

Advances in Antenna Array Processing for Radar 2014

Guest Editors: Hang Hu, Haiming Qi, Michelangelo Villano,
and Ahmed Shaharyar Khwaja





**Advances in Antenna Array Processing
for Radar 2014**

International Journal of Antennas and Propagation

**Advances in Antenna Array Processing
for Radar 2014**

Guest Editors: Hang Hu, Haiming Qi, Michelangelo Villano,
and Ahmed Shaharyar Khwaja



Copyright © 2015 Hindawi Publishing Corporation. All rights reserved.

This is a special issue published in "International Journal of Antennas and Propagation." All articles are open access articles distributed under the Creative Commons Attribution License, which permits unrestricted use, distribution, and reproduction in any medium, provided the original work is properly cited.

Editorial Board

Ana Alejos, Spain
Mohammad Ali, USA
Jaume Anguera, Spain
Ercument Arvas, USA
Alexei Ashikhmin, USA
Herve Aubert, France
Paolo Baccarelli, Italy
Xiulong Bao, Ireland
Toni Björninen, Finland
Djuradj S. Budimir, UK
Paolo Burghignoli, Italy
Shah N. Burokur, France
Giuseppe Castaldi, Italy
Felipe Cátedra, Spain
Chih-Hua Chang, Taiwan
Deb Chatterjee, USA
Shih Yuan Chen, Taiwan
Yu Jian Cheng, China
Renato Cicchetti, Italy
Lorenzo Crocco, Italy
Claudio Curcio, Italy
Francesco D'Agostino, Italy
Maria E. De Cos, Spain
Tayeb A. Denidni, Canada
Giuseppe Di Massa, Italy
Michele D'Urso, Italy
Francisco Falcone, Spain
Quanyuan Feng, China
Miguel Ferrando Bataller, Spain
Flaminio Ferrara, Italy
Vincenzo Galdi, Italy

Feifei Gao, China
Junping Geng, China
Claudio Gennarelli, Italy
Rocco Guerriero, Italy
Kerim Guney, Turkey
Song Guo, Japan
Qian He, China
Mohamed Himdi, France
Heng-Tung Hsu, Taiwan
Jun Hu, China
Tamer S. Ibrahim, USA
Mohammad T. Islam, Malaysia
Weixiang Jiang, China
M. R. Kamarudin, Malaysia
Kyeong Jin Kim, USA
Ahmed A. Kishk, Canada
Slawomir Koziel, Iceland
Luis Landesa, Spain
Ding-Bing Lin, Taiwan
Angelo Liseno, Italy
Giampiero Lovat, Italy
Lorenzo Luini, Italy
Atsushi Mase, Japan
Diego Masotti, Italy
Giuseppe Mazzeola, Italy
C. F. Mecklenbräuker, Austria
Massimo Migliozi, Italy
Mark Mirotznik, USA
Ahmed T. Mobashsher, Australia
Ananda S. Mohan, Australia
Jose-Maria Molina-Garcia-Pardo, Spain

Marco Mussetta, Italy
N. Nasimuddin, Singapore
Miguel Navarro-Cia, UK
Mourad Nedil, Canada
Symeon Nikolaou, Cyprus
Giacomo Oliveri, Italy
Athanasios D. Panagopoulos, Greece
Ikmo Park, Korea
Matteo Pastorino, Italy
Mugen Peng, China
Massimiliano Pieraccini, Italy
Xianming Qing, Singapore
Ahmad Safaai-Jazi, USA
Safieddin Safavi-Naeini, Canada
Magdalena Salazar-Palma, Spain
Stefano Selleri, Italy
John J. Shynk, USA
Prabhakar Singh, India
Raffaele Solimene, Italy
Seong-Youp Suh, USA
Sheng Sun, Hong Kong
Larbi Talbi, Canada
Luciano Tarricone, Italy
Parveen Wahid, USA
Yuanxun Ethan Wang, USA
Wen-Qin Wang, China
Shiwen Yang, China
Yuan Yao, China
Jingjing Zhang, Denmark

Contents

Advances in Antenna Array Processing for Radar 2014, Hang Hu, Haiming Qi, Michelangelo Villano, and Ahmed Shaharyar Khwaja
Volume 2015, Article ID 196910, 2 pages

Aspects of the Subarrayed Array Processing for the Phased Array Radar, Hang Hu
Volume 2015, Article ID 797352, 21 pages

An Improved Peak Sidelobe Reduction Method for Subarrayed Beam Scanning, Hang Hu, Xuepeng Luan, Guanglei Zhang, Ke Song, Weihui Liu, and Chenghu Mou
Volume 2015, Article ID 464521, 6 pages

Two-Dimensional DOA Estimation for Uniform Rectangular Array Using Reduced-Dimension Propagator Method, Ming Zhou, Xiaofei Zhang, Xiaofeng Qiu, and Chenghua Wang
Volume 2015, Article ID 485351, 10 pages

Research on Polarization Cancellation of Nonstationary Ionosphere Clutter in HF Radar System, Xingpeng Mao, Hong Hong, Weibo Deng, and Yongtan Liu
Volume 2015, Article ID 631217, 12 pages

The Application of JDL to Suppress Sea Clutter for Shipborne HFSWR, Zhenyuan Ji, Chunlei Yi, Junhao Xie, and Yang Li
Volume 2015, Article ID 825350, 6 pages

Statistical Angular Resolution Limit for Ultrawideband MIMO Noise Radar, Xiaoli Zhou, Hongqiang Wang, Yongqiang Cheng, Yuliang Qin, and Haowen Chen
Volume 2015, Article ID 906313, 12 pages

Beamspace Unitary ESPRIT Algorithm for Angle Estimation in Bistatic MIMO Radar, Dang Xiaofang, Chen Baixiao, Yang Minglei, and Zheng Guimei
Volume 2015, Article ID 621358, 9 pages

Ship-Borne Phased Array Radar Using GA Based Adaptive α - β - γ Filter for Beamforming Compensation and Air Target Tracking, J. Mar, Chen-Chih Liu, and M. B. Basnet
Volume 2015, Article ID 563726, 16 pages

Joint Phased-MIMO and Nested-Array Beamforming for Increased Degrees-of-Freedom, Chenglong Zhu, Hui Chen, and Huaizong Shao
Volume 2015, Article ID 989517, 11 pages

Multitarget Direct Localization Using Block Sparse Bayesian Learning in Distributed MIMO Radar, Bin Sun, Haowen Chen, Xizhang Wei, and Xiang Li
Volume 2015, Article ID 903902, 12 pages

Direct Data Domain Sparsity-Based STAP Utilizing Subaperture Smoothing Techniques, Zhaocheng Yang, Rui Fa, Yuliang Qin, Xiang Li, and Hongqiang Wang
Volume 2015, Article ID 171808, 10 pages

An Improved Antenna Array Pattern Synthesis Method Using Fast Fourier Transforms, Xucun Wang, Yiguo Zhou, and Yanfei Wang
Volume 2015, Article ID 316962, 9 pages

A Generalized Oblique Projection Filter with Flexible Parameter for Interference Suppression, Yi-ming Wang, Xing-peng Mao, Hong Hong, Jie Zhang, and Yu-mei Cui
Volume 2015, Article ID 320769, 11 pages

Two-Dimensional Direction of Arrival (DOA) Estimation for Rectangular Array via Compressive Sensing Trilinear Model, Huaxin Yu, Xiaofeng Qiu, Xiaofei Zhang, Chenghua Wang, and Gang Yang
Volume 2015, Article ID 297572, 10 pages

Knowledge-Aided STAP Using Low Rank and Geometry Properties, Zhaocheng Yang, Rodrigo C. de Lamare, Xiang Li, and Hongqiang Wang
Volume 2014, Article ID 196507, 14 pages

Spatial Spectrum-Based Imaging for UWB Through-the-Wall MIMO Arrays, Biying Lu, Xin Sun, Yang Zhao, and Zhimin Zhou
Volume 2014, Article ID 825403, 13 pages

Joint 2D Direction-of-Arrival and Range Estimation for Nonstationary Sources, Jian Chen, Hui Zhao, Xiaoying Sun, and Guohong Liu
Volume 2014, Article ID 849039, 7 pages

Joint DOD and DOA Estimation for High Speed Target Using Bistatic MIMO Radar, Jinli Chen, Jiaqiang Li, Peng Li, Yanping Zhu, and Weijun Long
Volume 2014, Article ID 914327, 10 pages

SAGE-Based Algorithm for Direction-of-Arrival Estimation and Array Calibration, Kunlai Xiong, Zheng Liu, and Wenli Jiang
Volume 2014, Article ID 217482, 8 pages

Editorial

Advances in Antenna Array Processing for Radar 2014

Hang Hu,¹ Haiming Qi,² Michelangelo Villano,³ and Ahmed Shaharyar Khwaja⁴

¹*School of Electronics and Information Engineering, Harbin Institute of Technology, Harbin 150001, China*

²*The Earth Observation System and Data Center, China National Space Administration, Beijing 100101, China*

³*Microwaves and Radar Institute, German Aerospace Center (DLR), Oberpfaffenhofen, 82234 Wessling, Germany*

⁴*Department of Electrical and Computer Engineering, Ryerson University, Toronto, ON, Canada M5B 2K3*

Correspondence should be addressed to Hang Hu; huhang@hit.edu.cn

Received 17 March 2015; Accepted 17 March 2015

Copyright © 2015 Hang Hu et al. This is an open access article distributed under the Creative Commons Attribution License, which permits unrestricted use, distribution, and reproduction in any medium, provided the original work is properly cited.

Arrays today are the configuration for nearly all kinds of sensors (electromagnetic, acoustic, optical, etc.). Consequently, array processing is today one of the most important and dynamic fields of research. For radar, RAP (radar array processing) has received attention for nearly four decades and considerable results have been obtained. However, we are still far from a full understanding of all effects and promising improvement seems to be possible. RAP comprises theoretical and more academic issues as well as practical issues of implementation and aspects of system engineering.

The topics of RAP include nearly all aspects of radar processing: antenna aspects, signal processing aspects, and radar data processing and radar management aspects. Particular topics are as follows: pattern shaping and sidelobe reduction; adaptive interference suppression, including ABF (adaptive beam forming), ASLB (adaptive sidelobe blanking), and fast-time STAP (space-time adaptive processing); clutter mitigation (slow-time STAP); adaptive detection; parameter estimation (adaptive monopulse and superresolution direction finding); array error calibration; optimization of array configurations, and so forth.

Today, the main characteristics of RAP are as follows.

- (1) The achievable capabilities of the algorithms for different applications are constrained by some hardware factors, for example, channel errors.
- (2) The amalgamation and integration of multiple RAP techniques are a trend, such as the combination of ABF, adaptive monopulse, and superresolution.
- (3) The subarray optimization is still a complicated and open problem, compared with the algorithms due

to constraints with very little flexibility: mechanical constraints, feasibility of production, and cost.

- (4) The exploitation of knowledge of RAP features in radar data processing can exploit the full potential of array systems (for instance, in adaptive tracking). This can improve the overall performance significantly.
- (5) MIMO (multiple-input multiple-output) radar offers a multitude of applications for RAP. Hybrid MIMO-PAR (phased array radar) can promote and deepen the development of the RAP.

The current challenging works in RAP are in the following areas:

- (1) RAP to counter MLJ (mainlobe jamming);
- (2) joint cancellation of mixed interferences like CW (continuous wave) interference; impulsive interference, and clutter;
- (3) amalgamation of modern RAP and adaptive detection;
- (4) RAP for thinned arrays;
- (5) RAP for conformal arrays (e.g., used for seekers);
- (6) subarray optimization;
- (7) RAP for dual/multiple use antennas, for example, combining radar and communication functions;
- (8) DSP and FPGA implementation.

The special issue “Advances in Antenna Array Processing for Radar” was published in 2013 for the first time. It presented

research achievements in the field of RAP, in particular, including contributions of world's leading radar experts, as U. Nickel, P. Lombardo, A. Farina, F. Colone, Y. L. Wang, and so forth. Inspired by this, we decided to edit this special issue.

In this 2014 special issue, we have collected 19 papers covering various aspects of the latest RAP research and development. We received 53 submissions with an acceptance rate of 35.8%, to guarantee the standard of the journal.

We would like to thank all authors for their highly professional contributions and all reviewers for their time and effort. A special thank goes to Dr. U. Nickel for his constructive guidance. We hope that this special issue will stimulate interest and draw valuable ideas to solve open research problems in the area of RAP and its applications.

Hang Hu
Haiming Qi
Michelangelo Villano
Ahmed Shaharyar Khwaja

Review Article

Aspects of the Subarrayed Array Processing for the Phased Array Radar

Hang Hu

School of Electronics and Information Engineering, Harbin Institute of Technology, Harbin 150001, China

Correspondence should be addressed to Hang Hu; huhang@hit.edu.cn

Received 20 June 2014; Revised 25 November 2014; Accepted 25 November 2014

Academic Editor: Michelangelo Villano

Copyright © 2015 Hang Hu. This is an open access article distributed under the Creative Commons Attribution License, which permits unrestricted use, distribution, and reproduction in any medium, provided the original work is properly cited.

This paper gives an overview on the research status, developments, and achievements of subarrayed array processing for the multifunction phased array radar. We address some issues concerning subarrayed adaptive beamforming, subarrayed fast-time space-time adaptive processing, subarray-based sidelobe reduction of sum and difference beam, subarrayed adapted monopulse, subarrayed superresolution direction finding, subarray configuration optimization in ECCM (electronic counter-countermeasure), and subarrayed array processing for MIMO-PAR. In this review, several viewpoints relevant to subarrayed array processing are pointed out and the achieved results are demonstrated by numerical examples.

1. Introduction

PAR (phased array radar) and especially MFPAR (multifunction PAR) often adopt a subarrayed antenna array. SASP (subarrayed array signal processing) is one of the key technologies in modern PARs and plays a key role in the MFPAR.

In this paper we consider the modern MFPAR with an element number of the order of 1000 (assume that the subarrays are compact and nonoverlapping) and with amplitude tapering (e.g., Taylor weighting) applied at the elements for low sidelobes. And the steering into the look direction is done by phase shifting at the elements. Assume the MFPAR with many modes of operation (e.g., search, track, and high resolution) and all processing to be performed digitally with the subarray outputs.

The key technologies and issues of SASP include subarray weighting for quiescent pattern synthesis and PSL (peak sidelobe) reduction, subarrayed adaptive interference suppression with subarrayed ABF (adaptive beamforming) or ASLB (adaptive sidelobe blanking), subarrayed adaptive detection, subarrayed parameter estimation, for instance, adaptive monopulse and superresolution direction finding, optimization of subarray configuration, and an expansion of the SASP, that is, application in MIMO- (multiple-input multiple-output-) PAR, and so forth.

Nickel is the pioneer and trailblazer in the field of the SASP. Since the 1990s, he has firstly systematically performed a series of thorough researches which theoretically and technically lay the solid foundation of the SASP. His research achievements represent the development level of SASP technology [1]. Nickel's researches covered all kinds of key technologies in SASP, including subarray weighting for PSL reduction [2], adaptive interference suppression (ABF and ASLB) [3–5], slow- and fast-time STAP (space-time adaptive processing) [6–9], influence of channel errors [6, 10], multiple BF (beam forming) with low sidelobes [11], adaptive detection [5, 8], adaptive monopulse [9, 12–18], superresolution [6, 19], adaptive tracking [20–24], and design of optimum subarrays [2]. The achievements have formed a complete theoretical system and framework of the SASP.

Similarly, Farina with different coauthors has given creative and pioneering contributions to the following aspects, including subarrayed weighting for SLC [25, 26], subarrayed adaptation and superresolution [25–27], and subarray optimization [25, 28]. Lombardo and his co-authors contributed great achievements to subarrayed adaptive processing and pattern control [29, 30], SASP for thinned arrays [31, 32], while Massa et al. contributed in the fields of subarrayed weighting, synthesis of sum and difference patterns for monopulse [33–36]; Liao et al. in the field of subarrayed

ABF, subarrayed STAP and subarray architectures [23, 37, 38]; Wang et al. in the field of subarrayed STAP and subarray configuration [39–42]; Klemm in the field of the design of the subarray configuration for STAP [43], and so forth.

SASP possesses a good application prospect for millimeter wave PAR seeker, airborne multifunction radar, and space-borne early-warning radar. A famous and outstanding example is the tri-national X-band AMSAR project for a future European airborne radar [7].

This paper summarizes the research achievements in the field of SASP including the study results of the author. The relevant issues focus on subarrayed ABF, subarrayed fast-time STAP, subarrayed PSL reduction for sum and difference beam, PSL reduction for subarrayed beam scanning, subarrayed adapted monopulse, subarrayed superresolution direction finding, subarray optimization for ECCM (electronic counter-countermeasure), and the SASP for MIMO-PAR.

In this review, viewpoints and innovative ways are presented which are relevant to the SASP. For the proposed algorithms we give examples.

2. Subarrayed ABF

In this section we investigate subarrayed ABF and adaptive interference suppression. Actually, the adaptive weighting is implemented at subarray level. The subarrayed ABF has three configurations, that is, DSW (direct subarray weighting), SLC (sidelobe canceller), and GSLC (generalized SLC) types [16]. The three concepts are shown in Figure 1.

The limitation of DSW configuration is that it requires an estimation of the interference-plus-noise covariance matrix. The matrix is necessary for the estimation of adaptive weights. The limitation of the subarrayed SLC configuration is that equipment with auxiliary antennas and auxiliary channels is required, as indicated in Figure 1(b). The advantage of subarrayed GSLC is less equipment complexity compared with subarrayed SLC, because the auxiliary channels need not single elements but may be generated from the array itself by subarrays as indicated in Figure 1(c). Furthermore, compared with the DSW, the SLC and the GSLC do not need an estimation of interference plus noise covariance matrix (since the jammer signal can be subtracted from the main channel by the weighted sum of auxiliary channels outputs, Figures 1(b) and 1(c)).

This section is devoted to the DSW and GSLC configurations.

2.1. DSW Type Subarrayed ABF

2.1.1. Subarrayed Optimum ABF. First consider the subarrayed optimum BF (optimum adaptive filter [30]), in which weight vector \mathbf{w} is obtained by direct weighting of the subarray outputs. From the likelihood ratio test criterion, the probability of detection is maximized if the weight vector maximizes the SINR for a desired signal [1]. As a consequence, $\mathbf{w} = \mu \widehat{\mathbf{R}}^{-1} \mathbf{a}(\theta_0, \varphi_0)$, where $\widehat{\mathbf{R}}$ is an estimate of the interference-plus-noise covariance matrix at subarray level, $\mathbf{a}(\theta_0, \varphi_0)$ denotes the steering vector at look direction, and μ is a nonzero constant. The maximum likelihood estimate

of covariance matrix is $\widehat{\mathbf{R}}_{\text{SMI}}$, that is, taking the average over the subarray output data [1]. This method is also called the subarrayed SMI (sample matrix inverse).

2.1.2. Improved Versions of Subarrayed SMI. The shortcoming of the subarrayed SMI is that the sidelobe level of adapted pattern is increased remarkably compared with quiescent pattern with tapering weighting due to subarrayed weighting (assuming the subarray transformation matrix \mathbf{T} is not normalized), especially in the case of the absence of the jamming.

Suppose that we have an array with N elements divided into L subarrays. \mathbf{T} can be written by

$$\mathbf{T} = \Phi \mathbf{W} \mathbf{T}_0 \quad (1)$$

with $\Phi = \text{diag}[\varphi_n(\theta_0, \varphi_0)]_{n=0, \dots, N-1}$; hereinto $\varphi_n(\theta_0, \varphi_0)$ represents the effect of the phase shifting of the n th element; $\mathbf{W} = \text{diag}(w_n)_{n=0, \dots, N-1}$, where w_n is the weight of the n th element used to suppress sidelobe level of sum pattern. \mathbf{T}_0 is the $N \times L$ -dimensional subarray forming matrix, in all the elements of the l th ($l = 0, \dots, L-1$) column, only if the element belongs to l th subarray the element value is 1; otherwise it is 0.

On the other hand, the subarrayed SMI has only asymptotically a good performance. In practice, we have to draw on a variety of techniques to provide robust performance in the case of small sample size. The improved versions of subarrayed SMI comprise the subarrayed LSMI (load sample matrix inversion), the subarrayed LMI (lean matrix inversion), and so forth. The subarrayed LSMI and the subarrayed LMI are the extensions of LSMI [44] and LMI [45], respectively.

2.1.3. Quiescent Pattern Control Approaches. Quiescent pattern control approaches are another kind of the improved versions of subarrayed optimum ABF. The approaches preserve the desired quiescent pattern in the absence of jammer. Therefore, they make system automatically converge to the nonadapting mode. Thus the conversion problem between the two working modes of the subarrayed ABF is resolved [30]. Furthermore, quiescent pattern control approaches improve the PSL remarkably compared with subarrayed optimum ABF in the presence of jammers [46].

The pattern control approaches include normalization method, MOD (mismatched optimum detector), and SSP (subspace projection). Therein, the starting point of the normalization method [2, 25, 29, 30] is the amplitude taper combined with the different number of elements for each subarray, which implies the receiver noise level is different at the subarray output. The subarrayed ABF tries to find a weight giving equal noise power in all subarrays and cancels the low sidelobe taper; that is, the adapted weight tends to be the vector with uniform tapering. Then we can adopt normalization method to overcome this effect, that is, to normalize the outputs of subarrays before adaptation so that the noise powers at the subarray outputs are equal.

The MOD [29] introduces a mismatched steering vector, so that the adaptive beamformer detects such a mismatched target and yields quiescent pattern in the absence of jammers.

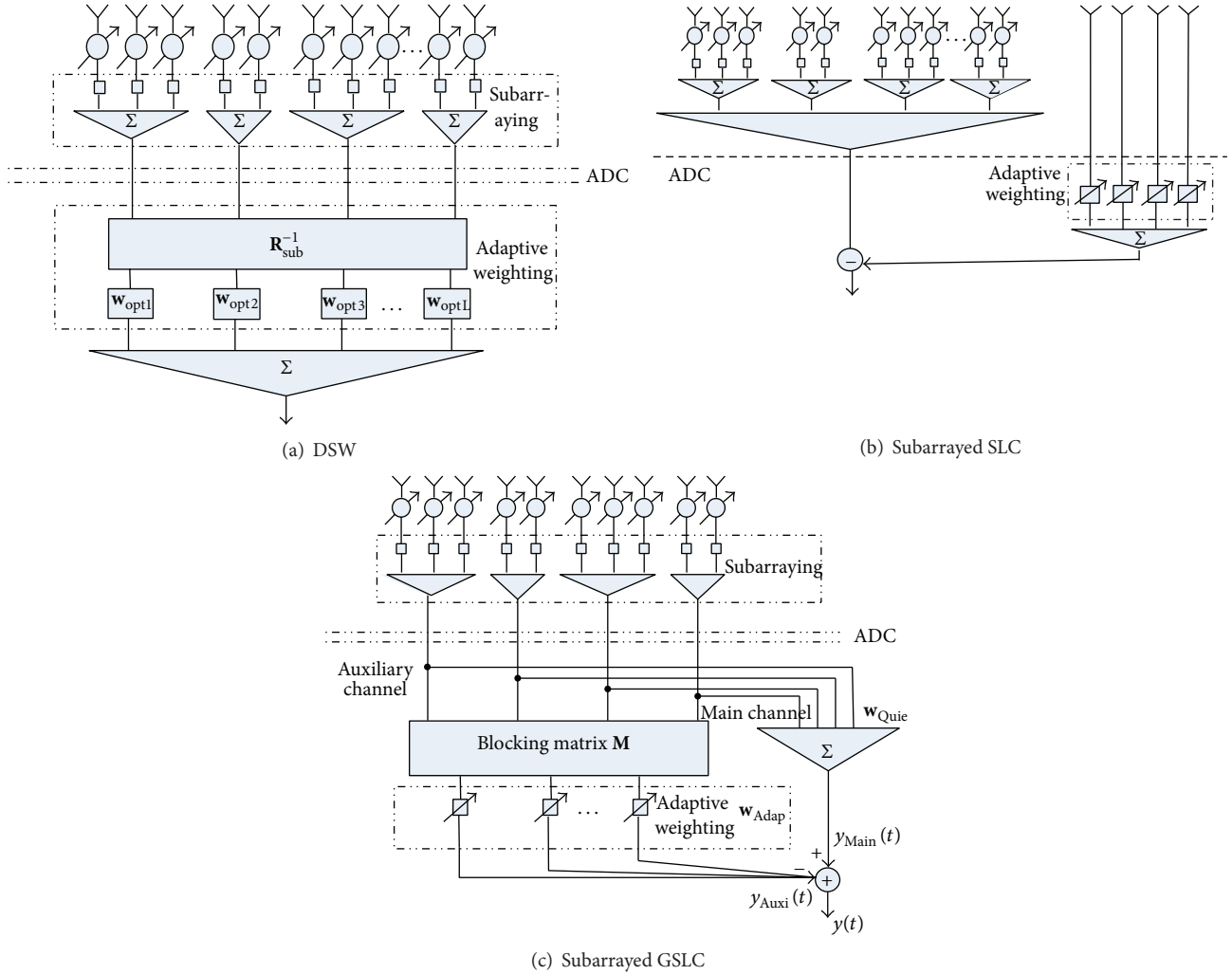


FIGURE 1: Configurations of subarrayed ABF.

The mismatched steering vector is written by $\mathbf{a}'(\theta_0, \varphi_0) = \mathbf{R}_{\text{SMI}}^{(0)} \mathbf{q}$, the superscript (0) indicates the absence of jammer. Assume that \mathbf{q} denotes the quiescent control vector, namely, the $L \times 1$ column vector, in which all the elements are equally 1. As a consequence, in the case of absence of jammer, the adaptive weights are $\mathbf{w}^{(0)} = \mu \mathbf{q}$. Thereby, the quiescent pattern control is achieved. Compared with the normalization method, the MOD does not need preprocessing and a recovery operator; therefore the computational cost is reduced remarkably.

The SSP [29] consists of the following steps: (1) obtaining the first subspace and getting the quiescent patterns by using \mathbf{q} to combine subarray outputs, (2) finding the subspace which distorts the quiescent pattern and discarding it, and (3) making the optimum interference suppression in the remaining $L - 2$ dimensional space which does not impact the quiescent pattern.

Table 1 presents the contrast of the performance for the quiescent pattern control approaches, obviously, in which the MOD is suitable for the overlapped subarrays and has small computational burden compared with other models.

2.1.4. *The Approach Combining the Subarrayed Optimum ABF with the Quiescent Pattern Control [46].* Following we present an improvement of quiescent pattern control approaches. For the pattern control, the PSL reduction capability is at the cost of degradation of adaptation. This results in an output SINR loss. On the other hand, for the subarrayed optimum ABF, the anti-jamming capability is optimum. In order to compromise PSL and adaptation capability, we put forward the methods combining subarrayed optimum ABF and quiescent pattern control. The adaptive weight is

$$\mathbf{w}^{(\text{com})} = K_{\text{Opt}} \mathbf{w}_{\text{Opt}} + K_{\text{QPC}} \mathbf{w}_{\text{QPC}}, \quad (2)$$

where \mathbf{w}_{Opt} and \mathbf{w}_{QPC} denote the weights of the subarrayed optimum ABF and quiescent pattern control approach, respectively. And $K_{\text{Opt}} + K_{\text{QPC}} = 1.0$.

The combined method unifies subarrayed optimum ABF and quiescent pattern control, both of which are two extreme cases of the combined method. The combined method improves the flexibility of the PSL reduction for adaptive pattern and makes the trade-off between PSL and SINR according to real requirements. When we want to obtain

TABLE 1: Performance contrast of quiescent pattern control approaches.

	Suitability for overlapped subarrays	Computational burden
MOD	Suitable	Very small
Normalization method	Nonsuitable	Large
SSP	Suitable	Very heavy

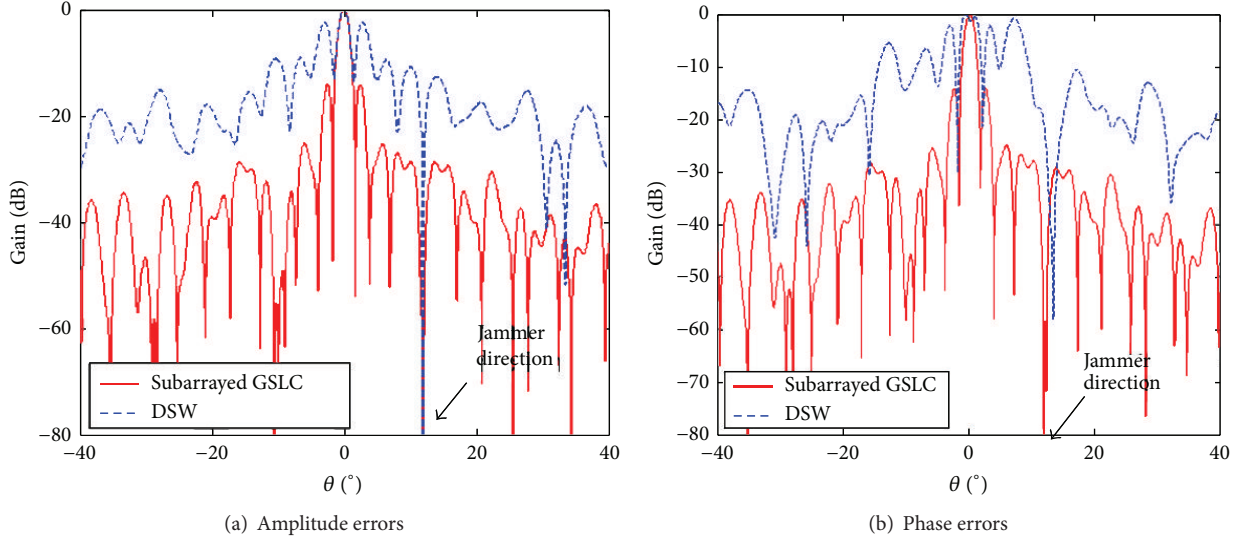


FIGURE 2: Adaptive patterns with I/Q errors.

better PSL reduction capability, we can choose higher value of K_{QPC} ; otherwise, we can set a higher value of K_{Opt} to reduce SINR loss. Through choosing appropriate parameters, combined method can reduce PSL effectively, and the achieved SINR is closely approximate to the SINR of subarrayed optimum ABF as well.

The above-mentioned quiescent pattern control method and the combining method can be extended into subarrayed fast-time STAP, as will be shown in Section 3.

2.2. GSLC-Based Subarrayed ABF. In the subarrayed GSLC, the blocking matrix in auxiliary channel (Figure 1(c)) is used for removing the desired signal component from this channel, in which simplest form is only difference operation of adjacent subarray outputs [47]. However, its blocking capability is poor. Consequently, residual signal component would be cancelled which leads to the degradation of output SINR. For this reason we introduce the Householder transform to determine the blocking matrix [48].

Let

$$\mathbf{e} = [1, 0, \dots, 0]^T_{L \times 1},$$

$$\mathbf{p} = \frac{\mathbf{a}(\theta_0, \varphi_0) - \|\mathbf{a}(\theta_0, \varphi_0)\|_2 \mathbf{e}}{\|\mathbf{a}(\theta_0, \varphi_0) - \|\mathbf{a}(\theta_0, \varphi_0)\|_2 \mathbf{e}\|_2}, \quad (3)$$

where $\|\cdot\|_2$ is 2-norm. Then the Householder matrix is

$$\mathbf{H} = \mathbf{I} - 2\mathbf{p}\mathbf{p}^T, \quad (4)$$

of which the first column is $\mathbf{a}(\theta_0, \varphi_0)$ and the remaining $L - 1$ ones are orthogonal to $\mathbf{a}(\theta_0, \varphi_0)$, respectively. Accordingly, \mathbf{M} in Figure 1(c) is

$$\mathbf{M} = \mathbf{H} \begin{bmatrix} 0 & \dots & 0 & 0 \\ 1 & \dots & 0 & 0 \\ \vdots & \ddots & \vdots & \vdots \\ 0 & \dots & 1 & 0 \\ 0 & \dots & 0 & 1 \end{bmatrix}_{L \times (L-1)}. \quad (5)$$

The adaptive patterns and output SINR obtained by Householder transform-based GSLC are the same as that of the optimum ABF-based DSW [48]. On the other hand, the robustness of the subarrayed GSLC is much better than DSW. We assume a ULA (uniform linear array) comprising 92 elements is partitioned into 10 nonoverlapped subarrays. Then -40 dB Taylor weighting is applied. The jammer direction θ_j is 12° , JNR (jammer-to-noise ratio) is 35 dB, signal power $p_s = 1$, and the noise at element is AGWN (additional Gaussian white noise). Following we consider the errors at subarray level produced by the receivers which create the I- and Q-channels. Assume the amplitude errors obey the distribution of $N(0, 0.1)$ with the ideal error-free amplitude gain of the I- and Q-channel being 1 and a normalized parameter being 0.1, while phase errors obey the distribution of $N(0, 1)$ with the unit of degree. Figure 2 shows the adaptive patterns of the subarrayed GSLC with Householder transform. It is obvious that all respects such as the look direction, the beam shape,

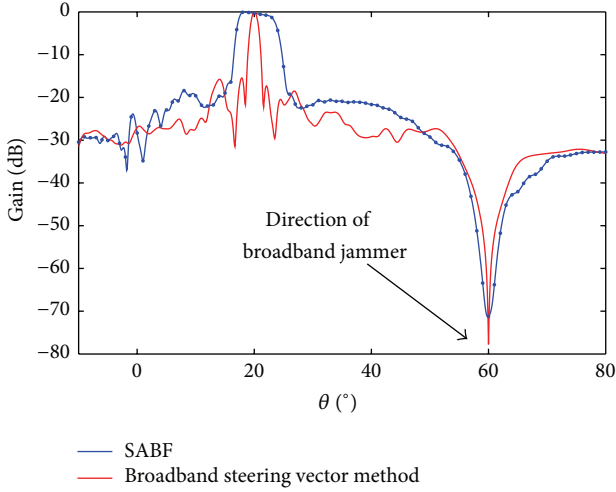


FIGURE 3: Adapted pattern obtained with subarrayed broadband ABF.

the direction and depth of jammer notch, and the PSL are much better than those of optimum ABF-based DSF.

The subarrayed GSLC with Householder transform is valid no matter it is with amplitude errors or phase errors, which is insensitive to phase errors even.

2.3. The Subarrayed Broadband ABF. For the broadband array, additional time delays at subarray outputs are adopted in order to compensate phase difference of internal subarray of each frequency component. The look direction is controlled by subarray time-delay and phase shifter together for whole working bandwidth.

The adaptive weights of subarrayed broadband ABF can be obtained through broadband steering vector method. This method controls the look direction for each frequency of working bandwidth and realizes gain condition constraints, that is, makes the gain for each frequency to be equal. Assume bandwidth of all jammers is B and the power spectrum density obeys the uniform distribution in $[f_0 - B/2, f_0 + B/2]$; then the subarrayed steering vector is

$$\mathbf{a}(\theta, \varphi) = \int_{f_0 - B/2}^{f_0 + B/2} \mathbf{T}_D^H \mathbf{a}_{\text{ele}}(f, \theta, \varphi) df, \quad (6)$$

where \mathbf{T}_D represents subarray transformation matrix with subarray time-delay effect; $\mathbf{a}_{\text{ele}}(f, \theta, \varphi) = [1, \dots, e^{-j2\pi f \tau_n(\theta, \varphi)}, \dots, e^{-j2\pi f \tau_{N-1}(\theta, \varphi)}]^T$; hereinto $\tau_n(\theta, \varphi)$ is the time difference relative to reference element.

Assume that a ULA consisting of 99 elements is partitioned into 25 nonuniform subarrays; the relative bandwidth is $B/f_0 = 10\%$; element spacing is $\lambda_0/2$ (λ_0 is wavelength at f_0). And -40 dB Taylor weighting is applied. Let $\theta_0 = -60^\circ$ and $\theta_j = -20^\circ$. Figure 3 illustrates a resulting adapted pattern obtained with broadband steering vector method-based subarrayed broadband ABF [49]. It is drawn that the look direction and mainlobe shape of the adapted pattern is maintained, whereas the subarrayed ABF (SABF for short) has an obvious mainlobe broadening.

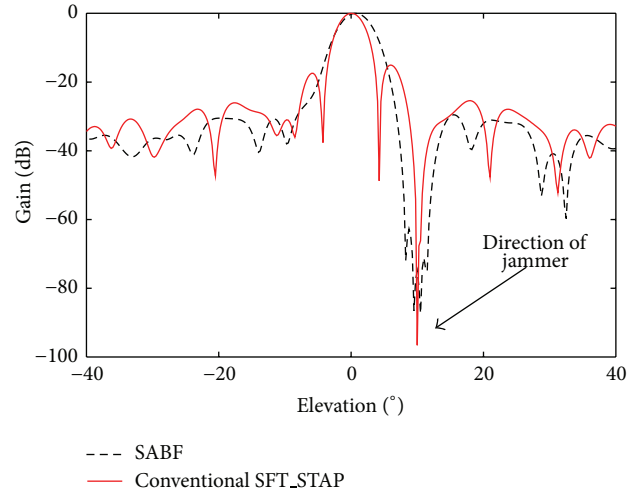


FIGURE 4: Adaptive patterns in the case of broadband jammer (cut patterns in azimuth plane).

3. Subarrayed Fast-Time STAP

In the recent twenty years, extensive and thorough research on slow-time STAP used for clutter mitigation in airborne radar has been carried out [40, 43]. This paper only focuses on the fast-time STAP and this section is concerned with the subarrayed fast-time STAP.

In the presence of broadband jammers, subarrayed ABF would form broad adaptive nulls, which consumes spatial degrees of freedom and distorts the beam shape as indicated in Figure 3. For this reason, we should adopt subarrayed fast-time STAP [6].

The subarrayed ABF methods presented in Section 2 can be applied analogously in the space-time domain. The subarrayed fast-time STAP includes three kinds of structures, namely, DSF, SLC, and GSLC type. For example, for the DSF type subarrayed fast-time STAP, delay-weighting network is used at each subarray output (the number of delays is equal for each subarray). The delays aim to provide phase compensation for each frequency component in bandwidth. Meanwhile, adaptive weights are applied at all delay outputs of each subarray to achieve broadband interference suppression.

To give an example, suppose a UPA (uniform planar array) with 32×34 elements, and in both x and y directions the element spacing is $\lambda_0/2$. A -40 dB Taylor weighting is applied in both x and y directions. Array is partitioned into 6×6 nonuniform subarrays, each of which is a rectangle planar array. Suppose $B/f_0 = 10\%$ for the jammer. We set the number of delay $K = 4$. Figure 4 plots patterns in the presence of SLJ (sidelobe jamming), where SFT_STAP is an abbreviation of subarrayed fast-time STAP. By comparing two approaches, we see a narrow null of subarrayed fast-time STAP, while subarrayed ABF results in rather wide null.

On the other hand, for broad array, similar to subarrayed broadband ABF, the subarrayed fast-time STAP should adopt time delays at subarray outputs to compensate phase difference. This is subarrayed fast-time STAP with broadband

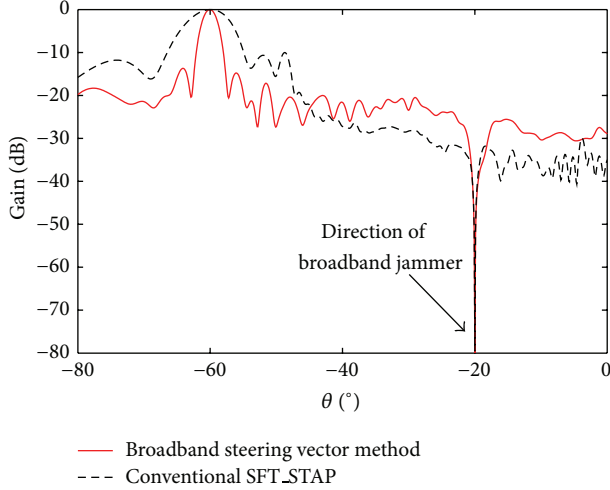


FIGURE 5: Adaptive pattern by broadband steering vector-based subarrayed fast-time STAP.

steering vector method [50]. Here, broadband steering vector method modifies constraint condition of conventional LCMV criterion, so that the gain of the pattern in desired signal direction is a constant within the whole receiving bandwidth.

We give the simulation results, in which the parameters of array are set the same as Figure 3. The central frequency of the bandwidth of array is the same as that of the bandwidth of jammer. Adaptive pattern obtained with broadband steering vector method-based subarrayed fast-time STAP is illustrated in Figure 5 [50]. It is seen that the look direction and mainlobe shape are preserved, which is impossible for the conventional subarrayed fast-time STAP (conventional SFT_STAP for short).

The optimum adaptive weights of subarrayed fast-time STAP can be determined by the LCMV criterion [51]. However the PSL is very high which is similar to optimum subarrayed ABF. Therefore, we adopt the approach combining the optimum subarrayed fast-time STAP and subarrayed fast-time STAP with the quiescent pattern control capability, in order to make a trade-off between the PSL and the broadband jammer suppression capability.

The adaptive pattern in the case of broadband SLJ is given in Figure 6 [50]; meanwhile K_{Opt} is chosen to be 0.6 for the combined subarrayed fast-time STAP. It is seen that the PSL of combined subarrayed fast-time STAP is improved remarkably, namely, by 13.2 dB in comparison with the optimum one.

4. The Subarray Weighting-Based Sidelobe Reduction of Sum and Difference Beam

The sidelobe reduction of patterns is the basic task for the PAR systems. In this section, we deal with subarray weighting-based algorithms for the PSL reduction of sum and difference beam. The goal is to obtain a trade-off between hardware complexity and achievable sidelobe level.

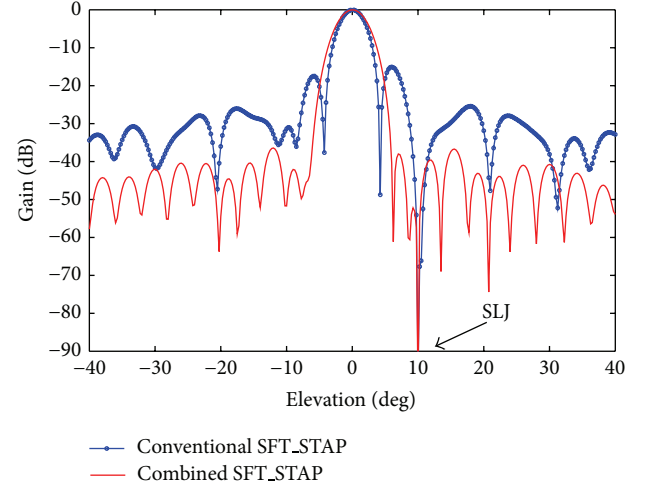


FIGURE 6: Comparison of combined subarrayed fast-time STAP with the optimum one.

One function of subarray weighting is to reduce the PSL of both the sum and the difference beam simultaneously for a monopulse PAR, in which digital subarray weighting substitutes the analog element amplitude weighting. Accordingly, hardware cost and complexity are greatly reduced.

In this section, two techniques are presented as follows.

4.1. Full Digital Weighting Scheme. This approach completely substitutes the element weighting adopting subarray weighting (for instance, a Taylor and Bayliss weighting for sum and difference beam, resp.). We assume that no amplitude weighting at element level is possible. The two schemes for determining subarray weights are as follows.

4.1.1. The Analytical Approach. The analytical approach includes two ways, namely, weight approximation and pattern approximation. The former makes the subarray weight to approximate the Taylor or Bayliss weight in LMS (least mean square) sense, while the latter makes the patterns obtained with the subarray weights approximate to that obtained by the Taylor or Bayliss weight in LMS sense [2].

The weight approximation-based subarray weights are determined by

Sum beam:

$$\mathbf{w}_{\Sigma_WA}^{(\text{opt})} = \arg \min_{\mathbf{w}_{\Sigma_WA}} \left\| \mathbf{T}\mathbf{w}_{\Sigma_WA} - \mathbf{w}_{\text{Taylor}} \right\|_2^2, \quad (7)$$

Difference beam:

$$\mathbf{w}_{\Delta_WA}^{(\text{opt})} = \arg \min_{\mathbf{w}_{\Delta_WA}} \left\| \mathbf{T}\mathbf{w}_{\Delta_WA} - \mathbf{w}_{\text{Bayliss}} \right\|_2^2, \quad (8)$$

$$\mathbf{a}^H(\theta_0, \varphi_0) (\mathbf{T}\mathbf{w}_{\Delta_WA}^{(\text{opt})}) = \mathbf{0},$$

where $\mathbf{w}_{\text{Taylor}}$, $\mathbf{w}_{\text{Bayliss}}$ denote Taylor weigh vector, Bayliss weigh vector, respectively.

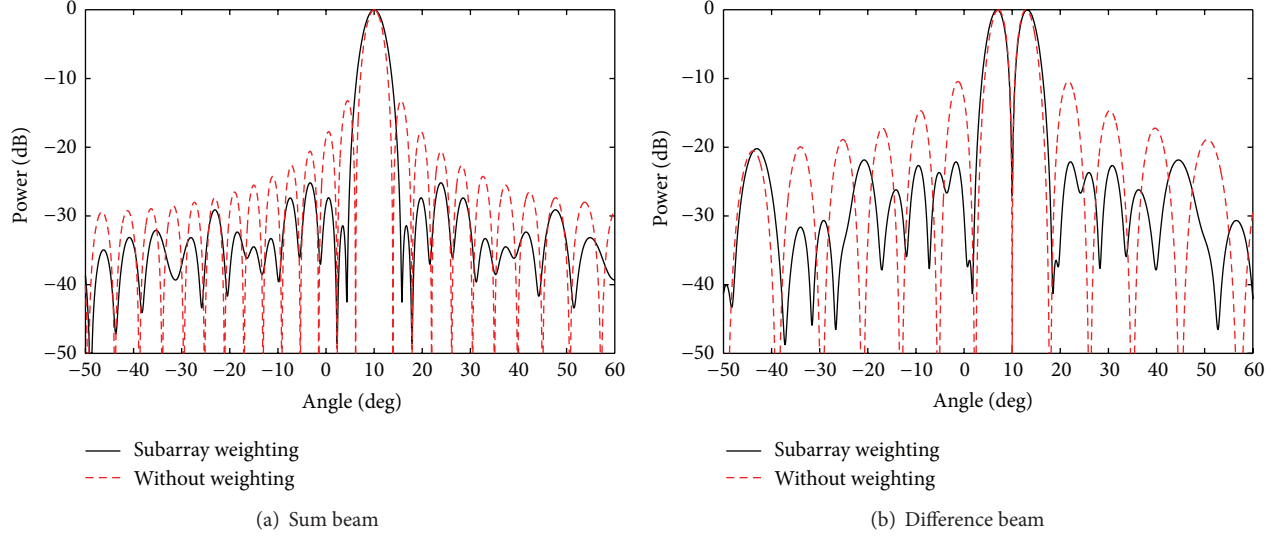


FIGURE 7: Subarrayed weighting-based quiescent patterns.

Take the sum beam for example, the pattern approximation-based subarray weights are determined by

$$\begin{aligned} & \mathbf{w}_{\Sigma_PA}^{(opt)} \\ &= \arg \min_{\mathbf{w}_{\Sigma_PA}} \int_{-\pi/2}^{\pi/2} \int_{-\pi/2}^{\pi/2} \left| \mathbf{w}_{\Sigma_PA}^H \mathbf{T}^H \mathbf{a}(\theta, \varphi) - \mathbf{w}_{Tay}^H \mathbf{a}(\theta, \varphi) \right|^2 \\ & \quad \times P(\theta, \varphi) d\theta d\varphi, \end{aligned} \quad (9)$$

where $P(\theta, \varphi)$ is the directional weighted function. It could adjust the approximation of pattern obtained by the pattern approximation method and the pattern obtained by the Taylor weights in a certain direction area which leads to better sidelobe reduction capability.

Assume a ULA with 30 omnidirectional elements with $\lambda/2$ of element spacing. The look direction is 10° , and the array is divided into 11 nonuniform subarrays. Figure 7 shows patterns obtained by pattern approximation method which are used for approximating the patterns obtained by -30 dB Taylor and -30 dB Bayliss weighting, respectively. The PSL is -25.18 dB for the sum beam (Figure 7(a)) which is improved by 11.95 dB compared with that without weighting, while PSL is -20.22 dB for the difference beam (Figure 7(b)) which is improved by 9.78 dB compared with that without weighting. It is seen that the PSL reduction effect of difference beam is inferior to the one of the sum beam for the subarray weighting method, since the constraint for the null restricts a further improvement of PSL.

Note the subarray weighting-based PSL reduction capability cannot be the same as that with element weighting, which is a price required for reducing the hardware cost. This approach is more suitable for the difference beam which is used for target tracking.

4.1.2. GA (Genetic Algorithm). This approach optimizes the subarray weights using GA. The GA could achieve global

optimum solution which is unconstrained by issues related solution.

Here, fitness function has a great influence to PSL reduction capability. We choose two kinds of fitness functions: (1) the weight approximation-based fitness function, that is, $f_{WA} = \|\mathbf{T}\mathbf{w}_{sub} - \mathbf{w}_{ele}\|_2^2$, where \mathbf{w}_{sub} and \mathbf{w}_{ele} are the subarray weights and element weights, respectively; (2) the PA-based fitness function, namely, making PSL of pattern obtained by subarray weighting as low as possible, which turns to be more reasonable. Meanwhile, main beam broadening should be limited in a certain range. Furthermore, it should form a notch with enough null depth in a certain direction for the difference beam. For example, for difference beam, the fitness function is designed as $f_{patt} = k_{SLL}(\Delta_{SLL})^2 + k_{BW}(\Delta_{BW})^2 + k_{ND}(\Delta_{ND})^2$, where Δ_{PSL} , Δ_{BW} , and Δ_{ND} are difference between expected value and practice value of PSL, beamwidth, and null depth, respectively, k_{SLL} , k_{BW} , and k_{ND} are used for adjusting the weighing coefficients of Δ_{SLL} , Δ_{BW} , and Δ_{ND} , respectively.

Adopting f_{weight} as fitness function brings high operating efficiency; however, the PSL reduction performance is unsatisfactory because only the weight vector is optimized. While adopting f_{patt} as the fitness function can improve the performance, because the PSL itself is optimized in this case. However, its drawbacks are that the genetic operation is easily constrained on local optimal solution and the computing efficiency is poor.

In order to overcome the limitation of two approaches mentioned above, we present an improved GA, that is, partition genetic process into two stages whose process is as below. The first stage is used for the preliminary optimization using f_{weight} as fitness function. Then we turn into stage 2 which is used for improving PSL reduction capability further; namely, according to descending order of fitness values of the first stage, select a certain scale of excellent filial generations among optimizing results to compose new

TABLE 2: The PLSs of sum beam with several approaches.

	Without weighing	Conventional GA (with fitness function f_{WA})	Conventional GA (with fitness function f_{patt})	Improved GA
PSL (dB)	-13.43	-26.18	-27.70	-27.77

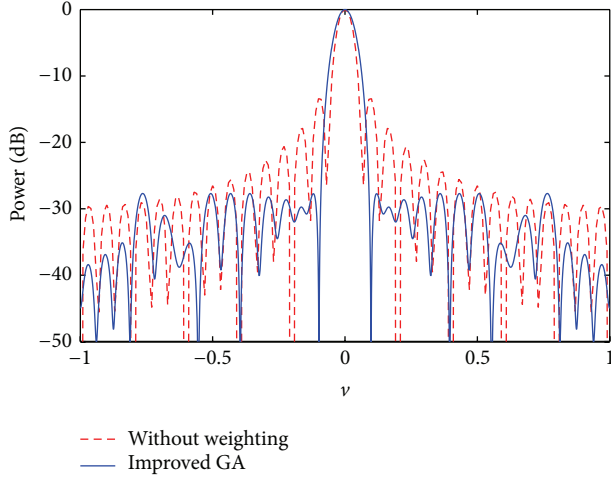


FIGURE 8: Sum patterns: improved GA.

population. Afterwards, continue to optimize by using f_{patt} as fitness function.

There is a UPA containing 30×30 omnidirectional elements with the element spacing $d = \lambda/2$ in the direction of x and y . The beam direction is $(0^\circ, 0^\circ)$. The array is divided into 10×10 nonuniform subarrays. The improved GA-based subarray weights are used to approximate -30 dB Taylor weights, in which number of generations is 1300 in first stage and 20 in second one, respectively. Figure 8 reports the sum pattern; it is seen that obtained PSL is close to the expected -30 dB.

Table 2 shows the PSLs with several methods, in which PSL reduction capability with f_{patt} fitness function is better than that with f_{WA} (it is improved by 1.58 dB) for conventional GA. And PSL reduction performance of improved GA quite is close to the one of conventional GA with f_{patt} (meanwhile, improved GA enhances calculation efficiency greatly), which is degraded only by 2.23 dB compared with expected Taylor weight.

4.2. Combining of Element and Subarray Weighting. The scheme generates sum and difference channels simultaneously only using an analog weighting. In order to determine the analog weights, it is assumed that the supposed interferences locate within the sidelobe area of sum and difference beams [25]. Then the supposed interferences are adaptively suppressed (e.g., based on LCMV criterion). And the obtained adaptive weight is regarded as the desired analog weight. Furthermore, the subarray weighting is adopted; that is, analog weight is combined with the digital weights in order to improve the PSL reduction capability. The subarray weighting has two forms which are used for sum and difference beam, respectively. Then the subarray weights could

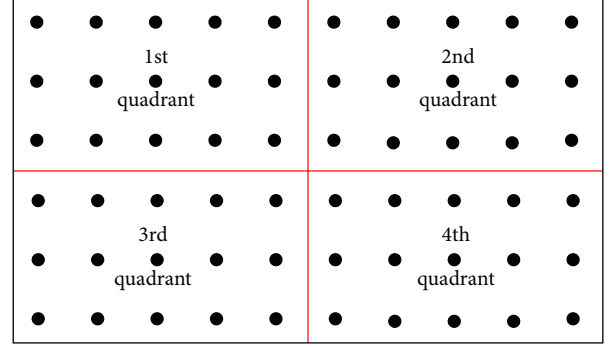


FIGURE 9: The division of planar array into four quadrants.

be determined by the weight approximation or the pattern approximation approach, as mentioned in Section 4.1.

The literature [25] presented above-mentioned approach for the ULA. Next we focus on planar array [52]. Consider a UPA with $N_x \times N_y = N$ elements. First the array is divided into four equal quadrants as shown in Figure 9. And then we number the elements as $1 \leq n \leq N/4$ in the first quadrant, $N/4 + 1 \leq n \leq N/2$ for the elements in the second quadrant, $N/2 + 1 \leq n \leq 3N/4$ for the elements in the third quadrant, and $3N/4 + 1 \leq n \leq N$ for the elements in the fourth quadrant. The sum and difference channels are shown in Figure 10.

Assume coordinate of n th ($n = 1, \dots, N$) element is (x_n, y_n) . The analog weight is $\mathbf{w}_{ele} = \mu \mathbf{R}^{-1} \mathbf{a}(\theta_0, \varphi_0)$, where μ is a nonzero constant; $\mathbf{a}(\theta_0, \varphi_0)$ is the steering vector into the look direction; $\mathbf{R} = \mathbf{R}_{x_\Sigma} + \mathbf{J}_\Delta \mathbf{R}_{x_\Delta} \mathbf{J}_\Delta$ with $\mathbf{J}_\Delta = \text{diag}(\underbrace{\mathbf{q} \ \mathbf{p} \ \cdots \ \mathbf{q} \ \mathbf{p}}_{N_y/2}, \underbrace{\mathbf{p} \ \mathbf{q} \ \cdots \ \mathbf{p} \ \mathbf{q}}_{N_y/2})$, and \mathbf{q} is $N_x/2$ -

dimensional unit row vector, while \mathbf{p} is $N_y/2$ -dimensional row vector in which every element is -1 . Assuming the interferences are with uniform distribution, let $\mathbf{R}_{x_\Sigma} = (r_{ik-\Sigma})_{i,k=1,2,\dots,N}$; then we have

$$r_{ik-\Sigma} = \begin{cases} \pi (1 - R_\Sigma^2) \sigma_{L-\Sigma}^2 + \sigma_n^2, & i = k \\ 2\pi e^{j\pi[(x_i-x_k)u_0 + (y_i-y_k)v_0] (l_0 - R_\Sigma l_\Sigma) \sigma_{L-\Sigma}^2}, & i \neq k \end{cases} \quad (10)$$

with $l_0 = J_1(c_{ik})/c_{ik}$, $l_\Sigma = J_1(c_{ik}R_\Sigma)/c_{ik}$, where $J_1(\cdot)$ is first order Bessel function of the first kind and $c_{ik} = 2\pi \sqrt{(x_i - x_k)^2 + (y_i - y_k)^2} / \lambda$; R_Σ is mainlobe radius of sum beam; $\sigma_{L-\Sigma}^2$ is power of interference imposing on sum beam; σ_n^2 is thermal noise power. Similarly, we can obtain $r_{ik-\Delta}$ with $\mathbf{R}_{x_\Delta} = (r_{ik-\Delta})_{i,k=1,2,\dots,N}$.

It should be pointed out that the PSL reduction effect with only analog weighting approach is determined by the selected design parameters, such as JNR and spatial distribution of supposed interferences.

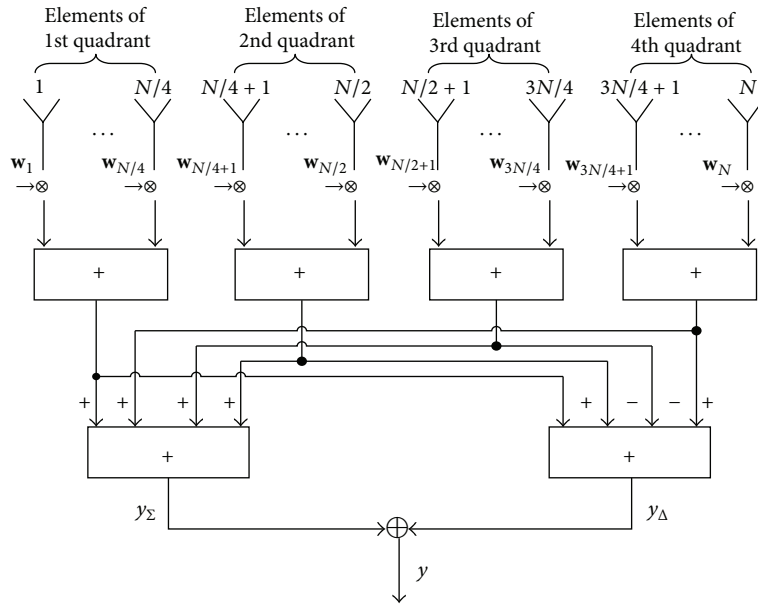


FIGURE 10: Construction of sum and difference channels.

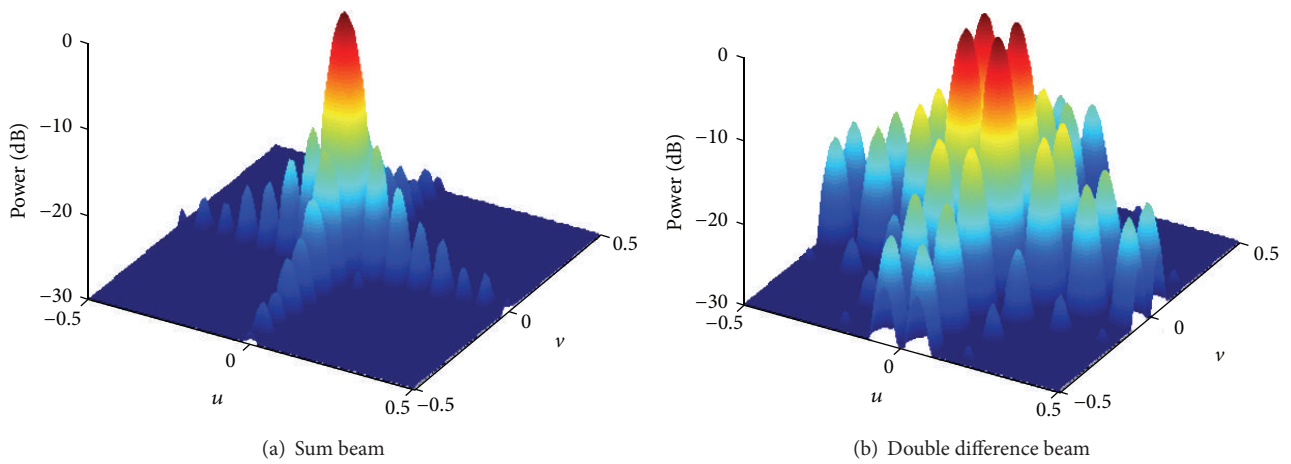


FIGURE 11: Patterns obtained by only analog weighting.

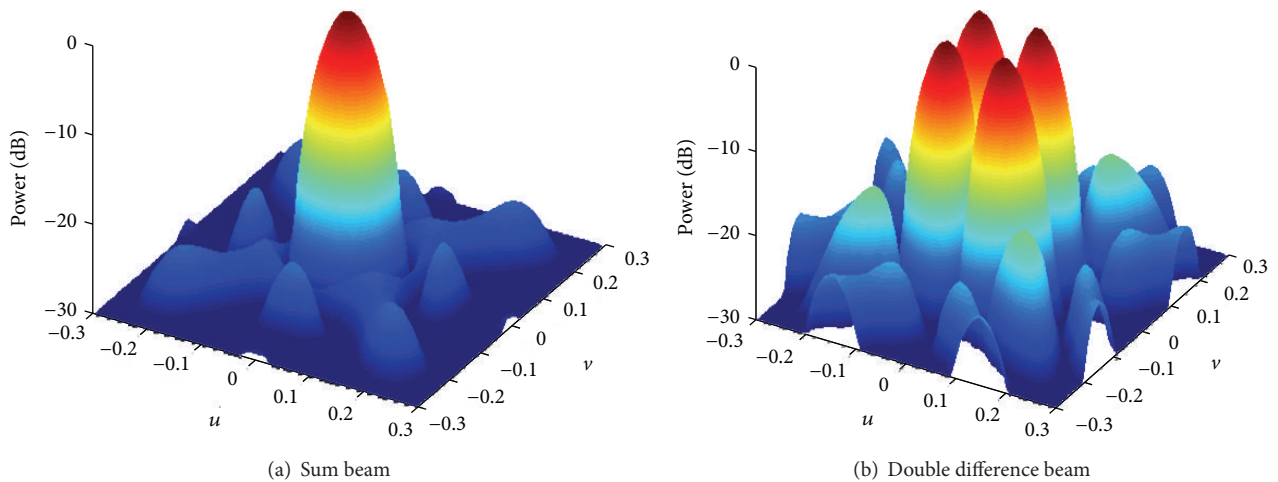


FIGURE 12: Patterns obtained by analog and digital weighting (with weight approximation approach).

Assume that a UPA consists of 30×30 elements on a rectangular grid at half wavelength spacing configured into 10×10 uniform subarrays. The look direction is $(0^\circ, 0^\circ)$. For sum and double difference beam (double difference beam is useful for main beam ECCM application, for instance, the mainlobe canceller), the JNRs of supposed interferences are both of 30 dB. Figure 11 shows patterns generated by only analog weighting. The PSLs of the sum and difference pattern are -14.51 dB and -10.77 dB, respectively. Figure 12 shows the results of adopting both element weighting and weight approximation-based subarray weighting, in which the PSLs of sum and double difference patterns are improved by 8.34 dB and 5.27 dB, respectively, compared with Figure 11.

In fact the PSL reduction capabilities of weight approximation- and pattern approximation-based subarray weighting are quite close.

5. The Sidelobe Reduction for Subarrayed Beam Scanning

The look direction is usually controlled by phase shifters for PAR. However further subarrayed digital beam scanning may be required for forming multiple beams and many other applications which are used for a limited sector of look directions around the presteered direction.

Typically with subarrayed scanning, the PSL will increase rapidly with the scanning direction departing from the original look direction. The larger the scan angle is, the greater the PSL increase is [11]. Therefore the requirement for sidelobe reduction arises.

In this section, we discuss the PSL reduction approaches for subarrayed beam scanning, namely, beam clusters created at subarray level.

With subarrayed scanning, the resulting pattern is composed of the pattern of each subarray. Each subarray pattern has a high PSL which contributes to a high PSL of the array pattern. If pattern of each subarray would be superimposed properly in the main beam and has a low PSL, the PSL of the array pattern could be reduced effectively.

Therefore, one can post-process the subarray outputs using a weighting network, consequently creating new subarrays with the patterns with similar shape within the main beam and with PSLs as low as possible. The starting point is to make the new subarray patterns to approximate the desired one.

The natural form of desired subarray pattern is the ISP (ideal subarray pattern) which is constant within the mainlobe and zero else [11]. It has two kinds of forms: (1) projection of mainlobe in array plane is a rectangular area, and (2) projection of mainlobe is a circular area.

As an example, assume that a UPA consists of 32×34 omnidirectional elements on a rectangular grid at half wavelength spacing. A -40 dB Taylor weighting is applied in both x and y directions. The array is divided into 6×6 nonuniform subarrays and each of which is a rectangular array. Assume $(u_0, v_0) = (-0.5, 0)$.

By using the ISP based on rectangular projection, we give an example for reducing the sidelobes in Figure 13(a).

Obviously, the shape and beamwidth of the main beam of all subarrays are very similar, but the gain of the different subarrays makes a great difference in the results. Figure 13(b) shows patterns obtained by ISP based circular projection. Obviously, the shape, the beamwidth, and the gains of the main beam of all subarrays are very similar, which is superior to rectangular projection method.

Figure 14 shows array patterns after scanning carried out in u direction. Subplots (a), (b), and (c) show the patterns obtained without the weighting network processing, with ISP based rectangular projection and ISP based on circular projection, respectively. The different curves are given for nonscanning and scan angles of $0.5 B_w$ and $1.0 B_w$, respectively, where B_w is the 3 dB beam width. Compared to the case without-weighting network, for ISP based on rectangular projection the PSL is reduced by 1.34 dB for $0.5 B_w$ scanning and 1.72 dB for the $1 B_w$, while for ISP based circular projection the PSL is reduced by 1.99 dB and 2.39 dB, respectively.

It is seen from above-mentioned examples that the PSL reduction capability with ISP is not satisfied. For the reason, we adopt GSP- (Gaussian subarray pattern-) based approach [53]. Therein desired pattern is the Gaussian pattern, which is more smooth than the ISP [11].

The result obtained with the GSP approach is shown in Figure 15. Comparing Figure 15 with Figure 14(b), we see that the PSL by GSP is improved obviously compared with ISP based rectangular projection; namely, PSL is reduced by 1.49 dB for the $0.5 B_w$ scanning and 2.05 dB for the $1 B_w$, respectively. Consequently, the GSP improves remarkably ISP as PSL of the latter is only reduced by more than 1 dB compared with non-weighting network; meanwhile the computational burden is equivalent to the latter [53].

6. The Subarrayed Adaptive Monopulse

In order to ensure the accuracy of angle estimation of monopulse PAR in jammer environments, we should adopt subarrayed adaptive monopulse technique. The subarrayed ABF can improve SINR and detection capability. However, under circumstances of MLJ (mainlobe jamming) the adaptive null will distort the main beam of pattern greatly, thus leading to serious deviation of the angle estimation. Thereby, the subarrayed adaptive monopulse should be applied.

Existing approaches usually take the adaptive patterns into account to avoid the degradation of monopulse performance near the null. For example, one can use LMS-based target direction search to determine adaptively the weights of optimum difference beam [54]. This kind of methods needs to adopt the outputs of the sum and difference beam to achieve the corrected monopulse ratio and it needs higher computational cost. Subarrayed linearly constrained adaptive monopulse is generalized from the linearly constrained adaptive monopulse [55]. But it reduces degree of freedom by adopting adaptive difference beam constraints.

The reined subarrayed adaptive monopulse methods with higher monopulse property have been suggested, for example, the approximative maximum-likelihood angle estimators

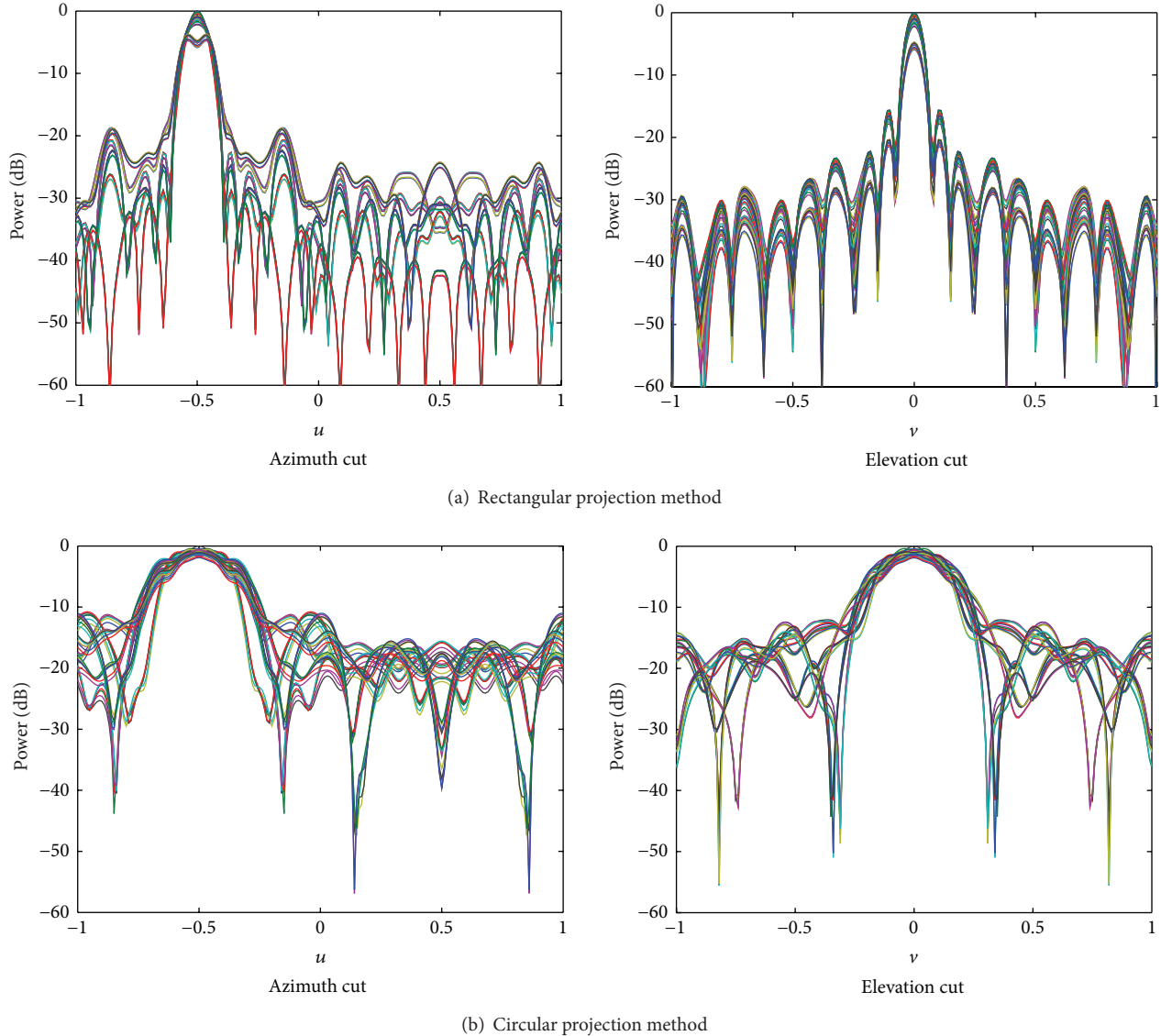


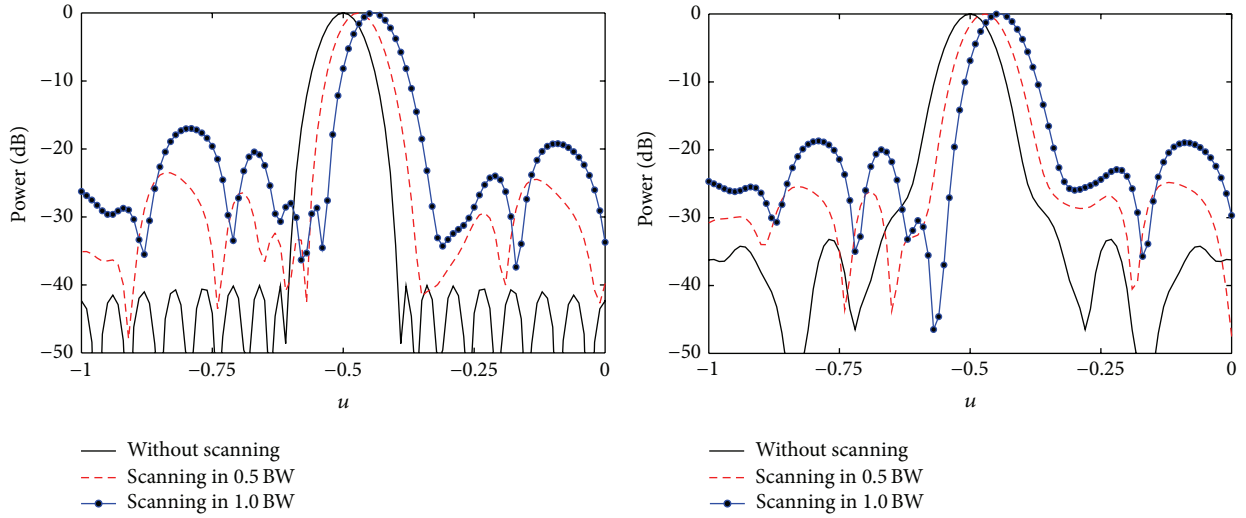
FIGURE 13: Subarray patterns obtained by ISP.

[12, 13, 15, 16] proposed by Nickel. In this section, we focus on two-stage subarrayed adaptive monopulse. Here we improve the conventional two-stage subarrayed adaptive monopulse which is an extension of the two-stage adaptive monopulse technique [56].

The realization process of the two-stage subarrayed adaptive monopulse is as follows: firstly, the subarrayed ABF is used to suppress the SLJ, while maintaining the mainlobe shape; secondly, the MLJ is suppressed, while maintaining the monopulse performance; that is, the jammers are canceled with nulls along one direction (elevation or azimuth) and undistorted monopulse ratio along the orthogonal direction (azimuth or elevation) is preserved. The two-stage subarrayed adaptive monopulse requires four channels, in which the delta-delta channel is used as an auxiliary channel for the mainlobe cancellation.

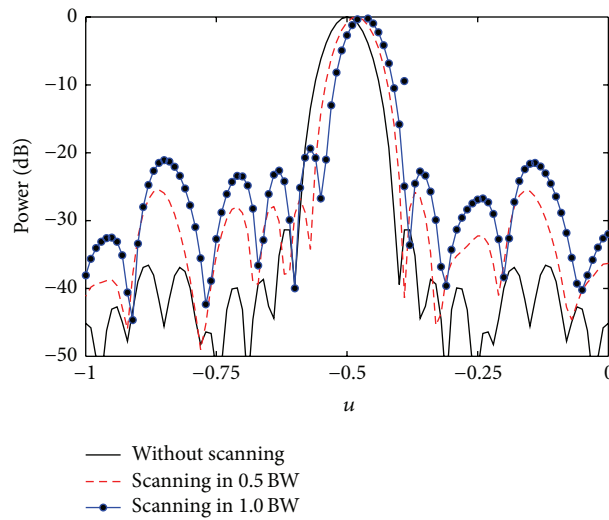
However, the method possesses two limitations: (1) after the first-stage processing, the PSLs of patterns increase greatly, and (2) the monopulse performance is undesirable, for there exists serious distortion in deviation of the look direction for adaptive monopulse ratio; the reason is that the MLM (mainlobe maintaining) effect is not ideal. Therefore, in the first-stage processing, subarrayed optimum ABF is substituted by MOD; consequently, the monopulse performance would be improved greatly [57].

Suppose a rectangular UPA with 56×42 elements and the element spacing is $\lambda/2$. A -40 dB Taylor weighting is applied in x and a -30 dB in the y direction. Array is partitioned into 6×6 nonuniform subarrays and each subarray is a rectangular array: $(\theta_0, \varphi_0) = (0^\circ, 0^\circ)$. Assuming that MLJ and SLJ are located at $(1^\circ, 2^\circ)$ and $(10^\circ, 15^\circ)$, respectively, then all the JNRS are 30 dB.



(a) Non-weighing network

(b) Rectangular projection method



(c) Circular projection method

FIGURE 14: Array patterns with beam scanning obtained by ISP method (azimuth cut).

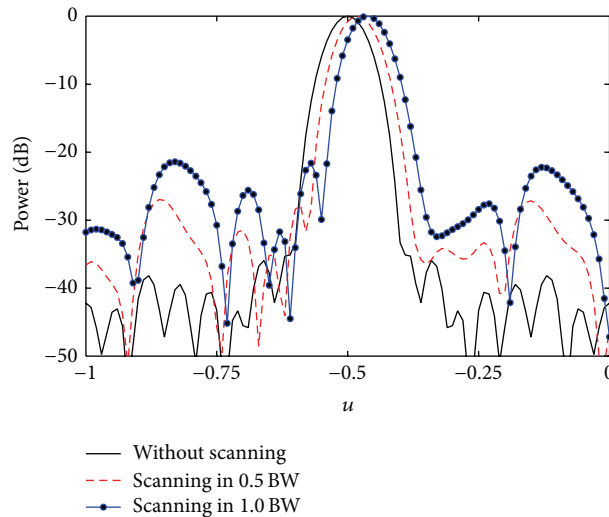


FIGURE 15: Array patterns with beam scanning obtained by GSP (azimuth cut).

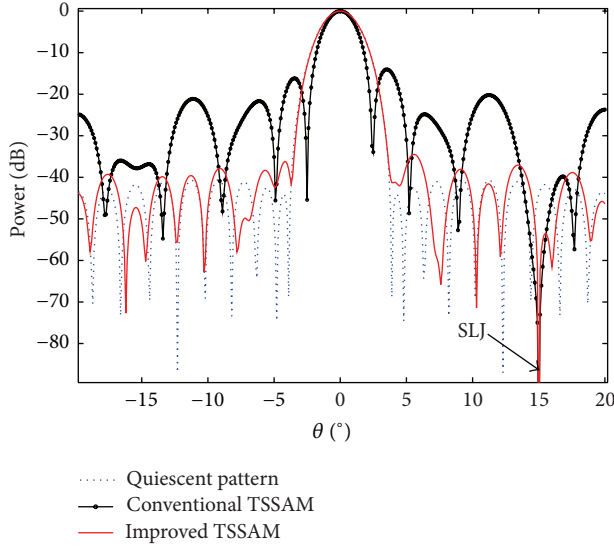


FIGURE 16: Adaptive patterns of elevation sum beam obtained by first-stage adaptive processing.

Next we illustrate the simulation results taking the elevation direction as an example. Figure 16 is the cut of the adaptive patterns of elevation sum beam applying first-stage processing. It is obvious that the conventional two-stage subarrayed adaptive monopulse (TSSAM for short), namely the subarrayed optimum ABF combined with MLM obviously increases the PSL, compared with the quiescent pattern, and the mainlobe width shows apparent reduction, which leads to the distortion of adaptive monopulse ratio around the look direction. The PSL is improved greatly by using the MOD, and more important the remarkable improvement of the MLM effect makes the mainlobe shape close to that of the quiescent pattern; therefore a greater improvement of adaptive monopulse ratio can be obtained.

Figure 17 presents an elevation monopulse ratio obtained by the two-stage subarrayed adaptive monopulse. Let $u = \cos \theta \sin \varphi$ and $v = \sin \theta$, where φ and θ are the azimuth and elevation angle correspondingly. The monopulse ratio along elevation direction is $K_E(u, v) = F_{\Delta_E}(u, v)/F_{\Sigma}(u, v)$, where $F_{\Sigma}(u, v)$ and $F_{\Delta_E}(u, v)$ denote the pattern of sum beam and elevation difference beam, respectively. The two-dimensional antenna patterns are separable; therefore, $K_E(u, v) = F_{\Sigma_A}(u)F_{\Delta_E}(v)/[F_{\Sigma_A}(u)F_{\Sigma_E}(v)] = F_{\Delta_E}(v)/F_{\Sigma_E}(v)$ [56].

Since the subarrayed optimum ABF combined with MLM is used in the first-stage processing, the monopulse ratio deviated from the look direction shows serious distortion. Undoubtedly, the MOD combined with MLM is an appropriate choice to enhance adaptive monopulse ratio, for its similarity to quiescent monopulse ratio and the small distortion when deviated from the look direction. And the relative error of adaptive monopulse ratio with improved two-stage monopulse (MOD+MLM for first-stage processing) is only 3.49% compared with quiescent monopulse ratio when the elevation is -2.7° , while the conventional two-stage monopulse (subarrayed optimum ABF+MLM for the first-stage processing) is as much as 69.70%. So, improved

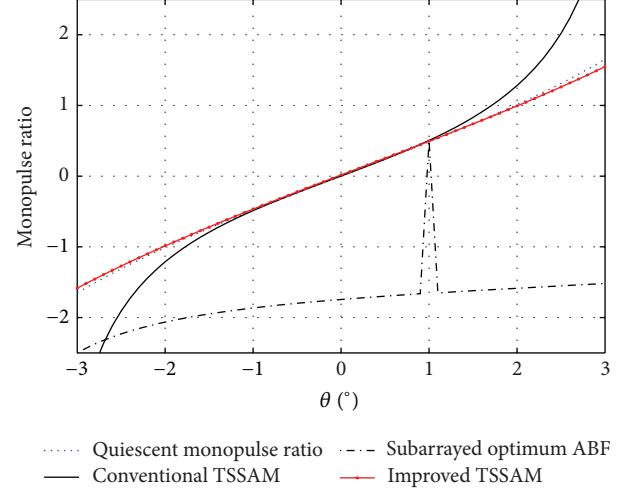


FIGURE 17: Elevation monopulse ratio obtained by two-stage adaptive processing.

method monopulse reduces error of monopulse ratio greatly compared with conventional method. The numerical results demonstrate that, in the range of 3 dB bandwidth of patterns, for the improved method monopulse, the relative error of adaptive monopulse ratio is less 1% and even reaches 0.01% compared with quiescent monopulse ratio.

Two-stage subarrayed adaptive monopulse integrates several techniques, including subarrayed ABF, MLM, quiescent pattern control, and four-channel MJC. The SLJ and MLJ are suppressed, respectively, so it is unnecessary to design the sophisticated monopulse techniques to match the mainlobe of patterns.

For the wideband MLJs, the SLC type STAP can be used to form both sum and difference beam. If auxiliary array is separated from the main array by distances that are sufficiently large, the array can place narrow nulls on the MLJ while maintaining peak gain on a closely spaced target [58]. Consequently, it can suppress MLJs effectively while preserving superior monopulse capability.

7. The Subarrayed Superresolution

To address angle superresolution issues, a variety of methods have been developed. This paper only focuses on subarrayed superresolution. In this section, two types of the approaches are described: the first refers to the narrowband superresolution; the second approach presents the broadband superresolution [6].

7.1. The Subarrayed Superresolution. The subarrayed superresolution direction finding could be achieved by extending the conventional superresolution algorithms into the subarray level. However, this kind of algorithms has to calibrate the whole array manifold. But for the active calibration technique the realization is very complicated and costly, while for the self-calibrate solutions there are limitations, for example, difficulty of implementation; high computational burden (some algorithms are many times more than original

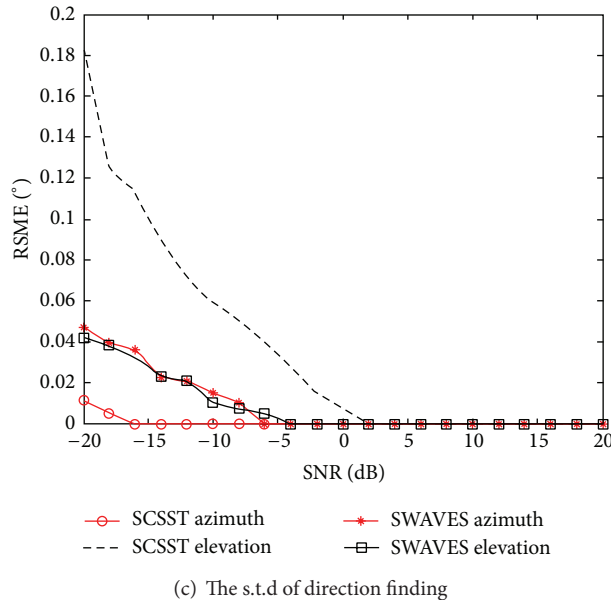
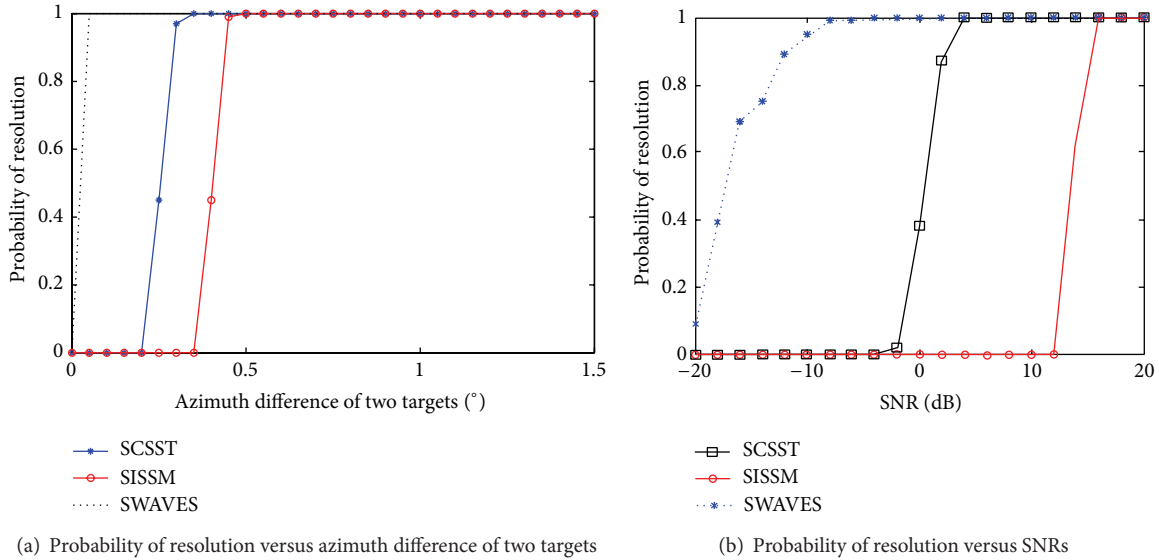


FIGURE 18: Contrast of performances of three broadband subarrayed superresolution algorithms.

superresolution algorithms even); the convergence problems for some iterative algorithms; the performances are limited in the case of a lot of array position errors; some are only effective for specific errors of one or two kinds only [59].

Thus, simplified array manifolds can be used. The essence of these methods is to treat the whole array as a superarray and each subarray as a superelement. The idea is to approximate the patterns at subarray outputs by those of superelements located at the subarray centres [19]. The simplified array manifolds are only determined by phase centers and gain of subarrays [19]. Because the calibration needs to be implemented only inside the subarrays, the calibration cost and complexity are reduced greatly.

These methods can eliminate uncertain information in sidelobe area. The available region of direction finding of them is within 3 dB beamwidth of patterns around the

center of the look direction. However, combined with beam scanning by element phase shifting, superresolution can be achieved in any possible direction, that is, make the superresolution be carried out repeatedly by changing look direction. The advantage is suppressing sidelobe sources in complicated situation such as multipathway reflection; consequently, number of sources and dimension of parameter estimation are reduced and the process of superresolution is simplified [19]. Meanwhile we can use beam scanning to find the area with no signal source and wipe it off in advance; therefore 2-D peak searching cost is reduced greatly.

The available direction finding area of direct simplified array manifold-based subarrayed superresolution is fixed which cannot be adjusted and the sidelobe sources cannot be suppressed completely. Changing subarray patterns can overcome the limitations, but it is unable to be achieved by

restructuring the subarray structure. The subarray structure is an optimized result based on various factors and hardware is fixed. Therefore, we post-process the subarray outputs by introducing a weighting network which constructs required new subarray patterns. This kind of methods improved the flexibility of array processing greatly and the optimization of subarrays for different purpose and distinct processing tasks can be achieved based the same hardware [19].

Compared with the method based direct simplified array manifold, the ISP and GSP methods can adjust the available region of direction estimation and suppress sidelobe sources better [19, 60, 61]. On the other hand, compared with the ISP and GSP methods, the approximate ISP and approximate GSP methods reduce the computational cost greatly, while the precision of direction finding and resolution probability are very close to ISP and GSP [62, 63], respectively.

7.2. The Broadband Subarrayed Superresolution. The subarrayed superresolution approaches presented in the Section 7.1 are based on the scenario of narrowband signals. Next let us consider the broadband subarrayed superresolution which includes three kinds of approaches, namely, subband processing, space-time processing, and subarray time-delaying processing [6].

The subarrayed ISSM (incoherent signal subspace method), subarrayed CSST (coherent signal subspace transform), and subarrayed WAVES (weighted average of signal subspace) translate broadband problems into a subband processing. All these algorithms need to make delay-weighting for outputs of subbands. The subarrayed ISSM only averages the direction finding results of each subband obtained by subarrayed MUSIC. The subarrayed CSST and subarrayed WAVES should choose the suitable focusing transformation matrix and therefore need to preestimate source direction. If the preestimated direction is erroneous, the direction finding performance will be degraded. The subarrayed WAVES determines a joint space from all subspaces of subband covariance matrix, which is only one representative optimum signal subspace [6]. The mentioned-above subband processing methods can be combined with simplified array manifolds. Consequently, the broadband subarrayed superresolution can be achieved.

The broadband superresolution based on subarray time delay does not need any subband processing. Accordingly, it has less calculation which is easy to be implemented but needs a focusing transform. For the simplified array manifold-based approaches, they have better performance if the preestimated target direction is near the look direction; otherwise the performance would be degraded rapidly.

The narrowband subarrayed superresolution can be extended to the space-time superresolution (such as the subarrayed space-time MUSIC). Through compensating the phase using a subarray delay network, this kind of algorithms reduces the frequency-angle ambiguities. Then use the space-time steering vector to calculate the space-time covariance matrix and extract the dominant signal subspace [6]. The space-time broadband subarrayed superresolution does not need any focusing transform and direction preestimation, but the computation is costly.

To give an example, suppose a UPA with $19 \times 43 = 817$ elements, and the element spacing is $\lambda_0/2$. A -40 dB Taylor weighting is applied in x and a -30 dB in the y direction. Array is partitioned into $7 \times 11 = 77$ nonuniform subarrays and each subarray is a rectangular array. Assume look direction is $(5^\circ, 45^\circ)$. The sources are incoherent, broadband with $B = 0.2f_0$ and with equal power. Suppose there are two targets; in both the elevation is 43.0° and the azimuth difference varies from 5.0° to 0° and SNR (signal-to-noise ratio) is 0 dB.

Two targets are deemed to be separable if their peak values of spatial spectrum both are greater than the value in the central direction of targets. Namely, targets are resolvable if the following two conditions are both met: $P(\theta_1) > P((\theta_1 + \theta_2)/2)$ and $P(\theta_2) > P((\theta_1 + \theta_2)/2)$, where θ_1 and θ_2 are directions of spectrum peaks of the targets, respectively. And the probability of resolution is the probability that the two targets are successfully resolved.

Figure 18(a) plots the probability of resolution curves obtained by several algorithms [64]. It can be seen that the angle resolution capability of subarrayed WAVES (SWAVES for short) is the best, while subarrayed ISSM (SISSM for short) is the worst. Assuming two targets located at $(4.0^\circ, 45.0^\circ)$ and $(5^\circ, 43.0^\circ)$, Figure 18(b) shows the curves of the probability of resolution versus SNRs. From the figure it can be found that probability of resolution of subarrayed WAVES is the best, followed by subarrayed CSST (SCSST for short), and subarrayed ISSM is the worst. Figure 18(c) gives the curves of RMSE of direction estimation versus SNRs, in which RMSEs are the average value of the estimations of the two targets [64].

8. Subarray Configuration Optimization for ECCM

For the PAR equipped with ABE, the optimization of subarray configuration is a key problem and challenge in the field of the SASP.

For its obvious influence on the performance of PAR, the optimization of subarray configuration can bring much improvement of the system performances such as sidelobe level, detection capability, accuracy of angle estimation, ECCM capability (anti-MLJ), and so forth. The subarray division is a system design problem; the optimized result has to take into account various factors. However, different capabilities may be contradictory mutually.

There are different solutions to this contradiction. In this section we briefly overview the MOEA (multiobjective evolutionary algorithm) procedure working on this issue. MOEA might make an optimal trade-off between above-mentioned capabilities.

The objective functions in the MOEA could be the mean P_d for different positions of the target, the mean CRB (Cramer-Rao Bound) of the target azimuth/elevation estimation, the mean PSLs of sum adapted pattern in the azimuth/elevation plane, and so forth [28]. But the set of optimum solutions is obtained after the subarray optimization through MOEA. Therefore, we need to determine posteriorly an optimized array through optimizing the

specific capability or introducing constraints (such as the geometric structures or the realization cost and complexity of array).

On the other hand, several issues should be considered on engineering realization: for example, all the subarrays are nonoverlapped and array is the fully filled, subarray configuration is relatively regular, and all elements inside a subarray are relatively concentrative (subarray's shapes should not be disjointed). Therefore, multiple constraints should be set during the process of genetic optimization.

The process of optimizing subarray is quite complicated for the great amount of elements in a PAR and the large searching space. Thus we can adopt the improved GA to make optimizing with a characteristic of adaptive crossover combination, which is based on the adaptive crossover operator; this will result in remarkable enhancement on convergence speed of optimization and calculation efficiency [65].

Suppose a UPA with $30 \times 32 = 960$ omnidirectional elements and element spacing is $\lambda/2$. A -40 dB Taylor weighting is applied in x and in the y direction. The subarray number is 64, $(\theta_0, \varphi_0) = (0^\circ, 0^\circ)$. The original subarray structure is selected randomly. Suppose that the direction of the MLJ is $(1^\circ, 1^\circ)$ and $\text{JNR} = 35$ dB.

We optimize the five objective functions simultaneously based on the MOEA. Hereinto, the first objective function is the PSL of adapted sum pattern in $u = 0$ cut. Figure 19(a) shows the adapted sum pattern obtained by the optimized subarray configuration and the original one, respectively. Here the original and optimized PSL are -12.36 and -22.37 dB, respectively; namely, the PSL is improved by 10.01 dB. The second objective function is the PSL of adapted sum pattern in $v = 0$ cut. Figure 19(b) shows the adapted sum pattern cut obtained by the optimized subarray configuration and the original one, respectively, in which the original and optimized PSL are -8.93 dB and -15.98 dB, respectively; therefore the PSL is improved by 7.05 dB. Note here the PSL is the third high sidelobe in the patterns, because the second one is caused by adaptive null.

On the other hand, for the PAR with subarrayed ABE, the ideal optimum subarray configuration should keep system's performances be optimal for various interference environments interference environments. But this is impossible to realize in principle.

9. The Subarrayed Processing for MIMO-PAR

Historically, the SASP techniques are mainly used for the PAR systems. In this section, we discuss the concept of the SASP suitable for MIMO-PAR system. Creating this technique is an impetus following from previous sections.

The MIMO structure is impracticable when the array is composed of hundreds or thousands of elements due to the huge quantity of independent transmitting signals and transmitting and receiving channels. Hardware cost and algorithmic complexity will exceed the acceptable level.

Therefore, we present the subarrayed MIMO-PAR. It is an extension of the subarrayed PAR. The MIMO-PAR is the combination of MIMO radar and PAR: the array is divided into several subarrays; inside each subarray a coherent signal

is transmitted, working as PAR mode; orthogonal signals are transmitted between subarrays to form a MIMO system. The MIMO-PAR presented in this paper adopts Tx/Rx array modules, and transmitting and receiving arrays have the same subarray configuration, while both at the transmitting and receiving ends the SASP techniques are be applied.

9.1. The Characteristics of MIMO-PAR. The features of MIMO-PAR are listed as follows.

- (1) It maintains advantages of MIMO radar as well as the characteristics of PAR (such as the coherent processing gain).
- (2) Compared with MIMO radar, the MIMO-PAR reduces the cost and complexity of the hardware (the number of the transmitting and receiving channels) and the computational burden greatly. For example, the dimension of optimization algorithms for designing transmitting signals is reduced to subarray number, while it is the same as the element number in MIMO. Typically element number has an order of magnitude from several hundreds to several thousands and subarray number is only a few dozens of magnitude.
- (3) Hardware cost and algorithm complexity can be flexibly controlled by adjusting the number of the subarrays. The ability of coherent processing (SNR) and the characteristics of waveform diversity (angle resolution) can be compromised by adjusting the subarray structure and subarray number.
- (4) Compared with MIMO radar, the transmitting signals of different subarrays can be combined with independent beam look directions to improve the capability of beam control, producing more flexible transmitting beam patterns, thus improving the flexibility of object tracking.
- (5) The characteristics with further advantages over MIMO radar, such as lower PSL of total pattern, can be achieved by design of the weighting of subarrayed transmitting/receiving BF. Moreover, MIMO-PAR can enhance the anti-jamming capability and generate higher output SINR under strong interference, and realize low PSL without expense of mainlobe gain loss.
- (6) The performance of the system can be enhanced by optimizing the structure of subarray, such as transmitting diversity, SNR, PSL of total pattern, the performance of transmitting beam, and the ECCM capability.
- (7) The exiting research achievements related to receiving SASP for PAR can be generalized to the MIMO-PAR. This is a promising direction of further studies.
- (8) The configuration of MIMO-PAR with Tx/Rx modules can be easily made compatible with existing subarrayed PAR.

9.2. The Research Topics of SASP for MIMO-PAR. The research topics are as follows.

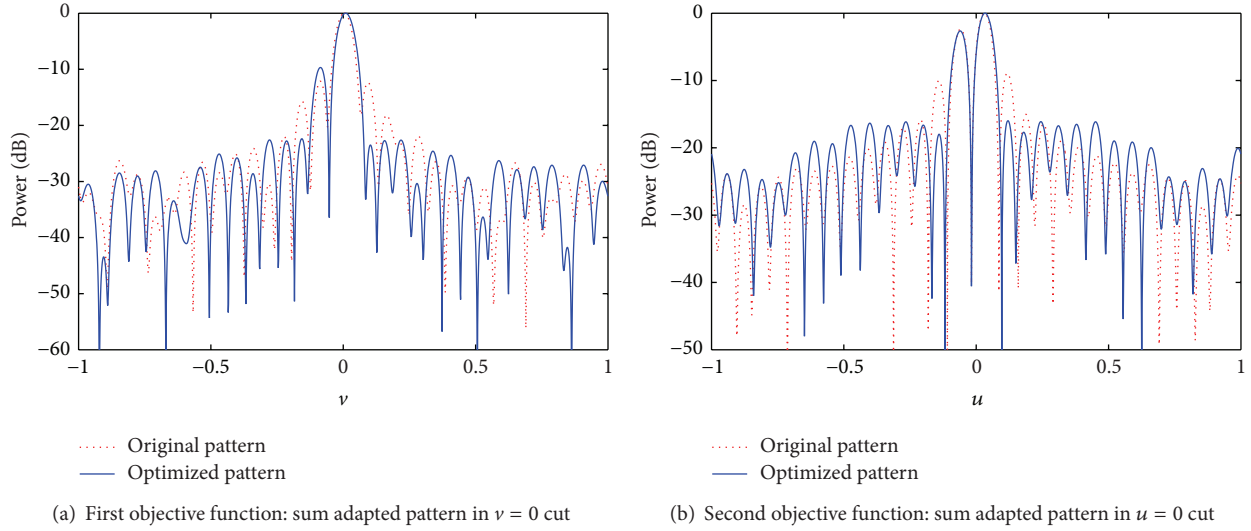


FIGURE 19: Optimized results based on MOEA.

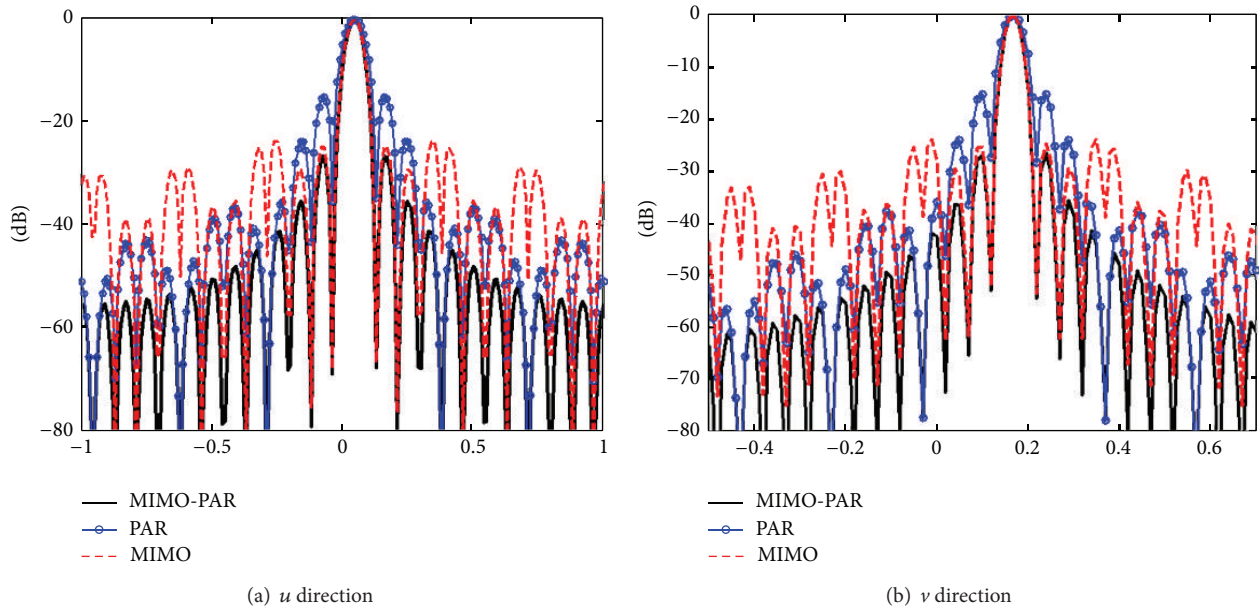


FIGURE 20: Total patterns of PAR, MIMO, and MIMO-PAR.

9.2.1. Subarrayed Transmitting/Receiving BF

(1) *Subarrayed Transmitting BF.* The use of robust subarrayed transmitting BF can minimize the transmitted power. The starting point is minimizing the norm of the transmitting BF weight vector while restricting the upper bound of sidelobes [66].

(2) *Subarrayed Receiving BF.* The subarrayed ABF for PAR is described in Section 2 can be employed for MIMO-PAR. Furthermore, the subarrayed LSMI and subarrayed CAPS (constrained adaptive pattern synthesis) and so forth [1] can also be applied to MIMO-PAR.

(3) *The Characteristic of the Transmitting/Waveform Diversity/Receiving Total Pattern.* The virtual array steering vector of the MIMO-PAR is decided by the coherent processing gain vector, the waveform diversity vector, and the steering vector of the receiving array. And the total patterns are the production of transmitting pattern, wave diversity patterns, and receiving patterns.

Assume a UPA of Tx/Rx community with 960 omnidirectional elements on a rectangular grid at half wavelength spacing. The array is divided into $8 \times 8 = 64$ uniform subarrays, each of which is a rectangular array. Figure 20 illustrates the total pattern for the three radar models [67]. Table 3 shows the results of the comparison. It is seen that

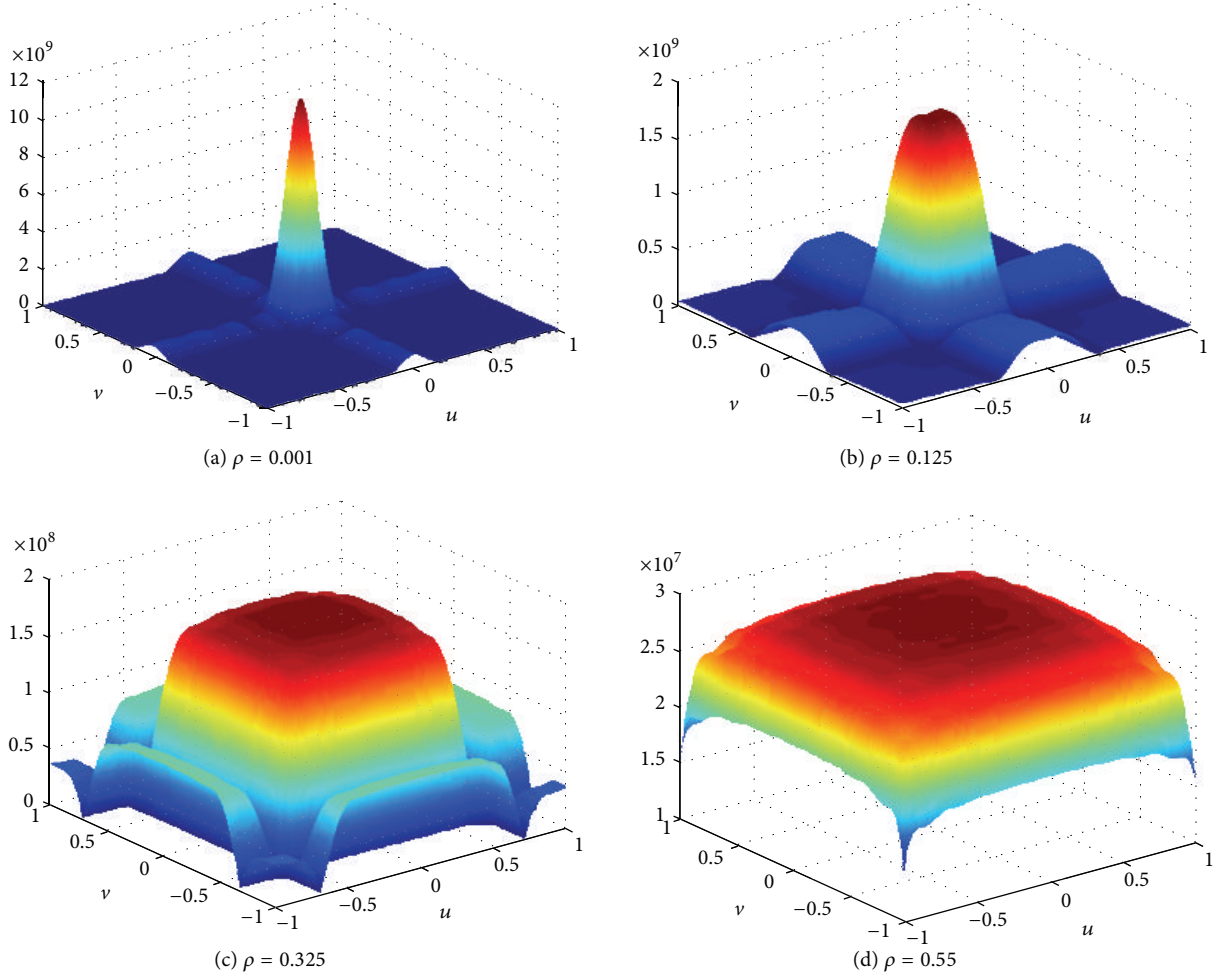


FIGURE 21: Transmit beam patterns based on synthesis of subarray transmitted signal.

TABLE 3: PSLs of total pattern for different radar models (dB).

Radar model	PAR	MIMO	MIMO-PAR
PSLs in u direction	-15.00	-24.66	-26.56
PSLs in v direction	-15.16	-25.26	-26.95

MIMO-PAR is superior to the PAR and the MIMO in terms of the PSL.

9.2.2. Synthesis of Transmitting Beam Pattern. The rectangle transmitting beam pattern can be used to radiate the maximum transmitting energy to interesting areas, so as to improve the exploring ability. As a result, a rectangle transmitting beam pattern can be synthesized from cross-correlation matrix of transmit signals [68].

The transmitting beam control includes two scenarios. (1) Each subarray has different beam directions to form a broad transmitting beam (for radar search mode). (2) Each subarray has the same beam direction to focus on transmitting beam (for tracking mode).

Aiming at a UPA, Figure 21 shows the transmitting beam patterns with different signal correlation coefficient ρ [69]. We observe that the beam width can be adjusted.

The performance evaluation of transmitted signal includes (1) orthogonality and (2) range resolution and multiple-target resolution (pulse compressing performance). On the other hand, the orthogonality degrades with increase of the subarray number.

9.2.3. Optimization of the Subarray Configuration. In the MIMO-PAR, when the element number and subarray number are fixed, the subarray structure has a significant impact on the system performance. Then the subarray structure has to be optimized. While in the MOEA method, the following constraints can be chosen as objective functions: (1) the waveform diversity capability, (2) the coherent processing gain, (3) the PSL of the total pattern in elevation direction, (4) the PSL of the total pattern in azimuth direction, and (5) the RMSE of the transmitting beam pattern and the rectangular pattern.

10. Conclusions and Remarks

In this paper, we describe some aspects of the SASP. From these investigations, we draw the concluding remarks as follows.

- (1) For the SASP the achievable capabilities in application are constrained by some hardware factors, for example, channel errors.
- (2) The amalgamation as well as integration of multiple SASP techniques is a trend, such as the combination of subarrayed ABF, adaptive monopulse, and superresolution. Consequently, the performance of the SASP could be improved.
- (3) The subarray optimization is still a complicated and hard problem, compared with the algorithms.
- (4) The extension of the SASP into MIMO-PAR could promote and deepen development of the SASP.

Furthermore, we point out the problems to be dealt with. The challenging works are in the following areas.

- (1) The more thorough study of subarray optimization should be carried out. It is important for improving capabilities of system (including ECCM).
- (2) The SASP for anti-MLJs is still a hard research topic.
- (3) The SASP techniques for the thinned arrays should be further developed.
- (4) At present, the research focuses mainly on the planar arrays which are only suitable for small angle of view (for instance, $\pm 45^\circ$). The SASP should be extended to the conformal arrays (e.g., seekers).

List of Acronyms

ABF:	Adaptive beamforming
ADC:	Analogue-to-digital conversion
ASLB:	Adaptive sidelobe blanking
BF:	Beam forming
CAPS:	Constrained adaptive pattern synthesis
CSST:	Coherent signal subspace transform
CRB:	Cramer-Rao Bound
DSW:	Direct subarray weighting
ECCM:	Electronic counter-countermeasure
GA:	Genetic algorithm
GSLC:	Generalized sidelobe canceller
GSP:	Gaussian subarray pattern
ISP:	Ideal subarray pattern
ISSM:	Incoherent signal subspace method
JNR:	Jammer-to-noise ratio
LCMV:	Linearly constrained minimum variance
LMI:	Lean matrix inversion
LMS:	Least mean square
LSMI:	Load sample matrix inversion
MFPAR:	Multifunction phased array radar
MIMO:	Multiple-input multiple-output
MLJ:	Mainlobe jamming
MLM:	Mainlobe maintaining
MOD:	Mismatched optimum detector
MOEA:	Multiobjective evolutionary algorithm
PAR:	Phased array radar
PSL:	Peak sidelobe level

SASP:	Subarrayed array signal processing
SINR:	Signal-to-interference-plus-noise ratio
SLC:	Sidelobe canceller
SLJ:	Sidelobe jamming
SMI:	Sample matrix inverse
SNR:	Signal-to-noise ratio
SSP:	Subspace projection
STAP:	Space-time adaptive processing
ULA:	Uniform linear array
UPA:	Uniform planar array
WAVES:	Weighted average of signal subspace.

Conflict of Interests

The author declares that there is no conflict of interests regarding the publication of this paper.

Acknowledgments

The author would like to thank Dr. Ulrich Nickel of Fraunhofer FKIE, Germany, for his insightful comments and useful discussions. This work has been partially supported by “the Fundamental Research Funds for the Central Universities” (Grant no. HIT.NSRIF.201152), the ASFC (Aeronautical Science Foundation of China, no. 20132077016), and the SAST Foundation (no. SAST201339).

References

- [1] U. Nickel, “Array processing for radar: achievements and challenges,” *International Journal of Antennas and Propagation*, vol. 2013, Article ID 261230, 21 pages, 2013.
- [2] U. R. O. Nickel, “Subarray configurations for digital beamforming with low sidelobes and adaptive interference suppression,” in *Proceedings of the IEEE International Radar Conference*, pp. 714–719, IEEE, Alexandria, VA, USA, May 1995.
- [3] U. Nickel, “Adaptive beamforming for phased array radars,” in *Proceedings of the International Radar Symposium*, pp. 897–906, Munich, Germany, September 1998.
- [4] U. Nickel, “Subarray configurations for interference suppression with phased array radar,” in *Proceedings of the International Conference on Radar*, pp. 82–86, Paris, France, 1989.
- [5] U. Nickel, “Detection with adaptive arrays with irregular digital subarrays,” in *Proceedings of the IEEE Radar Conference*, pp. 635–640, Waltham, Mass, USA, April 2007.
- [6] U. Nickel, “Super-resolution and jammer suppression with broadband arrays for multi-function radar,” in *Applications of Space-Time Adaptive Processing*, R. Klemm, Ed., chapter 16, pp. 543–599, IEE, 2004.
- [7] U. Nickel, P. G. Richardson, J. C. Medley, and E. Briemle, “Array signal processing using digital subarrays,” in *Proceedings of the IET Conference on Radar Systems*, Edinburgh, UK, October 2007.
- [8] W. Bürger and U. Nickel, “Space-time adaptive detection for airborne multifunction radar,” in *Proceedings of the IEEE Radar Conference (RADAR '08)*, pp. 1–5, Rome, Italy, May 2008.
- [9] R. Klemm and U. Nickel, “Adaptive monopulse with STAP,” in *Proceedings of the CIE International Conference on Radar (CIE ICR '06)*, Shanghai, China, October 2006.

- [10] U. Nickel, "On the influence of channel errors on array signal processing methods," *International Journal of Electronics and Communication*, vol. 47, no. 4, pp. 209–219, 1993.
- [11] U. R. O. Nickel, "Properties of digital beamforming with subarrays," in *Proceedings of the International Conference on Radar (ICR '06)*, Shanghai, China, October 2006.
- [12] U. Nickel, "Monopulse estimation with adaptive arrays," *IEE Proceedings, Part F: Radar and Signal Processing*, vol. 140, no. 5, pp. 303–308, 1993.
- [13] U. Nickel, "Monopulse estimation with sub-array adaptive arrays and arbitrary sum- and difference beams," *IEE Proceedings—Radar, Sonar and Navigation*, vol. 143, no. 4, pp. 232–238, 1996.
- [14] U. Nickel, "Performance of corrected adaptive monopulse estimation," *IEE Proceedings Radar, Sonar and Navigation*, vol. 146, no. 1, pp. 17–24, 1999.
- [15] U. Nickel, "Performance analysis of space-time-adaptive monopulse," *Signal Processing*, vol. 84, Special section on new trends and findings in antenna array processing for radar, no. 9, pp. 1561–1579, 2004.
- [16] U. Nickel, "Overview of generalized monopulse estimation," *IEEE Aerospace and Electronic Systems Magazine*, vol. 21, no. 6, pp. 27–55, 2006.
- [17] U. R. O. Nickel, E. Chaumette, and P. Larzabal, "Statistical performance prediction of generalized monopulse estimation," *IEEE Transactions on Aerospace and Electronic Systems*, vol. 47, no. 1, pp. 381–404, 2011.
- [18] E. Chaumette, U. Nickel, and P. Larzabal, "Detection and parameter estimation of extended targets using the generalized monopulse estimator," *IEEE Transactions on Aerospace and Electronic Systems*, vol. 48, no. 4, pp. 3389–3417, 2012.
- [19] U. Nickel, "Spotlight MUSIC: super-resolution with subarrays with low calibration effort," *IEE Proceedings: Radar, Sonar and Navigation*, vol. 149, no. 4, pp. 166–173, 2002.
- [20] R. Klemm, W. Koch, and U. Nickel, "Ground target tracking with adaptive monopulse radar," in *Proceedings of the European Microwave Association*, vol. 3, pp. 47–56, 2007.
- [21] W. R. Blanding, W. Koch, and U. Nickel, "Adaptive phased-array tracking in ECM using negative information," *IEEE Transactions on Aerospace and Electronic Systems*, vol. 45, no. 1, pp. 152–166, 2009.
- [22] M. Feldmann and U. Nickel, "Target parameter estimation and tracking with adaptive beamforming," in *Proceedings of the International Radar Symposium (IRS '11)*, pp. 585–590, September 2011.
- [23] G. S. Liao, Z. Bao, and Y. H. Zhang, "On clutter DOF for phased array airborne early warning radars," *Journal of Electronics*, vol. 10, no. 4, pp. 307–314, 1993.
- [24] W. Blanding, W. Koch, and U. Nickel, "On adaptive phased-array tracking in the presence of main-lobe jammer suppression," in *Signal and Data Processing of Small Targets*, vol. 6236 of *Proceedings of SPIE*, Orlando, Fla, USA, April 2006.
- [25] A. Farina, G. Golino, S. Immediata, L. Ortenzi, and L. Timmoneri, "Techniques to design sub-arrays for radar antennas," in *Proceedings of the 12th International Conference on Antennas and Propagation (ICAP '03)*, vol. 1, pp. 17–23, 2003.
- [26] A. Farina, "Electronic counter-countermeasures," in *Radar Handbook*, M. I. Skolnik, Ed., chapter 24, McGraw-Hill, 3rd edition, 2008.
- [27] A. Farina, G. Golino, and L. Timmoneri, "Maximum likelihood approach to the estimate of target angular co-ordinates under a main beam interference condition," in *Proceedings of the International Conference on Radar*, pp. 834–838, Beijing, China, 2001.
- [28] G. Golino, "Improved genetic algorithm for the design of the optimal antenna division in sub-arrays: a multi-objective genetic algorithm," in *Proceedings of the IEEE International Radar Conference*, pp. 629–634, Washington, DC, USA, 2005.
- [29] P. Lombardo and D. Pastina, "Pattern control for adaptive antenna processing with overlapped sub-arrays," in *Proceedings of the International Conference on Radar*, pp. 188–193, Adelaide, Australia, September 2003.
- [30] P. Lombardo and D. Pastina, "Quiescent pattern control in adaptive antenna processing at sub-array level," in *Proceedings of the IEEE International Symposium on Phased Array Systems and Technology*, pp. 176–181, Boston, Mass, USA, October 2003.
- [31] P. Lombardo, R. Cardinali, M. Bucciarelli, D. Pastina, and A. Farina, "Planar thinned arrays: optimization and subarray based adaptive processing," *International Journal of Antennas and Propagation*, vol. 2013, Article ID 206173, 13 pages, 2013.
- [32] P. Lombardo, R. Cardinali, D. Pastina, M. Bucciarelli, and A. Farina, "Array optimization and adaptive processing for sub-array based thinned arrays," in *Proceedings of the International Conference on Radar (Radar '08)*, pp. 197–202, Adelaide, Australia, September 2008.
- [33] A. Massa, M. Pastorino, and A. Randazzo, "Optimization of the directivity of a monopulse antenna with a subarray weighting by a hybrid differential evolution method," *IEEE Antennas and Wireless Propagation Letters*, vol. 5, no. 1, pp. 155–158, 2006.
- [34] S. Caorsi, A. Massa, M. Pastorino, and A. Randazzo, "Optimization of the difference patterns for monopulse antennas by a hybrid real/integer-coded differential evolution method," *IEEE Transactions on Antennas and Propagation*, vol. 53, no. 1, pp. 372–376, 2005.
- [35] L. Manica, P. Rocca, and A. Massa, "Design of subarrayed linear and planar array antennas with SLL control based on an excitation matching approach," *IEEE Transactions on Antennas and Propagation*, vol. 57, no. 6, pp. 1684–1691, 2009.
- [36] L. Manica, P. Rocca, and A. Massa, "Excitation matching procedure for sub-arrayed monopulse arrays with maximum directivity," *IET Radar, Sonar and Navigation*, vol. 3, no. 1, pp. 42–48, 2009.
- [37] Y. F. Kong, C. Zeng, G. S. Liao, and H. H. Tao, "A new reduced-dimension GSC for target tracking and interference suppression," in *Proceedings of the 6th International Conference on Radar (RADAR '11)*, pp. 785–788, Chengdu, China, October 2011.
- [38] Z. Y. Xu, Z. Bao, and G. S. Liao, "A method of designing irregular subarray architectures for partially adaptive processing," in *Proceedings of the CIE International Conference on Radar (ICR '96)*, pp. 461–464, Beijing, China, October 1996.
- [39] Y. Wang, K. Duan, and W. Xie, "Cross beam STAP for non-stationary clutter suppression in airborne radar," *International Journal of Antennas and Propagation*, vol. 2013, Article ID 276310, 5 pages, 2013.
- [40] W.-C. Xie and Y.-L. Wang, "Optimization of subarray partition based on genetic algorithm," in *Proceedings of the 8th International Conference on Signal Processing (ICSP '06)*, Beijing, China, November 2006.
- [41] Z. H. Zhang, J. B. Zhu, and Y. L. Wang, "Local degrees of freedom of clutter for airborne space-time adaptive processing radar with subarrays," *IET Radar, Sonar and Navigation*, vol. 6, no. 3, pp. 130–136, 2012.

- [42] L. Y. Dai, R. F. Li, and C. Rao, "Combining sum-difference and auxiliary beams for adaptive monopulse in jamming," *Journal of Systems Engineering and Electronics*, vol. 24, no. 3, pp. 372–381, 2013.
- [43] R. Klemm, *Principles of Space-Time Adaptive Processing*, IEE, 3rd edition, 2006.
- [44] B. D. Carlson, "Covariance matrix estimation errors and diagonal loading in adaptive arrays," *IEEE Transactions on Aerospace and Electronic Systems*, vol. 24, no. 4, pp. 397–401, 1988.
- [45] C. H. Gierull, "Fast and effective method for low-rank interference suppression in presence of channel errors," *Electronics Letters*, vol. 34, no. 6, pp. 518–520, 1998.
- [46] H. Hu and X. H. Deng, "An effective ADBF method at subarray level for plane phased array," in *Proceedings of the 8th International Conference on Signal Processing (ICSP '06)*, vol. 4, Beijing, China, November 2006.
- [47] H. Hu, E. Liu, and Y. Xiao, "ADBF at subarray level using a generalized sidelobe canceller," in *Proceedings of the 3rd IEEE International Symposium on Microwave, Antenna, Propagation and EMC Technologies for Wireless Communications*, pp. 697–700, Beijing, China, October 2009.
- [48] H. Hu and E. X. Liu, "An improved GSLC at subarray level," Submitted.
- [49] H. Hu and X. Qu, "An improved subarrayed broadband ABF," Submitted.
- [50] H. Hu and X. Qu, "An improved subarrayed fast-time STAP algorithm," Submitted.
- [51] D. Wang, H. Hu, and X. Qu, "Space-time adaptive processing method at subarray level for broadband jammer suppression," in *Proceedings of the 2nd IEEE International Conference on Microwave Technology and Computational Electromagnetics (ICMTCE '11)*, pp. 281–284, Beijing, China, May 2011.
- [52] H. Hu and W. H. Liu, "A novel analog and digital weighting approach for sum and difference beam of planar array at subarray level," *Chinese Journal of Electronics*, vol. 19, no. 3, pp. 468–472, 2010.
- [53] H. Hu, W.-H. Liu, and Q. Wu, "A kind of effective side lobe suppression approach for beam scanning at sub-array level," *Journal of Electronics & Information Technology*, vol. 31, no. 8, pp. 1867–1871, 2009 (Chinese).
- [54] A. S. Paine, "Minimum variance monopulse technique for an adaptive phased array radar," *IEE Proceedings—Radar, Sonar and Navigation*, vol. 145, no. 6, pp. 374–380, 1998.
- [55] R. L. Fante, "Synthesis of adaptive monopulse patterns," *IEEE Transactions on Antennas and Propagation*, vol. 47, no. 5, pp. 773–774, 1999.
- [56] K. B. Yu and D. J. Murrow, "Adaptive digital beamforming for angle estimation in jamming," *IEEE Transactions on Aerospace and Electronic Systems*, vol. 37, no. 2, pp. 508–523, 2001.
- [57] H. Hu and H. Zhang, "An improved two-stage processing approach of adaptive monopulse at subarray level," *Acta Electronica Sinica*, vol. 37, no. 9, pp. 1996–2003, 2009 (Chinese).
- [58] R. L. Fante, R. M. Davis, and T. P. Guella, "Wideband cancellation of multiple mainbeam jammers," *IEEE Transactions on Antennas and Propagation*, vol. 44, no. 10, pp. 1402–1413, 1996.
- [59] C. M. See and A. B. Gershman, "Direction-of-arrival estimation in partly calibrated subarray-based sensor arrays," *IEEE Transactions on Signal Processing*, vol. 52, no. 2, pp. 329–337, 2004.
- [60] H. Hu and X. W. Jing, "2-D WSF method at subarray level based on ideal patterns," in *Proceedings of the International Conference on Radar*, pp. 1161–1164, Beijing, China, 2006.
- [61] H. Hu and X. W. Jing, "2-D spatial spectrum estimation methods at subarray level for phased array," *Acta Electronica Sinica*, vol. 35, pp. 415–419, 2007 (Chinese).
- [62] H. Hu and X. W. Jing, "An improved super-resolution direction finding method at subarray level for coherent sources," in *Proceedings of the CIE International Conference on Radar (ICR '06)*, pp. 525–528, Shanghai, China, October 2006.
- [63] H. Hu and X.-W. Jing, "A new super-resolution method at subarray level in planar phased array for coherent source," *Acta Electronica Sinica*, vol. 36, no. 6, pp. 1052–1057, 2008 (Chinese).
- [64] H. Hu, X. Liu, and L. J. Liang, "Study on the broadband superresolution direction finding at subarray level," Submitted.
- [65] H. Hu, W. C. Qin, and S. Feng, "Optimizing the architecture of planar phased array by improved genetic algorithm," in *Proceedings of the IEEE International Symposium on Microwave, Antenna, Propagation, and EMC Technologies for Wireless Communications (MAPE '07)*, pp. 676–679, Hangzhou, China, August 2007.
- [66] A. Hassanien and S. A. Vorobyov, "Phased-MIMO radar: a tradeoff between phased-array and MIMO radars," *IEEE Transactions on Signal Processing*, vol. 58, no. 6, pp. 3137–3151, 2010.
- [67] X. P. Luan, H. Hu, and X. Hu, "Analysis on pattern features of MIMO-phased array hybrid radar," Submitted.
- [68] D. R. Fuhrmann, J. P. Browning, and M. Rangaswamy, "Signaling strategies for the hybrid MIMO phased-array radar," *IEEE Journal on Selected Topics in Signal Processing*, vol. 4, no. 1, pp. 66–78, 2010.
- [69] X. P. Luan, H. Hu, and N. Xiao, "A synthesis algorithm of transmitting beam pattern for MIMO-PAR," Submitted.

Research Article

An Improved Peak Sidelobe Reduction Method for Subarrayed Beam Scanning

Hang Hu,¹ Xuepeng Luan,² Guanglei Zhang,³ Ke Song,⁴ Weihui Liu,¹ and Chenghu Mou⁴

¹School of Electronics and Information Engineering, Harbin Institute of Technology, Harbin 150001, China

²College of Computer & Information Science, Three Gorges University, Yichang, Hubei 443002, China

³RAA Integrated Microwave RF Simulation System, Radar and Avionics Institute of AVIC, Wuxi, Jiangsu 214063, China

⁴No. 802 Institute of SAST, Shanghai 200090, China

Correspondence should be addressed to Hang Hu; huhang@hit.edu.cn

Received 20 June 2014; Accepted 6 December 2014

Academic Editor: Ahmed Shaharyar Khwaja

Copyright © 2015 Hang Hu et al. This is an open access article distributed under the Creative Commons Attribution License, which permits unrestricted use, distribution, and reproduction in any medium, provided the original work is properly cited.

This paper focused on PSL (peak sidelobe level) reduction for subarrayed beam scanning in phased array radars. The desired GSP (Gaussian Subarray Patterns) are achieved by creating a subarray weighting network. The GSP-based method could reduce PSL of array pattern; compared with the method based on the desired subarray pattern which is defined by ideal space-domain filter, the PSL reduction performance is improved remarkably. Further, based on the concept adopting super-element patterns to approximately express original subarray patterns, the simplified GSP-based method is proposed. So the dimension of each matrix required for creating the weighting network, which was originally the same as the element number, could be reduced to the same as the subarray number. Consequently, we achieve remarkable reduction of the computation burden; simultaneously, the PSL mitigation performance is degraded slightly. Simulation results demonstrate the validity of the introduced methods.

1. Introduction

In modern PAR (phased array radars) and particularly multi-functional PAR, the subarray structure is usually adopted [1–4] and subarrayed array processing is a key technique [5–9]. For subarrayed PAR, the look direction is usually controlled by the phase shifters [1]. However, further digital scanning at subarray level is required for forming multiple beams and many other applications. The look direction is steered into a certain direction by the phase shifters and then SBS (subarrayed beam scanning) is used for a limited sector of look directions around the presteered direction.

Typically with SBS, the PSL will increase rapidly with the scanning direction departing from the original look direction. Therefore, the requirement for PSL reduction arises. The resulting array pattern is composed of the pattern of each subarray. Usually, the shape and beamwidth of the subarray patterns are different. Each subarray pattern has a high PSL which contributes to a high PSL of the array pattern. If the

pattern of each subarray would have good coherence in the main beam and have a low PSL, the PSL of the array pattern could be reduced for SBS.

Nickel made a first investigation for reducing the PSL with SBS. In his paper [4], the SLL with SBS was reduced to some degree by inserting a matrix operation with the objective of making the new subarray pattern approach an ideal one based on LMS criterion. Therein, the ideal subarray pattern is set as Ideal Space-Domain Filter (ISDF in short) which is constant within the main lobe and zero otherwise.

This paper introduces Gaussian Subarray Pattern (GSP for short) [5] as the desired pattern in order to improve the PSL with SBS. For the GSP, the gain is set very low outside the main beam which is better suited to reduce the PSL. However, in GSP-based method, the dimension of the matrix for creating WN (weighting network) is the same as the element number. Therefore, the computational burden is enormous for the PAR containing hundreds or even thousands of elements.

Therefore, this paper adopts the methodology of regarding the array as a superarray and each subarray as a superelement, and representing the superelements by the corresponding subarray's phase center and gain. When creating the WN, the superelement pattern approximately represents the pattern for the new subarray obtained by WN. By using this simplification, the dimension of each matrix for creating WN would be reduced to the subarray number. Therefore, the simplification could reduce the computational burden remarkably, compared with GSP-based one. This simplification method is named Simplified GSP (SGSP for short) in this paper.

2. Array Pattern of SBS

Assuming a planar phased array with M omnidirectional elements located on the xoy plane, take the first element as the origin of the coordinate system and let (x_m, y_m) be the coordinate of the m th ($m = 1, \dots, M$) element. Amplitude weighting at element is used for reducing the PSL of the sum beam. The weight of the m th element is $w_{\text{ele},m}$ and array look direction is (θ_0, φ_0) .

Let the phased array be divided into L subarrays, and let \mathbf{T}_0 represent the subarray forming matrix of $M \times L$ dimension. Let $\mathbf{W}_{\text{ele}} = \text{diag}(w_{\text{ele},m})_{m=1,2,\dots,M}$; denote $\varphi_m(\theta, \varphi) = \exp\{-j2\pi[x_m \sin \theta \cos \varphi + y_m \sin \theta \sin \varphi]/\lambda\}$ and $\Phi_0 = \text{diag}[\varphi_m^*(\theta_0, \varphi_0)]_{m=1,\dots,M}$; then, subarray transformation matrix is

$$\mathbf{T} = \Phi_0 \mathbf{W}_{\text{ele}} \mathbf{T}_0. \quad (1)$$

We consider the array as a superarray and each subarray as a superelement. The superelement position is defined as the phase centre of the subarray. For the l th subarray, the phase center is denoted by $\xi_{l,x}$ and $\xi_{l,y}$ along the x and y direction, respectively, and the gain is denoted by g_l . Then, one obtains [5]

$$\xi_{l,p} = \frac{\sum_{m \in U_l} w_{\text{ele},m} p_m}{\sum_{m \in U_l} w_{\text{ele},m}}, \quad \text{for } p = x \text{ or } y, \quad (2)$$

$$g_l = \sum_{m \in U_l} w_{\text{ele},m},$$

where U_l denotes the set of indices of elements in the l th subarray.

We introduce $a_m(u, v) = e^{j2\pi(x_m u + y_m v)/\lambda}$ and define $\mathbf{a}(u, v) = [a_1(u, v), \dots, a_m(u, v), \dots, a_M(u, v)]^T$. Suppose that $f_l(u, v)$ is the pattern of the l th subarray and we let $\mathbf{f}_{\text{sub}}(u, v) = [f_1(u, v), \dots, f_l(u, v), \dots, f_L(u, v)]^T$; then,

$$\mathbf{f}_{\text{sub}}(u, v) = \mathbf{T}^H \mathbf{a}(u, v). \quad (3)$$

The array pattern is

$$F(u, v) = \sum_{l=1}^L f_l(u, v) e^{j2\pi(\xi_{l,x}u + \xi_{l,y}v)}. \quad (4)$$

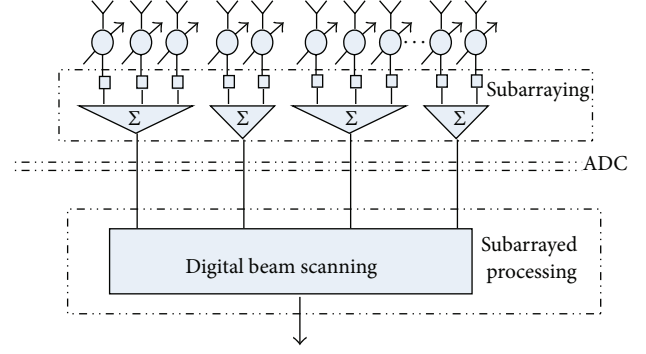


FIGURE 1: Structure of subarrayed beam scanning.

SBS is implemented by performing subarrayed digital phase shift while taking a superelement as reference element. The array pattern after scanning in this way is

$$F_{\text{Scan}}(u, v) = \sum_{l=1}^L f_l(u, v) e^{j2\pi[\xi_{l,x}(u+\Delta u) + \xi_{l,y}(v+\Delta v)]} \quad (5)$$

in which Δu and Δv represent the scan angles in u and v direction.

The concept of the subarrayed beam scanning is indicated in Figure 1.

3. SGSP-Based SLL Reduction for SBS

To suppress the PSL after SBS, a way is postprocessing the subarray outputs, which creates new subarrays with new patterns and new superelement. This is designed to make the new subarray pattern approximate to a desired subarray pattern according to the LMS criterion. The starting point of creating the WN is to make the new subarrays have a pattern with similar shape within the main beam and with PSLs as low as possible.

3.1. GSP-Based Weighting Network. Firstly, the desired array pattern is set as one with a shape of a Gaussian function. For l th subarray, it is expressed as [5]

$$f_l^{(\text{GSP})}(u, v) = \frac{1}{\pi\sigma^2} e^{-[(u-u_0)^2 + (v-v_0)^2]/\sigma^2} \cdot e^{j2\pi[\xi_{l,x}(u-u_0) + \xi_{l,y}(v-v_0)]/\lambda}, \quad (6)$$

where σ^2 represents the variance of Gaussian distribution function which is used to adjust the beamwidth.

The WN $\mathbf{W} = (\mathbf{w}_1, \dots, \mathbf{w}_L)$ in which \mathbf{w}_l is an L -dimensional column vector. The pattern of the l th new subarray is

$$f_{\text{new},l}(u, v) = (\mathbf{w}_l)^H \mathbf{f}_{\text{sub}}(u, v). \quad (7)$$

We consider the objective function

$$Y_l = \int_V |f_{\text{new},l}(u, v) - f_l^{(\text{GSP})}(u, v)|^2 du dv, \quad (8)$$

where $V = \{(u, v) \in \mathbb{R}^2 \mid u^2 + v^2 \leq 1\}$. Then, we have [5]

$$\mathbf{W} = (\mathbf{T}^H \mathbf{T})^{-1} \mathbf{T}^H \mathbf{C}^{-1} \mathbf{V}, \quad (9)$$

where

$$\mathbf{C} = \int_V \mathbf{a}(u, v) \mathbf{a}^H(u, v) du dv \quad (10)$$

and $\mathbf{V} = (\mathbf{v}_1, \dots, \mathbf{v}_l, \dots, \mathbf{v}_L)$, where $\mathbf{v}_l = (v_{1,l}, \dots, v_{m,l}, \dots, v_{M,l})^T$ and

$$v_{m,l} = \frac{1}{\pi\sigma^2} e^{j2\pi(x_m u_0 + y_m v_0)/\lambda} \cdot \int_V e^{j2\pi[(x_m - \xi_{l,x})(u - u_0) + (y_m - \xi_{l,y})(v - v_0)]/\lambda} \cdot e^{-[(u - u_0)^2 + (v - v_0)^2]/\sigma^2} du dv, \quad 1 \leq m \leq M. \quad (11)$$

Considering the formula (9), \mathbf{T} , \mathbf{C} , and \mathbf{V} have the dimensions $M \times L$, $M \times M$, and $M \times L$, respectively. Usually, M has an order of magnitude from several hundred to several thousand, so their extensive computations are needed to calculate \mathbf{W} .

3.2. SGSP-Based Weighting Network. A method of reducing the computational cost is proposed in the following. The idea is to represent the pattern function of the new subarray in (7) approximately. We use $\mathbf{A}_{se}(u_0, v_0)$ denoting the steering vector matrix of the superarray in the look direction:

$$\mathbf{A}_{se}(u_0, v_0) = \text{diag} \left(e^{j2\pi(\xi_{l,x}u_0 + \xi_{l,y}v_0)/\lambda} \right)_{l=1, \dots, L}. \quad (12)$$

And let

$$\mathbf{G}_{se} = \text{diag} (g_l)_{l=1, \dots, L}. \quad (13)$$

Phase shifts and gains are combined into

$$\mathbf{B}_{se} = \mathbf{A}_{se}^H(u_0, v_0) \mathbf{G}_{se}. \quad (14)$$

The steering vector of superarray is expressed as

$$\mathbf{a}_{se}(u, v) = [a_{se,1}(u, v), \dots, a_{se,l}(u, v), \dots, a_{se,L}(u, v)]^T, \quad (15)$$

where $a_{se,l}(u, v) = e^{j2\pi(\xi_{l,x}u + \xi_{l,y}v)/\lambda}$.

Let

$$\mathbf{f}'_{sub}(u, v) = \mathbf{B}_{se} \mathbf{a}_{se}(u, v) \quad (16)$$

and denote $\mathbf{f}'_{sub}(u, v) = [f'_1(u, v), \dots, f'_l(u, v), \dots, f'_L(u, v)]^T$. Substituting (14) and (15) into (16), one obtains

$$f'_l(u, v) = g_l e^{j2\pi[\xi_{l,x}(u - u_0) + \xi_{l,y}(v - v_0)]/\lambda}. \quad (17)$$

So $\mathbf{f}'_{sub}(u, v)$ is used to express the subarray pattern approximately.

Next, we adopt the WN \mathbf{W}' and denote it as $\mathbf{W}' = (\mathbf{w}'_1, \dots, \mathbf{w}'_l, \dots, \mathbf{w}'_L)$. The pattern of the new subarray obtained by \mathbf{W}' is

$$f'_{new,l}(u, v) = (\mathbf{w}'_l)^H \mathbf{f}'_{sub}(u, v). \quad (18)$$

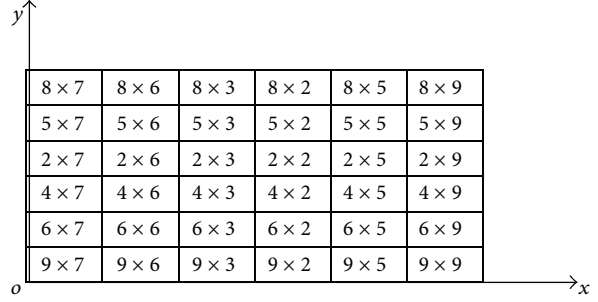


FIGURE 2: Antenna with 1088 elements on rectangular grid configured into 36 subarrays.

We determine the subarray weight such that a desired pattern is approximated in a LMS sense:

$$Y'_l = \int_V |f'_{new,l}(u, v) - f_l^{(GSP)}(u, v)|^2 du dv. \quad (19)$$

Similarly, we can obtain [5]

$$\mathbf{W}' = (\mathbf{B}_{se} \mathbf{B}_{se}^H)^{-1} \mathbf{B}_{se} (\mathbf{C}_{se})^{-1} \mathbf{V}_{se}, \quad (20)$$

where

$$\mathbf{C}_{se} = \int_V \mathbf{a}_{se}(u, v) \mathbf{a}_{se}^H(u, v) du dv \quad (21)$$

and $\mathbf{V}_{se} = (\mathbf{v}'_1, \dots, \mathbf{v}'_l, \dots, \mathbf{v}'_L)$, where $\mathbf{v}'_l = (v'_{1,l}, \dots, v'_{n,l}, \dots, v'_{L,l})^T$ and

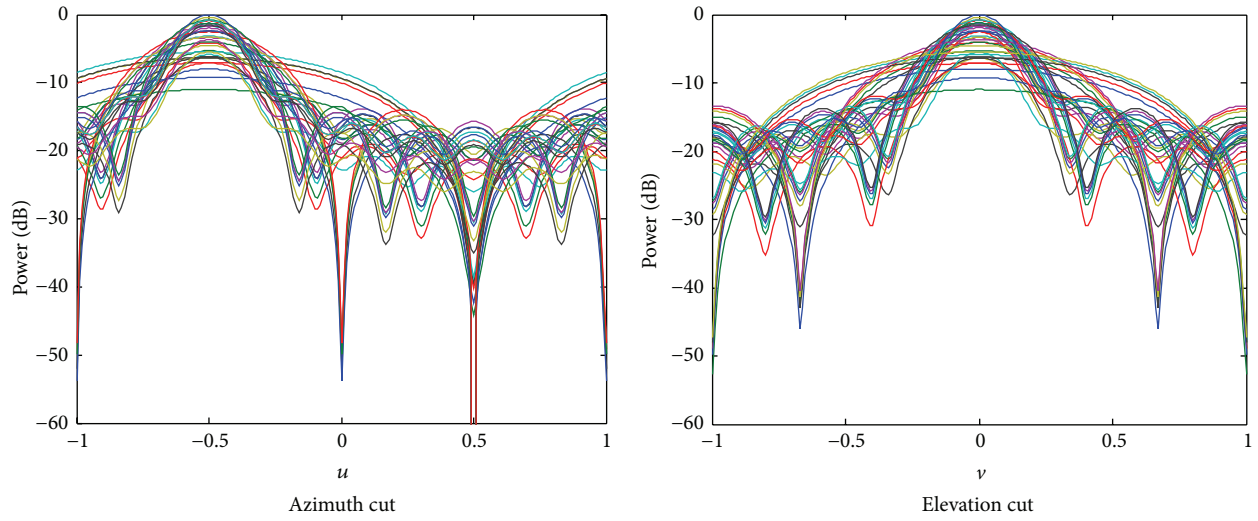
$$v'_{n,l} = \frac{1}{\pi\sigma^2} e^{j2\pi(\xi_{n,x}u_0 + \xi_{n,y}v_0)/\lambda} \cdot \int_V e^{j2\pi[(\xi_{n,x} - \xi_{l,x})(u - u_0) + (\xi_{n,y} - \xi_{l,y})(v - v_0)]/\lambda} \cdot e^{-[(u - u_0)^2 + (v - v_0)^2]/\sigma^2} du dv, \quad 1 \leq n \leq L. \quad (22)$$

Considering formula (20), the matrices required in creating \mathbf{W}' , that is, \mathbf{V}_{se} , \mathbf{B}_{se} , and \mathbf{C}_{se} , are all of dimension $L \times L$. Usually L is only a few dozens of magnitude and therefore the computational burden with \mathbf{W}' is reduced remarkably compared with \mathbf{W} .

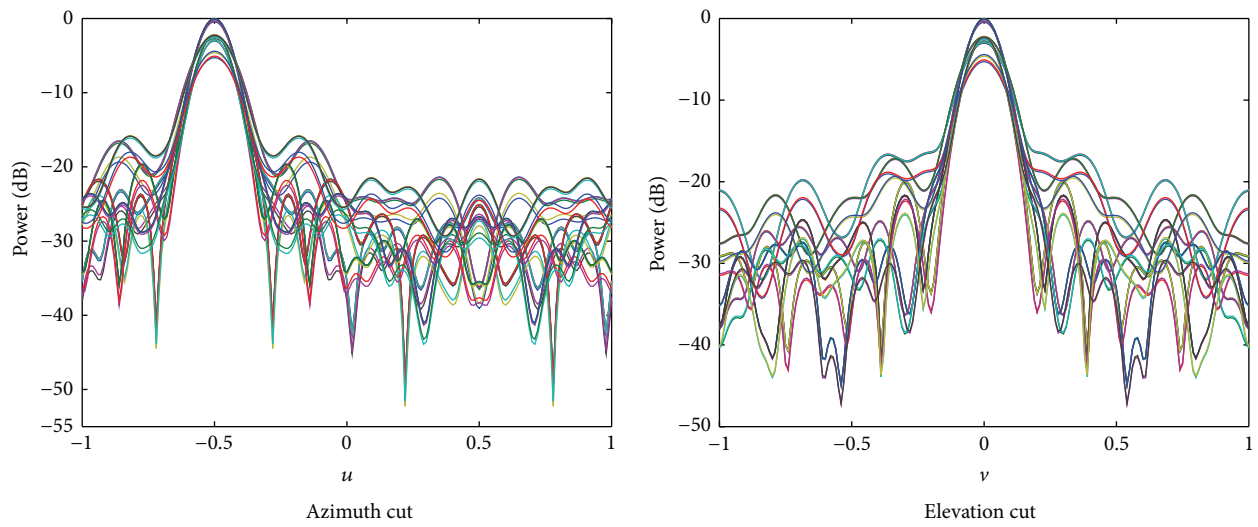
4. Simulation Results

Assume a planar array with 32×34 omnidirectional elements placed at rectangle grid on xoy plane, and the spacing between adjacent elements is $\lambda/2$. A -40 dB Taylor weighting is applied in both x and y directions. The array is divided into 6×6 subarrays and each of which is a rectangular array. The element distribution and the subarray arrangement are shown in Figure 2. We assume that the look direction is $(-0.5, 0)$, BW is the 3 dB beam width of the pattern, and σ^2 is chosen as 0.2 BW in both the GSP and the SGSP cases.

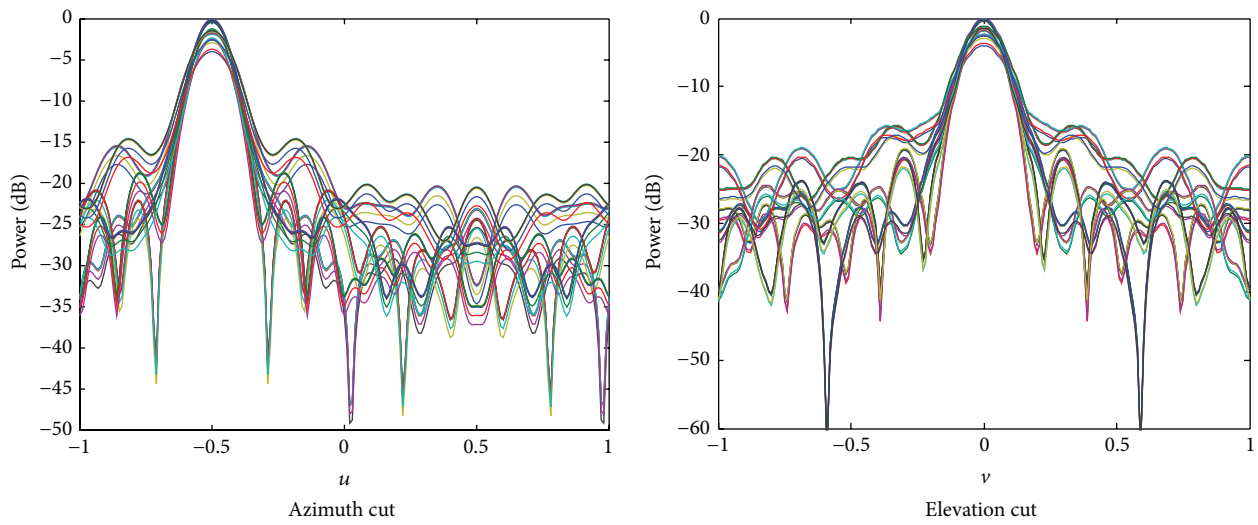
4.1. Subarray Patterns. Figure 3 shows subarray patterns obtained by different methods. Figure 3(a) shows the original



(a) Original patterns



(b) GSP



(c) SGSP

FIGURE 3: Subarray patterns obtained by several methods.

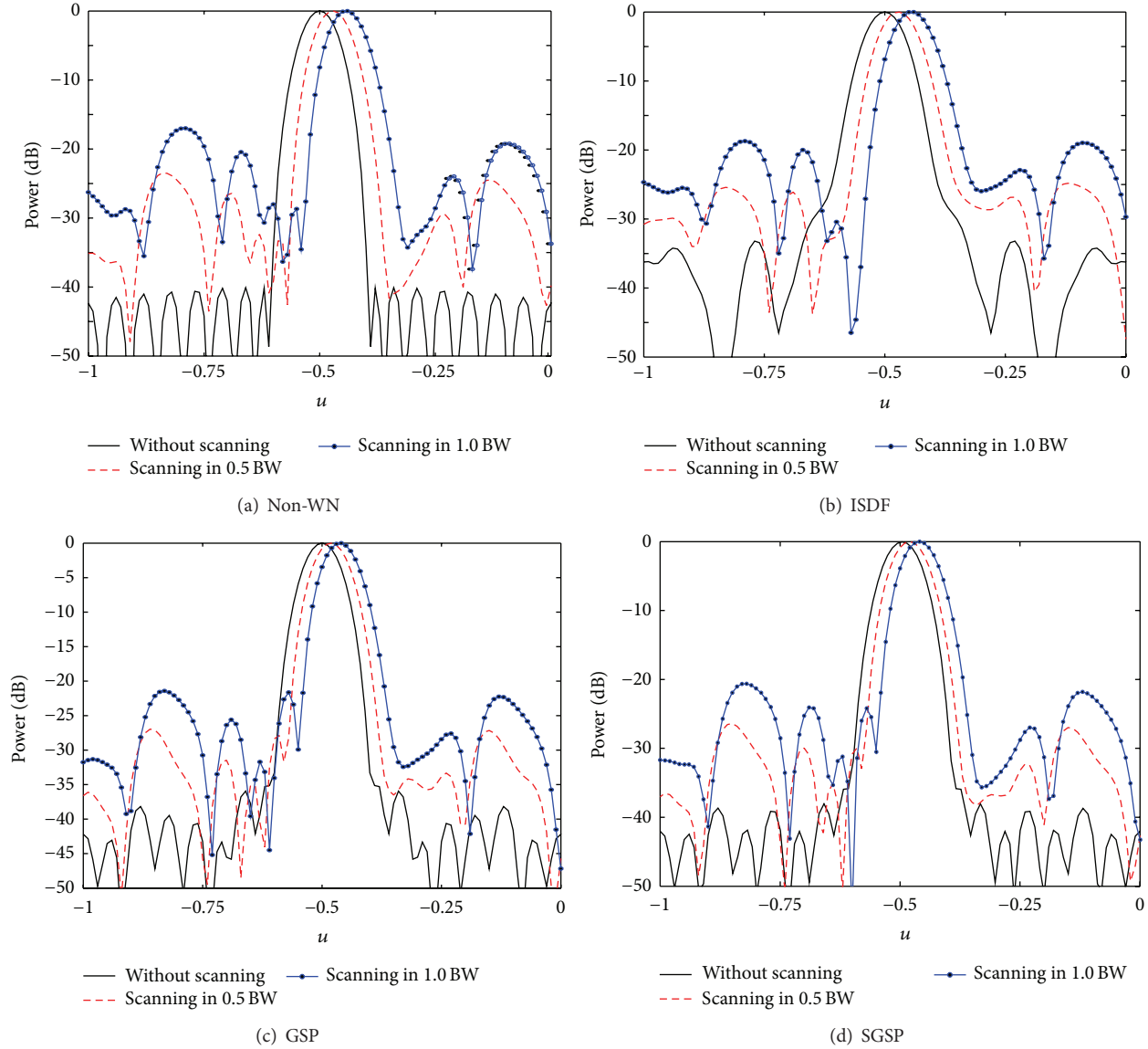


FIGURE 4: Array patterns with SBS obtained by different methods (azimuth cut).

subarray patterns. Obviously the shape and the beamwidth of each subarray pattern differ from each other greatly, and the PSL is high. Figure 3(b) shows the subarray patterns obtained by GSP. Obviously, the beam shape and beamwidth of all subarrays are very similar, and the shape of each main beam is similar to Gaussian function while the SLL is reduced effectively. Figure 3(c) shows the subarray patterns obtained by SGSP. We can see that it is very close to Figure 3(b). The beam shape, beamwidth, and gain within the main beam of each subarray are very similar, while the SLL is reduced as well. However, its SLL is slightly higher compared with Figure 3(b).

4.2. The PSL Performance after SBS. Next, simulations after SBS are given, in which scanning is carried out in u direction and the scan angle is set as 0.5 BW and 1.0 BW, respectively.

Figure 4 shows the array patterns after scanning. Subplots (a), (b), (c), and (d) show the array patterns obtained without the WN processing, with ISDF, GSP, and SGSP, respectively. The different curves are given for nonscanning and scan angles of 0.5 BW and 1.0 BW, respectively. Comparing subplots (c) and (d) with (a), it is obvious that the PSL of the pattern after scanning is reduced using both GSP and SGSP compared to the case without a WN. Comparing subplots (c) and (d) with (b), it is seen that both GSP and SGSP are superior to ISDF in the aspect of the PSL reduction capability. It can be seen that the PSL reduction of SGSP is degraded slightly compared with GSP, which can be seen from subplots (c) and (d).

The PSL values of each pattern in Figure 4 after scanning are shown in Table 1. It can be seen compared to the case without WN that for ISDF the PSL is reduced by 1.3 dB for

TABLE 1: The PSL of array pattern with SBS (dB).

Scanning range (BW)	Non-WN	ISDF		GSP		SGSP	
		PSL	Improvement	PSL	Improvement	PSL	Improvement
0.5	-23.5	-24.8	1.3	-27.0	3.5	-26.4	2.9
1.0	-17.0	-18.7	1.7	-21.4	4.4	-20.6	3.6

0.5 BW scanning and 1.7 dB for 1 BW, while for GSP the PSL is reduced by 3.5 dB and 4.4 dB, respectively. Thus, the PSL of GSP is improved by 2.1 dB for 0.5 BW scanning and 2.7 dB for the 1 BW compared with ISDF. Consequently, the GSP improves remarkably ISDF as PSL of the latter is only reduced by more than 1 dB compared with non-WN. SGSP has a good PSL reduction, too, which PSL is just degraded by 0.6 dB for 0.5 BW scanning and 0.8 dB for 1 BW, compared with GSP.

5. Conclusions

- (1) The GSP can reduce the PSL of the array pattern with SBS effectively, while the computational cost is equivalent compared with the ISDF method. For SGSP, the dimension of each matrix for creating the WN is the same as the subarray number. Consequently, the computational cost is reduced remarkably compared with GSP in which the matrix dimension is equal to the element number. Furthermore, the PSL reduction of SGSP degrades only slightly compared with the latter.
- (2) For the WN-based method, the construction of more effective desired subarray pattern is the way to improve the PSL mitigation performance further.

Conflict of Interests

The authors declare that there is no conflict of interests regarding the publication of this paper.

Acknowledgments

The authors would like to thank Dr. Ulrich Nickel of Fraunhofer FKIE, Germany, for his insightful comments and useful discussions. This work has been partially supported by the Fundamental Research Funds for the Central Universities (Grant no. HIT.NSRIF.201152), the ASFC (Aeronautical Science Foundation of China, no. 20132077016), and the SAST Foundation (no. SAST201339).

References

- [1] U. Nickel, "Array processing for radar: achievements and challenges," *International Journal of Antennas and Propagation*, vol. 2013, Article ID 261230, 21 pages, 2013.
- [2] A. Farina, G. Golino, and S. Immediata, "Techniques to design sub-arrays for radar antennas," in *Proceedings of the International Conference on Antennas and Propagation*, pp. 17–23, Exeter, UK, 2003.
- [3] P. Lombardo and D. Pastina, "Pattern control for adaptive antenna processing with overlapped sub-arrays," in *Proceedings of the International Conference on Radar*, pp. 188–193, Adelaide, Australia, 2003.
- [4] U. Nickel, "Properties of digital beamforming with subarrays," in *Proceedings of the International Conference on Radar (CIE '06)*, pp. 1–5, Shanghai, China, October 2006.
- [5] U. Nickel, "Spotlight MUSIC: super-resolution with subarrays with low calibration effort," *IEE Proceedings: Radar, Sonar and Navigation*, vol. 149, no. 4, pp. 166–173, 2002.
- [6] R. L. Fante, R. M. Davis, and T. P. Guella, "Wideband cancellation of multiple mainbeam jammers," *IEEE Transactions on Antennas and Propagation*, vol. 44, no. 10, pp. 1402–1413, 1996.
- [7] H. Hu and W. H. Liu, "A novel analog and digital weighting approach for sum and difference beam of planar array at subarray level," *Chinese Journal of Electronics*, vol. 19, no. 3, pp. 468–472, 2010.
- [8] L. Manica, P. Rocca, and A. Massa, "Design of subarrayed linear and planar array antennas with SLL control based on an excitation matching approach," *IEEE Transactions on Antennas and Propagation*, vol. 57, no. 6, pp. 1684–1691, 2009.
- [9] Y. L. Wang, K. Q. Duan, and W. C. Xie, "Cross beam STAP for nonstationary clutter suppression in airborne radar," *International Journal of Antennas and Propagation*, vol. 2013, Article ID 276310, 5 pages, 2013.

Research Article

Two-Dimensional DOA Estimation for Uniform Rectangular Array Using Reduced-Dimension Propagator Method

Ming Zhou,¹ Xiaofei Zhang,¹ Xiaofeng Qiu,² and Chenghua Wang¹

¹Key Laboratory of Radar Imaging and Microwave Photonics (Nanjing University of Aeronautics and Astronautics), Ministry of Education, Nanjing 210016, China

²Institute of Command Information System, PLA University of Science and Technology, Nanjing 210007, China

Correspondence should be addressed to Ming Zhou; zm_nuaa2012@163.com

Received 17 May 2014; Revised 3 August 2014; Accepted 17 August 2014

Academic Editor: Ahmed Shaharyar Khwaja

Copyright © 2015 Ming Zhou et al. This is an open access article distributed under the Creative Commons Attribution License, which permits unrestricted use, distribution, and reproduction in any medium, provided the original work is properly cited.

A novel algorithm is proposed for two-dimensional direction of arrival (2D-DOA) estimation with uniform rectangular array using reduced-dimension propagator method (RD-PM). The proposed algorithm requires no eigenvalue decomposition of the covariance matrix of the receive data and simplifies two-dimensional global searching in two-dimensional PM (2D-PM) to one-dimensional local searching. The complexity of the proposed algorithm is much lower than that of 2D-PM. The angle estimation performance of the proposed algorithm is better than that of estimation of signal parameters via rotational invariance techniques (ESPRIT) algorithm and conventional PM algorithms, also very close to 2D-PM. The angle estimation error and Cramér-Rao bound (CRB) are derived in this paper. Furthermore, the proposed algorithm can achieve automatically paired 2D-DOA estimation. The simulation results verify the effectiveness of the algorithm.

1. Introduction

Direction-of-arrival (DOA) estimation is a fundamental problem in array signal processing and has been widely used in many fields [1–5]. Till now, many algorithms have been proposed for DOA estimation with uniform linear array. Among them, multiple signal classification (MUSIC) algorithm [6] and estimation of signal parameters via rotational invariance technique (ESPRIT) algorithm [7] are widely used superresolution methods. The two-dimensional DOA (2D-DOA) estimation problem, which plays an important role in array signal processing, has received more attention. This problem is usually considered with rectangular array, two parallel uniform linear arrays, L-shape array, and so forth. Also, many algorithms have been considered for 2D-DOA estimation, which include 2D-MUSIC algorithm [8], 2D Unitary ESPRIT algorithm [9], modified 2D-ESPRIT algorithm [10], matrix pencil methods [11, 12], maximum likelihood method [13], parallel factor (PARAFAC) algorithm [14], and high order cumulant method [15].

Propagator method, which is known as a low complexity method without eigenvalue decomposition (EVD) of

the covariance matrix of the received data, has been proposed for DOA estimation through peak searching [17–20]. Due to its low complexity, PM algorithms are widely used for 2D-DOA estimation. In [21], a PM-based DOA estimation algorithm is proposed for two parallel uniform linear arrays via the rotational invariance property of propagator matrix, which requires extra pairing match. Reference [22] presents an efficient 2D-DOA estimation algorithm with two parallel uniform linear arrays using PM. In [23], an improved PM algorithm is proposed for 2D-DOA estimation, which has better angle estimation performance than the algorithms in [21, 22]. The above-mentioned PM algorithms can be extended to the rectangular array for 2D-DOA estimation; however, they only employ the rotational invariance property of propagator matrices, and as a result of that, the accuracy of angle estimation performance is not sufficient in some cases, especially with low signal to noise ratio (SNR). Two-dimensional PM (2D-PM) algorithm through peak searching can be extended for 2D-DOA estimation; however, the high computational complexity caused by 2D peak searching makes it inefficient.

In this paper, we derive a reduced-dimension PM (RD-PM) algorithm, which reduces the high complexity for 2D-DOA estimation with uniform rectangular array compared with 2D-PM algorithm. The proposed algorithm applies the rotational invariance property of propagator matrix to get the initial angle estimation and then employs one-dimensional local searching to get more accurate angle and finally obtains the other angle via least square (LS) method and estimate azimuth and elevation angles. The proposed algorithm has the following advantages: (1) the proposed algorithm has lower computational complexity than 2D-PM algorithm since it requires no EVD of the covariance matrix of the receive data and it only requires one-dimensional local searching; (2) the angle estimation performance of the proposed algorithm is better than that of ESPRIT algorithm and the PM algorithms in [21, 23], also very close to that of 2D-PM algorithm; (3) it can obtain automatically paired parameters estimation.

The remainder of this paper is structured as follows: Section 2 shows the data model for uniform rectangular array, while Section 3 proposes the RD-PM algorithm for 2D-DOA estimation. The angle estimation error is derived as well as CRB in Section 4. In Section 5, the simulation results verify the feasibility and effectiveness of the proposed algorithm, and the conclusions are showed in Section 6.

Notion. $(\cdot)^T$, $(\cdot)^H$, $(\cdot)^{-1}$, and $(\cdot)^+$ denote transpose, conjugate-transpose, inverse, and pseudoinverse operations, respectively; $\text{diag}(\mathbf{v})$ stands for diagonal matrix whose diagonal element is a vector \mathbf{v} ; $\mathbf{1}_P$, \mathbf{I}_P , and $\mathbf{0}_P$ denote a $P \times 1$ vector of ones, a $P \times P$ identity matrix, and a $P \times 1$ vector of zeros, respectively. \otimes , \circ , and \odot are the Kronecker product, the Khatri-Rao product, and the Hadamard product, respectively; $\angle(\cdot)$ is to get the phase angle.

2. Data Model

As illustrated in Figure 1, consider a uniform rectangular array having $M \times N$ sensors; M and N are the numbers of sensors in x -axis and y -axis, respectively. The distance between the two adjacent elements is d in both x -axis and y -axis. Assume that there are K uncorrelated sources, and θ_k , ϕ_k are the elevation and azimuth angles of the k th source.

The received signal of the first subarray $\mathbf{x}_1(t)$ can be expressed as

$$\mathbf{x}_1(t) = \mathbf{A}_x \mathbf{s}(t) + \mathbf{n}_1(t), \quad (1)$$

where $\mathbf{A}_x = [\mathbf{a}_x(\phi_1, \theta_1), \mathbf{a}_x(\phi_2, \theta_2), \dots, \mathbf{a}_x(\phi_K, \theta_K)]$, $\mathbf{a}_x(\phi_k, \theta_k) = [1, e^{-j2\pi d \sin \theta_k \cos \phi_k / \lambda}, \dots, e^{-j2\pi(M-1)d \sin \theta_k \cos \phi_k / \lambda}]^T$, and λ is the wavelength. $\mathbf{n}_1(t)$ is the additive white Gaussian noise of the first subarray and $\mathbf{s}(t) \in \mathbb{C}^{K \times 1}$ is the source vector.

Similarly, the received signal of the n th subarray $\mathbf{x}_n(t)$ in the rectangular array is also denoted as

$$\mathbf{x}_n(t) = \mathbf{A}_x \Phi^{n-1} \mathbf{s}(t) + \mathbf{n}_n(t), \quad (2)$$

where $\Phi = \text{diag}(e^{-j2\pi d \sin \theta_1 \sin \phi_1 / \lambda}, \dots, e^{-j2\pi d \sin \theta_K \sin \phi_K / \lambda})$ and $\mathbf{n}_n(t)$ is the additive white Gaussian noise of the n th subarray.

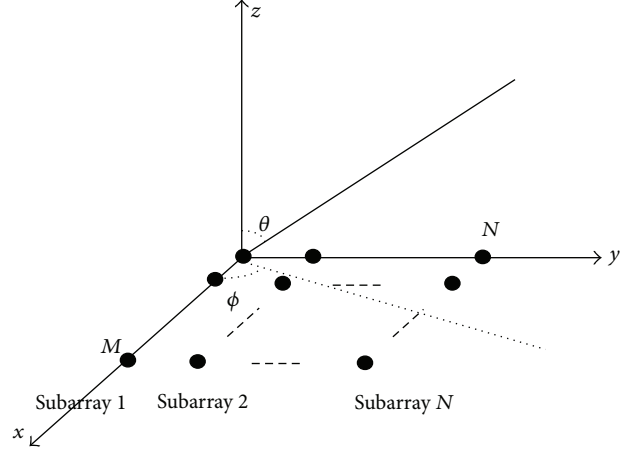


FIGURE 1: The structure of uniform rectangular array [16].

So the integrated received signal of the rectangular array is shown as follows:

$$\mathbf{x}(t) = \begin{bmatrix} \mathbf{x}_1(t) \\ \mathbf{x}_2(t) \\ \vdots \\ \mathbf{x}_N(t) \end{bmatrix} = \begin{bmatrix} \mathbf{A}_x \\ \mathbf{A}_x \Phi \\ \vdots \\ \mathbf{A}_x \Phi^{N-1} \end{bmatrix} \mathbf{s}(t) + \begin{bmatrix} \mathbf{n}_1(t) \\ \mathbf{n}_2(t) \\ \vdots \\ \mathbf{n}_N(t) \end{bmatrix}, \quad (3)$$

where $\mathbf{x}_i(t)$ ($i = 1, \dots, N$) stands for the received signal of the i th subarray. Equation (3) is also denoted as

$$\begin{aligned} \mathbf{x}(t) &= [\mathbf{A}_y \circ \mathbf{A}_x] \mathbf{s}(t) + \mathbf{n}(t) \\ &= \mathbf{A} \mathbf{s}(t) + \mathbf{n}(t), \end{aligned} \quad (4)$$

where $\mathbf{A} = \mathbf{A}_y \circ \mathbf{A}_x$, $\mathbf{A}_y = [\mathbf{a}_y(\phi_1, \theta_1), \mathbf{a}_y(\phi_2, \theta_2), \dots, \mathbf{a}_y(\phi_K, \theta_K)]$, $\mathbf{a}_y(\phi_k, \theta_k) = [1, e^{-j2\pi d \sin \theta_k \sin \phi_k / \lambda}, \dots, e^{-j2\pi(M-1)d \sin \theta_k \sin \phi_k / \lambda}]^T$, and $\mathbf{n}(t) = [\mathbf{n}_1(t)^T, \mathbf{n}_2(t)^T, \dots, \mathbf{n}_N(t)^T]^T$.

For the signal model in (4), we collect J snapshots to get the covariance matrix $\widehat{\mathbf{R}}_x$ as

$$\widehat{\mathbf{R}}_x = \frac{1}{J} \sum_{j=1}^J \mathbf{x}(t_j) \mathbf{x}^H(t_j). \quad (5)$$

3. Two-Dimensional DOA Estimation Algorithm

3.1. 2D-PM Algorithm. In this section, we give a brief introduction of 2D-PM algorithm.

Partition the matrix \mathbf{A} as

$$\mathbf{A} = \begin{bmatrix} \mathbf{A}_1 \\ \mathbf{A}_2 \end{bmatrix}, \quad (6)$$

where $\mathbf{A}_1 \in \mathbb{C}^{K \times K}$ and $\mathbf{A}_2 \in \mathbb{C}^{(MN-K) \times K}$. Since \mathbf{A}_1 is a $K \times K$ nonsingular matrix, \mathbf{A}_2 is a linear transformation of \mathbf{A}_1 as [17]

$$\mathbf{A}_2 = \mathbf{P}^H \mathbf{A}_1, \quad (7)$$

where $\mathbf{P} \in \mathbb{C}^{K \times (MN-K)}$ is the propagator matrix. We define the matrix \mathbf{Q} as

$$\mathbf{Q} = \begin{bmatrix} \mathbf{P} \\ -\mathbf{I}_{MN-K} \end{bmatrix}. \quad (8)$$

According to (6) and (7), we have

$$\mathbf{Q}^H \mathbf{A} = \mathbf{0}_{(MN-K) \times K}. \quad (9)$$

Then, we construct the function of the 2D-PM spatial spectrum as

$$F_{2D-PM}(\theta, \phi) = \frac{1}{[\mathbf{a}_y(\phi) \otimes \mathbf{a}_x(\theta)]^H \mathbf{Q} \mathbf{Q}^H [\mathbf{a}_y(\phi) \otimes \mathbf{a}_x(\theta)]}. \quad (10)$$

By searching ϕ and θ , the K largest peaks of the costing function in (10) correspond to the angles information. However, the high computational cost caused by the 2D peak searching makes this algorithm inefficient.

For estimating the propagator matrix \mathbf{P} , we partition the covariance matrix $\widehat{\mathbf{R}}_x$ as

$$\widehat{\mathbf{R}}_x = [\widehat{\mathbf{G}}, \widehat{\mathbf{H}}], \quad (11)$$

where $\widehat{\mathbf{G}} \in \mathbb{C}^{MN \times K}$, $\widehat{\mathbf{H}} \in \mathbb{C}^{MN \times (MN-K)}$. The propagator matrix $\widehat{\mathbf{P}}$ meets the minimization problem $J_{\text{csm}}(\widehat{\mathbf{P}}) = \|\widehat{\mathbf{H}} - \widehat{\mathbf{G}}\widehat{\mathbf{P}}\|^2$, and the estimation of $\widehat{\mathbf{P}}$ is

$$\widehat{\mathbf{P}} = (\widehat{\mathbf{G}}^H \widehat{\mathbf{G}})^{-1} \widehat{\mathbf{G}}^H \widehat{\mathbf{H}}. \quad (12)$$

3.2. Reduced-Dimension Propagator Method for 2D-DOA Estimation

3.2.1. Initial Estimation. Define

$$u \triangleq \sin \theta \cos \phi, \quad v \triangleq \sin \theta \sin \phi. \quad (13)$$

Then, $\mathbf{a}_x(\phi, \theta)$ and $\mathbf{a}_y(\phi, \theta)$ can be rewritten as

$$\mathbf{a}_x(v) = [1, e^{-j2\pi dv/\lambda}, \dots, e^{-j2\pi(N-1)dv/\lambda}]^T \quad (14)$$

$$\mathbf{a}_y(u) = [1, e^{-j2\pi du/\lambda}, \dots, e^{-j2\pi(M-1)du/\lambda}]^T.$$

Construct matrix \mathbf{P}_c as

$$\mathbf{P}_c = \begin{bmatrix} \mathbf{I}_K \\ \mathbf{P}^H \end{bmatrix}. \quad (15)$$

Divide \mathbf{P}_c into N blocks as $\mathbf{P}_c = [\mathbf{P}_{c1}^T, \mathbf{P}_{c2}^T, \dots, \mathbf{P}_{cN}^T]^T$, and every block contains $M \times K$ elements. Construct $\mathbf{P}_1 = [\mathbf{P}_{c1}^T, \mathbf{P}_{c2}^T, \dots, \mathbf{P}_{c(N-1)}^T]^T$ and $\mathbf{P}_2 = [\mathbf{P}_{c2}^T, \mathbf{P}_{c3}^T, \dots, \mathbf{P}_{cN}^T]^T$; then we have

$$\mathbf{P}_2 = \mathbf{P}_1 \mathbf{T}^{-1} \Phi \mathbf{T}, \quad (16)$$

where $\Phi = \text{diag}(e^{-j2\pi du_1/\lambda}, \dots, e^{-j2\pi du_k/\lambda})$. Use EVD of $\mathbf{P}_1^+ \mathbf{P}_2$ and obtain the k th eigenvalue as p_k ; then the initial estimation of $\widehat{u}_k^{\text{ini}}$ is

$$\widehat{u}_k^{\text{ini}} = \frac{-\text{angle}(p_k) \lambda}{(2\pi d)}. \quad (17)$$

3.2.2. 2D-DOA Estimation. Define

$$\mathbf{V}(u, v) = [\mathbf{a}_y(u) \otimes \mathbf{a}_x(v)]^H \mathbf{Q} \mathbf{Q}^H [\mathbf{a}_y(u) \otimes \mathbf{a}_x(v)]. \quad (18)$$

Equation (18) can also be denoted as

$$\begin{aligned} \mathbf{V}(u, v) &= \mathbf{a}_x(v)^H [\mathbf{a}_y(u) \otimes \mathbf{I}_M]^H \mathbf{Q} \mathbf{Q}^H [\mathbf{a}_y(u) \otimes \mathbf{I}_M] \mathbf{a}_x(v) \\ &= \mathbf{a}_x(v)^H \mathbf{C}(u) \mathbf{a}_x(v), \end{aligned} \quad (19)$$

where $\mathbf{C}(u) = [\mathbf{a}_y(u) \otimes \mathbf{I}_M]^H \mathbf{Q} \mathbf{Q}^H [\mathbf{a}_y(u) \otimes \mathbf{I}_M]$. Equation (19) is the problem of quadratic optimization. We consider the constraint $\mathbf{e}_1^H \mathbf{a}_x(v) = 1$, where $\mathbf{e}_1 = [1, 0, \dots, 0]^T \in \mathbb{R}^{M \times 1}$. The optimization problem can be reconstructed via linearly constrained minimum variance as [24]

$$\begin{aligned} \min_{u, v} \quad & \mathbf{a}_x(v)^H \mathbf{C}(u) \mathbf{a}_x(v), \\ \text{s.t.} \quad & \mathbf{e}_1^H \mathbf{a}_x(v) = 1. \end{aligned} \quad (20)$$

The costing function is

$$L(u, v) = \mathbf{a}_x(v)^H \mathbf{C}(u) \mathbf{a}_x(v) - \omega (\mathbf{e}_1^H \mathbf{a}_x(v) - 1), \quad (21)$$

where ω is a constant. We have

$$\frac{\partial}{\partial \mathbf{a}_x(v)} L(u, v) = 2\mathbf{C}(u) \mathbf{a}_x(v) + \omega \mathbf{e}_1 = 0. \quad (22)$$

According to (22), we obtain $\mathbf{a}_x(v) = \mu \mathbf{C}^{-1}(u) \mathbf{e}_1$, where μ is also a constant. As $\mathbf{e}_1^H \mathbf{a}_x(v) = 1$, $\mu = 1/\{\mathbf{e}_1^H \mathbf{C}^{-1}(u) \mathbf{e}_1\}$. Then, $\mathbf{a}_x(v)$ can be expressed as

$$\mathbf{a}_x(v) = \frac{\mathbf{C}^{-1}(u) \mathbf{e}_1}{\mathbf{e}_1^H \mathbf{C}^{-1}(u) \mathbf{e}_1}. \quad (23)$$

Combining (20) and (23), the estimation of u is

$$\widehat{u} = \arg \min_u \frac{1}{\mathbf{e}_1^H \mathbf{C}(u)^{-1} \mathbf{e}_1} = \arg \max_u \mathbf{e}_1^H \mathbf{C}^{-1}(u) \mathbf{e}_1. \quad (24)$$

Equation (24) also can be present as

$$\widehat{u}_k = \arg \max \mathbf{e}_1^H \mathbf{C}^{-1}(u) \mathbf{e}_1, \quad k = 1, 2, \dots, K. \quad (25)$$

We find the K largest peaks of the (1, 1) element of $\mathbf{C}^{-1}(u)$ through searching $u \in [\widehat{u}_k^{\text{ini}} - \Delta u, \widehat{u}_k^{\text{ini}} + \Delta u]$, where Δu is a small value. The K largest peaks (u_1, u_2, \dots, u_K) correspond to the estimations of $\sin \theta_k \sin \phi_k$ ($k = 1, 2, \dots, K$); then we obtain K vectors of $\widehat{\mathbf{a}}_x(v_1), \widehat{\mathbf{a}}_x(v_2), \dots, \widehat{\mathbf{a}}_x(v_K)$ via (23). Since $\mathbf{a}_x(v_k) = [1, e^{-j2\pi dv_k/\lambda}, \dots, e^{-j2\pi(N-1)dv_k/\lambda}]^T$, we have

$$\begin{aligned} \mathbf{g}_k &= -\text{angle}(\mathbf{a}_x(v_k)) \\ &= \left[0, \frac{2\pi dv_k}{\lambda}, \dots, \frac{2\pi(M-1)dv_k}{\lambda} \right]^T \\ &= v_k \mathbf{Q}, \end{aligned} \quad (26)$$

where $\mathbf{q} = [0, 2\pi d/\lambda, \dots, 2\pi(M-1)d/\lambda]^T$. Normalize $\hat{\mathbf{a}}_x(v_K)$ and use LS method to estimate v_K ; the LS fitting is

$$\min_{\hat{\mathbf{c}}_k} \|\mathbf{E}\hat{\mathbf{c}}_k - \hat{\mathbf{g}}_k\|_F^2, \quad (27)$$

where $\hat{\mathbf{g}}_k = -\text{angle}(\hat{\mathbf{a}}_x(v_K))$, $\mathbf{c}_k = [c_{k0}, c_{k1}]^T \in \mathbb{R}^{2 \times 1}$, $\mathbf{E} = [\mathbf{I}_M, \mathbf{q}]$, and c_{k1} is the estimation of v_k . The solution to \mathbf{c}_k is

$$[c_{k0}, v_k]^T = (\mathbf{E}^T \mathbf{E})^{-1} \mathbf{E}^T \hat{\mathbf{g}}_k. \quad (28)$$

Finally, we get the estimation of θ_k, ϕ_k as

$$\begin{aligned} \hat{\theta}_k &= \sin^{-1}(\text{abs}(\hat{v}_k + j\hat{u}_k)) \\ \hat{\phi}_k &= \text{angle}(\hat{v}_k + j\hat{u}_k). \end{aligned} \quad (29)$$

Till now, we have achieved the proposed algorithm for 2D-DOA estimation. The major steps and complexity of the algorithm are shown as follows:

- (1) construct the covariance matrix $\hat{\mathbf{R}}_x$ via (5);...
 $O\{JM^2N^2\}$;
- (2) partition the $\hat{\mathbf{R}}_x$ to get \mathbf{P} ; then construct $\mathbf{Q}, \mathbf{P}_c, \mathbf{P}_1, \mathbf{P}_2$ and obtain the initial estimation of \hat{u}_k^{ini} from the EVD of $\mathbf{P}_1^+ \mathbf{P}_2; \dots, O\{KM^2N^2 + K^2MN + 2K^2M(N-1) + 2K^3\}$;
- (3) find the K largest peaks of the (1, 1) element of $\mathbf{Q}^{-1}(u)$ through searching $u \in [\hat{u}_k^{\text{ini}} - \Delta u, \hat{u}_k^{\text{ini}} + \Delta u]$ and obtain the estimation of $\hat{u}_k; \dots, O\{n_1K[(M^2N + M^2)(MN - K) + M^2]\}$;
- (4) compute $\hat{\mathbf{a}}_x(v_K)$ via (23), and then \hat{v}_k can be estimated through the LS fitting;... $O\{6M + 12\}$;
- (5) estimate $\hat{\theta}_k, \hat{\phi}_k$ via (29).

Remark 1. In this paper, we assume that the target number K is a prior known parameter. If not, we can estimate K by applying the method in [25, 26].

Remark 2. The proposed algorithm gets the estimation of \hat{u}_k through searching $u \in [\hat{u}_k^{\text{ini}} - \Delta u, \hat{u}_k^{\text{ini}} + \Delta u]$ and then obtains the corresponding $\hat{\mathbf{a}}_x(v_K)$ and estimates corresponding \hat{v}_k . Since \hat{u}_k and \hat{v}_k are correspondence, the proposed algorithm can obtain automatically paired parameters estimation.

Remark 3. The proposed algorithm requires u_k, v_k ($k = 1, \dots, K$) being different. If the sources have the same u or v , then the direction matrix $\mathbf{A} = \mathbf{A}_x \circ \mathbf{A}_y$ is a matrix of rank loss according to the property of Khatri-Rao product [27]. That will lead many algorithms invalid, such as ESPRIT, PMs in [21, 23], and our algorithm.

3.3. Complexity Analysis. The proposed algorithm has much lower complexity than 2D-PM algorithm. The major complexity of the proposed algorithm is $O\{n_1K[(M^2N + M^2)(MN - K) + M^2] + JM^2N^2 + 2K^2M(N-1) + 2K^3 + M^2N^2K + K^2MN\}$, where n_1 is the number of steps within the local searching range; 2D-PM algorithm requires $O\{JM^2N^2 +$

$M^2N^2K + 2K^3 + n_2[(MN + 1)(MN - K)]\}$, where n_2 is the number of steps within the global searching range and $n_2 \gg n_1$, while ESPRIT algorithm costs $O\{JM^2N^2 + M^3N^3 + 2K^3(M-1)N + 6K^3 + 2K^2(N-1)M\}$.

The complexity comparison with different parameters is shown in Figures 2 and 3. From Figures 2 and 3, we can find that the proposed algorithm has much lower complexity than 2D-PM algorithm since the proposed algorithm only requires a one-dimensional local searching.

4. Performance Analysis

This section aims at analyzing the theoretic estimation error of the proposed algorithm and deriving the Cramér-Rao bound (CRB).

4.1. Error Analysis. Assume that the receive data in (1) can be written as

$$\tilde{\mathbf{X}} = \mathbf{X} + \Delta\mathbf{X}, \quad (30)$$

where $\tilde{\mathbf{X}}$ is the noisy data matrix and $\Delta\mathbf{X}$ is the additive perturbation matrix with mean zero and variance σ^2 statistically independent. Since $\hat{\mathbf{R}}_x = (1/J) \sum_{j=1}^J \mathbf{x}(t_j)\mathbf{x}^H(t_j)$, we have

$$\begin{aligned} \hat{\mathbf{R}}_x &= \frac{(\mathbf{X} + \Delta\mathbf{X})(\mathbf{X} + \Delta\mathbf{X})^H}{J} \\ &= \frac{\mathbf{X}\mathbf{X}^H}{J} + \frac{\Delta\mathbf{X}\Delta\mathbf{X}^H}{J} \\ &= \mathbf{R}_x + \Delta\mathbf{R}_x, \end{aligned} \quad (31)$$

where $\mathbf{R}_x = \mathbf{X}\mathbf{X}^H/J$ and $\Delta\mathbf{R}_x = \Delta\mathbf{X}\Delta\mathbf{X}^H/J$. According to (11), we also have

$$\hat{\mathbf{G}} = \mathbf{G} + \Delta\mathbf{G}, \quad \hat{\mathbf{H}} = \mathbf{H} + \Delta\mathbf{H}. \quad (32)$$

The estimation of propagator matrix \mathbf{P} can be denoted as

$$\hat{\mathbf{P}} = [(\mathbf{G} + \Delta\mathbf{G})(\mathbf{G} + \Delta\mathbf{G})^H]^{-1} (\mathbf{G} + \Delta\mathbf{G})(\mathbf{H} + \Delta\mathbf{H})^H. \quad (33)$$

With a first-order expansion in $\Delta\mathbf{G}$ and $\Delta\mathbf{H}$, $\hat{\mathbf{P}}$ is rewritten as

$$\hat{\mathbf{P}} = \mathbf{P} + \Delta\mathbf{P}, \quad (34)$$

where $\Delta\mathbf{P} = (\mathbf{G}\mathbf{G}^H)^{-1}\mathbf{G}(\Delta\mathbf{H}^H - \Delta\mathbf{G}^H\mathbf{P})$. We also obtain

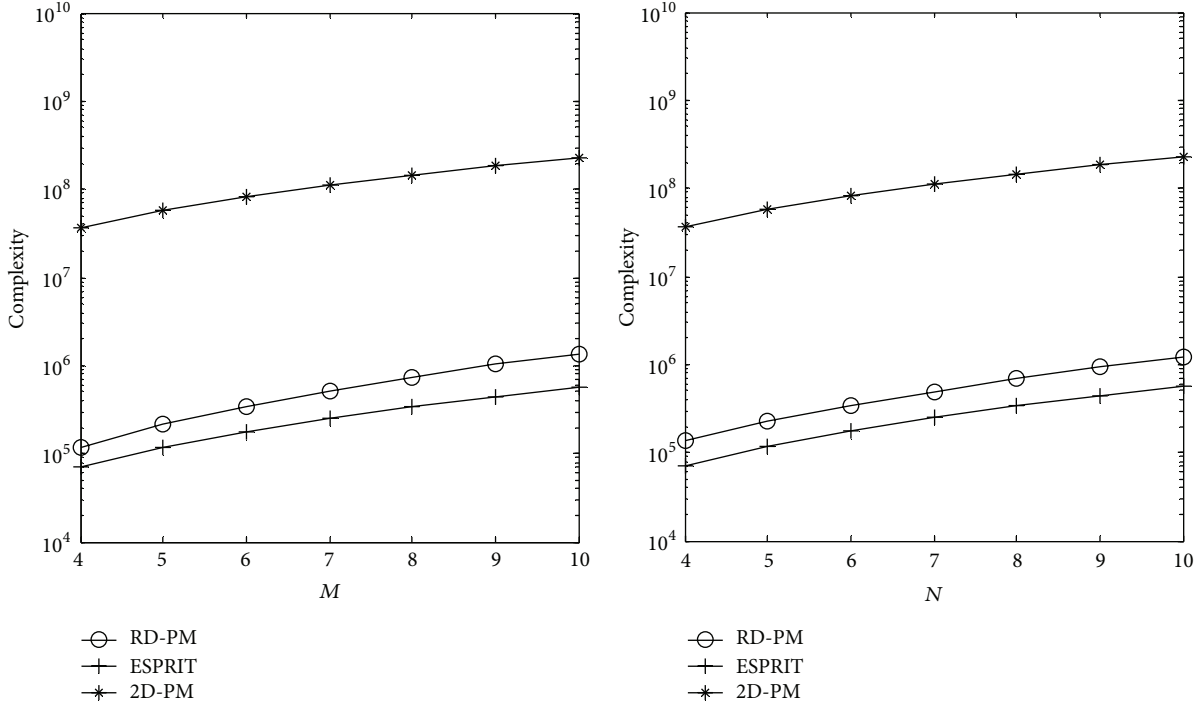
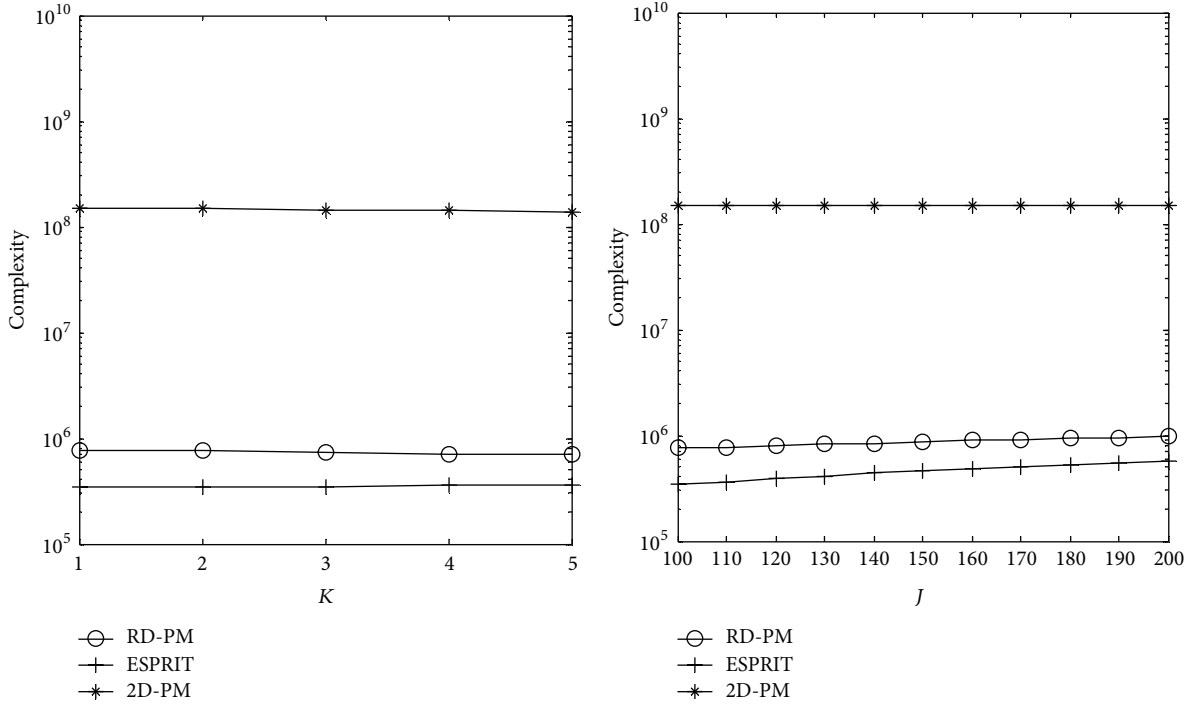
$$\hat{\mathbf{Q}} = \begin{bmatrix} \hat{\mathbf{P}} \\ -\mathbf{I}_{MN-K} \end{bmatrix} = \mathbf{Q} + \Delta\mathbf{Q}, \quad (35)$$

where $\Delta\mathbf{Q} = \mathbf{T}\Delta\mathbf{X}^H\mathbf{Q}$ with $\mathbf{T} = -\begin{bmatrix} (\mathbf{G}\mathbf{G}^H)^{-1}\mathbf{G} \\ \mathbf{0}_{MN-K} \end{bmatrix}$.

Since $\hat{\mathbf{C}} = \hat{\mathbf{Q}}\hat{\mathbf{Q}}^H = \mathbf{C} + \Delta\mathbf{C}$, using first-order expansion we obtain

$$\Delta\mathbf{C} = \mathbf{Q}\Delta\mathbf{Q}^H + \Delta\mathbf{Q}\mathbf{Q}^H. \quad (36)$$

The proposed algorithm has the same cost function as 2D-PM algorithm, which is a reduced-dimension form of 2D-PM


 FIGURE 2: Complexity comparison of different algorithms with different values of M/N .

 FIGURE 3: Complexity comparison of different algorithms with different values of K/J .

algorithm. For simplification, we derive the theoretical error of the proposed algorithm through the cost function of 2D-PM algorithm.

The function from which we search for the minima in order to determine the estimates is

$$W(u, v) = [\mathbf{a}_y(u) \otimes \mathbf{a}_x(v)]^H \widehat{\mathbf{C}}^H [\mathbf{a}_y(u) \otimes \mathbf{a}_x(v)]. \quad (37)$$

Define $\mathbf{r} = [u, v]^T$, $\nabla_{\mathbf{r}} = [\partial/\partial u, \partial/\partial v]^T$, $\mathbf{d}_u(k) = \partial \mathbf{a}_k / \partial u_k$, and $\mathbf{d}_v(k) = \partial \mathbf{a}_k / \partial v_k$. Use $r_i = [u_i, v_i]$ to denote the true angles corresponding to the i th target and $\hat{r}_i = [\hat{u}_i, \hat{v}_i]$ denotes the estimated ones. Then,

$$\nabla_{\mathbf{r}} W(u, v) \Big|_{\hat{\mathbf{r}}_i} = \mathbf{0}. \quad (38)$$

After the Taylor expansion around r_i (use W instead of $W(u, v)$ for simplification),

$$\mathbf{0} = \nabla_r W|_{r_i} + \nabla_r (\nabla_r W)^T|_{r_{i\xi}} (\hat{r}_i - r_i), \quad (39)$$

where $r_{i\xi}$ is a vector of some value on the line segment joining \hat{r}_i and r_i .

Define

$$\mathbf{H}_i = \lim_{N \rightarrow \infty} \nabla_r (\nabla_r W)^T|_{r_i}. \quad (40)$$

Under large sample, $(\hat{r}_i - r_i)$ is asymptotically zero-mean Gaussian distributed [17–19], so the associated asymptotic covariance matrix is given by

$$\begin{aligned} \Phi_{ik} &= \lim_{N \rightarrow \infty} E [(\hat{r}_i - r_i)(\hat{r}_k - r_k)^T] \\ &= (\mathbf{H}_i)^{-1} \lim_{N \rightarrow \infty} E \left[\nabla_{r_i} f(\nabla_{r_k} f)^T \right] |_{r_i, r_k} (\mathbf{H}_k)^{-1}. \end{aligned} \quad (41)$$

According to (36) and (41) and taking into account that $\mathbf{a}_i^H \mathbf{Q} = 0$, we can determine

$$\begin{aligned} \Phi_{ik} &= \frac{\sigma^4}{2w(i)w(k)} \begin{bmatrix} \mathbf{d}_v^H(i) \mathbf{P}_A^\perp \mathbf{d}_v(i) & \rho(i) \\ \rho(i) & \mathbf{d}_u^H(i) \mathbf{P}_A^\perp \mathbf{d}_u(i) \end{bmatrix} \\ &\times \text{Re} \left\{ \left(\mathbf{a}_i^H \mathbf{T} \mathbf{T}^H \mathbf{a}_k \right) \begin{bmatrix} \mathbf{d}_u^H(k) \mathbf{P}_A^\perp \mathbf{d}_u(i) & \mathbf{d}_v^H(k) \mathbf{P}_A^\perp \mathbf{d}_u(i) \\ \mathbf{d}_u^H(k) \mathbf{P}_A^\perp \mathbf{d}_v(i) & \mathbf{d}_v^H(k) \mathbf{P}_A^\perp \mathbf{d}_v(i) \end{bmatrix} \right\} \\ &\times \begin{bmatrix} \mathbf{d}_v^H(k) \mathbf{P}_A^\perp \mathbf{d}_v(k) & \rho(k) \\ \rho(k) & \mathbf{d}_u^H(k) \mathbf{P}_A^\perp \mathbf{d}_u(k) \end{bmatrix}, \end{aligned} \quad (42)$$

where $w(i) = \mathbf{d}_u^H(i) \mathbf{P}_A^\perp \mathbf{d}_u(i) \mathbf{d}_v^H(i) \mathbf{P}_A^\perp \mathbf{d}_v(i) - (1/4) [\mathbf{d}_u^H(i) \mathbf{P}_A^\perp \mathbf{d}_v(i) + \mathbf{d}_v^H(i) \mathbf{P}_A^\perp \mathbf{d}_u(i)]^2$, $\mathbf{P}_A^\perp = \mathbf{I} - \mathbf{A}(\mathbf{A}^H \mathbf{A})^{-1} \mathbf{A}^H$, and $\rho(i) = -[\mathbf{d}_u^H(i) \mathbf{P}_A^\perp \mathbf{d}_v(i) + \mathbf{d}_v^H(i) \mathbf{P}_A^\perp \mathbf{d}_u(i)]/2$.

That is, $E[(\partial u_k)^2] = \Phi_{kk}(1, 1)$, $E[(\partial v_k)^2] = \Phi_{kk}(2, 2)$, and $E[\partial v_k \partial u_k] = \Phi_{kk}(2, 1)$.

According to (29), the mean square error (MSE) of azimuth and elevation can be derived as

$$\begin{aligned} E[\partial \phi_k^2] &= \frac{1}{2 \sin^2 \theta_k} \left[E[\partial u_k^2] + E[\partial v_k^2] \right. \\ &\quad \left. - \text{Re} \left\{ \left(E[\partial v_k^2] + 2jE[\partial v_k \partial u_k] \right. \right. \right. \\ &\quad \left. \left. \left. - E[\partial u_k^2] \right) e^{-j2\phi_k} \right\} \right] \\ &= \frac{1}{2 \sin^2 \theta_k} \left[\cos^2 \phi_k \Phi_{kk}(1, 1) \right. \\ &\quad \left. + \sin^2 \phi_k \Phi_{kk}(2, 2) - \sin 2\phi_k \Phi_{kk}(2, 1) \right] \\ E[\partial \theta_k^2] &= \frac{1}{\sin^2 \theta_k \cos^2 \theta_k} \\ &\quad \times \left(u^2 E[\partial u^2] + v^2 E[\partial v^2] + 2uv E[\partial v \partial u] \right) \\ &= \frac{1}{\cos^2 \theta_k} \left[\sin^2 \phi_k \Phi_{kk}(1, 1) + \cos^2 \phi_k \Phi_{kk}(2, 2) \right. \\ &\quad \left. + \sin 2\phi_k \Phi_{kk}(2, 1) \right]. \end{aligned} \quad (43)$$

The comparison of theoretical estimation error and simulation results will be shown in Section 5.

4.2. CRB. According to [28], we can derive the CRB for uniform rectangular array

$$\text{CRB} = \frac{\sigma^2}{2J} \left\{ \text{Re} \left[\mathbf{D}^H \mathbf{\Pi}_A^\perp \mathbf{D} \odot \mathbf{P}^T \right] \right\}^{-1}, \quad (44)$$

where $\mathbf{D} = [\partial \mathbf{a}_1 / \partial \theta_1, \partial \mathbf{a}_2 / \partial \theta_2, \dots, \partial \mathbf{a}_K / \partial \theta_K, \partial \mathbf{a}_1 / \partial \phi_1, \partial \mathbf{a}_2 / \partial \phi_2, \dots, \partial \mathbf{a}_K / \partial \phi_K]$ and \mathbf{a}_k is the k th column of \mathbf{A} ; $\mathbf{P} = \begin{bmatrix} \mathbf{P}_s & \mathbf{P}_s \\ \mathbf{P}_s & \mathbf{P}_s \end{bmatrix}$, $\hat{\mathbf{P}}_s = (1/J) \sum_{t=1}^J \mathbf{b}(t) \mathbf{b}^H(t)$, $\mathbf{\Pi}_A^\perp = \mathbf{I}_{MN} - \mathbf{A}(\mathbf{A}^H \mathbf{A})^{-1} \mathbf{A}^H$, and σ^2 is the covariance of the noise. \odot is the Hadamard product.

5. Simulation and Analysis

5.1. Simulation Results. We present 1000 Monte Carlo simulations to assess the angle estimation performance of the RD-PM algorithm. Define root mean square error (RMSE):

$$\text{RMSE} = \frac{1}{K} \sum_{k=1}^K \sqrt{\frac{1}{1000} \sum_{l=1}^{1000} \left[(\hat{\theta}_{k,l} - \theta_k)^2 + (\hat{\phi}_{k,l} - \phi_k)^2 \right]}, \quad (45)$$

where $\hat{\theta}_{k,l}$, $\hat{\phi}_{k,l}$ are the estimates of θ_k , ϕ_k in the l th Monte Carlo trial, respectively. We assume that there are $K = 3$ noncoherent sources with $(\theta_1, \phi_1) = (10^\circ, 15^\circ)$, $(\theta_2, \phi_2) = (20^\circ, 25^\circ)$, and $(\theta_3, \phi_3) = (30^\circ, 35^\circ)$; the spacing between two

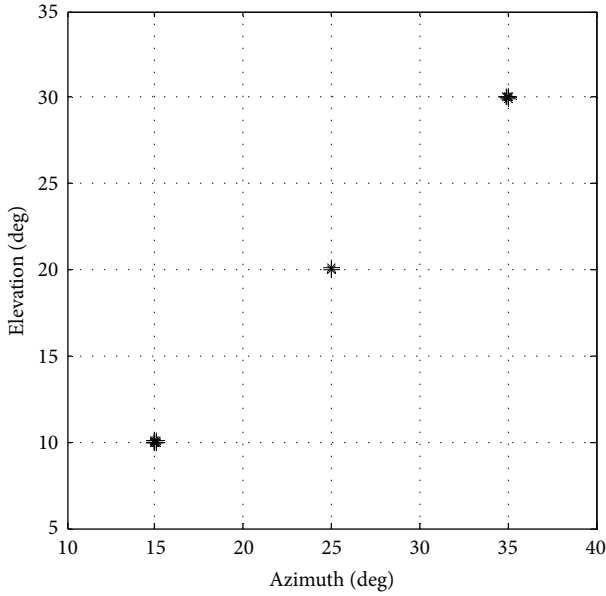


FIGURE 4: Angle estimation performance of the proposed algorithm with SNR = 20 dB.

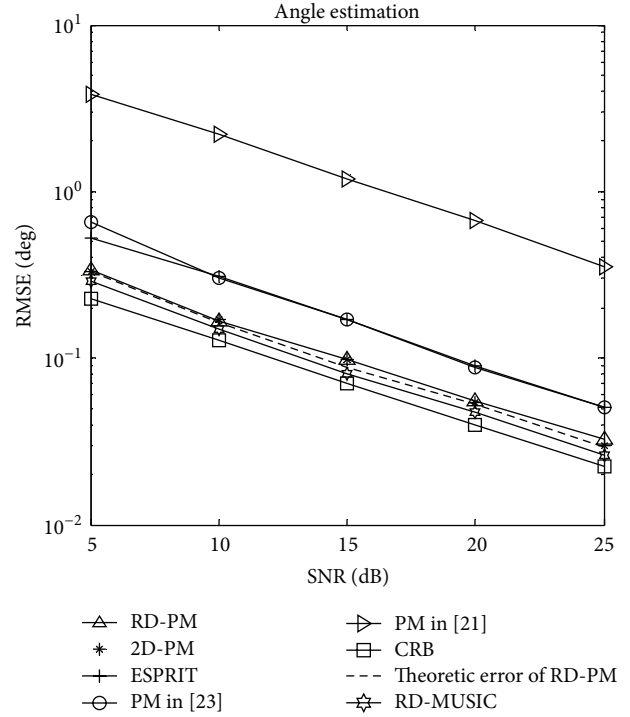


FIGURE 6: Angle estimation performance comparison ($M = 8$, $N = 10$, $J = 120$, and $K = 2$).

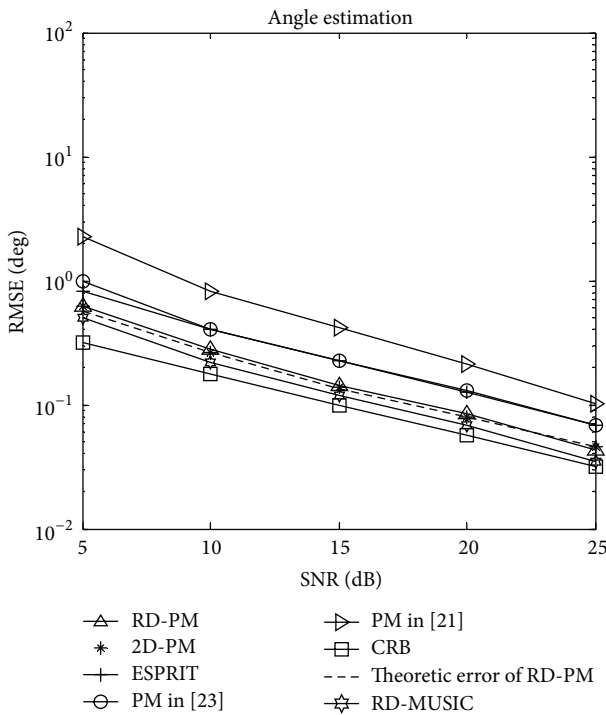


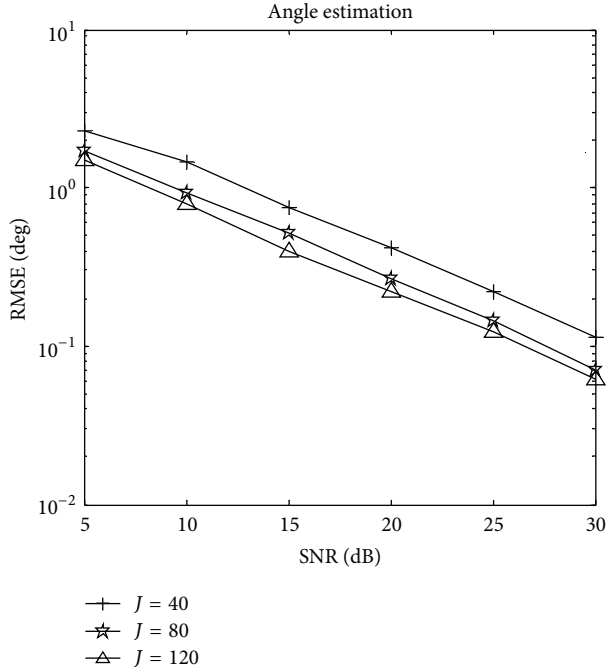
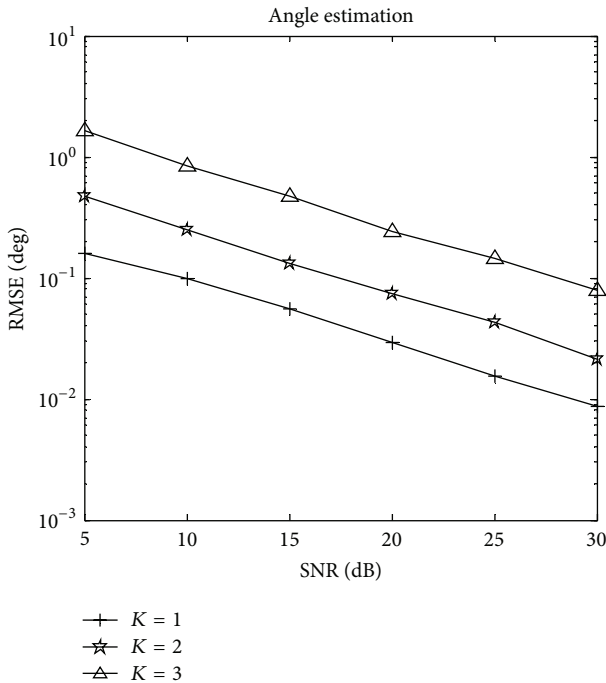
FIGURE 5: Angle estimation performance comparison ($M = 8$, $N = 8$, $J = 100$, and $K = 3$).

adjacent elements is $d = \lambda/2$. Note that M and N are the numbers of sensors in x -axis and y -axis, respectively. J is the number of snapshots.

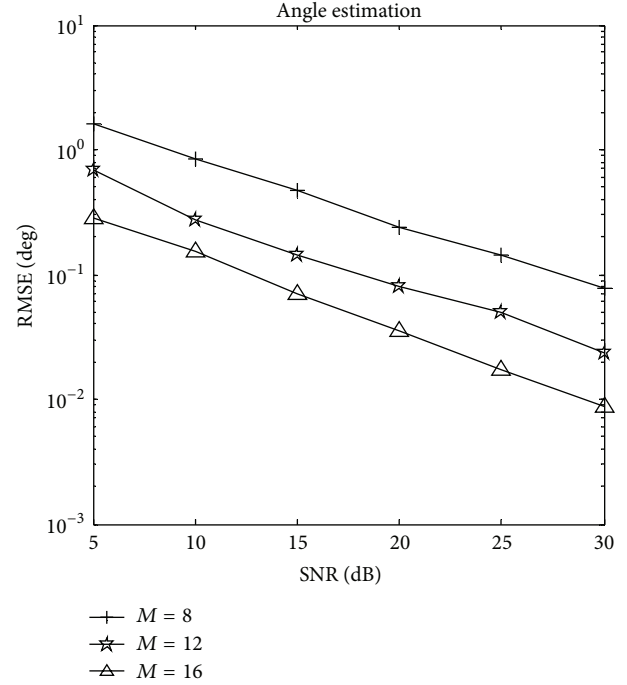
Simulation 1. Figure 4 depicts angle estimation performance of the proposed algorithm with $M = 8$, $N = 10$, $J = 100$, and SNR = 20 dB. The results show that elevation and azimuth angles can be clearly observed.

Simulation 2. Figures 5 and 6 present angle estimation performance comparison among the proposed algorithm, 2D-PM algorithm, the PM algorithm in [21], the PM algorithm in [23], ESPRIT algorithm, RD-MUSIC algorithm, CRB, and the theoretic estimation error of RD-PM. We can see that the estimation performance of the proposed algorithm is better than ESPRIT algorithm and the PM algorithms in [21, 23] and is very close to 2D-PM algorithm and RD-MUSIC algorithm. Compared with 2D-PM algorithm, the proposed algorithm has the same costing function and simplifies two-dimensional global searching to one-dimensional local searching. As a result of that, our algorithm has very close angle estimation performance to 2D-PM algorithm and greatly reduces complexity. Furthermore, Figures 5 and 6 also show that the RMSE of the proposed algorithm is almost the same as the theoretic estimation error.

Simulation 3. Figure 7 presents angle estimation performance of the proposed algorithm with $M = 8$, $N = 8$, $K = 3$, and different values of J . We can find that the angle estimation performance is improved when J increases. When J increases, we get more samples to estimate more accurate propagator matrix \mathbf{P} , and the angle estimation performance is enhanced.

FIGURE 7: Angle estimation performance with different values of J .FIGURE 8: Angle estimation performance with different values of K .

Simulation 4. Figure 8 shows angle estimation performance of the proposed algorithm with $M = 8$, $N = 8$, $J = 100$, and different values of K . It is shown that the angle estimation performance of the proposed algorithm is improved when K decreases. More sources enhance the interference, so the

FIGURE 9: Angle estimation performance with $N = 8$ and different values of M .

angle estimation performance of the proposed algorithm is affected.

Simulation 5. Figures 9 and 10 investigate angle estimation performance of the proposed algorithm with $K = 3$, $J = 100$, and different values of M or N , respectively. It is indicated that the performance of the proposed algorithm is improved when M or N increases. Multiple sensors enhance the aperture of the array as well as diversity gain, so the angle estimation performance is improved.

Simulation 6. Figure 11 depicts angle estimation performance of the proposed algorithm when the two sources are closely spaced with $M = 8$, $N = 8$, $J = 100$, and $\text{SNR} = 20$ dB. It is shown in Figure 11 that our algorithm works well for the closely spaced sources.

6. Conclusions

In this paper, we have presented a novel algorithm for 2D-DOA estimation for uniform rectangular array using RD-PM algorithm. The proposed algorithm, which only requires one-dimensional local searching and avoids the EVD of the covariance matrix of the receive data, has a much lower complexity than 2D-PM algorithm. Simulation results show that the angle estimation performance of the proposed algorithm is better than that of ESPRIT algorithm and conventional PM algorithms, also very close to that of 2D-PM algorithm. Furthermore, the proposed algorithm can achieve paired 2D-DOA estimation automatically.

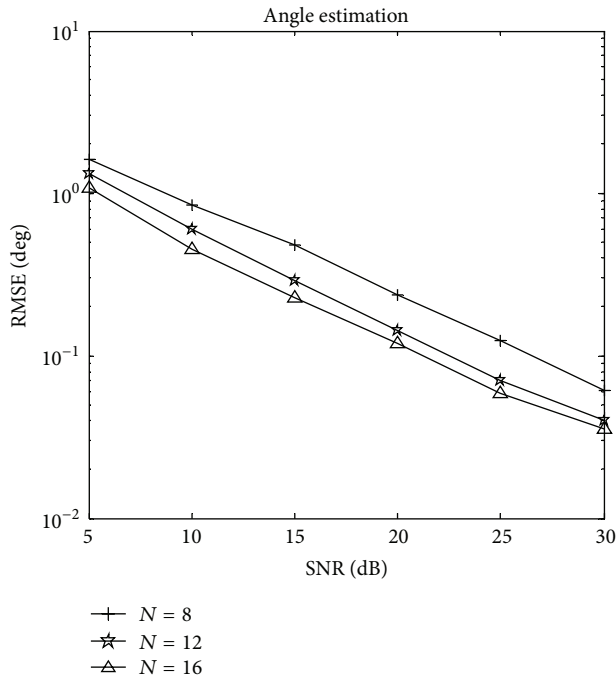


FIGURE 10: Angle estimation performance with $M = 8$ and different values of N .

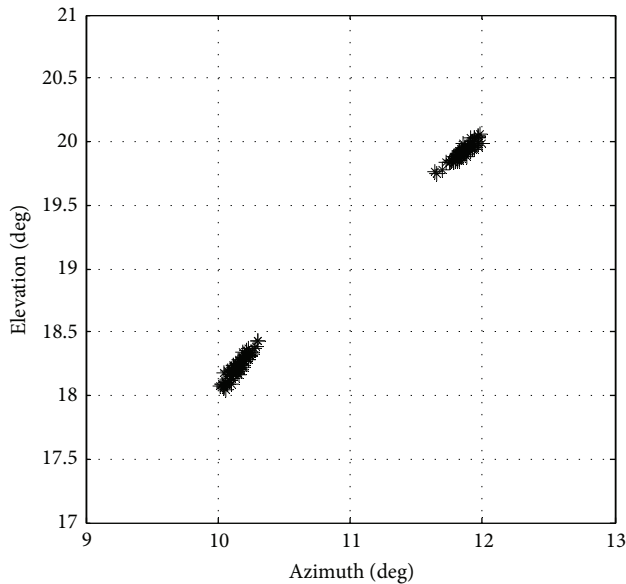


FIGURE 11: Angle estimation performance of the proposed algorithm with the closely spaced sources.

Conflict of Interests

The authors declare that there is no conflict of interests regarding the publication of this paper.

Acknowledgments

This work is supported by China NSF Grants (61371169, 61301108, 61471191, 61471192, and 61271327), Jiangsu Planned Projects for Postdoctoral Research Funds (1201039C), China Postdoctoral Science Foundation (2012M521099, 2013M541661), Open Project of Key Laboratory of Modern Acoustic of Ministry of Education (Nanjing University), the Aeronautical Science Foundation of China (20120152001), Qing Lan Project, priority academic program development of Jiangsu high education institutions, and the Fundamental Research Funds for the Central Universities (NZ2012010, NS2013024, kfj130114, kfj130115).

References

- [1] H. Y. Kang, Y. S. Kim, and C. J. Kim, "Spatially close signals separation via array aperture expansions and spatial spectrum averaging," *ETRI Journal*, vol. 26, no. 1, pp. 45–47, 2004.
- [2] V. S. Kedia and B. Chandna, "A new algorithm for 2-D DOA estimation," *Signal Processing*, vol. 60, no. 3, pp. 325–332, 1997.
- [3] R. Rajagopal and P. R. Rao, "Generalised algorithm for DOA estimation in a passive sonar," *IEE Proceedings. F. Radar and Signal Processing*, vol. 140, no. 1, pp. 12–20, 1993.
- [4] J. H. Winters, "Smart antennas for wireless systems," *IEEE Personal Communications*, vol. 5, no. 1, pp. 23–27, 1998.
- [5] S. C. Swales, M. A. Beach, D. J. Edwards, and J. P. McGeehan, "Performance enhancement of multibeam adaptive base-station antennas for cellular land mobile radio systems," *IEEE Transactions on Vehicular Technology*, vol. 39, no. 1, pp. 56–67, 1990.
- [6] R. O. Schmidt, "Multiple emitter location and signal parameter estimation," *IEEE Transactions on Antennas and Propagation*, vol. 34, no. 3, pp. 276–280, 1986.
- [7] R. Roy and T. Kailath, "ESPRIT-estimation of signal parameters via rotational invariance techniques," *IEEE Transactions on Acoustics, Speech and Signal Processing*, vol. 37, no. 7, pp. 984–995, 1989.
- [8] M. Wax, T.-J. Shan, and T. Kailath, "Spatio-temporal spectral analysis by eigenstructure methods," *IEEE Transactions on Acoustics, Speech, and Signal Processing*, vol. 32, no. 4, pp. 817–827, 1984.
- [9] M. D. Zoltowski, M. Haardt, and C. P. Mathews, "Closed-form 2-D angle estimation with rectangular arrays in element space or beamspace via unitary ESPRIT," *IEEE Transactions on Signal Processing*, vol. 44, no. 2, pp. 316–328, 1996.
- [10] X. Zhang, X. Gao, and W. Chen, "Improved blind 2D-direction of arrival estimation with L-shaped array using shift invariance property," *Journal of Electromagnetic Waves and Applications*, vol. 23, no. 5-6, pp. 593–606, 2009.
- [11] J. E. F. del Rio and M. F. C tedra-P rez, "The matrix pencil method for two-dimensional direction of arrival estimation employing an l-shaped array," *IEEE Transactions on Antennas and Propagation*, vol. 45, no. 11, pp. 1693–1694, 1997.
- [12] P. F. C. Krekel and E. F. Deprettere, "Two-dimensional version of the matrix pencil method to solve the DOA problem," in *Proceedings of the European Conference on Circuit Theory and Design*, pp. 435–439, September 1989.
- [13] M. P. Clark and L. L. Scharf, "Two-dimensional modal analysis based on maximum likelihood," *IEEE Transactions on Signal Processing*, vol. 42, no. 6, pp. 1443–1452, 1994.

- [14] Z. Xiaofei, L. Jianfeng, and X. Lingyun, "Novel two-dimensional DOA estimation with L-shaped array," *EURASIP Journal on Advances in Signal Processing*, vol. 2011, article 50, pp. 1–7, 2011.
- [15] T. Bin, X. Xianci, and S. Taihe, "A novel method for estimating spatial 2-D direction of arrival," *Acta Electronica Sinica*, vol. 27, no. 3, pp. 104–106, 1999.
- [16] X. Zhang, F. Wang, W. Chen et al., *Theory and Application of Array Signal Processing*, National Defense Industry Press, Beijing, China, 2nd edition, 2013.
- [17] S. Marcos, A. Marsal, and M. Benidir, "The propagator method for source bearing estimation," *Signal Processing*, vol. 42, no. 2, pp. 121–138, 1995.
- [18] S. Marcos, A. Marsal, and M. Benidir, "Performances analysis of the propagator method for source bearing estimation," in *Proceedings of the International Conference on Acoustics, Speech, and Signal Processing*, vol. 4, pp. 237–240, April 1994.
- [19] J. Sanchez-Araujo and S. Marcos, "Statistical analysis of the propagator method for DOA estimation without eigendecomposition," in *Proceedings of the 8th IEEE Signal Processing Workshop on Statistical Signal and Array Processing (SSAP '96)*, pp. 570–573, June 1996.
- [20] N. Tayem and H. M. Kwon, "2-D DOA estimation with propagator method for correlated sources under unknown symmetric toeplitz noise," in *Proceedings of the IEEE Vehicular Technology Conference*, vol. 61, pp. 1–5, 1999.
- [21] Y. Wu, G. Liao, and H. C. So, "A fast algorithm for 2-D direction-of-arrival estimation," *Signal Processing*, vol. 83, no. 8, pp. 1827–1831, 2003.
- [22] H. Cao, L. Yang, X. Tan, and S. Yang, "Computationally efficient 2-D DOA estimation using two parallel uniform linear arrays," *ETRI Journal*, vol. 31, no. 6, pp. 806–808, 2009.
- [23] J. Li, X. Zhang, and H. Chen, "Improved two-dimensional DOA estimation algorithm for two-parallel uniform linear arrays using propagator method," *Signal Processing*, vol. 92, no. 12, pp. 3032–3038, 2012.
- [24] X. Zhang, L. Xu, L. Xu, and D. Xu, "Direction of departure (DOD) and direction of arrival (DOA) estimation in MIMO radar with reduced-dimension mUSIC," *IEEE Communications Letters*, vol. 14, no. 12, pp. 1161–1163, 2010.
- [25] J. Xin, N. Zheng, and A. Sano, "Simple and efficient nonparametric method for estimating the number of signals without eigendecomposition," *IEEE Transactions on Signal Processing*, vol. 55, no. 4, pp. 1405–1420, 2007.
- [26] H. T. Wu, J. F. Yang, and F. K. Chen, "Source number estimator using Gerschgorin disks," in *Proceedings of the IEEE International Conference on Acoustics, Speech, and Signal Processing (ICASSP '94)*, vol. 4, pp. IV/261–IV/264, 1994.
- [27] X. D. Zhang, *Matrix Analysis and Applications (Version 2)*, Tsinghua University Press, Beijing, China, 2013.
- [28] P. Stoica and A. Nehorai, "Performance study of conditional and unconditional direction-of-arrival estimation," *IEEE Transactions on Acoustics, Speech, and Signal Processing*, vol. 38, no. 10, pp. 1783–1795, 1990.

Research Article

Research on Polarization Cancellation of Nonstationary Ionosphere Clutter in HF Radar System

Xingpeng Mao, Hong Hong, Weibo Deng, and Yongtan Liu

School of Electronic and Information Engineering, Harbin Institute of Technology, Harbin, Heilongjiang 150001, China

Correspondence should be addressed to Xingpeng Mao; mxp@hit.edu.cn

Received 25 April 2014; Revised 20 August 2014; Accepted 9 September 2014

Academic Editor: Hang Hu

Copyright © 2015 Xingpeng Mao et al. This is an open access article distributed under the Creative Commons Attribution License, which permits unrestricted use, distribution, and reproduction in any medium, provided the original work is properly cited.

Oblique projection polarization filter (OPPF) can be applied as an effective approach for interference cancellation in high-frequency surface wave radar (HFSWR) and other systems. In order to suppress the nonstationary ionosphere clutter further, a novel OP PF based clutter suppressing scheme is proposed in this paper. The polarization and nonstationary characteristic of the clutter are taken into account in the algorithms referred to as range-Doppler domain polarization suppression (RDDPS) and the range-time domain polarization suppression (RTDPS) method, respectively. The RDDPS is designed for weak ionosphere clutter and implemented in the range-Doppler domain directly, whereas the RTDPS algorithm is designed to suppress the powerful ionosphere clutter with a multisegment estimation and suppression scheme. About 15–23 dB signal to interference ratio (SIR) improvement can be expected when using the proposed method, whereas the targets can be more easily detected in the range-Doppler map. Experimental results demonstrate that the scheme proposed is effective for nonstationary ionosphere clutter and is proven to be a practical interference cancellation technique for HFSWR.

1. Introduction

By exploiting the long-range propagation of vertically polarized electromagnetic wave in the band of 2–15 MHz, high-frequency surface wave radar (HFSWR) is able to receive vessel and low-flying aircraft echoes over the horizon. However, the signal environment of high-frequency (HF) band is far from satisfactory. The powerful shortwave radio interference, ionosphere clutter, and industrial interference that dominate the pure receiver noise in the HF band cause a significant limit of detection capability. Ionosphere clutter, which is often observed to mask multiple successive range and Doppler cells, is one of the main interference sources. In some cases, the power of the clutter is so high that even the target echoes are overwhelmed, resulting in poor detection and tracking performance [1, 2].

Adaptive beamforming schemes have been developed by using the space information of ionosphere clutter [3–5]. However, when the target is overlapped by ionosphere clutter from the same or close direction, such approaches are not ideal. According to the fact that the echoes of targets arriving along the surface of ocean used to be vertically

polarized while ionosphere clutter is elliptically polarized, polarization filtering can be applied to improve the HF radar performance. By utilizing the polarization difference between the target and the clutter, polarization filter can be used to suppress interference [6–9]. However, a severe loss of coherent integration occurs when a conventional polarization filter is applied to coherent systems such as HFSWR, as an additional amplitude and/or phase distortion of the target signal will be introduced. In order to solve this problem, null phase-shift polarization filter (NPPF) [10] is proposed and then extended to a frequency domain null phase-shift multinotch polarization filter in [11, 12]. Such improvement effectively keeps the temporal coherence of the target within coherent integration time (CIT) and successfully paved a way for the application of polarization filtering in HFSWR. To improve the flexibility and convenience, oblique projection polarization filter (OPPF) [13] is further proposed to deal with nonorthogonal signals. Successful experimental evaluation of OP PF for suppressing shortwave radio interference in HFSWR is reported in [14].

However, the ionosphere clutter cancellation method, which meets the requirement of practical HFSWR system,

is still an open issue, as the ionosphere clutter is usually nonstationary. In this paper, two types of clutter cancellation approaches are given to suppress the nonstationary ionosphere clutter. The range-Doppler domain polarization suppression (RDDPS) is designed for weak ionosphere clutter and performed in the range-Doppler domain, while the range-time domain polarization suppression (RTDPS) is designed for strong ionosphere clutter. The procedure of clutter polarization estimation and clutter suppression in segments for the RTDPS is emphasized in our research. And the segmentation parameter optimization is also discussed in detail to obtain a balance between the clutter cancellation and the target restoration. The specific utilization of RDDPS or RTDPS depends on the type of the clutter at the corresponding range cell.

The remainder of this paper is organized as follows. In Section 2, the design of OPPF is introduced and the impact on the performance of the OPPF by the estimation error is analyzed. The nonstationary ionosphere clutter cancellation scheme is proposed in Section 3, whereas the applications of RDDPS and RTDPS are discussed in detail in Section 4. Then the experimental performance evaluation of the proposed scheme is given in Section 4. Finally, the conclusions are drawn in Section 5.

2. Oblique Projection Polarization Filter

2.1. Received Signal Model. Suppose the received wavefront is a completely polarized wave and its polarization angle and polarization angle difference are γ and η , respectively. Ignoring the absolute phase, the incident signal $\mathbf{E}(t)$ can be described by Jones vector as in [10] as

$$\begin{aligned} \mathbf{E}(t) &= \begin{bmatrix} S(t) \cos \gamma \\ S(t) \sin \gamma \exp(j\eta) \end{bmatrix} \\ &= \begin{bmatrix} \cos \gamma \\ \sin \gamma \exp(j\eta) \end{bmatrix} S(t) = \mathbf{a}S(t), \end{aligned} \quad (1)$$

where $S(t) \cos \gamma$ is the horizontally polarized component of $\mathbf{E}(t)$ while $S(t) \sin \gamma \exp(j\eta)$ is the vertically polarized component of $\mathbf{E}(t)$. Vector \mathbf{a} is defined as the polarization steering vector of $\mathbf{E}(t)$, and

$$\mathbf{a} = \begin{bmatrix} \cos \gamma \\ \sin \gamma e^{j\eta} \end{bmatrix}. \quad (2)$$

2.2. OPPF and Error Analysis. Suppose the polarization steering vectors of the target and interference are \mathbf{a}_S and \mathbf{a}_I , respectively. If the two steering vectors satisfy $\mathbf{a}_S \neq \mathbf{a}_I$, a corresponding polarization oblique projection operator can be constructed by [13]

$$\mathbf{H} = \mathbf{a}_S (\mathbf{a}_S^H \mathbf{P}_{\mathbf{a}_I}^\perp \mathbf{a}_S)^{-1} \mathbf{a}_S^H \mathbf{P}_{\mathbf{a}_I}^\perp, \quad (3)$$

where $\mathbf{P}_{\mathbf{a}_I}^\perp = \mathbf{E} - \mathbf{a}_I (\mathbf{a}_I^H \mathbf{a}_I)^{-1} \mathbf{a}_I^H$ and \mathbf{E} represents the unit matrix.

The fundamental property of this polarization oblique projection operator can be given as

$$\mathbf{H} \mathbf{a}_S = \mathbf{a}_S, \quad \mathbf{H} \mathbf{a}_I = 0. \quad (4)$$

The scalar form of (4) can be given as

$$(\mathbf{A}_S^\dagger \mathbf{H}) \mathbf{a}_S = 1, \quad (\mathbf{A}_S^\dagger \mathbf{H}) \mathbf{a}_I = 0, \quad (5)$$

where $\mathbf{A}_S^\dagger = (\mathbf{a}_S^H \mathbf{a}_S)^{-1} \mathbf{a}_S^H$.

Usually, the received signal is a linear combination of the target $\mathbf{E}_S(t) = \mathbf{a}_S S(t)$, interference $\mathbf{E}_I(t) = \mathbf{a}_I I(t)$, and noise $\mathbf{n}(t)$. According to (4), the output of the OPPF can be given as

$$\begin{aligned} \widehat{\mathbf{E}}_S(t) &= \mathbf{H} (\mathbf{E}_S(t) + \mathbf{E}_I(t) + \mathbf{n}(t)) \\ &= \mathbf{H} \mathbf{a}_S S(t) + \mathbf{H} \mathbf{a}_I I(t) + \mathbf{H} \mathbf{n}(t) \\ &= \mathbf{E}_S(t) + \mathbf{H} \mathbf{n}(t). \end{aligned} \quad (6)$$

When scalar form is required, the filtering process can be rewritten as

$$\begin{aligned} \widehat{S}(t) &= \mathbf{A}_S^\dagger \mathbf{H} (\mathbf{E}_S(t) + \mathbf{E}_I(t) + \mathbf{n}(t)) \\ &= \mathbf{A}_S^\dagger \mathbf{H} \mathbf{a}_S S(t) + \mathbf{A}_S^\dagger \mathbf{H} \mathbf{a}_I I(t) + \mathbf{A}_S^\dagger \mathbf{H} \mathbf{n}(t). \end{aligned} \quad (7)$$

According to (5), (7) can be simplified as

$$\widehat{S}(t) = S(t) + \mathbf{A}_S^\dagger \mathbf{H} \mathbf{n}(t). \quad (8)$$

Equations (6) and (8) indicate that the interference can be completely cancelled and the target is restored without distortion when the polarization steering vectors of the target and interference, which are utilized to build the subspaces of desired ranges and null spaces, are estimated accurately.

If the estimation accuracy is uncertain, in order to analyze the performance loss of OPPF that was caused by the estimation error, the mean square error (MSE) of the target can be defined as $\text{MSE} = \mathbf{E}\{\|\widehat{S}(t) - S(t)\|_F^2\}$, where $\widehat{S}(t)$ is the recovered signal of the target $S(t)$ and $\mathbf{E}(\cdot)$ and $\|\cdot\|_F$ denote the mathematical expectation and the Frobenius norm. Substituting (7) into MSE, the general form of MSE of the target $S(t)$ can be given as

$$\text{MSE} = \mathbf{E} \left\{ \left\| \widehat{\mathbf{A}}_S^\dagger \widehat{\mathbf{H}} \mathbf{a}_S S(t) + \widehat{\mathbf{A}}_S^\dagger \widehat{\mathbf{H}} \mathbf{a}_I I(t) + \widehat{\mathbf{A}}_S^\dagger \widehat{\mathbf{H}} \mathbf{n}(t) - S(t) \right\|_F^2 \right\}, \quad (9)$$

where $\widehat{\mathbf{H}} = \widehat{\mathbf{a}}_S (\widehat{\mathbf{a}}_S^H \widehat{\mathbf{P}}_{\widehat{\mathbf{a}}_I}^\perp \widehat{\mathbf{a}}_S)^{-1} \widehat{\mathbf{a}}_S^H \widehat{\mathbf{P}}_{\widehat{\mathbf{a}}_I}^\perp$, $\widehat{\mathbf{A}}_S^\dagger = (\widehat{\mathbf{a}}_S^H \widehat{\mathbf{a}}_S)^{-1} \widehat{\mathbf{a}}_S^H$, \mathbf{a}_S and \mathbf{a}_I are the real polarization steering vectors of the target and the interference, and $\widehat{\mathbf{a}}_S$ and $\widehat{\mathbf{a}}_I$ are the estimated values, respectively.

Supposing the target signal, interference, and noise are uncorrelated, (9) can be simplified as

$$\text{MSE} = |x|^2 \sigma_s^2 + |y|^2 \sigma_i^2 + |z|^2 \sigma^2, \quad (10)$$

where

$$x = \widehat{\mathbf{A}}_S^\dagger \widehat{\mathbf{H}} \mathbf{a}_S - 1, \quad (11)$$

$$y = \widehat{\mathbf{A}}_S^\dagger \widehat{\mathbf{H}} \mathbf{a}_I, \quad (12)$$

$$z = \sqrt{\frac{1}{\sin^2 \psi}}, \quad (13)$$

$$\psi = \arccos \left(\left| \widehat{\mathbf{a}}_S^H \widehat{\mathbf{a}}_I \right| \right). \quad (14)$$

And σ_s^2 , σ_I^2 , and σ^2 are the power of the target, interference, and noise, respectively. Define x and y as the coefficients of σ_s^2 and σ_I^2 . The error analysis of the MSE will be discussed in three cases as follows.

2.2.1. MSE without Estimation Error: $\hat{\mathbf{a}}_S = \mathbf{a}_S$, $\hat{\mathbf{a}}_I = \mathbf{a}_I$. Supposing the polarization steering vectors of the target and the interference are both accurately estimated, according to (11) and (12), we have $x = y = 0$. The MSE gets to its minimum as

$$\text{MSE} = |z|^2 \sigma^2. \quad (15)$$

2.2.2. MSE with Target Estimation Error: $\hat{\mathbf{a}}_S \neq \mathbf{a}_S$, $\hat{\mathbf{a}}_I = \mathbf{a}_I$. In this case, we have $x \neq 0$ and $y = 0$, which indicates that the interference can be completely suppressed while the target is restored with distortion. Then the MSE can be simplified from (10) as

$$\text{MSE} = |x|^2 \sigma_s^2 + |z|^2 \sigma^2. \quad (16)$$

Ignoring the noise term, the MSE is mainly determined by x and σ_s^2 . According to the properties of oblique projection [15], it is beneficial to decompose vector \mathbf{a}_S into two specific components: the component that locates in the subspace spanned by $\hat{\mathbf{a}}_S$ and the one which lies in the subspace spanned by \mathbf{a}_I . Therefore, \mathbf{a}_S can be decomposed as

$$\mathbf{a}_S = (\alpha + \beta) \hat{\mathbf{a}}_S + \nu \mathbf{a}_I, \quad (17)$$

where

$$\begin{aligned} \alpha &= \frac{\hat{\mathbf{a}}_S^H \mathbf{a}_S}{(|\hat{\mathbf{a}}_S|^2 |\mathbf{a}_S|)}, \\ \beta &= \frac{(|\mathbf{a}_I|^2 \hat{\mathbf{a}}_S^H \mathbf{d} - \hat{\mathbf{a}}_S^H \mathbf{a}_I \mathbf{a}_I^H \mathbf{d})}{(|\hat{\mathbf{a}}_S|^2 |\mathbf{a}_I|^2 - \hat{\mathbf{a}}_S^H \mathbf{a}_I \mathbf{a}_I^H \hat{\mathbf{a}}_S)}, \\ \nu &= \frac{(|\hat{\mathbf{a}}_S|^2 \mathbf{a}_I^H \mathbf{d} - \mathbf{a}_I^H \hat{\mathbf{a}}_S \hat{\mathbf{a}}_S^H \mathbf{d})}{(|\hat{\mathbf{a}}_S|^2 |\mathbf{a}_I|^2 - \hat{\mathbf{a}}_S^H \mathbf{a}_I \mathbf{a}_I^H \hat{\mathbf{a}}_S)}, \\ \mathbf{d} &= \mathbf{a}_S - \alpha \hat{\mathbf{a}}_S. \end{aligned} \quad (18)$$

According to [13], the first part in (17), which locates in the target subspace, will be reserved as a whole, whereas the second part will be cancelled by $\hat{\mathbf{H}}$ to null. Substituting (17) into (11), x can be rewritten as

$$x = \hat{\mathbf{A}}_S^+ \hat{\mathbf{H}} ((\alpha + \beta) \hat{\mathbf{a}}_S + \nu \mathbf{a}_I) - 1 = \alpha + \beta - 1. \quad (19)$$

Therefore, (16) can be rewritten as

$$\text{MSE} = |\alpha + \beta - 1|^2 \sigma_s^2 + |z|^2 \sigma^2. \quad (20)$$

Equation (20) indicates that the MSE is mainly affected by the term of $|\alpha + \beta - 1|^2 \sigma_s^2$, which is the product of the target power σ_s^2 and its corresponding coefficient x . The lower the estimation accuracy of target's polarization state is, the larger the value of x will be, and the MSE increases. However, when the target is estimated with no error, (20) will be identical to (15).

2.2.3. MSE with Interference Estimation Error: $\hat{\mathbf{a}}_S = \mathbf{a}_S$, $\hat{\mathbf{a}}_I \neq \mathbf{a}_I$. Supposing the target signal is accurately estimated while the interference is not, we have $\hat{\mathbf{A}}_S^+ \hat{\mathbf{H}} \mathbf{a}_S = 1$ and $\hat{\mathbf{A}}_S^+ \hat{\mathbf{H}} \mathbf{a}_I \neq 0$, which makes $x = 0$, $y \neq 0$. In this case, the target is perfectly restored while the interference is partly suppressed by OPPF. Decomposing vector \mathbf{a}_I into two specific components, we have

$$\mathbf{a}_I = (\alpha' + \beta') \hat{\mathbf{a}}_I + \nu' \mathbf{a}_S, \quad (21)$$

where

$$\begin{aligned} \alpha' &= \frac{\hat{\mathbf{a}}_I^H \mathbf{a}_I}{(|\hat{\mathbf{a}}_I|^2 |\mathbf{a}_I|)}, \\ \beta' &= \frac{(|\mathbf{a}_S|^2 \hat{\mathbf{a}}_I^H \mathbf{d} - \hat{\mathbf{a}}_I^H \mathbf{a}_S \mathbf{a}_S^H \mathbf{d}')}{(|\hat{\mathbf{a}}_I|^2 |\mathbf{a}_S|^2 - \hat{\mathbf{a}}_I^H \mathbf{a}_S \mathbf{a}_S^H \hat{\mathbf{a}}_I)}, \\ \nu' &= \frac{(|\hat{\mathbf{a}}_I|^2 \mathbf{a}_S^H \mathbf{d} - \mathbf{a}_S^H \hat{\mathbf{a}}_I \hat{\mathbf{a}}_I^H \mathbf{d}')}{(|\hat{\mathbf{a}}_I|^2 |\mathbf{a}_S|^2 - \hat{\mathbf{a}}_I^H \mathbf{a}_S \mathbf{a}_S^H \hat{\mathbf{a}}_I)}, \\ \mathbf{d}' &= \mathbf{a}_I - \alpha' \hat{\mathbf{a}}_I. \end{aligned} \quad (22)$$

Substituting (21) into (12), y can be rewritten as

$$y = \hat{\mathbf{A}}_S^+ \hat{\mathbf{H}} (\alpha' + \beta') \hat{\mathbf{a}}_I + \hat{\mathbf{A}}_S^+ \hat{\mathbf{H}} \nu' \mathbf{a}_S = \nu'. \quad (23)$$

The MSE can be simplified as

$$\begin{aligned} \text{MSE} &= |\nu'|^2 \sigma_I^2 + |z|^2 \sigma^2 \\ &= \sigma_s^2 \left(\frac{|\nu'|^2}{\text{SIR}} + \frac{|z|^2}{\text{SNR}} \right), \end{aligned} \quad (24)$$

where $\text{SIR} = \sigma_s^2 / \sigma_I^2$ and $\text{SNR} = \sigma_s^2 / \sigma^2$ refers to the signal to noise ratio (SNR).

Equation (24) demonstrates that the interference cannot be suppressed completely when it is estimated with error. The degree of interference suppression is determined by the component $(\alpha' + \beta') \hat{\mathbf{a}}_I$ in (21). The smaller the estimation deviation is, the larger this component will be and the performance of OPPF will be better.

Moreover, fixing the SIR and SNR and the power of the target, according to (14), it can be noticed that the part of $|z|^2 \sigma^2$ in (15), (20), and (24) will increase and the MSE will become larger, when the polarization state of the target and the interference are getting close.

3. Polarization Cancellation for Ionosphere Clutter

To apply an OPPF in ionosphere clutter cancellation, it is necessary to accurately estimate the polarization state of the target and the ionosphere clutter, so that the clutter can be suppressed to the maximum whereas the target can be effectively restored. With regard to the nonstationary characteristic of the ionosphere clutter, the polarization estimation methods and ionosphere clutter cancellation scheme should be properly designed.

3.1. Polarization and Nonstationary Characteristic of Ionosphere Clutter. Ionosphere clutter, which is a kind of self-generated interference in HFSWR, is the radar signals reflecting back from the ionosphere. The polarization plane of the electromagnetic wave is usually rotated by the ionosphere along the radio propagation path, which makes the high power vertically polarized radar signals change into elliptically polarized ones. However, the echoes of targets arriving along the surface of ocean remain vertically polarized. Evident difference between the elliptical polarized ionosphere clutters and the vertically polarized target signals can be found in the dual-polarized HFSWR. That is, the power of the horizontally polarized component of ionosphere clutter is close to that of the vertically polarized part or even stronger. However, the power of the horizontally polarized component of the target echoes propagating along the ocean surface is quite weak compared with that of the vertically polarized component [16, 17].

Affected by the irregular activities of the free electrons and charged ions, the electron concentration of the ionosphere is unstable, which leads to the nonstationary feature of the ionosphere clutter [3]. The following characteristics of the ionosphere clutter are usually observed.

- (1) The ionosphere clutter is not stable in a CIT, and its duration time varies from several pulse periods to the whole CIT.
- (2) In each single pulse, some clutters occupy less range cells whereas some occupy more.
- (3) The nonstationary feature also leads to the different frequency spread in Doppler spectrum; some clutters locate in multiple successive Doppler cells while some exist in fewer Doppler cells.
- (4) The ionosphere clutter is usually elliptically polarized but its polarization state is unstable in the whole CIT [5]. As a result, it behaves as a partially polarized wave in a long time observation.

3.2. Nonstationary Ionosphere Clutter Polarization Cancellation Scheme. According to the characteristics of ionosphere clutter discussed above, a novel OPPF based polarization cancellation scheme for nonstationary ionosphere clutter is proposed. Figure 1 gives the basic structure of this scheme. In Figure 1, the raw data is pretreated first to obtain the polarization information of the clutters and the targets, which is necessary for building the RDDPS or RTDPS; then the signals are filtered in range or range-Doppler domain, and the output of the filter will be utilized to perform range and Doppler processing in RTDPS or given as the result in RDDPS, respectively. Five steps are needed to finish the clutter cancellation.

- (1) Because of the weak power of radar echoes, range processing and Doppler processing need to be carried out first. Range-Doppler maps are generated from the raw data of each horizontal and vertical channel, respectively.
- (2) The state of all the samples in the range-Doppler map is then estimated, including the power value and

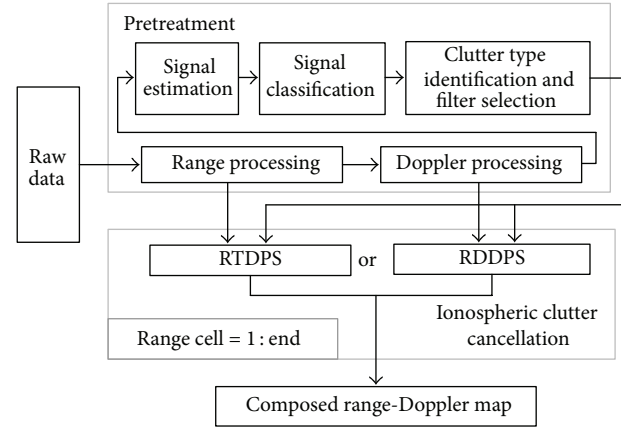


FIGURE 1: Structure of ionosphere clutter cancellation scheme.

polarization parameters. By using the basic characteristic of the signals in the range-Doppler map, the target and other clutters, such as ground clutter, ocean clutter, and ionosphere clutter, can be preliminarily separated and classified.

- (3) Based on the power estimation, the type of ionosphere clutter is identified cell by cell in range domain. The specific utilization of RDDPS or RTDPS at each range cell is determined by the clutter type at each range cell.
- (4) RDDPS and RTDPS algorithms, designed for different types of ionosphere clutter, will be used to suppress the clutter. The former one is designed for the ionosphere clutter with low power and the filtering process is carried out in range-Doppler domain directly. The latter one is designed for powerful clutter, and the filtering process is mainly carried out in the range-time domain. In a practical HFSWR system, the two types of ionosphere clutter may exist simultaneously and locate at different range cells. Therefore, the selection of RDDPS or RTDPS is decided by the clutter type at the corresponding range cell. Because of the adaptive scheme in this part, an optimal filtering effect can be obtained.
- (5) After all the range cells are treated with the procedure in (4), the final range-Doppler map is composed for RDDPS, whereas a range-Doppler processing is needed for RTDPS to obtain the final range-Doppler map.

3.3. Pretreatment. As drawn in Figure 1, pretreatment includes the range-Doppler processing, the signal parameters estimation, signal classification, determination of ionosphere clutter type, and the selection of filtering method. Different from conventional processing, in a dual-polarized HFSWR system, the radar raw data of both the horizontal polarization channel and vertical polarization channel are recorded simultaneously. Then range-Doppler map of each channel can be obtained, respectively. Then the power value and polarization state of all the signals in the range-Doppler map can be estimated and stored. After all the signals are

classified, the target (big enough or separated from the clutter), ground/ocean clutter, and ionosphere clutter will be separated apart. Suppose the range-Doppler map is composed by J range cells and R Doppler cells. The samples of the vertical and horizontal polarization channel at the current range-Doppler cell (j, r) are defined as $V(j, r)$ and $H(j, r)$, where $1 \leq j \leq J$ and $1 \leq r \leq R$, respectively. The estimation values of the power value $d(j, r)$, polarization angle $\gamma(j, r)$, and polarization angle difference $\eta(j, r)$ of range-Doppler cell (j, r) can be given as

$$\begin{aligned}\hat{d}(j, r) &= \sqrt{(V(j, r))^2 + (H(j, r))^2}, \\ \hat{\gamma}(j, r) &= \arctan\left(\frac{\text{abs}(V(j, r))}{\text{abs}(H(j, r))}\right), \\ \hat{\eta}(j, r) &= \text{angle}(V(j, r)) - \text{angle}(H(j, r)),\end{aligned}\quad (25)$$

where $\text{angle}()$ is the function to obtain the complex phase of $V(j, r)$ and $H(j, r)$.

After the parameters have been estimated, all the signals will be classified. Firstly, a power value gate is set by d_L to reduce the impact of noise. All the samples that satisfy $\hat{d}(j, r) \geq d_L$ are determined to be valid while the other samples are considered to be noise. Secondly, the ocean clutter can be separated by utilizing the relationship between the radar transmitting frequency and the Bragg frequency [18]. Thirdly, by using the polarization characteristic of the ionosphere clutter, a polarization angle gate γ_L is further defined. Those valid samples that satisfy $\hat{\gamma}(j, r) \leq \gamma_L$ are determined as ionosphere clutter while the others are considered as echoes returning along the ocean and/or the mixed signal. In this way, the target, ocean clutter, and ionosphere clutter are preliminarily separated from each other in the range-Doppler map.

The ionosphere clutter is checked cell by cell. For the range cells that ionosphere clutter exists in, polarization cancellation scheme will be applied. In order to decide which polarization filtering algorithm will be taken, define function F_n , of which the logic is set to $\{1, 0\}$. If $F_n = 1$, RDDPS algorithm is chosen; if $F_n = 0$, RTDPS algorithm will be applied.

The criterion of algorithm selection is based on the relationship of the power between the target and the ionosphere clutter. At the corresponding range cell, if the maximum value of the ionosphere clutter power is smaller than the average power of the target, the clutter is considered to be weak and $F_n = 1$. On the contrary, the clutter is considered to be strong and $F_n = 0$. Suppose the set of power values of all the ionosphere clutters and targets at the corresponding range cell are defined as D_I and D_S , respectively; F_n can be specified as

$$F_n = \begin{cases} 1, & \max(D_I) < \text{mean}(D_S) \\ 0, & \max(D_I) \geq \text{mean}(D_S). \end{cases} \quad (26)$$

However, in certain range cells, the target may be non-existent; the value of F_n in (26) will be uncertain. Therefore,

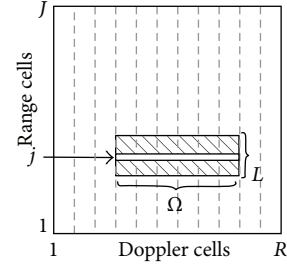


FIGURE 2: Diagrammatic illustration of RDDPS.

considering the Bragg scattering lines have the similar polarization characteristic with the target, (26) can be modified as

$$F_n = \begin{cases} 1, & \max(D_I) < \max(D_{\text{Bragg},L}, D_{\text{Bragg},R}) \\ 0, & \max(D_I) \geq \max(D_{\text{Bragg},L}, D_{\text{Bragg},R}), \end{cases} \quad (27)$$

where $D_{\text{Bragg},L}$ and $D_{\text{Bragg},R}$ are the power value of left and right Braggs at the current range cell, respectively.

3.4. Range-Doppler Domain Polarization Suppression. To illustrate the potential advantages of range-Doppler domain suppression, three main aspects are given as follows.

- (1) Due to the time-frequency invariance of the signal's polarization characteristic [12, 19], the estimation of the signal's polarization parameters can be performed in range-Doppler domain.
- (2) In range-Doppler domain the power of each signal can be concentrated on limited range and Doppler cells, respectively, which significantly increases the SNR and interference to noise ratio (INR). In this way, the polarization estimation accuracy of both the target and the clutter will be improved effectively. As mentioned in Section 2, the improvement of estimation accuracy is beneficial for the clutter suppression and the restoration of the targets as well.
- (3) In range-Doppler domain, the multiple clutters and targets can be isolated in different cells, providing a possibility of individual polarization estimation and suppression for each clutter, and the polarization degree of the signals is improved.

Based on the analysis above, polarization filtering in range-Doppler domain is considered to be more suitable to process the ionosphere clutter with weak power. The improved SIR and INR will significantly enhance the estimation accuracy and the performance of the filter.

The illustration of RDDPS is drawn in Figure 2. Supposing there are some ionosphere clutters existing at the range cell j , a range-Doppler window ($L \times \Omega$) is first set in the range-Doppler map ($J \times R$), as shown in Figure 2. In the center of the window is the clutter area to be processed. The polarization state of clutters at the range cell j will be estimated in the adjacent cells, as the characteristic of the ionosphere clutter in the neighbor range-Doppler is similar [3].

In the range-Doppler window, the polarization estimation is performed cell by cell in range for L times. In each range cell, the samples that have the maximum power value are used for polarization estimation. To avoid the influence of target-like signal, the range-Doppler domain data in the window are excluded with the target and ground/ocean clutter. In this way, a sum of L polarization parameters is obtained and the corresponding L OPPF operators are generated. Ignoring the noise and supposing there are Q clutters at range cell j , the composite input signal $\mathbf{E}(j, \omega)$ can be expressed as

$$\begin{aligned} \mathbf{E}(j, \omega) &= \mathbf{E}_S(j, \omega) + \mathbf{E}_I(j, \omega) \\ &= \mathbf{E}_S(j, \omega) + \sum_{q=1}^Q \mathbf{E}_{I,q}(j, \omega) \\ &= \mathbf{a}_S S(j, \omega) + \sum_{q=1}^Q \mathbf{a}_{I,q} I_q(j, \omega), \end{aligned} \quad (28)$$

where ω is the Doppler frequency, $\mathbf{E}_S(j, \omega)$ and $\mathbf{E}_I(j, \omega)$ are the target and the ionosphere clutters at range cell j , and $\mathbf{E}_{I,q}(j, \omega)$ is the q th clutter of $\mathbf{E}_I(j, \omega)$, where \mathbf{a}_S , $\mathbf{a}_{I,q}$, $S(j, \omega)$, and $I_q(j, \omega)$ are the polarization steering vector and range-Doppler spectrum of the target and the q th clutter $\mathbf{E}_{I,q}(j, \omega)$, respectively.

For simplicity, suppose $L = Q$ and the generated L OPPF operators have one-to-one correspondence with the Q clutters. Specifically, the l th OPPF operator \mathbf{H}_l is generated to suppress the q th clutter, when $l = q$. According to (3), the corresponding OPPF operator can be given as $\mathbf{H}_l = \mathbf{a}_S (\mathbf{a}_S^H \mathbf{P}_{\mathbf{a}_{I,l}}^\perp \mathbf{a}_S)^{-1} \mathbf{a}_S^H \mathbf{P}_{\mathbf{a}_{I,l}}^\perp$, $l = 1, 2, \dots, L$. According to (6), the output of l th OPPF at range cell j can be expressed as

$$\begin{aligned} \mathbf{Y}_l(j, \omega) &= \mathbf{H}_l \mathbf{E}(j, \omega) \\ &= \mathbf{H}_l \left(\mathbf{a}_S S(j, \omega) + \mathbf{a}_{I,l} I_l(j, \omega) \right. \\ &\quad \left. + \sum_{q=1}^{l-1} \mathbf{a}_{I,q} I_q(j, \omega) + \sum_{q=l+1}^Q \mathbf{a}_{I,q} I_q(j, \omega) \right) \\ &= \mathbf{E}_S(j, \omega) + \mathbf{H}_l \sum_{q=1, q \neq l}^Q \mathbf{E}_{I,q}(j, \omega), \end{aligned} \quad (29)$$

where $\mathbf{Y}_l(j, \omega)$ is the l th range-Doppler spectrum, in which the l th ionosphere clutter $\mathbf{E}_{I,l}(j, \omega)$ is completely suppressed.

Equation (29) indicates that the l th clutter $\mathbf{E}_{I,l}(j, \omega)$ can be effectively cancelled by \mathbf{H}_l while the rest of $Q - 1$ clutters are still left in $\mathbf{Y}_l(j, \omega)$. Obviously, when all OPPF operators are applied to $\mathbf{E}_I(j, \omega)$ in turn, L filtering results will be obtained and only the clutter that matches $\mathbf{a}_{I,l}$ will be suppressed to the maximum. Suppose all the clutters are not overlapping with each other in the Doppler spectrum. In order to obtain a composite result from the above L filtering results, logic product process [12], which reserves the smallest points in

Doppler spectrum from the L filtering results, can be applied. Therefore, all the Q ionosphere clutters will be suppressed simultaneously in the Doppler spectrum. Moreover, as shown in (29), the target $\mathbf{E}_S(j, \omega)$ can be completely restored in each filtering result. In this way, the logic product process will not influence $\mathbf{E}_S(j, \omega)$ in the final result. And the output of RDDPS $\mathbf{Y}_{\text{RDDPS}}(j, \omega)$ can be expressed as

$$\mathbf{Y}_{\text{RDDPS}}(j, \omega) = \sum_{r=1}^R \left\{ \delta(\omega - \omega_r) \min_{l=1}^L (\mathbf{H}_l \mathbf{E}(j, \omega)) \right\}, \quad (30)$$

where ω_r is the Doppler frequency of Doppler cell r .

When the actual number of the clutters is less than L , ($L > Q$), which is the most common situation for RDDPS, the amount of estimated parameters is more than the amount of clutters. Clearly, for some clutters, their polarization state will be estimated for more than once in the range-Doppler window. And the corresponding filtering results will be similar. Note that the OPPF, which is generated by the estimated parameters approaching the real values, will suppress the clutter deeper; the recovered $\mathbf{Y}_{\text{RDDPS}}(j, \omega)$ in fact can be considered as an optimized result of the L filter outputs.

3.5. Range-Time Domain Polarization Suppression. The scheme of RDDPS takes advantage of the characteristic of the ionosphere clutter in range-Doppler domain and hence is suitable for ionosphere clutter cancellation of low power in HFSWR. However, the nonstationary characteristic of ionosphere clutter will degrade the performance of RDDPS, as a result of the decline of clutter's polarization degree. To solve this problem, another scheme which is referred to as range-time domain polarization suppression (RTDPS) is proposed.

Rather than estimating the polarization state in a CIT, the nonstationary characteristic of ionosphere clutter can be relaxed when the clutter is observed under a smaller time scale. By dividing the time domain data into many segments, the polarization degree in each segment can be improved. Thus, for a RTDPS, data segmentation is performed prior to the estimation and filtering process. The range-Doppler map is used to find the position (range and Doppler frequency) of the clutter, and the polarization state of the clutter is estimated in the corresponding range-Doppler cell of each segment, whereas the filtering process is performed in the range-time domain. To guarantee the estimation accuracy, a higher INR is required to compensate the decreased coherent integration time in each segment. That is why the RTDPS is more suitable for suppressing the strong ionosphere clutters. For the case of single clutter in the corresponding range cell, RTDPS is applied in the mode of single-notch mode, whereas a mult notch filtering mode of RTDPS will be taken when more clutters exist. It is necessary to emphasize that the notch is in the Doppler domain rather than in the polarization domain, which is completely different from the definition in [12].

3.5.1. Single-Notch RTDPS. As shown in Figure 3, the single-notch RTDPS contains the following parts: setting of notch

in Doppler domain, time domain segmentation, polarization estimation and clutter suppressing in each segment, and the final time domain data reconstruction.

Based on the results of the pretreatment step, a Doppler notch is set first to cover the region of several successive Doppler cells where the ionosphere clutter locates. In this way, the polarization steering vector of the ionosphere clutter can be estimated from the samples in the Doppler notch. After being processed by RTDPS, the ionosphere clutter in this area will be suppressed heavily, forming a “notch” in the Doppler spectrum.

After the Doppler notch has been set, the time domain data is divided into P segments. In each segment, Doppler processing and polarization estimation are carried out to generate the corresponding OPPF operator. As shown in Figure 3, the ionosphere clutters in the Doppler notch will be suppressed by the OPPF within each segment. It should be noticed that the polarization estimation is finished in Doppler domain, whereas the filter is used in time domain.

Suppose the sum of time domain samples at the current range cell j is N and the number of segments is P (suppose N can be exactly divided by P). The ionosphere clutter $\mathbf{E}_I(j, n)$ can be described as

$$\mathbf{E}_I(j, n) = \sum_{p=1}^P \mathbf{E}_{I,p}(j, n), \quad \frac{N(p-1)}{P} < n \leq \frac{Np}{P}, \quad (31)$$

where $\mathbf{E}_{I,p}(j, n)$ is the clutter in segment p in range-time domain.

In each segment, it is convenient to decompose $\mathbf{E}_{I,p}(j, n)$ into the completely polarized component $\mathbf{E}_{I,CP,p}(j, n)$ and the completely unpolarized component $\mathbf{E}_{I,UP,p}(j, n)$; $\mathbf{E}_I(j, n)$ can be rewritten as

$$\begin{aligned} \mathbf{E}_I(j, n) &= \sum_{p=1}^P (\mathbf{E}_{I,CP,p}(j, n) + \mathbf{E}_{I,UP,p}(j, n)) \\ &= \sum_{p=1}^P (\mathbf{a}_{I,p} I_p(j, n) + \mathbf{E}_{I,UP,p}(j, n)), \end{aligned} \quad (32)$$

$$\frac{N(p-1)}{P} < n \leq \frac{Np}{P},$$

where $\mathbf{a}_{I,p}$ and $I_p(j, n)$ are the polarization steering vector and the corresponding time domain data of the completely polarized component $\mathbf{E}_{I,CP,p}(j, n)$.

Meanwhile, the highly polarized target $\mathbf{E}_S(j, n)$ can be described as

$$\mathbf{E}_S(j, n) = \sum_{p=1}^P \mathbf{E}_{S,p}(j, n) = \sum_{p=1}^P \mathbf{a}_S S_p(j, n), \quad (33)$$

$$\frac{N(p-1)}{P} < n \leq \frac{Np}{P},$$

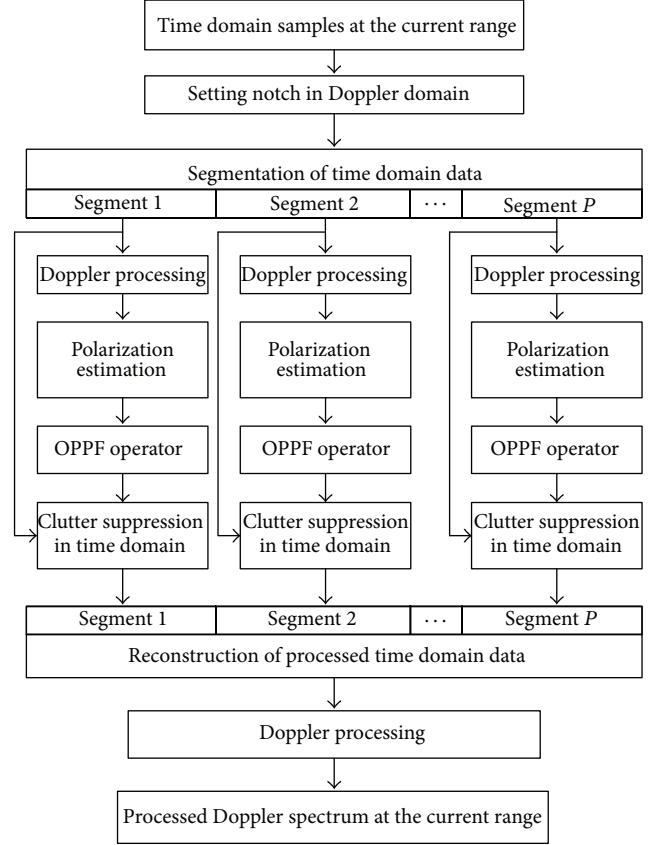


FIGURE 3: Principle of single-notch RTDPS.

where \mathbf{a}_S is the polarization steering vector of the target and $S_p(j, n)$ is the corresponding time domain data of $\mathbf{E}_{S,p}(j, n)$ in segment p , respectively.

Then the OPPF operators of each segment can be obtained as $\mathbf{H}_p = \mathbf{a}_S (\mathbf{a}_S^H \mathbf{P}_{\mathbf{a}_{I,p}}^\perp \mathbf{a}_S)^{-1} \mathbf{a}_S^H \mathbf{P}_{\mathbf{a}_{I,p}}^\perp$, where $\mathbf{P}_{\mathbf{a}_{I,p}}^\perp = \mathbf{I} - \mathbf{a}_{I,p} (\mathbf{a}_{I,p}^H \mathbf{a}_{I,p})^{-1} \mathbf{a}_{I,p}^H$ and $p = 1, 2, \dots, P$. According to (6), the filtering process of single-notch RTDPS can be given as

$$\begin{aligned} \hat{\mathbf{E}}_S(j, n) &= \sum_{p=1}^P \{ \mathbf{H}_p (\mathbf{E}_{S,p}(j, n) + \mathbf{E}_{I,p}(j, n)) \} \\ &= \sum_{p=1}^P \{ \mathbf{H}_p \mathbf{a}_S S_p(j, n) + \mathbf{H}_p \mathbf{a}_{I,p} I_p(j, n) \\ &\quad + \mathbf{H}_p \mathbf{E}_{I,UP,p}(j, n) \} \\ &= \sum_{p=1}^P \{ \mathbf{a}_S S_p(j, n) + \mathbf{H}_p \mathbf{E}_{I,UP,p}(j, n) \} \\ &= \mathbf{E}_S(j, n) + \sum_{p=1}^P \mathbf{H}_p \mathbf{E}_{I,UP,p}(j, n). \end{aligned} \quad (34)$$

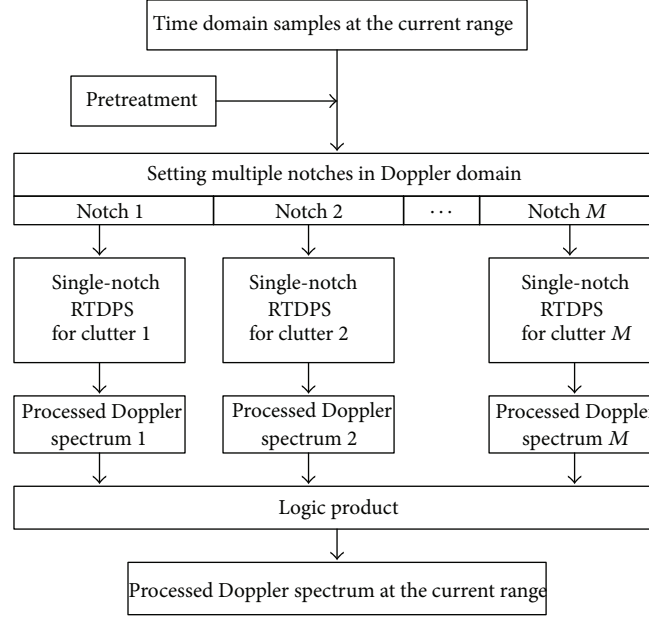


FIGURE 4: Principle of multinotch RTDPS.

After the Doppler processing, the final output of single-notch RTDPS can be expressed as

$$\mathbf{Y}_{\text{RTDPS_single}}(j, \omega) = \text{FFT} \left[\mathbf{E}_S(j, n) + \sum_{p=1}^P \mathbf{H}_p \mathbf{E}_{I_UP,p}(j, n) \right]. \quad (35)$$

The second component in (35) is the completely unpolarized part of the ionosphere clutter, which will be kept as stochastic noise. Meanwhile, the completely polarized part, described as the first component in (32), can be completely cancelled when $\mathbf{a}_{i,p}$ is accurately estimated.

By dividing the range-time domain data into segments, the estimation and suppression scheme is performed in separate segments and the polarization degree of the ionosphere clutter in each segment can be increased. As a result, the estimation accuracy of the clutter's polarization will be improved and the clutter can be suppressed more completely as the completely unpolarized part is unable to be suppressed.

3.5.2. Multinotch RTDPS. Multinotch RTDPS is implemented for more clutters at the current range cell, as drawn in Figure 4. The quantity and distribution state of the ionosphere clutters at the current range cell are estimated in the pretreatment step. After the locations and sizes of the Doppler notches are decided, single-notch RTDPS is implemented for each clutter. And the final Doppler spectrum is generated by the logic product process.

Supposing the sum of ionosphere clutters is M , M filtering results can be obtained by utilizing single-notch RTDPS shown in (35). Supposing all the clutters are not

overlapping with each other in the Doppler spectrum, the result of multinotch RTDPS $\mathbf{Y}_{\text{RTDPS_multi}}(j, \omega)$ can be given as

$$\mathbf{Y}_{\text{RTDPS_multi}}(j, \omega) = \sum_{r=1}^R \left\{ \delta(\omega - \omega_r) \min_{m=1}^M (\mathbf{Y}_{\text{RTDPS_single},m}(j, \omega)) \right\}, \quad (36)$$

where M and N represent the number of clutters and that of the time domain samples at the current range cell j , respectively; ω_r is the frequency of Doppler cell r and $\mathbf{Y}_{\text{RTDPS_single},m}(j, \omega)$ is the output of the single-notch RTDPS for the m th clutter.

3.5.3. Clutter Polarization Estimation within Each Segment. Supposing the width of the Doppler notch is K , the parameters of the samples in this Doppler notch are defined as $(\gamma_{I,k,p}, \eta_{I,k,p}, d_{I,k,p}), k \in [1, K]$, where the first and second parameters are the polarization angle and angle difference and the third parameter is the power value of the sample. To be clear, the subscript of I denotes the ionosphere clutter, k is the serial number of the Doppler notch, and p represents the serial number of the current segment, respectively.

For each segment, the polarization steering vector of the ionosphere clutter within the Doppler notch can be estimated by

$$\mathbf{a}_{I,p}(\gamma_{I,h,p}, \eta_{I,h,p}) = \begin{bmatrix} \cos \gamma_{I,h,p} \\ \sin \gamma_{I,h,p} \exp(j\eta_{I,h,p}) \end{bmatrix}, \quad (37)$$

where

$$d_{I,h,p} = \max [d_{I,k,p}], \quad k, h \in [1, K]. \quad (38)$$

The estimated values are determined by the sample that has the maximum power within the Doppler notch.

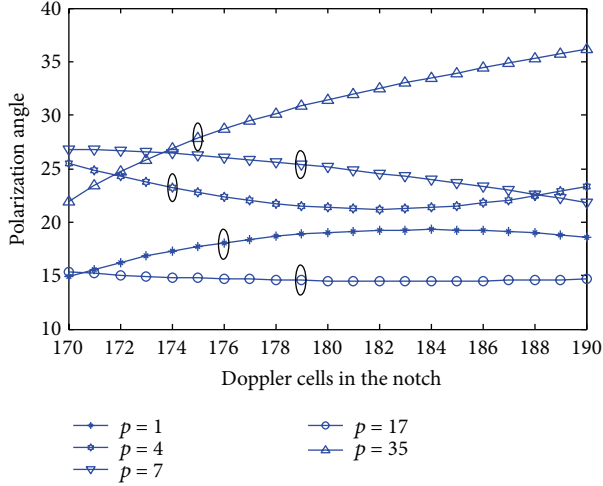


FIGURE 5: Selection of polarization parameters in Doppler notch.

Derived from the experimental HFSWR data, Figure 5 gives polarization angles in segments 1, 4, 7, 17, and 35, when total 40 segments are used. The horizontal axis is the Doppler cells whereas the vertical axis is the polarization angle. By using the definition in (38), the samples of the maximum power in the 5 segments are selected and marked with ellipses as shown in Figure 5. According to (37), the polarization steering vectors of each of the corresponding segments can be estimated as $\mathbf{a}_{I,1}(\gamma_{I,176,1}, \eta_{I,176,1})$, $\mathbf{a}_{I,4}(\gamma_{I,174,4}, \eta_{I,174,4})$, $\mathbf{a}_{I,7}(\gamma_{I,179,7}, \eta_{I,179,7})$, $\mathbf{a}_{I,17}(\gamma_{I,179,17}, \eta_{I,179,17})$, and $\mathbf{a}_{I,35}(\gamma_{I,175,35}, \eta_{I,175,35})$, respectively.

3.5.4. Set of Segment Numbers. In Figure 5, an obvious fluctuating, which is caused by the nonstationary polarization characteristic of the ionosphere clutter, can be found, whereas a plain curve is expected to suppress the clutter with different Doppler frequency together within the notch.

To improve the polarization stationarity or the polarization degree of the clutter in each segment, more segments number should be used. As given in Figure 6, the variance of polarization angle distribution of the clutter decreases when the segment number increases. However, more segments indicate shorter time in coherent integration and result in more estimation error, which degrades the performance of the filter.

Therefore, a satisfied performance of clutter cancellation can be only obtained by properly selecting the number of time domain segment. There is a trade-off between the improvement of polarization degree and reduction of estimation error, which should be balanced in practical application.

4. Experimental Performance Evaluation

To evaluate the performance of the proposed method, experimental data of a dual-polarized HFSWR in the east coastal region of China [20] are utilized. The HFSWR is installed by Harbin Institute of Technology and is equipped with

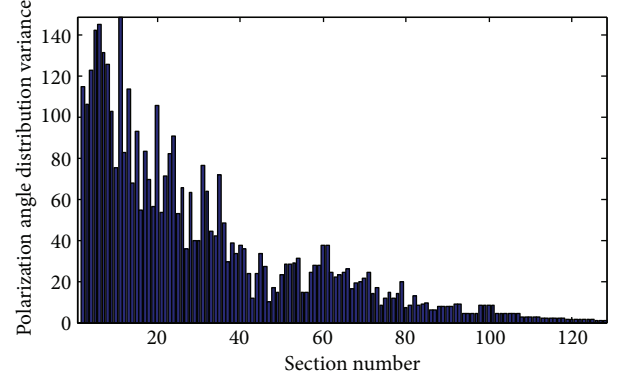


FIGURE 6: Polarization stationarity under different segment numbers.

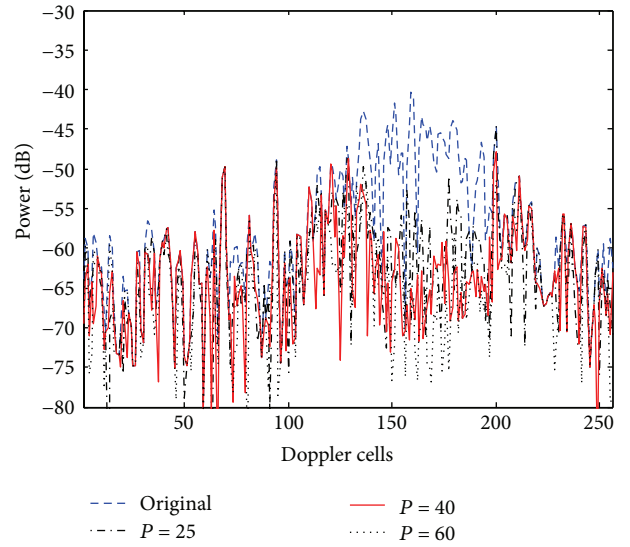


FIGURE 7: Clutter cancellation performance by different segment numbers.

eight-element vertically polarized receiving antenna array and two mutual-orthogonal horizontal polarized antennas to carry out various experiments of interference cancellation.

4.1. Segmentation Setting of RTDPS. Set a group of successive notches that cover the ionosphere clutters region locating in Doppler cells 132–195 at the range cell 157. Figure 7 gives the original Doppler spectrum and the outputs of the RTDPS by using 25, 40, and 60 segments, respectively. The average power of the four curves in the region is -48 dB, -61 dB, -64 dB, and -66 dB, respectively. It can be found that the clutter can be suppressed effectively, and the suppressed capability depends on the segment number used. The SIR improvement is about 13 dB, 16 dB, and 18 dB when the segment number is 25, 40, and 60, respectively.

In each segment, the target signal with an ideal polarization will be recovered without any distortion. However, the polarization of some targets may be different with an ideal one and a distortion of amplitude and phase will be introduced

in these segments. As a result, the targets (or Braggs) are also suppressed when the segment number increases (see Doppler cell 200 in Figure 7).

Therefore, while the segmentation of RTDPS improves the performance of clutter cancellation, the coherent integration of the targets with polarization mismatching will be influenced. Then the segment number should be balanced between the clutter suppressing and target restoration. In our simulation, the segmentation number is set as

$$P_{\text{opt}} = 40. \quad (39)$$

4.2. Ionosphere Clutter Cancellation. Figure 8 gives the result of two typical types of ionosphere clutter suppression at the range cell 69, by the RDDPS and RTDPS, respectively. In Figure 8, the blue dashed line is the original Doppler spectrum, whereas the black solid line and the red dotted line are the results of RDDPS and RTDPS, respectively. In order to evaluate the effectiveness of the clutter cancellation and the target preservation, a synthetic target is also added to the raw data, which locates in the range cell 69 Doppler cell 32 with the power of -22 dB.

In Figure 8, the peak at the Doppler cell 64 with the power of -36 dB (64, -36 dB) is the left Bragg peak and the one at the Doppler cell 198 with the power of -30 dB (198, -30 dB) is the right Bragg peak of the ocean clutter, whereas the peaks at around (80, -41 dB), (83, -33 dB), (118, -45 dB), (172, -31 dB), and (177, -25 dB) are the signals of the targets. At the current range cell, the ionosphere clutter is weak and masks almost all the Doppler cells. In Figure 8, the power of the background noise of RDDPS and RTDPS degrades to about -73 dB and -66 dB, respectively, and the SIR improvement is about 14 dB for RDDPS and 7 dB for RTDPS. No matter what methods are used, the targets and Braggs can be well restored and the peaks are clearer after process.

Figure 9 gives the results of RDDPS and RTDPS at the range cell 158, respectively. A synthetic target is also added to the raw data, which locates in the Doppler cell 32 with the power of -42 dB. Different from the range cell 69, the ionosphere clutter occupying Doppler cells 110–190 reveals higher power value (-44 dB in average), of which the maximum power is as high as -35 dB, which is 9 dB higher than the target signal (94, -44 dB). In Figure 9, the targets at Doppler cells 94 and 32 are completely restored independent of the method. However, the background noise of RDDPS and RTDPS in Doppler cells 110–190 is about -59 dB and -66 dB, respectively, indicating a better performance of RTDPS.

Figure 10 gives the original range-Doppler map and the final result. The same as in Figures 8 and 9, two synthetic targets at range cells 69 and 158 are added to the raw data. To be specified, a light blue line is attached and divides the original range-Doppler map into two parts. The ionosphere clutter is estimated to be stronger than the targets and Braggs in the upper part, so $F_n = 0$ and RTDPS is applied in the range cells 156–200, whereas $F_n = 1$ in the lower part of the map and the RDDPS is utilized in the rest of range cells. Processed with the proposed method, the weak ionosphere clutter that masks range cells 25–155 is suppressed close to the power of background noise, and the SIR improvement is about 15 dB

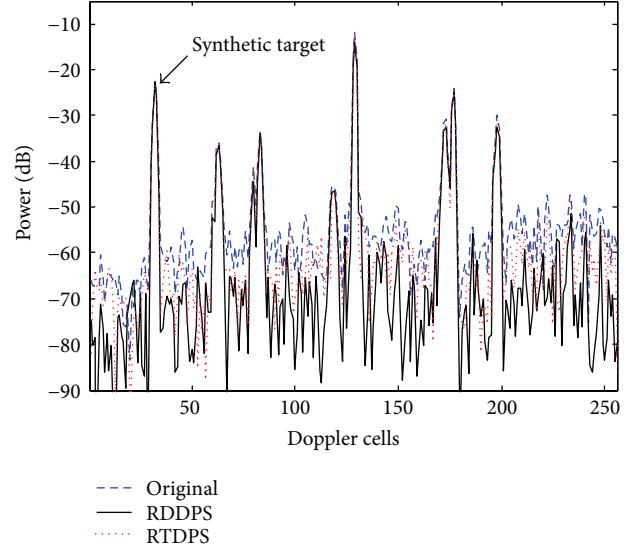


FIGURE 8: Results of RDDPS and RTDPS at range cell 69.

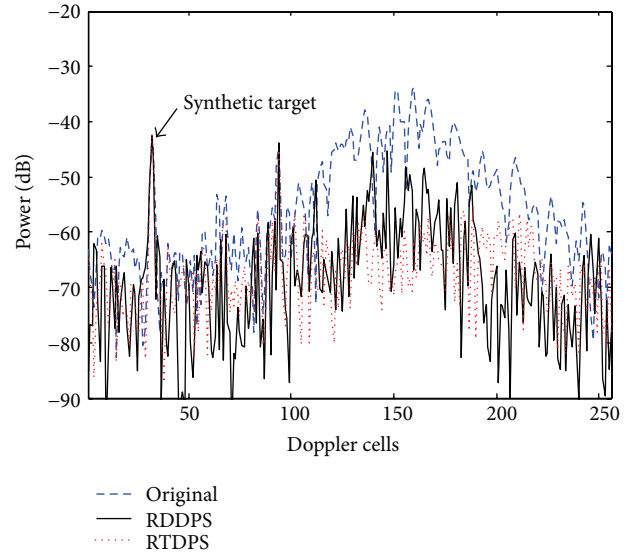


FIGURE 9: Results of RTDPS at range cell 158.

in average. Meanwhile, the powerful ionosphere clutters that cover range cells from 156 to 180 are also suppressed, while the SIR improvement is about 22 dB in average. As a result, all the targets are more clear and easier to be detected and tracked in the range-Doppler map.

5. Conclusion

In this paper, a novel ionosphere clutter cancellation scheme is proposed. Two types of ionosphere clutter cancellation methods, RDDPS and RTDPS, are designed based on the theory of OPPE. RTDPS is suitable in dealing with powerful ionosphere clutter, whereas the RDDPS performs a stable filtering effect to suppress the clutter of low power. The selection of RDDPS or RTDPS algorithm is determined by

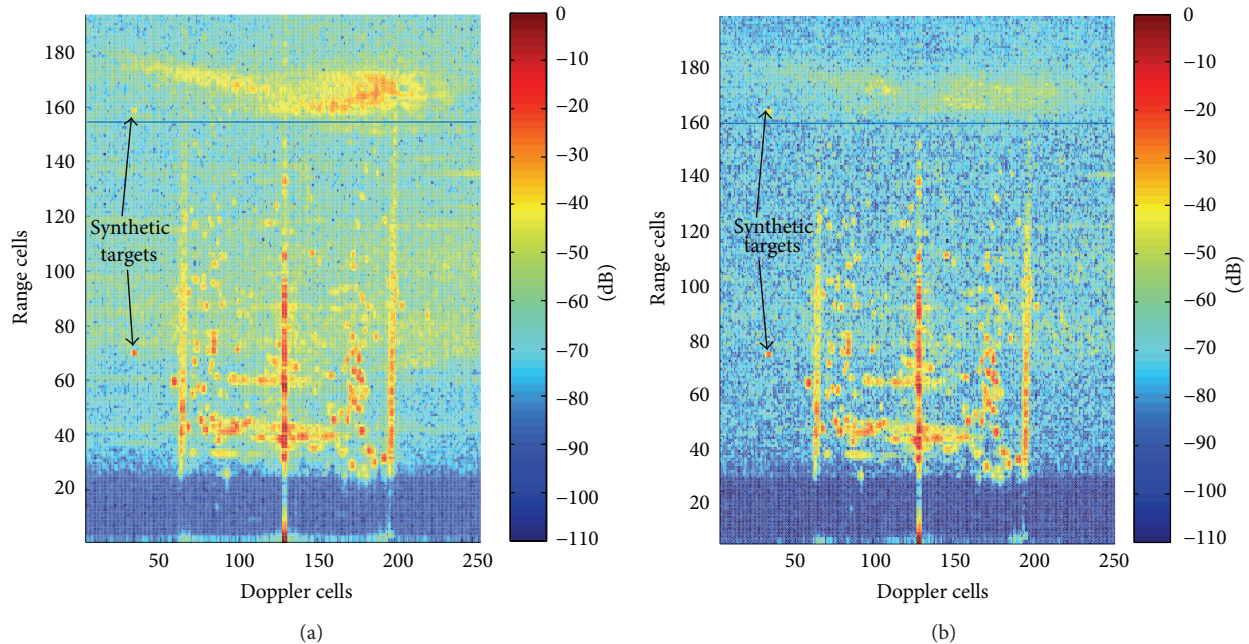


FIGURE 10: The original and the processed range-Doppler map.

the clutter type at the corresponding range cell. Combining the RDDPS and RTDPS together, the ionosphere clutters can be suppressed deeply. Theoretical analysis and experimental results demonstrate that the proposed scheme is valid and the SIR can be increased more than 15 dB. It is indicated that the proposed method may serve as a suitable method for ionosphere clutter cancellation in a practical HFSWR system.

Conflict of Interests

The authors declare that there is no conflict of interests regarding the publication of this paper.

Acknowledgment

This project is sponsored by the National Natural Science Foundation of China (no. 61171180).

References

- [1] H. C. Chan, "Characterization of ionospheric clutter in HF surface wave radar," Defence R&D Canada-Ottawa Technical Report, DRDC Ottawa TR, 2003.
- [2] W. Shen, B.-Y. Wen, Z.-L. Li, X.-J. Huang, and J. Yang, "Ionospheric measurement with HF ground wave radar system," *Chinese Journal of Radio Science*, vol. 23, no. 1, pp. 1–5, 2008.
- [3] X. Guo, H. Sun, and T. S. Yeo, "Interference cancellation for high-frequency surface wave radar," *IEEE Transactions on Geoscience and Remote Sensing*, vol. 46, no. 7, pp. 1879–1891, 2008.
- [4] H.-T. Su and Z. Bao, "Adaptive HF-communication interference mitigation in HF-GWR," *Chinese Journal of Radio Science*, vol. 18, no. 3, pp. 270–274, 2003.
- [5] G. A. Fabrizio, A. B. Gershman, and M. D. Turley, "Robust adaptive beamforming for HF surface wave over-the-horizon radar," *IEEE Transactions on Aerospace and Electronic Systems*, vol. 40, no. 2, pp. 510–525, 2004.
- [6] A. J. Poelman, "Virtual polarisation adaptation—a method of increasing the detection capability of a radar system through polarization-vector processing," *IEE Proceedings of Communications, Radar and Signal Processing*, vol. 128, no. 5, pp. 261–270, 1981.
- [7] M. Gherardelli, D. Giuli, and M. Fossi, "Suboptimum adaptive polarisation cancellers for dual-polarisation radars," *IEE Proceedings, Part F: Communications, Radar and Signal Processing*, vol. 135, no. 1, pp. 60–72, 1988.
- [8] G. Y. Zhang and Y. T. Liu, "Study of the polarization filtering technique of HF ground wave radar," *Journal of Systems of Engineering and Electronics*, vol. 22, no. 3, pp. 55–57, 2000.
- [9] R. Tian and X. Tian, "Novel polarization filter design for wideband radar," *Journal of Systems Engineering and Electronics*, vol. 23, no. 4, pp. 522–528, 2012.
- [10] X.-P. Mao, Y.-T. Liu, W.-B. Deng, C.-J. Yu, and Z.-L. Ma, "Null phase-shift instantaneous polarization filter," *Acta Electronica Sinica*, vol. 32, no. 9, pp. 1495–1498, 2004.
- [11] X.-P. Mao and Y.-T. Liu, "Null phase-shift polarization filtering for high-frequency radar," *IEEE Transactions on Aerospace and Electronic Systems*, vol. 43, no. 4, pp. 1397–1408, 2007.
- [12] X.-P. Mao, Y.-T. Liu, and W.-B. Deng, "Frequency domain null phase-shift multinotch polarization filter," *Acta Electronica Sinica*, vol. 36, no. 3, pp. 537–542, 2008.
- [13] X.-P. Mao, A.-J. Liu, W.-B. Deng, B. Cao, and Q.-Y. Zhang, "An oblique projecting polarization filter," *Acta Electronica Sinica*, vol. 38, no. 9, pp. 2003–2008, 2010.
- [14] X.-P. Mao, A.-J. Liu, and H.-J. Hou, "Oblique projection polarisation filtering for interference suppression in high-frequency surface wave radar," *IET Radar, Sonar and Navigation*, vol. 6, no. 2, pp. 71–80, 2012.

- [15] R. T. Behrens and L. L. Scharf, "Signal processing applications of oblique projection operators," *IEEE Transactions on Signal Processing*, vol. 42, no. 6, pp. 1413–1424, 1994.
- [16] K. Davies, *Ionospheric Radio*, pp. 225–230, Peter Peregrinus, London, UK, 1990.
- [17] M. Xingpeng, L. Yongtan, D. Weibo, Y. Changjun, and M. Zilong, "Sky wave interference of high-frequency surface wave radar," *Electronics Letters*, vol. 40, no. 15, pp. 968–969, 2004.
- [18] S. Leinwoll, *Shortwave Propagation*, John Lyder Publisher, New York, NY, USA, 1959.
- [19] A. Roueff, J. Chanussot, and J. I. Mars, "Estimation of polarization parameters using time-frequency representations and its application to waves separation," *Signal Processing*, vol. 86, no. 12, pp. 3714–3731, 2006.
- [20] Y. T. Liu, R. Q. Xu, and N. Zhang, "Progress in HFSWR research at Harbin institute of technology," in *Proceeding of the IEEE Radar Conference*, pp. 522–528, Adelaide, Australia, September 2003.

Research Article

The Application of JDL to Suppress Sea Clutter for Shipborne HFSWR

Zhenyuan Ji, Chunlei Yi, Junhao Xie, and Yang Li

Department of Electronic Engineering, Harbin Institute of Technology, Harbin 150001, China

Correspondence should be addressed to Junhao Xie; xj@hit.edu.cn

Received 25 April 2014; Revised 27 October 2014; Accepted 28 October 2014

Academic Editor: Michelangelo Villano

Copyright © 2015 Zhenyuan Ji et al. This is an open access article distributed under the Creative Commons Attribution License, which permits unrestricted use, distribution, and reproduction in any medium, provided the original work is properly cited.

This paper deals with the problem of sea clutter suppression for shipborne high frequency surface wave radar (HFSWR) based on the joint domain localized (JDL) adaptive processing algorithm. The performance of the novel method is compared with 2D FFT plus digital beamforming (FFT-DBF) and orthogonal weight in different azimuths. The results based on simulated and real data show that the novel method provides higher detection performance than others.

1. Introduction

HFSWR can be classified into onshore HFSWR and shipborne HFSWR according to the platform where HFSWR is located. There are many literatures about target detection and tracking based on onshore HFSWR [1, 2]. When HFSWR is mounted on a moving shipborne platform, the first-order Bragg lines are spread in Doppler domain [3]. Besides, the sea clutter spectrum is spatially temporally coupled with each other. The background for the detection of high-velocity targets such as aircrafts and missiles is still the high-order sea clutter and noise because of their large Doppler shift. These targets can be handled just like onshore HFSWR. However, for the targets located among the spread first-order sea clutter spectrum, they are more difficult to be detected. The sea clutter suppression of space-time adaptive processing (STAP) may be better than that of the cascaded space-time processing.

STAP was proposed by Brennan and Reed in 1970s [4], which was first used in the airborne radar, to suppress ground clutter. To reduce the computational complexity of STAP, reduced-dimension STAP is used generally. For the homogeneous clutter, reduced-dimension STAP methods mainly contain JDL [5, 6], space-time multiple-beam (STMB) algorithm [7], linear equations [8], and the two-data-set (TDS) algorithm [9]. For the nonhomogeneous clutter, there are the direct data domain (D3) [10], AR model [11], and so on.

Among the shipborne radar clutters, sea clutter is considered to be more complex. However, the research of the sea clutter suppression for shipborne HFSWR is very limited. The orthogonal weight algorithm proposed in [12] is effective, but it is one-dimensional processing. The simulation of STAP technique has been given based on a conventional architecture of processing [13]. However, the computational complexity of the conventional STAP is rather large.

Consider a line array antenna with N spatial channels and M pulses per coherent processing interval (CPI). Conventional STAP algorithm uses all NM degrees of freedom (DOF). In practice, $2NM$ independent, identically distributed (i.i.d.) secondary data samples are needed to approach the optimal performance (-3 dB loss) [14]. Because of the estimation error between real sea clutter covariance matrix in interested range cell and the estimated one using the samples around interested range bin, this method exists the signal-to-noise ratio loss depending on the number of secondary data samples to some extent. Obtaining such a large number of i.i.d. samples is difficult especially for shipborne HFSWR. Generally, if M is 512 and N is 7, that needs at least 7168 range data samples to estimate clutter covariance. Furthermore, even if i.i.d. samples are available, the associated computation expense makes this fully adaptive algorithm impractical. Then, a reduced-dimension STAP algorithm JDL is first used to suppress sea clutter of shipborne HFSWR in this paper. Adaptive processing is restricted to

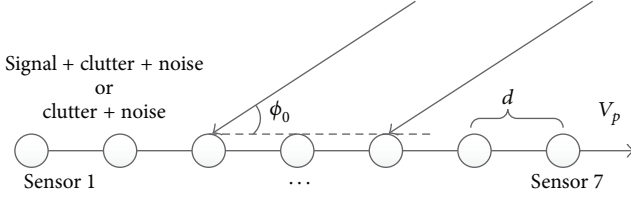


FIGURE 1: Shipborne line array.

a localised processing region (LPR) in the angle-Doppler domain for JDL, which reduces the DOF while retaining maximal gain against thermal noise [6]. The reduced DOF leads to corresponding reductions in the required samples and computation load in the conventional STAP.

This work is organized in five sections. Section 2 introduces space-time distribution of the first-order sea clutter spectrum. Section 3 discusses the theory of JDL algorithm. Section 4 introduces performance comparison and discussion. Section 5 provides the conclusion.

2. Space-Time Distribution of the First-Order Sea Clutter Spectrum

For the shipborne line array, the sketch map of the receiving array is depicted in Figure 1. V_p is the velocity of a platform (m/s). ϕ_0 is the angle between the incident direction of radar returns and the vector of the platform velocity. d is the distance between two receiving sensors (m). The storage format of data is not one-dimensional for shipborne HFSWR, but three-dimensional. The first dimension is the data of sensors, the second dimension is the data of time-domain sweeps, and the last one is the data of range bins. In this paper, we only analyse the two-dimensional data in the range cell.

For shipborne HFSWR, platform motion causes the shift of Doppler frequency. Under ideal conditions, the space-time distribution of the first-order sea clutter spectrum in the receiving sensors can be denoted by two lines [12] as

$$f_d = f_{dp} \cos \phi_0 \pm f_B, \quad (1)$$

where $f_{dp} = 2V_p/\lambda$, $\phi_0 \in [0, \pi]$, $f_B \approx 0.102\sqrt{f_0}$, λ is the radar wavelength (m), and f_0 is the carrier frequency (MHz).

From (1), the Doppler frequency spread of the spectrum of the first-order sea clutter in the receiving sensors should be $[-f_B - f_{dp}, -f_B + f_{dp}]$ and $[f_B - f_{dp}, f_B + f_{dp}]$.

3. Joint Domain Localized (JDL) Processing

For certain range cell, defining the sample vector in the time domain $\mathbf{x}_n = [x_{n1} \cdots x_{nM}]^T$ for sensor n , the whole sample vector ($NM \times 1$) is given by

$$\mathbf{x} = [\mathbf{x}_1^T, \mathbf{x}_2^T \cdots \mathbf{x}_N^T]^T. \quad (2)$$

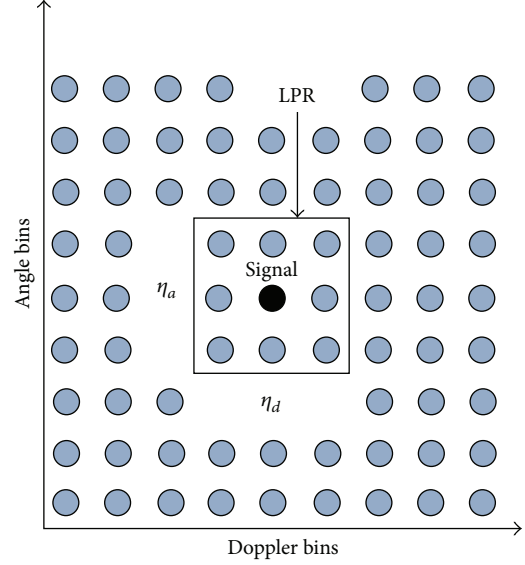


FIGURE 2: Localized processing region in JDL.

According to the definition above, the output of \mathbf{x} at the azimuth ϕ_0 and Doppler frequency f_{d0} can be obtained through the following equations:

$$\begin{aligned} x_0(\phi_0, f_{d0}) &= \mathbf{s}^H \mathbf{x}, \\ \mathbf{s} &= \mathbf{s}_t(f_{d0}) \otimes \mathbf{s}_s(\phi_0), \\ \mathbf{s}_t(f_{d0}) &= e^{j2\pi f_{d0} T_r [0,1,\dots,M-1]^T}, \\ \mathbf{s}_s(\phi_0) &= e^{j2\pi(d/\lambda) \cos(\phi_0) [0,1,\dots,N-1]^T}, \end{aligned} \quad (3)$$

where $\mathbf{s}_s(\phi_0)$, $\mathbf{s}_t(f_{d0})$ are steering vectors with azimuth ϕ_0 and Doppler frequency f_{d0} in the space and time domains, respectively, T_r is the pulse repetition period, and \otimes denotes Kronecker product.

In JDL, radar signals are processed in the angle-Doppler domain. The signal vector, corresponding to the angle-Doppler of interest is transformed to a single point in the angle-Doppler space. A LPR, as shown in Figure 2, is formed around the signal point and interference is suppressed in this region.

In Figure 2, the LPR covers η_a angle bins and η_d Doppler bins. The adaptive weights are calculated by

$$\mathbf{w} = \mathbf{R}^{-1} \mathbf{s}_0, \quad (4)$$

where \mathbf{R} is the estimated covariance matrix corresponding to the LPR of interest and \mathbf{s}_0 is the steering vector for the adaptive process.

In Figure 2, the process is finished by the following matrix:

$$\begin{aligned} \mathbf{T} &= [\mathbf{h}\mathbf{n} \odot \mathbf{s}_t(f_{d-1}), \mathbf{h}\mathbf{n} \odot \mathbf{s}_t(f_{d0}), \mathbf{h}\mathbf{n} \odot \mathbf{s}_t(f_{d+1})] \\ &\quad \otimes [\mathbf{s}_s(\phi_{-1}), \mathbf{s}_s(\phi_0), \mathbf{s}_s(\phi_{+1})], \end{aligned} \quad (5)$$

where $\mathbf{h}\mathbf{n}$ is Hanning window ($M \times 1$) and \odot represents the Hadamard product.

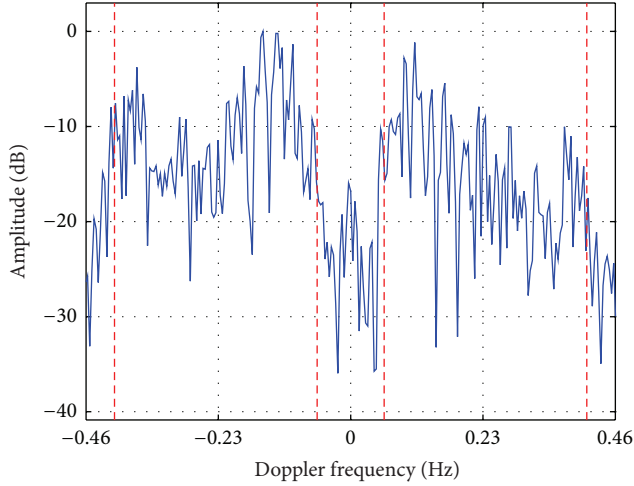


FIGURE 3: Spread spectrum of real first-order sea clutter.

So,

$$\begin{aligned} \mathbf{s}_0 &= \mathbf{T}^H \mathbf{s}, \\ \mathbf{x}_{\text{LPR}} &= \mathbf{T}^H \mathbf{x}, \\ \mathbf{R} &= E \left[\mathbf{x}_{\text{LPR}} \mathbf{x}_{\text{LPR}}^H \right]. \end{aligned} \quad (6)$$

In a practical situation, \mathbf{R} can be estimated by using secondary data from range cells surrounding the range cell of interest. 3° spacing is chosen in the angle domain. The spacing of Doppler frequency is 0.0037 Hz. And the adaptive weights in (4) are used to find a statistic for detection by hypothesis testing. The paper uses the modified sample matrix inversion (MSMI) statistic [6]:

$$\rho_{\text{MSMI}} = \frac{|\mathbf{w}^H \mathbf{x}_{\text{LPR}}|^2}{\mathbf{w}^H \mathbf{s}_0}, \quad (7)$$

where \mathbf{x}_{LPR} ($\eta_a \eta_d \times 1$) is the angle-Doppler data vector from the LPR in the range cell of interest.

4. Performance Comparison and Discussion

In order to evaluate the performance of new method, the real data is from the shipborne radar experiment conducted from 6 to 10 September, 1998, on the Yellow Sea of China. The whole experimental system was mounted on a large barge, towed by a tugboat.

Based on the measured radar data, the spread spectrum of first-order sea clutter at 4th sensor and 17th range bin (2D FFT) is shown in Figure 3. What is more, the space-time spectrum of sea clutter at 17th range bin (FFT-DBF) is also shown in Figure 4. The number of real data file used here is 1057. In addition, the units of the third dimension in all the figures are normalized amplitude in dB.

In Figure 3, it is the first-order sea clutter spectrum between the two red lines. The first-order spectrum spreads obviously. In Figure 4, the space-time coupling of first-order spectrum is very strong. So the target located in Figure 4

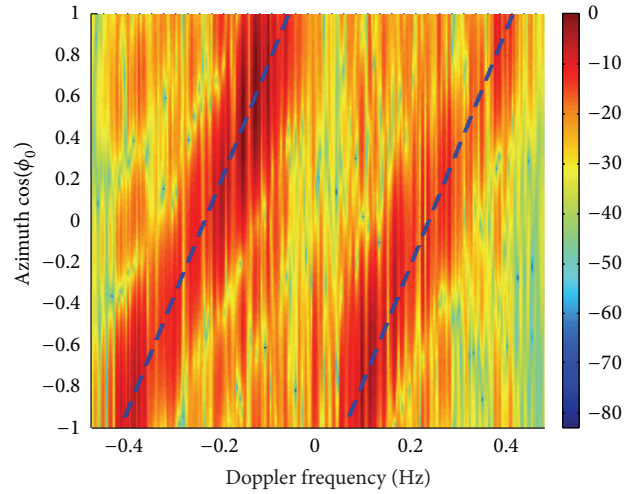


FIGURE 4: Space-time spectrum of real sea clutter. - - denotes the theoretical value of first-order sea clutter in (1).

is hard to be detected no matter only in spatial domain or frequency domain. This provides a good theoretical basis for the application of STAP algorithm.

In order to prove the truth of JDL algorithm for shipborne HFSWR, the parameters of simulated and measured data are introduced as follows. The pulse repetition interval (T_r) is 0.26 s, the distance of two receiving sensors (d) is 14 m, the carrier frequency (f_0) is 5.283 MHz, bandwidth (B) is 30 kHz, the number of receiving sensors (N) is 7, the number of sweeps (M) is 1024, the velocity of platform (V_p) is 5 m/s, and the frequency resolution is 0.0037 Hz. The azimuth of first-order sea clutter is approximately 80° when Doppler frequency is -0.2044 Hz. The positive and negative signs mean that first-order sea clutter or targets move towards and away from shipborne HFSWR, respectively. For simulated targets, they are all added at 17th range bin, Doppler frequencies are all -0.2044 Hz, and the azimuths are 95° and 130° , respectively. Besides, the SCNR (signal to clutter plus noise ratio) of added target is -15 dB. It can be obtained by (8). x_{nm} in (9) does not contain any targets, and the added signal matrix is also shown in (10):

$$\text{SCNR} = 20 \log_{10} \left(\frac{p_s}{p_{cn}} \right), \quad (8)$$

$$p_{cn} = \frac{1}{MN} \sum_{m=1}^M \sum_{n=1}^N |x_{nm}|, \quad (9)$$

$$\text{sig} = p_s (\mathbf{s}_s(\phi_0) \mathbf{s}_t(f_{d0})^T), \quad (10)$$

where p_s is the amplitude of added signal, p_{cn} is the average amplitude of clutter plus noise, and sig is added signal in the range cell of interest.

4.1. Simulated Sea Clutter Plus a Simulated Target. In this part, the performance is compared among JDL, FFT-DBF, and orthogonal weight [12]. First, the space-time spectrum

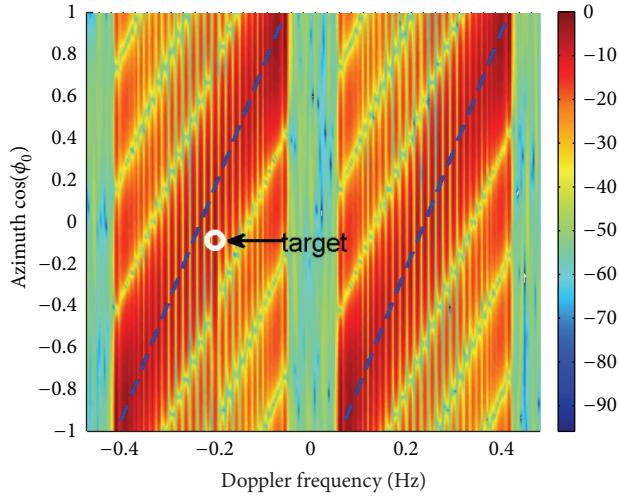


FIGURE 5: Space-time spectrum of simulated sea clutter plus a simulated target.

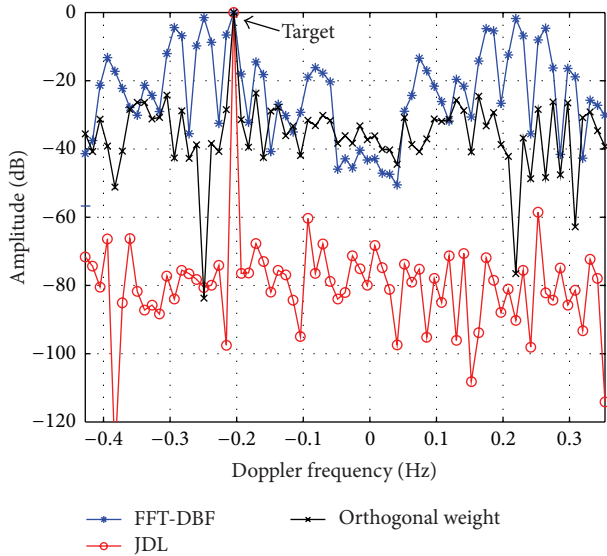


FIGURE 6: Compared Doppler results (simulated sea clutter, target azimuth 95°).

of simulated sea clutter with a simulated target (azimuth 95°) is shown to prove the validity of simulated data in Figure 5.

Then, the compared results are also shown in Figures 6 and 7. Because Hanning window is applied to range transform, the real target information is mainly contained in the neighbouring 3 range cells. Here, \mathbf{R} is estimated using 14 secondary data cells on both sides of the range bin of interest, neglecting the first range cell on each side. The estimation methods of \mathbf{R} are identical in both simulated and real data. From the two figures, FFT-DBF cannot detect the target. However, compared with orthogonal weight, the amplitude of sea clutter around the target is lower, and the first-order sea clutter is suppressed more greatly for JDL. So JDL provides the best performance of the three techniques considered.

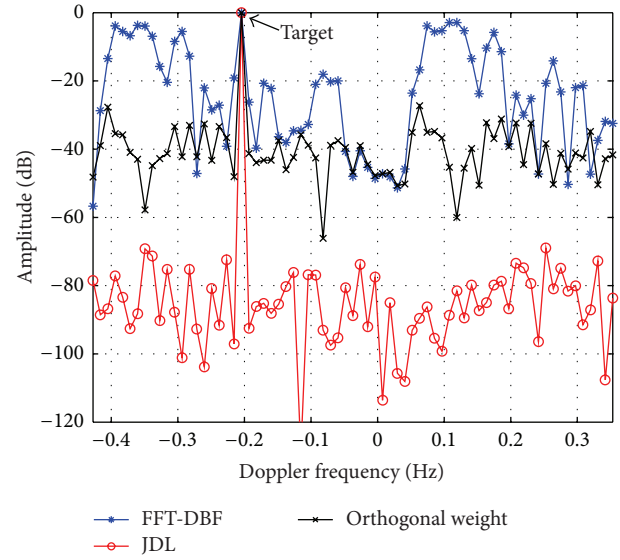


FIGURE 7: Compared Doppler results (simulated sea clutter, target azimuth 130°).

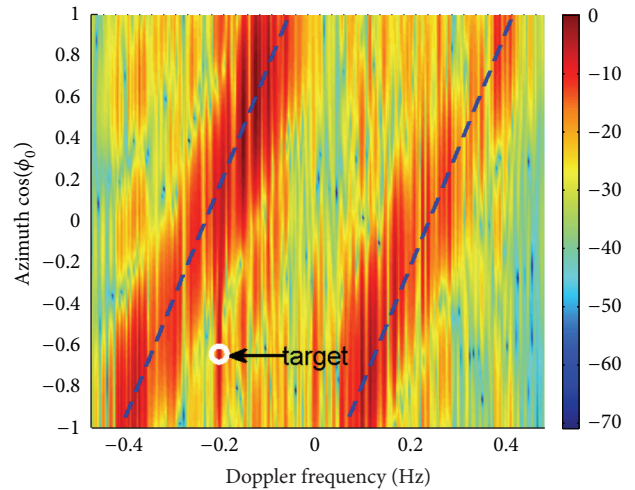


FIGURE 8: Space-time spectrum with a simulated target (real clutter data file 1057, target azimuth 130°).

4.2. Real Sea Clutter Plus a Simulated Target. The real sea clutter data is from file 1057; then a simulated target with azimuth 130° is added to the real clutter data. The position of the target is shown in Figure 8. It depicts the Doppler results in Figure 9. After that, a target with the azimuth 95° is added to the real clutter data. The Doppler results of three methods are provided in Figure 10. From the figures, it is obvious that the performance of JDL is better than other methods in terms of the amplitude of sea clutter.

4.3. Measured Data. In this part, measured data is applied to illustrate the validity of JDL. The number of real data file is 1128. The Doppler frequency of the target is -0.2044 Hz. The azimuths of real target and the first-order sea clutter are approximately 95° and 80° , respectively. The position of

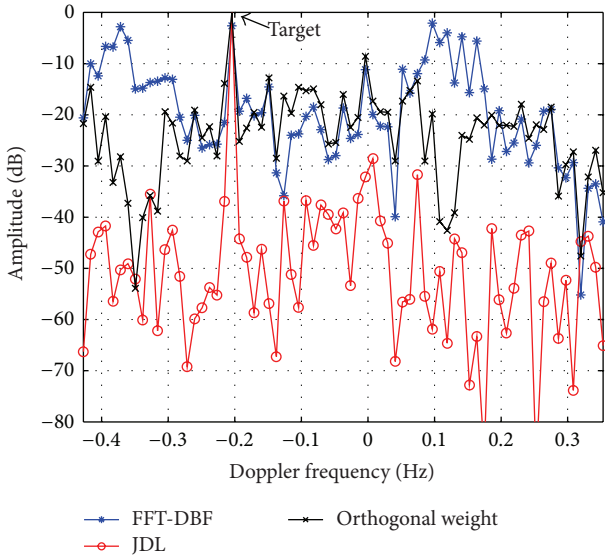


FIGURE 9: Compared Doppler results (real sea clutter, target azimuth 130°).

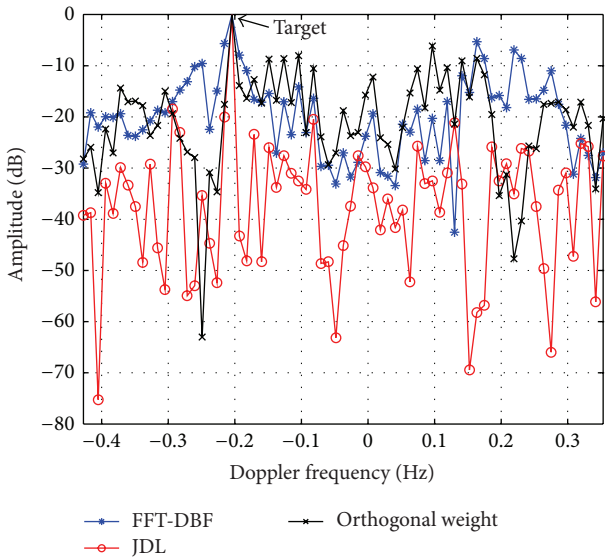


FIGURE 10: Compared Doppler results (real sea clutter, target azimuth 95°).

the target is shown in Figure 11. In azimuth 95°, the Doppler results of three methods are shown in Figure 12. From the figure, the SCNR of JDL is the highest, so the performance of sea clutter suppression is the best.

4.4. Performance Analysis. The performance of three methods is compared in different azimuths using simulated and real data. The conclusion can be drawn that the performance of sea clutter suppression for JDL is better than other methods from the Doppler results. This is because orthogonal weight suppresses sea clutter in one dimension, and FFT-DBF does not suppress sea clutter, but JDL suppresses sea clutter in two dimensions (STAP). Whether the performance of orthogonal

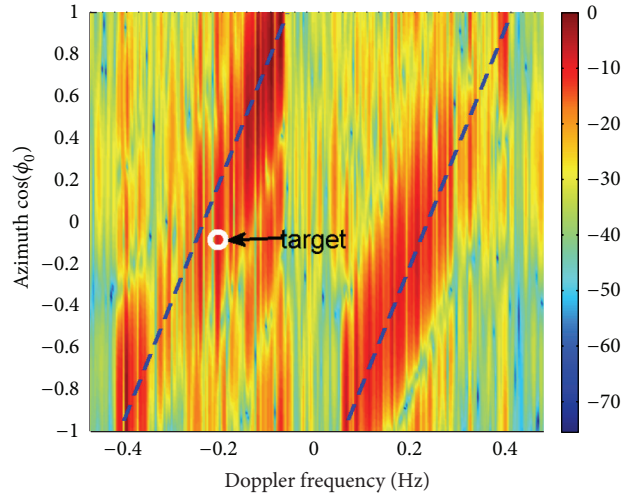


FIGURE 11: Space-time spectrum with a real target (target azimuth 95°).

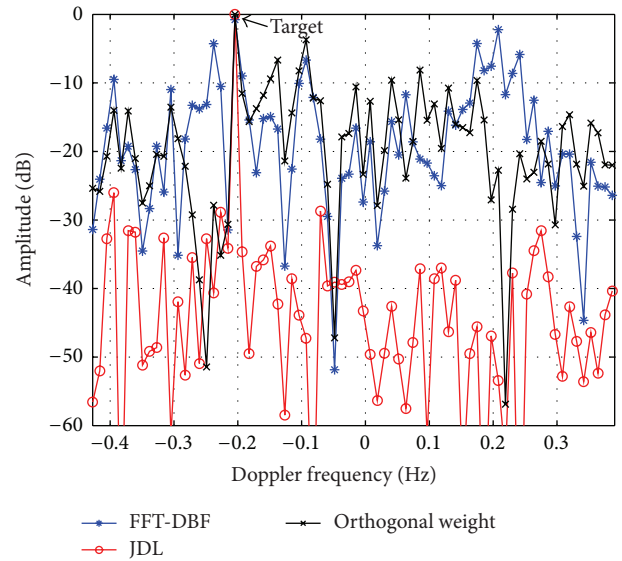


FIGURE 12: Compared Doppler results (target azimuth 95°).

weight outweighs that of FFT-DBF depends on the azimuth spacing between targets and the first-order sea clutter. For example, when the simulated target is far away first-order sea clutter in azimuth such as 130°, it can be seen that the suppression effect of orthogonal weight is better than FFT-DBF from Figures 7 and 9. However, the advantage of orthogonal weight degrades when the target is near the first-order sea clutter in azimuth such as 95° (first-order sea clutter and the target are within the same main beam) in Figures 6 and 10. This is because there is almost no loss of target gain for orthogonal weight when the azimuth of the target is far away first-order sea clutter. However, the suppression of sea clutter near the target for orthogonal weight results in loss of target gain, which is unfavourable for target detection. Because the orthogonal weight technique causes a notch in the azimuth of first-order sea clutter when the first-order sea

clutter is lied in the same main beam with the target. The phenomenon is called main beam split. Then the main beam looks like two beams. The split in the main beam of the target leads to difficulty in azimuth estimation. But the problem for orthogonal weight can be solved by amplitude comparison of the two split beams [12].

5. Conclusion

In this paper, JDL algorithm is first applied to sea clutter suppression of HFSWR. The simulated and real data are used to test the performance of JDL, FFT-DBF, and orthogonal weight, which is compared in different azimuthes. Compared with FFT-DBF and orthogonal weight, the performance of sea clutter for JDL is the best. The advantage of JDL is more obvious when the target is near first-order sea clutter in azimuth. However, JDL algorithm is only available in homogenous environments [6], and its performance depends on the accuracy of estimated covariance matrix of sea clutter plus noise (\mathbf{R}).

Conflict of Interests

The authors declare that there is no conflict of interests regarding the publication of this paper.

Acknowledgments

This project is supported by the state key program of the Natural Science Foundation of China (Grant no. 61132005) and the National Natural Science Foundation of China (Grant no. 61102158).

References

- [1] Y. Liu, "Target detection and tracking with a high frequency ground wave over-the-horizon radar," in *Proceedings of the CIE International Conference of Radar Proceedings (ICR '96)*, pp. 29–33, October 1996.
- [2] R. H. Khan, "Target detection and tracking with HF radar using reciprocal SAR techniques," *IEEE Aerospace and Electronic Systems Magazine*, vol. 12, no. 1, pp. 40–43, 1997.
- [3] J. H. Xie, Y. S. Yuan, and Y. T. Liu, "Experimental analysis of sea clutter in shipborne HFSWR," *IEE Proceedings: Radar, Sonar and Navigation*, vol. 148, no. 2, pp. 67–71, 2001.
- [4] L. E. Brennan and L. S. Reed, "Theory of adaptive radar," *IEEE Transactions on Aerospace and Electronic Systems*, vol. 9, no. 2, pp. 237–252, 1973.
- [5] H. Wang and L. Cai, "On adaptive spatial-temporal processing for airborne surveillance radar systems," *IEEE Transactions on Aerospace and Electronic Systems*, vol. 30, no. 3, pp. 660–669, 1994.
- [6] R. S. Adve, T. B. Hale, and M. C. Wicks, "Practical joint domain localized processing in homogeneous and non-homogeneous environments," *IEE Proceedings—Radar, Sonar and Navigation*, vol. 147, no. 2, pp. 57–74, 2000.
- [7] X.-K. Fan and Y. Fan, "A robust space-time multiple-beam STAP algorithm," in *Proceedings of the 2nd International Conference on Signal Processing Systems (ICSPS '10)*, pp. V1-44–V1-47, Dalian, China, July 2010.
- [8] H. Yao, "A reduced-rank STAP method based on solution of linear equations," in *Proceedings of the International Conference on Computer Design and Applications (ICCCA '10)*, pp. 235–238, IEEE, Qinhuaogdao, China, June 2010.
- [9] E. Aboutanios and B. Mulgrew, "Hybrid detection approach for STAP in heterogeneous clutter," *IEEE Transactions on Aerospace and Electronic Systems*, vol. 46, no. 3, pp. 1021–1033, 2010.
- [10] R. Dong and Z. Bao, "Direct data domain STAP algorithm for airborne radar applications," in *Proceedings of the CIE International Conference on Radar Proceedings*, pp. 770–772, October 2001.
- [11] K.-Q. Duan, W.-C. Xie, and Y.-L. Wang, "A new STAP method for nonhomogeneous clutter environment," in *Proceedings of the 2nd International Conference on Industrial Mechatronics and Automation (ICIMA '10)*, pp. 66–70, May 2010.
- [12] J. Xie, Y. Yuan, and Y. Liu, "Suppression of sea clutter with orthogonal weighting for target detection in shipborne HFSWR," *IEE Proceedings: Radar, Sonar and Navigation*, vol. 149, no. 1, pp. 39–44, 2002.
- [13] M. Lesturgie, "Use of STAP techniques to enhance the detection of slow targets in shipborne HFSWR," in *Proceedings of the International Radar Conference*, pp. 504–509, 2003.
- [14] I. S. Reed, J. D. Mallett, and L. E. Brennan, "Rapid convergence rate in adaptive arrays," *IEEE Transactions on Aerospace and Electronic Systems*, vol. 10, no. 6, pp. 853–863, 1974.

Research Article

Statistical Angular Resolution Limit for Ultrawideband MIMO Noise Radar

Xiaoli Zhou, Hongqiang Wang, Yongqiang Cheng, Yuliang Qin, and Haowen Chen

School of Electronic Science and Engineering, National University of Defense Technology, Changsha 410073, China

Correspondence should be addressed to Hongqiang Wang; oliverwhq1970@gmail.com

Received 23 April 2014; Accepted 15 October 2014

Academic Editor: Michelangelo Villano

Copyright © 2015 Xiaoli Zhou et al. This is an open access article distributed under the Creative Commons Attribution License, which permits unrestricted use, distribution, and reproduction in any medium, provided the original work is properly cited.

The two-dimensional angular resolution limit (ARL) of elevation and azimuth for MIMO radar with ultrawideband (UWB) noise waveforms is investigated using statistical resolution theory. First, the signal model of monostatic UWB MIMO noise radar is established in a 3D reference frame. Then, the statistical angular resolution limits (SARLs) of two closely spaced targets are derived using the detection-theoretic and estimation-theoretic approaches, respectively. The detection-theoretic approach is based on the generalized likelihood ratio test (GLRT) with given probabilities of false alarm and detection, while the estimation-theoretic approach is based on Smith's criterion which involves the Cramér-Rao lower bound (CRLB). Furthermore, the relationship between the two approaches is presented, and the factors affecting the SARL, that is, detection parameters, transmit waveforms, array geometry, signal-to-noise ratio (SNR), and parameters of target (i.e., radar cross section (RCS) and direction), are analyzed. Compared with the conventional radar resolution theory defined by the ambiguity function, the SARL reflects the practical resolution ability of radar and can provide an optimization criterion for radar system design.

1. Introduction

As a novel class of radar system, multiple-input multiple-output (MIMO) radar has gained popularity and attracted attention [1]. MIMO radar can offer additional degrees of freedom by employing multiple transmit and receive antennas, and it possess significant potentials for fading mitigation, resolution enhancement, and interference, and jamming suppression. Fully exploiting these potentials can improve target detection, parameter estimation, and target tracking and recognition performance [2]. MIMO radar uses multiple antennas to simultaneously transmit noncoherent waveforms, while the ultrawideband (UWB) noise waveform is an ideal candidate for MIMO operation [3]. Recently, there has been some active research on using UWB noise radar in MIMO configuration [3–5]. A UWB noise radar, transmitting a noise or noise-like waveform with a fractional bandwidth of over 25% or an absolute bandwidth of over 500 MHz [3], has high range resolution, uncoupled ambiguity function (AF), low probabilities of interception and detection, and immunity from interference [5, 6]. Combing the benefits of MIMO radar and UWB noise radar, UWB MIMO noise

radar satisfies some important military requirements and is considered to be a promising technique for high resolution target detection and estimation [4].

For UWB MIMO noise radar, a typical function is target localization [2, 7], and there exists performance improvement in this application, while it is necessary to know the performance level of target localization expected from a particular radar configuration, and resolution limit is an important performance measure indicating the capability to resolve closely spaced targets. Among the tools characterizing the resolution limit, the classic AF is commonly used to describe the inherent resolution properties of time delay and Doppler for a specific waveform [8]. Early, AF concentrated on the monostatic narrowband applications. Owing to the potential advantages of the UWB waveform and MIMO radar system, wideband/UWB AF [6, 9, 10] and MIMO AF [10–12] are then investigated.

Although AF describes the resolving ability of radar waveform and MIMO AF can simultaneously characterize the effects of array geometry, transmitted waveform, and target scattering on resolution performance [2], the effect of environment noise is neglected. Moreover, the conventional

resolution limit (i.e., AF) is limited by the Rayleigh limit, whereas the super-resolution theory indicates that resolution beyond the Rayleigh limit is possible under certain conditions related to signal-to-noise ratio (SNR).

The statistical resolution limit (SRL) [13], deduced from the statistical characteristic of radar measurement and where the uncertainty of measurement is taken into account, has attracted much attention recently. The SRL can be used to analyze the statistical resolution capability beyond the Rayleigh's criterion and reflect the practical resolution ability of radar. There are mainly three approaches to define the SRL. The earliest approach is based on the mean null spectrum [14] which is quite simple, whereas its application is limited to the specific estimation algorithm. In practical applications, there exist another two commonly used approaches, independent of the algorithm, to define the SRL. (I) One is based on detection theory; the resolution problem is modeled as a hypothesis test to decide if the two sources are resolvable. And the resolution limit is defined by the probability of error or right criterion [15–21]. (II) The other is based on estimation accuracy; the SRL is given with the Cramér-Rao lower bound (CRLB) [13, 15, 16, 22–24]. There are two main criteria based on the CRLB: Lee's criterion [25] and Smith's criterion [13].

In recent years, the SRLs of DOD (direction of departure) and DOA (direction of arrival) for MIMO radar have been deeply researched [21, 24], whereas the majority of this published work has assumed narrowband signal scenarios, which cannot be applied to the wideband/UWB situation directly. The SRL of wideband/UWB MIMO radar has not been investigated, not to mention UWB MIMO noise radar.

In this paper, the 2D statistical angular resolution limits (SARLs) of elevation and azimuth for UWB MIMO noise radar in a 3D reference frame are derived. The prespecified detection-theoretic and estimation-theoretic approaches are used in the derivations, which are based on GLRT with the constraints on probabilities of false alarm and detection, and CRLB with the constraint on Smith's criterion, respectively. The closed-form expressions of SARL are achieved, which are compact and can provide useful qualitative information on the behavior of resolution limit. Moreover, the relationships between SARL and different factors (i.e., SNR, detection parameters, array geometry, and the radar cross section (RCS) and direction of target) are analyzed. As for the application, the SARL presented in this paper can be used to evaluate the performance of sensor arrays in target localization (such as in radar and sonar), and the approaches may be applied to general detection and parameter estimation problems.

This paper is organized as follows. In Section 2, we introduce the signal model and the related assumptions which are used in the derivations. In Section 3, detection-theoretic approach is presented to investigate the SARL. Then the SARL is further derived based on CRLB with the Smith's criterion, and the relationship between the two approaches is discussed in Section 4. In Section 5, the results obtained in Sections 3 and 4 are discussed to provide further insight into the SARL, and some insightful properties revealed by the results of simulations are given. Finally, some comments and conclusions are presented in Section 6.

A comment on notation is as follows: we use boldface lowercase letters for vectors and boldface uppercase letters for matrices. $(\cdot)^H$, $(\cdot)^*$, $(\cdot)^T$, and $(\cdot)^{-1}$ denote the conjugate transpose, conjugate, transpose, and inverse of a matrix, respectively. $E\{\cdot\}$ is used for expectation with respect to the random variable. $\Re\{\cdot\}$ and $\Im\{\cdot\}$ denote the real and imaginary parts, respectively. Finally, $\|\cdot\|$ denotes the Frobenius norm of a vector and \mathbf{I}_N is the N th-order identity matrix.

2. Problem Setup

2.1. Assumptions. Throughout the paper, it is assumed that the following assumptions hold.

- (1) The radar is operated in monostatic configuration and then the DOD is approximately equal to the DOA.
- (2) The targets are point targets located in the far-field of the radar array.
- (3) The background noise is an independent additive wide-sense stationary (WSS) complex circular white Gaussian random process with zero-mean and variance σ_n^2 .
- (4) All transmit waveforms are mutually orthogonal band-limited noise waveforms with equal power σ_s^2 and bandwidth B_w . Meanwhile, the signal spectral components at different frequencies are also mutually orthogonal.
- (5) The channel attenuation is ignored.
- (6) The coherent processing time for signal and noise is sufficient.

2.2. Signal Model. Consider two closely spaced targets in the far-field for MIMO radar. Target T1 is assumed as the reference target with a known direction $\boldsymbol{\theta}_1 = (\varphi_1, \phi_1)$ and RCS, while target T2, whose direction $\boldsymbol{\theta}_2 = (\varphi_2, \phi_2)$ is unknown, is close to T1. $\varphi_i \in [0, \pi/2]$ and $\phi_i \in [0, 2\pi]$ denote the elevation and azimuth of the i th target ($\forall i \in \{1, 2\}$), respectively.

The MIMO radar geometry is shown in Figure 1. Both the N -element transmitters and M -element receivers, which are located in the same plane, are circular arrays (but not limited to circular array) with radii r_t and r_r , respectively. The origin O of the Cartesian coordinate system is set up as the center of the arrays, wherein the radar array and targets are considered as point objects.

In this paper, a single snapshot is considered. Then the demodulated baseband signal received by the m th receiver can be expressed as [7]:

$$y_m(t) = \sum_{i=1}^2 \alpha_i \sum_{n=1}^N s_n(t - \tau_{mn}^i) e^{-j2\pi f_c t_{mn}^i} + w_m(t), \quad (1)$$

where $s_n(t)$ is the baseband stochastic signal transmitted by the n th transmitter with the bandwidth B_w , w_m is the noise received by the m th receiver, and f_c is the carrier frequency of the transmit waveforms. α_i denotes the complex amplitude proportional to the RCS of the i th target.

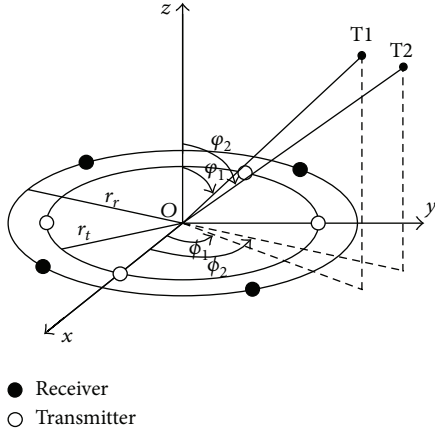


FIGURE 1: Geometry of monostatic MIMO radar with circular arrays.

$\tau_{mn}^i = \sin \varphi_i (r_r \cos(\phi_i - \vartheta_{rm}) + r_t \cos(\phi_i - \vartheta_{tn})) / c$ is the relative propagation delay corresponding to the n th transmitter (located at $\theta_{tn} = (\pi/2, \vartheta_{tn})$) and the m th receiver (located at $\theta_{rm} = (\pi/2, \vartheta_{rm})$) with respect to the reference point O , where c is the speed of wave propagation.

Since $s_n(t)$ is an UWB stochastic signal which is not convenient to analysis, thus $s_n(t)$ is expressed as the spectral representation $s_n(t) = \int_f e^{j2\pi f t} dS_n(f)$ in the frequency domain. $dS_n(f)$ denotes a measure of the signal spectrum at frequency f , which is independent of variable t and will simplify the derivations involving the stochastic signal.

3. SARL Based on Detection-Theoretic Approach

In this section, the 2D SARL, based on the hypothesis test (more precisely, GLRT), is derived using the signal model in Section 2.

3.1. Statistic of the Observation. From the statistical signal processing theory we know that the sufficient statistic is the effective summarization and makes the probability density function (PDF) be independent with the unknown parameters. For UWB MIMO noise radar, one of the sufficient statistics for targets resolving is

$$\mathbf{E} \triangleq \mathbf{y}(t) = \mathbf{x}(t) + \mathbf{w}(t), \quad (2)$$

where $\mathbf{y}(t) = [y_1(t), \dots, y_M(t)]^T$, $\mathbf{x}(t) = [x_1(t), \dots, x_M(t)]^T$, $\mathbf{w}(t) = [w_1(t), \dots, w_M(t)]^T$, $x_m(t) = \sum_{i=1}^2 \alpha_i \sum_{n=1}^N s_n(t - \tau_{mn}^i) e^{-j2\pi f_c \tau_{mn}^i}$.

3.2. Linear Form of the Signal Model. The 2D SARL can be expressed as $\boldsymbol{\delta} \triangleq [\delta_\varphi \ \delta_\phi]^T$, where $\delta_\varphi \triangleq \varphi_2 - \varphi_1$ and $\delta_\phi \triangleq \phi_2 - \phi_1$. The derivation of δ_φ and δ_ϕ is a nonlinear optimization problem which is analytically intractable. We therefore approximate the model to be linear w.r.t. the unknown parameters.

Substituting $s_n(t) = \int_f e^{j2\pi f t} dS_n(f)$ into $x_m(t)$, the first order Taylor expansion of $x_m(t)$ around $\boldsymbol{\delta} = \mathbf{0}$ is given as

$$\begin{aligned} x_m(t) \approx & (\alpha_1 + \alpha_2) \sum_{n=1}^N \int_f e^{j2\pi(f(t-\tau_{nm}^1) - f_c \tau_{nm}^1)} dS_n(f) \\ & - j2\pi\alpha_2 \delta_\varphi \cos \varphi_1 \sum_{n=1}^N \int_f a_{mn}(f + f_c) \\ & \quad \times e^{j2\pi(f(t-\tau_{nm}^1) - f_c \tau_{nm}^1)} dS_n(f) \\ & + j2\pi\alpha_2 \delta_\phi \sin \varphi_1 \sum_{n=1}^N \int_f b_{mn}(f + f_c) \\ & \quad \times e^{j2\pi(f(t-\tau_{nm}^1) - f_c \tau_{nm}^1)} dS_n(f). \end{aligned} \quad (3)$$

Then, the sufficient statistic can be expressed as

$$\mathbf{y} = \mathbf{G}\boldsymbol{\zeta} + \mathbf{w}, \quad (4)$$

$$\boldsymbol{\zeta} = [\alpha_1 + \alpha_2 \quad \alpha_2 \boldsymbol{\delta}^T]^T,$$

$$\mathbf{G} = [\mathbf{B} \quad \mathbf{C} \quad \mathbf{D}],$$

$$B_m = \sum_{n=1}^N \int_f e^{j2\pi(f(t-\tau_{nm}^1) - f_c \tau_{nm}^1)} dS_n(f),$$

$$\begin{aligned} C_m = & -j2\pi \cos \varphi_1 \sum_{n=1}^N \int_f a_{mn}(f + f_c) \\ & \quad \times e^{j2\pi(f(t-\tau_{nm}^1) - f_c \tau_{nm}^1)} dS_n(f), \end{aligned} \quad (5)$$

$$\begin{aligned} D_m = & j2\pi \cos \varphi_1 \sum_{n=1}^N \int_f b_{mn}(f + f_c) \\ & \quad \times e^{j2\pi(f(t-\tau_{nm}^1) - f_c \tau_{nm}^1)} dS_n(f), \end{aligned}$$

where B_m , C_m , and D_m represent the m th element of \mathbf{B} , \mathbf{C} , and \mathbf{D} , respectively. a_{mn} and b_{mn} are denoted by

$$\begin{aligned} a_{mn} &= \frac{(r_r \cos(\phi_1 - \vartheta_{rm}) + r_t \cos(\phi_1 - \vartheta_{tn}))}{c}, \\ b_{mn} &= \frac{(r_r \sin(\phi_1 - \vartheta_{rm}) + r_t \sin(\phi_1 - \vartheta_{tn}))}{c}. \end{aligned} \quad (6)$$

3.3. Derivation of the SARL. It is a common sense that the targets can be resolved easily and the probability of detection is higher if the spacing between the two targets is larger. In this sense, the probability of detection can be used to represent the resolvability of two closely spaced targets. Consequently, the resolution problem can be modeled as a hypothesis test problem, and the relationships between the minimal resolvable $\boldsymbol{\delta}$ and the factors affecting the resolution limit can be obtained. Denoting that $\mathbf{P} = [\mathbf{0}, \mathbf{I}_2]$, as $\mathbf{P}\boldsymbol{\zeta} = \alpha_2 \boldsymbol{\delta}$

and $\alpha_2 \neq 0$, the corresponding hypothesis for the resolution problem is given by

$$\begin{aligned} \mathcal{H}_0: \quad & \mathbf{P}\zeta = \mathbf{0} \\ \mathcal{H}_1: \quad & \mathbf{P}\zeta \neq \mathbf{0}, \end{aligned} \quad (7)$$

where \mathcal{H}_1 and \mathcal{H}_0 indicate that the two targets are resolvable or not, respectively.

A basic method for hypothesis test is the classical approach based on Neyman-Pearson (NP) lemma [26]. According to the NP lemma, the optimum solution to the above hypothesis test problem is the likelihood ratio test (LRT). However, since δ is unknown, it is impossible to give the PDF exactly under \mathcal{H}_1 and design an optimal detector in the NP sense. A common approach is the GLRT in this case. GLRT first computes the maximum likelihood estimates (MLEs) of the unknown parameters and then uses the estimated values to form the standard NP detector. Although GLRT is not optimal, it is an asymptotically uniformly most powerful (UMP) test among all the invariant statistical tests [26], and its performance is very close to that of an ideal detector, to which the values of all the parameters in the model are known. Hence, the performance of the described detector can be reasonably considered as an approximate performance bound in practice. According to (7), the expression of GLRT is

$$L(\mathbf{y}) = \frac{\max_{\delta} p(\mathbf{y}; \zeta, \mathcal{H}_1)}{\max_{\delta} p(\mathbf{y}; \mathcal{H}_0)} = \frac{p(\mathbf{y}; \hat{\zeta}, \mathcal{H}_1)}{p(\mathbf{y}; \mathcal{H}_0)} \stackrel{\mathcal{H}_1}{\geq} \eta, \quad (8)$$

where $p(\mathbf{y}; \zeta, \mathcal{H}_1)$ and $p(\mathbf{y}; \mathcal{H}_0)$ are the PDFs under \mathcal{H}_1 and \mathcal{H}_0 , respectively. η is detection threshold. $\hat{\zeta} = (\mathbf{G}^H \mathbf{G})^{-1} \mathbf{G}^H \mathbf{y}$ is the MLE of ζ when $p(\mathbf{y}; \hat{\zeta}, \mathcal{H}_1)$ is maximized. Equivalently, the GLRT in (8) can be rewritten as

$$T(\mathbf{y}) = 2 \ln L(\mathbf{y}) \stackrel{\mathcal{H}_1}{\geq} \eta' = 2 \ln \eta. \quad (9)$$

Then the GLRT statistic for the approximated model yields [26]

$$T(\mathbf{y}) = \frac{2}{\sigma_n^2} (\mathbf{P}\hat{\zeta})^H (\mathbf{P}(\mathbf{G}^H \mathbf{G})^{-1} \mathbf{P}^H)^{-1} \mathbf{P}\hat{\zeta}. \quad (10)$$

To choose the value of η' , the asymptotic performance of the test [26] is formed as (11), as the expression of GLRT may be generally complicated and its performance may be difficult to analyze. Consider

$$T(\mathbf{y}) \sim \begin{cases} \chi_{2M}^2, & \mathcal{H}_0 \\ \chi_{2M}^{\prime 2}(\lambda(p_{fa}, p_d)), & \mathcal{H}_1, \end{cases} \quad (11)$$

where χ_{2M}^2 and $\chi_{2M}^{\prime 2}(\lambda(p_{fa}, p_d))$ are the central and non-central chi-square distribution with $2M$ degrees of freedom, respectively. The noncentrality parameter is $\lambda(p_{fa}, p_d)$ which is critical in illuminating the relationship between the SNR and SARL. Then η' is conditioned by the probabilities of

false alarm and detection, which are defined as $p_{fa} = Q_{\chi_{2M}^2}(\eta')$ and $p_d = Q_{\chi_{2M}^{\prime 2}(\lambda(p_{fa}, p_d))}(\eta')$, respectively. $Q_{\chi_{2M}^2}(\cdot)$ and $Q_{\chi_{2M}^{\prime 2}(\lambda(p_{fa}, p_d))}(\cdot)$ denote the right tail probabilities of χ_{2M}^2 and $\chi_{2M}^{\prime 2}(\lambda(p_{fa}, p_d))$, respectively. Then $\lambda(p_{fa}, p_d)$ can be computed as the solution of

$$Q_{\chi_{2M}^2}^{-1}(p_{fa}) = Q_{\chi_{2M}^{\prime 2}(\lambda(p_{fa}, p_d))}^{-1}(p_d). \quad (12)$$

On the other hand, $\lambda(p_{fa}, p_d)$ can be given as

$$\lambda(p_{fa}, p_d) = \frac{2}{\sigma_n^2} (\mathbf{P}\zeta)^H (\mathbf{P}(\mathbf{G}^H \mathbf{G})^{-1} \mathbf{P}^H)^{-1} (\mathbf{P}\zeta). \quad (13)$$

From the viewpoint of statistics, it is impossible to resolve the two closely spaced targets at 100 percent, whereas they are resolvable at a given probability. Since the constraints on p_{fa} and p_d for test (7) are assigned, the SRL can be rigorously defined by the constraints; otherwise, the resolution limit can be arbitrarily low and the result may be meaningless [20]. Based on the constraints, we may claim that the two targets are statistically resolved under the constraints on p_{fa} and p_d . In other words, the probability to resolve both targets is p_d for a given p_{fa} . There definitely exists a minimum δ so that both constraints can be satisfied. If δ is lower than the minimum value, the constraints on p_{fa} and p_d will be broken. The minimum δ , therefore, can be taken as the SRL.

When computing $(\mathbf{P}(\mathbf{G}^H \mathbf{G})^{-1} \mathbf{P}^H)^{-1}$, it is necessary to obtain $\mathbf{B}^H \mathbf{B}$, $\mathbf{B}^H \mathbf{C}$, $\mathbf{B}^H \mathbf{D}$, $\mathbf{C}^H \mathbf{C}$, $\mathbf{C}^H \mathbf{D}$, and $\mathbf{D}^H \mathbf{D}$. Since $s_n(t)$ is a stochastic signal, the expectation operator is applied to calculate $(\mathbf{P}(\mathbf{G}^H \mathbf{G})^{-1} \mathbf{P}^H)^{-1}$. As we have assumed that the spectral components at different frequencies are mutually orthogonal in Section 2, then [27]

$$E[dS_n(f) dS_n^*(f')] = \begin{cases} \rho_n(f) df, & f = f' \\ 0, & f \neq f', \end{cases} \quad (14)$$

where $\rho_n(f)$ is the power spectrum density (PSD) of $s_n(t)$ at the frequency f . From (5) and (14), we can obtain

$$E\{\mathbf{B}^H \mathbf{B}\} = MN\sigma_s^2, \quad (15)$$

where $\sigma_s^2 = \int_f \rho_n(f) df$ is the power of each transmitter. The same way is used to obtain $E\{\mathbf{B}^H \mathbf{C}\}$, $E\{\mathbf{B}^H \mathbf{D}\}$ and so on.

The total SNR is defined as $\text{SNR} = (N\sigma_s^2)/(M\sigma_n^2)$, where σ_n^2 can be obtained from (13). Finally, the relationship between the SARL δ and the minimum SNR, which is required to resolve two closely spaced targets, is given by

$$\text{SNR} = \frac{N\lambda(p_{fa}, p_d)}{8\pi^2 M \|\alpha_2\|^2 \delta^T (f_c^2 (\boldsymbol{\varepsilon}_1 - \boldsymbol{\varepsilon}_2/MN) + B_{\text{rms}}^2 \boldsymbol{\varepsilon}_1) \boldsymbol{\delta}}, \quad (16)$$

where $B_{\text{rms}} = \sqrt{\int_f f^2 \rho(f) df / \int_f \rho(f) df}$ is the root mean square (RMS) bandwidth. The RMS bandwidth, which is not equivalent to bandwidth B_w , is commonly used as a basic

quantitative characteristic to describe the feature of power spectra. Consider

$$\begin{aligned}\boldsymbol{\varepsilon}_1 &= \begin{bmatrix} (\cos \varphi_1)^2 \varepsilon_1 & -\sin \varphi_1 \cos \varphi_1 \varepsilon_3 \\ -\sin \varphi_1 \cos \varphi_1 \varepsilon_3 & (\sin \varphi_1)^2 \varepsilon_2 \end{bmatrix}, \\ \boldsymbol{\varepsilon}_2 &= \begin{bmatrix} (\cos \varphi_1)^2 \varepsilon_4^2 & -\sin \varphi_1 \cos \varphi_1 \varepsilon_4 \varepsilon_5 \\ -\sin \varphi_1 \cos \varphi_1 \varepsilon_4 \varepsilon_5 & (\sin \varphi_1)^2 \varepsilon_5^2 \end{bmatrix}, \\ \varepsilon_1 &= \sum_{m=1}^M \sum_{n=1}^N a_{mn}^2, \quad \varepsilon_2 = \sum_{m=1}^M \sum_{n=1}^N b_{mn}^2, \quad \varepsilon_3 = \sum_{m=1}^M \sum_{n=1}^N a_{mn} b_{mn}, \\ \varepsilon_4 &= \sum_{m=1}^M \sum_{n=1}^N a_{mn}, \quad \varepsilon_5 = \sum_{m=1}^M \sum_{n=1}^N b_{mn}.\end{aligned}\quad (17)$$

From (16), the SARL depends not only on SNR, but also on the detection parameters, transmit waveforms, array geometry, RCS, and direction of target. In Particular, $\varepsilon_1 = \varepsilon_2 = MN(r_t^2 + r_r^2)/(2c^2)$ and $\varepsilon_3 = \varepsilon_4 = \varepsilon_5 = 0$ for uniform circular array (UCA) when $M, N \neq 1$. Then the SARL can be given by

$$\begin{aligned}\cos^2 \varphi_1 \delta_\varphi^2 + \sin^2 \varphi_1 \delta_\phi^2 \\ = \frac{c^2 \lambda (p_{fa}, p_d)}{4\pi^2 M^2 \|\alpha_2\|^2 (r_t^2 + r_r^2) (f_c^2 + B_{rms}^2) \text{SNR}}.\end{aligned}\quad (18)$$

Then we can conclude that the SARL is independent of the azimuth of target for UCA.

To complement the results in this section, we carry out the Fisher information matrix (FIM) derivation for the general signal model to achieve the SARL expression from the parameter estimation perspective in the following.

4. SARL Based on Estimation-Theoretic Approach

In this section, we derive and analyze the SARL for UWB MIMO noise radar, based on the Smith's criterion which involves the CRLB. The SARL can be defined as the solution of the Smith equation $\delta = \sqrt{\text{CRLB}(\delta)}$. To solve the equation, we need to have a closed-form expression of $\text{CRLB}(\delta)$. The derivation process is as follows. First, the FIM derivation for the general signal model is carried out. Then, the closed-form expression of the CRLB for the considered problem is achieved. Finally, we derive in closed form the analytic SARL under the assumption of UCA.

4.1. FIM Derivation. Since T1 is considered as the reference target, α_1 , φ_1 , and ϕ_1 are assumed to be known. Thus, the vector of unknown parameters in (2) is

$$\boldsymbol{\xi} = \left[\underbrace{\alpha_2^R \quad \alpha_2^I}_{\boldsymbol{\alpha}} \quad \underbrace{\delta_\varphi \quad \delta_\phi}_{\boldsymbol{\delta}} \right]^T, \quad (19)$$

where $\alpha_2^R = \Re\{\alpha_2\}$ and $\alpha_2^I = \Im\{\alpha_2\}$ denote the real and imaginary parts of α_2 ; that is, $\alpha_2 = \alpha_2^R + j\alpha_2^I$. In (19), we identify two sets of parameters: parameters of interest $\boldsymbol{\delta} \triangleq [\delta_\varphi \quad \delta_\phi]^T$ and nuisance parameters $\boldsymbol{\alpha} \triangleq [\alpha_2^R \quad \alpha_2^I]^T$.

The FIM $\mathbf{J}(\boldsymbol{\xi})$ with respect to the vector $\boldsymbol{\xi}$ is given by [7]

$$\mathbf{J}(\boldsymbol{\xi}) = E_{\mathbf{y}|\boldsymbol{\xi}} \left\{ \left[\frac{\partial}{\partial \boldsymbol{\xi}} \log p(\mathbf{y} | \boldsymbol{\xi}) \right] \left[\frac{\partial}{\partial \boldsymbol{\xi}} \log p(\mathbf{y} | \boldsymbol{\xi}) \right]^H \right\}, \quad (20)$$

where $p(\mathbf{y} | \boldsymbol{\xi})$ is the joint PDF of \mathbf{y} conditioned on $\boldsymbol{\xi}$ and $E_{\mathbf{y}|\boldsymbol{\xi}}\{\cdot\}$ is the conditional expectation of \mathbf{y} given $\boldsymbol{\xi}$.

The received signals \mathbf{y} are parameterized by the unknown parameters $\boldsymbol{\xi}$. The conditional joint PDF of the observations at the receivers, given by (1), is

$$p(\mathbf{y} | \boldsymbol{\xi}) \propto \exp \left\{ -\frac{1}{\sigma_n^2} \sum_{m=1}^M \int_T \|\mathbf{y}_m(t) - \mathbf{x}_m(t)\|^2 dt \right\}. \quad (21)$$

Then we develop the FIM for $\boldsymbol{\xi}$, based on the conditional PDF in (21). The expression for (20) is obtained using

$$\begin{aligned}[\mathbf{J}(\boldsymbol{\xi})]_{ij} = [\mathbf{J}(\boldsymbol{\xi})]_{ji} = -E_{\mathbf{y}|\boldsymbol{\xi}} \left\{ \frac{\partial^2 \log p(\mathbf{y} | \boldsymbol{\xi})}{\partial \xi_i \partial \xi_j} \right\} \\ i, j = 1, 2, 3, 4.\end{aligned}\quad (22)$$

Before the derivation continues, some conclusions should be made. Denote $\dot{s}_n(t - \tau_{mn}^l) = \partial s_n(t - \tau_{mn}^l) / \partial \tau_{mn}^l$, as described in Section 2; $s_n(t) = \int_f e^{j2\pi f t} dS_n(f)$; then, $\dot{s}_n(t - \tau_{mn}^l)$ can be expressed as

$$\dot{s}_n(t - \tau_{mn}^l) = \int_f -j2\pi f e^{j2\pi f (t - \tau_{mn}^l)} dS_n(f). \quad (23)$$

According to the conclusion described in (14), the conclusions can be drawn as follows:

$$\begin{aligned}E \left\{ \int_T \dot{s}_n(t - \tau_{mn}^l) s_n^*(t - \tau_{mn}^l) dt \right\} = \int_f -j2\pi f \rho_n df = 0, \\ E \left\{ \int_T \dot{s}_n(t - \tau_{mn}^l) \dot{s}_n^*(t - \tau_{mn}^l) dt \right\} = \int_f (2\pi f)^2 \rho_n df \\ = 4\pi^2 B_{rms}^2 \sigma_s^2.\end{aligned}\quad (24)$$

Based on (14) and (24), the expression for the FIM $\mathbf{J}(\boldsymbol{\xi})$ is derived in the Appendix.

4.2. CRLB Derivation. The CRLB provides a lower bound for the MSE of any unbiased estimator for unknown parameters. Given a vector parameter $\boldsymbol{\xi}$, the CRLB is defined as

$$\text{CRLB}(\boldsymbol{\xi}) = [\mathbf{J}(\boldsymbol{\xi})]^{-1}. \quad (25)$$

To give an insight into the terms in the expression of FIM, $\mathbf{J}(\boldsymbol{\xi})$ defined by (20) can be partitioned as

$$\mathbf{J}(\boldsymbol{\xi}) = \begin{bmatrix} \mathbf{J}_{\boldsymbol{\alpha}\boldsymbol{\alpha}} & \mathbf{J}_{\boldsymbol{\alpha}\boldsymbol{\delta}}^H \\ \mathbf{J}_{\boldsymbol{\alpha}\boldsymbol{\delta}} & \mathbf{J}_{\boldsymbol{\delta}\boldsymbol{\delta}} \end{bmatrix}, \quad (26)$$

where the elements $\mathbf{J}_{\alpha\alpha}$, $\mathbf{J}_{\alpha\delta}$, and $\mathbf{J}_{\delta\delta}$ are defined as

$$\mathbf{J}_{\alpha\alpha} = 2MN\text{snr}\mathbf{I}_2$$

$$\mathbf{J}_{\alpha\delta} = \mathbf{J}_{\alpha\delta}^H = 4\pi f_c \text{snr} \begin{bmatrix} \alpha_2^I \cos \varphi_1 \varepsilon_4 & -\alpha_2^R \cos \varphi_1 \varepsilon_4 \\ -\alpha_2^I \sin \varphi_1 \varepsilon_5 & \alpha_2^R \sin \varphi_1 \varepsilon_5 \end{bmatrix}$$

$$\begin{aligned} \mathbf{J}_{\delta\delta} &= 8\pi^2 \|\alpha_2\|^2 (B_{\text{rms}}^2 + f_c^2) \\ &\times \text{snr} \begin{bmatrix} \cos^2 \varphi_1 \varepsilon_1 & -\sin \varphi_1 \cos \varphi_1 \varepsilon_3 \\ -\sin \varphi_1 \cos \varphi_1 \varepsilon_3 & \sin^2 \varphi_1 \varepsilon_2 \end{bmatrix}, \end{aligned} \quad (27)$$

where $\text{snr} = \sigma_s^2/\sigma_n^2$ and \mathbf{I}_2 is the identity matrix. Then, the CRLB of the parameters of interest $\boldsymbol{\xi}$ can be expressed as

$$\begin{aligned} \text{CRLB}(\boldsymbol{\delta}) &= [\mathbf{J}_{\delta\delta} - \mathbf{J}_{\alpha\delta} \mathbf{J}_{\alpha\alpha}^{-1} \mathbf{J}_{\alpha\delta}^H]^{-1} \\ &= \frac{N}{8\pi^2 \|\alpha_2\|^2 M \text{SNR}} \begin{bmatrix} \left((B_{\text{rms}}^2 + f_c^2) \varepsilon_1 - \frac{f_c^2 \varepsilon_4^2}{MN} \right) \cos^2 \varphi_1 & - \left((B_{\text{rms}}^2 + f_c^2) \varepsilon_3 - \frac{f_c^2 \varepsilon_4 \varepsilon_5}{MN} \right) \sin \varphi_1 \cos \varphi_1 \\ - \left((B_{\text{rms}}^2 + f_c^2) \varepsilon_3 - \frac{f_c^2 \varepsilon_4 \varepsilon_5}{MN} \right) \sin \varphi_1 \cos \varphi_1 & \left((B_{\text{rms}}^2 + f_c^2) \varepsilon_2 - \frac{f_c^2 \varepsilon_5^2}{MN} \right) \sin^2 \varphi_1 \end{bmatrix}^{-1}. \end{aligned} \quad (28)$$

According to the Smith's criterion, the 2D SARLs in this case are

$$\begin{aligned} \delta_\varphi &= \sqrt{\text{CRLB}(\varphi)} = \sqrt{[\text{CRLB}(\boldsymbol{\delta})]_{11}}, \\ \delta_\phi &= \sqrt{\text{CRLB}(\phi)} = \sqrt{[\text{CRLB}(\boldsymbol{\delta})]_{22}}. \end{aligned} \quad (29)$$

As is shown in (28), the derivation of SARL in closed form is difficult in the context of MIMO radar. However, in the case of UCA, $\varepsilon_1 = \varepsilon_2 = MN(r_t^2 + r_r^2)/(2c^2)$ and $\varepsilon_3 = \varepsilon_4 = \varepsilon_5 = 0$. Then, the CRLB can be simplified as

$$\begin{aligned} \text{CRLB}(\boldsymbol{\delta}) &= \frac{c^2}{4\pi^2 \|\alpha_2\|^2 M^2 \|\alpha_2\|^2 (r_t^2 + r_r^2) (B_{\text{rms}}^2 + f_c^2) \text{SNR}} \\ &\times \begin{bmatrix} \frac{1}{\cos^2 \varphi_1} & 0 \\ 0 & \frac{1}{\sin^2 \varphi_1} \end{bmatrix}. \end{aligned} \quad (30)$$

Consequently, the SARLs of elevation and azimuth are

$$\delta_\varphi = \frac{c}{2\pi M \|\alpha_2\| \cos \varphi_1} \sqrt{\frac{1}{(r_t^2 + r_r^2) (f_c^2 + B_{\text{rms}}^2) \text{SNR}}}, \quad (31)$$

$$\delta_\phi = \frac{c}{2\pi M \|\alpha_2\| \sin \varphi_1} \sqrt{\frac{1}{(r_t^2 + r_r^2) (f_c^2 + B_{\text{rms}}^2) \text{SNR}}}. \quad (32)$$

4.3. Relationship between the SARL Based on Detection-Theoretic and Estimation-Theoretic Approaches. The SARLs have been derived based on the detection-theoretic and

estimation-theoretic approaches, respectively. As described in [26], the noncentrality parameter $\lambda(p_{fa}, p_d)$ is given as

$$\lambda(p_{fa}, p_d) = (\boldsymbol{\delta} - 0)^T \left([\mathbf{J}^{-1}(\boldsymbol{\xi})]_{\delta\delta} \right)^{-1} (\boldsymbol{\delta} - 0), \quad (33)$$

where $[\mathbf{J}^{-1}(\boldsymbol{\xi})]_{\delta\delta}$ denotes the $\mathbf{J}_{\delta\delta}$ defined in (26). As the observation time is sufficiently long, (33) is equivalent to

$$\begin{aligned} \lambda(p_{fa}, p_d) &\cong (\boldsymbol{\delta} - 0)^T \left([\mathbf{J}^{-1}(\boldsymbol{\xi})]_{\delta\delta} \Big|_{\boldsymbol{\delta}=0} \right)^{-1} (\boldsymbol{\delta} - 0) \\ &= \boldsymbol{\delta}^T (\text{CRLB}(\boldsymbol{\delta})|_{\boldsymbol{\delta}=0})^{-1} \boldsymbol{\delta}, \end{aligned} \quad (34)$$

where “ \cong ” stands for “asymptotically equal.”

The conclusion in (34) can be verified by (16) and (28). Moreover, $\sqrt{\lambda(p_{fa}, p_d)}$, the proportionality constant corresponding to a given couple (P_{fa}, P_d) , is called “translation factor” (from CRLB to the SRL) in [20]. Thus, the asymptotic SRL based on the hypothesis test approach is consistent with the SRL based on the CRLB approach (i.e., using the Smith's criterion). Furthermore, the SRL based on Smith's criterion is equivalent to an asymptotically UMP test among all invariant statistical tests when $\lambda(p_{fa}, p_d) = 1$. Consequently, (34) shows that the detection-based approach is unified with the estimation-based approach [20].

5. Discussion and Numerical Analysis

The 2D SARLs for UWB MIMO noise radar have been derived in Sections 3 and 4. In this section, the results expressed in (16) and (28) are discussed. Then some numerical simulations are made to analysis the factors impacting the 2D SARLs.

TABLE 1: RMS bandwidth for different signals.

Types of spectra	Expression	RMS bandwidth
Rectangular low-frequency spectrum	$\rho(f) = \begin{cases} \rho_0, & f \leq B_w/2 \\ 0, & f > B_w/2 \end{cases}$	$B_w/2\sqrt{3}$
Gaussian spectrum	$\rho(f) = \rho_0 \exp(-2f^2/\sigma^2 B_w^2)$	$\sigma B_w/2$

5.1. *Discussion.* The following comments are intended to provide further insight into the results obtained in Sections 3 and 4.

- (A1) Since the SARL is inversely proportional to RMS bandwidth B_{rms} and carrier frequency f_c , increasing B_{rms} and f_c will improve the SARL, while for narrowband signals, $B_{\text{rms}}/f_c \ll 1$, the SARL is inversely proportional to f_c and independent of B_{rms} . As B_{rms} is the integration over the range of frequencies with nonzero signal content, B_{rms} is determined by both the bandwidth B_w and the distribution of PSD. As is shown in Table 1, the RMS bandwidth of noise waveforms for different distributions of PSD is different, which leads to different SARL.
- (A2) As is shown in (28), the off-diagonal elements of the 2×2 -order CRLB(δ) corresponding to δ_ϕ and δ_θ are not equivalent to zero, which means the CRLB is coupled and the SARL of one direction parameter (δ_ϕ or δ_θ) is degraded by the uncertainty of another. The uncoupling is important which means that the SARL of one parameter is independent of others [28]. Since both diagonal and off-diagonal elements of $\mathbf{J}_{\delta\delta}$ depend on the array geometry, the optimum array geometry can be found to get the best resolution limit. As the off-diagonal elements of $\mathbf{J}_{\delta\delta}$ are zero, the array geometry for monostatic MIMO radar with UCA configuration satisfies the uncoupling conditions in [1].
- (A3) The SARL is strongly reliant on the relative geometry of antennas versus target location. This dependency is incorporated in the terms of ϕ_1 and φ_1 . Moreover, it is apparent from (28) that there is a tradeoff between the SARLs of the azimuth and elevation. For example, a set of antennas' locations that increases the SARL of azimuth may result in a low SARL of elevation, as we expect intuitively. This is caused by the fact that δ_θ is summation of sine functions and δ_ϕ is summation of cosine functions. In order to truly determine the minimum achievable SARLs in both azimuth and elevation, we need to minimize the overall SARL, defined as the total SARL in the next part.
- (A4) As the SARLs in (16) and (28) are achieved for the coherent processing approach, the phase information is used which leads to the resolution limit improvement comparing with the noncoherent processing approach. However, both time synchronization and phase synchronization between the transmitters and receivers are necessary in this case, while only time

synchronization is necessary in the noncoherent case [7], which is a challenge for the radar system.

- (A5) The SARL, as expressed by CRLB, provides a tight bound at high SNR, while the CRLB is not tight at low-SNR case; thus, a more rigid bound is necessary for the estimation accuracy in this case, which is beyond this paper.

5.2. *Numerical Simulation.* The factors, impacting the 2D SARLs of MIMO radar with UWB noise waveforms, are analyzed by numerical simulations as follows. The transmit signals are set up as ideal bandlimited Gaussian noise waveforms with $f_c = 9$ GHz and $B_w = 0.2f_c$; then, the RMS bandwidth is $B_{\text{rms}} = B_w/2\sqrt{3}$. And we consider the case that the number of antennas is $M = N = 4$ and all antennas lie on a disk of radius $r_t = r_r = r = 1$ m.

First, the SARLs for different target directions and array geometry configurations are simulated to verify the comments A2 and A3. Assume that the transmitters and receivers are configured in the same array geometry. Consider four relative geometries of antennas versus target location in Figure 2, where "x" represents the target location with the azimuth ϕ_1 from the vertical view.

It can be shown from Figure 3 that the SARL is strongly related to array geometry and target location. As for UCA in type (d), $\varepsilon_3 = \varepsilon_4 = \varepsilon_5 = 0$ satisfies the uncoupling conditions described in [1], while the array geometries described in Figures 2(a)~2(c) are coupling configurations. As discussed above, the coupling increases the parameter uncertainty which degrades the SARL, and the conclusion is verified in Figure 3. Meanwhile, the aperture size of the array for type (d) is bigger than the other types of array geometry. Furthermore, comparing Figure 3(a) with Figure 3(b), the SARL of elevation degrades with the elevation of target, while the SARL of azimuth is enhanced by the increasing elevation. The contradiction makes it hard to design the array geometry versus the target direction.

As described in [20], the SARL (in the two-target case) is asymptotically proportional to the square root of the lower bound of the MSAE (in the single-target case). The MSAE is defined as

$$\text{MSAE}_{\text{CRLB}} \triangleq \sin^2 \varphi \text{CRLB}(\phi) + \text{CRLB}(\varphi), \quad (35)$$

where $\text{CRLB}(\phi)$ and $\text{CRLB}(\varphi)$ are the CRLBs on ϕ and φ (in the single-target case, $\phi = \phi_1 = \phi_2$ and $\varphi = \varphi_1 = \varphi_2$), respectively. $\sqrt{\text{MSAE}_{\text{CRLB}}}$ contains the CRLBs of the azimuth and elevation and provides an overall measure of the resolution limit; thus, $\sqrt{\text{MSAE}_{\text{CRLB}}}$ can be used as the "total SARL." Moreover, it is also a very useful quality measure for gaining physical insight into the SARL in 3D space. Figure 4 shows that $\sqrt{\text{MSAE}_{\text{CRLB}}}$ varies with the elevation and azimuth of target for different types of array geometry. There are some lowest points in each subfigure, which can be chosen as the tradeoff between the SARLs of azimuth and elevation in certain applications. And the tradeoff elevation and azimuth differ for different array geometry configurations. When designing the radar system, the radar plane can be adjusted to

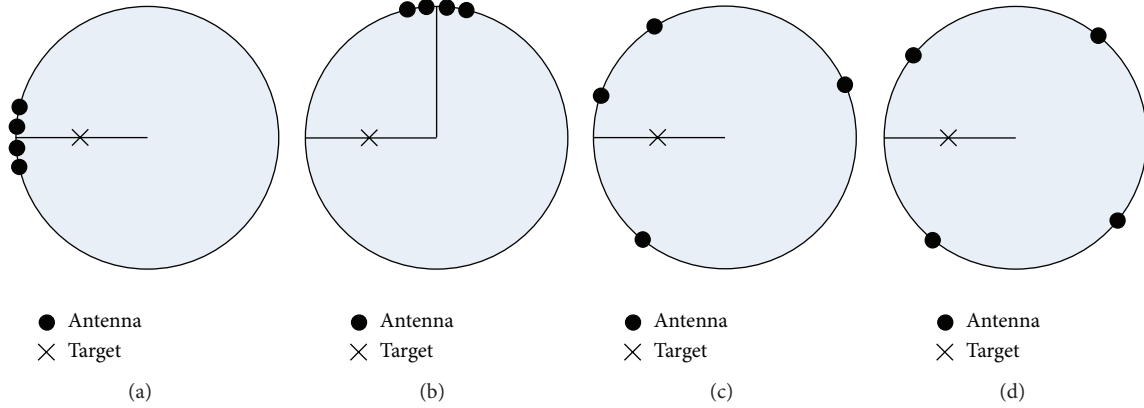


FIGURE 2: Different types of antenna geometry. (a) All elements concentrated at locations $re^{j\phi_1}$ or $re^{j(\phi_1+\pi)}$. (b) All elements concentrated at locations $re^{j(\phi_1+\pi/2)}$ or $re^{j(\phi_1-\pi/2)}$. (c) The elements are randomly located at the disk. (d) The elements are uniformly located on the disk.

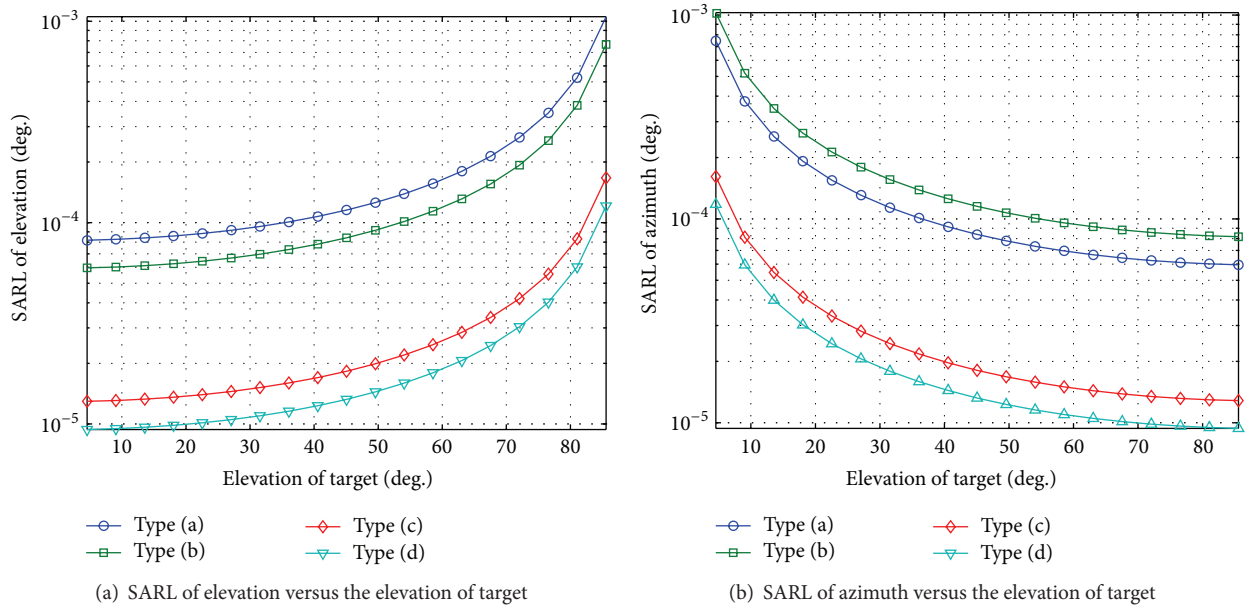


FIGURE 3: SARLs of elevation and azimuth versus the elevation of target for different types of array geometry.

make the target located at the tradeoff elevation and azimuth from the plane, which will lead to the best SARL.

Next, we focus on the effects of other factors on the SARL. In the simulations, both the transmitters and receivers are assumed to be arranged in UCA, and the SARL based on detection approach is considered.

The effect of RCS on the resolution limit can be concluded directly from (16) and (28). The SARL is improved as the RCS increases. Although RCS does not affect the transmit waveform, the received signal power and the probability of detection increase as the RCS increases, which induces a better resolution limit. Thus the target characteristic indeed could affect the resolution limit which is ignored by the conventional radar resolution theory. In the framework of our derivations, target T1 is assumed as the reference target with a known direction and RCS, while target T2 is

unknown and is close to T1; thus, the SARL is independent of the RCS of T2. However, the RCS values of both targets could affect the SARL as the received signal power and SNR will increase if the RCS values increase. In our future work, we consider the resolution of two targets in case that both the targets are unknown although the derivations become complex. Some related work has been published in [29].

Figure 5 shows the effect of detection parameters where only δ_ϕ is considered (the same way is done for δ_θ). From Figure 5, the resolution limit decreases as p_d increases and p_{fa} decreases, since increasing p_d and decreasing p_{fa} lead to a more selective decision. Then the resolution limit can be improved by increasing p_{fa} and calling for a lower p_d . However, the performance of detection will be depressed in this case.

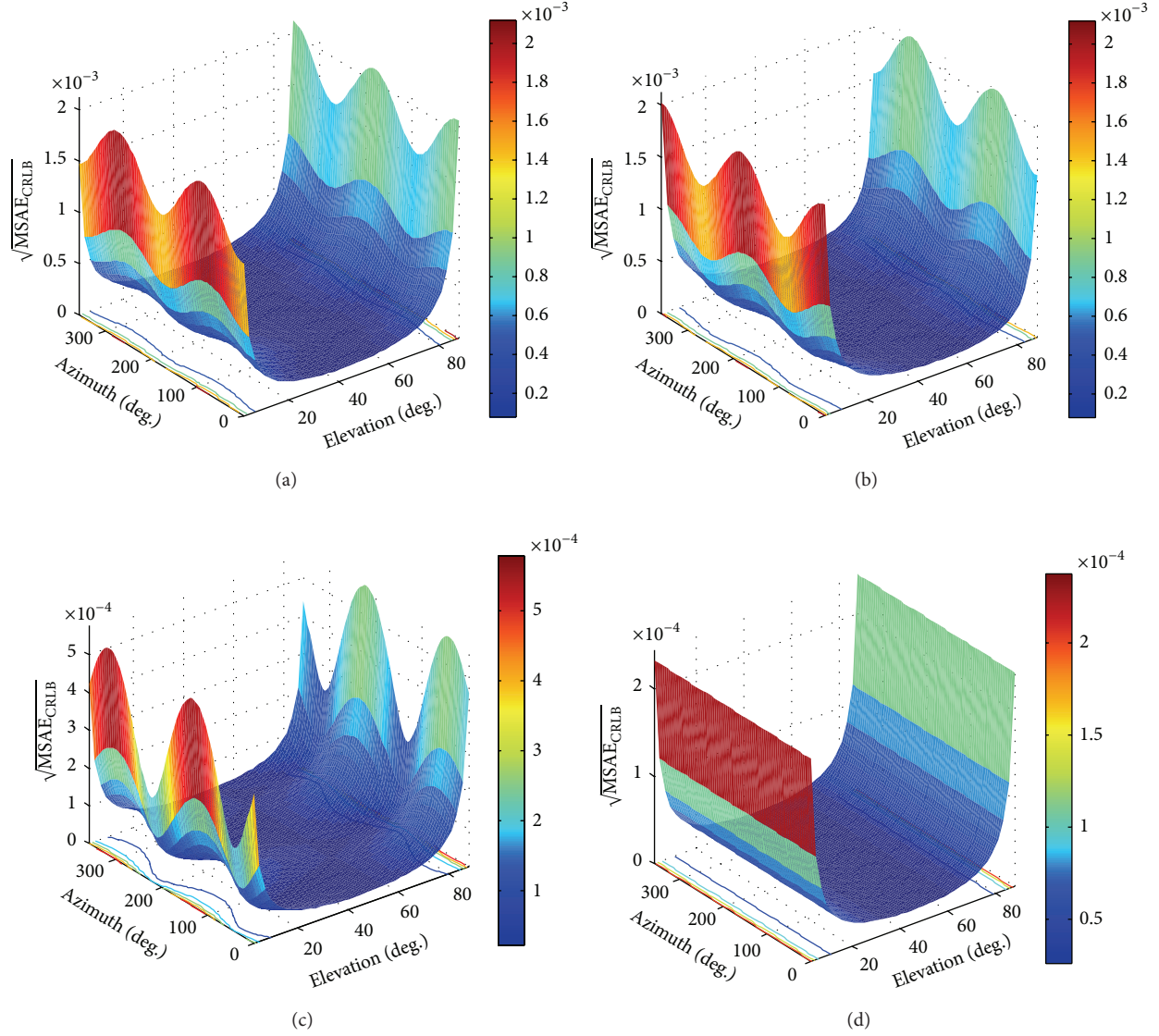


FIGURE 4: $\sqrt{MSAE_{CRLB}}$ versus the elevation and azimuth of target for different types of array geometry.

Figure 6 shows the resolution cells for different target directions and SNR with $(p_{fa}, p_d) = (0.01, 0.99)$. For visual convenience, δ_φ and δ_ϕ are scaled up to 120 times. Obviously, increasing SNR can improve the SARL. Meanwhile, the SARL varies with the target direction because of the spatial diversity of radar, which means that the SARL is “nonuniform” on the whole space. Moreover, the resolution cell is ellipse which means that the SARL varies at different directions for a given target location.

Consider the SARL of elevation δ_ϕ as shown in (31), the relationship between SARL and the radius of the arrays is simulated in Figure 7. The simulation parameters are configured as $M = N = 4$, $r_t = r_r = r \in \{1 \text{ m}, 2 \text{ m}, 3 \text{ m}\}$, and $\varphi_1 = 1^\circ$. Figure 7 represents that increasing the radius of the arrays will lead to the resolution limit improvement, since a larger virtual aperture is achieved in this case, according to the MIMO radar virtual aperture theory.

6. Conclusion

Resolution limit can be interpreted as the minimal difference to resolve two closely spaced targets and is a critical quantity to evaluate the performance of a radar system. In this paper, we have derived the explicit expressions for 2D SARLs of elevation and azimuth for UWB MIMO noise radar, which are defined using GLRT based on hypothesis test and estimation approach based on Smith’s criterion, respectively. The relationship between the two approaches has been proved and verified. Meanwhile, we have analyzed the effects of SNR, detection parameters, transmit waveforms, and array geometry and the parameters of target on the SAR and some significant conclusions are achieved as follows. (1) The SARLs based on the detection and estimation approaches are unified. (2) The array geometry is an important factor that impacts the SARL. (3) There is a tradeoff between the SARLs of

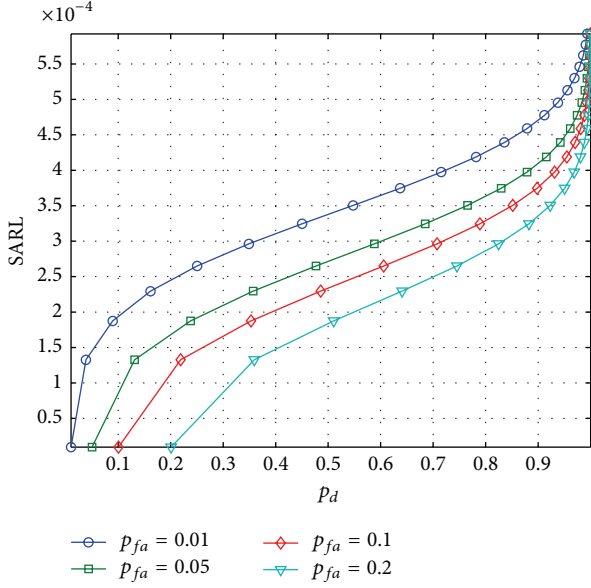


FIGURE 5: SARL as a function of detection parameters (p_{fa} , p_d) for SNR = 20 dB and $\varphi_1 = 1^\circ$.

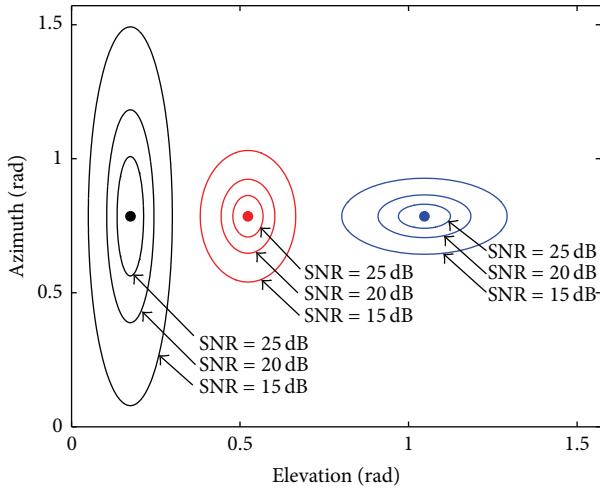


FIGURE 6: Resolution cell versus target direction for elevation $\varphi_1 \in \{10^\circ, 30^\circ, 60^\circ\}$ and $(p_{fa}, p_d) = (0.01, 0.99)$.

elevation and azimuth, which can be determined by the total SARL $\sqrt{\text{MSAE}_{\text{CRLB}}}$. (4) The SARLs of MIMO radar on the whole space and at different directions are “nonuniform”. (5) The target characteristic and detection parameters (if the detection approach is used) can impact the resolution limit. (6) Increasing the bandwidth and SNR will result in the SARL improvement. Compared with the conventional radar resolution theory, the SRL reflects not only the effect of transmit waveforms, but also SNR, parameters of target, and measurement approach. Therefore, the SRL describes the practical resolution ability of radar effectively and provides the optimization criterion for radar system design.

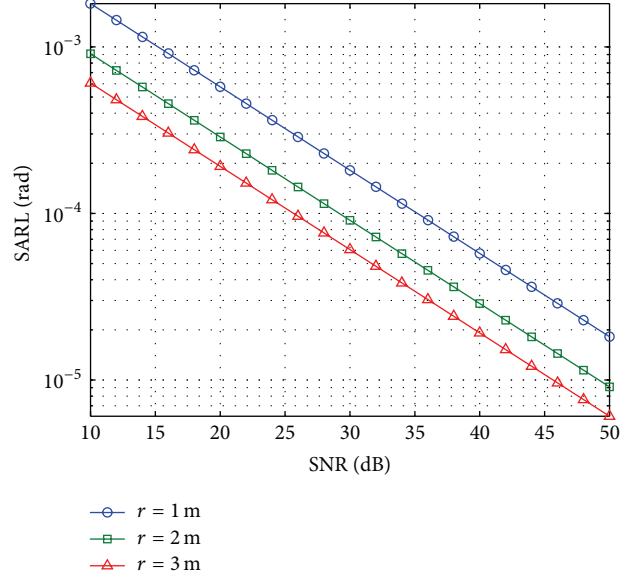


FIGURE 7: SARL as a function of r and SNR (in dB).

Appendix

Derivation of the FIM in (20) is as follows.

The first derivative of $\log p(\mathbf{y} | \boldsymbol{\xi})$ with respect to the elements of $\boldsymbol{\xi}$ is

$$\begin{aligned} & \frac{\partial \log p(\mathbf{y} | \boldsymbol{\xi})}{\partial \alpha_2^R} \\ &= \frac{2}{\sigma_n^2} \sum_{m=1}^M \int_T \text{Re} \left\{ \left(y_m(t) - \sum_{l=1}^2 \alpha_l \sum_{n=1}^N s_n(t - \tau_{mn}^l) e^{-j2\pi f_c \tau_{mn}^l} \right) \right. \\ & \quad \left. \times \left(\sum_{n=1}^N s_n(t - \tau_{mn}^2) e^{-j2\pi f_c \tau_{mn}^2} \right)^* \right\} dt, \end{aligned} \quad (\text{A.1})$$

$$\begin{aligned} & \frac{\partial \log p(\mathbf{y} | \boldsymbol{\xi})}{\partial \alpha_2^I} \\ &= \frac{2}{\sigma_n^2} \sum_{m=1}^M \int_T \text{Re} \left\{ \left(y_m(t) - \sum_{l=1}^2 \alpha_l \sum_{n=1}^N s_n(t - \tau_{mn}^l) e^{-j2\pi f_c \tau_{mn}^l} \right) \right. \\ & \quad \left. \times \left(j \sum_{n=1}^N s_n(t - \tau_{mn}^2) e^{-j2\pi f_c \tau_{mn}^2} \right)^* \right\} dt, \end{aligned} \quad (\text{A.2})$$

$$\begin{aligned} & \frac{\partial \log p(\mathbf{y} | \boldsymbol{\xi})}{\partial \delta_\varphi} \\ &= \frac{-2 \cos \varphi_1}{\sigma_n^2} \\ & \quad \times \sum_{m=1}^M \int_T \text{Re} \\ & \quad \times \left\{ \left(y_m(t) - \sum_{l=1}^2 \alpha_l \sum_{n=1}^N s_n(t - \tau_{mn}^l) e^{-j2\pi f_c \tau_{mn}^l} \right) \right. \end{aligned}$$

$$\times \left(\alpha_2 \sum_{n=1}^N a_{mn} \left(\dot{s}_n(t - \tau_{mn}^2) + j2\pi f_c s_n(t - \tau_{mn}^2) \right) \times e^{-j2\pi f_c \tau_{mn}^2} \right)^* \Bigg\} dt, \quad (\text{A.3})$$

$$\begin{aligned} & \frac{\partial \log p(\mathbf{y} | \boldsymbol{\xi})}{\partial \delta_\phi} \\ &= \frac{2 \sin \varphi_1}{\sigma_n^2} \\ & \times \sum_{m=1}^M \int_T \text{Re} \left\{ \left(y_m(t) - \sum_{l=1}^2 \alpha_l \sum_{n=1}^N s_n(t - \tau_{mn}^l) e^{-j2\pi f_c \tau_{mn}^l} \right) \right. \\ & \quad \times \left(\alpha_2 \sum_{n=1}^N b_{mn} \left(\dot{s}_n(t - \tau_{mn}^2) \right. \right. \\ & \quad \left. \left. + j2\pi f_c s_n(t - \tau_{mn}^2) \right) \times e^{-j2\pi f_c \tau_{mn}^2} \right)^* \Bigg\} dt. \end{aligned} \quad (\text{A.4})$$

Denote $\text{snr} = \sigma_s^2 / \sigma_n^2$ and use the conclusions in (24) and then apply the second derivative to (A.1)~(A.4) to define FIM $\mathbf{J}(\boldsymbol{\xi})$ with the following elements:

$$[\mathbf{J}(\boldsymbol{\xi})]_{11} = -E_{\mathbf{y}|\boldsymbol{\xi}} \left\{ \frac{\partial^2 \log p(\mathbf{y} | \boldsymbol{\xi})}{(\partial \alpha_2^R)^2} \right\} \Bigg|_{\delta_\phi=0, \delta_\phi=0} \quad (\text{A.5})$$

$$= 2MN \text{snr},$$

$$[\mathbf{J}(\boldsymbol{\xi})]_{22} = -E_{\mathbf{y}|\boldsymbol{\xi}} \left\{ \frac{\partial^2 \log p(\mathbf{y} | \boldsymbol{\xi})}{(\partial \alpha_2^I)^2} \right\} \Bigg|_{\delta_\phi=0, \delta_\phi=0} \quad (\text{A.6})$$

$$= 2MN \text{snr},$$

$$[\mathbf{J}(\boldsymbol{\xi})]_{21} = [\mathbf{J}(\boldsymbol{\xi})]_{12} = -E_{\mathbf{y}|\boldsymbol{\xi}} \left\{ \frac{\partial^2 \log p(\mathbf{y} | \boldsymbol{\xi})}{\partial \alpha_2^R \partial \alpha_2^I} \right\} \Bigg|_{\delta_\phi=0, \delta_\phi=0} \quad (\text{A.7})$$

$$= \frac{2}{\sigma_n^2} \text{Re} \{-jMN\sigma_s^2\}$$

$$= 0,$$

$$[\mathbf{J}(\boldsymbol{\xi})]_{31} = [\mathbf{J}(\boldsymbol{\xi})]_{13} = -E_{\mathbf{y}|\boldsymbol{\xi}} \left\{ \frac{\partial^2 \log p(\mathbf{y} | \boldsymbol{\xi})}{\partial \alpha_2^R \partial \delta_\phi} \right\} \Bigg|_{\delta_\phi=0, \delta_\phi=0} \quad (\text{A.8})$$

$$= 4\pi f_c \alpha_2 \text{snr} \cos \varphi_1 \varepsilon_4,$$

$$[\mathbf{J}(\boldsymbol{\xi})]_{41} = [\mathbf{J}(\boldsymbol{\xi})]_{14} = -E_{\mathbf{y}|\boldsymbol{\xi}} \left\{ \frac{\partial^2 \log p(\mathbf{y} | \boldsymbol{\xi})}{\partial \alpha_2^R \partial \delta_\phi} \right\} \Bigg|_{\delta_\phi=0, \delta_\phi=0} \quad (\text{A.9})$$

$$= -4\pi f_c \alpha_2^I \text{snr} \sin \varphi_1 \varepsilon_5,$$

$$[\mathbf{J}(\boldsymbol{\xi})]_{32} = [\mathbf{J}(\boldsymbol{\xi})]_{23} = -E_{\mathbf{y}|\boldsymbol{\xi}} \left\{ \frac{\partial^2 \log p(\mathbf{y} | \boldsymbol{\xi})}{\partial \alpha_2^I \partial \delta_\phi} \right\} \Bigg|_{\delta_\phi=0, \delta_\phi=0} \quad (\text{A.10})$$

$$= -4\pi f_c \alpha_2^R \text{snr} \cos \varphi_1 \varepsilon_4,$$

$$[\mathbf{J}(\boldsymbol{\xi})]_{42} = [\mathbf{J}(\boldsymbol{\xi})]_{24} = -E_{\mathbf{y}|\boldsymbol{\xi}} \left\{ \frac{\partial^2 \log p(\mathbf{y} | \boldsymbol{\xi})}{\partial \alpha_2^I \partial \delta_\phi} \right\} \Bigg|_{\delta_\phi=0, \delta_\phi=0} \quad (\text{A.11})$$

$$= 4\pi f_c \alpha_2^R \text{snr} \sin \varphi_1 \varepsilon_5,$$

$$[\mathbf{J}(\boldsymbol{\xi})]_{33} = -E_{\mathbf{y}|\boldsymbol{\xi}} \left\{ \frac{\partial^2 \log p(\mathbf{y} | \boldsymbol{\xi})}{(\partial \delta_\phi)^2} \right\} \Bigg|_{\delta_\phi=0, \delta_\phi=0} \quad (\text{A.12})$$

$$= 8\pi^2 \|\alpha_2\|^2 (B_{\text{rms}}^2 + f_c^2) \text{snr} \cos^2 \varphi_1 \varepsilon_1,$$

$$[\mathbf{J}(\boldsymbol{\xi})]_{44} = -E_{\mathbf{y}|\boldsymbol{\xi}} \left\{ \frac{\partial^2 \log p(\mathbf{y} | \boldsymbol{\xi})}{(\partial \delta_\phi)^2} \right\} \Bigg|_{\delta_\phi=0, \delta_\phi=0} \quad (\text{A.13})$$

$$= 8\pi^2 \|\alpha_2\|^2 (B_{\text{rms}}^2 + f_c^2) \text{snr} \sin^2 \varphi_1 \varepsilon_2,$$

$$[\mathbf{J}(\boldsymbol{\xi})]_{34} = [\mathbf{J}(\boldsymbol{\xi})]_{34} = -E_{\mathbf{y}|\boldsymbol{\xi}} \left\{ \frac{\partial^2 \log p(\mathbf{y} | \boldsymbol{\xi})}{\partial \delta_\phi \partial \delta_\phi} \right\} \Bigg|_{\delta_\phi=0, \delta_\phi=0} \quad (\text{A.14})$$

$$= -8\pi^2 \|\alpha_2\|^2 (B_{\text{rms}}^2 + f_c^2) \text{snr} \sin \varphi_1 \cos \varphi_1 \varepsilon_3.$$

Conflict of Interests

The authors declare that there is no conflict of interests regarding the publication of this paper.

Acknowledgments

This work was supported by the National Natural Science Foundation of China (no. 61302149 and no. 61101182) and the Research Fund for the Doctoral Program of Higher Education of China (20124307110013). The authors would like to thank the editors and reviewers for their insightful comments.

References

- [1] H. Chen, X. Li, H. Wang, and Z. Zhuang, "Performance bounds of direction finding and its applications for multiple-input multiple-output radar," *IET Radar, Sonar & Navigation*, vol. 8, no. 3, pp. 251–263, 2014.
- [2] J. Li and P. Stoica, Eds., *MIMO Radar Signal Processing*. John Wiley & Sons, New York, NY, USA, 2008.
- [3] W. J. Chen and R. M. Narayanan, "Comparison of the estimation performance of coherent and non-coherent ambiguity functions for an ultrawideband multi-input-multi-output noise radar," *IET Radar, Sonar and Navigation*, vol. 6, no. 1, pp. 49–59, 2012.
- [4] W.-J. Chen and R. M. Narayanan, "CGLRT plus TDL beamforming for ultrawideband MIMO noise radar," *IEEE Transactions on Aerospace and Electronic Systems*, vol. 48, no. 3, pp. 1858–1869, 2012.
- [5] W.-J. Chen and R. M. Narayanan, "Antenna placement for minimizing target localization error in UWB MIMO noise radar," *IEEE Antennas and Wireless Propagation Letters*, vol. 10, pp. 135–138, 2011.
- [6] M. Dawood and R. M. Narayanan, "Generalised wideband ambiguity function of a coherent ultrawideband random noise radar," *IEE Proceedings: Radar, Sonar and Navigation*, vol. 150, no. 5, pp. 379–386, 2003.
- [7] H. Godrich, A. M. Haimovich, and R. S. Blum, "Target localization accuracy gain in MIMO radar-based systems," *IEEE Transactions on Information Theory*, vol. 56, no. 6, pp. 2783–2803, 2010.
- [8] P. Woodward, *Probability and Information Theory: With Applications to Radar*, Pergamon, New York, NY, USA, 1957.
- [9] J. M. Speiser, "Wideband ambiguity functions," *IEEE Transactions on Information Theory*, vol. 13, no. 1, pp. 122–123, 1967.
- [10] H. Yan, G. Shen, R. Zetik, O. Hirsch, and R. S. Thoma, "Ultra-wideband MIMO ambiguity function and its factorability," *IEEE Transactions on Geoscience and Remote Sensing*, vol. 51, no. 1, pp. 504–519, 2013.
- [11] G. S. Antonio, D. R. Fuhrmann, and F. C. Robey, "MIMO radar ambiguity functions," *IEEE Journal on Selected Topics in Signal Processing*, vol. 1, no. 1, pp. 167–177, 2007.
- [12] Y. I. Abramovich and G. J. Frazer, "Bounds on the volume and height distributions for the MIMO radar ambiguity function," *IEEE Signal Processing Letters*, vol. 15, pp. 505–508, 2008.
- [13] S. T. Smith, "Statistical resolution limits and the complexified Cramér-Rao bound," *IEEE Transactions on Signal Processing*, vol. 53, no. 5, pp. 1597–1609, 2005.
- [14] H. Cox, "Resolving power and sensitivity to mismatch of optimum array processors," *Journal of the Acoustical Society of America*, vol. 54, no. 3, pp. 771–785, 1973.
- [15] M. N. El Korso, R. Boyer, A. Renaux, and S. Marcos, "Statistical resolution limit for the multidimensional harmonic retrieval model- hypothesis test and Cramér-Rao bound approaches," *EURASIP Journal on Advances in Signal Processing*, vol. 2011, article 12, 2011.
- [16] M. Shahram and P. Milanfar, "Statistical and information-theoretic analysis of resolution in imaging," *IEEE Transactions on Information Theory*, vol. 52, no. 8, pp. 3411–3437, 2006.
- [17] M. N. El Korso, R. Boyer, A. Renaux, and S. Marcos, "On the asymptotic resolvability of two point sources in known subspace interference using a GLRT-based framework," *Signal Processing*, vol. 92, no. 10, pp. 2471–2483, 2012.
- [18] A. Amar and A. J. Weiss, "Fundamental limitations on the resolution of deterministic signals," *IEEE Transactions on Signal Processing*, vol. 56, no. 11, pp. 5309–5318, 2008.
- [19] M. Shahram and P. Milanfar, "On the resolvability of sinusoids with nearby frequencies in the presence of noise," *IEEE Transactions on Signal Processing*, vol. 53, no. 7, pp. 2579–2588, 2005.
- [20] Z. Liu and A. Nehorai, "Statistical angular resolution limit for point sources," *IEEE Transactions on Signal Processing*, vol. 55, no. 11, pp. 5521–5527, 2007.
- [21] M. N. El Korso, R. Boyer, A. Renaux, and S. Marcos, "Statistical resolution limit for source localization with clutter interference in a MIMO radar context," *IEEE Transactions on Signal Processing*, vol. 60, no. 2, pp. 987–992, 2012.
- [22] N. D. Tran, R. Boyer, S. Marcos, and P. Larzabal, "On the angular resolution limit for array processing in the presence of modeling errors," *IEEE Transactions on Signal Processing*, vol. 61, no. 19, pp. 4701–4706, 2013.
- [23] M. N. El Korso, R. Boyer, A. Renaux, and S. Marcos, "Statistical resolution limit of the uniform linear cocompact orthogonal loop and dipole array," *IEEE Transactions on Signal Processing*, vol. 59, no. 1, pp. 425–431, 2011.
- [24] R. Boyer, "Performance bounds and angular resolution limit for the moving colocated MIMO radar," *IEEE Transactions on Signal Processing*, vol. 59, no. 4, pp. 1539–1552, 2011.
- [25] H. B. Lee, "The Cramer-Rao bound on frequency estimates of signals closely spaced in frequency," *IEEE Transactions on Signal Processing*, vol. 40, no. 6, pp. 1508–1517, 1992.
- [26] S. M. Kay, *Fundamentals of Statistical Signal Processing: Volume II: Detection Theory*, chapter 6, Prentice-Hall, Englewood Cliffs, NJ, USA, 1993.
- [27] D. C. Bell and R. M. Narayanan, "Theoretical aspects of radar imaging using stochastic waveforms," *IEEE Transactions on Signal Processing*, vol. 49, no. 2, pp. 394–400, 2001.
- [28] M. Hawkes, "Effects of sensor placement on acoustic vector-sensor array performance," *IEEE Journal of Oceanic Engineering*, vol. 24, no. 1, pp. 33–40, 1999.
- [29] H. Chen, W. Zhou, J. Yang, Y. Peng, and X. Li, "Manifold studies on fundamental limits of direction-finding multiple-input multiple-output radar systems," *IET Radar, Sonar and Navigation*, vol. 6, no. 8, pp. 708–718, 2012.

Research Article

Beamspace Unitary ESPRIT Algorithm for Angle Estimation in Bistatic MIMO Radar

Dang Xiaofang, Chen Baixiao, Yang Minglei, and Zheng Guimei

National Laboratory of Radar Signal Processing, Xidian University, Xi'an, Shaanxi 710071, China

Correspondence should be addressed to Dang Xiaofang; xiaofang_dang@sina.cn

Received 28 February 2014; Revised 5 September 2014; Accepted 21 October 2014

Academic Editor: Hang Hu

Copyright © 2015 Dang Xiaofang et al. This is an open access article distributed under the Creative Commons Attribution License, which permits unrestricted use, distribution, and reproduction in any medium, provided the original work is properly cited.

The beamspace unitary ESPRIT (B-UESPRIT) algorithm for estimating the joint direction of arrival (DOA) and the direction of departure (DOD) in bistatic multiple-input multiple-output (MIMO) radar is proposed. The conjugate centrosymmetrized DFT matrix is utilized to retain the rotational invariance structure in the beamspace transformation for both the receiving array and the transmitting array. Then the real-valued unitary ESPRIT algorithm is used to estimate DODs and DOAs which have been paired automatically. The proposed algorithm does not require peak searching, presents low complexity, and provides a significant better performance compared to some existing methods, such as the element-space ESPRIT (E-ESPRIT) algorithm and the beamspace ESPRIT (B-ESPRIT) algorithm for bistatic MIMO radar. Simulation results are conducted to show these conclusions.

1. Introduction

Multiple-input multiple-output (MIMO) radar [1–6] is developed on the basis of MIMO communication theory, which has gained increasing attention and wide investigation in recent years. MIMO radar can emit orthogonal waveforms simultaneously through multiple antennas and also extract the orthogonal waveforms by using a bank of matched filters. Compared with the traditional phased array radars, a lot of potential advantages of MIMO radars, such as more degrees of freedom (DOFs) [2], better parameter identifiability [2], and higher angular estimation accuracy [3], increasingly appear. According to the configuration of transmitting/receiving arrays, MIMO radars can be grouped into two classes: the former is called statistical MIMO radar, where the transmitting and receiving antennas are widely spaced [1, 3, 4]. It aims at overcoming the radar cross section (RCS) scintillation effect which was encountered in radar systems by capitalizing on the spatial diversity [5]. The latter is known as monostatic MIMO radar or bistatic MIMO radar [2, 6–10], where the transmitting and receiving antennas are closely spaced. Monostatic or bistatic MIMO radar, which can form receiving beam and virtual transmitting beam jointly at the receiver [2], has many advantages, such as narrower

beamwidth, lower sidelobes, higher angular resolution, and higher angular estimation accuracy [6, 11]. And this paper focuses on the bistatic MIMO radar.

For the bistatic MIMO radar, one of the most important issues is to estimate the directions of departure and arrival of multiple targets from the received signals corrupted by noise. So far various approaches have been put forward. In [7], the two-dimensional (2D) Capon estimator is introduced to estimate the DOAs and the DODs of the targets in bistatic MIMO radar. To reduce the computational cost, a polynomial rooting estimator is introduced in [8]. The 2D multiple signal classification (MUSIC) algorithm and reduced-dimension MUSIC (RD-MUSIC) algorithm are discussed in [12, 13]. To alleviate the computational burden, the ESPRIT algorithm [14] is used for target direction estimation by utilizing the invariance property of both the transmitting array and the receiving array. Nevertheless, an additional matched pair is required in the ESPRIT algorithm. In order to solve this problem, a unitary ESPRIT algorithm for bistatic MIMO radar is proposed in [15], which fully exploits the real-valued rotational invariance equations of signal subspace to estimate DODs and DOAs that are paired automatically. When some a priori knowledge of the angle information of sources is known, the beamspace ESPRIT (B-ESPRIT) [16] algorithm

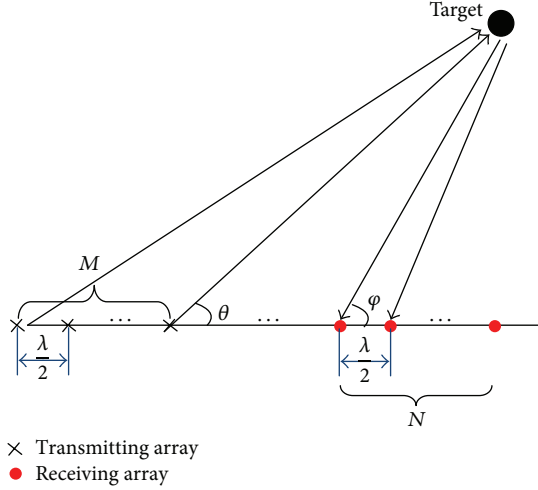


FIGURE 1: The configuration of bistatic MIMO radar.

is raised to reduce computational complexity; however, an additional pair matching is also needed and a degradation of the algorithm's performance can be observed as well.

To overcome the aforementioned problems, a beamspace unitary ESPRIT algorithm is developed to estimate DODs and DOAs of the targets in bistatic MIMO radar in this paper. First, the conjugate centrosymmetrized DFT matrix is employed to retain the rotational invariance structure in the beamspace transformation for both the receiving array and the transmitting array. Then the DODs and DOAs can be estimated in accordance with a new version of ESPRIT for the bistatic MIMO radar. The ESPRIT algorithm works in the beamspace and involves only real-valued computation from start to finish. Over the beamspace ESPRIT algorithm, the proposed algorithm has better performance that can be paired automatically for DODs and DOAs estimation. In some situation, the proposed algorithm also has a better performance over the element ESPRIT.

And the structure of the rest of the paper will be organized as follows. The bistatic MIMO radar signal model is presented in Section 2. The proposed beamspace unitary ESPRIT for DODs and DOAs estimation is proposed in Section 3. Section 4 gives the computational complexity analysis of the proposed algorithm, unitary ESPRIT, and beamspace ESPRIT; advantages and disadvantages of the proposed algorithm also have been discussed in Section 4. And simulation results are provided to verify the performance of the proposed algorithm in Section 5; the Cramer-Rao Bound (CRB) also has been derived in this section. Finally, Section 6 concludes this paper.

2. Signal Model of the Bistatic MIMO Radar

Considering a narrowband bistatic MIMO radar system with an M -element transmitting array and an N -element receiving array, we found that both are half-wave length spaced uniform linear arrays (Figure 1).

At the transmitting site, M different orthogonal narrow-band waveforms are emitted simultaneously. In each receiver, the echoes are processed for all of the transmitted waveforms. Assume that there are P uncorrelated targets in the same range bin, located in the far field of the array. The DOD and DOA of the p th target with respect to the transmitting array and the receiving array are denoted by θ_p and φ_p , respectively. Thus, the output of all the matched filters in receivers can be written as

$$\mathbf{X}(t) = \mathbf{A}\mathbf{S}(t) + \mathbf{N}(t), \quad (1)$$

where $\mathbf{A} = [\mathbf{a}_1, \mathbf{a}_2, \dots, \mathbf{a}_P]$ is an $MN \times P$ matrix, the column vectors \mathbf{a}_p , $p = 1, \dots, P$ are P steering vectors, which can be written as $\mathbf{a}_p = \mathbf{a}_r(\mu_p) \otimes \mathbf{a}_t(\nu_p)$, is the combined steering vector of p th target, where $\mathbf{a}_r(\mu_p) = [1 \ e^{j\mu_p} \ \dots \ e^{j(N-1)\mu_p}]^T \in \mathbb{C}^{N \times 1}$ and $\mathbf{a}_t(\nu_p) = [1 \ e^{j\nu_p} \ \dots \ e^{j(M-1)\nu_p}]^T \in \mathbb{C}^{M \times 1}$ are the receiving and transmitting steering vector of the p th target, and $\mu_p = \pi \sin \varphi_p$ and $\nu_p = \pi \sin \theta_p$, respectively; \otimes denotes the Kronecker product; $\mathbf{S}(t) = [s_1(t) \ s_2(t) \ \dots \ s_P(t)]^T$ is a column vector consisted of the amplitudes and phases of the P sources at time t ; $s_p(t)$ is usually in the form of $s_p(t) = \alpha_p e^{j\omega_p t}$ with α_p being the complex amplitude and ω_p the Doppler frequency of the p th target; $\mathbf{N}(t)$ is the additive noise, which is modeled as a zero-mean, spatially white Gaussian process with covariance matrix $\sigma_n^2 \mathbf{I}_{MN}$, where \mathbf{I}_{MN} denotes an $MN \times MN$ identity matrix.

Note that the dimension of \mathbf{X} will be $MN \times J$, and J is the number of time samples. When M and N are large, the computational load and time will be huge. To overcome this shortcoming, the beamspace unitary ESPRIT is proposed as follows.

3. Proposed Method for DOD and DOA Estimation

In a radar application, the operation of reducing dimension could be facilitated in beamspace when a priori information on the general angular locations of the signal arrivals presents. In this case, by utilizing the beamspace transform matrix, beams, which involve the sector of interest, would be formed, thereby reducing computational complexity. And if there is no a priori information, one may apply angle estimation algorithm via parallel processing to each of the number of sets of successive overlapped sectors, which will also reduce computational complexity.

To retain the rotational invariance structure in the beamspace transformation, in this paper, the conjugate centrosymmetrized DFT matrix is applied as the beamspace transformed matrix. Let \mathbf{W}_r^H be the receiving beamspace transformed matrix and let \mathbf{W}_t^H be the transmitting

beamspace transformed matrix. The m th row of \mathbf{W}_r^H and \mathbf{W}_t^H is formulated as [17]

$$\begin{aligned} \mathbf{w}_{r,m}^H &= e^{j((N-1)/2)m(2\pi/N)} \\ &\cdot [1, e^{-jm(2\pi/N)}, \dots, e^{-j(N-1)m(2\pi/N)}], \\ & \quad m = 0, \dots, N-1 \\ \mathbf{w}_{t,m}^H &= e^{j((M-1)/2)m(2\pi/M)} \\ &\cdot [1, e^{-jm(2\pi/M)}, \dots, e^{-j(M-1)m(2\pi/M)}], \\ & \quad m = 0, \dots, M-1. \end{aligned} \quad (2)$$

Both \mathbf{W}_r^H and \mathbf{W}_t^H are conjugate centrosymmetrized matrixes and their m th row vector represents a DFT beam steered at the spatial frequency $\mu = m(2\pi/N)$ and $\nu = m(2\pi/M)$, respectively. An important property of the Kronecker operator that will prove useful throughout the transformation is

$$(\mathbf{A} \otimes \mathbf{B})(\mathbf{C} \otimes \mathbf{D}) = \mathbf{AC} \otimes \mathbf{BD}, \quad (3)$$

where \mathbf{A} is an $m \times n$ matrix, which is not the matrix \mathbf{A} mentioned above in (1). \mathbf{B} is a $p \times q$ matrix, which is also not the matrix \mathbf{B} mentioned below in (5). \mathbf{C} is an $n \times r$ matrix and \mathbf{D} is a $q \times s$ matrix.

The receiving beamspace manifold is defined as $\mathbf{B}_r = \mathbf{W}_r^H \mathbf{A}_r$ and the transmitting beamspace manifold is defined as $\mathbf{B}_t = \mathbf{W}_t^H \mathbf{A}_t$, respectively. Then the final beamspace manifold can be written as

$$\begin{aligned} \mathbf{B} &= \mathbf{W}^H \mathbf{A} = \mathbf{B}_r \otimes \mathbf{B}_t \\ &= \mathbf{W}_r^H \mathbf{A}_r \otimes \mathbf{W}_t^H \mathbf{A}_t. \end{aligned} \quad (4)$$

According to property (3), the equation $\mathbf{W}_r^H \mathbf{A}_r \otimes \mathbf{W}_t^H \mathbf{A}_t = (\mathbf{W}_r^H \otimes \mathbf{W}_t^H)(\mathbf{A}_r \otimes \mathbf{A}_t)$ holds. Thus, the final beamspace transformed matrix is defined as

$$\mathbf{W}^H = \mathbf{W}_r^H \otimes \mathbf{W}_t^H. \quad (5)$$

\mathbf{W} is an $K_t K_r \times MN$ matrix, where K_t and K_r are the number of transmitting beam and receiving beam, respectively. A new beamspace received signal is defined as

$$\begin{aligned} \mathbf{Y}(t) &= \mathbf{W}^H \mathbf{A} \mathbf{S}(t) + \bar{\mathbf{N}}(t) \\ &= \mathbf{B} \mathbf{S}(t) + \bar{\mathbf{N}}(t), \end{aligned} \quad (6)$$

where $\bar{\mathbf{N}}(t) = \mathbf{W}^H \mathbf{N}(t)$ is the noise of beamspace.

Next the rotational invariance structure in the beamspace will be examined. Considering the receiving beamspace manifold $\mathbf{B}_r = [\mathbf{b}_r(\mu_1), \dots, \mathbf{b}_r(\mu_p)]$, the p th component of \mathbf{B}_r

is $\mathbf{b}_r(\mu_p) = [b_{r,0}(\mu_p), \dots, b_{r,N-1}(\mu_p)]^T$. And the m th elements of $\mathbf{b}_r(\mu_p)$ are

$$b_{r,m}(\mu_p) = \mathbf{w}_{r,m}^H \mathbf{a}_r(\mu) = \frac{\sin[(N/2)(\mu_p - m(2\pi/N))]}{\sin[(1/2)(\mu_p - m(2\pi/N))]} \quad (7)$$

Comparing (7) with $b_{r,m+1}(\mu_p)$, it is observed that the numerator of $b_{r,m+1}(\mu_p)$ is the negative of that of $b_{r,m}(\mu_p)$. Then the two adjacent components of $\mathbf{b}_r(\mu_p)$ are related as [18]

$$\begin{aligned} \sin\left[\frac{1}{2}\left(\mu_p - m\frac{2\pi}{N}\right)\right] b_{r,m}(\mu_p) \\ + \sin\left[\frac{1}{2}\left(\mu_p - (m+1)\frac{2\pi}{N}\right)\right] b_{r,m+1}(\mu_p) = 0. \end{aligned} \quad (8)$$

Trigonometric equations lead to

$$\begin{aligned} \tan\left(\frac{\mu_p}{2}\right) \left\{ \cos\left(m\frac{\pi}{N}\right) b_{r,m}(\mu_p) \right. \\ \left. + \cos\left((m+1)\frac{\pi}{N}\right) b_{r,m+1}(\mu_p) \right\} \\ = \sin\left(m\frac{\pi}{N}\right) b_{r,m}(\mu_p) + \sin\left((m+1)\frac{\pi}{N}\right) b_{r,m+1}(\mu_p). \end{aligned} \quad (9)$$

Due to the fact that the beams with indices $m = 0$ and $m = N-1$ are steered at the spatial frequencies $\mu_{p,0} = 0$ and $\mu_{p,N-1} - 2\pi = (N-1)(2\pi/N) - 2\pi = -2\pi/N$, where the two beams are physically adjacent to each other. First, we observe that

$$\begin{aligned} b_N(\mu_p) &= \frac{\sin[(N/2)(\mu_p - N(2\pi/N))]}{\sin[(1/2)(\mu_p - N(2\pi/N))]} \\ &= \frac{\sin((N/2)\mu_p - N\pi)}{\sin((1/2)\mu_p - \pi)} \\ &= \frac{(-1)^N \sin((N/2)\mu_p)}{-\sin((1/2)\mu_p)} = (-1)^{N-1} \cdot b_0(\mu_p). \end{aligned} \quad (10)$$

Then, the first and the last elements of $\mathbf{b}_r(\mu_p)$ are related by setting $m = N-1$ in (9), and there is

$$\begin{aligned} \tan\left(\frac{\mu_p}{2}\right) \left\{ \cos\left((N-1)\frac{\pi}{N}\right) b_{r,N-1}(\mu_p) \right. \\ \left. + \cos(\pi)(-1)^{(N-1)} b_{r,0}(\mu_p) \right\} \\ = \sin\left((N-1)\frac{\pi}{N}\right) b_{r,N-1}(\mu_p) \\ + \sin(\pi)(-1)^{(N-1)} b_{r,0}(\mu_p). \end{aligned} \quad (11)$$

All N equations ($0 \leq m \leq N-1$) lead to an invariance relationship for the $\mathbf{b}_r(\mu_p)$ as follows:

$$\tan\left(\frac{\mu_p}{2}\right) \mathbf{\Gamma}_1 \mathbf{b}_r(\mu_p) = \mathbf{\Gamma}_2 \mathbf{b}_r(\mu_p), \quad (12)$$

where $\mathbf{\Gamma}_1$ and $\mathbf{\Gamma}_2$ are the two selection matrixes defined as

$$\mathbf{\Gamma}_1 = \begin{bmatrix} 1 & \cos\left(\frac{\pi}{N}\right) & 0 & 0 & \cdots & 0 & 0 \\ 0 & \cos\left(\frac{\pi}{N}\right) & \cos\left(\frac{2\pi}{N}\right) & 0 & \cdots & 0 & 0 \\ 0 & 0 & \cos\left(\frac{2\pi}{N}\right) & \cos\left(\frac{3\pi}{N}\right) & \cdots & 0 & 0 \\ \vdots & \vdots & \vdots & \vdots & \cdot & \vdots & \vdots \\ 0 & 0 & 0 & 0 & \cdots & \cos\left((N-2)\frac{\pi}{N}\right) & \cos\left((N-1)\frac{\pi}{N}\right) \\ (-1)^N & 0 & 0 & 0 & \cdots & 0 & \cos\left((N-1)\frac{\pi}{N}\right) \end{bmatrix}, \quad (13)$$

$$\mathbf{\Gamma}_2 = \begin{bmatrix} 0 & \sin\left(\frac{\pi}{N}\right) & 0 & 0 & \cdots & 0 & 0 \\ 0 & \sin\left(\frac{\pi}{N}\right) & \sin\left(\frac{2\pi}{N}\right) & 0 & \cdots & 0 & 0 \\ 0 & 0 & \sin\left(\frac{2\pi}{N}\right) & \sin\left(\frac{3\pi}{N}\right) & \cdots & 0 & 0 \\ \vdots & \vdots & \vdots & \vdots & \cdot & \vdots & \vdots \\ 0 & 0 & 0 & 0 & \cdots & \sin\left((N-2)\frac{\pi}{N}\right) & \sin\left((N-1)\frac{\pi}{N}\right) \\ 0 & 0 & 0 & 0 & \cdots & 0 & \sin\left((N-1)\frac{\pi}{N}\right) \end{bmatrix}.$$

When some a priori knowledge of the angle information of sources is known, a reduced dimension processing can be achieved by applying a subset of row vectors defined in (4) to the data matrix \mathbf{X} . Hence, only those subblocks of the selection matrices $\mathbf{\Gamma}_1$ and $\mathbf{\Gamma}_2$ which are correlated with the corresponding components of $\mathbf{b}_r(\mu_p)$ will be used.

With P targets, (12) translates into the receiving beamspace matrix relation:

$$\mathbf{\Gamma}_1 \mathbf{B}_r \mathbf{\Omega}_\mu = \mathbf{\Gamma}_2 \mathbf{B}_r, \quad (14)$$

where $\mathbf{\Omega}_\mu = \text{diag}\{\tan(\mu_1/2), \dots, \tan(\mu_P/2)\}$ is a real-valued diagonal matrix whose diagonal elements contain the desired DOA information. Similar to the relation of receiving beamspace matrix, the relation of transmit beamspace matrix is

$$\mathbf{\Gamma}_3 \mathbf{B}_t \mathbf{\Omega}_\nu = \mathbf{\Gamma}_4 \mathbf{B}_t, \quad (15)$$

where $\mathbf{\Gamma}_3$ and $\mathbf{\Gamma}_4$ are defined similar to (13) with N replaced by M and $\mathbf{\Omega}_\nu = \text{diag}\{\tan(\nu_1/2), \dots, \tan(\nu_P/2)\}$ is a real-valued diagonal matrix whose diagonal elements contain the desired DOD information.

According to the use of the property of the Kronecker operator in (3), we find that the whole beamspace manifold \mathbf{B} satisfies

$$\begin{aligned} \mathbf{\Gamma}_{\mu_1} \mathbf{B} \mathbf{\Omega}_\mu &= \mathbf{\Gamma}_{\mu_2} \mathbf{B} \\ \mathbf{\Gamma}_{\nu_1} \mathbf{B} \mathbf{\Omega}_\nu &= \mathbf{\Gamma}_{\nu_2} \mathbf{B}, \end{aligned} \quad (16)$$

where $\mathbf{\Gamma}_{\mu_1} = \mathbf{\Gamma}_1 \otimes \mathbf{I}_M$ and $\mathbf{\Gamma}_{\mu_2} = \mathbf{\Gamma}_2 \otimes \mathbf{I}_M$ are the receiving beamspace selection matrices and $\mathbf{\Gamma}_{\nu_1} = \mathbf{I}_N \otimes \mathbf{\Gamma}_3$ and

$\mathbf{\Gamma}_{\nu_2} = \mathbf{I}_N \otimes \mathbf{\Gamma}_4$ are the transmitting beamspace selection matrices, respectively.

Looking back on the beamspace received signal $\mathbf{Y}(t)$ defined in (5), the proper $NM \times P$ matrix of signal subspace for the proposed algorithm can be formed by P "largest" left singular vectors of the real-valued matrix $[\text{Re}(\mathbf{Y}), \text{Im}(\mathbf{Y})]$. As we know, the signal subspace \mathbf{E}_s may be spanned by \mathbf{B} , which is expressed as

$$\mathbf{E}_s = \mathbf{B} \mathbf{T}, \quad (17)$$

where \mathbf{T} is an unknown $P \times P$ real-valued matrix. Substituting $\mathbf{B} = \mathbf{E}_s \mathbf{T}^{-1}$ into (16) yields

$$\begin{aligned} \mathbf{\Gamma}_{\mu_1} \mathbf{E}_s \mathbf{\Psi}_\mu &= \mathbf{\Gamma}_{\mu_2} \mathbf{E}_s, \\ \mathbf{\Gamma}_{\nu_1} \mathbf{E}_s \mathbf{\Psi}_\nu &= \mathbf{\Gamma}_{\nu_2} \mathbf{E}_s, \end{aligned} \quad (18)$$

where $\mathbf{\Psi}_\mu = \mathbf{T}^{-1} \mathbf{\Omega}_\mu \mathbf{T}$ and $\mathbf{\Psi}_\nu = \mathbf{T}^{-1} \mathbf{\Omega}_\nu \mathbf{T}$. Equation (18) can be solved by the least squares (LS) or the total least squares (TLS) algorithm. Note the fact that all of the quantities of $\mathbf{\Psi}_\mu$ and $\mathbf{\Psi}_\nu$ are real-valued. Automatic pairing of the spatial frequency μ and ν estimation can be obtained by decomposing $\mathbf{\Psi}_\mu + j\mathbf{\Psi}_\nu$ as follows:

$$\mathbf{\Psi}_\mu + j\mathbf{\Psi}_\nu = \mathbf{T}^{-1} \{ \mathbf{\Omega}_\mu + j\mathbf{\Omega}_\nu \} \mathbf{T}. \quad (19)$$

Hence, the real and imaginary parts of the eigenvalues $\{\Omega_{\mu} + j\Omega_{\nu}\}$ are the estimation of $\{\mu_p, \nu_p\}$, $p = 1, \dots, P$. Then the DODs and DOAs of targets can be derived as follows:

$$\begin{aligned}\hat{\theta}_p &= \arcsin \left\{ \frac{2 \arctan [\Omega_{\nu}]_p}{\pi} \right\}, \quad p = 1, \dots, P, \\ \hat{\varphi}_p &= \arcsin \left\{ \frac{2 \arctan [\Omega_{\mu}]_p}{\pi} \right\}, \quad p = 1, \dots, P.\end{aligned}\quad (20)$$

The beamspace unitary ESPRIT algorithm based on this development is summarized below.

- (1) To form the beamspace transformed matrix $\mathbf{W}^H = \mathbf{W}_r^H \otimes \mathbf{W}_t^H$, where $\mathbf{W}^H \in K_t K_r \times MN$.
- (2) To transform the receiving data $\mathbf{X}(t)$ into beamspace $\mathbf{Y} = \mathbf{W}^H \mathbf{X}$, where $\mathbf{Y} \in K_t K_r \times J$, J is the number of time samples.
- (3) To compute the SVD of $[\text{Re}(\mathbf{Y}), \text{Im}(\mathbf{Y})]$. The P dominant left singular vectors will be called $\mathbf{E}_s \in K_t K_r \times P$. And if P is not known as the a priori information, the number of sources P should be estimated [19].
- (4a) To compute Ψ_{μ} by solving the overdetermined system of equation $\Gamma_{\mu_1} \mathbf{E}_s \Psi_{\mu} = \Gamma_{\mu_2} \mathbf{E}_s$ via the least squares or the total least squares algorithm. The selection matrices $\Gamma_{\mu_1} = \Gamma_1 \otimes \mathbf{I}_M$ and $\Gamma_{\mu_2} = \Gamma_2 \otimes \mathbf{I}_M$, where Γ_1 and Γ_2 are defined in (13). When one has the a priori information on the general angular locations of the signal arrivals, only the appropriate subblocks of Γ_1 and Γ_2 are employed.
- (4b) To compute Ψ_{ν} by solving the overdetermined system of equation $\Gamma_{\nu_1} \mathbf{E}_s \Psi_{\nu} = \Gamma_{\nu_2} \mathbf{E}_s$ by the least squares or the total least squares algorithm. The selection matrices are $\Gamma_{\nu_1} = \mathbf{I}_N \otimes \Gamma_3$ and $\Gamma_{\nu_2} = \mathbf{I}_N \otimes \Gamma_4$.
- (5) To compute the eigendecomposition of matrix $\Psi_{\mu} + j\Psi_{\nu}$. Then P largest eigenvalues λ_p , $p = 1, \dots, P$ could be obtained as $\lambda_p = \{[\Omega_{\nu}]_p + j[\Omega_{\mu}]_p\}$, where $[\Omega_{\nu}]_p$ and $[\Omega_{\mu}]_p$ are the real and imaginary parts of λ_p , respectively.
- (6) To compute the DODs and DOAs as the solution to $\hat{\theta}_p = \arcsin\{2 \arctan[\Omega_{\nu}]_p/\pi\}$, $p = 1, \dots, P$ and $\hat{\varphi}_p = \arcsin\{2 \arctan[\Omega_{\mu}]_p/\pi\}$, $p = 1, \dots, P$ which are paired automatically.

4. Computational Complexity Analysis

In Table 1, the beamspace unitary ESPRIT is compared against the unitary ESPRIT and the beamspace ESPRIT algorithm in terms of computational complexity. For the element ESPRIT and the unitary ESPRIT algorithm, the computational complexity of eigendecomposition is $O(M^3 N^3)$, which is very heavy. Unlike the element ESPRIT and the unitary ESPRIT algorithm, the beamspace ESPRIT and the beamspace unitary ESPRIT algorithm transform the original data vector into several lower-dimensional beamspaces. Since

the data processing of each beamspace is independent, it can be parallel processed. If only $K_t < M$ transmitting beams and $K_r < N$ receiving beams are selected, the computational complexity could be reduced from $O(M^3 N^3)$ to $O(K_t^3 K_r^3)$. It is noted that the computational saving is quite significant. Comparing the beamspace unitary ESPRIT with the beamspace ESPRIT algorithm, the proposed algorithm involves only real-valued computation from start to finish. So the computational complexity of beamspace unitary ESPRIT is slightly lower than the beamspace ESPRIT algorithm. And the beamspace unitary ESPRIT algorithm can estimate DOAs and DODs that are paired automatically, which need to be paired additionally in the beamspace ESPRIT algorithm, to save computational complexity.

4.1. Advantages and Disadvantages of the Proposed Algorithm.

The proposed algorithm has the following advantages.

- (1) The proposed algorithm involves only real-valued computation after the initial transformation of beamspace.
- (2) The proposed algorithm has a low complexity for the fact that peak searching is not required. And when a priori information is known, only several beams encompassing the sector of interest need to be formed, thereby yielding further reduced computational complexity.
- (3) The proposed algorithm can obtain automatically paired DOD and DOA angle estimations.
- (4) The proposed algorithm has a better angle estimation performance than B-ESPRIT algorithm which has been explained in the following section.

The proposed algorithm also has the following disadvantages.

- (1) The proposed algorithm shows that, due to the dramatic reduction in computational complexity, the performance degradation would appear.
- (2) The proposed algorithm is sensitive to array errors. The rotational invariance structure will be damaged in the presence of array errors.

5. Simulation Results

In this section, some numerical examples are presented to assess the effectiveness of the proposed method. In all

TABLE 1: Comparison of computational complexities of the beamspace unitary ESPRIT, the beamspace ESPRIT, and the unitary ESPRIT.

Algorithms	Beamspace transformation	Subspace decomposition	DOA and DOD estimation
The unitary ESPRIT	None	$O(M^3 N^3)$	$O(2^3 P^3)$
The beamspace ESPRIT	$O(JK_r K_r MN)$	$O(K_r^3 K_r^3)$	$O(2^3 P^3)$
The beamspace unitary ESPRIT	$O(JK_r K_r MN)$	$O(K_r^3 K_r^3)$	$O(P^3)$

simulations, 2000 Monte Carlo trials are performed. The RMSE is defined as

$$\begin{aligned} \text{RMSE}_t &= \frac{1}{P} \sum_{p=1}^P \sqrt{\frac{1}{1,000} \sum_{l=1}^{1,000} (\hat{\theta}_{p,l} - \theta_p)^2}, \\ \text{RMSE}_r &= \frac{1}{P} \sum_{p=1}^P \sqrt{\frac{1}{1,000} \sum_{l=1}^{1,000} (\hat{\varphi}_{p,l} - \varphi_p)^2}, \\ \text{RMSE} &= \frac{1}{P} \sum_{p=1}^P \sqrt{\frac{1}{1,000} \sum_{l=1}^{1,000} [(\hat{\theta}_{p,l} - \theta_p)^2 + (\hat{\varphi}_{p,l} - \varphi_p)^2]}, \end{aligned} \quad (21)$$

which are employed as the performance metric, where θ_p and φ_p denote the DOD and DOA of the p th source and $\hat{\theta}_{p,l}$ and $\hat{\varphi}_{p,l}$ are the estimation of θ_p and φ_p in the l th Monte Carlo trail, respectively. J denotes the number of snapshots. According to [16], the CRB for the angle estimation in bistatic MIMO radar is derived as follows:

$$\text{CRB}(\theta, \varphi) = \frac{\sigma^2}{2K} \left\{ \text{Re} \left[\mathbf{D}^H \mathbf{\Pi}_B^\perp \mathbf{D} \odot \hat{\mathbf{P}}_{SS}^T \right] \right\}^{-1}, \quad (22)$$

where $\mathbf{D} = [\partial \mathbf{b}_1 / \partial \theta_1, \partial \mathbf{b}_2 / \partial \theta_2, \dots, \partial \mathbf{b}_P / \partial \theta_P, \partial \mathbf{b}_1 / \partial \varphi_1, \partial \mathbf{b}_2 / \partial \varphi_2, \dots, \partial \mathbf{b}_P / \partial \varphi_P]$ with \mathbf{b}_p being the p th column of \mathbf{B} , $\mathbf{\Pi}_B^\perp = \mathbf{I}_{MN} - \mathbf{B}(\mathbf{B}^H \mathbf{B})^{-1} \mathbf{B}^H$, $\hat{\mathbf{P}}_{SS}^T = \begin{bmatrix} \hat{\mathbf{P}}_s & \hat{\mathbf{P}}_s \\ \hat{\mathbf{P}}_s & \hat{\mathbf{P}}_s \end{bmatrix}$, $\hat{\mathbf{P}}_s = (1/J) \sum_{t=1}^J \mathbf{S}(t) \mathbf{S}^H(t)$, σ^2 stands for the noise variance, and J is the number of time samples.

Assuming that there are $P = 3$ sources, whose angles are $(\theta_1, \varphi_1) = (30^\circ, -30^\circ)$, $(\theta_2, \varphi_2) = (20^\circ, -40^\circ)$, and $(\theta_3, \varphi_3) = (40^\circ, -36^\circ)$. For the B-ESPRIT and the proposed algorithm, there are five beams are formed, which involve the sector of interest.

Figures 2 and 3 depict the DOD and DOA estimation results of the proposed algorithm for the three sources in bistatic MIMO radar with $M = 8$, $N = 6$, $J = 64$, SNR = 15 dB, and 20 dB, respectively. It shows that the DODs and DOAs of sources can be clearly observed, and the performance will be improved as the SNR increases.

The proposed algorithm is compared against the beamspace ESPRIT algorithm, the element ESPRIT algorithm, the unitary ESPRIT, and CRB. And in this Simulation, a new source located at $(\theta_4, \varphi_4) = (36^\circ, -36^\circ)$ is added. Figures 4 and 5 present angle estimation performance comparison with $M = 8$, $N = 6$, and $J = 64$. It can be found that the angle estimation performance of proposed algorithm is better than the B-ESPRIT algorithm because unitary ESPRIT doubles the number of data samples

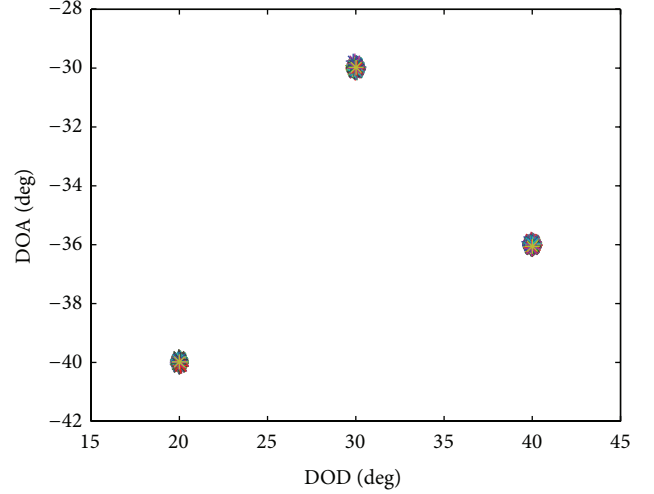


FIGURE 2: Angle estimation results with SNR = 15 dB.

effectively [20]. It is observed that the proposed algorithm performs slightly worse than the U-ESPRIT algorithm does in the DOD estimation in despite of the dramatic reduction in computational complexity (where the number of transmit antenna is $M = 8$ and the number of transmit beam is $L_t = 5 < M$). And the proposed algorithm and U-ESPRIT algorithm both have similar estimation performance of DOA due to the fact that the number of receiving beam is nearly equal to the number of transmitting antenna (where $L_r = 5$ and $N = 6$). Compared with the E-ESPRIT algorithm, although the beamspace unitary ESPRIT algorithm is a unitary algorithm, its performance will also be degraded because of the dramatic reduction in computational complexity. When the degradation is not large enough, the proposed algorithm also has a better performance over the element ESPRIT.

Figures 6 and 7 present the angle estimation performance of the proposed algorithm with different J , where $M = 8$, $N = 6$. The proposed algorithm is compared with the unitary ESPRIT algorithm. It illustrates that the angle estimation performance of our algorithm is improved as the number of snapshots increases. Meanwhile, it shows that performance of our algorithm is slightly worse than the unitary ESPRIT algorithm when the computational complexity is reduced all at once.

In Figure 8, values of transmitting array antennas $M = 6, 8$ and 10 ($N = 6$, $J = 64$) are examined for the SNR support. From Figure 8, it can be seen that the angle estimation performance of proposed algorithm will gradually increase with the increasing transmitting antenna number.

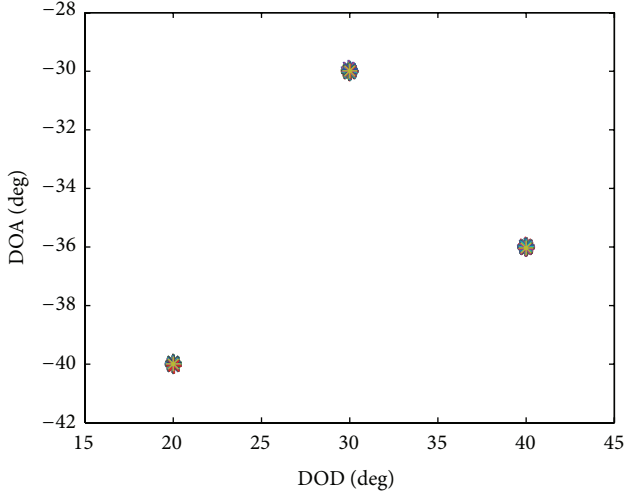


FIGURE 3: Angle estimation results with SNR = 20 dB.

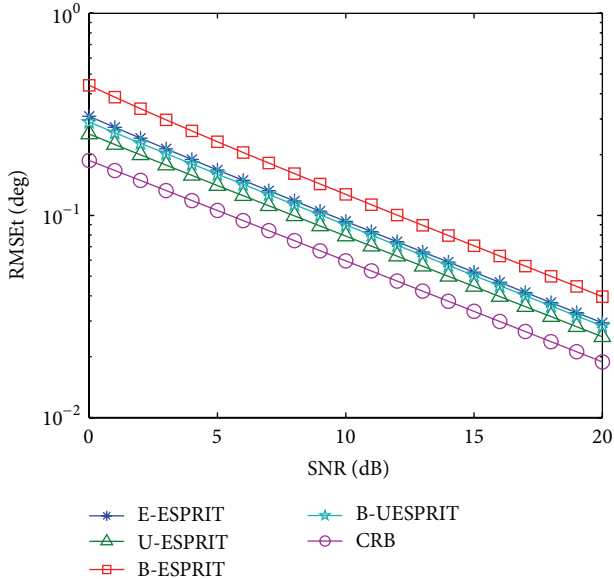


FIGURE 4: DOD estimation performance comparison.

Figure 9 gives the resolution performance of the proposed algorithm, the beamspace ESPRIT algorithm, the element ESPRIT algorithm, and the unitary ESPRIT algorithm. Considering a scenario with two uncorrelated sources of equal power, the angle parameters are $\theta_1 = \varphi_1 = -\delta/\sqrt{2}$ and $\theta_2 = \varphi_2 = \delta/\sqrt{2}$, and $J = 50$, SNR = 20 dB. Then the angular source separation is parameterized by [21]

$$2\delta = \sqrt{(\theta_1 - \theta_2)^2 + (\varphi_1 - \varphi_2)^2}. \quad (23)$$

The two sources are considered as resolved if the estimation of angle is close to the true angle parameter; that is,

$$(\hat{\theta}_1 - \theta_1)^2 + (\hat{\varphi}_1 - \varphi_1)^2 < \delta^2 \cap (\hat{\theta}_2 - \theta_2)^2 + (\hat{\varphi}_2 - \varphi_2)^2 < \delta^2. \quad (24)$$

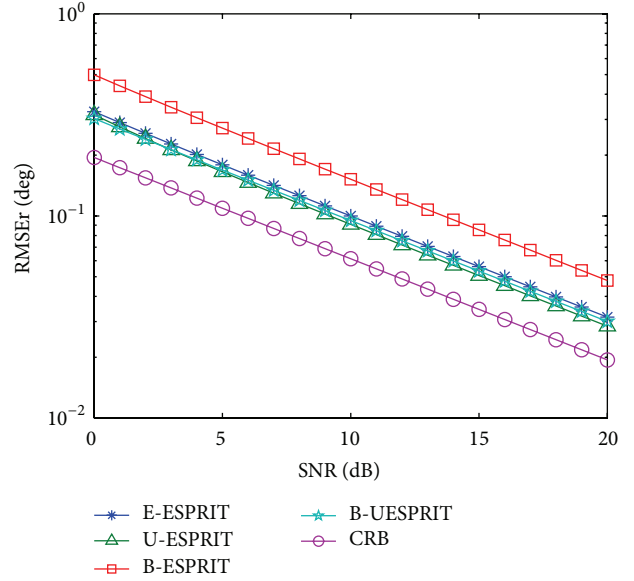


FIGURE 5: DOA estimation performance comparison.

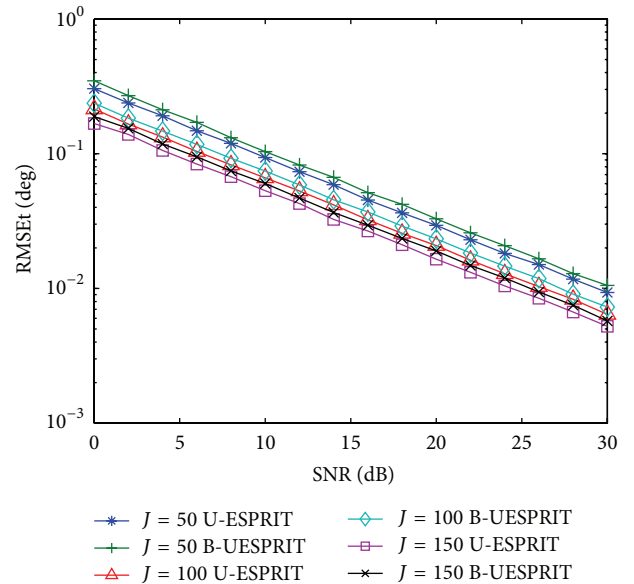


FIGURE 6: RMSE of DOD versus SNR for 3 sources with different values of sample.

It can be seen that the probability of resolution of proposed algorithm is better than both the beamspace ESPRIT algorithm and the element ESPRIT algorithm but slightly worse than the unitary ESPRIT algorithm.

Figure 10 depicts an evaluation of the computational complexity using TIC and TOC instructions that can serve for calculating the runtime of an algorithm in MATLAB. It can be seen that when all the beams are formed, the runtime of proposed algorithm is smaller than the U-ESPRIT algorithm in the case of the number of sensors is larger than 10. And when only five beams are formed, the runtime of proposed algorithm is much smaller than the U-ESPRIT

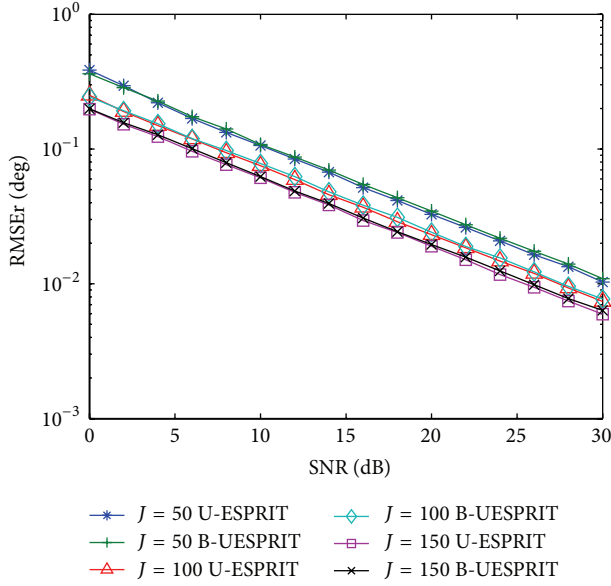


FIGURE 7: RMSE of DOA versus SNR for 3 sources with different values of sample.

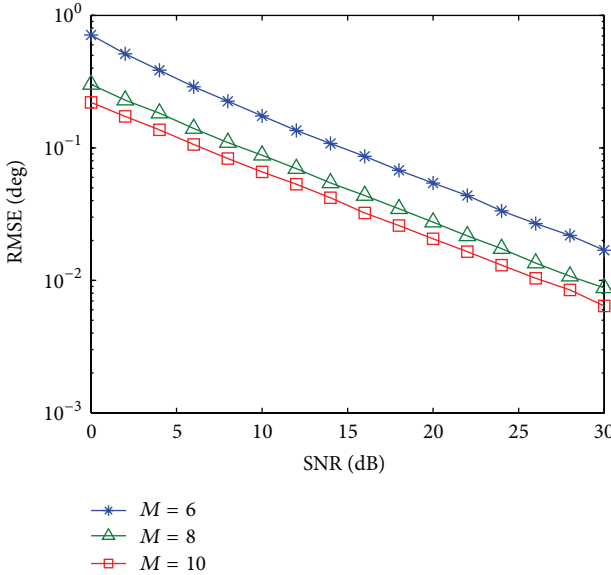


FIGURE 8: Total RMSE versus SNR for 3 sources with different values of M .

algorithm. Also, the runtime of the B-UESPRIT is smaller than the B-ESPRIT algorithm, which is still in the case of only five beams are formed. It is observed that as the number of sensors increases, the runtime of the proposed algorithm increases slowly. The reason is that the computational complexities and runtime of proposed algorithm are influenced by the number of beams formed, which is still five.

6. Conclusion

In this paper, a beamspace unitary ESPRIT is developed to estimate angles of the targets in bistatic MIMO radar.

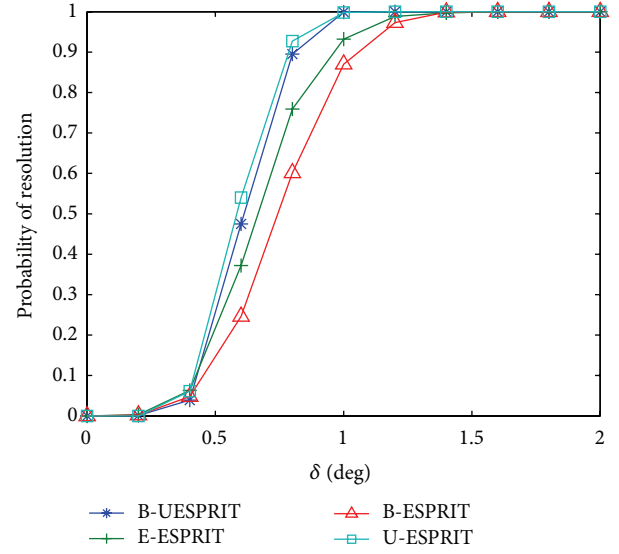


FIGURE 9: Probability of resolution versus angular separation δ , at SNR = 20 dB, $J = 50$.

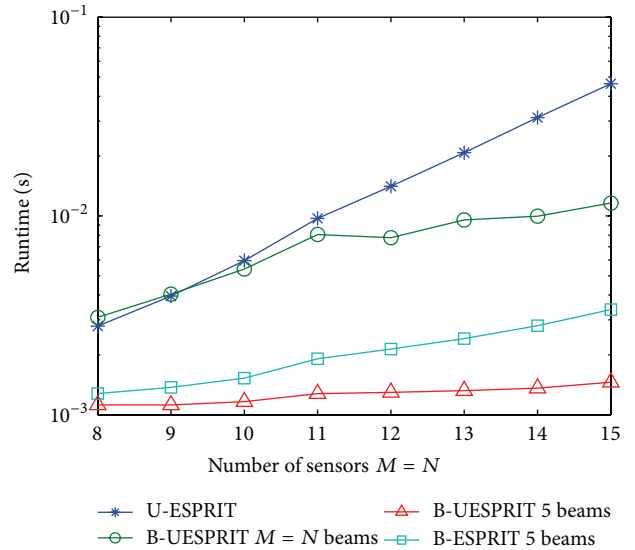


FIGURE 10: Runtime comparison against number of sensors $M = N$.

The conjugate centrosymmetrized DFT matrix is applied to transform the received data into beamspace. Then the invariance property of the transmitting beam and the receiving beam is exploited, respectively, to calculate the DODs and the DOAs of targets. Unlike the beamspace ESPRIT, the B-UESPRIT involves only real-valued computation from beginning to end. Therefore, a reduction of the computational complexity is obtained, which is demonstrated by the analysis of computational complexity and the runtime of algorithm. Furthermore, the simulation results prove that the B-UESPRIT requires no matched pair but possesses better angle estimation performance than the E-ESPRIT and the B-ESPRIT. Additionally, the CRB has been derived to analyze the performance.

Conflict of Interests

The authors declare that there is no conflict of interests regarding the publication of this paper.

References

- [1] E. Fishler, A. Haimovich, R. Blum, D. Chizhik, L. Cimini, and R. Valenzuela, "MIMO radar: an idea whose time has come," in *Proceedings of the IEEE Radar Conference*, pp. 71–78, Philadelphia, Pa, USA, April 2004.
- [2] I. Bekkerman and J. Tabrikian, "Target detection and localization using MIMO radars and sonars," *IEEE Transactions on Signal Processing*, vol. 54, no. 10, pp. 3873–3883, 2006.
- [3] E. Fishler, A. Haimovich, R. S. Blum, L. J. Cimini Jr., D. Chizhik, and R. A. Valenzuela, "Spatial diversity in radars—models and detection performance," *IEEE Transactions on Signal Processing*, vol. 54, no. 3, pp. 823–838, 2006.
- [4] A. M. Haimovich, R. S. Blum, and L. J. Cimini, "MIMO radar with widely separated antennas," *IEEE Signal Processing Magazine*, vol. 25, no. 1, pp. 116–129, 2008.
- [5] J. Li and P. Stoica, "MIMO radar—diversity means superiority," in *Proceedings of the 14th Adaptive Sensor Array Process Workshop (ASAP '06)*, pp. 1–64, Lexington, Mass, USA, December 2006.
- [6] J. Li and P. Stoica, "MIMO radar with colocated antennas," *IEEE Signal Processing Magazine*, vol. 24, no. 5, pp. 106–114, 2007.
- [7] H. Yan, J. Li, and G. Liao, "Multitarget identification and localization using bistatic MIMO radar systems," *EURASIP Journal on Advances in Signal Processing*, vol. 2008, Article ID 283483, 2008.
- [8] R. Xie, Z. Liu, and Z.-J. Zhang, "DOA estimation for monostatic MIMO radar using polynomial rooting," *Signal Processing*, vol. 90, no. 12, pp. 3284–3288, 2010.
- [9] J. Li, P. Stoica, L. Xu, and W. Roberts, "On parameter identifiability of MIMO radar," *IEEE Signal Processing Letters*, vol. 14, no. 12, pp. 968–971, 2007.
- [10] M. Jin, G. Liao, and J. Li, "Joint DOD and DOA estimation for bistatic MIMO radar," *Signal Processing*, vol. 89, no. 2, pp. 244–251, 2009.
- [11] L. Xu, J. Li, and P. Stoica, "Target detection and parameter estimation for MIMO radar systems," *IEEE Transactions on Aerospace and Electronic Systems*, vol. 44, no. 3, pp. 927–939, 2008.
- [12] X. Gao, X. Zhang, G. Feng, Z. Wang, and D. Xu, "On the MUSIC-derived approaches of angle estimation for bistatic MIMO radar," in *Proceedings of the International Conference on Wireless Networks and Information Systems (WNIS '09)*, pp. 343–346, December 2009.
- [13] A. Zahernia, M. J. Dehghani, and R. Javidan, "MUSIC algorithm for DOA estimation using MIMO arrays," in *Proceedings of the 6th International Conference on Telecommunication Systems, Services, and Applications (TSSA '11)*, pp. 149–153, October 2011.
- [14] C. Duofang, C. Baixiao, and Q. Guodong, "Angle estimation using ESPRIT in MIMO radar," *Electronics Letters*, vol. 44, no. 12, pp. 770–771, 2008.
- [15] G. Zheng, B. Chen, and M. Yang, "Unitary ESPRIT algorithm for bistatic MIMO radar," *Electronics Letters*, vol. 48, no. 3, pp. 179–181, 2012.
- [16] Y. D. Guo, Y. S. Zhang, and N. N. Tong, "Beamspace ESPRIT algorithm for bistatic MIMO radar," *Electronics Letters*, vol. 47, no. 15, pp. 876–878, 2011.
- [17] M. D. Zoltowski, M. Haardt, and C. P. Mathews, "Closed-form 2D angle estimation with rectangular arrays via DFT beamspace ESPRIT," in *Proceedings of the 28th Asilomar IEEE Conference on Signals, Systems, and Computers*, pp. 682–687, 1994.
- [18] M. D. Zoltowski, M. Haardt, and C. P. Mathews, "Closed-form 2-D angle estimation with rectangular arrays in element space or beamspace via unitary ESPRIT," *IEEE Transactions on Signal Processing*, vol. 44, no. 2, pp. 316–328, 1996.
- [19] G. Xu, R. H. Roy III, and T. Kailath, "Detection of number of sources via exploitation of centro-symmetry property," *IEEE Transactions on Signal Processing*, vol. 42, no. 1, pp. 102–112, 1994.
- [20] M. Haardt and J. A. Nosssek, "Unitary ESPRIT: how to obtain increased estimation accuracy with a reduced computational burden," *IEEE Transactions on Signal Processing*, vol. 43, no. 5, pp. 1232–1242, 1995.
- [21] P. Heidenreich, A. M. Zoubir, and M. RübSamen, "Joint 2-D DOA estimation and phase calibration for uniform rectangular arrays," *IEEE Transactions on Signal Processing*, vol. 60, no. 9, pp. 4683–4693, 2012.

Research Article

Ship-Borne Phased Array Radar Using GA Based Adaptive α - β - γ Filter for Beamforming Compensation and Air Target Tracking

J. Mar,^{1,2} Chen-Chih Liu,¹ and M. B. Basnet¹

¹Department of Communications Engineering, Yuan-Ze University, 135 Yuan-Tung Road, Jungli, Taoyuan 320, Taiwan

²Communication Research Center, Yuan-Ze University, 135 Yuan-Tung Road, Jungli, Taoyuan 320, Taiwan

Correspondence should be addressed to J. Mar; eejmar@saturn.yzu.edu.tw

Received 7 March 2014; Revised 27 August 2014; Accepted 11 September 2014

Academic Editor: Hang Hu

Copyright © 2015 J. Mar et al. This is an open access article distributed under the Creative Commons Attribution License, which permits unrestricted use, distribution, and reproduction in any medium, provided the original work is properly cited.

Beam pointing error caused by ship motion over the ocean affects the tracking performance of the ship-borne phased array radar. Due to the dynamic nature of the sea environments, the ship-borne phased array radar must be able to compensate for the ship's motion adaptively. In this paper, the adaptive α - β - γ filter is proposed for the ship-borne phased array radar to compensate for the beam pointing error and to track the air target. The genetic algorithm (GA) and the particle swarm optimization (PSO) methods are applied to estimate the gain parameters of adaptive α - β - γ filters, while achieving the optimum objective of minimum root mean square error (RMSE). The roll and pitch data measured from a gyroscope of the sea vehicle and generated from ship motion mathematical model are used in the experiments. The tracking accuracy of adaptive α - β - γ filter using the GA method is compared with PSO method under different ship motion conditions. The convergent time and tracking accuracy of ship-borne phased array radar using the proposed GA based adaptive α - β - γ filter are also compared with the adaptive extended Kalman filter (AEKF). Finally, it is proved that the proposed GA based adaptive α - β - γ filter is a real time applicable algorithm for ship-borne phased array radar.

1. Introduction

Sea wave causes the effect of roll and pitch motions on ships. These ship rotational motions result in measurement error in phased array radar aboard the ship. The antenna stabilization to achieve the beam pointing accuracy over the long dwell time is an important issue for ship-borne phased array radar [1]. There are two ship motion compensations: compensation for rotational motion (i.e., pitch, roll, and heading angle) and compensation for translational motion (i.e., radial speed relative to the earth). Gyroscope provides pitch, roll, heading angles of the ship, speed, course, and vertical velocity of antenna installed on the ship at a data rate of 10 Hz. To compensate for the translational motion, the speed, course, and vertical velocity acquired from the gyroscope are averaged for the duration of radar-dwell time. Then the Doppler shift introduced by the translational motion is estimated in the digital signal processor (DSP) of the radar to compensate the radial velocity. The radar

control computer (RCC) provides the target locations relative to earth, schedules beam directions, and predicts beam pointing error to the beam steering controller (BSC), which compensates for the beam pointing error and controls the phased array antenna to point the beam at the target direction relative to the ship coordinates.

The motion compensation method based on coordinate conversion has been described in [2, 3], which requires the measurement of a device's coordinates, the ship's coordinates, and the earth's coordinates systems to compensate the device errors due to motion disturbances. In [1], Kalman filtering along with coordinates conversion is applied to reduce the beam pointing error and to stabilize a tracking beam. The α - β - γ filter, which is more easily implemented than a generalized Kalman filter, is used for motion compensation under different sea states in [1]. The sea environments are very dynamic; hence, there is need of an adaptive system for controlling and compensating devices regardless of ship motion. Most recent works have used Kalman filtering (KF) [4]

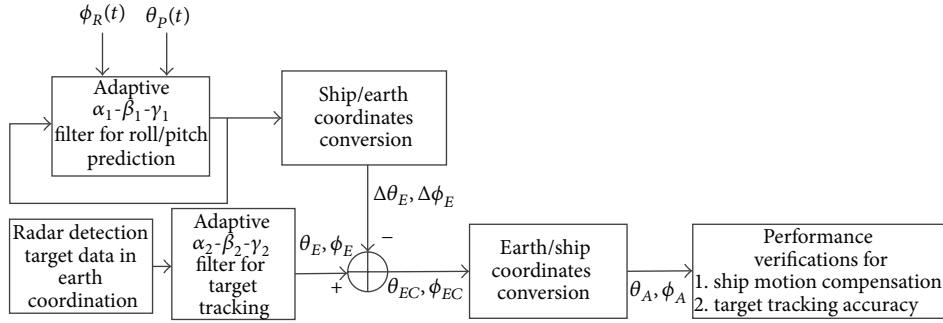


FIGURE 1: High level structure of ship rotational motion compensation for phased array radar.

and extended Kalman filtering (EKF) [5] to estimate the ship's attitude. Estimation accuracy of KF and EKF depends on the values of different parameters, such as error covariance matrices; thus, the KF and EKF require knowledge of covariance. In [6], the automatic beam pointing error compensation mechanism employs the parallel fuzzy basis function network (FBFN) architecture to estimate the beam pointing error caused by roll and pitch of the ship. The effect of automatic beam pointing error compensation mechanism on the tracking performance of adaptive extended Kalman filter (AEKF) implemented in ship-borne phased array radar is investigated. It shows that the tracking error of AEKF converges to less than about 20 m at 550 iterations (sec/iteration) and the estimation error will remain within the range of about 20 m when beam pointing error is compensated by FBFN controller.

The α - β - γ filter has a similar structure with the KF but depends on the gain value of α , β , and γ which are limited and interdependent [7–9]. The uses of various methods to adjust parameter values for Kalman filter, EKF, and α - β - γ filter have been proposed and implemented over the years. Fuzzy membership function is used in [10] to estimate and correct the target position for the signal being tracked. Genetic algorithm (GA) is used in [9] to search the suitable parameter values for the α - β - γ filter, which can provide the approximate position, velocity, and acceleration signal and simultaneously decrease the measurement noise. Particle swarm optimization (PSO) is used in [11] to tune the noise covariance of a Kalman filter. In [12], the PSO is used to find the optimal gain parameter values for an α - β - γ filter. PSO and GA methods are suitable for the real time application because they do not require differentiation and are less complicated than other methods.

In this paper, GA based adaptive α - β - γ filter is proposed for automatic beam pointing error correction and air target tracking in three-dimensional space. Continuous monitoring of the environment and adapting filter gain parameter with less computational burden is needed for real time application. The adaptive α - β - γ filter requires knowledge of the coefficients for which GA algorithm is used only in certain time intervals. GA is used to find the gain values by minimizing the objective function, that is, root mean square error (RMSE). The proposed adaptive α - β - γ filter algorithm

is implemented and compared with using PSO method. The roll and pitch data were recorded by a gyroscope of the sea vehicle to simulate the tracking performance of ship-borne phased array radar using the proposed adaptive α - β - γ filter. In addition, the roll and pitch data generated from ship motion mathematical model at sea states 2 and 3 are also applied for the proposed adaptive α - β - γ filter to verify the correctness of the test results.

The rest of this paper is organized as follows: the model of ship rotational motion, coordinates transform, and planar array antenna of ship-borne phased array radar are described in detail in Section 2. The algorithm of the proposed adaptive α - β - γ filter based on the GA is presented in Section 3, where the α - β - γ filter, GA gain estimator, PSO gain estimator, and optimization problem formulation are described. In Section 4, six different experimental cases are performed; the variations of roll and pitch angles in sea states 2 and 3 are analyzed; the GA and PSO methods are used to determine the optimal filter gain of adaptive α - β - γ filter that minimizes RMSE; the tracking performance of ship-borne phased array radar using the proposed adaptive α - β - γ filter is simulated. Finally, conclusions are made in Section 5.

2. Ship Rotational Motion Compensation

The ship-borne phased array radar must be able to compensate the ship's motion and track the maneuvering targets automatically. The adaptive α - β - γ filtering algorithm is designed to real time compensate the errors caused by the ship's motion. The block diagram of rotational motion compensation system for ship-borne phased array radar is shown in Figure 1, which consists of adaptive α - β - γ filter for beam pointing error prediction, ship coordinates/earth coordinates conversion, earth coordinates/ship coordinates conversion, and adaptive α - β - γ filter for target tracking. The roll angle $\phi_R(t)$ and the pitch angle $\theta_p(t)$ of the ship angular motion are measured by the gyroscope. (θ_A, ϕ_A) is the antenna beam pointing angle relative to the ship body, where θ_A is the angle off antenna boresight, and ϕ_A is the azimuth angle counterclockwise from the bow of the ship. Assume that the beam steering angle at a certain time instant is (θ_0, ϕ_0) , the antenna point angle offset caused by the ship motion (pitch,

TABLE 1: Sea state parameters.

	Roll		Pitch	
	A_R (°)	T_R (sec)	A_P (°)	T_P (sec)
Sea state 2	1	2.5	0.2	1.2
Sea state 3	1	2.0	0.2	0.6

roll) is (θ_e, ϕ_e) , and then the current antenna pointing angle is (θ_E, ϕ_E) with respect to the earth coordinates:

$$\theta_E = \theta_0 + \theta_e, \quad \phi_E = \phi_0 + \phi_e. \quad (1)$$

If the beam pointing error is predicted as $(\Delta\theta_E, \Delta\phi_E)$, then the beam pointing angle is corrected as

$$\theta_{EC} = \theta_0 + \theta_e - \Delta\theta_E, \quad \phi_{EC} = \phi_0 + \phi_e - \Delta\phi_E. \quad (2)$$

The value of (θ_{EC}, ϕ_{EC}) is approximate to (θ_0, ϕ_0) .

2.1. Ship Rotational Motion Model. Ship is affected by the waves in the ocean, resulting in six degrees of freedom of movement. In this paper, assuming zero yaw angle, the simplified roll and pitch model [1, 13] is adopted to describe the ship rotational motion in the earth coordinates. Ship's rotational motion is modeled with sinusoidal signal. The roll angle is

$$\phi_R(t) = A_R \sin(\omega_R t) + n_R(t). \quad (3)$$

The pitch angle is

$$\phi_P(t) = A_P \sin(\omega_P t) + n_P(t), \quad (4)$$

where A_R and A_P are the amplitude of ship's roll and pitch angles, $n_R(t)$ and $n_P(t)$ are assumed to be zero mean Gaussian noise, T_R and T_P are the roll and pitch periods, and $\omega_R = 2\pi/T_R$ and $\omega_P = 2\pi/T_P$ are the roll and pitch angular frequencies.

The random roll and pitch angle errors caused by other unknown factors, including the change of ship's traveling direction and weather, in the actual ship navigation environment will be considered into the standard deviation of the noise terms. The amplitude and period parameters of sea states 2 and 3 are listed in Table 1 [1].

2.2. Coordinates Transform. Since the phased array antenna is installed on the ship, the beam steering control employs the ship body coordinates. But the target tracking of adaptive α - β - γ filter employs the Earth coordinates. The Euler coordinates transform formula is used to convert antenna beam pointing angle relative to the earth (θ_E, ϕ_E) , where θ_E is the angle from vertical and ϕ_E is the angle clockwise from true north, into antenna beam pointing angle relative to the ship body (θ_A, ϕ_A) [13]:

$$\begin{bmatrix} \sin \theta_A \cos \phi_A \\ \sin \theta_A \sin \phi_A \\ \cos \theta_A \end{bmatrix} = T(\phi) T(\theta) T(\psi) \begin{bmatrix} \sin \theta_E \cos \phi_E \\ -\sin \theta_E \sin \phi_E \\ \cos \theta_E \end{bmatrix}, \quad (5)$$

where the coordinates transform matrices are defined as

$$\begin{aligned} T(\phi) &= \begin{bmatrix} 1 & 0 & 0 \\ 0 & \cos \phi & \sin \phi \\ 0 & -\sin \phi & \cos \phi \end{bmatrix}, \\ T(\theta) &= \begin{bmatrix} \cos \theta & 0 & \sin \theta \\ 0 & 1 & 0 \\ -\sin \theta & 0 & \cos \theta \end{bmatrix}, \\ T(\psi) &= \begin{bmatrix} \cos \psi & -\sin \psi & 0 \\ \sin \psi & \cos \psi & 0 \\ 0 & 0 & 1 \end{bmatrix}, \end{aligned} \quad (6)$$

where the ship roll angle ϕ is positive with downward roll of starboard, the ship pitch angle θ is positive with bow pitch upward, and the ship yaw angle ψ is positive clockwise from the north.

2.3. Planar Array Antenna. An $M \times N$ element planar array [6] is designed for the ship-borne phased array radar system, which includes the beamforming (BF) mode and direction of arrival (DOA) mode. The planar array can produce multibeams in the azimuth and elevation by using the beamformer network (BFN), which consists of a set of power dividers and phase shifters. The planar array using amplitude comparison method [14] generates the difference signal patterns for the DOA estimation. The difference signals obtained from two neighboring beams can measure the DOA of the target signal of the ship-borne phased array radar system. The beam pattern is expressed as [14, 15]

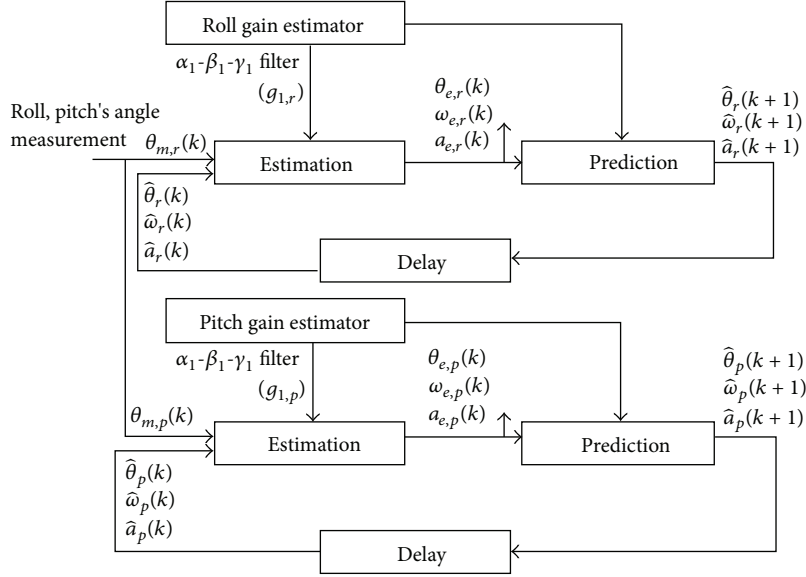
$$\begin{aligned} AF(\theta, \phi) &= \sum_{n=1}^N I_{1n} \left[\sum_{m=1}^M I_{m1} e^{j(m-1)(kd_x \sin \theta \cos \phi + \beta_x)} \right] \\ &\quad \times e^{j(n-1)(kd_y \sin \theta \sin \phi + \beta_y)} = S_{xm} S_{ym}, \end{aligned} \quad (7)$$

where

$$\begin{aligned} S_{xm} &= \sum_{m=1}^M I_{m1} e^{j(m-1)(kd_x \sin \theta \cos \phi + \beta_x)}, \\ S_{ym} &= \sum_{n=1}^N I_{1n} e^{j(n-1)(kd_y \sin \theta \sin \phi + \beta_y)}, \\ \beta_x &= -kd_x \sin \theta_t \cos \phi_t, \\ \beta_y &= -kd_y \sin \theta_t \sin \phi_t, \end{aligned} \quad (8)$$

where $I_{m1} = I_{1n} =$ Chebyshev weighting [13], $M =$ the number of array elements in the x -axis, $N =$ the number of array elements in y -axis, $\phi_t =$ the azimuth steering angle of the main beam, $\theta_t =$ the elevation steering angle of the main beam, $d_x =$ the interelement spacing in x -axis, $d_y =$ the interelement spacing in y -axis, $k = 2\pi/\lambda =$ the phase propagation constant, and λ is the wavelength of the carrier.

The phase of the RF signal at each array element is adjusted to steer the beam to the coordinates (θ_t, ϕ_t) .

FIGURE 2: Parallel adaptive α - β - γ filter for beam pointing error prediction.

3. Adaptive α - β - γ Filter

As shown in Figure 1, the adaptive α - β - γ filters are applied to beam pointing error prediction and target tracking, respectively.

3.1. Parallel Adaptive α - β - γ Filter for Beam Pointing Error Prediction. Figure 2 shows the beam pointing error prediction system, which consists of separate adaptive α - β - γ filters to predict the roll and pitch angles of ship motion and their outputs are fed into the beam steering controller (BSC). The BSC compensates the beam pointing errors of the phased array antenna onboard the ship to reduce the impact of the roll and pitch motion on the phased array radar. Roll and pitch data are random but they are similar in nature and they can be characterized with different amplitudes and frequencies [1]. The α - β - γ filter predicts the next positions using current error also known as innovation [8]. This innovation process has two steps: prediction and estimation.

The pitch prediction equations are expressed as

$$\begin{aligned}\hat{\theta}_p(k+1) &= \theta_{e,p}(k) + T_1 \omega_{e,p}(k) + \frac{T_1^2}{2} a_{e,p}(k), \\ \hat{\omega}_p(k+1) &= \omega_{e,p}(k) + T_1 a_{e,p}(k), \\ \hat{a}_p(k+1) &= a_{e,p}(k).\end{aligned}\quad (9)$$

The pitch estimation equations are expressed as

$$\begin{aligned}\theta_{e,p}(k) &= \hat{\theta}_p(k) + \alpha_{1,p} [\theta_{m,p}(k) - \hat{\theta}_p(k)] + n_{1,p}(k), \\ \omega_{e,p}(k) &= \hat{\omega}_p(k) + \frac{\beta_{1,p}}{T_1} [\theta_{m,p}(k) - \hat{\theta}_p(k)], \\ a_{e,p}(k) &= \hat{a}_p(k) + \frac{\gamma_{1,p}}{2T_1^2} [\theta_{m,p}(k) - \hat{\theta}_p(k)],\end{aligned}\quad (10)$$

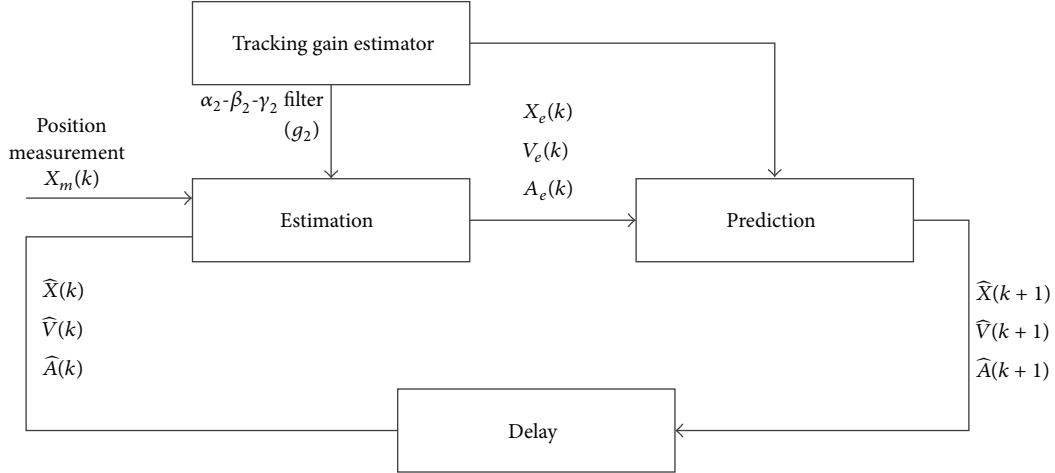
where $\hat{\theta}_p(k+1)$, $\hat{\omega}_p(k+1)$, and $\hat{a}_p(k+1)$ are pitch angular position, pitch angular velocity, and pitch angular acceleration values predicted at $(k+1)$ th interval, respectively. The sampling time $T_1 = 0.1$ sec, $\theta_{e,p}(k)$, $\omega_{e,p}(k)$, and $a_{e,p}(k)$ are pitch angular position, pitch angular velocity, and pitch angular acceleration estimated at k th interval. $\alpha_{1,p}$, $\beta_{1,p}$, and $\gamma_{1,p}$ are the smoothing parameters whose region of stability and parameter constraint have been studied in [8]. The relationship among $\alpha_{1,p}$, $\beta_{1,p}$, and $\gamma_{1,p}$ parameters can be related to pitch gain $g_{1,p}$, where $0 < g_{1,p} < 1$. The formula is described as follows:

$$\begin{aligned}\alpha_{1,p} &= 1 - g_{1,p}^3, \\ \beta_{1,p} &= 1.5 \cdot (1 + g_{1,p}) (1 - g_{1,p})^2, \\ \gamma_{1,p} &= (1 - g_{1,p})^3.\end{aligned}\quad (11)$$

The roll prediction equations, roll estimation equations, and roll smoothing parameters have similar forms as the pitch prediction equations, pitch estimation equations, and pitch smoothing parameters, respectively.

3.2. Adaptive α - β - γ Filter for Target Tracking in Three-Dimensional Space. The GA based α - β - γ filter algorithm for target tracking is used by ship-borne phased array radar to predict the next target positions using current error and further improves its tracking accuracy. The tracking process of α - β - γ filter is shown in Figure 3, where the prediction equations are

$$\begin{aligned}\hat{\mathbf{X}}(k+1) &= \mathbf{X}_e(k) + T_2 \mathbf{V}_e(k) + \frac{T_2^2}{2} \mathbf{A}_e(k), \\ \hat{\mathbf{V}}(k+1) &= \mathbf{V}_e(k) + T_2 \mathbf{A}_e(k), \\ \hat{\mathbf{A}}(k+1) &= \mathbf{A}_e(k).\end{aligned}\quad (12)$$

FIGURE 3: Adaptive α - β - γ filter for target tracking in three-dimensional space.

The estimation equations are

$$\begin{aligned} \mathbf{X}_e(k) &= \widehat{\mathbf{X}}(k) + \boldsymbol{\alpha}_2 [\mathbf{X}_m(k) - \widehat{\mathbf{X}}(k)] + \mathbf{n}_2(k), \\ \mathbf{V}_e(k) &= \widehat{\mathbf{V}}(k) + \frac{\boldsymbol{\beta}_2}{T_2} [\mathbf{X}_m(k) - \widehat{\mathbf{X}}(k)], \\ \mathbf{A}_e(k) &= \widehat{\mathbf{A}}(k) + \frac{\boldsymbol{\gamma}_2}{2T_2^2} [\mathbf{X}_m(k) - \widehat{\mathbf{X}}(k)], \end{aligned} \quad (13)$$

where $\mathbf{X}(k) = [x(k), y(k), z(k)]^T$, $\mathbf{V}(k) = [v_x(k), v_y(k), v_z(k)]^T$, and $\mathbf{A}(k) = [a_x(k), a_y(k), a_z(k)]^T$ are the position vector, velocity vector, and acceleration vector, respectively, at time instant k ; $\mathbf{n}_2(k)$ is the zero mean white Gaussian noise and the sampling time $T_2 = 1$ sec. The relationship among $\boldsymbol{\alpha}_2$, $\boldsymbol{\beta}_2$, and $\boldsymbol{\gamma}_2$ parameters can be related to gain factor vector $\mathbf{g}_2 = [g_{2,x}, g_{2,y}, g_{2,z}]^T$. The formula is described as follows:

$$\begin{aligned} \boldsymbol{\alpha}_2 &= \begin{bmatrix} \alpha_{2,x} & 0 & 0 \\ 0 & \alpha_{2,y} & 0 \\ 0 & 0 & \alpha_{2,z} \end{bmatrix} = \begin{bmatrix} 1 - g_2^3 & 0 & 0 \\ 0 & 1 - g_2^3 & 0 \\ 0 & 0 & 1 - g_2^3 \end{bmatrix}, \\ \boldsymbol{\beta}_2 &= \begin{bmatrix} \beta_{2,x} & 0 & 0 \\ 0 & \beta_{2,y} & 0 \\ 0 & 0 & \beta_{2,z} \end{bmatrix} = \begin{bmatrix} 1.5(1 + g_2)(1 - g_2)^2 & 0 & 0 \\ 0 & 1.5(1 + g_2)(1 - g_2)^2 & 0 \\ 0 & 0 & 1.5(1 + g_2)(1 - g_2)^2 \end{bmatrix}, \\ \boldsymbol{\gamma}_2 &= \begin{bmatrix} \gamma_{2,x} & 0 & 0 \\ 0 & \gamma_{2,y} & 0 \\ 0 & 0 & \gamma_{2,z} \end{bmatrix} = \begin{bmatrix} (1 - g_2)^3 & 0 & 0 \\ 0 & (1 - g_2)^3 & 0 \\ 0 & 0 & (1 - g_2)^3 \end{bmatrix}. \end{aligned} \quad (14)$$

3.3. GA Gain Estimator. The flow chart of GA roll/pitch gain estimators of adaptive α - β - γ filter is shown in Figure 4. The GA roll/pitch gain estimators are used to estimate the roll and pitch angles gain ($g_{1,r}/g_{1,p}$) of adaptive α_1 - β_1 - γ_1 filters. The GA tracking gain estimator is used to estimate the optimal gain \mathbf{g}_2 of adaptive α_2 - β_2 - γ_2 filter. The flow chart of GA tracking gain estimator is similar to Figure 4. The GA method uses selection, crossover, and mutation [16] techniques to find the solutions. At first, the initial population which contains randomly generated chromosomes is made. Chromosomes are chains of 0 and 1 bits whose length is defined as string length. Chromosomes number is defined as the population size. These chromosomes from the mating pool are shuffled to

create more randomness and then applied to the problem to find their outputs and fitness scores accordingly. Fitness value defines how well the chromosome solves the problem. Two chromosomes are selected from the mating pool depending on selection method. Depending on the crossover rate, all bits between two randomly chosen points selected from two different chromosomes are interchanged, which is known as two-point crossover. Chromosomes may undergo mutation where random bits of chromosomes are flipped depending on the mutation rate. Termination criteria are defined by the number of generations.

Selection is done usually by using two methods as follows: roulette wheel selection and tournament selection.

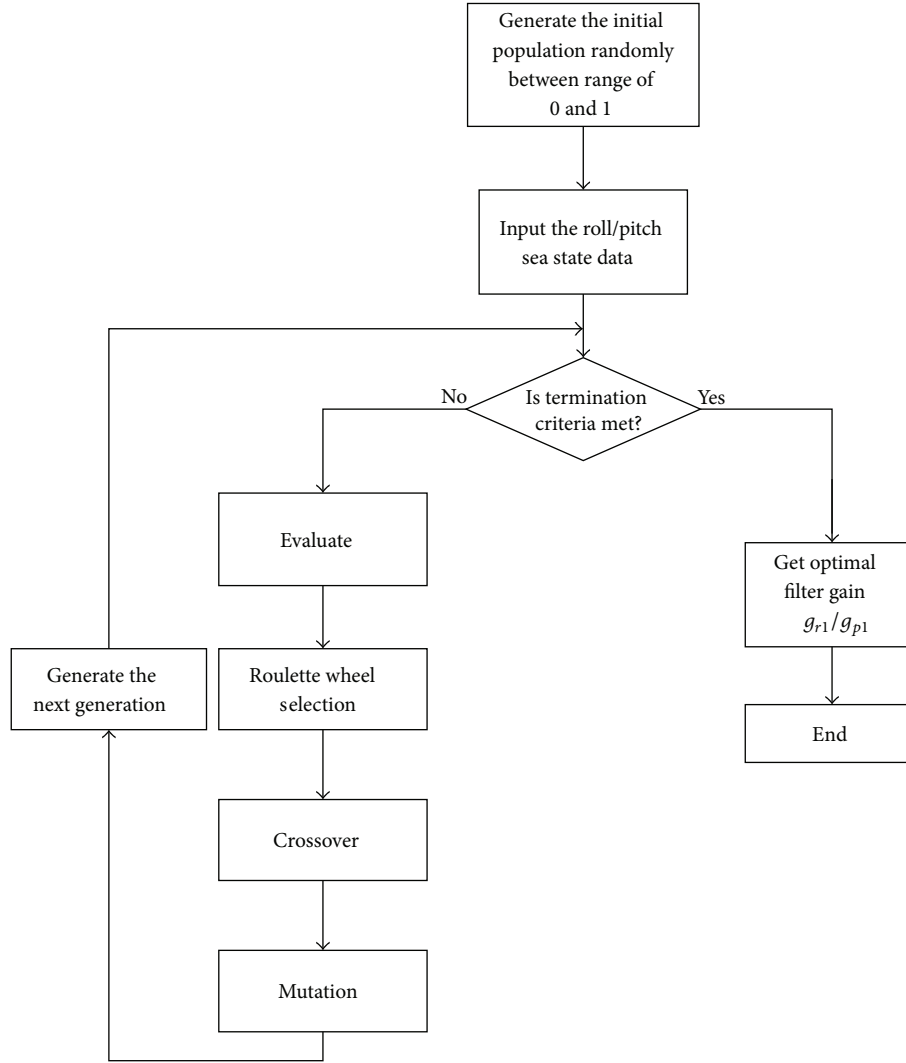


FIGURE 4: Flow chart of GA roll/pitch gain estimator.

In roulette wheel selection, the chromosomes selected from population are put into a mating pool. The chromosome selection probability is proportion to the fitness value. In tournament selection, chromosomes have to go through several tournaments. The chromosome, which has the fittest value, is selected and put into the mating pool. Here the roulette wheel selection method is chosen to determine the solution.

Two-point crossover calls for two random points selected from two different parent chromosome strings; all bits between two points are swapped for two parent chromosomes. Crossover rate is commonly chosen in a range of 0.60 to 0.80 [16]. Mutation rate describes the probability that a bit in a chromosome will be flipped (0 flips to 1 and 1 flips to 0). Mutation brings diversity to the population as mutation of a chromosome is a random process which will bring randomness to present chromosome group. Generation defines iteration, the GA method runs for a defined number of generations, and the final best solution is considered as the result.

3.4. *PSO Gain Estimator* [9, 12, 17]. PSO method was first proposed in [18]. PSO is based on the number of particles flying around the solution space to find the best solution that minimizes the cost function. Particles move around the solution space as soon as a particle detects a better solution; the information is passed to other particles and then particles change their position with respect to their best position observed among all the particles. Figure 5 describes the PSO method in detail. The PSO changes the velocity and position of the particle according to (15) and (17), respectively, to achieve the fitness [16]:

$$v_{id(n+1)} = K * \left[v_{id(n)} + c_1 \cdot \text{rand}() \cdot (p_{id(n)} - x_{id(n)}) + c_2 \cdot \text{Rand}() \cdot (p_{gd(n)} - x_{id(n)}) \right], \quad (15)$$

$$K = \frac{2}{\left| 2 - \varphi - \sqrt{\varphi^2 - 4\varphi} \right|}, \quad \text{where, } \varphi = c_1 + c_2, \varphi > 4, \quad (16)$$

$$x_{id(n+1)} = x_{id(n)} + v_{id(n)}, \quad (17)$$

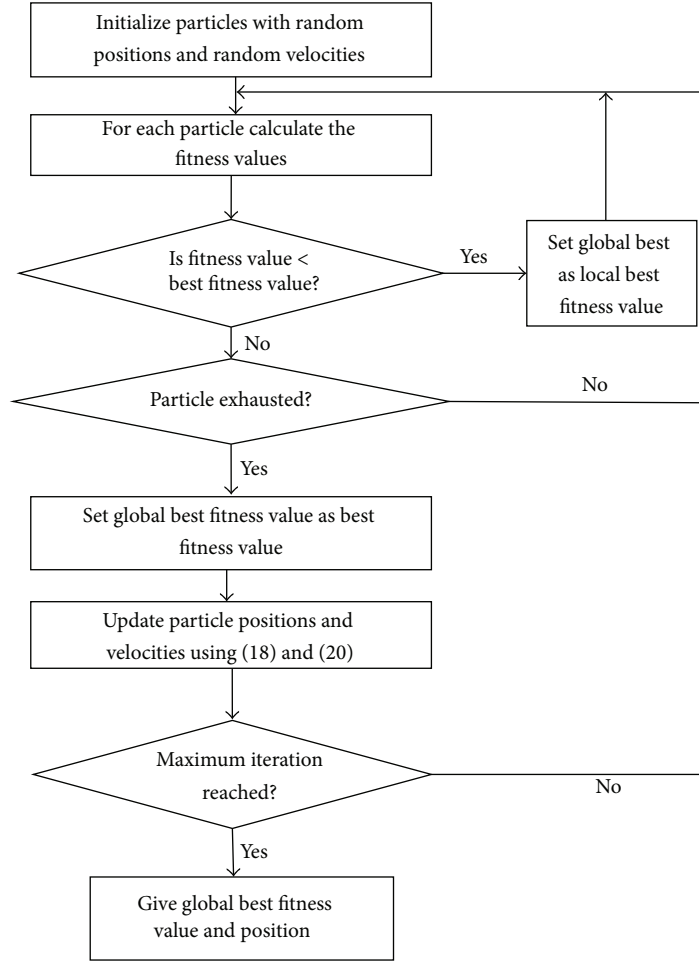


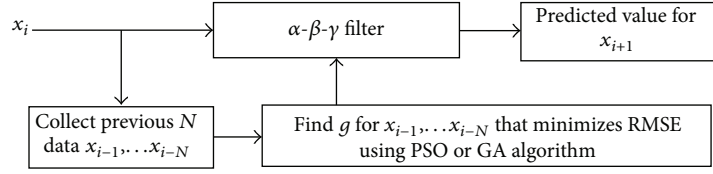
FIGURE 5: Flow chart of PSO method.

where $x_{id(n)}$ and $v_{id(n)}$ are position and velocity of (id)th particle at (n)th iteration, respectively. $p_{id(n)}$ and $p_{gd(n)}$ are the best position and global best position of (id)th particle at (n)th iteration, respectively. $\text{Rand}()$ and $\text{rand}()$ are random number between 0 and 1, respectively. Equation (15) updates the velocity of the particles and (17) updates the position of particles. K means inertia, c_1 and c_2 are correction factors, and swarm size means number of particles for an iteration, as described in [16].

Particles in the PSO method sometimes go out of constraints while changing their position. Reinitialization of the particle's position randomly to fall within the constraints is done as soon as a particle moves out of constraints. This ensures full use of particles and also increases the chance of discovering a better solution. To reduce the chance of getting trapped in a local minimum, the advantages of using PSO method are that it is derivative-free, easy to implement, and easy to comprehend and the solution is independent of the initial point [17]. One of the drawbacks of the PSO method is that it does not guarantee success; that is, the solution found may not be the best solution.

3.5. GA/PSO Based Adaptive α - β - γ Filter. The flow chart of the adaptive α - β - γ filter algorithm is shown in Figure 6, where N is the number of sampling data to determine the filter gain. In this algorithm, the parameters α , β , and γ , which are related to the filter gain g , are optimized by minimizing the RMSE using GA or PSO method. The proposed adaptive α - β - γ filter processes the current sampled data x_i which predicts the next sample data x_{i+1} as iteration continues. The adaptive GA or PSO process only occurs at certain time interval. The previous N data, that is, $x_p(i-N) \cdots x_p(i-1)$, is sent to the adaptive GA or PSO algorithm where the optimum value of filter gain (g) is determined for the α - β - γ filter. Then x_{i+1} is predicted and the process continues. The value of N determines running time and accuracy of the algorithm, so N must have small enough value to support real time implementation and large enough value to provide acceptable accuracy.

Since the roll and pitch angles of ship motion change over time randomly, in order to speed up the processing time and to reach the objectives of minimum estimation error, the filter gain values are real time updated by using the pipelined architecture. The recorded roll and pitch signals are

FIGURE 6: Block diagram of adaptive α - β - γ filter.

segmented into block of 1000 sampled data (100 sec) for linear trajectory target and 420 sampled data (42 sec) for circular trajectory target, respectively. The gain value of α_2 - β_2 - γ_2 filter in 101–200 sec is estimated by GA and PSO methods using the collected data during 1–100 sec, the gain value of α_2 - β_2 - γ_2 filter in 201–300 sec is estimated by the GA and PSO methods using the collected data in 101–200 sec, and so on. Similarly, the measured flight target signals are segmented into block of 100 sampled data (100 sec) for linear trajectory target and 42 sampled data (42 sec) for circular trajectory target, respectively. The gain value of α_2 - β_2 - γ_2 filter in 101–200 sec is estimated by the GA and PSO methods using the collected data during 1–100 sec, the gain value of α_2 - β_2 - γ_2 filter in the interval of 201–300 sec is estimated by the GA and PSO methods using the collected data in 101–200 sec, and so on.

For the PSO process, it was found that gain parameter converged within 100 iterations, so the number of iterations for an adaptive α - β - γ filter was kept at constant 100 iterations per processing cycle, swarm size = 30, inertia = 0.7298, and correction factors $c_1 = 2.1$, $c_2 = 2$. For the GA process, we have considered population size = 8, string length = 12, crossover rate = 0.8, and mutation rate = 0.05.

If $\theta_{i,p}$, $i = 1, 2, \dots, N$ and $\hat{\theta}_{i,p}$, $i = 1, 2, \dots, N$ are real measurement pitch's values and estimated pitch's values of adaptive α_1 - β_1 - γ_1 filter, respectively, then $\theta_{i,r}$, $i = 1, 2, \dots, N$ and $\hat{\theta}_{i,r}$, $i = 1, 2, \dots, N$ are real measurement roll's values and estimated roll's values of adaptive α_1 - β_1 - γ_1 filter, respectively, where i is the current iteration and N is the total number of sampling data. The RMSEs of pitch and roll estimations are defined as follows:

$$\text{RMSE}_p = \sqrt{\frac{1}{N} \sum_{i=1}^N (\hat{\theta}_{i,p} - \theta_{i,p})^2}, \quad (18)$$

$$\text{RMSE}_r = \sqrt{\frac{1}{N} \sum_{i=1}^N (\hat{\theta}_{i,r} - \theta_{i,r})^2}, \quad (19)$$

where the main purpose of GA and PSO methods is to find the optimum values of $g_{1,p}$ and $g_{1,r}$ which minimize the RMSE_p and RMSE_r , respectively.

If \mathbf{X}_i and $\hat{\mathbf{X}}_i$, $i = 1, 2, \dots, N$ are real measurement target position vector values and estimated target position vector

values of adaptive α_2 - β_2 - γ_2 filter, the RMSE of target tracking is defined as

$$\text{RMSE} = \sqrt{\frac{1}{N} \sum_{i=1}^N ((x_i - \hat{x}_i)^2 + (y_i - \hat{y}_i)^2 + (z_i - \hat{z}_i)^2)}, \quad (20)$$

where x_i , y_i , and z_i are the components of target position vector \mathbf{X}_i in x , y , and z axes. The main purpose of GA and PSO algorithms is to find the optimum gain value of \mathbf{g}_2 which minimizes the RMSE.

4. Experimental Results

Six scenarios are used to simulate the tracking performance of ship-borne phased array radar using the proposed adaptive α - β - γ filter for beam pointing error compensation and target tracking in three-dimensional space.

Case 1 (roll and pitch estimations using GA based adaptive α - β - γ filter and measured data). The roll and pitch data recorded by a gyroscope of the ship were used in the experiments. The total number of data is 1000 and the sampling time is 0.1 sec. The angle variation of roll and pitch signals measured by ship gyroscope are shown in Figure 7, which will result in the beam pointing errors of phased array antenna. The GA based adaptive α - β - γ filter is used to estimate the roll and pitch angles. Figures 8(a) and 8(b) show that the convergent time of roll and pitch angles are 3 sec and 5 sec, respectively, under simulated sea states 2 and 3 and measured data. The ship's roll and pitch signals are simulated according to (3) and (4) with roll and pitch angle parameters of sea states 2 and 3 listed in Table 1 and standard deviation of 0.01. It concludes that the proposed GA based adaptive α - β - γ filter is suitable to compensate the ship motion. As shown in Table 1, the period of sea state 2 is longer than sea state 3. Therefore, the convergent RMSE (about 0.19° for roll, about 0.1° for pitch) of sea state 2 is less than sea state 3 (about 0.29° for roll, about 0.22° for pitch) because the roll and pitch signals with shorter period in sea state 3 have rapid oscillations, which are more difficult to be predicted precisely.

Case 2 (tracking linear moving target in three-dimensional space using GA based adaptive α - β - γ filter (without beam pointing error)). Assuming the ship is not affected by the sea waves (antenna beam pointing error is zero), the tracking performance of GA based adaptive α - β - γ filter for a straight flight target trajectory is simulated. The initial position of radar is (0, 0, 0). The ship moves with a speed of 10 m/sec in

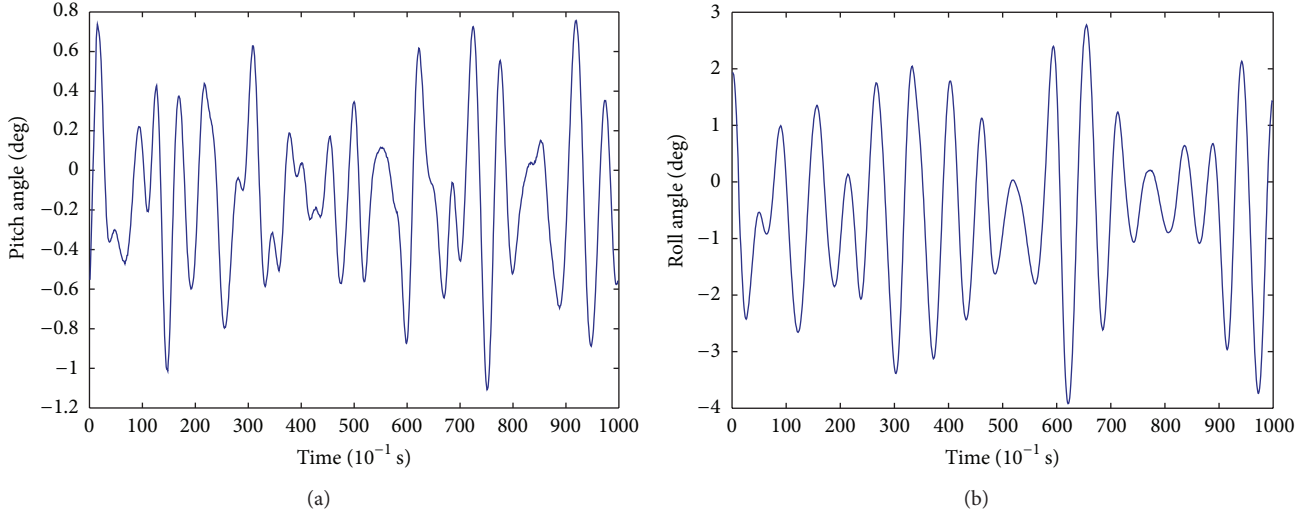


FIGURE 7: Demonstrating angle variation of (a) pitch and (b) roll signals measured by gyroscope.

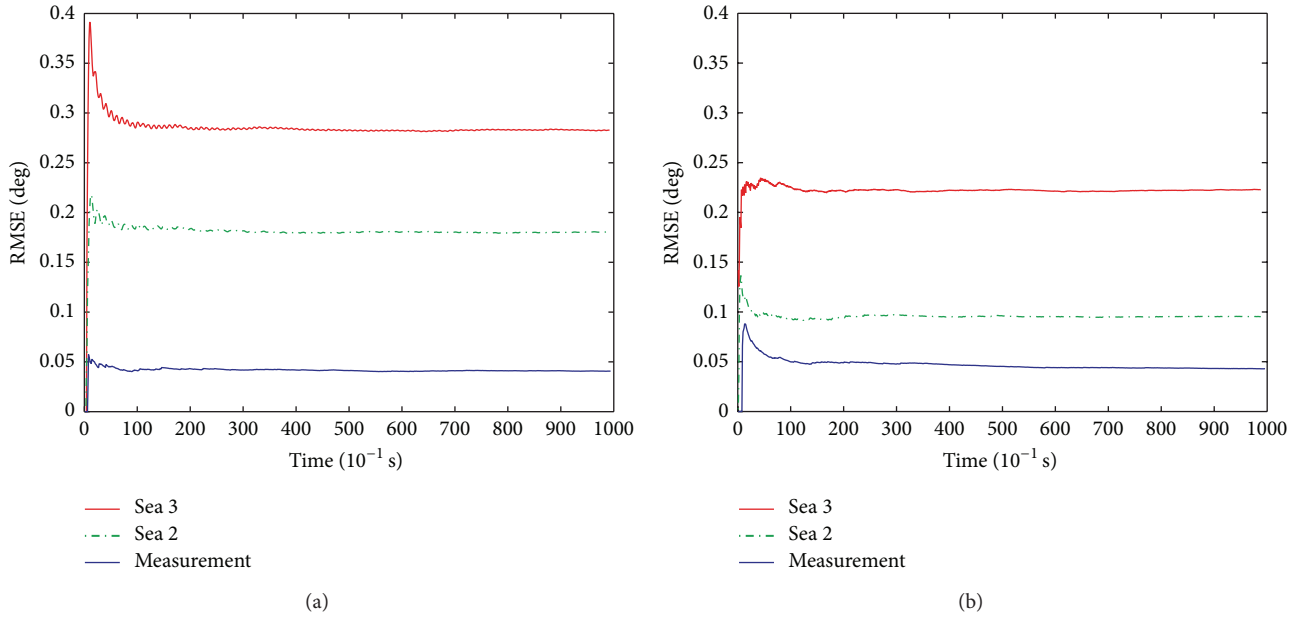


FIGURE 8: RMSE of (a) roll and (b) pitch under simulated data of sea states 2 and 3 and measured data.

the Y axial direction. The linear path equation of the ship is given by

$$\mathbf{X}_s(x_t, y_t, z_t) = \mathbf{X}_{0s} + \mathbf{V}_s t, \quad (21)$$

where $t = 1, 2, 3, \dots, 1000$ sec, \mathbf{V}_s is ship velocity vector and \mathbf{X}_{0s} is initial ship position vector in three-dimensional space. The radar position is updated every second. The initial position of flying target is $(-74840, -129620, 9100)$ m, which is about 150 km from the radar. The flight speed of target is 300 m/sec (X axial velocity of 150 m/sec and Y axial velocity of 260 m/sec). The target location is updated every second. The linear target trajectory equation is

$$\mathbf{X}_m(x_t, y_t, z_t) = \mathbf{X}_{0m} + \mathbf{V}_m t, \quad (22)$$

where \mathbf{V}_m is the target velocity vector and \mathbf{X}_{0m} is the initial target position vector in three-dimensional space. The tracking accuracy of GA based adaptive α - β - γ filter for a straight flight target is shown in Figure 9, where the trajectory estimation error is calculated by

$$E_t = \sqrt{(x_t - \hat{x}_t)^2 + (y_t - \hat{y}_t)^2 + (z_t - \hat{z}_t)^2}, \quad (23)$$

where (x_t, y_t, z_t) and $(\hat{x}_t, \hat{y}_t, \hat{z}_t)$ denote the real target location and estimated target location, respectively. It shows that the GA based adaptive α - β - γ filter converges to less than about 2 m after 5 sec.

TABLE 2: Estimated gain parameters for GA based adaptive α - β - γ filter.

Time (sec)	1~100	101~200	201~300	301~400	401~500	501~600	601~700	701~800	801~900	901~1000
$g_{r,1}$	0.574	0.6399	0.652	0.6904	0.6537	0.674	0.6286	0.6313	0.6044	0.5392
$g_{p,1}$	0.629	0.6664	0.622	0.7756	0.664	0.7399	0.663	0.6652	0.6816	0.6498
g_2	0.285	0.5827	0.3282	0.3851	0.0054	0.3480	0.2916	0.3736	0.547	0.4864

TABLE 3: Estimated gain parameters for PSO based adaptive α - β - γ filter.

Time (sec)	1~100	101~200	201~300	301~400	401~500	501~600	601~700	701~800	801~900	901~1000
$g_{r,1}$	0.557	0.5986	0.357	0.5345	0.6142	0.5774	0.5544	0.529	0.4592	0.5626
$g_{p,1}$	0.612	0.5898	0.4129	0.5675	0.5286	0.3953	0.5565	0.6199	0.5214	0.6285
g_2	0.326	0.07	0.1136	0.146	0.098	0.2365	0.21	0.2547	0.2474	0.1245

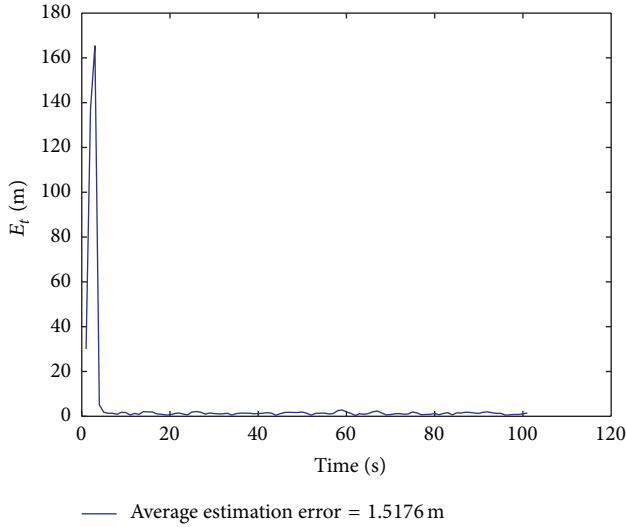


FIGURE 9: Estimation error for linear target trajectory without beam pointing error.

Case 3 (tracking circular moving target in three-dimensional space using GA based adaptive α - β - γ filter (without beam pointing error)). Figures 10(a) and 10(b) show the simulation scenario of beam pointing error compensation for circular maneuvering air target and linear moving ship. The ship has the same linear moving speed and path equation as Case 2. The flying target is parallel to the XY plane, the initial position of flying target is (8885, 4590, 9100) m, the velocity is 300 m/sec, and the angle (θ_0) between the initial position and the X-axis is 30° . The trajectory of the flight vehicle is a circle, which has a radius of 10 km. The center of circular trajectory is Y-axis. The rotational cycle time of the flight target is 209 seconds and the total observation time is 419 sec.

The circular trajectory equation is

$$\mathbf{X}_m(x_t, y_t, z_t) = (r \cos(\theta_0 - \omega t), r \sin(\theta_0 - \omega t), 9100), \quad (24)$$

where $t = 1, 2, 3, \dots, 418, 419$ sec, r is the circular flight radius in meter, θ_0 is the initial angle between the flight vehicle, and the X-axis, ω is the angular speed of flight vehicle. The accuracy of GA based adaptive α - β - γ filter for tracking a circular flight target is shown in Figure 11, where the GA based adaptive α - β - γ filter converges to less than 3 m after 8 sec. Therefore, using the GA based adaptive α - β - γ filter to track the circular trajectory target has the larger average estimation error and longer convergent time than linear trajectory target.

Case 4 (estimating roll and pitch angles and tracking linear trajectory target using GA/PSO based adaptive α - β - γ filter and measured data (with beam pointing error)). The measured roll and pitch signals shown in Figure 7 are used to evaluate the performance of GA/PSO based adaptive α - β - γ filter for estimating the roll and pitch angles and tracking the linear trajectory target. The beam of 6×6 planar array antenna is steered to track the linear trajectory target. The sampling frequency is set as 10 Hz. Therefore, the ship's roll and pitch signals are sampled 10000 points within 1000 seconds. As the scenario described in Case 2, the ship is along the Y axis of XY plane in the earth coordinates, the ship speed is 10 m/sec, and the flying target speed is 300 m/sec. The flying target is parallel to the XY plane, 9.1 km above the ground, and the angle between the flight direction and the Y-axis is 120° . The largest reconnaissance distance of ship-borne radar is 150 km. When the air target is flying within the radar detection range, the beam pointing error estimation and linear trajectory target tracking of ship-borne phased array radar are simulated.

Figure 12 is a simulation flow chart used to verify the effect of beam pointing error compensation on the tracking accuracy of adaptive α - β - γ filter. Tables 2 and 3 demonstrate the optimal gain parameters of adaptive α - β - γ filter for roll $g_{r,1}$, pitch $g_{p,1}$, and target tracking g_2 obtained by the GA and PSO methods, respectively, that minimizes the RMSE. Figures 13–17 show the estimation errors for five different gain values, which are summarized in Table 4. It demonstrates that the greater gain value ($g = 0.1, 0.75$ and 0.9) will generate the greater error and need the longer convergence time. The estimation errors

TABLE 4: Estimation errors for different gains.

	Calculated by GA	Calculated by PSO		Fixed gain	
$g_{r,1}$	0.5392~0.6904	0.357~0.6142	0.1	0.75	0.9
$g_{p,1}$	0.622~0.7756	0.3953~0.6285	0.1	0.75	0.9
g_2	0.054~0.5827	0.07~0.3259	0.1	0.75	0.9
Average E_t (m)	14.781	16.3224	16.9663	53.4804	399.1188

TABLE 5: Estimated gain parameters for GA based adaptive α - β - γ filter.

Time (sec)	1~100	101~200	201~300	301~400	401~500	501~600	601~700	701~800	801~900	901~1000
$g_{r,1}$	0.543	0.5653	0.5424	0.5455	0.5665	0.56	0.58	0.532	0.5414	0.5385
$g_{p,1}$	0.464	0.484	0.4459	0.422	0.4667	0.4654	0.4509	0.4459	0.4308	0.4651
g_2	0.161	0.0929	0.1937	0.0865	0.0241	0.0609	0.1174	0.1897	0.1713	0.1727

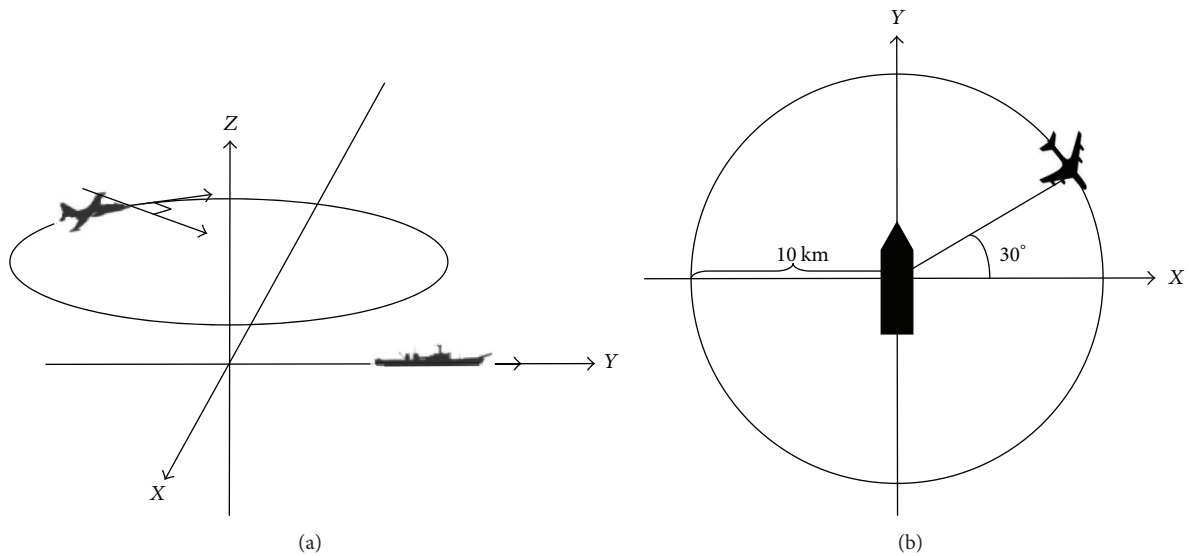


FIGURE 10: Simulation scenarios of Case 3 for (a) 3D and (b) top view diagrams.

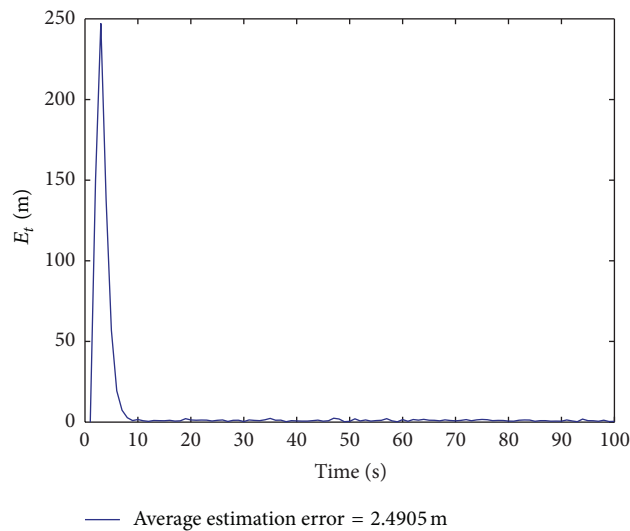


FIGURE 11: Estimation error for circular target trajectory without beam pointing error.

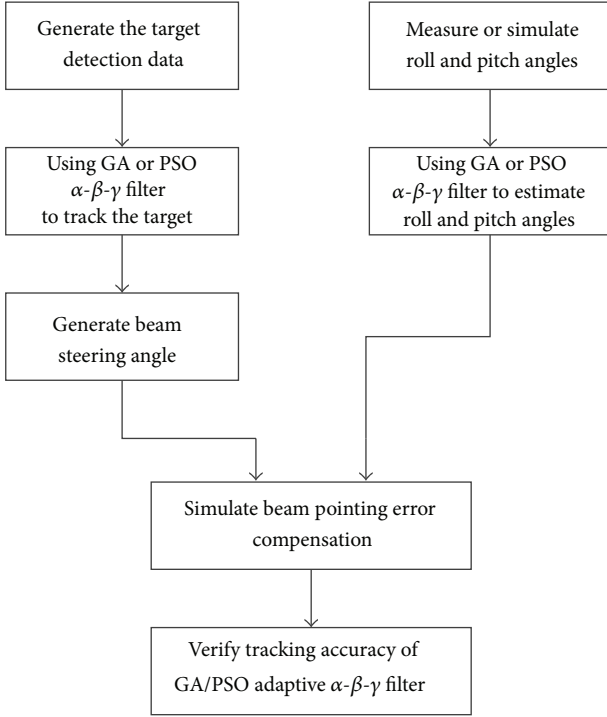


FIGURE 12: Flow chart of tracking performance simulation for Case 4 experiment.

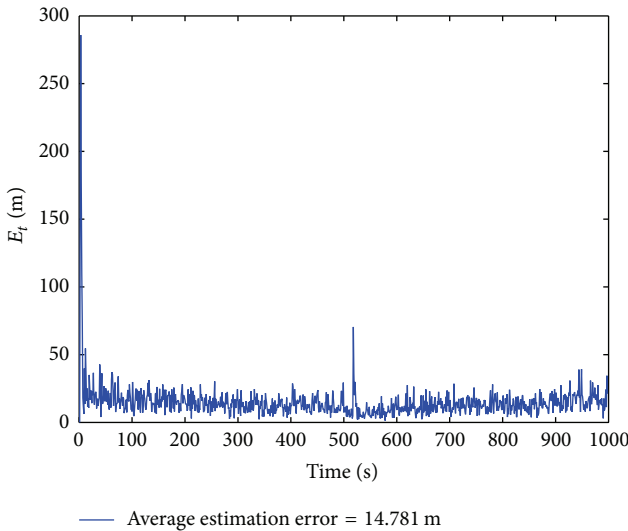


FIGURE 13: Estimation error of GA based adaptive α - β - γ filter.

presented in Figures 16 and 17 are too large to be applicable when the gain values are equal to 0.75 and 0.9. The GA and PSO have smaller errors compared with the fixed gain values, and the GA obtains the best estimation accuracy. The estimation errors of GA and PSO methods were found to be close. From Figures 13, 14, and 15, we can observe that there is a peak value that occurred at the time duration about 510 to 515 seconds, because the horizontal beam direction of ship-borne phased array

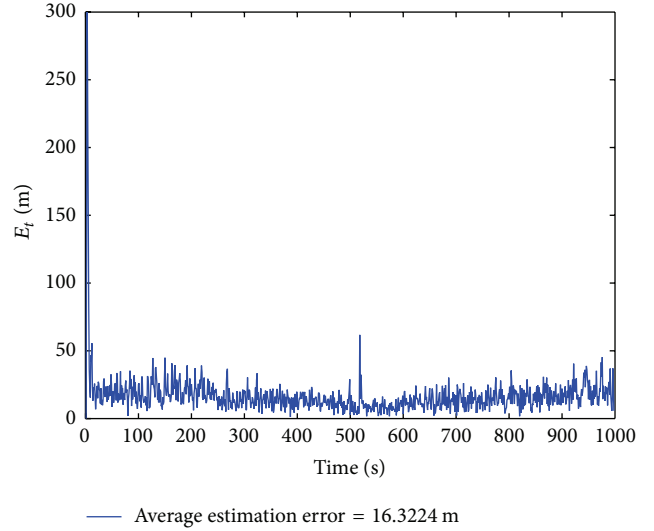


FIGURE 14: Estimation error of PSO based adaptive α - β - γ filter.

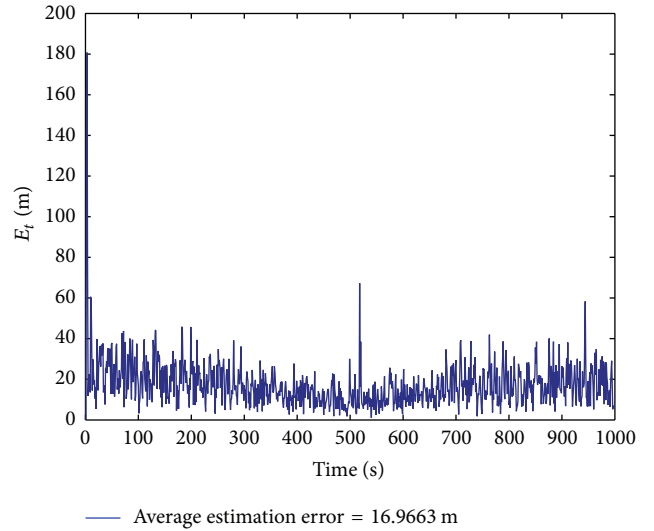


FIGURE 15: Estimation error of α - β - γ filter with $g_{r,1} = g_{p,1} = g_2 = 0.1$.

radar is steered according to the linear trajectory target, which is flying through sky just above the ship at the time instant of 510 second. As shown in Figure 18, the horizontal beam steering angle of ship-borne phased array radar at about the time of 510 second is changing from descending into ascending. When the GA based adaptive α - β - γ filter tracks the linear trajectory target, the estimation error values are less than 30 meters or less if the peak estimation errors during these 5 seconds are ignored.

Case 5 (estimating roll and pitch angles and tracking linear trajectory target using GA/PSO based adaptive α - β - γ filter and simulated data (with beam pointing error)). The ship's roll and pitch signals are simulated according to (3) and (4) with parameters of sea state 2 listed in Table 1 and standard

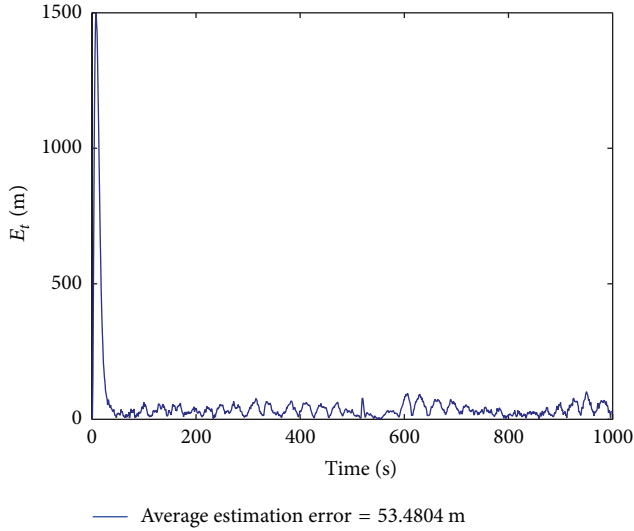


FIGURE 16: Estimation error of α - β - γ filter with $g_{r,1} = g_{p,1} = g_2 = 0.75$.

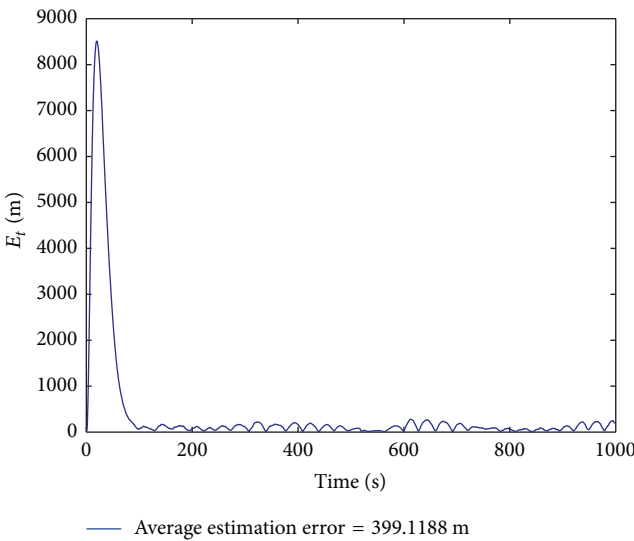


FIGURE 17: Estimation error of α - β - γ filter with $g_{r,1} = g_{p,1} = g_2 = 0.9$.

deviation of 0.01. The simulated ship's roll and pitch signals are applied for five different methods to estimate the gain of GA/PSO based adaptive α - β - γ filter. The total observation time is 1000 sec and sampling time is 0.1 sec. The simulation replicates 10000 times. The input samples are updated by one new sample for the next iteration. The other simulation scenario and parameters are the same as Case 4. Tables 5 and 6 demonstrate the optimal gain parameters of adaptive α - β - γ filter for roll gain $g_{r,1}$, pitch gain $g_{p,1}$, and target tracking gain vector \mathbf{g}_2 obtained by the GA and PSO methods, respectively, that minimizes RMSE. Figures 19, 20, 21, 22, and 23 show the estimation errors for five different gain values, which are summarized in Table 7. The estimation error of GA based adaptive α - β - γ filter for tracking a linear trajectory target is shown in Figure 19, where the convergence time of GA

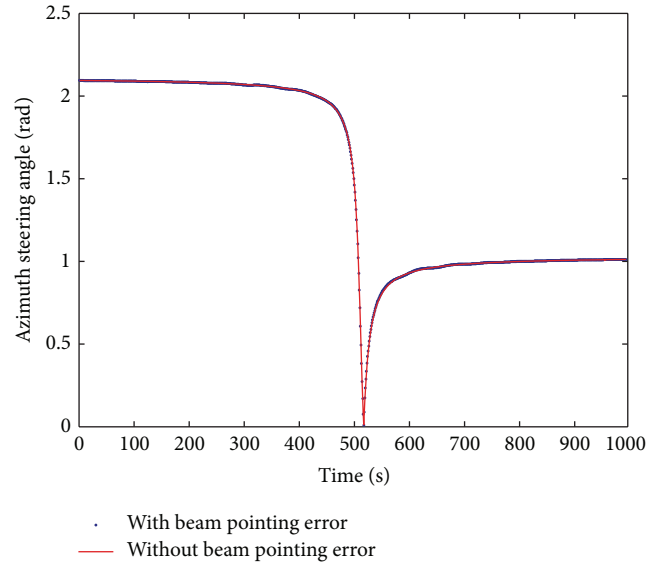


FIGURE 18: Azimuth beam steering angle of ship-borne phased array radar.

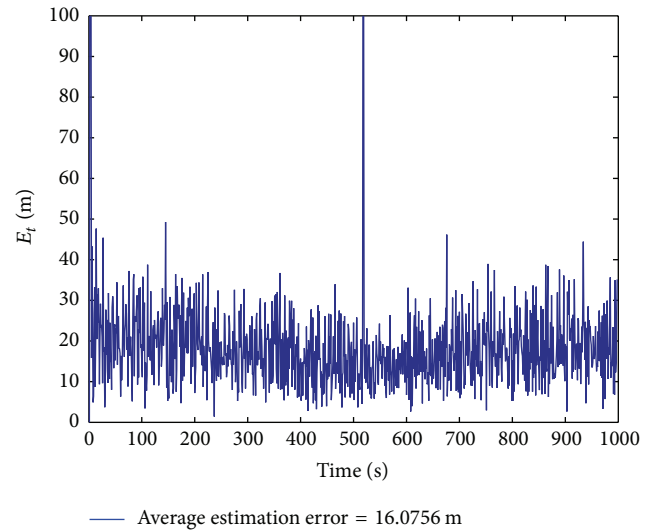
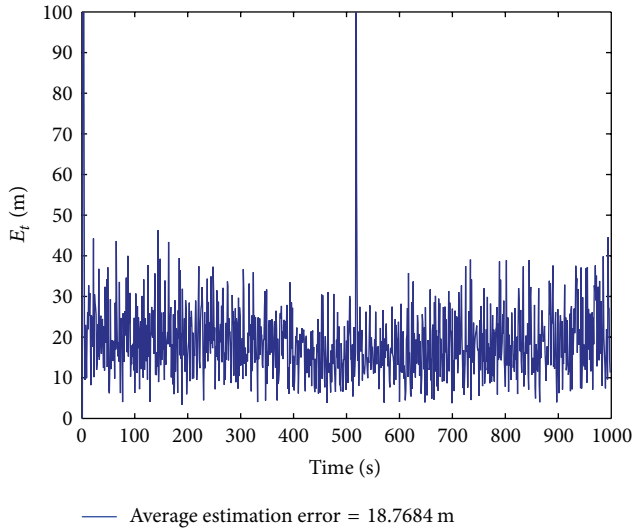
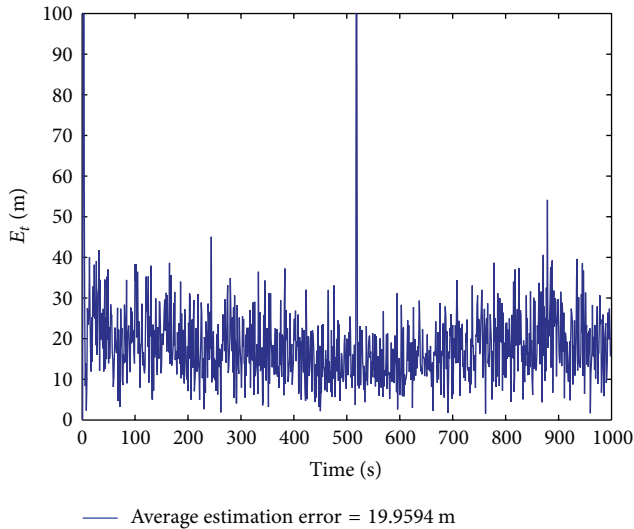


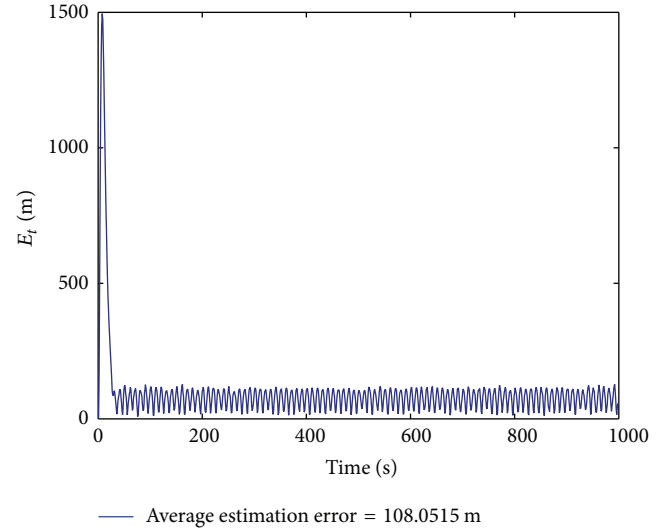
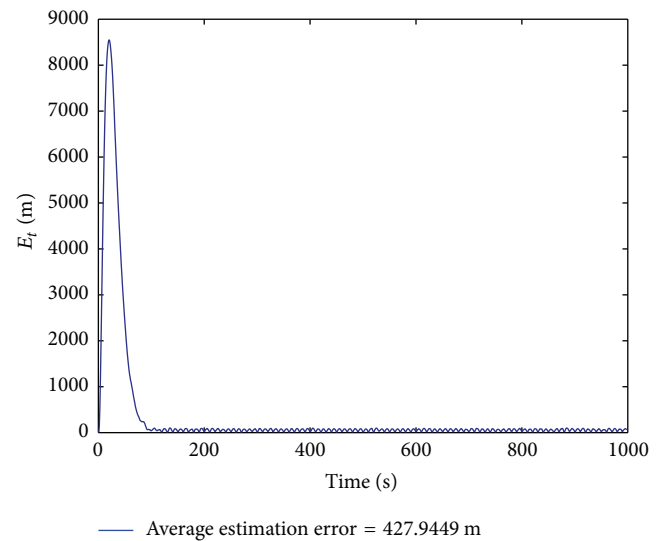
FIGURE 19: Estimation error of GA based adaptive α - β - γ filter.

based adaptive α - β - γ filter is about 3 sec and the average estimation error is about 16.0756 m. It concludes that the experimental results in Case 5 have the same trend as in Case 4; therefore, the simulated data can be used to observe the effect of ship motion on the tracking performance of ship-borne phased array radar under different sea state conditions. The convergence time and average estimation error of GA based adaptive α - β - γ filter are better than the method used in [6], where the tracking error of AEKF converges to less than about 20 m at 550 iterations (sec/iteration) and the estimation error will remain within the range of about 20 m when the beam pointing error is compensated by FBFN controller.

Case 6 (estimating roll and pitch angles and tracking circular moving target using GA based adaptive α - β - γ filter and

FIGURE 20: Estimation error of PSO based adaptive α - β - γ filter.FIGURE 21: Estimation error of α - β - γ filter with $g_{r,1} = g_{p,1} = g_2 = 0.1$.

measured data (with beam pointing error)). As the scenario described in Case 3, the measured roll and pitch signals shown in Figure 7 are used to evaluate the performance of GA based adaptive α - β - γ filter for estimating the roll and pitch angles and tracking the circular trajectory target. The estimation errors of α - β - γ filter with fixed gains of $g_{r,1} = g_{p,1} = g_2 = 0.1$ and $g_{r,1} = g_{p,1} = g_2 = 0.75$ are shown in Figures 24 and 25, respectively. The average estimation errors for fixed filter gains of 0.1 and 0.75 are about 4.1638 m and 57.2386 m, respectively. The optimal roll gain $g_{r,1}$, pitch gain $g_{p,1}$, and target tracking gain g_2 of adaptive α - β - γ filter estimated by the GA method during the observation time of 419 sec are listed in Table 8. The estimation error of GA based adaptive α - β - γ filter for tracking a circular flight target is shown in Figure 26, where the convergence time of GA based adaptive α - β - γ filter is about 5 sec and the average

FIGURE 22: Estimation error of α - β - γ filter with $g_{r,1} = g_{p,1} = g_2 = 0.75$.FIGURE 23: Estimation error of α - β - γ filter with $g_{r,1} = g_{p,1} = g_2 = 0.9$.

estimation error is about 3.6667 m. It concludes that the GA based adaptive α - β - γ filter can greatly improve the tracking accuracy and convergence time of the conventional α - β - γ filter for tracking the circular trajectory target.

5. Conclusions

This paper proposed an intelligent beam pointing error compensation mechanism for ship-borne phased array radar. The GA based adaptive α - β - γ filter estimates the roll and pitch angles of the ship moving in the sea and thus compensates for the antenna beam pointing error in order to enhance the tracking accuracy of phased array radar system.

TABLE 6: Estimated gain parameters for PSO based adaptive α - β - γ filter.

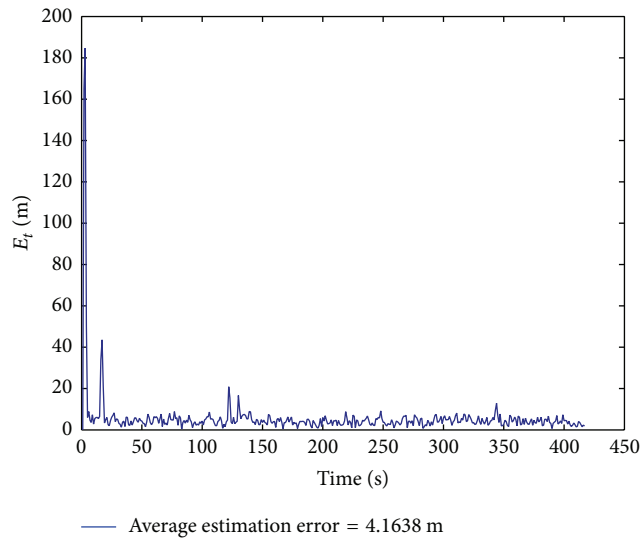
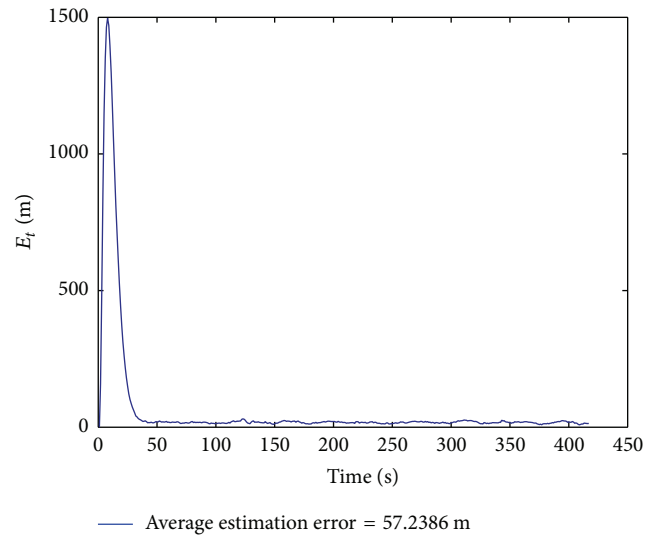
Time (sec)	1~100	101~200	201~300	301~400	401~500	501~600	601~700	701~800	801~900	901~1000
$g_{r,1}$	0.366	0.3645	0.532	0.4519	0.5151	0.5002	0.4797	0.5254	0.4146	0.5351
$g_{p,1}$	0.366	0.3647	0.3634	0.3644	0.3643	0.363	0.3644	0.3684	0.3643	0.3642
g_2	0.125	0.1271	0.2286	0.2166	0.1169	0.1799	0.1735	0.1564	0.0767	0.1346

TABLE 7: Estimation errors for different gains.

	Calculated by GA	Calculated by PSO	Fixed gain		
$g_{r,1}$	0.459~0.583	0.3645~0.5352	0.1	0.75	0.9
$g_{p,1}$	0.498~0.667	0.363~0.3684	0.1	0.75	0.9
g_2	0.0586~0.1697	0.0367~0.2291	0.1	0.75	0.9
Average E_t (m)	16.0756	18.7684	19.9594	108.0515	427.9449

TABLE 8: Estimated gain parameters for GA based adaptive α - β - γ filter.

Time (sec)	1~42	43~84	85~126	127~168	169~210	211~252	253~294	295~336	337~378	379~419
$g_{r,1}$	0.619	0.4996	0.5316	0.644	0.5052	0.5568	0.5316	0.4459	0.5092	0.5924
$g_{p,1}$	0.582	0.6727	0.7201	0.4913	0.4168	0.7169	0.5983	0.2036	0.5858	0.621
g_2	0.214	0.2215	0.1612	0.2474	0.1822	0.157	0.2073	0.1211	0.2278	0.1074

FIGURE 24: Estimation error of α - β - γ filter with $g_{r,1} = g_{p,1} = g_2 = 0.1$.FIGURE 25: Estimation error of α - β - γ filter with $g_{r,1} = g_{p,1} = g_2 = 0.75$.

Six experimental cases are conducted to verify the performance of ship-borne phased array radar using the proposed GA based adaptive α - β - γ filter. In Case 1, the GA based adaptive α - β - γ filter is used to estimate the roll and pitch angles with the simulated and measured roll and pitch signals, respectively. The simulation results show that the measurement data has the minimum estimation error, the estimation error in the sea state 2 is the second, and the estimation error in the sea state 3 is the worst. Cases 2 and 3 show that when the GA based adaptive α - β - γ filter is applied to estimate the beam pointing error and to track the target in a ship-borne phased array radar, the circular trajectory

target will be tracked with the larger average estimation error and longer convergence time than linear trajectory target. The experimental results of Cases 4 and 5 demonstrate that when a linear trajectory target is tracked by ship-borne phased array radar, the average estimation error and convergence time of ship-borne phased array radar using the GA based adaptive α - β - γ filter are better than PSO based adaptive α - β - γ filter and fixed filter gain α - β - γ filter. The convergence time and tracking accuracy of ship-borne phased array radar using the proposed GA based adaptive α - β - γ filter are superior to the AEKF significantly. In conclusions, the proposed GA based adaptive α - β - γ filter is a real time applicable algorithm

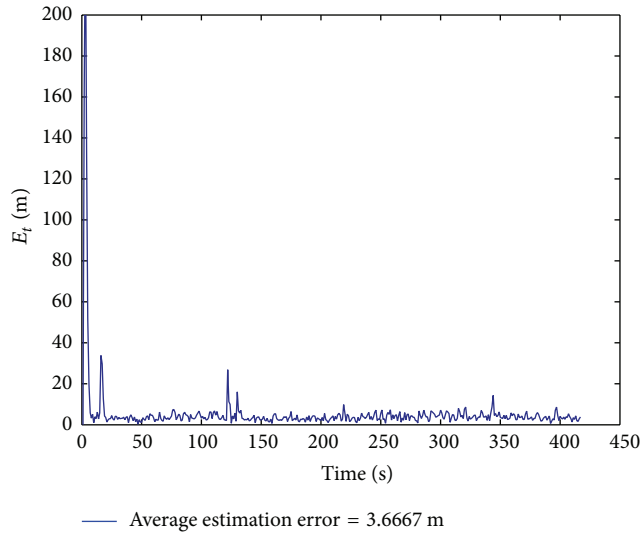


FIGURE 26: Estimation error of GA based adaptive α - β - γ filter.

whose accuracy is good with relatively less complexity. In addition, the roll and pitch signals measured in real operation environments can be replaced with the simulated roll and pitch signals to test all the relevant properties of practical ship motion compensation and air target tracking for ship-borne phased array radar.

Conflict of Interests

The authors declare that there is no conflict of interests regarding the publication of this paper.

Acknowledgment

This work is supported in part by research grants from National Science Council, China (NSC 102-2218-E-155-001).

References

- [1] Z. Fang and Q. Rundong, *Ship-borne Phased Array Radar Motion Compensation*, System Engineering and Electronic Technologies, 1998.
- [2] L. J. Love, J. F. Jansen, and F. G. Pin, "Compensation of wave induced motion and force phenomenon for ship based high performance robotic and human amplifying systems," Oak Ridge National Laboratory ORNL/TM-2003/233, 2003.
- [3] R. J. Hill, *Motion Compensation for Ship Borne Radars and Lidars*, U.S. Department of Commerce, National Oceanic and Atmospheric Administration, Office of Oceanic and Atmospheric Research, Earth System Research Laboratory, Physical Sciences Division, 2005.
- [4] T. I. Fossen and T. Perez, "Kalman filtering for positioning and heading control of ships and offshore rigs," *IEEE Control Systems Magazine*, vol. 29, no. 6, pp. 32–46, 2009.
- [5] S. K uchler, C. Pregizer, J. K. Eberharter, K. Schneider, and O. Sawodny, "Real-time estimation of a ship's attitude," in *Proceedings of the American Control Conference (ACC '11)*, pp. 2411–2416, San Francisco, Calif, USA, July 2011.
- [6] J. Mar, K. C. Tsai, Y. T. Wang, and M. B. Basnet, "Intelligent motion compensation for improving the tracking performance of shipborne phased array radar," *International Journal of Antennas and Propagation*, vol. 2013, Article ID 384756, 14 pages, 2013.
- [7] T. Dirk and S. Tarunraj, "Optimal design of α - β - γ filters," in *American Control Conference*, vol. 6, pp. 4348–4352, Chicago, Ill, USA, June 2000.
- [8] D. Tenne and T. Singh, "Characterizing performance of α - β - γ filters," *IEEE Transactions on Aerospace and Electronic Systems*, vol. 38, no. 3, pp. 1072–1087, 2002.
- [9] T. E. Lee, J. P. Su, and K. W. Yu, "Parameter optimization for a third-order sampled-data tracker," in *Proceedings of the 2nd International Conference on Innovative Computing, Information and Control*, p. 336, Kumamoto, Japan, September 2007.
- [10] Y. H. Lho and J. H. Painter, "A fuzzy tuned adaptive Kalman filter," in *Industrial Fuzzy Control and Intelligent System*, pp. 144–148, December 1993.
- [11] N. Ramakoti, A. Vinay, and R. K. Jatoth, "Particle swarm optimization aided Kalman filter for object tracking," in *Proceedings of the International Conference on Advances in Computing, Control and Telecommunication Technologies (ACT '09)*, pp. 531–533, Kerala, India, December 2009.
- [12] T.-E. Lee, J.-P. Su, and K.-W. Yu, "A particle swarm optimization-based state estimation scheme for moving objects," *Transactions of the Institute of Measurement and Control*, vol. 34, no. 2-3, pp. 236–254, 2012.
- [13] D. C. Law, S. A. McLaughlin, M. J. Post et al., "An electronically stabilized phased array system for shipborne atmospheric wind profiling," *Journal of Atmospheric and Oceanic Technology*, vol. 19, no. 6, pp. 924–933, 2002.
- [14] C. A. Balanis, *Antenna Theory: Analysis and Design*, John Wiley & Sons, New York, NY, USA, 3rd edition, 2005.
- [15] J. Mar and Y. R. Lin, "Implementation of SDR digital beam-former for microsatellite SAR," *IEEE Geoscience and Remote Sensing Letters*, vol. 6, no. 1, pp. 92–96, 2009.
- [16] R. C. Eberhart and Y. Shi, *Computational Intelligence: Concepts to Implementations*, Elsevier/Morgan Kaufmann, 2007.
- [17] K. Y. Lee and J.-B. Park, "Application of particle swarm optimization to economic dispatch problem: advantages and disadvantages," in *Proceedings of the IEEE PES Power Systems Conference and Exposition (PSCE '06)*, pp. 188–192, Atlanta, Ga, USA, November 2006.
- [18] R. C. Eberhart and J. Kennedy, "New optimizer using particle swarm theory," in *Proceedings of the 6th International Symposium on Micro Machine and Human Science*, pp. 39–43, Nagoya, Japan, October 1995.

Research Article

Joint Phased-MIMO and Nested-Array Beamforming for Increased Degrees-of-Freedom

Chenglong Zhu, Hui Chen, and Huaizong Shao

School of Communication and Information Engineering, University of Electronic Science and Technology of China, Chengdu 611731, China

Correspondence should be addressed to Chenglong Zhu; zhuchenglong01@126.com

Received 18 June 2014; Revised 7 December 2014; Accepted 18 January 2015

Academic Editor: Hang Hu

Copyright © 2015 Chenglong Zhu et al. This is an open access article distributed under the Creative Commons Attribution License, which permits unrestricted use, distribution, and reproduction in any medium, provided the original work is properly cited.

Phased-multiple-input multiple-output (phased-MIMO) enjoys the advantages of MIMO virtual array and phased-array directional gain, but it gets the directional gain at a cost of reduced degrees-of-freedom (DOFs). To compensate the DOF loss, this paper proposes a joint phased-array and nested-array beamforming based on the difference coarray processing and spatial smoothing. The essence is to use a nested-array in the receiver and then fully exploit the second order statistic of the received data. In doing so, the array system offers more DOFs which means more sources can be resolved. The direction-of-arrival (DOA) estimation performance of the proposed method is evaluated by examining the root-mean-square error. Simulation results show the proposed method has significant superiorities to the existing phased-MIMO.

1. Introduction

In recent years, multiple-input multiple-output (MIMO) has received much attention [1–4]. Many of MIMO superiorities are fundamentally due to the fact that it can utilize the waveform diversity to yield a virtual aperture that is larger than the physical array of its phased-array counterpart [5–8]. However, MIMO array misses directional gain selectivity. In contrast, phased-array has good direction gain but without spatial diversity gain. To overcome these disadvantages, intermediates between MIMO and phased-array are investigated by jointly exploiting their benefits [9–11]. Particularly, a transmit subaperturing approach was proposed in [11] for MIMO radar. The basic idea is to form multiple transmit beams which are steered toward the same direction [12]. In [9], the authors proposed a phased-MIMO technique, which enjoys the advantages of MIMO array without sacrificing the main advantages of phased-array in coherent processing gain. That is to say, phased-MIMO array offers a tradeoff between conventional phased-array and MIMO array.

However, the number of degrees-of-freedom (DOFs) is important criteria because more DOFs mean more sources can be resolved by the system. To compensate the sacrificed

DOFs of phased-MIMO radar, it is necessary to increase the DOFs in the receiver. In earlier works, the problem of increasing the DOFs of linear arrays has been investigated in [13, 14], but the augmented covariance matrix is not positive semidefinite anymore. The authors of [14] increase the DOFs with the minimum redundancy arrays [15] and constructing an augmented covariance matrix. Nonuniform and sparse array arrangements are also widely employed [16–21]. Solutions based on genetic algorithm [22, 23], random spacing [24], linear programming [25], and compressive sensing [26–28] have been proposed for phased-array thinning. But sparse array elements have the drawbacks of generating grating lobes. Moreover, it is not easy to extend them to any arbitrary array size. To mitigate these weaknesses, the authors of [29–31] propose a nested-array based on the concept of difference coarray [32], but there are no studies on the joint transmit and receive array design.

Inspired by the phased-MIMO [9] and nest-array [29], this paper proposes a joint phased-array and nested-array beamforming based on the difference coarray processing and spatial smoothing for increased DOFs and consequently more sources can be resolved. The main contribution of this work can be summarized as follows: (1) a joint phased-array

and nested-array beamforming is proposed. This approach optimally utilizes the advantages of MIMO, phased-array, and nested-array and overcomes their disadvantages. (2) Adaptive beamforming based on the spatial smoothing algorithm is presented to resolve the coherent noise problem caused by the difference coarray processing. (3) The direction-of-arrival (DOA) estimation performance of the proposed joint phased-array and nested-array beamforming is extensively evaluated by examining the root-mean-square error (RMSE).

The rest of this paper is organized as follows. In Section 2, we briefly introduce some background on the basic phased-MIMO and nested-array technique. In Section 3, the formulation and signal model of the joint phased-MIMO and nested-array are proposed. It can significantly increase the system DOFs, which means more interferences/targets can be suppressed/identified. Next, Section 4 develops the adaptive beamforming with a spatial smoothing algorithm. Section 5 performs extensive simulations to evaluate the proposed method in DOA estimation by examining the RMSE performance. Finally, conclusions are drawn in Section 6.

2. Preliminaries and Motivations

In this section, we provide an overview of basic phased-MIMO and nested-array.

2.1. Phased-MIMO. The main idea of the phased-MIMO is to divide the M transmit elements into $1 \leq K \leq M$ subarrays, which are allowed to overlap. All elements of the k ($1 \leq k \leq K$) subarrays are used to coherently emit the signal $\phi_k(t)$ in order to form a beam towards an interesting direction. At the same time, different waveforms are transmitted simultaneously by different subarrays.

The complex envelope of the signals emitted by the k th subarray can be modeled as

$$s_k(t) = \sqrt{\frac{M}{K}} \phi_k(t) \bar{\mathbf{w}}_k^*, \quad k = 1, \dots, K, \quad (1)$$

where $\bar{\mathbf{w}}_k$ is the $M \times 1$ unit-norm complex vector which is comprised of M_k (number of elements used in the k th subarray) nonzero and $M - M_k$ zeros and $(\cdot)^*$ is the conjugate operator. The $\sqrt{M/K}$ is used to obtain an identical transmit power constraint.

The signal reflected by a target located at angle θ in the far-field can then be modeled as

$$r(t, \theta) = \sqrt{\frac{M}{K}} \alpha(\theta) \sum_{k=1}^K \mathbf{w}_k^H \mathbf{a}_k(\theta) e^{-j\tau_k(\theta)} \phi_k(t), \quad (2)$$

where $\alpha(\theta)$ is the target coefficient and \mathbf{w}_k and $\mathbf{a}_k(\theta)$ are the $M_k \times 1$ beamforming vector and transmit steering vector, respectively. And $\tau_k(\theta)$ is the required signal propagation for the k th subarray. The reflection coefficient $\alpha(\theta)$ for a target is assumed to be constant during the whole pulse but varies from pulse to pulse; that is, it obeys the Swerling II target model [33].

Denoting

$$\mathbf{c}(\theta) \doteq [\mathbf{w}_1^H \mathbf{a}_1(\theta), \mathbf{w}_2^H \mathbf{a}_2(\theta), \dots, \mathbf{w}_K^H \mathbf{a}_K(\theta)]^T, \quad (3a)$$

$$\mathbf{d}(\theta) \doteq [e^{-j\tau_1(\theta)}, e^{-j\tau_2(\theta)}, \dots, e^{-j\tau_K(\theta)}]^T, \quad (3b)$$

with $(\cdot)^T$ being the transpose operator. Supposing that a target is located at θ_s and D interferences at θ_i , $1 \leq i \leq D$, for an N -element receive array we can get $KN \times 1$ data vector:

$$\mathbf{y} = \sqrt{\frac{M}{K}} \alpha_s(\theta_s) \mathbf{u}_{\text{pa-mimo}}(\theta_s) + \sum_{i=1}^D \sqrt{\frac{M}{K}} \alpha_i(\theta_i) \mathbf{u}_{\text{pa-mimo}}(\theta_i) + \mathbf{n}, \quad (4)$$

where \mathbf{n} is the $KN \times 1$ noise term. The $KN \times 1$ virtual steering vector is

$$\mathbf{u}_{\text{pa-mimo}} = [\mathbf{c}(\theta) \odot \mathbf{d}(\theta)] \otimes \mathbf{b}(\theta), \quad (5)$$

where \odot and \otimes denote the Hadamard product and Kronecker product, respectively. And $\mathbf{b}(\theta)$ is the $N \times 1$ actual receive steering vectors associated with the direction θ .

It can be noticed from (5) that phased-MIMO radar is a compromise between MIMO and phased-array radar and thus enjoys the advantages of MIMO radar extending the array aperture by virtual array and phased-array radar allowing for maximization of the coherent processing gain through transmit beamforming [34]. From (4), we can conclude that the complexity of the traditional processing algorithm is $O(K^4 N^2 L)$.

It would be specially mentioned that if $K = 1$ is chosen, then the signal model (4) simplifies to the signal model for the conventional phased-array radar. On the other hand if $K = M$ is chosen, the signal model (4) simplifies to the signal model for the MIMO radar. Thus we can conclude that the degrees of freedom can be got from aforementioned radar system as

$$\text{DOF}_{\text{pa-array}} = N + 1, \quad (6a)$$

$$\text{DOF}_{\text{pa-mimo}} = N + K, \quad (6b)$$

$$\text{DOF}_{\text{mimo}} = N + M. \quad (6c)$$

2.2. Nested-Array. The number of sources that can be resolved by an N -element ULA phased-array using conventional subspace-based methods is $N - 1$. However, according to the difference coarray scheme [32], the maximum attainable number of DOFs, denoted by DOF_{max} , is

$$\text{DOF}_{\text{max}} = N(N - 1) + 1. \quad (7)$$

Certainly, if a difference occurs more than once, it implies a decrease in the available DOFs. Consider a linear array with d being the minimum spacing of the underlying grid and define the function $c[m]$ which takes a value 1 if there is an element

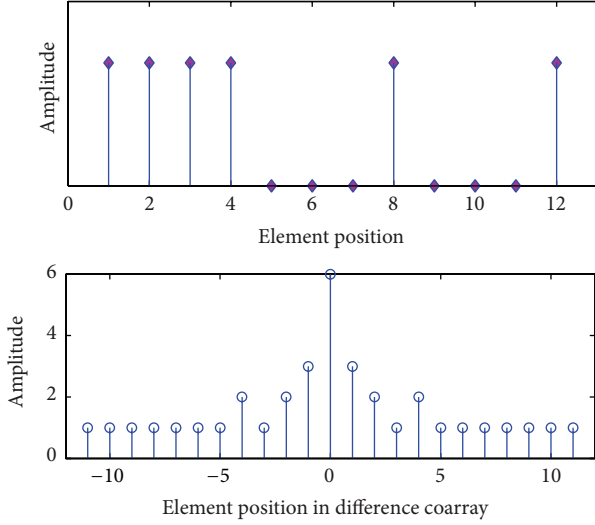


FIGURE 1: Illustration of a two-level nested-array with $N_1 = 3$ and $N_2 = 3$.

located at md and 0 otherwise. The number of same occurrences in each position, denoted by γ , can be expressed as

$$\gamma = c[m] \otimes c[-m], \quad (8)$$

where \otimes denotes the convolution operator. That is to say, the difference coarray of an N -element ULA is another ULA with $(2N - 1)$ elements. To achieve more DOFs, we can use the nested-array [29]. It is basically a concatenation of two ULAs, namely, inner and outer ULAs where they consist of N_1 and N_2 elements with spacing d_1 and spacing $d_2 = (N_1 + 1)d_1$, respectively. It is easily understood that the difference coarray of the two-level nested-array is a full ULA with $2N_2(N_1 + 1) - 1$ elements whose positions are

$$\{md_2, m = -N_e, -N_e + 1, \dots, N_e, N_e = N_2(N_1 + 1) - 1\}. \quad (9)$$

This is a systematic way to increase the DOFs and the details can be found in [29]. An illustration for a two-level nested arrays with $N_1 = 3$ and $N_2 = 3$ is shown in Figure 1.

In summary, phased-MIMO enjoys increased transmit coherent gain at a cost of reduced DOFs. Since a ULA phased-array receiver is used in the basic phased-MIMO, we can use a nested-array as the receiver and thus increase the DOFs by difference coarray processing technique to compensate the DOF loss. This is just the motivation of this paper. The increased DOFs can be obtained when the nested-array is applied at the receiving end. Thus the DOF for phased-MIMO radar joints with nested-array as well as others can be shown as [29]. Comparing with (6a), (6b), and (6c), we can see that the proposed method is capable of proving $O(N^2)$ DOF from

TABLE 1: Comparative DOF between the traditional method and the proposed method.

Method applied	Number of subarrays partitioned at the transmitting end	Number of sensors used at the receiving end	DOF
Traditional method	K	N	$O(N) + O(K)$
Proposed method	K	N	$O(N^2) + O(K)$

only $O(N)$ physical sensors and it is possible to get a dramatic increase in DOF:

$$\text{DOF}_{\text{nested-pa-array}} = \frac{N^2}{2} + N + 1, \quad (10a)$$

$$\text{DOF}_{\text{nested-pa-mimo}} = \frac{N^2 + 2N}{2} + 2K - 1, \quad (10b)$$

$$\text{DOF}_{\text{nested-mimo}} = \frac{N^2 - 2}{2} + N + 2M. \quad (10c)$$

A comparison concerning DOF between the proposed method and the traditional method is summarized in Table 1.

From the foregoing analysis, by applying a new structure of “nested-array” on the receiving end, the proposed method can provide $O(N^2)$ degrees of freedom for a receiving end with N physical sensors. It also can be generated easily in a systematic mode. So the problem of detecting more sources than physical sensors can be addressed in this way.

3. Difference Coarray Processing Based Phased-MIMO Signal Model

Figure 2 compares our proposal of joint phased-MIMO and nested-array and the basic phased-MIMO, where the minimum element spacing d is assumed to be half of the wavelength. For analysis convenience, we rewrite (4) as a more general equation

$$\mathbf{y} = \sum_{i=1}^L \sqrt{\frac{M}{K}} \alpha_i \mathbf{u}(\theta_i) + \mathbf{n}, \quad (11)$$

where $L = D + 1$ is the number of sources including target and interferences. Multiplying both sides by $\sqrt{K/M}$, we have

$$\tilde{\mathbf{y}} = \mathbf{y} \sqrt{\frac{K}{M}} = \sum_{i=1}^L \alpha_i \mathbf{u}(\theta_i) + \sqrt{\frac{K}{M}} \mathbf{n} = \mathbf{U} \boldsymbol{\alpha} + \sqrt{\frac{K}{M}} \mathbf{n}, \quad (12)$$

where \mathbf{U} denotes the virtual array manifold matrix and $\boldsymbol{\alpha} = [\alpha_1(\theta_1), \alpha_2(\theta_2), \dots, \alpha_L(\theta_L)]^T$. It is easily understood that $\tilde{\mathbf{y}}$ satisfies the statistical model of $\tilde{\mathbf{y}} \sim N_c(\boldsymbol{\mu}, \mathbf{R})$, where N_c stands for the complex multivariate circular Gaussian probability

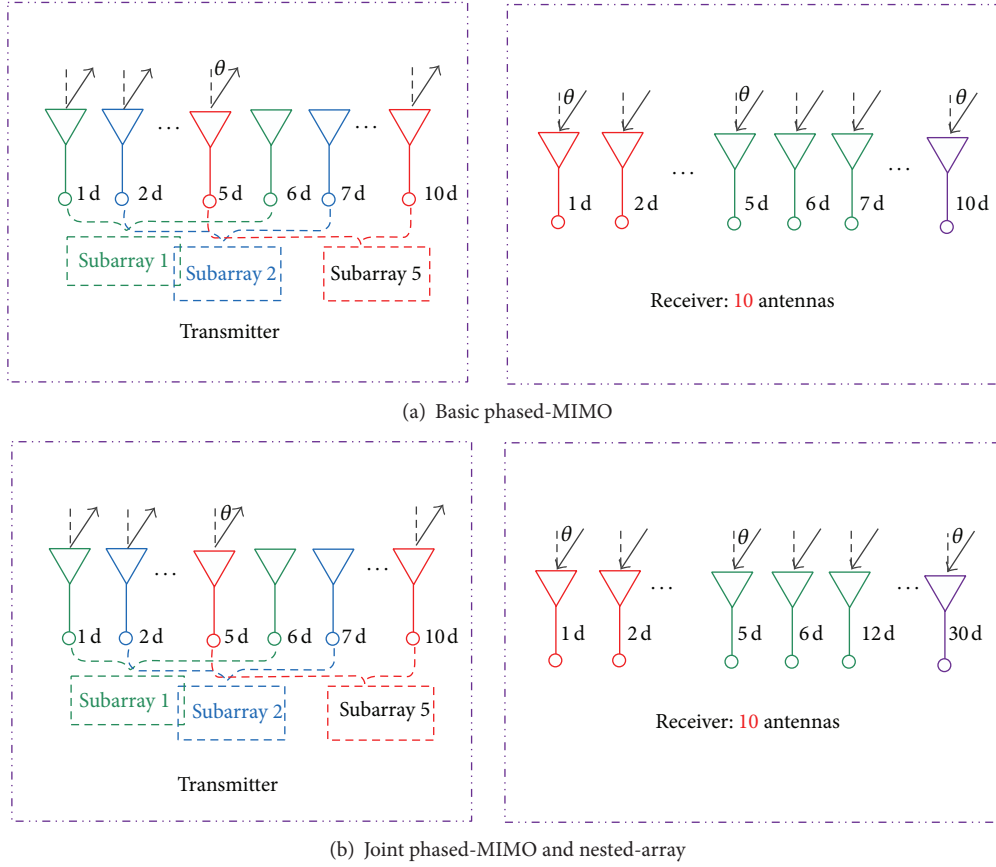


FIGURE 2: Comparisons between our proposal of joint phased-MIMO and nested-array and the basic phased-MIMO.

density function, μ is the mean of $\tilde{\mathbf{y}}$, and \mathbf{R} is its covariance matrix.

According to the difference coarray processing algorithm [32], we can get the autocorrelation matrix of $\tilde{\mathbf{y}}$ as

$$\begin{aligned}
 \mathbf{R}_{\tilde{\mathbf{y}}\tilde{\mathbf{y}}} &= E[\tilde{\mathbf{y}}\tilde{\mathbf{y}}^H] = E\left[\left(\mathbf{U}\boldsymbol{\alpha} + \sqrt{\frac{K}{M}}\mathbf{n}\right)\left(\mathbf{U}\boldsymbol{\alpha} + \sqrt{\frac{K}{M}}\mathbf{n}\right)^H\right] \\
 &= E\left[\left(\mathbf{U}\boldsymbol{\alpha} + \sqrt{\frac{K}{M}}\mathbf{n}\right)\left(\boldsymbol{\alpha}^H\mathbf{U}^H + \sqrt{\frac{K}{M}}\mathbf{n}^H\right)\right] \\
 &= \mathbf{U}\begin{bmatrix} \sigma_1^2 & & & \\ & \sigma_2^2 & & \\ & & \dots & \\ & & & \sigma_L^2 \end{bmatrix}\mathbf{U}^H + \frac{K}{M}\sigma_n^2\mathbf{I},
 \end{aligned} \tag{13}$$

where superscript $(\cdot)^H$ denotes transpose conjugate and σ_n^2 is the noise variance. The corresponding original array manifold matrix \mathbf{U} is given in (15).

Then we vectorize $\mathbf{R}_{\tilde{\mathbf{y}}\tilde{\mathbf{y}}}$ as the following vector:

$$\begin{aligned}
 \hat{\mathbf{y}} = \text{vec}(\mathbf{R}_{\tilde{\mathbf{y}}\tilde{\mathbf{y}}}) &= \text{vec}\left[\sum_{i=1}^L \sigma_i^2 \mathbf{u}(\theta_i) \mathbf{u}^H(\theta_i)\right] + \frac{K}{M} \sigma_n^2 \tilde{\mathbf{1}}_n \\
 &= (\mathbf{U}^* \oplus \mathbf{U}) \mathbf{p} + \frac{K}{M} \sigma_n^2 \tilde{\mathbf{1}}_n,
 \end{aligned} \tag{14}$$

where the sources power vector $\mathbf{p} = [\sigma_1^2, \sigma_2^2, \dots, \sigma_L^2]^T$ and $\tilde{\mathbf{1}}_n = [\mathbf{e}_1^T, \mathbf{e}_2^T, \dots, \mathbf{e}_N^T]^T$ whose element \mathbf{e}_i stands for a column vector of all zeros except a 1 at the i th position. And the symbol \oplus is used to denote the Khatri Rao (KR) product. Also, the new virtual array manifold $\mathbf{U}^* \oplus \mathbf{U}$ is derived in (16). Both of (15) and (16) are shown at bottom of the next page. We can see that the dimension of the new virtual array manifold $\mathbf{U}^* \oplus \mathbf{U}$ is $KN^2 \times L$. Obviously, the equivalent aperture has been significantly increased. More importantly, it is a ULA virtual array. Here, we can view $\hat{\mathbf{y}}$ as the observation vector comparing with (11). And \mathbf{p} which consists of the sources' powers represents the equivalent source signal vector.

Now we would like to consider the computation complexity of this proposed method. From (14), we can see that

K^2N^4L complex multiplication and $KN^2(L-1)$ addition of complex quantities have been increased. These considerations reveal that the complexity of the proposal is of $O(K^2N^4L)$. Due to the difference coarray processing, it takes

much resources to compute the autocorrelation matrix of the received data and is beneficial for us to make full use of the statistics:

$$\mathbf{U} = [\mathbf{u}(\theta_1), \dots, \mathbf{u}(\theta_L)]$$

$$= \begin{pmatrix} e^{-j(2\pi/\lambda)(d_{t1}+d_{r1}) \sin(\theta_1)} & \dots & e^{-j(2\pi/\lambda)(d_{t1}+d_{r1}) \sin(\theta_i)} & \dots & e^{-j(2\pi/\lambda)(d_{t1}+d_{r1}) \sin(\theta_L)} \\ \vdots & & \vdots & & \vdots \\ e^{-j(2\pi/\lambda)(d_{t1}+d_{rN}) \sin(\theta_1)} & \dots & e^{-j(2\pi/\lambda)(d_{t1}+d_{rN}) \sin(\theta_i)} & \dots & e^{-j(2\pi/\lambda)(d_{t1}+d_{rN}) \sin(\theta_L)} \\ \vdots & & \vdots & & \vdots \\ e^{-j(2\pi/\lambda)(d_{tK}+d_{r1}) \sin(\theta_1)} & \dots & e^{-j(2\pi/\lambda)(d_{tK}+d_{r1}) \sin(\theta_i)} & \dots & e^{-j(2\pi/\lambda)(d_{tK}+d_{r1}) \sin(\theta_L)} \\ \vdots & & \vdots & & \vdots \\ e^{-j(2\pi/\lambda)(d_{tK}+d_{rN}) \sin(\theta_1)} & \dots & e^{-j(2\pi/\lambda)(d_{tK}+d_{rN}) \sin(\theta_i)} & \dots & e^{-j(2\pi/\lambda)(d_{tK}+d_{rN}) \sin(\theta_L)} \end{pmatrix}_{KN \times L}, \quad (15)$$

$\mathbf{U}^* \oplus \mathbf{U}$

$$= \begin{pmatrix} e^{-j(2\pi/\lambda)(d_{t1}+d_{r1}-d_{t1}-d_{r1}) \sin(\theta_1)} & \dots & e^{-j(2\pi/\lambda)(d_{t1}+d_{r1}-d_{t1}-d_{r1}) \sin(\theta_i)} & \dots & e^{-j(2\pi/\lambda)(d_{t1}+d_{r1}-d_{t1}-d_{r1}) \sin(\theta_L)} \\ \vdots & & \vdots & & \vdots \\ e^{-j(2\pi/\lambda)(d_{tK}+d_{rN}-d_{t1}-d_{r1}) \sin(\theta_1)} & \dots & e^{-j(2\pi/\lambda)(d_{tK}+d_{rN}-d_{t1}-d_{r1}) \sin(\theta_i)} & \dots & e^{-j(2\pi/\lambda)(d_{tK}+d_{rN}-d_{t1}-d_{r1}) \sin(\theta_L)} \\ \vdots & & \vdots & & \vdots \\ e^{-j(2\pi/\lambda)(d_{t1}+d_{r1}-d_{tK}-d_{rN}) \sin(\theta_1)} & \dots & e^{-j(2\pi/\lambda)(d_{t1}+d_{r1}-d_{tK}-d_{rN}) \sin(\theta_i)} & \dots & e^{-j(2\pi/\lambda)(d_{t1}+d_{r1}-d_{tK}-d_{rN}) \sin(\theta_L)} \\ \vdots & & \vdots & & \vdots \\ e^{-j(2\pi/\lambda)(d_{tK}+d_{rN}-d_{tK}-d_{rN}) \sin(\theta_1)} & \dots & e^{-j(2\pi/\lambda)(d_{tK}+d_{rN}-d_{tK}-d_{rN}) \sin(\theta_i)} & \dots & e^{-j(2\pi/\lambda)(d_{tK}+d_{rN}-d_{tK}-d_{rN}) \sin(\theta_L)} \end{pmatrix}_{KN^2 \times L}. \quad (16)$$

For simplicity and without loss of generality, firstly we consider a special example where all subarrays have an equal aperture. In this case, the nonadaptive transmit beamformer weight vectors are given by

$$\mathbf{w}_k = \frac{\mathbf{a}_k(\theta_s)}{\|\mathbf{a}_k(\theta_s)\|}, \quad k = 1, 2, \dots, K. \quad (17)$$

Correspondingly, the normalized transmit coherent processing vector $\mathbf{c}(\theta_s)$ can be expressed as

$$\mathbf{c}(\theta_s) = \left[\frac{\mathbf{a}_1^H(\theta_s) \mathbf{a}_1(\theta_s)}{\|\mathbf{a}_1(\theta_s)\|}, \dots, \frac{\mathbf{a}_K^H(\theta_s) \mathbf{a}_K(\theta_s)}{\|\mathbf{a}_K(\theta_s)\|} \right]^T$$

$$= \left[\sqrt{M-K+1}, \dots, \sqrt{M-K+1} \right]^T. \quad (18)$$

We then have

$$\mathbf{c}(\theta_s) \odot \mathbf{d}(\theta_s) = \sqrt{M-K+1} \left[e^{-j\tau_1(\theta_s)}, \dots, e^{-j\tau_K(\theta_s)} \right]^T. \quad (19)$$

Substituting it to (5) yields

$$\mathbf{u}(\theta_s)$$

$$= (\mathbf{c}(\theta_s) \odot \mathbf{d}(\theta_s)) \otimes \mathbf{b}(\theta_s)$$

$$= \sqrt{M-K+1} \left[e^{-j(2\pi/\lambda)d_{t1} \sin(\theta_s)}, \dots, e^{-j(2\pi/\lambda)d_{tK} \sin(\theta_s)} \right]^T$$

$$\otimes \left[e^{-j(2\pi/\lambda)d_{r1} \sin(\theta_s)}, \dots, e^{-j(2\pi/\lambda)d_{rN} \sin(\theta_s)} \right]^T$$

$$= \sqrt{M-K+1} \left[e^{-j(2\pi/\lambda)(d_{t1}+d_{r1}) \sin(\theta_s)}, \dots, \right.$$

$$e^{-j(2\pi/\lambda)(d_{t1}+d_{rN}) \sin(\theta_s)},$$

$$e^{-j(2\pi/\lambda)(d_{t2}+d_{r1}) \sin(\theta_s)}, \dots,$$

$$e^{-j(2\pi/\lambda)(d_{t2}+d_{rN}) \sin(\theta_s)}, \dots,$$

$$e^{-j(2\pi/\lambda)(d_{tK}+d_{r1}) \sin(\theta_s)}, \dots,$$

$$\left. e^{-j(2\pi/\lambda)(d_{tK}+d_{rN}) \sin(\theta_s)} \right]^T. \quad (20)$$

4. Adaptive Beamforming

In order to maximize the output signal-plus-noise ratios (SINR), adaptive beamforming should be employed. Applying the beamformer weighter \mathbf{w}_p to (14), we can get

$$\begin{aligned}\tilde{\mathbf{Y}} &= \mathbf{w}_p^H \hat{\mathbf{y}} = \sum_{i=1}^L \mathbf{w}_p^H [\mathbf{u}^*(\theta_i) \otimes \mathbf{u}(\theta_i)] \sigma_i^2 + \frac{K}{M} \sigma_n^2 \mathbf{w}_p^H \tilde{\mathbf{I}}_n \\ &= \sum_{i=1}^L \mathbf{B}_{\text{power}}(\theta_i) \sigma_i^2 + \frac{K}{M} \sigma_n^2 \mathbf{w}_p^H \tilde{\mathbf{I}}_n,\end{aligned}\quad (21)$$

where $\mathbf{B}_{\text{power}}(\theta) = \mathbf{w}_p^H [\mathbf{u}^*(\theta) \otimes \mathbf{u}(\theta)]$. Equation (21) means that, though the incident interferences are originally assumed uncorrelated, after the difference coarray processing, they are represented by their powers vector \mathbf{p} which consists of the powers σ_i^2 in (14) and they behave like fully coherent sources. Consequently the resulting covariance matrix of the observation vector $\hat{\mathbf{y}}$ will be of rank 1. For the fact that the classic minimum variance distortionless response (MVDR) technique yields poor performance when the jammers are coherent, so the MVDR cannot be applied directly on $\hat{\mathbf{y}}$ for the beamforming. To address this problem, we perform spatial smoothing on $\hat{\mathbf{y}}$ as follows.

- (i) First, we construct a new matrix \mathbf{U}_1 of size $((N^2 - 2)/2 + N + 2K) \times L$ from the $\mathbf{U}^* \oplus \mathbf{U}$, where the repeated rows (after their first occurrence) have been removed.
- (ii) The elements in \mathbf{U}_1 are sorted, so that the i th row corresponds to the sensor location $(N^2/4 + N/2 + K - 1 + i)d$ in the difference coarray of the original virtual array. This is equivalent to removing the corresponding rows from the observation vector $\hat{\mathbf{y}}$ and sorting them to get a new vector $\hat{\mathbf{y}}_1$ given by

$$\hat{\mathbf{y}}_1 = \mathbf{U}_1 \mathbf{p} + \frac{K}{M} \sigma_n^2 \tilde{\mathbf{e}}', \quad (22)$$

where $\tilde{\mathbf{e}}' \in \mathbb{R}^{(2(N+K-1)-1) \times 1}$ is a vector of all zeros except a 1 at the $(N + K - 1)$ th position. After the sorting and replacement of repeated rows, the deterministic noise vector $\tilde{\mathbf{I}}_n$ in (14) has been changed to $\tilde{\mathbf{e}}'$ and the difference coarray of the original virtual array has equivalent elements located from $(-N^2/4 - N/2 - K + 1)d$ to $(N^2/4 + N/2 + K - 1)d$.

- (iii) We now divide this difference coarray into $(N^2/4 + N/2 + K)$ overlapping subarrays, each with $(N^2/4 + N/2 + K)$ elements, where the i th subarray has the elements corresponding to the $(N^2/4 + N/2 + K - 1 - i)$ th to $((N^2 - 2)/2 + N + 2K - 2 - i)$ th rows of $\hat{\mathbf{y}}_1$, which we denote by $\hat{\mathbf{y}}_{1i} = \mathbf{U}_{1i} \mathbf{p} + (K/M) \sigma_n^2 \mathbf{e}'_i$. The \mathbf{U}_{1i} is a $(N^2/4 + N/2 + K - 1) \times L$ matrix consisting of the $(N^2/4 + N/2 + K - 1 - i)$ th to $((N^2 - 2)/2 + N + 2K - 2 - i)$ th rows of \mathbf{U}_1 and \mathbf{e}'_i is a vector of all zeros except a 1 at the i th position. It is easy to prove that

$$\hat{\mathbf{y}}_{1i} = \mathbf{U}_{11} \Phi^{i-1} \mathbf{p} + \frac{K}{M} \sigma_n^2 \mathbf{e}'_i, \quad (23)$$

where

$$\begin{aligned}\Phi &= \begin{pmatrix} e^{-j(2\pi/\lambda)d \sin(\theta_1)} & & & \\ & e^{-j(2\pi/\lambda)d \sin(\theta_2)} & & \\ & & \ddots & \\ & & & e^{-j(2\pi/\lambda)d \sin(\theta_L)} \end{pmatrix}.\end{aligned}\quad (24)$$

- (iv) The covariance matrix of $\hat{\mathbf{y}}_{1i}$ is

$$\begin{aligned}\mathbf{R}_i &= E \{ \hat{\mathbf{y}}_{1i} \hat{\mathbf{y}}_{1i}^H \} \\ &= \mathbf{U}_{11} \Phi^{i-1} \mathbf{p} \mathbf{p}^H \Phi^{i-1H} \mathbf{U}_{11}^H + \frac{K^2}{M^2} \sigma_n^2 \mathbf{e}'_i \mathbf{e}'_i{}^H \\ &\quad + \frac{K}{M} \sigma_n^2 \mathbf{U}_{11} \Phi^{i-1} \mathbf{p} \mathbf{e}'_i{}^H + \frac{K}{M} \sigma_n^2 \mathbf{e}'_i \mathbf{p}^H \Phi^{i-1H} \mathbf{U}_{11}^H.\end{aligned}\quad (25)$$

The spatially smoothed covariance matrix \mathbf{R}_{ss} can then be obtained by taking the average of \mathbf{R}_i over all i :

$$\mathbf{R}_{ss} \triangleq \frac{1}{N + K - 1} \sum_{i=1}^{N+K-1} \mathbf{R}_i. \quad (26)$$

- (v) The \mathbf{R}_{ss} enables us to build a full rank covariance matrix which can be applied for performing MVDR beamforming on the received data of the joint phased-MIMO and nested-array. For instance, using the subarray with elements at nd , $n = 0, 1, \dots, (N^2/4 + N/2 + K - 1)$ as the reference subarray (we denote its steering vector as $\mathbf{a}_1(\theta)$), the MVDR beamform weighter can then be derived as

$$\mathbf{w}_p = \frac{\mathbf{R}_{ss}^{-1} \mathbf{a}_1(\theta_s)}{\mathbf{a}_1(\theta_s)^H \mathbf{R}_{ss}^{-1} \mathbf{a}_1(\theta_s)}. \quad (27)$$

Finally, the eigen decomposition of \mathbf{R}_{ss} is

$$\mathbf{R}_{ss} = \mathbf{E}_s \Lambda_s \mathbf{E}_s^H + \mathbf{E}_n \Lambda_n \mathbf{E}_n^H, \quad (28)$$

where the diagonal matrix Λ_s contains the L target eigenvalues and the columns of \mathbf{E}_s are the corresponding eigenvectors, while the diagonal matrix Λ_n contains the remaining $N^2/4 - N/2 + K - L$ eigenvalues and the columns of \mathbf{E}_n are the corresponding eigenvectors constructing the noise space. The DOA of targets can then be estimated from the peaks of the multiple signal classification (MUSIC) spectra

$$\mathbf{z}(\theta) = \frac{\mathbf{a}_1^H(\theta) \mathbf{a}_1(\theta)}{\mathbf{a}_1^H(\theta) \mathbf{P} \mathbf{a}_1(\theta)}, \quad (29)$$

where $\mathbf{P} = \mathbf{E}_n \mathbf{E}_n^H = \mathbf{I} - \mathbf{E}_s \mathbf{E}_s^H$ is the projection matrix onto the noise subspace.

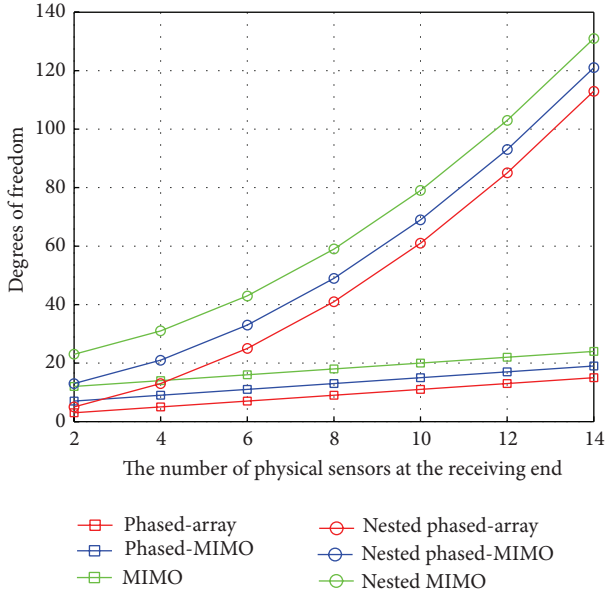


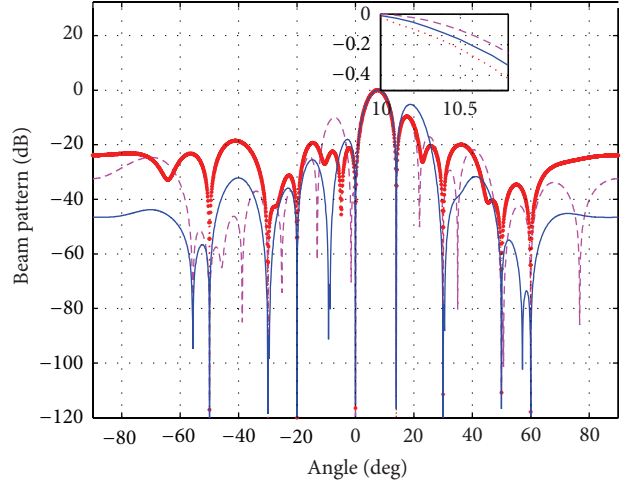
FIGURE 3: Comparative DOF versus sensors' number.

5. Simulation Results

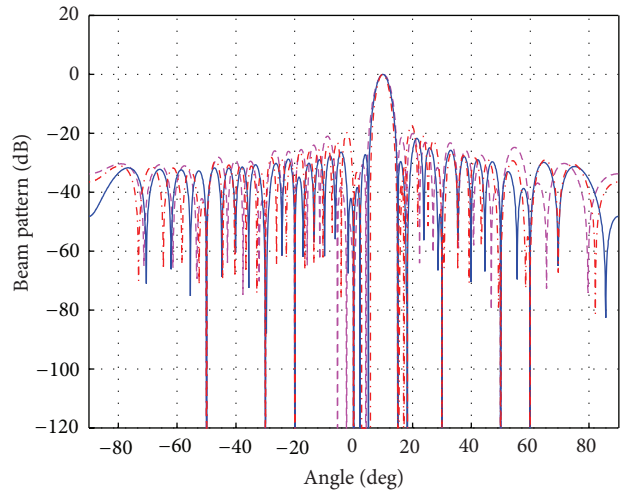
Throughout our simulations, we assume a ULA of $M = 10$ omnidirectional antennas used for transmitting the based-band waveforms $\{\phi_k(t) = Q(T_0)\exp^{j2\pi(k/T_0)t}\}_{k=1}^K$, where $Q(T_0) = \sqrt{1/T_0}$ and $K = 5$. $N = 10$ omnidirectional receiving phased-array elements are used in the simulations, except Example 2 where $N = 5$ is used. The additive Gaussian white noise is assumed to be zero-mean and unit-variance. All the statistical results are computed based on 300 independent runs.

5.1. DOF Comparison. Firstly, we would like to demonstrate the superior capability of the proposal which can provide a dramatic increase in the DOF. We compare the phased-MIMO technique with the phased-array and the MIMO radar when the nested-array structure is applied at the receiving end. According to the relationship concerning DOF and the number of sensors obtained in Section 2, the notable difference can be shown in Figure 3. It can be seen from the figure that the proposal obtains much more DOF than the traditional method. Moreover, as the number of physical sensors increases, the difference between proposal and the traditional method tends to increase. On the other hand, the MIMO radar exhibits DOF performance which is better than two other techniques. Because the transmit array of the MIMO radar is divided into M subarrays which is the most subarrays. The main drawback of MIMO radar is that it sacrifices the coherent processing gain as compared to phased-MIMO technique.

5.2. Adaptive Beamforming. Suppose a target of interest is located at 10° and eight interferences located at $\{-50^\circ, -30^\circ, -20^\circ, 0^\circ, 15^\circ, 30^\circ, 50^\circ, 60^\circ\}$. The target power is fixed to 0 dB



(a) Basic phased-MIMO



(b) Joint phased-MIMO and nested-array

FIGURE 4: Comparative MVDR beam pattern when $D = 8$.

while the interference power is fixed to 50 dB. Figure 4 compares the MVDR beam pattern between the basic phased-MIMO and our proposal of joint phased-MIMO and nested-array. The comparison between Figures 4(a) and 4(b) suggests that our proposal yields significant performance improvements such as much narrower main beamwidth and lower sidelobe levels. From the amplifying subgraph in Figure 4(a), we can see that there are some difference for the width of the main lobe among the three different techniques. Also, we can notice that both of the MIMO ($K = M = 10$) and phased-MIMO ($K = 5$) offer lower sidelobe levels than the phased-array ($K = 1$). More importantly, our proposal can offer more notches. This means that more interferences can be effectively suppressed or more targets can be identified.

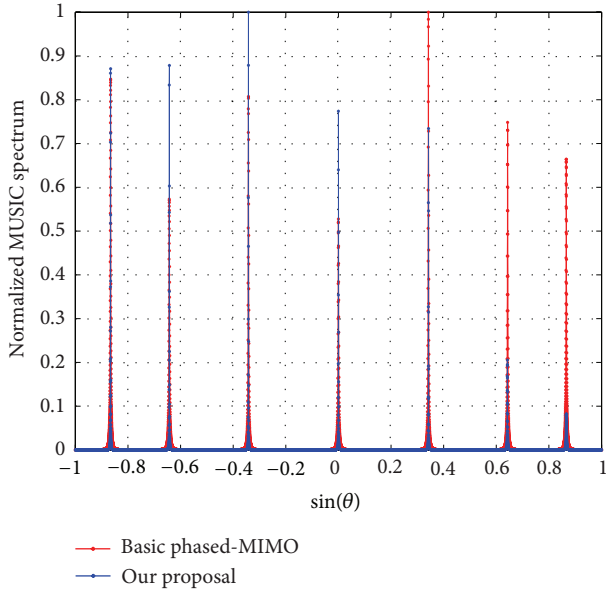


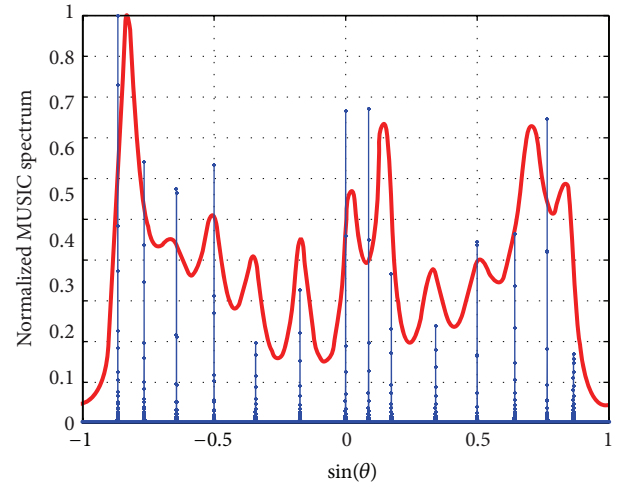
FIGURE 5: Comparative MUSIC spectra when $L = 7$.

5.3. DOA Estimation. Here, we provide two examples to show the superior performance of our proposal.

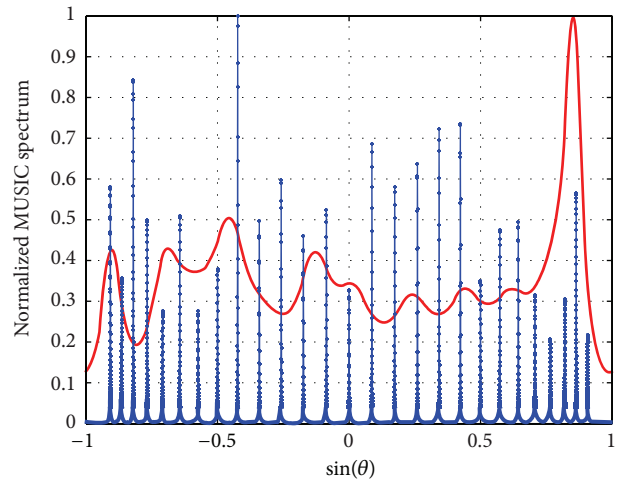
Example 1. Consider $N = 10$. First, we consider 7 sources with the DOAs of $\{-60^\circ, -40^\circ, -20^\circ, 0^\circ, 20^\circ, 40^\circ, 60^\circ\}$ and the signal-to-noise (SNR) is assumed to be 0 dB. Figure 5 compares the MUSIC spectra of our proposal to the basic phased-MIMO. We can see that both of them can resolve the 7 targets clearly. This is because they can resolve up to $(N + K - 1)$ and $(N^2/4 + N/2 + K - 1)$ sources, respectively. Therefore, our proposal can resolve more sources. For instance, Figure 6 compares the MUSIC spectra when there are $L = 14$ and $L = 27$ sources, respectively. Obviously, the basic phased-MIMO fails to detect many sources, but our proposal reveals a superior performance with more clearly discernible peaks of the MUSIC spectra.

Example 2. Consider $N = 5$. Furthermore, we consider an alternative receive array by reducing the $N = 10$ elements to $N = 5$ elements. The elements are arranged as Figure 7, where the receiving elements are located in receiver as a vector $[1, 0, 1, 0, 0, 1, 0, 0, 1, 1]$. Here 1 means that the antenna with an index corresponding to the location of that 1 in the vector belongs to the receive array while 0 means it does not. Suppose also that there are 7 targets with the DOAs of $\{-60^\circ, -40^\circ, -20^\circ, 0^\circ, 20^\circ, 40^\circ, 60^\circ\}$. Figure 8 compares this alternative arrangement with the basic phased-MIMO that still keeps the $N = 10$ elements in the receiver (see Figure 2). It is noticed that both of the two arrangements can resolve the 7 sources sufficiently well, but our proposal uses only 5 elements in the receiver whereas 10 elements are used in the basic phased-MIMO to get an equivalent performance.

It is necessary to analyze the RMSE performance. Suppose there is one source located at 30° . The system parameters



(a) $L = 14$



(b) $L = 27$

FIGURE 6: DOF comparisons in MUSIC spectra.

used in Examples 1 and 2 are simulated, respectively. Their comparative RMSE versus SNR results are given in Figures 9 and 10. We can see that our proposal achieves much better performance than the basic phased-MIMO.

6. Conclusion

In this paper, we propose a joint phased-MIMO and nested-array for increased DOFs to resolve more sources. The essence of the proposal is to apply the difference coarray processing to the joint phased-MIMO and nested-array to generate more virtual array elements. Additionally, a spatial

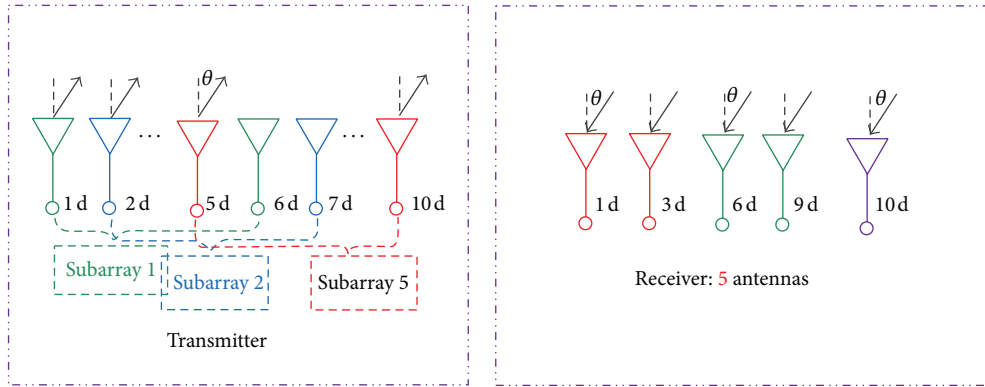


FIGURE 7: Alternative receiving array with 5 elements for joint phased-array and nested-array.

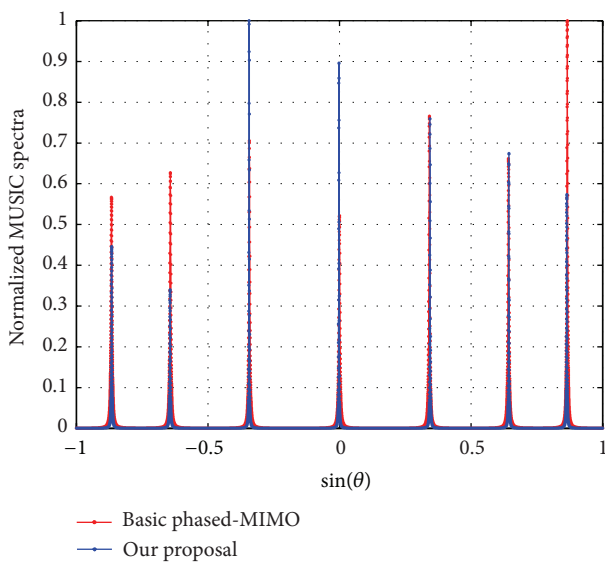


FIGURE 8: Comparative MUSIC spectra for the alternative receiving array.

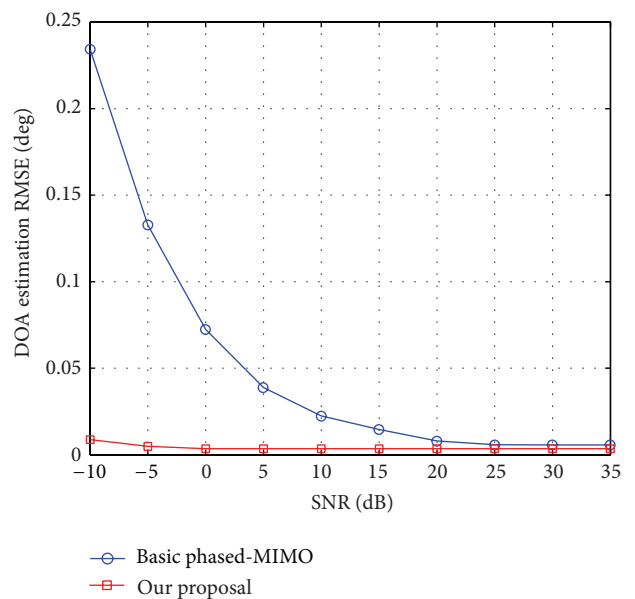


FIGURE 9: Comparative RMSE versus SNR for Example 1.

smoothing algorithm is used to overcome the interference coherent problem in the difference coarray data. Extensive simulation results show that our proposal allows to achieve more DOFs and better source localization performance. Meanwhile, our proposal yields superior DOA estimation RMSE performance. In our proposed design, the real array element spacing is integer multiple of half-wavelength. The spacing is implementable in practical array systems. However, coupling is ignored in the algorithm development. As a future work, we will study the coupling effects and other physical realizability issues. Another research direction is to extend the linear array to other arrays.

Conflict of Interests

The authors declare that there is no conflict of interests regarding the publication of this paper.

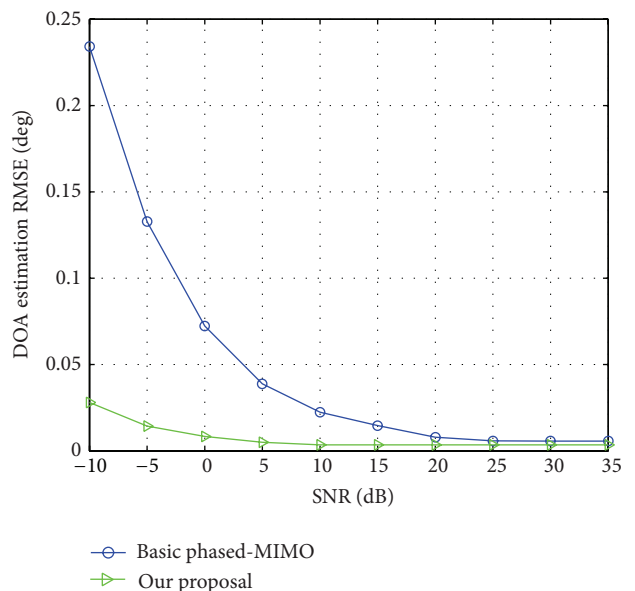


FIGURE 10: Comparative RMSE versus SNR for Example 2.

Acknowledgments

The work described in this paper was supported by the National Natural Science Foundation of China under Grant 41101317, the Program for New Century Excellent Talents in University under Grant NCET-12-0095, and Sichuan Province Science Fund for Distinguished Young Scholars under Grant 2013JQ0003.

References

- [1] C. Redondo and L. de Haro, "On the analysis and design of reconfigurable multimode MIMO microstrip antennas," *IEEE Transactions on Antennas and Propagation*, vol. 62, no. 1, pp. 119–129, 2014.
- [2] W.-Q. Wang, "Large-area remote sensing in high-altitude high-speed platform Using MIMO SAR," *IEEE Journal of Selected Topics in Applied Earth Observations and Remote Sensing*, vol. 6, no. 5, pp. 2146–2158, 2013.
- [3] L. Liu, S. W. Cheung, and T. I. Yuk, "Compact MIMO antenna for portable devices in UWB applications," *IEEE Transactions on Antennas and Propagation*, vol. 61, no. 8, pp. 4257–4264, 2013.
- [4] O. N. Alrabadi, J. Perruisseau-Carrier, and A. Kalis, "MIMO transmission using a single RF source: theory and antenna design," *IEEE Transactions on Antennas and Propagation*, vol. 60, no. 2, pp. 654–664, 2012.
- [5] M. Webb, M. Q. Yu, and M. Beach, "Propagation characteristics, metrics, and statistics for virtual MIMO performance in a measured outdoor cell," *IEEE Transactions on Antennas and Propagation*, vol. 59, no. 1, pp. 236–244, 2011.
- [6] W.-Q. Wang, "Virtual antenna array analysis for MIMO synthetic aperture radars," *International Journal of Antennas and Propagation*, vol. 2012, Article ID 587276, 10 pages, 2012.
- [7] M. Contu and P. Lombardo, "Sidelobe control for a MIMO radar virtual array," in *Proceedings of the IEEE Radar Conference*, pp. 1–6, Ottawa, Canada, May 2013.
- [8] S. Sugiura, "Coherent versus non-coherent reconfigurable antenna aided virtual MIMO systems," *IEEE Signal Processing Letters*, vol. 21, no. 4, pp. 390–394, 2014.
- [9] A. Hassanien and S. A. Vorobyov, "Phased-MIMO radar: a tradeoff between phased-array and MIMO radars," *IEEE Transactions on Signal Processing*, vol. 58, no. 6, pp. 3137–3151, 2010.
- [10] D. R. Fuhrmann, J. P. Browning, and M. Rangaswamy, "Signaling strategies for the hybrid MIMO phased-array radar," *IEEE Journal on Selected Topics in Signal Processing*, vol. 4, no. 1, pp. 66–78, 2010.
- [11] H. Li and B. Himed, "Transmit subaperturing for MIMO radars with co-located antennas," *IEEE Journal on Selected Topics in Signal Processing*, vol. 4, no. 1, pp. 55–65, 2010.
- [12] W.-Q. Wang and H. C. So, "Transmit subaperturing for range and angle estimation in frequency diverse array radar," *IEEE Transactions on Signal Processing*, vol. 62, no. 8, pp. 2000–2011, 2014.
- [13] S. U. Pillai, Y. B. Ness, and F. Haber, "A new approach to array geometry for improved spatial spectrum estimation," *Proceedings of the IEEE*, vol. 73, no. 10, pp. 1522–1524, 1985.
- [14] A. Moffet, "Minimum-redundancy linear arrays," *IEEE Transactions on Antennas and Propagation*, vol. 16, no. 2, pp. 172–175, 1968.
- [15] J. Dong, Q. X. Li, and W. Guo, "A combinatorial method for antenna array design in minimum redundancy MIMO radars," *IEEE Antennas and Wireless Propagation Letters*, vol. 8, pp. 1150–1153, 2009.
- [16] G. Oliveri, F. Caramanica, M. D. Migliore, and A. Massa, "Synthesis of nonuniform MIMO arrays through combinatorial sets," *IEEE Antennas and Wireless Propagation Letters*, vol. 11, no. 11, pp. 728–731, 2012.
- [17] W. Roberts, L. Z. Xu, J. Li, and P. Stoica, "Sparse antenna array design for MIMO active sensing applications," *IEEE Transactions on Antennas and Propagation*, vol. 59, no. 3, pp. 846–858, 2011.
- [18] N. Hu, Z. F. Ye, X. Xu, and M. Bao, "DOA estimation for sparse array via sparse signal reconstruction," *IEEE Transactions on Aerospace and Electronic Systems*, vol. 49, no. 2, pp. 760–773, 2013.
- [19] L. F. Yepes, D. H. Covarrubias, M. A. Alonso, and R. Ferrus, "Hybrid sparse linear array synthesis applied to phased antenna arrays," *IEEE Antennas and Wireless Propagation Letters*, vol. 13, pp. 185–188, 2014.
- [20] A. A. Khan and A. K. Brown, "Null steering in irregularly spaced sparse antenna arrays using aperture distributed subarrays and hybrid optimiser," *IET Microwaves, Antennas and Propagation*, vol. 8, no. 2, pp. 86–92, 2014.
- [21] O. M. Bucci, T. Isernia, and A. F. Morabito, "An effective deterministic procedure for the synthesis of shaped beams by means of uniform-amplitude linear sparse arrays," *IEEE Transactions on Antennas and Propagation*, vol. 61, no. 1, pp. 169–175, 2013.
- [22] L. Cen, Z. L. Yu, W. Ser, and W. Cen, "Linear aperiodic array synthesis using an improved genetic algorithm," *IEEE Transactions on Antennas and Propagation*, vol. 60, no. 2, part 2, pp. 895–902, 2012.
- [23] G. Oliveri and A. Massa, "Genetic algorithm (GA)-enhanced almost difference set (ADS)-based approach for array thinning," *IET Microwaves, Antennas & Propagation*, vol. 5, no. 3, pp. 305–315, 2011.
- [24] L. Carin, D. H. Liu, and B. Guo, "Coherence, compressive sensing, and random sensor arrays," *IEEE Antennas and Propagation Magazine*, vol. 53, no. 4, pp. 28–39, 2011.
- [25] S. Holm, B. Elgetun, and G. Dahl, "Properties of the beam-pattern of weight- and layout-optimized sparse arrays," *IEEE Transactions on Ultrasonics, Ferroelectrics, and Frequency Control*, vol. 44, no. 5, pp. 983–991, 1997.
- [26] G. Oliveri, M. Carlin, and A. Massa, "Complex-weight sparse linear array synthesis by Bayesian compressive sampling," *IEEE Transactions on Antennas and Propagation*, vol. 60, no. 5, pp. 2309–2326, 2012.
- [27] F. Viani, G. Oliveri, and A. Massa, "Compressive sensing pattern matching techniques for synthesizing planar sparse arrays," *IEEE Transactions on Antennas and Propagation*, vol. 61, no. 9, pp. 4577–4587, 2013.
- [28] G. Oliveri and A. Massa, "ADS-based array design for 2-D and 3-D ultrasound imaging," *IEEE Transactions on Ultrasonics, Ferroelectrics, and Frequency Control*, vol. 57, no. 7, pp. 1568–1582, 2010.
- [29] P. Pal and P. P. Vaidyanathan, "Nested arrays: a novel approach to array processing with enhanced degrees of freedom," *IEEE Transactions on Signal Processing*, vol. 58, no. 8, pp. 4167–4181, 2010.

- [30] P. Pal and P. P. Vaidyanathan, "A novel array structure for directions-of-arrival estimation with increased degrees of freedom," in *Proceedings of the IEEE International Conference on Acoustics, Speech, and Signal Processing (ICASSP '10)*, pp. 2606–2609, IEEE, Dallas, Tex, USA, March 2010.
- [31] P. Pal and P. P. Vaidyanathan, "Beamforming using passive nested arrays of sensors," in *Proceedings of the IEEE International Symposium on Circuits and Systems: Nano-Bio Circuit Fabrics and Systems (ISCAS '10)*, pp. 2840–2843, Paris, France, June 2010.
- [32] R. T. Hoctor and S. A. Kassam, "Unifying role of the coarray in aperture synthesis for coherent and incoherent imaging," *Proceedings of the IEEE*, vol. 78, no. 4, pp. 735–752, 1990.
- [33] D. Nion and N. D. Sidiropoulos, "A PARAFAC-based technique for detection and localization of multiple targets in a MIMO radar system," in *Proceedings of the IEEE International Conference on Acoustics, Speech, and Signal Processing (ICASSP '09)*, pp. 2077–2080, Taipei, Taiwan, April 2009.
- [34] W.-Q. Wang, "Phased-MIMO radar with frequency diversity for range-dependent beamforming," *IEEE Sensors Journal*, vol. 13, no. 4, pp. 1320–1328, 2013.

Research Article

Multitarget Direct Localization Using Block Sparse Bayesian Learning in Distributed MIMO Radar

Bin Sun, Haowen Chen, Xizhang Wei, and Xiang Li

School of Electronic Science and Engineering, National University of Defense Technology, Changsha, Hunan 410073, China

Correspondence should be addressed to Bin Sun; sunbin0616@gmail.com

Received 16 April 2014; Revised 14 August 2014; Accepted 22 August 2014

Academic Editor: Michelangelo Villano

Copyright © 2015 Bin Sun et al. This is an open access article distributed under the Creative Commons Attribution License, which permits unrestricted use, distribution, and reproduction in any medium, provided the original work is properly cited.

The target localization in distributed multiple-input multiple-output (MIMO) radar is a problem of great interest. This problem becomes more complicated for the case of multitarget where the measurement should be associated with the correct target. Sparse representation has been demonstrated to be a powerful framework for direct position determination (DPD) algorithms which avoid the association process. In this paper, we explore a novel sparsity-based DPD method to locate multiple targets using distributed MIMO radar. Since the sparse representation coefficients exhibit block sparsity, we use a block sparse Bayesian learning (BSBL) method to estimate the locations of multitarget, which has many advantages over existing block sparse model based algorithms. Experimental results illustrate that DPD using BSBL can achieve better localization accuracy and higher robustness against block coherence and compressed sensing (CS) than popular algorithms in most cases especially for dense targets case.

1. Introduction

Multiple-input multiple-output (MIMO) radar study has received considerable attention over the past few years [1–7]. MIMO radar is typically used in two antenna configurations, namely, colocated [1, 2] and distributed [3, 4]. Colocated MIMO radar with closely spaced antennas exploits the waveform diversity and increased degrees of freedom (DOF) to obtain better angular resolution due to the virtual aperture [1]. The proximity of the antenna arrays allows considering the same target response for each transmitter-receiver pair [8]. Unlike colocated MIMO radar, distributed MIMO radar exploits angular diversity by capturing information from different aspect angles of target with widely spaced antennas [3] and supports accurate target location and velocity estimation [9]. In distributed MIMO radar, targets display different radar cross-sections (RCS) in different transmit-receive channels, and thus better detection performance is ensured by averaging the target scintillations from different angles [3]. In this paper, we are concerned with solving multiple stationary targets localization problem using distributed MIMO radar.

Location estimation technique is one important problem for MIMO radar systems due to its great potential to

enable different kinds of localization applications. The traditional approach to solve the localization problem consists of a two-step procedure. The signal parameters such as direction of arrival (DOA), time of arrival (TOA), and time difference of arrival (TDOA) are estimated firstly at several receivers independently and then the coordinates of targets are calculated by exploiting the explicit geometric relationship. The authors in [10, 11] studied target localization with MIMO radar systems by utilizing bistatic TOA for multilateration and the Cramér-Rao bound (CRB) for the target localization accuracy was derived. It has been shown that localization by coherent MIMO radar provides significantly better performance than noncoherent processing where the phase information is ignored. Coherent processing, however, entails the challenge of ensuring multisite systems phase synchronization [12] and the impact of static phase errors at the transmitters and receivers over the CRB has been well analyzed [13, 14]. Literature [15] has demonstrated that even the noncoherent MIMO radar provides significant performance improvement over a monostatic phased array radar with high range and azimuth resolutions. Although most publications on localization algorithms concentrate on the two-step method, it is suboptimal in general [16].

The problem becomes more complicated and challenging for multiple dense targets scenario using the method given in [11], where parameters as TOAs should be assigned to the correct targets, which is called ‘‘Data Association’’ [17] and it is an important problem especially for multiple target applications. A multiple-hypothesis- (MH-) based algorithm for multitarget localization was proposed to estimate the number and states of targets [18].

On the contrary, the direct position determination (DPD) method suggested by Weiss in [16] and Bar-Shalom and Weiss in [19] does not need intermediate parameters as DOAs or TOAs. The position estimates of interest are obtained directly by minimizing a cost function using the grid-search method, which can improve the estimation accuracy with respect to the two-step method. A maximum likelihood (ML) based DPD method dealing with one moving target is developed [20]. Moreover, the DPD method can provide superior localization capability in the context of multitarget scenarios since the data association step is avoided. Despite these advantages, the DPD method did not receive enough attention due to its intensive computation load. Recently, sparsity-based representation DPD framework is exploited for target/source localization problem. In fact, since the number of unknown targets is small in the radar scene, it can be modeled as an ideal sparse vector in the localization problem. Therefore, sparse modeling for distributed MIMO radar is firstly presented in [21] and the location estimates can be obtained by searching for the block sparse solution of underdetermined model using block matching pursuit (BMP) method. In [22], the multisource localization problem using TDOA measurements is formulated to be a sparse recovery problem and the problem of the data association and multisource localization is solved in a joint fashion. The method of block sparse Bayesian learning (BSBL) method in [23] motivates us to consider its application to multitarget localization problem in distributed MIMO radar. By exploiting the intrablock correlation, BSBL can achieve a superior performance over other algorithms for off-grid DOA estimation [24]. Simulation results showed that the BSBL method significantly outperforms competitive algorithms in different experiments.

In this paper, motivated by [21], we propose to apply the BSBL algorithm [23] for solving multitarget direct localization problem by employing block sparse modeling and we demonstrate the superiority of BSBL for multitarget localization problem through sufficient numerical experiments from many aspects. Specifically, we demonstrate the robustness of BSBL against compressed sampling and capability of dealing with dense targets localization. The effect of parameter estimation based on the off-grid model is also shown.

The remainder of the paper is organized as follows. We introduce the signal model for a distributed MIMO radar and formulate the block sparse representation of signal in Section 2. In Section 3, we review existing sparse recovery algorithms for this problem. Then, the sparsity-aware multitarget localization using BSBL is presented in Section 4. The comparison of performance based on Monte Carlo simulations is shown in Section 5. Finally, concluding remarks and future work are addressed in Section 6.

Notations used in this paper are as follows. Boldface letters are reserved for vectors and matrices. $\|\cdot\|_1$ and $\|\cdot\|_2$ denote the ℓ_1 norm and ℓ_2 norm, respectively. $|\mathbf{A}|$, $\text{Tr}(\mathbf{A})$ are the determinant and trace of a matrix \mathbf{A} , respectively. $\text{diag}\{\mathbf{A}_1, \dots, \mathbf{A}_g\}$ denotes a block matrix with principal diagonal blocks being the $\mathbf{A}_1, \dots, \mathbf{A}_g$ in turn. $\mathbf{v} \geq \mathbf{0}$ means each elements in the vector \mathbf{v} is nonnegative. $\mathbf{1}_M$ denotes $M \times 1$ vector of all ones and \mathbf{I}_M denotes $M \times M$ identity matrix.

2. Signal Model

Consider a distributed MIMO radar network consisting of M_T transmitters, located at $\{\mathbf{t}_m = [x_m^t, y_m^t]\}_{m=1}^{M_T}$, M_R receivers, located at $\{\mathbf{r}_l = [x_l^r, y_l^r]\}_{l=1}^{M_R}$, and K targets, located at $\{\mathbf{p}_k = [x_k, y_k]\}_{k=1}^K$ in a two-dimensional (2D) plane. Without loss of generality, we can extend the analysis in this paper to the three-dimensional (3D) case. A set of orthogonal narrow-band waveforms $\{s_m(\hat{t})\}_{m=1}^{M_T}$ are transmitted from different transmitters where \hat{t} denotes the fast time. Suppose that the m th transmitter generates a linearly frequency-modulated (LFM) signal

$$s_m(\hat{t}) = \text{rect}\left(\frac{\hat{t}}{T_p}\right) \exp\left(j2\pi\left(f_m\hat{t} + \frac{1}{2}\mu\hat{t}^2\right)\right), \quad (1)$$

where

$$\text{rect}\left(\frac{\hat{t}}{T_p}\right) = \begin{cases} 1, & |\hat{t}| \leq \frac{T_p}{2}, \\ 0, & \text{otherwise} \end{cases} \quad (2)$$

denotes the window function, $j = \sqrt{-1}$, $\mu = B/T_p$ is the chirp rate, B represents the bandwidth, T_p denotes the pulse duration, and f_m is the carrier frequency of the m th transmitter. Further, we assume that the cross correlations between these waveforms are close to zeros for different delays; namely,

$$\int_{-\infty}^{\infty} s_m(\hat{t}) s_k^*(\hat{t} - \tau) dt = 0, \quad \forall m \neq k, \tau, \quad (3)$$

where $(\cdot)^*$ denotes the conjugate operator. Let α_{ml}^k denote the complex RCS value corresponding to the k th target between the m th transmitter and the l th receiver and each target is modeled as a collection of $M_T M_R$ various reflection coefficients. In this work, we are interested in Rician target model [25], which describes one dominant scatterer together with a number of small scatterers, and target returns are assumed to be deterministic and unknown.

For coherent processing, we obtain the bandpass signal arriving at the l th receiver taking account of the phase errors as

$$y_l(\hat{t}) = \sum_{k=1}^K \sum_{m=1}^{M_T} \alpha_{ml}^k \exp(j\theta_m^t + j\theta_l^r) \text{rect}\left(\frac{\hat{t} - \tau_{ml}^k}{T_p}\right) \times \exp\left(j2\pi\left(f_m(\hat{t} - \tau_{ml}^k) + \frac{1}{2}\mu(\hat{t} - \tau_{ml}^k)^2\right)\right) + \varepsilon_l(\hat{t}), \quad (4)$$

where τ_{ml}^k is the time delay corresponding to the k th target in the (m, l) th transmit-receive pair

$$\tau_{ml}^k = \frac{1}{c} \left(\|\mathbf{p}^k - \mathbf{t}_m\|_2 + \|\mathbf{p}^k - \mathbf{r}_l\|_2 \right), \quad (5)$$

and c is the speed of the propagation of the wave in the medium. θ_m^t and θ_l^r in (4) denote the phase error induced by the m th transmitter or l th receiver, respectively. The noise $\varepsilon_i(t)$ is assumed to be complex Gaussian with power spectral density (PSD) σ_ε^2 and is assumed to be independent for different l .

The received signals at each receiver can be decomposed by a bank of M_T matched filters. Then we take N samples within a range bin T_g centered at τ_{ml}^0 in the (m, l) th transmit-receive pair as

$$\begin{aligned} y_{ml}(n) &= \sum_{k=1}^K \tilde{\alpha}_{mn}^k \text{rect} \left(\frac{nT_s - \tau_{ml}^0}{T_g} \right) \text{Sinc} \left(B \left(\hat{\tau}_{ml}^0 + nT_s - \tau_{ml}^k \right) \right) \\ &\quad \times \exp \left(-j2\pi f_m \tau_{ml}^k \right) + \varepsilon_{ml}(n), \\ m &= 1, \dots, M_T; \quad l = 1, \dots, M_R; \quad n = 1, \dots, N, \end{aligned} \quad (6)$$

where n and T_s denote the sample index and sampling interval, respectively, $\tau_{ml}^0 = 1/c(\|\mathbf{p}^0 - \mathbf{t}_m\|_2 + \|\mathbf{p}^0 - \mathbf{r}_l\|_2)$, $\mathbf{p}^0 = [x^0, y^0]$ is selected as the center of K targets, $\hat{\tau}_{ml}^0$ is the sampling start time of corresponding range gate, and $\varepsilon_{ml}(n)$ is the noise component at the output of the matched filter. Note that unknown phase errors are absorbed in the unknown reflection coefficient as $\tilde{\alpha}_{mn}^k \triangleq \alpha_{mn}^k \exp(j\theta_m^t + j\theta_l^r)$. Plus, the waveform term s_m is no longer present in this equation as it is integrated out of the matched filter being a sinc function. This model is more practical than that in [21] by taking account of the effect of sampling deviation from the location of peaks.

We discretize the planar area into a grid of uniform cells where each of the targets is located at one of the cells. If there are K targets in the area and is given a fine grid of G cells such that the cell's occupancy is exclusive, the distribution of the targets in the plane is sparse; that is, out of G cells only $K \ll G$ contain the targets. This implies the spatial sparsity model as depicted in Figure 1. Denoting the signal attributed to the target located at cell g at sample index n as $\mathbf{w}^g(n)$ and concatenating the signals corresponding to each cells, the signal vector coming from all the 2D plane can be formed as $\mathbf{w}(n) = [(\mathbf{w}^1(n))^T, \dots, (\mathbf{w}^G(n))^T]^T$, where $\{\mathbf{w}^g(n)\}_{g=1}^G \in \mathbb{C}^{M_T M_R \times 1}$ and $[\cdot]^T$ stands for the transpose operator. Further, $\mathbf{w}^g(n)$ is defined as

$$w_{ml}^g(n) = \begin{cases} \tilde{\alpha}_{ml}^k, & k\text{th target is at grid } g \\ 0, & \text{otherwise.} \end{cases} \quad (7)$$

There are $M_T M_R$ reflection coefficients corresponding to the one particular cell where the target is located and there are only $K \ll G$ targets. We characterize sparsity with such structure as block sparsity. Figure 1 illustrates the particular block sparsity model exhibited in representation of signals coming from all over the grid as described above.

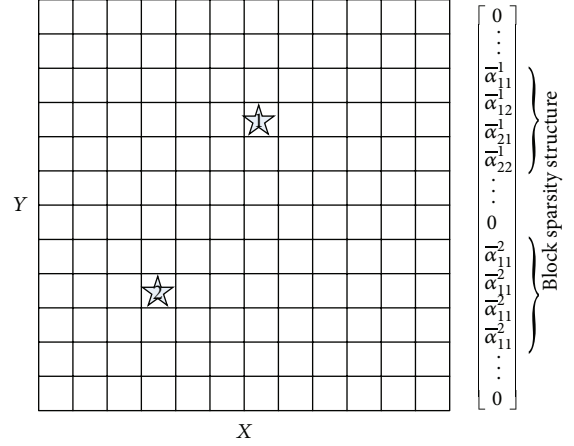


FIGURE 1: The spatial sparsity of the targets inside the area is illustrated through discretization of the area into a grid of G cells. The targets occupy only two cells marked as 1 and 2. Hence, the spatial representation of the target reflection coefficients is sparse. We can see that support of \mathbf{w} exhibits the block sparsity structure as there are only two blocks of nonzero elements corresponding to the two targets. The size of each block is the number of transmit-receive pairs.

For the coherent processing, the dictionary elements at the g th grid at sample index n in the (m, l) th pair is given as

$$\begin{aligned} \Psi_{ml}^g(n) &= \text{rect} \left(\frac{nT_s - \tau_{ml}^0}{T_g} \right) \text{Sinc} \left(B \left(\hat{\tau}_{ml}^0 + nT_s - \tau_{ml}^g \right) \right) \\ &\quad \times \exp \left(-j2\pi f_m \tau_{ml}^g \right). \end{aligned} \quad (8)$$

The dictionary $\{\Psi(n)\}_{n=1}^N \in \mathbb{C}^{M_T M_R \times G M_T M_R}$ is partitioned accordingly into

$$\Psi(n) = [\Psi^1(n), \Psi^2(n), \dots, \Psi^G(n)], \quad n = 1, \dots, N, \quad (9)$$

where

$$\begin{aligned} \Psi^g(n) &= \text{diag} \{ \Psi_{1l}^g(n), \dots, \Psi_{M_T M_R}^g(n) \}, \quad g = 1, \dots, G, \\ \Psi_l^g(n) &= \text{diag} \{ \Psi_{1l}^g(n), \dots, \Psi_{M_T l}^g(n) \}, \quad l = 1, \dots, M_R. \end{aligned} \quad (10)$$

Further, we arrange $\mathbf{y}_{ml}(n)$ ($m = 1, \dots, M_T; l = 1, \dots, M_R$) and $\varepsilon_{ml}(n)$ ($m = 1, \dots, M_T; l = 1, \dots, M_R$) in (6) into $M_T M_R$ dimensional column vectors $\mathbf{y}(n)$ and $\boldsymbol{\varepsilon}(n)$, respectively. Therefore, we can express the received vector at n as

$$\mathbf{y}(n) = \Psi(n) \mathbf{w}(n) + \boldsymbol{\varepsilon}(n), \quad n = 1, \dots, N, \quad (11)$$

where $\mathbf{w}(n)$ is a block sparse vector with only K nonzero blocks and each block containing $M_T M_R$ entries. We have expressed our observed data at n using sparse representation. It is further assumed that the target reflection coefficients remain constant across the range bin. In order to make the model more concise, we stack $\{\mathbf{y}(n)\}_{n=1}^N$, $\{\boldsymbol{\varepsilon}(n)\}_{n=1}^N$, and

$\{\Psi(n)\}_{n=1}^N$ into $\mathbf{y} = [(\mathbf{y}(1))^T, \dots, (\mathbf{y}(N))^T]^T$, $\boldsymbol{\varepsilon} = [(\boldsymbol{\varepsilon}(1))^T, \dots, (\boldsymbol{\varepsilon}(N))^T]^T$, and $\Psi = [(\Psi(1))^T, \dots, (\Psi(N))^T]^T$ to obtain sparse representation as

$$\mathbf{y} = \Psi \mathbf{w} + \boldsymbol{\varepsilon}, \quad (12)$$

where $\boldsymbol{\varepsilon} \in \mathbb{C}^{NM_T M_R \times 1}$, $\mathbf{y} \in \mathbb{C}^{NM_T M_R \times 1}$, and $\mathbf{w} \in \mathbb{C}^{GM_T M_R \times 1}$.

Note that, in the above expression for the measurement vector, $\Psi \in \mathbb{C}^{NM_T M_R \times GM_T M_R}$ is known and only \mathbf{w} depends on the actual targets present in the illuminated area. The nonzero entries of \mathbf{w} represent the target RCS values and the corresponding indices determine the positions. We assume that the number of targets K is unknown. The problem of target localization is therefore turned into sparse vector recovery problem. Recovery methods for block sparse signals will be addressed in the next section.

3. Existing Sparse Support Recovery

In the previous section, we have expressed that the signal received across M_R receive antennas over N snapshots using sparse representation. In order to find the locations of the targets, we need to recover the sparse vector \mathbf{w} from the measurements \mathbf{y} . Since the sampling number N is much smaller than the grid number G , the inversion of (12) is an ill-posed problem. In addition, \mathbf{w} has block/group structure. The exact sparsity of the signal \mathbf{w} denoted by $\|\mathbf{w}\|_0$, that is, the ℓ_0 norm of \mathbf{w} , is equal to the number of nonzero elements in \mathbf{w} and is employed to get the inversion of (12). Then, the signal vector can be obtained by solving the following optimization problem:

$$\hat{\mathbf{w}} = \arg \min_{\mathbf{w}} \left\{ \|\mathbf{y} - \Psi \mathbf{w}\|_2^2 + \beta \|\mathbf{w}\|_0 \right\}, \quad (13)$$

where β is the regularization factor proportional to the noise level. The optimization problem requires combinatorial search and is widely known as NP-hard. In order to simplify the optimization problem, some convex relaxation is often made. The most extensively used one is the ℓ_1 -norm relaxation as follows:

$$\hat{\mathbf{w}} = \arg \min_{\mathbf{w}} \left\{ \|\mathbf{y} - \Psi \mathbf{w}\|_2^2 + \beta \|\mathbf{w}\|_1 \right\}. \quad (14)$$

Since (13) is nonconvex, matching pursuit (MP) and orthogonal MP are preferred. The aforementioned two methods use a greedy strategy that iteratively selects the basis vector. After ℓ_1 -norm relaxation, many methods, such as basis pursuit (BP) denoising, least absolute shrinkage, and selection operator (LASSO), and gradient projection for sparse reconstruction can be used to find the solution. These algorithms recover sparse vectors but do not exploit the knowledge of the block sparsity. It is known that exploiting such block partition property can further improve recovery performance. Recently, block-MP (BMP) algorithm has been proposed [26] which exploits the knowledge of block sparsity.

Nevertheless, the BMP algorithm is effective on noiseless scenarios. In practice, measurements are inevitably contaminated with noise and underlying uncertainties. Besides, the

performance of the sparsity based estimation approaches is determined by the correlations between columns of the dictionary matrix Ψ and the distance between the adjacent grids. High dictionary coherence can potentially disrupt BMP or Group-Lasso algorithms [27]. More importantly, one should note that when one target belongs to the g th grid, not only the target reflection coefficient block \mathbf{w}_g is a nonzero block, but also its elements are correlated in amplitude. The correlation arises because the coefficients of the g th grid are belonging to the same target, and thus the elements in \mathbf{w}_g are mutually dependent. It is shown that exploiting the correlation within blocks can further improve the estimation quality of $\hat{\mathbf{w}}$ [23].

Therefore, in this paper we propose to use BSBL [23] to estimate $\hat{\mathbf{w}}$ by exploiting the block structure and the correlation within blocks. In the next section we briefly introduce BSBL and its algorithm.

4. Block SBL Based Target Localization

This section briefly describes the BSBL framework and corresponding algorithm.

4.1. BSBL Framework. BSBL is an extension of the basic SBL framework, which exploits a block structure and intrablock correlation in the coefficient vector \mathbf{w} . It is based on the assumption that \mathbf{w} can be partitioned into G nonoverlapping blocks as

$$\mathbf{w} = \left[\underbrace{w_1^1, \dots, w_d^1}_{(\mathbf{w}^1)^T}, \dots, \underbrace{w_1^G, \dots, w_d^G}_{(\mathbf{w}^G)^T} \right]^T. \quad (15)$$

For sparse model in this paper, $d = M_T M_R$. Then, each block $\mathbf{w}^g \in \mathbb{C}^{d \times 1}$ is assumed to satisfy a parameterized multivariate Gaussian distribution

$$p(\mathbf{w}^g; \nu_g, \mathbf{Q}_g) \sim \mathcal{CN}(\mathbf{0}, \nu_g \mathbf{Q}_g), \quad g = 1, \dots, G, \quad (16)$$

with the unknown parameters ν_g and \mathbf{Q}_g . Here ν_g is a non-negative parameter controlling the block sparsity of \mathbf{w} . When $\nu_g = 0$, the g th block becomes zero. During the learning procedure most ν_g tend to be zero, due to the mechanism of automatic relevance determination. Thus sparsity at the block level is encouraged. $\mathbf{Q}_g \in \mathbb{C}^{d \times d}$ is a positive definite and symmetrical matrix, capturing the intrablock correlation of the g th block. Under the assumption that blocks are mutually uncorrelated, the prior of \mathbf{w} is $p(\mathbf{w}; \{\nu_g, \mathbf{Q}_g\}_{g=1}^G) \sim \mathcal{CN}(\mathbf{0}, \boldsymbol{\Sigma}_0)$, where $\boldsymbol{\Sigma}_0 = \text{diag}\{\nu_1 \mathbf{Q}_1, \dots, \nu_G \mathbf{Q}_G\}$. Assume the noise vector $\boldsymbol{\varepsilon}$ satisfies $p(\boldsymbol{\varepsilon}; \lambda) \sim \mathcal{CN}(\mathbf{0}; \lambda \mathbf{I})$, where λ is a positive scalar to be estimated. Therefore the posterior of \mathbf{w} is given by

$$p(\mathbf{w} | \mathbf{y}; \lambda, \{\nu_g, \mathbf{Q}_g\}_{g=1}^G) = \mathcal{CN}(\boldsymbol{\mu}_w, \boldsymbol{\Sigma}_w) \quad (17)$$

with

$$\begin{aligned} \boldsymbol{\mu}_w &= \boldsymbol{\Sigma}_0 \Psi^T (\lambda \mathbf{I} + \Psi \boldsymbol{\Sigma}_0 \Psi^T)^{-1} \mathbf{y}, \\ \boldsymbol{\Sigma}_w &= \left(\boldsymbol{\Sigma}_0^{-1} + \frac{1}{\lambda} \Psi^T \Psi \right)^{-1}. \end{aligned} \quad (18)$$

Therefore, the estimate of \mathbf{w} can be directly obtained by using the the maximum a posteriori (MAP) estimation, providing all the parameters $\lambda, \{\nu_g, \mathbf{Q}_g\}_{g=1}^G$. The parameters $\lambda, \{\nu_g, \mathbf{Q}_g\}_{g=1}^G$ can be estimated by a Type II maximum likelihood procedure [28]. This is equivalent to minimizing the following cost function:

$$\begin{aligned} \mathcal{L}(\Theta) &\triangleq -2 \log \int p(\mathbf{y} | \mathbf{w}; \lambda) p(\mathbf{w}; \{\nu_g, \mathbf{Q}_g\}_g) d\mathbf{w} \\ &= \log |\lambda \mathbf{I} + \Psi \Sigma_0 \Psi^T| + \mathbf{y}^T (\lambda \mathbf{I} + \Psi \Sigma_0 \Psi^T)^{-1} \mathbf{y}, \end{aligned} \quad (19)$$

where $\Theta \triangleq \{\lambda, \{\nu_g, \mathbf{Q}_g\}_{g=1}^G\}$ denotes all the parameters. This framework is called the BSBL framework. The algorithm derived from this framework includes three learning rules, that is, the learning rules for ν_g , \mathbf{Q}_g , and λ . The correlation matrix \mathbf{Q}_g is modeled as a Toeplitz matrix. There are several optimization methods to minimize the cost function, such as the expectation-maximum (EM) method, the bound-optimization (BO) method, and the duality method.

4.2. Advantages of BSBL. Compared to Lasso-type algorithms (such as Group-Lasso based on ℓ_1 -minimization) and greedy algorithms (such as Group-MP based on ℓ_0 -minimization), BSBL has the following advantages.

- (1) BSBL provides large flexibility to model and exploit intrablock correlation structure in signals. By exploiting the correlation structures, recovery performance is significantly improved [29].
- (2) BSBL has the unique ability to find less-sparse and nonsparse true solutions with very small errors [30]. This is attractive for practical use, since in practice the true solutions may not be very sparse and existing sparse signal recovery algorithms generally fail in this case.
- (3) Its recovery performance is robust to the characteristics of the dictionary Ψ , while other algorithms are not. This advantage is very attractive to sparse representation and other applications, since in some applications there is a trade-off between the resolution (grid size) and the block coherence measure [21]. When the grid points come closer, the resolution is improved but blocks within Ψ are highly coherent.

Therefore, BSBL is promising for multitarget localization. In the following we choose the BSBL- ℓ_1 algorithm [23], which transforms the BSBL cost function from the ν space to the \mathbf{w} space by treating λ and \mathbf{Q}_g as regularizers. Since it only takes few iterations and each iteration is a standard Group-Lasso type problem, it is much faster and is more suitable for large-scale datasets than BSBL-EM and BSBL-BO algorithms [23].

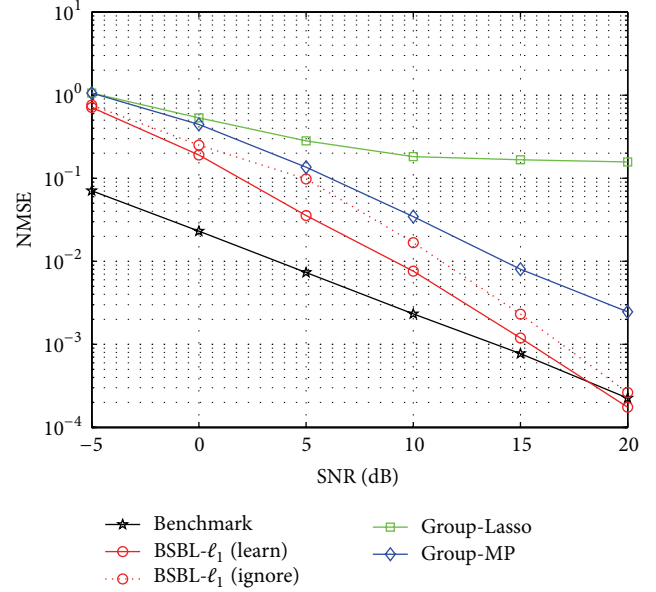


FIGURE 2: Comparison of NMSE versus SNR. Grid distance is 10 m.

5. Experiments

To demonstrate the superior performance of BSBL, this section tests the performance of sparse recovery based multi-target localization algorithms by conducting a wide range of numerical experiments. Three algorithms are used, which are the Group-Lasso method for solving (14), the Group/block-MP for solving (13) [21], and the BSBL- ℓ_1 method.

We use the same radar configuration as in [21]. Consider a 2×2 MIMO radar system in a common Cartesian coordinate system. The transmitters are located at $\mathbf{t}_1 = [100, 0]$ m and $\mathbf{t}_2 = [200, 0]$ m, respectively. The receivers are located at $\mathbf{r}_1 = [0, 200]$ m and $\mathbf{r}_2 = [0, 100]$ m, respectively. The three targets are located at $\mathbf{p}_1 = [120, 260]$ m, $\mathbf{p}_2 = [60, 320]$ m, and $\mathbf{p}_3 = [80, 240]$ m. The carrier frequency of these two transmitters are $f_1 = 1$ GHz and $f_2 = 1.5$ GHz. The pulse duration is $T_p = 0.2 \mu\text{s}$ and signal bandwidth is $B = 10$ MHz.

The phase errors $\{\theta_m^t\}_{m=1}^{M_T}$ and $\{\theta_l^r\}_{l=1}^{M_R}$ are assumed to be 0. We choose the range gate is $T_g = 6T_p$ and snapshots number is $N = 24$ for the simulation results. Therefore, \mathbf{y} has 96 entries. We divide the planar area into 13×13 grid points. Therefore, the total number of possible target states is $G = 169$. Hence, the 676 dimensional sparse vector \mathbf{w} has only 12 nonzero entries corresponding to the targets. The k th target reflection coefficients follow a Rician distribution with pdf $p(\alpha^k; \zeta^k, \sigma_0) = (\alpha^k / \sigma_0^2) \exp(-((\alpha^k)^2 + (\zeta^k)^2) / 2\sigma_0^2) I_0(\alpha^k \zeta^k / \sigma_0^2)$, where the fixed-amplitude part of three targets in all transmit-receive paths are $\zeta^1 = 5 \times \mathbf{1}_4$, $\zeta^2 = 3 \times \mathbf{1}_4$, and $\zeta^3 = \mathbf{1}_4$, and the power of Rayleigh part is $\sigma_0 = 0.05$ for all three targets. Our definition of signal-to-noise ratio (SNR) is $\text{SNR}[\text{dB}] = 10 \log_{10}(\|\Psi \mathbf{w}\|^2 / \sigma_\varepsilon^2)$ and the noise is generated independently from Gaussian distribution. We combine energies of reconstructed signal corresponding to different

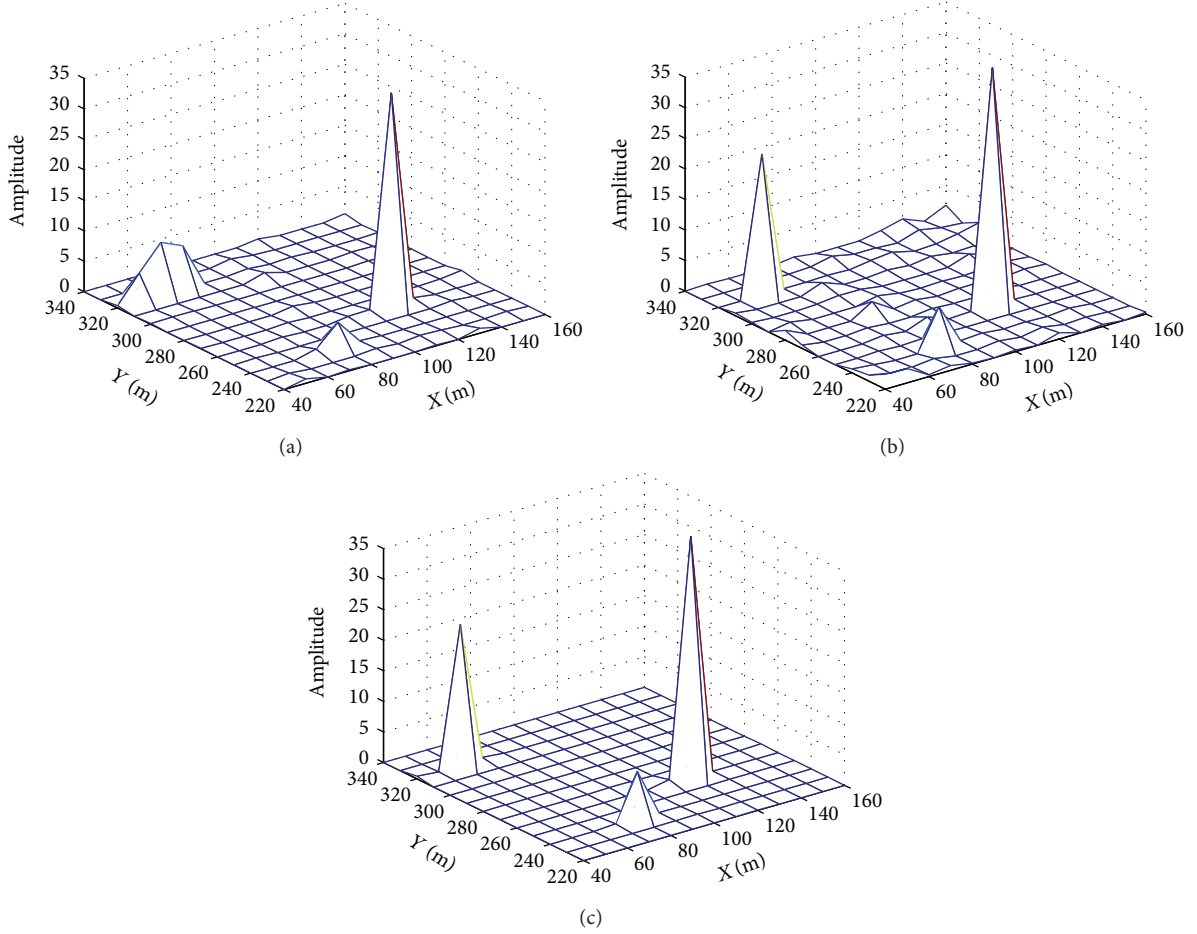


FIGURE 3: Comparison of reconstructed target reflection coefficients. SNR = 10 dB, grid distance is 10 m. (a) Group-Lasso, (b) Group-MP, and (c) BSBL- ℓ_1 exploiting correlation.

transmit-receive paths for each grid point in the target state space and define a new vector as

$$\tilde{\mathbf{w}}(g) = \sum_{m=1}^{M_T} \sum_{l=1}^{M_R} \|\tilde{\mathbf{w}}(M_T M_R (g-1) + M_R (l-1) + m)\|_2, \quad g = 1, \dots, G. \quad (20)$$

In the following, each experiment was repeated for 100 trials. In [21] a metric is given below to analyze the performance:

$$\Delta = \frac{\min \tilde{\mathbf{w}}^*}{\max \tilde{\mathbf{w}}^*}, \quad (21)$$

where $\tilde{\mathbf{w}}^*$ contains the values that $\tilde{\mathbf{w}}$ carries at the correct K indices and $\tilde{\mathbf{w}}^*$ takes 0 at the correct K indices and takes the same values as $\tilde{\mathbf{w}}$ at every other index. And the authors in [21] claimed that $\Delta > 1$ can guarantee exact estimation of the position. Since Δ can only represent the mean value of accuracy in the 100 trials, so we define the success rate as a new localization accuracy performance index, defined as the

percentage of successful trials in the 100 trials (a successful trial was defined as the one when $\Delta > 1$).

5.1. Comparison with Different Sparse Recovery Algorithms. We start by comparing the BSBL- ℓ_1 method with two classical methods, including Group-MP, Group-Lasso methods. Also we examine the benefit of exploiting intrablock correlation using BSBL- ℓ_1 algorithm. The normalized mean square error (NMSE) is used as a performance index, defined by $\|\tilde{\mathbf{w}} - \mathbf{w}\|_2^2 / \|\mathbf{w}\|_2^2$.

Figure 2 depicts the NMSE results using different recovery algorithms. As a benchmark result, the ‘‘pentagram’’ result is calculated, which is the least-square estimate of \mathbf{w} given its true support. The BSBL algorithm exhibits significant performance gains over non-BSBL algorithms. Figure 3 shows the reconstructed reflection coefficients of three targets for an SNR of 10 dB using different algorithms. From Figure 3 we can see that three algorithms are capable of estimating the positions of targets but the performance of Group-Lasso and Group-MP are intuitively poorer than BSBL- ℓ_1 method. In order to quantitatively analyze the performance of the three algorithms, we plot the metrics Δ and success rate

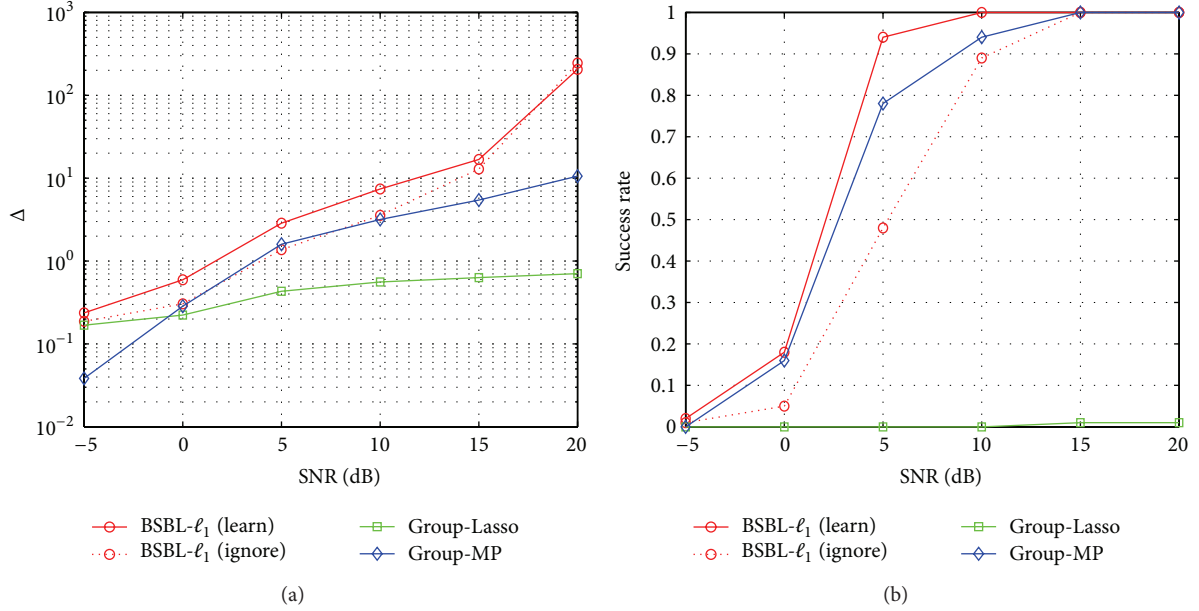


FIGURE 4: Comparison of metrics versus SNR. Grid distance is 10 m. (a) Δ ; (b) success rate.

versus SNR in Figure 4. BSBL- ℓ_1 is applied with and without correlation exploitation. In the first case, it adaptively learned and exploited the intrablock correlation. In the second case, it ignored the correlation, that is, fixing $\mathbf{Q}_g = \mathbf{I}$ ($\forall g$). As can be seen, the BSBL- ℓ_1 algorithm exhibits significant performance gains over non-BSBL algorithms. In Figure 4(a), the value of Δ remains above 1 for lower SNR for BSBL- ℓ_1 algorithm when compared with Group-MP and Group Lasso methods. In Figure 4(b), it is worth noting that when $\text{SNR} \geq 5$ dB, BSBL- ℓ_1 exactly recovers block sparse signals with a high success rate ($\geq 92\%$). Also we see that exploiting the intrablock correlation greatly improves the performance of the BSBL- ℓ_1 in terms of both metrics.

5.2. Ability for Dense Targets Scenario. In this subsection, we investigate the robust ability to find less-sparse solutions with small errors in the case of dense targets. Three targets are relocated at $\mathbf{p}_1 = [120, 300]$ m, $\mathbf{p}_2 = [100, 300]$ m, and $\mathbf{p}_3 = [110, 280]$ m and the RCS values remain unchanged.

Figure 5 demonstrates that BSBL- ℓ_1 is capable of exactly recovering less-sparse signals even for dense targets localization with respect to other algorithms. Figure 6 compares the location estimation performance in terms of the two metrics for different algorithms when the targets are located densely. As shown, its advantage over other conventional recovering algorithms is manifested in terms of larger Δ and higher success rate. The BSBL- ℓ_1 is accordingly suitable for dense targets localization problem.

5.3. Robustness against Block Coherence Measure. The following experiments are devoted to the performance evaluation for the case of robustness of BSBL to the block coherence measure [26], and it increases as the grid distance reduces [21].

TABLE 1: Comparison of computational time and NMSE.

Grid size (m)	BSBL		Group-MP	
	Time (s)	NMSE	Time (s)	NMSE
10	0.928	0.0169	0.653	0.0707
5	34.182	0.0177	11.178	0.279

Figure 7(b) shows the reconstructed reflection coefficients with smaller grid distance than that in Figure 7(a). Accordingly, Figure 7(d) illustrates that the resolution is improved compared with Figure 7(c). We plot the performance versus SNR with reduced grid distance in Figure 8. As expected, we note from Figure 8 that when the blocks of Ψ are highly coherent, BSBL exploiting intrablock correlation still maintains good performance compared with Figure 4, while other algorithms have seriously degraded performance in these two metrics.

Table 1 gives the computational time comparison of two algorithms on a computer with dual-core 2.5 GHz CPU, 2.0 GiB RAM, and Windows 7 OS, and $\text{SNR} = 10$ dB. It shows BSBL- ℓ_1 needs extra time to obtain better estimate performance compared with Group-MP algorithm. Also, we note that as the grid distance decreases, the computational time of two algorithms increases due to the larger dimensional dictionary matrix, and the NMSE of BSBL shows little change, while NMSE of Group-MP degraded significantly, which is caused by the highly coherent dictionary.

5.4. Robustness against Compressed Sensing. In this experiment, we consider the case for compressed sensing (CS)

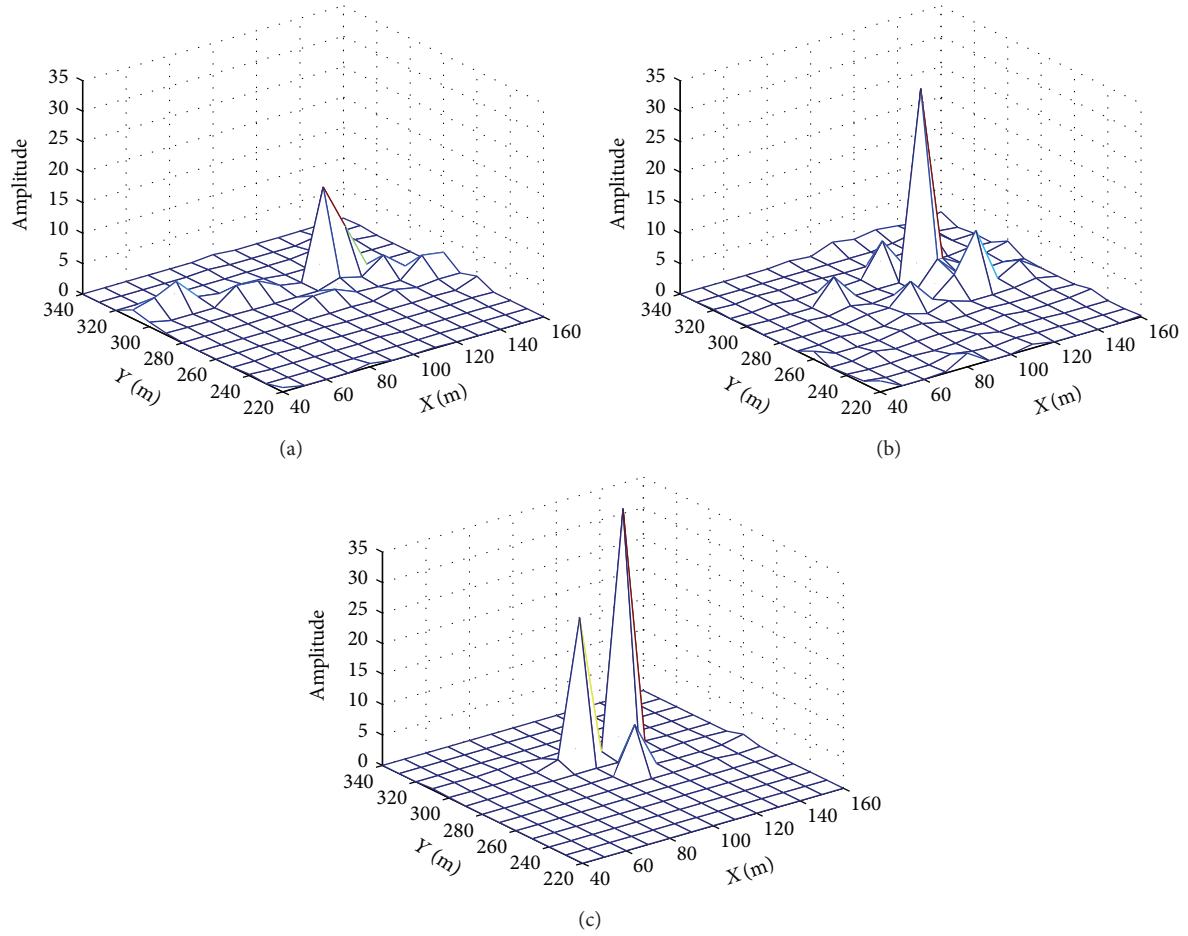


FIGURE 5: Comparison of reconstructed target reflection coefficients in dense targets case. SNR = 10 dB, grid distance is 10 m. (a) Group-Lasso, (b) Group-MP, and (c) BSBL- ℓ_1 exploiting correlation.

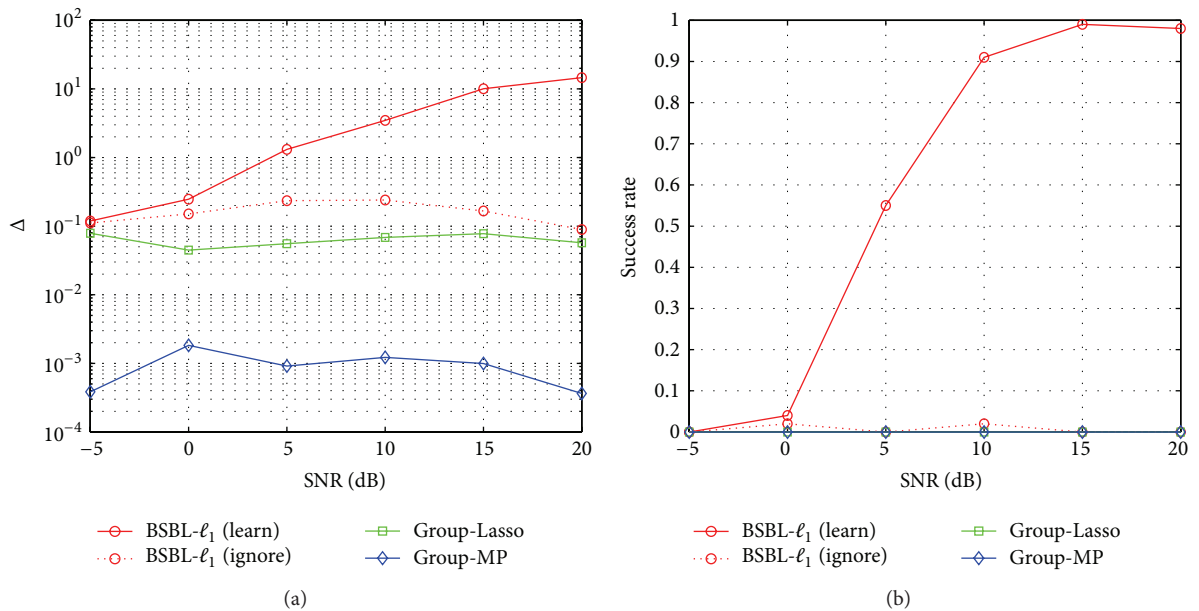


FIGURE 6: Comparison of metrics versus SNR in dense targets case. Grid distance is 10 m. (a) Δ ; (b) success rate.

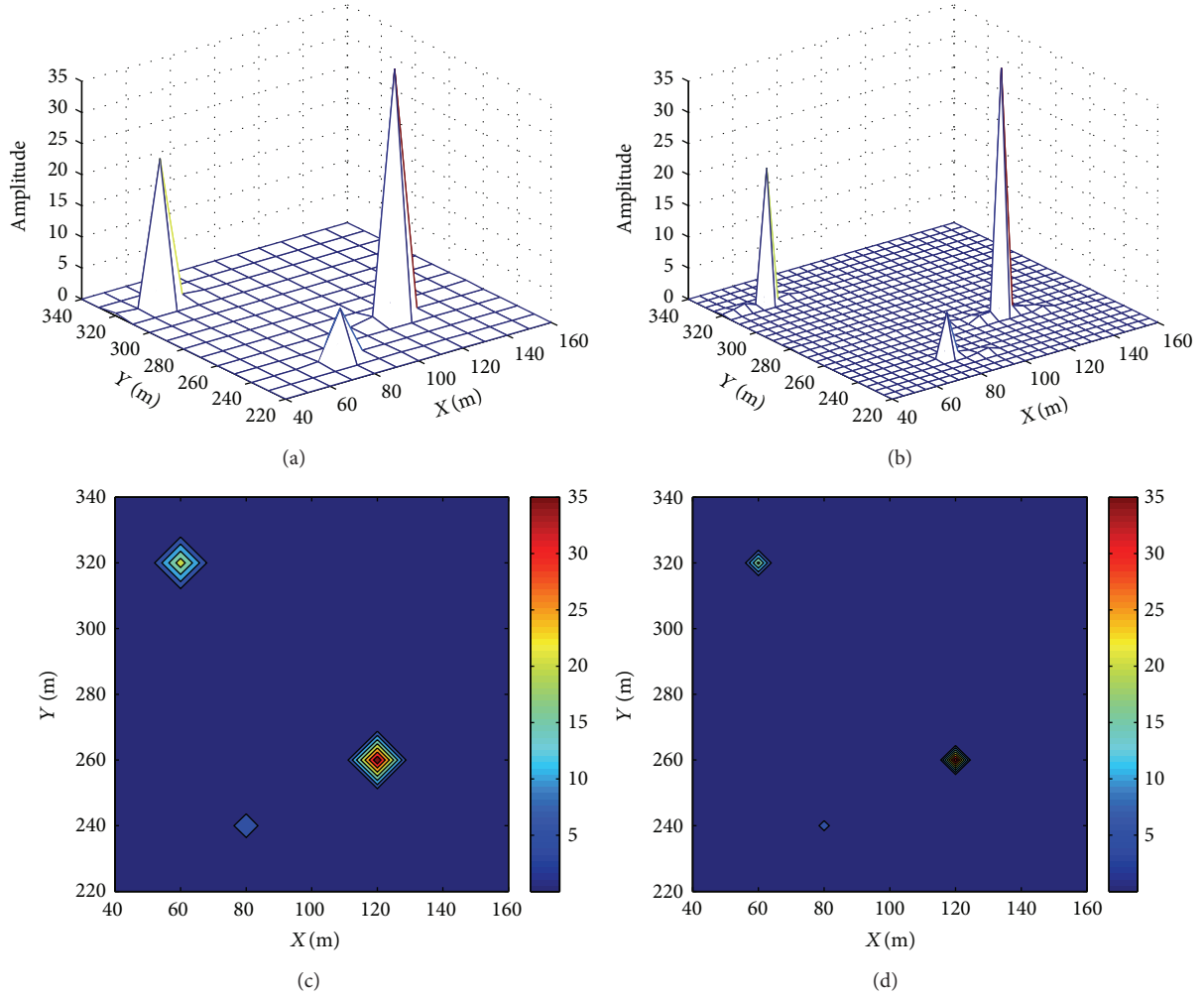


FIGURE 7: Comparison of reconstructed target reflection coefficients using BSBL- ℓ_1 method with different grid distance. SNR = 10 dB. (a) Grid distance is 10 m (3-D), (b) grid distance is 5 m (3-D), (c) grid distance is 10 m (contour plot), and (d) grid distance is 5 m (contour plot).

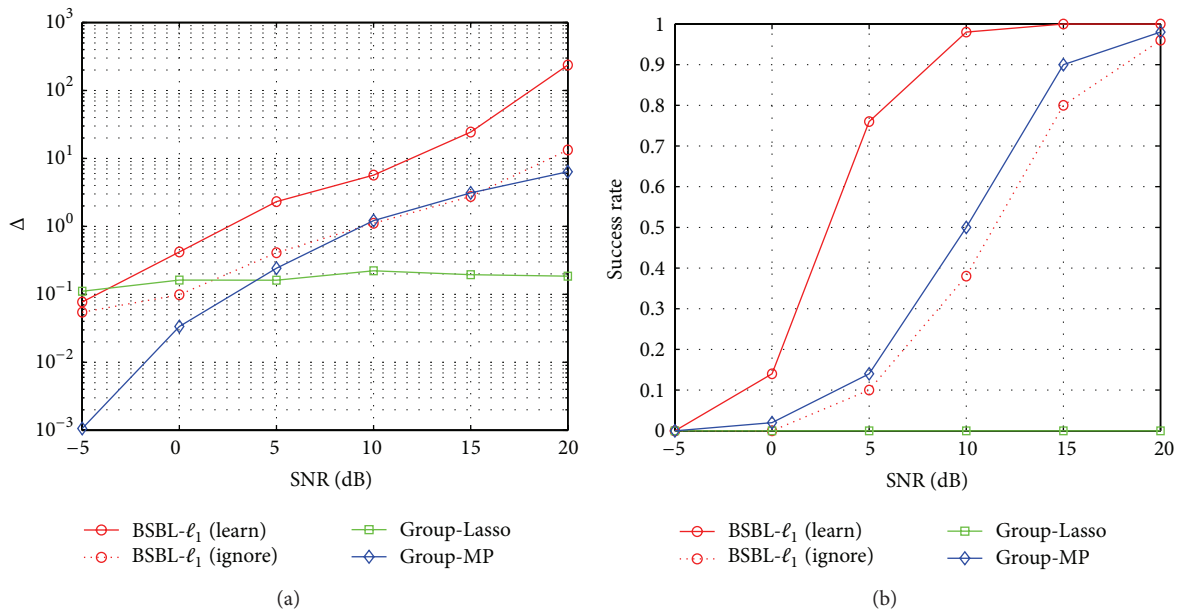


FIGURE 8: Comparison of metrics versus SNR. Grid distance is 5 m. (a) Δ ; (b) success rate.

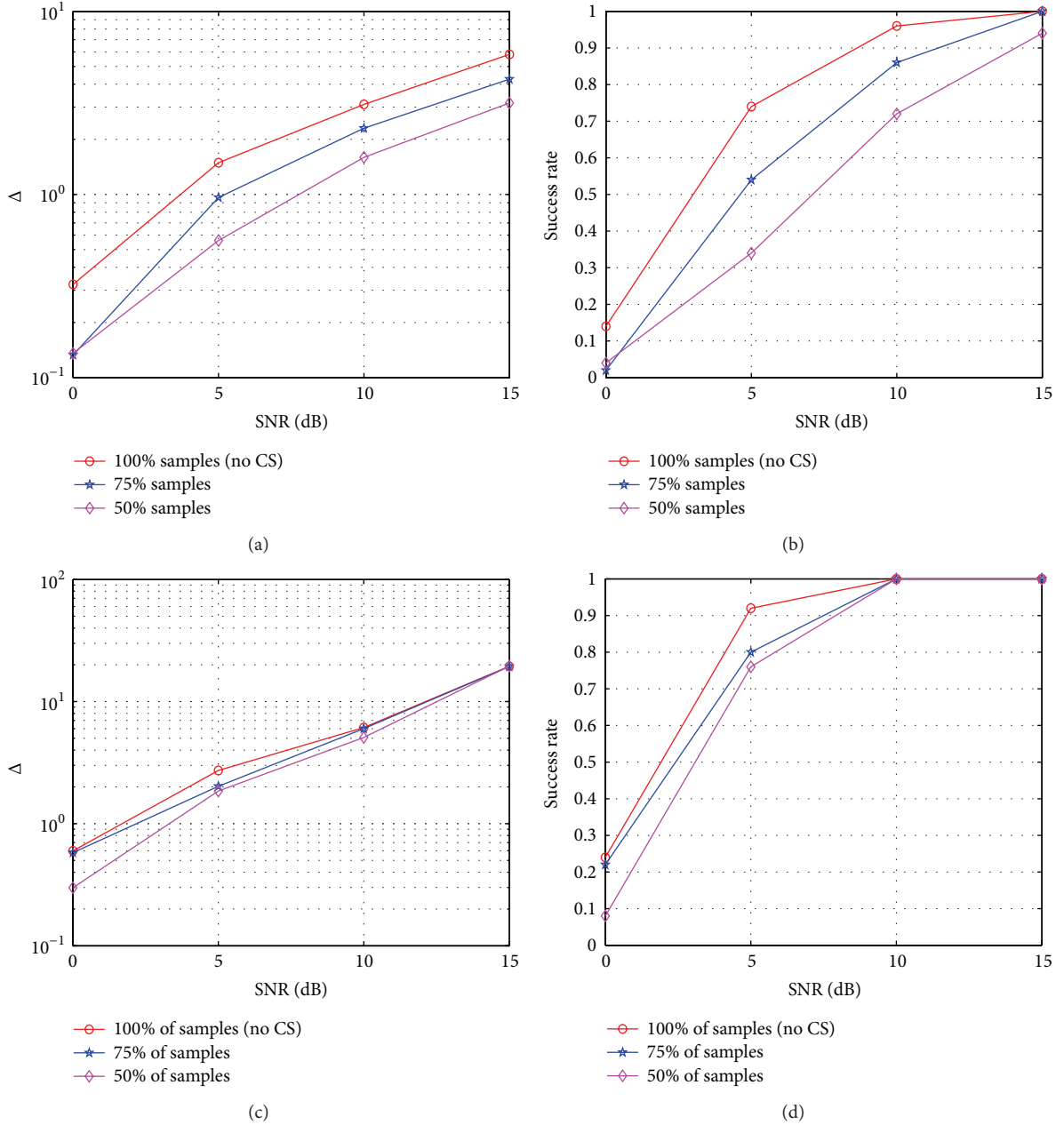


FIGURE 9: Comparison of metrics versus SNR for different percentages of samples. Grid distance is 10 m. (a) Group-MP, Δ ; (b) Group-MP, success rate; (c) BSBL- ℓ_1 , Δ ; (d) BSBL- ℓ_1 , success rate.

technique. The percentage of samples used is given as $N_{CS}/(NM_T M_R)$, where $N_{CS} \ll NM_T M_R$ is the CS sample number. For reconstruction of \mathbf{w} , we use Group-MP and BSBL- ℓ_1 methods.

As is clear from Figure 9, on one hand, the performance degrades as the percentage of samples reduces for both algorithms; on the other hand, the performance for Group-MP method dropped much more significantly than that for BSBL- ℓ_1 . In other words, the reconstructed estimates of the position using BSBL- ℓ_1 match the true values better while using only 50% of the samples.

5.5. Impact of Off-Grid Mismatch Errors. Finally, we consider the impact of off-grid mismatch errors. In the above experiments, we assume that all the targets are exactly located on the selected grid. The grid size is 10 m. Here, three targets are relocated at $\mathbf{p}_1 = [120, 262]$ m, $\mathbf{p}_2 = [63, 323]$ m, and $\mathbf{p}_3 = [80, 240]$ m and the RCS values remain unchanged, where \mathbf{p}_1 and \mathbf{p}_2 are beyond the fixed grid.

Compared with Figure 3(c), note that in Figure 10 when the true locations are beyond the fixed grid, we cannot obtain the exact location estimates due to errors caused by off-grid mismatches, though three location estimates can be

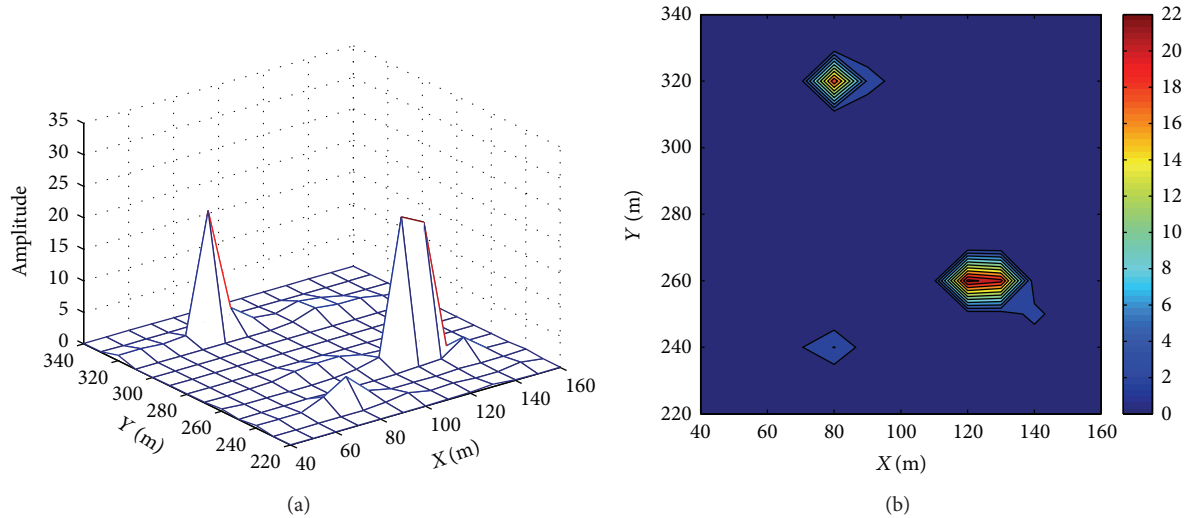


FIGURE 10: Off-grid reconstructed target reflection coefficients using BSBL- ℓ_1 method. SNR = 10 dB. (a) 3-D plot, (b) 2-D contour plot.

obtained according to three peaks projection. To deal with this problem, we could employ smaller grid size to make the targets located on the grid or approximate the error using linearization method [24].

6. Conclusions

Multitarget direct localization using distributed MIMO radar systems was discussed in this paper. Previous works generally focused on the use of two-step procedures with exact data association. In this paper, we introduced the block sparse Bayesian learning algorithm for multitarget direct localization by employing a new sparse modeling within a range bin. The success rate was defined to analyze the performance of the radar system. We experimentally demonstrated that BSBL algorithm significantly outperforms some algorithms by exploiting intrablock correlation in signals, especially when the targets were located densely and the blocks of dictionary were highly coherent. Finally, the CS technique was applied to the block sparse recovery. Results showed the BSBL was more robust than other algorithms when few samples were used.

In future work, we will consider dealing with off-grid target localization problem, where the targets are no longer constrained in the sampling grid set. Further, we will consider the problem of target localization for distributed MIMO radar in the presence of phase synchronization mismatch.

Conflict of Interests

The authors declare that there is no conflict of interests regarding the publication of this paper.

Acknowledgments

This work was partially supported by the National Natural Science Foundation of China (nos. 61302142 and 61271442)

and the National Science Fund for Distinguished Young Scholars (no. 61025006). The authors thank Dr. Z. L. Zhang at University of California, San Diego and Dr. W.G.Su at National University of Defense Technology for their helpful discussions and insights and sharing the source code of BSBL- ℓ_1 algorithm online.

References

- [1] J. Li and P. Stoica, "MIMO radar with colocated antennas," *IEEE Signal Processing Magazine*, vol. 24, no. 5, pp. 106–114, 2007.
- [2] J. Li, P. Stoica, L. Xu, and W. Roberts, "On parameter identifiability of MIMO radar," *IEEE Signal Processing Letters*, vol. 14, no. 12, pp. 968–971, 2007.
- [3] E. Fishler, A. Haimovich, R. S. Blum, L. J. Cimini Jr., D. Chizhik, and R. A. Valenzuela, "Spatial diversity in radars—models and detection performance," *IEEE Transactions on Signal Processing*, vol. 54, no. 3, pp. 823–838, 2006.
- [4] A. M. Haimovich, R. S. Blum, and L. J. Cimini, "MIMO radar with widely separated antennas," *IEEE Signal Processing Magazine*, vol. 25, no. 1, pp. 116–129, 2008.
- [5] I. Bekkerman and J. Tabrikian, "Target detection and localization using MIMO radars and sonars," *IEEE Transactions on Signal Processing*, vol. 54, no. 10, pp. 3873–3883, 2006.
- [6] M. Akcakaya and A. Nehorai, "MIMO radar sensitivity analysis for target detection," *IEEE Transactions on Signal Processing*, vol. 59, no. 7, pp. 3241–3250, 2011.
- [7] B. Sun, H. Chen, X. Wei, H. Wang, and X. Li, "Power allocation for range-only localization in distributed multiple-input multiple-output radar networks—a cooperative game approach," *IET Radar, Sonar & Navigation*, vol. 8, no. 7, pp. 708–718, 2014.
- [8] F. Belfiori, W. Rossum, and P. Hoogeboom, "Coherent MUSIC technique for range/angle information retrieval: application to a frequency-modulated continuous wave MIMO radar," *IET Radar, Sonar & Navigation*, vol. 8, no. 2, pp. 75–83, 2014.
- [9] Q. He, R. S. Blum, H. Godrich, and A. M. Haimovich, "Target velocity estimation and antenna placement for MIMO radar with widely separated antennas," *IEEE Journal on Selected Topics in Signal Processing*, vol. 4, no. 1, pp. 79–99, 2010.

- [10] H. Godrich, A. M. Haimovich, and R. S. Blum, "Target localization techniques and tools for multiple-input multiple-output radar," *IET Radar, Sonar and Navigation*, vol. 3, no. 4, pp. 314–327, 2009.
- [11] H. Godrich, A. M. Haimovich, and R. S. Blum, "Target localization accuracy gain in MIMO radar-based systems," *IEEE Transactions on Information Theory*, vol. 56, no. 6, pp. 2783–2803, 2010.
- [12] Y. Yang and R. S. Blum, "Phase synchronization for coherent MIMO radar: algorithms and their analysis," *IEEE Transactions on Signal Processing*, vol. 59, no. 11, pp. 5538–5557, 2011.
- [13] H. Godrich, A. M. Haimovich, and H. Vincent Poor, "An analysis of phase synchronization mismatch sensitivity for coherent MIMO radar systems," in *Proceedings of the 3rd IEEE International Workshop on Computational Advances in Multi-Sensor Adaptive Processing (CAMSAP '09)*, pp. 153–156, Aruba, Dutch Antilles, December 2009.
- [14] Q. He and R. S. Blum, "Cramer-rao bound for MIMO radar target localization with phase errors," *IEEE Signal Processing Letters*, vol. 17, no. 1, pp. 83–86, 2010.
- [15] R. Niu, R. S. Blum, P. K. Varshney, and A. L. Drozd, "Target localization and tracking in noncoherent multiple-input multiple-output radar systems," *IEEE Transactions on Aerospace and Electronic Systems*, vol. 48, no. 2, pp. 1466–1489, 2012.
- [16] A. J. Weiss, "Direct position determination of narrowband radio frequency transmitters," *IEEE Signal Processing Letters*, vol. 11, no. 5, pp. 513–516, 2004.
- [17] Y. Kalkan and B. Baykal, "Multiple target localization and data association for frequency-only widely separated," *Elsevier Digital Signal Processing*, vol. 49, no. 4, pp. 2179–2194, 2013.
- [18] A. A. Gorji, R. Tharmarasa, and T. Kirubarajan, "Widely separated MIMO versus multistatic radars for target localization and tracking," *IEEE Transactions on Aerospace and Electronic Systems*, vol. 49, no. 4, pp. 2179–2194, 2013.
- [19] O. Bar-Shalom and A. J. Weiss, "Direct positioning of stationary targets using MIMO radar," *Signal Processing*, vol. 91, no. 10, pp. 2345–2358, 2011.
- [20] A. Hassani, S. A. Vorobyov, and A. B. Gershman, "Moving target parameters estimation in noncoherent MIMO radar systems," *IEEE Transactions on Signal Processing*, vol. 60, no. 5, pp. 2354–2361, 2012.
- [21] S. Gogineni and A. Nehorai, "Target estimation using sparse modeling for distributed MIMO radar," *IEEE Transactions on Signal Processing*, vol. 59, no. 11, pp. 5315–5325, 2011.
- [22] H. Jamali-Rad and G. Leus, "Sparsity-aware multi-source TDOA localization," *IEEE Transactions on Signal Processing*, vol. 61, no. 19, pp. 4874–4887, 2013.
- [23] Z. Zhang and B. D. Rao, "Extension of SBL algorithms for the recovery of block sparse signals with intra-block correlation," *IEEE Transactions on Signal Processing*, vol. 61, no. 8, pp. 2009–2015, 2013.
- [24] Y. Zhang, Z. Ye, X. Xu, and N. Hu, "Off-grid DOA estimation using array covariance matrix and block-sparse Bayesian learning," *Signal Processing*, vol. 98, pp. 197–201, 2014.
- [25] X. Song, W. D. Blair, P. Willett, and S. Zhou, "Dominant-plus-rayleigh models for RCS: swerling III/IV versus rician," *IEEE Transactions on Aerospace and Electronic Systems*, vol. 49, no. 3, pp. 2058–2064, 2013.
- [26] Y. C. Eldar, P. Kuppinger, and H. Bolcskei, "Block-sparse signals: uncertainty relations and efficient recovery," *IEEE Transactions on Signal Processing*, vol. 58, no. 6, pp. 3042–3054, 2010.
- [27] D. P. Wipf, "Sparse estimation with structured dictionaries," in *Proceedings of the 24th Conference on Advances in Neural Information Processing Systems*, pp. 2016–2024, 2011.
- [28] M. E. Tipping, "Sparse Bayesian learning and the relevance vector machine," *Journal of Machine Learning Research*, vol. 1, no. 3, pp. 211–244, 2001.
- [29] Z. Zhang, *Sparse signal recovery exploiting spatiotemporal correlation [Ph.D. thesis]*, University of California, San Diego, Calif, USA, 2012.
- [30] Z. Zhang, T.-P. Jung, S. Makeig, and B. D. Rao, "Compressed sensing for energy-efficient wireless telemonitoring of non-invasive fetal ECG via block sparse bayesian learning," *IEEE Transactions on Biomedical Engineering*, vol. 60, no. 2, pp. 300–309, 2013.

Research Article

Direct Data Domain Sparsity-Based STAP Utilizing Subaperture Smoothing Techniques

Zhaocheng Yang,¹ Rui Fa,² Yuliang Qin,¹ Xiang Li,¹ and Hongqiang Wang¹

¹Research Institute of Space Electronics, Electronics Science and Engineering School,
National University of Defense Technology, Changsha 410073, China

²Department of Electrical Engineering and Electronics, The University of Liverpool, Liverpool L69 3GJ, UK

Correspondence should be addressed to Zhaocheng Yang; yangzhaocheng@gmail.com

Received 25 April 2014; Revised 6 October 2014; Accepted 16 October 2014

Academic Editor: Hang Hu

Copyright © 2015 Zhaocheng Yang et al. This is an open access article distributed under the Creative Commons Attribution License, which permits unrestricted use, distribution, and reproduction in any medium, provided the original work is properly cited.

We propose a novel direct data domain (D3) sparsity-based space-time adaptive processing (STAP) algorithm utilizing subaperture smoothing techniques for airborne radar applications. Different from either normal sparsity-based STAP or D3 sparsity-based STAP, the proposed algorithm firstly uses only the snapshot in the cell under test (CUT) to generate multiple subsnapshots by exploiting the space-time structure of the steering vector and the uncorrelated nature of the components of the interference covariance matrix. Since the interference spectrum is sparse in the whole angle-Doppler plane, by employing a sparse regularization, the generated multiple subsnapshots are jointly used to recover the interference spectrum. The interference covariance matrix is then estimated from the interference spectrum, followed by the space-time filtering and the target detection. Simulation results illustrate that the proposed algorithm outperforms the generalized forward/backward method, the conventional D3 least squares STAP algorithm, and the existing D3 sparsity-based STAP algorithm. Furthermore, compared with the normal sparsity-based STAP algorithm using multiple snapshots, the proposed algorithm can also avoid the performance degradation caused by discrete interferers merely appearing in the CUT.

1. Introduction

Space-time adaptive processing (STAP) is considered to be an effective tool for detection of weak targets by airborne radar systems in strong interference environments [1–4]. The problem is essentially that it usually assumes a homogeneous environment over the range cells. However, the assumptions are often not satisfied in realistic radar scenarios. Many factors, such as clutter edges, moving scatterers, shadowing and obstruction, and chaff, can render the clutter returns nonhomogeneous, resulting in performance degradation of conventional STAP algorithms [4].

Direct data domain least-squares (D3-LS) STAP approach is considered to be a powerful and effective method in nonhomogeneous environments [5–8]. It only uses the snapshot in the cell under test (CUT) rather than training data, which can avoid the nonhomogeneity in the training data and eliminate the impacts of nonhomogeneous environments. However, this configuration degrades the system performance since

the system degrees of freedom (DOFs) are reduced. By combining the STAP algorithms using the training data and the D3-LS STAP algorithms, the hybrid detection approach is introduced with improved robustness to nonhomogeneous environments [9, 10]. Knowledge-aided (KA) STAP approaches using digital land classification data and digital elevation data were proposed to select training data to obtain improved STAP performance [11]. Another KA-STAP method, called model-based approach (see [12–19] and the references therein), basically employs some prior knowledge to form the simplified general clutter model (GCM) and then blends the GCM with the measured observations to design the STAP filter or directly uses it to design the STAP filter. This method can obtain good performance in a small-sample-support condition with accurate prior knowledge. However, the formed GCM usually does not contain the information of discrete interferers because the discrete interferers can appear at arbitrary positions in the angle-Doppler plane, which results in the increase of false alarms. Moreover, in practice,

one cannot guarantee the accuracy of the prior knowledge, which is very important to the performance.

Recently, sparse recovery (SR) methods have been considered for STAP problems, such as sparsity-based STAP algorithms in [20–29] and L1-regularized STAP filters in [30, 31]. The sparsity-based STAP algorithms are highly related to the model-based approach but do not require the knowledge (such as the clutter ridge) to form the GCM and can be applied to arbitrary array geometries and random slow-time samples [21]. In fact, supposing that no prior knowledge of the interference is available, they discretize the whole angle-Doppler plane into many small grids, exploit the sparsity of the interference spectrum in all discretized angle-Doppler grids, and utilize the sparse recovery algorithms to recover the interference spectrum. Usually, there are two types of sparsity-based STAP in the literature: one type is the D3 STAP based on sparse recovery (D3-SR-STAP) algorithm which uses only the snapshot in the CUT [20–24]; the other is the normal STAP based on sparse recovery (NSR-STAP) that uses multiple snapshots adjacent to the CUT [24–29]. Both types exhibit significantly better performance than conventional STAP algorithms in limited training situations. However, for the D3-SR-STAP, the estimated interference covariance matrix is not stable since only one snapshot is employed; for the NSR-STAP, the presence of discrete interferers merely in the CUT will degrade the performance significantly.

In this paper, we propose a new D3-SR-STAP using the subaperture smoothing (SASM) techniques, which can overcome aforementioned drawbacks of both types of sparsity-based STAP. The proposed algorithm uses only snapshot in the CUT as conventional D3-SR-STAP does. Additionally, it uses the decimation techniques [32, 33] to generate multiple subsnapshots by exploiting the space-time structure of steering vector and the uncorrelated nature of the components of the interference covariance matrix. Then, the generated multiple subsnapshots are jointly used to recover the interference spectrum. Inspired by the SASM techniques used in the spectral estimation [34], the proposed algorithm can reduce the variance of the estimated interference spectrum resulting in improved signal-to-interference-plus-noise ratio (SINR). Moreover, thanks to the rapid convergence of sparsity-based STAP algorithms [25, 26, 28], the proposed algorithm does not reduce much the number of DOFs to increase the subsnapshots, which will benefit the recovery of the interference spectrum from single subsnapshot. It should be noted that another method, called the generalized forward/backward (F/B) method [35], also employs the SASM techniques and uses multiple training snapshots adjacent to the CUT to generate multiplicative improvement in the snapshots resulting in improved performance in sample limited cases. However, when the training snapshots have different statistics with that in the CUT, the performance of the generalized F/B method will degrade significantly. Simulation results illustrate the effectiveness of the proposed algorithm.

The rest of the paper is organized as follows. In Section 2, the STAP signal model and the principle of sparsity-based STAP algorithms are introduced. Section 3 details the proposed SASM D3-SR-STAP algorithm. Simulated data are used to evaluate the performance of the proposed algorithm

in Section 4. Section 5 provides the summary and conclusions.

2. Signal Model and Problem Formulation

In this section, we will introduce the signal model used in the paper and discuss the principle of the sparsity-based STAP algorithms.

2.1. Signal Model. In airborne radar systems, ignoring the impact of range ambiguities, a general model for the space-time interference (clutter and discrete interferers) plus noise snapshot \mathbf{x} in a target-free range cell is given by [3]

$$\mathbf{x} = \mathbf{x}_c + \mathbf{x}_I + \mathbf{n} = \sum_{n=1}^{N_c} \sigma_{c;n} \mathbf{v}(f_{c;d,n}, \phi_{c;n}) + \sum_{m=1}^{N_I} \sigma_{I;m} \mathbf{v}(f_{I;d,m}, \phi_{I;m}) + \mathbf{n}, \quad (1)$$

where \mathbf{n} is the Gaussian white noise vector with the noise power σ_n^2 on each channel and pulse; N_c and N_I denote the numbers of independent clutter patches and independent discrete interferers over the iso-range of interest; $\sigma_{c;n}$, $\phi_{c;n}$, and $f_{c;d,n}$ are the random complex amplitude, the angle-of-arrival (AOA), and the Doppler frequency of the n th clutter patch, respectively; $\sigma_{I;m}$, $\phi_{I;m}$, and $f_{I;d,m}$ are the random complex amplitude, the AOA, and the Doppler frequency of the m th discrete interferer, respectively; $\mathbf{v}(f_d, \phi)$ is the $NM \times 1$ space-time steering vector with the AOA ϕ and the Doppler frequency f_d and is defined by (for a uniform linear array (ULA))

$$\mathbf{v}(f_d, \phi) = \begin{bmatrix} 1 \\ \vdots \\ e^{j2\pi(M-1)f_s} \\ e^{j2\pi f_d} \\ \vdots \\ e^{j2\pi((N-1)f_d + (M-1)f_s)} \end{bmatrix}, \quad (2)$$

where N is the number of pulses in a coherent process interval (CPI), M is the number of array elements, and f_s corresponds to the spatial frequency related to the AOA ϕ . Let the inner spacing of array elements be d_a ; then the relationship between the spatial frequency and the AOA is $f_s = (d_a/\lambda_c) \sin \phi$, where λ_c is the operating wavelength.

2.2. Principle of Sparsity-Based STAP Algorithms. Recently developed sparsity-based STAP algorithms provide an effective approach to estimate interference (clutter, discrete interferers) covariance matrix. It first discretizes the whole angle-Doppler plane into $N_s = \rho_s M$, $N_d = \rho_d N$ ($\rho_s, \rho_d > 1$) grids, where N_s and N_d are the number of angle and Doppler bins, respectively. Then the received data in (1) can be rewritten as [22–29]

$$\mathbf{x} = \Phi \boldsymbol{\gamma} + \mathbf{n}, \quad (3)$$

where $\boldsymbol{\gamma} = [\gamma_{1,1}, \gamma_{1,2}, \dots, \gamma_{N_d, N_s}]^T$ denotes the $N_d N_s \times 1$ angle-Doppler profile with nonzero elements representing the interference, and the $NM \times N_d N_s$ matrix Φ is the overcompleted space-time steering dictionary including all the possible space-time steering vectors, as given by

$$\Phi = [\mathbf{v}(f_{d,1}, \phi_1), \dots, \mathbf{v}(f_{d,1}, \phi_{N_s}), \dots, \mathbf{v}(f_{d,N_d}, \phi_{N_s})]. \quad (4)$$

Here, the symbols $f_{d,i}$, $1 \leq i \leq N_d$ and ϕ_k , $1 \leq k \leq N_s$ denote the uniformly quantized Doppler frequencies and the AOAs. Herein, the interference plus noise covariance matrix can be expressed as

$$\mathbf{R} = E[\mathbf{x}\mathbf{x}^H] = \Phi\Gamma\Phi^H + \sigma_n^2\mathbf{I}, \quad (5)$$

where $\Gamma = E[\boldsymbol{\gamma}\boldsymbol{\gamma}^H] = \text{diag}(\mathbf{a})$ and $\mathbf{a} = E[\boldsymbol{\gamma} \odot \boldsymbol{\gamma}^*]$ is the interference spectral distribution vector under the assumptions of statistical independence between the clutter patches, the discrete interferers, and the noise [3, 4]. Here, $\text{diag}(\mathbf{a})$ stands for a diagonal matrix with the main diagonal taken from the elements of the vector \mathbf{a} , and \odot denotes the Hadamard product.

To estimate \mathbf{R} , the sparsity-based STAP algorithms try to calculate the parameter \mathbf{a} using the computed angle-Doppler profile from the CUT or angle-Doppler profiles from adjacent target-free range cells, which can be obtained via the sparse recovery algorithms by exploiting the intrinsic sparsity of the interference spectral distribution, for example, the sparse interference spectrum computed by using the Mountain Top dataset [36], as shown in Figure 1. The whole angle-Doppler plane shows a high degree of sparsity and only a small number of angle-Doppler grids of the interference spectrum are occupied. Mathematically, the angle-Doppler profile can be estimated by solving the following minimal optimization problem known as the least absolute shrinkage and selection operator (LASSO) [23–26]

$$\hat{\boldsymbol{\gamma}} = \arg \min_{\boldsymbol{\gamma}} \|\boldsymbol{\gamma}\|_1 \quad \text{s.t.} \quad \|\mathbf{x} - \Phi\boldsymbol{\gamma}\|_2 \leq \epsilon, \quad (6)$$

or the basis pursuit denoising (BPDN) [20, 22, 24, 26, 27, 29], given as

$$\hat{\boldsymbol{\gamma}} = \arg \min_{\boldsymbol{\gamma}} \left\{ \frac{1}{2} \|\mathbf{x} - \Phi\boldsymbol{\gamma}\|_2^2 + \kappa \|\boldsymbol{\gamma}\|_1 \right\}, \quad (7)$$

where $\|\cdot\|_p$ ($p = 1, 2$) denotes the l_p -norm, ϵ is the noise error allowance, and κ is a positive regularization parameter that provides a tradeoff between the approximation error and the sparsity.

For the D3-SR-STAP algorithm in [20–24], it is hard to obtain a stable and good estimation of interference covariance matrix estimate by using only one snapshot. For the NSR-STAP algorithm using multiple snapshots [24–29], although it can obtain a good performance by effectively suppressing the interference in homogeneous environments, it will lead to significant performance degradation in presence of discrete interferers only in the CUT. It is worthy of noting that, for the developed algorithm in [22], the exact prior knowledge

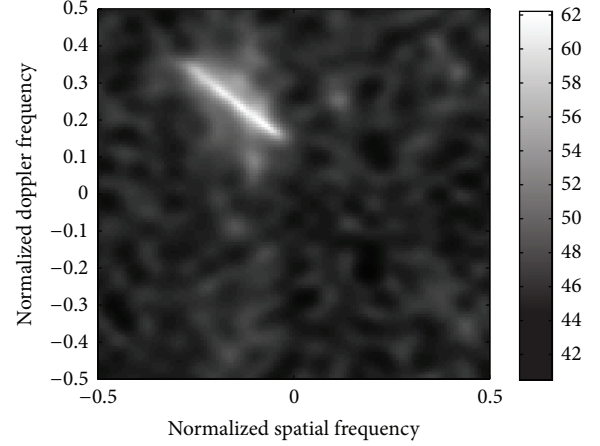


FIGURE 1: The estimated interference spectrum using the Mountain Top dataset.

of the clutter ridge in the angle-Doppler plane is required; however, it is hard to obtain in practice. Thus, we focus on sparsity-based STAP algorithms in [20, 21, 23–29] without prior knowledge of clutter ridge in this paper.

3. Proposed SASM D3-SR-STAP Algorithm

To overcome the above two drawbacks of existing sparsity-based STAP algorithms, we propose a novel SASM D3-SR-STAP algorithm in this section. The proposed algorithm uses the snapshot in the CUT as the conventional D3-SR-STAP algorithm does but can obtain better performance than the conventional D3-SR-STAP algorithm by utilizing SASM techniques. Because the proposed algorithm does not need any training snapshots, it can avoid the increase of false alarms caused by discrete interferers only appearing in the CUT, whereas the NSR-STAP can not avoid that in this case.

3.1. Multiple Subsnapshots Generation. To form multiple subsnapshots with the snapshot in the CUT, the SASM techniques are utilized to exploit the space-time structure of the steering vector together with the uncorrelated nature of the components of the interference covariance matrix [5–8, 35]. With \mathbf{x} defined in (3), let $\mathbf{x}_{p,q}$ denote the subsnapshot generated using N' consecutive pulses starting from the p th pulse and M' antenna elements starting from the q th antenna element (where $1 \leq p \leq N - N' + 1$ and $1 \leq q \leq M - M' + 1$). This subsnapshot can be realized by a $N'M' \times NM$ decimation matrix $\mathbf{D}_{p,q}$ with the form of

$$\mathbf{D}_{p,q} = [\mathbf{d}_{p,q,1}, \mathbf{d}_{p,q,2}, \dots, \mathbf{d}_{p,q,N'M'}]^T, \quad (8)$$

where

$$\mathbf{d}_{p,q,l} = \begin{bmatrix} \underbrace{0, \dots, 0}_{z_{p,q,l}}, 1, \underbrace{0, \dots, 0}_{NM - z_{p,q,l} - 1} \end{bmatrix}^T, \quad l = 1, \dots, N'M', \quad (9)$$

where $z_{p,q,l}$ is the number of zeros before the only element equal to one. We can set the value of $z_{p,q,l}$ in three ways, that is, utilizing subtemporal, subspatial, and subspatial-temporal aperture smoothing techniques, respectively, as shown in Figure 2. Suppose that the total number of the subsnapshots is K , which is equivalent to

$$K = (N - N' + 1)(M - M' + 1), \quad (10)$$

where $N' < N$ and $M' = M$ correspond to the case that uses subtemporal aperture smoothing, $N' = N$ and $M' < M$ correspond to the case that uses subspatial aperture smoothing, $N' < N$ and $M' < M$ correspond to the case that uses all three types of aperture smoothing, and $N' = N$ and $M' = M$ correspond to the conventional D3-SR-STAP algorithm presented in [23]. From Figure 2, we observe that the value of $z_{p,q,l}$ can be determined by

$$z_{p,q,l} = \left(p + \left\lfloor \frac{l}{M'} \right\rfloor - 1 \right) M + q + \text{mod}(l, M') - 1, \quad (11)$$

where the brackets $\lfloor \cdot \rfloor$ denote the floor operator and $\text{mod}(l, M') = l - \lfloor l/M' \rfloor M'$ denotes the modulo operator.

After determining the decimation matrix $\mathbf{D}_{p,q}$, we can obtain the (p, q) th subsnapshot by

$$\mathbf{x}_{p,q} = \mathbf{D}_{p,q} \mathbf{x}. \quad (12)$$

Note that $\mathbf{x}_{p,q}$ is of the size $N'M' \times 1$ and can be further expressed as

$$\begin{aligned} \mathbf{x}_{p,q} &= \mathbf{D}_{p,q} \Phi \boldsymbol{\gamma} + \mathbf{D}_{p,q} \mathbf{n} \\ &= \sum_{i=1}^{N_d} \sum_{k=1}^{N_s} \gamma_{i,k} \mathbf{D}_{p,q} \mathbf{v}(f_{d,i}, \phi_k) + \mathbf{n}_{p,q} \\ &= \sum_{i=1}^{N_d} \sum_{k=1}^{N_s} \bar{\gamma}_{p,q,i,k} \bar{\mathbf{v}}(f_{d,i}, \phi_k) + \mathbf{n}_{p,q}, \end{aligned} \quad (13)$$

where $\mathbf{n}_{p,q} = \mathbf{D}_{p,q} \mathbf{n}$, $\bar{\gamma}_{p,q,i,k} = e^{j2\pi[(p-1)Mf_{d,i} + (q-1)f_{s,k}]}\gamma_{i,k}$, and

$$\bar{\mathbf{v}}(f_{d,i}, \phi_k) = \begin{bmatrix} 1 \\ \vdots \\ e^{j2\pi(M'-1)f_{s,k}} \\ \vdots \\ e^{j2\pi[\lfloor l/M' \rfloor Mf_{d,i} + \text{mod}(l-1, M')f_{s,k}]} \\ \vdots \\ e^{j2\pi[(N'-1)Mf_{d,i} + (M'-1)f_{s,k}]} \end{bmatrix}, \quad (14)$$

with $l = 1, 2, \dots, N'M'$. Thus, the generated subsnapshot can be rewritten as

$$\mathbf{x}_{p,q} = \bar{\Phi} \bar{\boldsymbol{\gamma}}_{p,q} + \mathbf{n}_{p,q}, \quad (15)$$

where

$$\bar{\Phi} = [\bar{\mathbf{v}}(f_{d,1}, \phi_1), \bar{\mathbf{v}}(f_{d,1}, \phi_2), \dots, \bar{\mathbf{v}}(f_{d,N_d}, \phi_{N_s})]. \quad (16)$$

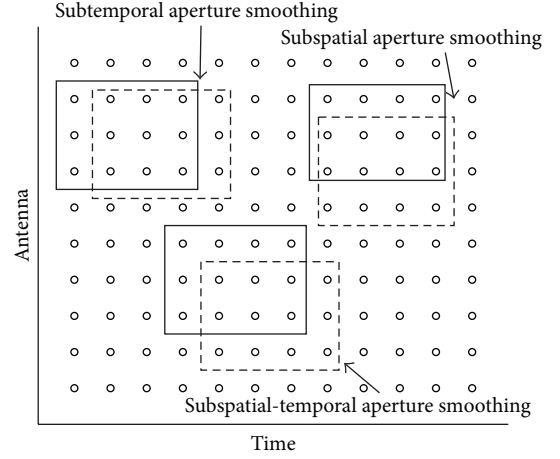


FIGURE 2: Generation of the subsnapshots from the space-time snapshot in the CUT using SASM techniques.

Comparing the formulations between $\bar{\boldsymbol{\gamma}}_{p,q}$ and $\boldsymbol{\gamma}$, we find that there is only a phase difference $e^{j2\pi[(p-1)Mf_{d,i} + (q-1)f_{s,k}]}$ among the corresponding elements, which results in $\boldsymbol{\gamma} \odot \boldsymbol{\gamma}^* = \bar{\boldsymbol{\gamma}}_{p,q} \odot \bar{\boldsymbol{\gamma}}_{p,q}^*$. In other words, different subsnapshots have the same angle-Doppler profile amplitude $|\boldsymbol{\gamma}|$. From the point of sparse recovery, these subsnapshots are called multiple measurement vectors (MMV) and the solutions share a common sparsity profile [37].

3.2. Interference Covariance Matrix Estimation and Filter Design. Based on the above discussions, the interference covariance matrix of the (p, q) th subsnapshot can be written as

$$\begin{aligned} \mathbf{R}_{p,q} &= E[\mathbf{x}_{p,q} \mathbf{x}_{p,q}^H] \\ &= \bar{\Phi} E[\bar{\boldsymbol{\gamma}}_{p,q} \bar{\boldsymbol{\gamma}}_{p,q}^H] \bar{\Phi}^H + E[\mathbf{n}_{p,q} \mathbf{n}_{p,q}^H] \\ &= \bar{\Phi} E[\text{diag}(\boldsymbol{\gamma}_{p,q} \odot \boldsymbol{\gamma}_{p,q}^*)] \bar{\Phi}^H + \sigma_n^2 \mathbf{I}_{N'M'} \\ &= \bar{\Phi} E[\text{diag}(\boldsymbol{\gamma} \odot \boldsymbol{\gamma}^*)] \bar{\Phi}^H + \sigma_n^2 \mathbf{I}_{N'M'} \\ &= \bar{\Phi} \Gamma \bar{\Phi}^H + \sigma_n^2 \mathbf{I}_{N'M'}. \end{aligned} \quad (17)$$

In the above derivation, we have used the fact that (i) different elements in the (p, q) th angle-Doppler profile are independent of each other, as well as different elements in the (p, q) th thermal noise vector $\mathbf{n}_{p,q}$; and (ii) $\boldsymbol{\gamma} \odot \boldsymbol{\gamma}^* = \bar{\boldsymbol{\gamma}}_{p,q} \odot \bar{\boldsymbol{\gamma}}_{p,q}^*$. From (17), we find that different subsnapshots share the same interference covariance matrix. Furthermore, it is noted that the full dimension (with the DOFs of NM) interference covariance matrix can be obtained according to (5) if the parameter $\Gamma = \text{diag}(\mathbf{a}) = E[\boldsymbol{\gamma} \odot \boldsymbol{\gamma}^*]$ is known. In other words, although we use the subsnapshots to recover the angle-Doppler profile, we can obtain the interference covariance matrix estimate exactly the same as what we get using the full snapshot. This will lead to no DOFs loss in the proposed algorithm. For the real applications, we can

not obtain the true parameter \mathbf{a} but can estimate it using the generated subsnapshots with the form of

$$\hat{\mathbf{a}} = \frac{1}{K} \sum_{p=1}^{N-N'+1} \sum_{q=1}^{M-M'+1} \bar{\mathbf{y}}_{p,q} \odot \bar{\mathbf{y}}_{p,q}^* \quad (18)$$

There are several aspects which should be noted about the recovery of angle-Doppler profile $\bar{\mathbf{y}}_{p,q}$ in (18). First, the values of N' and M' not only decide the number of subsnapshots but also are related to the accuracy of the recovered angle-Doppler profile. However, there is no theoretic argument in current literature to determine how large the size of the subsnapshot could be to obtain a unique recovery of the angle-Doppler profile, since the columns of the space-time steering dictionary $\bar{\Phi}$ are highly correlated and the samples are contaminated by the thermal noise. The following simulations will show that there is such a range of N' and M' that the angle-Doppler profiles will be well recovered from the subsnapshots. Second, since the convergence of the sparsity-based STAP algorithms is very fast (e.g., a good estimation of the interference covariance matrix can be obtained with the number of subsnapshots K equal to 3 or 4 [25, 26]), the size of $N'M'$ can be slightly smaller than NM . It is said that we can employ negligible loss in system DOFs to obtain multiplicative increment in the snapshots.

Thirdly, the subsnapshots are generated only using the received data in the CUT. On one hand, all subsnapshots satisfy a common sparsity profile, which is very important especially in presence of discrete interferers merely in the CUT. In this case, the snapshots adjacent to the CUT will have different sparsity profiles with the snapshot in the CUT, which results in significant bias between the estimated interference covariance matrix and the true interference covariance matrix of the CUT. On the other hand, because the recovered angle-Doppler profile in the CUT may also contain the information of target, it is necessary to eliminate the impacts of the target signal present in the CUT. This can be performed as the approach described in [23], which first determines the signal of interest area Ω in the angle-Doppler plane using the prior knowledge of the target signal (it is usually assumed to be known for STAP problem) as

$$\Omega = \left\{ (i_{n_1}, k_{n_1}), (i_{n_2}, k_{n_2}), \dots, (i_{n_{N_{\text{SOI}}}}, k_{n_{N_{\text{SOI}}}}) \right\}, \quad (19)$$

where (i_{n_m}, k_{n_m}) , $1 \leq m \leq N_{\text{SOI}}$ denote the possible indexes of the target signal in the discretized angle-Doppler plane. The size of N_{SOI} reflects the uncertainty along the angle and Doppler frequency axes. Then, the target signal is eliminated from the estimated interference spectrum by marking zero coefficients corresponding to Ω in the recovered angle-Doppler profile $\bar{\mathbf{y}}_{p,q}$.

After that, the interference plus noise covariance matrix can be estimated by

$$\hat{\mathbf{R}} = \sum_{i=1, k=1}^{N_d, N_s} \hat{a}_{i,k} \mathbf{v}(f_{d,i}, \phi_k) \mathbf{v}^H(f_{d,i}, \phi_k) + \hat{\sigma}_n^2 \mathbf{I}, \quad i, k \notin \Omega, \quad (20)$$

where $\hat{\sigma}_n^2$ is the estimated thermal noise power level.

After we obtain the estimated clutter plus noise covariance matrix, the idea behind linear constraint minimum variance (LCMV) approach is to minimize the interference plus noise output power whilst constraining the gain in the direction of the desired signal, which leads to the following minimization with constraints:

$$\min_{\mathbf{w}} \mathbf{w}^H \hat{\mathbf{R}} \mathbf{w} \quad \text{s.t.} \quad \mathbf{w}^H \mathbf{s} = 1, \quad (21)$$

where $\mathbf{s} = \mathbf{v}(f_{d,t}, \phi_t)$ represents the space-time steering vector in the target direction ($f_{d,t}$ and ϕ_t are the target Doppler frequency and the target AOA, resp.). Using the method of Lagrange multipliers, the LCMV STAP filter weight vector is given by

$$\hat{\mathbf{w}} = \frac{\hat{\mathbf{R}}^{-1} \mathbf{s}}{\mathbf{s}^H \hat{\mathbf{R}}^{-1} \mathbf{s}}. \quad (22)$$

Thus, the target can be detected by the adaptive matched filter (AMF) detector with the form

$$\frac{|\mathbf{s}^H \hat{\mathbf{R}}^{-1} \mathbf{x}|^2}{\mathbf{s}^H \hat{\mathbf{R}}^{-1} \mathbf{s}} \underset{H_0}{\overset{H_1}{\geq}} \xi_{\text{AMF}}, \quad (23)$$

where H_0 is the null hypothesis (i.e., target absence), H_1 is the alternative hypothesis (i.e., target presence), and ξ_{AMF} represents the target detection threshold.

It is remarked that the conventional D3-LS STAP methods [5–8] firstly eliminate the target signal effects and then employ the SASM technique to generate a number of subsnapshots. The proposed algorithm directly employs the SASM technique for the received data in the CUT to generate multiple subsnapshots and uses these subsnapshots to recover the interference spectrum. After determining the target of interest area Ω in the angle-Doppler plane using the prior knowledge, the target signal can be eliminated from the estimated interference spectrum by marking zero coefficients corresponding to Ω in the recovered angle-Doppler profile. This approach will obtain better accuracy of the estimated interference spectrum than the method that eliminates the target signal before sparse recovery. This is because of the fact that if we eliminate the target signal before sparse recovery as in the D3-LS approach, some interference components correlated with the target signal will also be canceled. On the other hand, if we directly recover the interference spectrum, one can expect to obtain simultaneously good estimation of the interference components and the target signals, for example, the recovered results in [23].

3.3. Complexity Analysis. For the proposed algorithm, the computational complexity mainly comes from the recovery of the angle-Doppler profile $\bar{\mathbf{y}}_{p,q}$. If we use the SR algorithms with single measurement vector (SMV-SR) to recover $\bar{\mathbf{y}}_{p,q}$ one by one, the computational complexity will be K times of that of recovering single angle-Doppler profile. This will lead to very high computational complexity. However, if we use the SR algorithms with MMV (MMV-SR) [37], the computational complexity will be significantly reduced compared with that of recovering the angle-Doppler profiles one by one.

TABLE 1: Radar system parameters.

Parameter	Value
Antenna array	side-looking ULA
Antenna array spacing	$\lambda_c/2$
Number of elements in ULA	12
Number of pulses in one CPI	12
Carrier wavelength	$\lambda_c = 0.3$ m
Instantaneous bandwidth	5 MHz
Transmit taper	Uniform
Pulse repetition frequency (PRF)	4000 Hz
Platform velocity	300 m/s
Platform height	3000 m
Clutter-to-noise ratio (CNR)	30 dB
The target AOA	0°

Of course, the computational complexity of the MMV-SR algorithms is still higher than that of recovering single angle-Doppler profile.

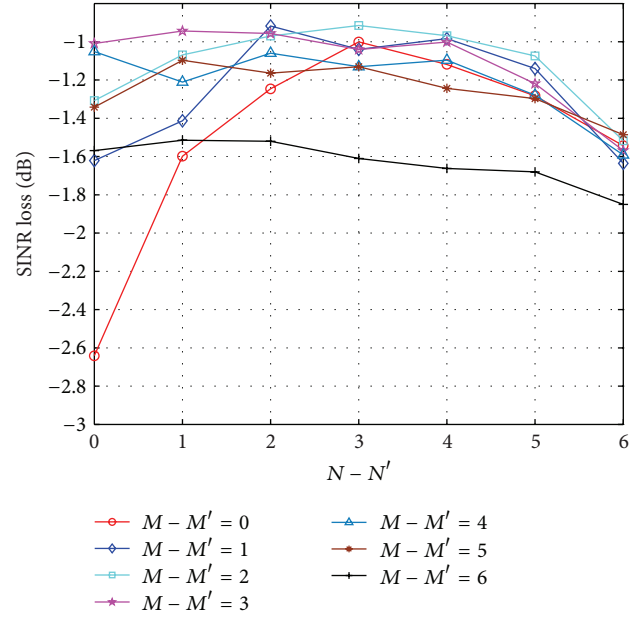
4. Simulation Results

In this section, we assess the output SINR and probability of detection (P_d) performance of the proposed algorithm using simulated data and compare it with the generalized F/B method in [35], the NSR-STAP algorithm in [25, 26], the D3-LS STAP method in [7], and the D3-SR-STAP algorithm in [23]. The parameters of the airborne radar systems are shown in Table 1. The thermal noise is modeled as a Gaussian white noise with unity power. The clutter and target powers are referred to as the thermal noise power. In the simulations, the diagonal loading factor $\hat{\sigma}_n^2$ is set to the noise level for all algorithms. For the sparsity-based STAP algorithms, we set $\rho_d = \rho_s = 4$ and use recently developed fast sparse recovery algorithm, called focal underdetermined system solution (FOCUSS) [37, 38], with the same parameters setting to compute the angle-Doppler profiles. For the NSR-STAP algorithm and the generalized F/B method, the numbers of training snapshots are set to 4 and 30, respectively. In addition, $N' = 11$ and $M' = 11$ for the generalized F/B method and $N' = 8$ and $M' = 8$ for the D3-LS STAP method. The output SINR loss is defined to be its output SINR performance relative to the matched filter SNR_{opt} in an interference-free environment [1], given as

$$\text{SINR} = \frac{|\hat{\mathbf{w}}^H \mathbf{s}|^2}{\text{SNR}_{\text{opt}} |\hat{\mathbf{w}}^H \mathbf{R} \hat{\mathbf{w}}|} = \frac{|\hat{\mathbf{w}}^H \mathbf{s}|^2}{NM |\hat{\mathbf{w}}^H \mathbf{R} \hat{\mathbf{w}}|}, \quad (24)$$

where \mathbf{R} is the true interference covariance matrix.

4.1. Setting of the Size of $N'M'$. In this subsection, we investigate the selection of the size of $N'M'$ in the proposed SASM D3-SR-STAP algorithm. In the example, consider homogeneous environments with none discrete interferers and the target with the AOA 0° and normalized Doppler frequency 0.25. When $N' < N$ and $M' = M$, the subsnapshots are only

FIGURE 3: SINR loss versus the sizes of $N - N'$ and $M - M'$.

generated using the subtemporal smoothing technique; when $N' = N$ and $M' < M$, the subsnapshots are only generated using the subspectral smoothing technique; when $N' < N$ and $M' < M$, the subsnapshots are generated by the subtemporal smoothing, subspectral smoothing, and subspectral-temporal smoothing techniques. The simulation results are plotted in Figure 3. It is seen from the curves that (i) the output SINR performance of the proposed SASM D3-SR-STAP algorithm is better than that of the conventional D3-SR-STAP algorithm corresponding to the case of $N' = N$ and $M' = M$ since the proposed algorithm uses multiple subsnapshots to estimate the interference covariance matrix. (ii) There is a range of the sizes of N' and M' to obtain a good SINR performance, which leads to a relaxing parameter setting of N' and M' . (iii) When $M - M' > 5$ or $N - N' > 5$, the performance of the proposed algorithm degrades because of too many DOFs reduced (corresponding to not enough observation data to recover the angle-Doppler profile). Therefore, for our simulations, it is best to select the size of $N'M'$ by making the ratio of $(N'M')/(NM)$ as big as possible whilst keeping $K = (N - N' + 1)(M - M' + 1) > 3$.

4.2. Comparison with Existing Algorithms. In the first example, we focus on the impact of discrete interferers only in presence of the CUT to the proposed algorithm. Consider two different cases: case 1, the homogeneous environments with none discrete interferers where the ideal spectral distribution of the interference is a diagonal line in the angle-Doppler plane; case 2, the nonhomogeneous environments. In this case, the snapshot in the CUT is a sum of clutter, one discrete interferer (the AOA -30° , the normalized Doppler frequency 0.3, and the power 25 dB), and the thermal noise, while the snapshots adjacent to the CUT are only a sum of clutter and thermal noise. Thus, the spectral distribution of the

snapshots adjacent to the CUT is different from that of the snapshot in the CUT, where the ideal spectral distribution of the interference in the CUT is the clutter ridge plus the discrete interferers. In the example, according to the results of the above subsection, we set $M' = M$ and $N - N' = 3$ for the proposed algorithm. The results that plot the SINR loss performance against the target Doppler frequency of the proposed algorithm and the existing algorithms are shown in Figures 4 and 5, which are averaged over 100 independent Monte Carlo runs. In Figure 5, the “No discrete interferer” denotes the approach that uses the precise clutter plus noise covariance matrix without discrete interferers information.

From the figures, we see that the proposed SASM D3-SR-STAP algorithm, the conventional D3-LS-STAP algorithm, and the D3-SR-STAP algorithm are robust to the case that the discrete interferers merely appear in the CUT, but the performance of the generalized F/B method, the NSR-STAP algorithm, and the approach of “No discrete interferer” is significantly degraded in this case. This is because the estimated covariance matrices that use the generalized F/B method, the NSR-STAP algorithm, and the approach of “No discrete interferer” do not include the discrete interferers information and can not effectively suppress the discrete interferers in the CUT. The D3 STAP algorithms (like the proposed SASM D3-SR-STAP algorithm, the conventional D3-LS-STAP algorithm, and the D3-SR-STAP algorithm) use only the snapshot in the CUT, thereby including both the clutter and discrete interferers information, and can suppress both the clutter and discrete interferers. We also observe that the proposed SASM D3-SR-STAP algorithm outperforms the generalized F/B method, the conventional D3-LS-STAP algorithm, and the D3-SR-STAP algorithm in most of Doppler bins in both cases but performs slightly worse than the generalized F/B method in the Doppler range of -0.1 to 0.1 . Although the proposed SASM D3-SR-STAP algorithm achieves worse SINR performance than the NSR-STAP algorithm in homogeneous environments, it obtains a much better SINR performance in nonhomogeneous environments. The cause for this is that the NSR-STAP algorithm uses more observed snapshots than the proposed algorithm and can achieve better performance than the proposed algorithm in homogeneous environments. However, in nonhomogeneous environments, the NSR-STAP algorithm does have a good estimation of the clutter covariance matrix, but it has no information of the discrete interferers resulting in a significant performance reduction.

In the second example, we focus on the impact of model mismatch, such as the ICM and the channel mismatch, to the proposed SASM D3-SR-STAP algorithm. The ICM can be formulated as a general model proposed by Ward in [1], which is suitable over the water scenario. The temporal autocorrelation of the fluctuations is Gaussian in shape with the form

$$\zeta(m) = \exp \left\{ -\frac{8\pi^2 \sigma_v^2 T_r^2}{\lambda_c^2} m^2 \right\}, \quad (25)$$

where T_r is the pulse repetition interval and σ_v is the velocity standard deviation (in the example, we set $\sigma_v = 1$ corresponding to a moderate clutter Doppler spreading situation).

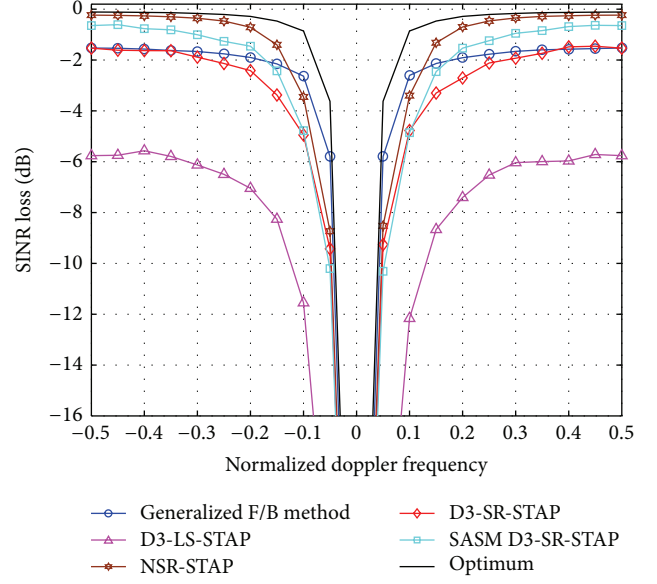


FIGURE 4: SINR loss against the target Doppler frequency in homogeneous environments.

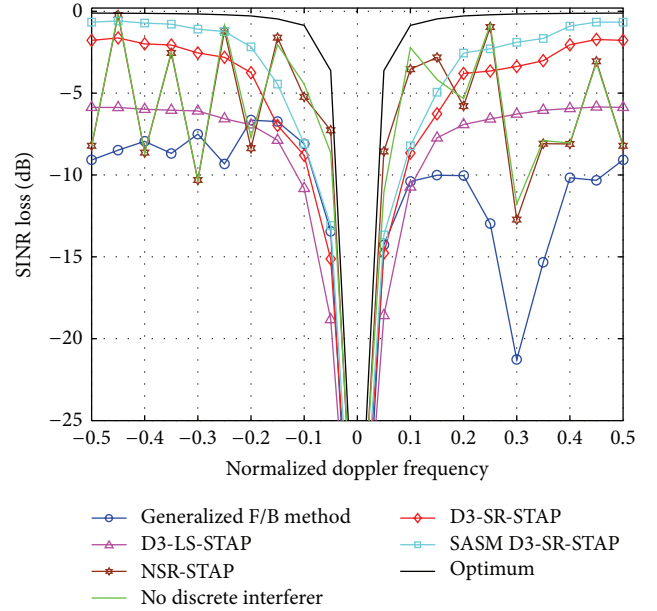


FIGURE 5: SINR loss against the target Doppler frequency in nonhomogeneous environments.

With regard to the channel mismatch, we only consider the angle-independent array errors described in [2]; that is, the amplitude and phase errors are modeled as a narrowband case as follows:

$$p(\delta_{\epsilon_a}) = \begin{cases} \frac{1}{\Delta\epsilon_a}, & \text{for } 0 \leq \delta_{\epsilon_a} \leq \Delta\epsilon_a, \\ 0, & \text{elsewhere,} \end{cases} \quad (26)$$

$$p(\delta_{\epsilon_p}) = \begin{cases} \frac{1}{\Delta\epsilon_p}, & \text{for } -\frac{\Delta\epsilon_p}{2} \leq \delta_{\epsilon_p} \leq \frac{\Delta\epsilon_p}{2}, \\ 0, & \text{elsewhere,} \end{cases}$$

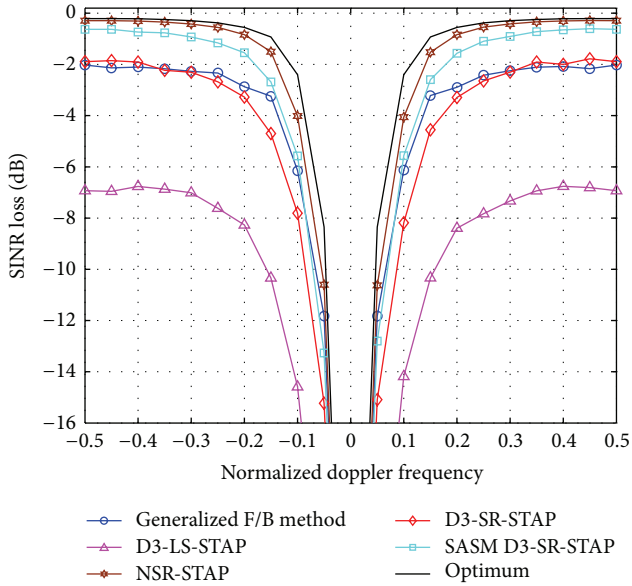


FIGURE 6: SINR loss against the target Doppler frequency considering ICM.

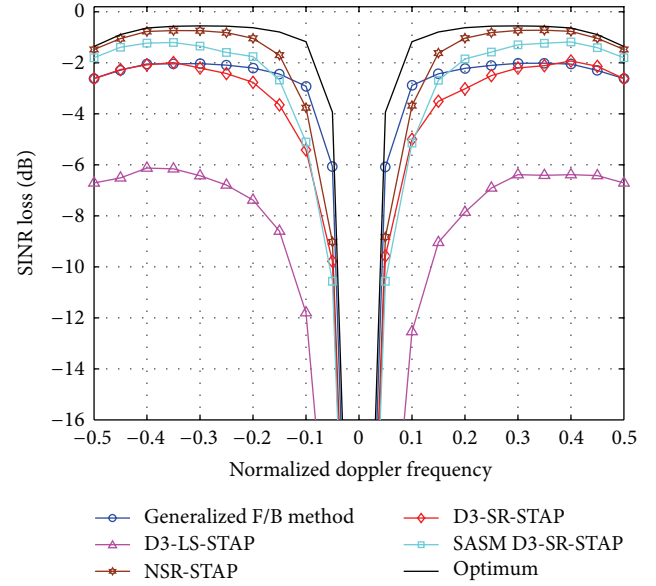


FIGURE 7: SINR loss against the target Doppler frequency considering channel mismatch.

where $p(\delta_{\epsilon_a})$ and $p(\delta_{\epsilon_p})$ are the probability density functions (pdfs) (uniform) associated with the amplitude and phase errors, respectively. The sparsity-based STAP algorithms can be easily extended to the situation in which the array has been calibrated. In fact, we only have to modify the space-time steering vectors in the space-time steering dictionary. Therefore, in the example, we set $\Delta\epsilon_a = 0.01$ and $\Delta\epsilon_p = 2^\circ$ corresponding to the general case after the array has been calibrated [16]. In severe channel mismatch cases, the array must be calibrated before using the proposed approach. The general calibration-on-clutter methods are summarized in Table 3 in [16]. Interested readers are referred to [16] for details. The other parameters are the same as those in Table 1.

Figures 6 and 7 depict the SINR loss performance against the target Doppler frequency of all algorithms under the cases considering the ICM and the channel mismatch, respectively. Compared with the case without ICM and channel mismatch in Figure 4, the curves show that the performance of all algorithms have some degradations because of the ICM and the channel mismatch. However, the performance of the proposed algorithm is still better than the generalized F/B method, the conventional D3-LS-STAP algorithm, and the D3-SR-STAP algorithm. Although the proposed algorithm performs worse than the NSR-STAP algorithm, it will not suffer performance decrease in presence of discrete interferers only in the CUT. In addition, the NSR-STAP algorithm requires the training snapshots to satisfy independent and identical distribution resulting in snapshots selection problem, whereas the proposed algorithm can avoid this problem. Furthermore, we present the P_d versus the target signal-to-noise ratio (SNR) for all algorithms considering different cases in Figure 8 (the ideal case with no ICM and channel mismatch), Figure 9 (the case with ICM), and Figure 10 (the case with channel mismatch). The false alarm rate P_{fa} is

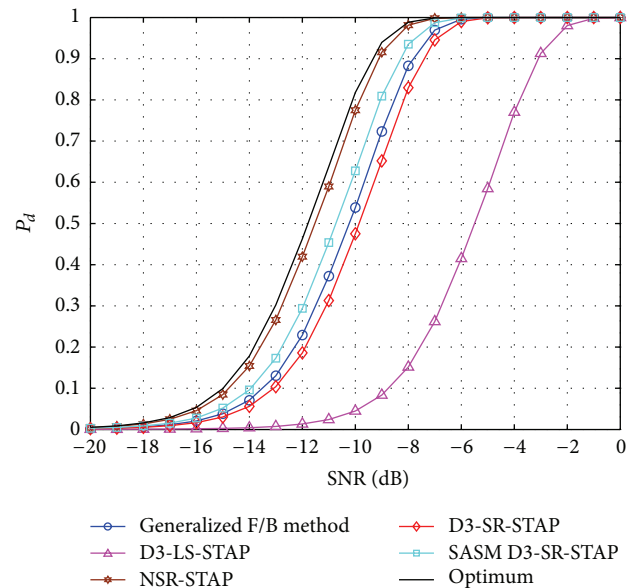
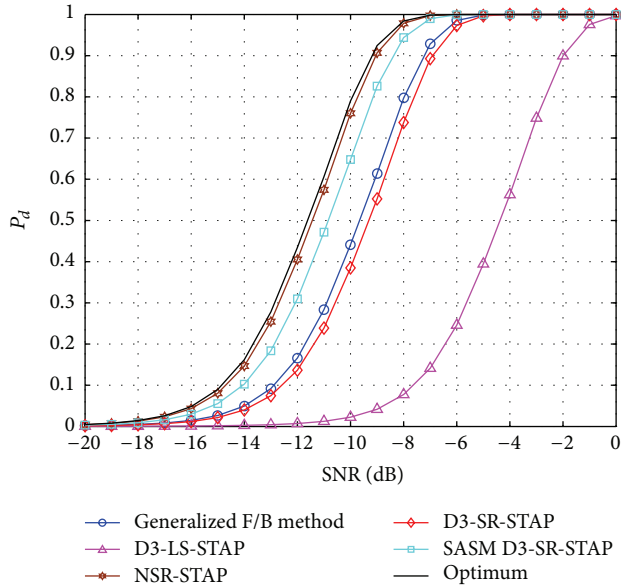
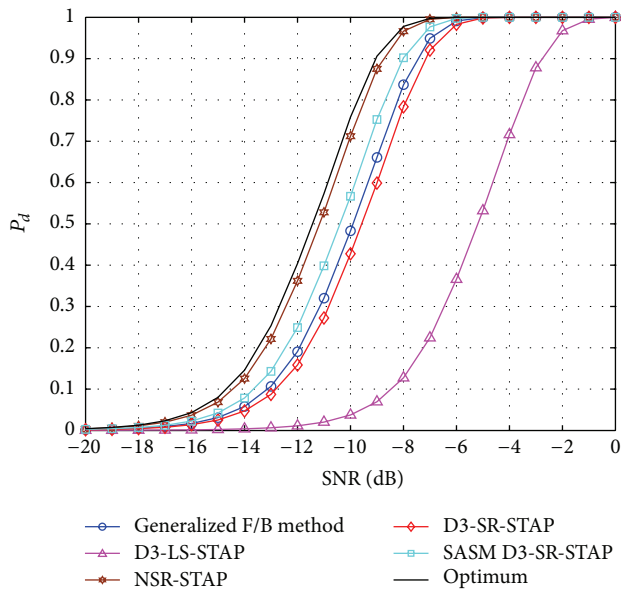


FIGURE 8: P_d versus the target SNR in the ideal case.

set to 10^{-4} and for simulation purposes the threshold and P_d estimates are based on 10,000 samples. We suppose the target is injected in the boresight with normalized Doppler frequency 0.25. The figure illustrates that the proposed algorithm provides higher detection rate than the generalized F/B method, the conventional D3-LS-STAP algorithm, and the D3-SR-STAP algorithm in all three cases, but a slightly lower detection rate than the NSR-STAP algorithm. However, as one can expect, the proposed algorithm will obtain better detection rate when the discrete interferers merely appear in the CUT.

FIGURE 9: P_d versus the target SNR considering ICM.FIGURE 10: P_d versus the target SNR considering channel mismatch.

5. Conclusions

In this paper, we proposed a novel D3-SR-STAP algorithm utilizing the SASM techniques for airborne radar applications. Different from either NSR-STAP or D3-SR-STAP, the proposed algorithm generates multiple subsnapshots with the snapshot in the CUT by exploiting the space-time structure of the steering vector and the uncorrelated nature of the components of the interference covariance matrix. By jointly using these multiple subsnapshots and the sparsity of interference spectrum in the angle-Doppler plane, the proposed algorithm can obtain a better interference spectrum estimate, thereby a higher output SINR, than the D3-SR-STAP algorithm.

Simulation results have shown that the proposed algorithm outperforms the generalized F/B method, the conventional D3-LS-STAP algorithm, and the D3-SR-STAP algorithm in both homogeneous and nonhomogeneous environments and provides better performance than the NSR-STAP algorithm in presence of discrete interferers merely in the CUT. Since the model mismatch is only considered in simulations in the paper, further investigation about the theoretical analysis of the model mismatch impacts on sparsity-based STAP algorithms is required.

Conflict of Interests

The authors declare that there is no conflict of interests regarding the publication of this paper.

Acknowledgment

This work is funded in part by the National Natural Science Foundation of China (61101182, 61201334, and 61401478).

References

- [1] J. Ward, "Space-time adaptive processing for airborne radar," Technical Report 1015, MIT Lincoln laboratory, Lexington, Mass, USA, 1994.
- [2] J. R. Guerci, *Space-Time Adaptive Processing for Radar*, Artech House, 2003.
- [3] W. L. Melvin, "A STAP overview," *IEEE Aerospace and Electronic Systems Magazine*, vol. 19, no. 1, pp. 19–35, 2004.
- [4] R. Klemm, *Principles of Space-Time Adaptive Processing*, Institute of Electrical Engineering, London, UK, 2006.
- [5] T. K. Sarkar and N. Sangruji, "Adaptive nulling system for a narrow-band signal with a look-direction constraint utilizing the conjugate gradient method," *IEEE Transactions on Antennas and Propagation*, vol. 37, no. 7, pp. 940–944, 1989.
- [6] H. Wang, Y. Zhang, and Q. Zhang, "View of current status of space-time processing algorithms research," in *Proceedings of the IEEE International Radar Conference*, pp. 635–640, Alexandria, Va, USA, May 1995.
- [7] T. K. Sarkar, H. Wang, S. Park et al., "A deterministic least-squares approach to space-time adaptive processing (STAP)," *IEEE Transactions on Antennas and Propagation*, vol. 49, no. 1, pp. 91–103, 2001.
- [8] D. Cristallini and W. Burger, "A robust direct data domain approach for STAP," *IEEE Transactions on Signal Processing*, vol. 60, no. 3, pp. 1283–1294, 2012.
- [9] E. Aboutanios and B. Mulgrew, "Hybrid detection approach for STAP in heterogeneous clutter," *IEEE Transactions on Aerospace and Electronic Systems*, vol. 46, no. 3, pp. 1021–1033, 2010.
- [10] E. Yang, R. Adve, J. Chun, and J. Chun, "Hybrid direct data domain sigma-delta space-time adaptive processing algorithm in non-homogeneous clutter," *IET Radar, Sonar and Navigation*, vol. 4, no. 4, pp. 611–625, 2010.
- [11] C. T. Capraro, G. T. Capraro, I. Bradaric, D. D. Weiner, M. C. Wicks, and W. J. Baldygo, "Implementing digital terrain data in knowledge-aided space-time adaptive processing," *IEEE Transactions on Aerospace and Electronic Systems*, vol. 42, no. 3, pp. 1080–1097, 2006.

- [12] A. Farina, P. Lombardo, and M. Pirri, "Nonlinear nonadaptive space-time processing for airborne early warning radar," *IEEE Proceedings-Radar, Sonar and Navigation*, vol. 145, no. 1, pp. 9–18, 1998.
- [13] A. Farina, P. Lombardo, and M. Pirri, "Nonlinear STAP processing," *Electronics & Communication Engineering Journal*, vol. 11, no. 1, pp. 41–48, 1999.
- [14] K. Gerlach and M. L. Picciolo, "Airborne/spacebased radar STAP using a structured covariance matrix," *IEEE Transactions on Aerospace and Electronic Systems*, vol. 39, no. 1, pp. 269–281, 2003.
- [15] J. S. Bergin, C. M. Teixeira, P. M. Techau, and J. R. Guerci, "Improved clutter mitigation performance using knowledge-aided space-time adaptive processing," *IEEE Transactions on Aerospace and Electronic Systems*, vol. 42, no. 3, pp. 997–1009, 2006.
- [16] W. L. Mevin and G. A. Showman, "An approach to knowledge-aided covariance estimation," *IEEE Transactions on Aerospace and Electronic Systems*, vol. 42, no. 3, pp. 1021–1042, 2006.
- [17] Z. Yang, R. C. de Lamare, X. Li, and Q. Wang, "Knowledge-aided STAP using low rank and geometry properties," *International Journal of Antennas and Propagation*, vol. 2014, Article ID 196507, 14 pages, 2014.
- [18] W. Xie, K. Duan, F. Gao, Y. Wang, and Z. Zhang, "Clutter suppression for airborne phased radar with conformal arrays by least squares estimation," *Signal Processing*, vol. 91, no. 7, pp. 1665–1669, 2011.
- [19] W. L. Melvin and J. R. Guerci, "Knowledge-aided signal processing: a new paradigm for radar and other advanced sensors," *IEEE Transactions on Aerospace and Electronic Systems*, vol. 42, no. 3, pp. 983–995, 2006.
- [20] S. Maria and J.-J. Fuchs, "Application of the global matched filter to STAP data: an efficient algorithmic approach," in *Proceedings of the IEEE International Conference on Acoustics, Speech and Signal Processing (ICASSP '06)*, May 2006.
- [21] J. Li, X. Zhu, P. Stoica, and M. Rangaswamy, "High resolution angle-doppler imaging for MTI radar," *IEEE Transactions on Aerospace and Electronic Systems*, vol. 46, no. 3, pp. 1544–1556, 2010.
- [22] I. W. Selesnick, S. U. Pillai, K. Y. Li, and B. Himed, "Angle-Doppler processing using sparse regularization," in *Proceedings of the IEEE International Conference on Acoustics, Speech, and Signal Processing (ICASSP '10)*, pp. 2750–2753, Dallas, Tex, USA, March 2010.
- [23] K. Sun, H. Meng, Y. Wang, and X. Wang, "Direct data domain STAP using sparse representation of clutter spectrum," *Signal Processing*, vol. 91, no. 9, pp. 2222–2236, 2011.
- [24] Z. Yang, X. Li, and H. Wang, "Space-time adaptive processing based on weighted regularized sparse recovery," *Progress in Electromagnetics Research B*, vol. 42, pp. 245–262, 2012.
- [25] K. Sun, H. Zhang, G. Li, H. Meng, and X. Wang, "A novel STAP algorithm using sparse recovery technique," in *Proceedings of the IEEE International Geoscience and Remote Sensing Symposium (IGARSS '09)*, pp. 336–339, July 2009.
- [26] Z. Yang, X. Li, H. Wang, and L. Nie, "Sparsity-based space-time adaptive processing using complex-valued homotopy technique for airborne radar," *IET Signal Processing*, vol. 8, no. 5, pp. 552–564, 2014.
- [27] Z. Yang, X. Li, H. Wang, and W. Jiang, "On clutter sparsity analysis in space-time adaptive processing airborne radar," *IEEE Geoscience and Remote Sensing Letters*, vol. 10, no. 5, pp. 1214–1218, 2013.
- [28] Z. Yang, X. Li, H. Wang, and W. Jiang, "Adaptive clutter suppression based on iterative adaptive approach for airborne radar," *Signal Processing*, vol. 93, no. 12, pp. 3567–3577, 2013.
- [29] S. Sen, "OFDM radar space-time adaptive processing by exploiting spatio-temporal sparsity," *IEEE Transactions on Signal Processing*, vol. 61, no. 1, pp. 118–130, 2013.
- [30] Z. Yang, R. C. de Lamare, and X. Li, " L_1 -regularized STAP algorithms with a generalized sidelobe canceler architecture for airborne radar," *IEEE Transactions on Signal Processing*, vol. 60, no. 2, pp. 674–686, 2012.
- [31] Z. Yang, R. C. de Lamare, and X. Li, "Sparsity-aware space-time adaptive processing algorithms with L_1 -norm regularization for airborne radar," *IET Signal Processing*, vol. 6, no. 5, pp. 413–423, 2012.
- [32] R. C. de Lamare and R. Sampaio-Neto, "Adaptive reduced-rank processing based on joint and iterative interpolation, decimation, and filtering," *IEEE Transactions on Signal Processing*, vol. 57, no. 7, pp. 2503–2514, 2009.
- [33] R. Fa, R. C. de Lamare, and L. Wang, "Reduced-rank STAP schemes for airborne radar based on switched joint interpolation, decimation and filtering algorithm," *IEEE Transactions on Signal Processing*, vol. 58, no. 8, pp. 4182–4194, 2010.
- [34] P. Stoica and R. Moses, *Spectral Analysis of Signals*, Prentice Hall, Upper Saddle River, NJ, USA, 2005.
- [35] S. U. Pillai, Y. L. Kim, and J. R. Guerci, "Generalized forward/backward subaperture smoothing techniques for sample starved STAP," *IEEE Transactions on Signal Processing*, vol. 48, no. 12, pp. 3569–3574, 2000.
- [36] G. W. Titi and D. F. Marshall, "The ARPA/NAVY mountain program: adaptive signal processing for airborne early warning radar," in *Proceedings of the IEEE International Conference on Acoustics, Speech, and Signal Processing (ICASSP '96)*, pp. 1165–1168, May 1996.
- [37] S. F. Cotter, B. D. Rao, K. Engan, and K. Kreutz-Delgado, "Sparse solutions to linear inverse problems with multiple measurement vectors," *IEEE Transactions on Signal Processing*, vol. 53, no. 7, pp. 2477–2488, 2005.
- [38] I. F. Gorodnitsky and B. D. Rao, "Sparse signal reconstruction from limited data using FOCUSS: a re-weighted minimum norm algorithm," *IEEE Transactions on Signal Processing*, vol. 45, no. 3, pp. 600–616, 1997.

Research Article

An Improved Antenna Array Pattern Synthesis Method Using Fast Fourier Transforms

Xucun Wang,^{1,2} Yiguo Zhou,¹ and Yanfei Wang¹

¹*Institute of Electronics, Chinese Academy of Sciences, Beijing 100190, China*

²*University of Chinese Academy of Sciences, Beijing 100190, China*

Correspondence should be addressed to Xucun Wang; wangxucun1900@126.com

Received 21 April 2014; Revised 18 August 2014; Accepted 22 August 2014

Academic Editor: Michelangelo Villano

Copyright © 2015 Xucun Wang et al. This is an open access article distributed under the Creative Commons Attribution License, which permits unrestricted use, distribution, and reproduction in any medium, provided the original work is properly cited.

An improved antenna array pattern synthesis method using fast Fourier transform is proposed, which can be effectively applied to the synthesis of large planar arrays with periodic structure. Theoretical and simulative analyses show that the original FFT method has a low convergence rate and the converged solution can hardly fully meet the requirements of the desired pattern. A scaling factor is introduced to the original method. By choosing a proper value for the scaling factor, the convergence rate can be greatly improved and the final solution is able to fully meet the expectations. Simulation results are given to demonstrate the effectiveness of the proposed algorithm.

1. Introduction

In order to solve complex antenna pattern synthesis problems, various methods using various optimization algorithms have been developed. In [1], a quadratic program is formed for arbitrary array pattern synthesis. In [2], a convex optimization problem [3] is formulated for pattern synthesis subject to arbitrary upper bounds. For certain cases, the convex programming problem can be reduced to a linear programming problem [4]. In [5] an effective hybrid optimization method is proposed for footprint pattern synthesis of very large planar antenna arrays [6]. The methods mentioned above all adopt conventional optimization algorithms [7]. Global optimization algorithms such as genetic algorithms [8–10] and particle swarm optimization algorithms [11–13] have also been successfully applied in pattern synthesis problems. To approximate the desired pattern for an array, we need to discretize the angular space. The bigger the elements number is, the greater the required discrete density needs to be. Usually, the computational complexity would grow greatly as the elements number increases. As a consequence, normal synthesis techniques using local or global optimization algorithms are usually not suitable for large planar arrays.

As we know, fast Fourier transforms (FFT) are able to quickly compute the radiation pattern of an array with periodic structure. Once the number of FFT points is specified, the computation time is barely affected by the element number. In [14], an FFT method suitable for large planar arrays is proposed. The operation is very straightforward, which mainly involves direct and inverse fast Fourier transforms. In [15], a modified iterative FFT technique is proposed for leaky-wave antenna pattern synthesis. In [16], FFT is used for the pattern synthesis of nonuniform antenna arrays. The iterative FFT method is very efficient as shown in [14], and many examples are presented, but why the method is effective has not been explained.

In this paper, both theoretical and simulative analyses of the FFT method are presented. It is found that, though effective, it is a slow-convergence method and can hardly converge to the optimum solution. Based on the analyses, we introduce a scaling factor and the performance can be greatly improved.

2. Original FFT Method for Pattern Synthesis

First, we establish the relationship between a certain point in the FFT result and the corresponding angle of the radiation

pattern. Consider a planar array with $M \times N$ elements arranging in a rectangular grid and spacing d_x and d_y between rows and columns. Assume the element pattern is isotropic. The array factor is given by

$$F(\theta, \phi) = \sum_{m=0}^{M-1} \sum_{n=0}^{N-1} I_{mn} e^{j2\pi[m((d_x/\lambda) \sin \theta \cos \phi) + n((d_y/\lambda) \sin \theta \sin \phi)]}, \quad (1)$$

where I_{mn} is the complex excitation of the m th element and λ is the wavelength. If the (u, v) coordinates ($u = \sin \theta \cos \phi$, $v = \sin \theta \sin \phi$) are used, the array pattern can be written as

$$F(u, v) = \sum_{m=0}^{M-1} \sum_{n=0}^{N-1} I_{mn} e^{j2\pi[m((d_x/\lambda)u) + n((d_y/\lambda)v)]}. \quad (2)$$

Performing $K_{\text{fft}} \times L_{\text{fft}}$ points 2D inverse fast Fourier transform (IFFT) on the excitations, we get

$$IF(k, l) = \frac{1}{K_{\text{fft}} L_{\text{fft}}} \sum_{m=0}^{M-1} \sum_{n=0}^{N-1} I_{mn} e^{j2\pi[m(k/K_{\text{fft}}) + n(l/L_{\text{fft}})]} \quad (3)$$

$$(k = 0, 1, \dots, K_{\text{fft}} - 1; l = 0, 1, \dots, L_{\text{fft}} - 1).$$

If we want to represent the array factor using $IF(k, l)$, then the coordinates (u, v) and (k, l) are related by

$$\frac{d_x}{\lambda} u = \frac{k}{K_{\text{fft}}} + S_k \quad (4)$$

$$\frac{d_y}{\lambda} v = \frac{l}{L_{\text{fft}}} + S_l,$$

where S_k and S_l are integers, making sure both sides of the equations have the same value range. Suppose that both K_{fft} and L_{fft} are even numbers. Define

$$k' = \begin{cases} k + \frac{K_{\text{fft}}}{2}, & k < \frac{K_{\text{fft}}}{2} \\ k - \frac{K_{\text{fft}}}{2}, & k \geq \frac{K_{\text{fft}}}{2} \end{cases} \quad (5)$$

$$l' = \begin{cases} l + \frac{L_{\text{fft}}}{2}, & l < \frac{L_{\text{fft}}}{2} \\ l - \frac{L_{\text{fft}}}{2}, & l \geq \frac{L_{\text{fft}}}{2} \end{cases}.$$

Combining (4) and (5) and considering the value ranges of u and v , we have

$$u = \frac{\lambda}{d_x} \left(\frac{k'}{K_{\text{fft}}} - \frac{1}{2} \right) \quad (6)$$

$$v = \frac{\lambda}{d_y} \left(\frac{l'}{L_{\text{fft}}} - \frac{1}{2} \right).$$

So, the relation between the array factor and the IFFT of the array excitation is

$$F(u, v) = K_{\text{fft}} L_{\text{fft}} \cdot IF(k', l'). \quad (7)$$

Finally, the visible space is given by

$$\left(\frac{\lambda}{d_x} \right)^2 \left(\frac{k'}{K_{\text{fft}}} - \frac{1}{2} \right)^2 + \left(\frac{\lambda}{d_y} \right)^2 \left(\frac{l'}{L_{\text{fft}}} - \frac{1}{2} \right)^2 \leq 1. \quad (8)$$

Note that the indices change in (5) is in fact the fftshift operation in Matlab.

Once the corresponding relationship is established, the procedure of the FFT method for pattern synthesis is given as follows.

- (1) Specify dimension of the array $M \times N$, the initial excitation $I_{mn}^{(1)}$, the FFT points $K_{\text{fft}} \times L_{\text{fft}}$, and the maximum iteration times N_{max} .
- (2) Perform IFFT on the excitation of the i th iteration $I_{mn}^{(i)}$ and obtain the array factor $F_{kl}^{(i)}$.
- (3) Extract the amplitude $|F_{kl}^{(i)}|$ and phase $\phi_{kl}^{(i)}$ of $F_{kl}^{(i)}$.
- (4) Compare $|F_{kl}^{(i)}|$ with the desired pattern F_{kl}^e . If the computed pattern fully meets the requirements or the maximum iteration time is reached, terminate the procedure; otherwise go to the next step.
- (5) Obtain the new pattern $F_{kl}^{(i)'}$ by replacing the undesired $F_{kl}^{(i)}$ with $F_{kl}^e \cdot e^{j\phi_{kl}^{(i)}}$ as follows:

$$F_{kl}^{(i)'} = \begin{cases} F_{kl}^e \cdot e^{j\phi_{kl}^{(i)}}, & (k, l) \in U \\ F_{kl}^{(i)}, & (k, l) \notin U, \end{cases} \quad (9)$$

where U is a set containing all the points where the pattern is undesired. For example, if (k^*, l^*) is a point within the side lobe region and $|F_{k^*l^*}^{(i)}| > F_{k^*l^*}^e$, then it means that the side lobe level exceeds the desired level and that $(k^*, l^*) \in U$.

- (6) Perform $K_{\text{fft}} \times L_{\text{fft}}$ points 2-D FFT on $F_{kl}^{(i)'}$ and choose the first $M \times N$ points as the initial excitation for the next iteration $I_{mn}^{(i+1)}$. Constraints can be easily made for amplitude-only or phase-only synthesis.
- (7) Go to step (2).

The procedure is also illustrated in Figure 1.

3. Algorithm Analysis

The procedure is simple yet effective. In this section, the method is carefully examined. Without loss of generality, take an N -element linear array for example. Suppose that in the i th iteration the excitation sequence is $\mathbf{I}^{(i)}$ which has been extended to M_{fft} ($M_{\text{fft}} > N$) points by zero padding. M_{fft} is the number of the FFT points. After comparing the obtained pattern $\mathbf{F}^{(i)}$ with the desired pattern, we can obtain the error pattern $\Delta \mathbf{F}^{(i)}$. Now we will find the relation between the error pattern in the next iteration $\Delta \mathbf{F}^{(i+1)}$ and $\Delta \mathbf{F}^{(i)}$. It is difficult to

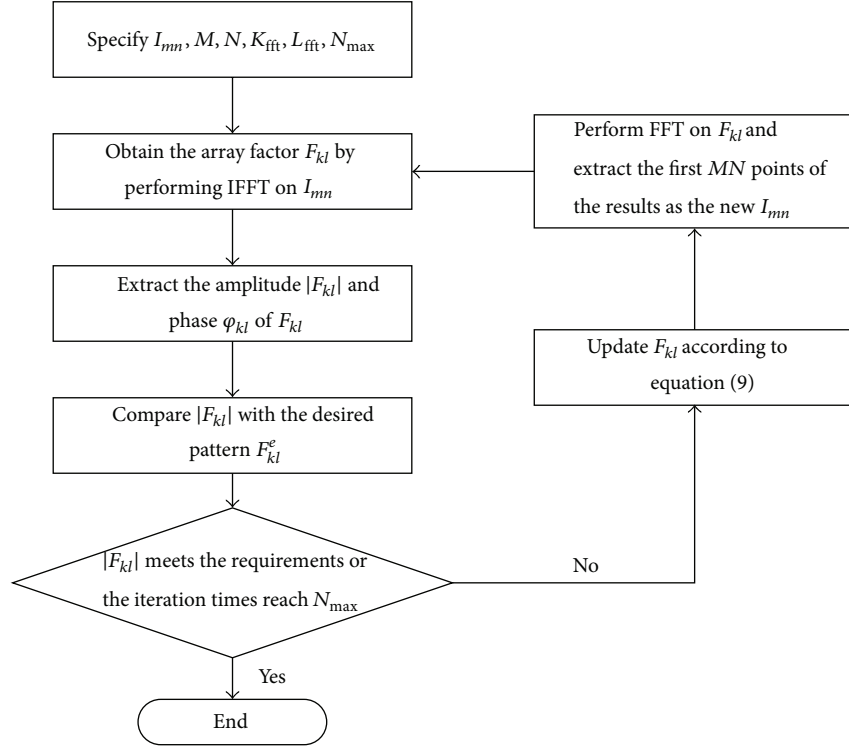


FIGURE 1: Flowchart of the FFT procedure for pattern synthesis.

precisely compute $\Delta \mathbf{F}^{(i+1)}$ through the above assumption. Let $\Delta \mathbf{I}^{(i)}$ be the corresponding error excitation for $\Delta \mathbf{F}^{(i)}$. Then

$$\Delta \mathbf{F}^{(i)} = \text{IFFT} [\Delta \mathbf{I}^{(i)}], \quad (10)$$

where $\Delta \mathbf{I}^{(i)}$ contains M_{fft} points. Consider the elements in $\Delta \mathbf{F}^{(i)}$

$$\Delta F_m^{(i)} = \begin{cases} (F_m^e - |F_m^{(i)}|) \cdot e^{j\varphi_m^{(i)}}, & m \in U \\ 0, & m \notin U. \end{cases} \quad (11)$$

If the set U only contains points representing the side lobe region, then the magnitude values of the elements in $\Delta \mathbf{F}^{(i)}$ are very small, as well as $\Delta \mathbf{I}^{(i)}$. So the variation in $\mathbf{I}^{(i+1)}$ from $\mathbf{I}^{(i)}$ is very little. Then we can use $\mathbf{F}^{(i)} + \Delta \mathbf{F}^{(i)}$ as the desired pattern in the $i + 1$ th iteration and obtain the error pattern

$$\Delta \mathbf{F}^{(i+1)} \approx \mathbf{F}^{(i)} + \Delta \mathbf{F}^{(i)} - \mathbf{F}^{(i+1)} = \text{IFFT} [\mathbf{I}^{(i)} + \Delta \mathbf{I}^{(i)} - \mathbf{I}^{(i+1)}]. \quad (12)$$

For complex weighting using both amplitude and phase, $\mathbf{I}^{(i+1)}$ is given as

$$\mathbf{I}^{(i+1)} = \mathbf{I}^{(i)} + [\Delta \mathbf{I}^{(i)} - \Delta \mathbf{I}^{(i)'}], \quad (13)$$

where $\Delta \mathbf{I}^{(i)'}$ is a sequence by setting the first N elements in $\Delta \mathbf{I}^{(i)}$ to zero. So

$$\Delta \mathbf{F}^{(i+1)} \approx \text{IFFT} [\Delta \mathbf{I}^{(i)'}. \quad (14)$$

As a result, we have

$$\|\Delta \mathbf{F}^{(i+1)}\|_2^2 \approx \frac{1}{M_{\text{fft}}} \|\Delta \mathbf{I}^{(i)'}\|_2^2 \leq \frac{1}{M_{\text{fft}}} \|\Delta \mathbf{I}^{(i)}\|_2^2 = \|\Delta \mathbf{F}^{(i)}\|_2^2, \quad (15)$$

where $\|\cdot\|_2$ denotes the l_2 -norm.

It is seen from (15) that the method has the ability to converge. However, as M_{fft} increases the difference between $\|\Delta \mathbf{I}^{(i)'}\|_2^2$ and $\|\Delta \mathbf{I}^{(i)}\|_2^2$ decreases. We can conclude that the method has a lower converge rate for larger FFT points. For amplitude-only synthesis, the analysis is similar and (15) still holds. For phase-only analysis, the excitation of the $i + 1$ th iteration is

$$\mathbf{I}^{(i+1)} = \mathbf{I} \cdot e^{j \arg[\mathbf{I}^{(i)} + \Delta \mathbf{I}^{(i)} - \Delta \mathbf{I}^{(i)'}]}, \quad (16)$$

where \mathbf{I} is the given amplitude. Since the magnitude value of $\Delta \mathbf{I}^{(i)}$ can be very small compared to \mathbf{I} , $\mathbf{I}^{(i+1)}$ can be approximated by

$$\mathbf{I}^{(i+1)} \approx \mathbf{I}^{(i)} + [\Delta \mathbf{I}^{(i)} - \Delta \mathbf{I}^{(i)'}]. \quad (17)$$

So the convergence properties are similar to amplitude-only or complex tapering.

To verify our analysis, we will give an example. Consider a linear array with 60 elements spacing by half wavelength. For the amplitude-only synthesis, the desired pattern has a maximum side lobe level of -40 dB. For the phase-only case, the maximum side lobe level is -18 dB. We use the uniform taper as the initial excitation and set the maximum iteration

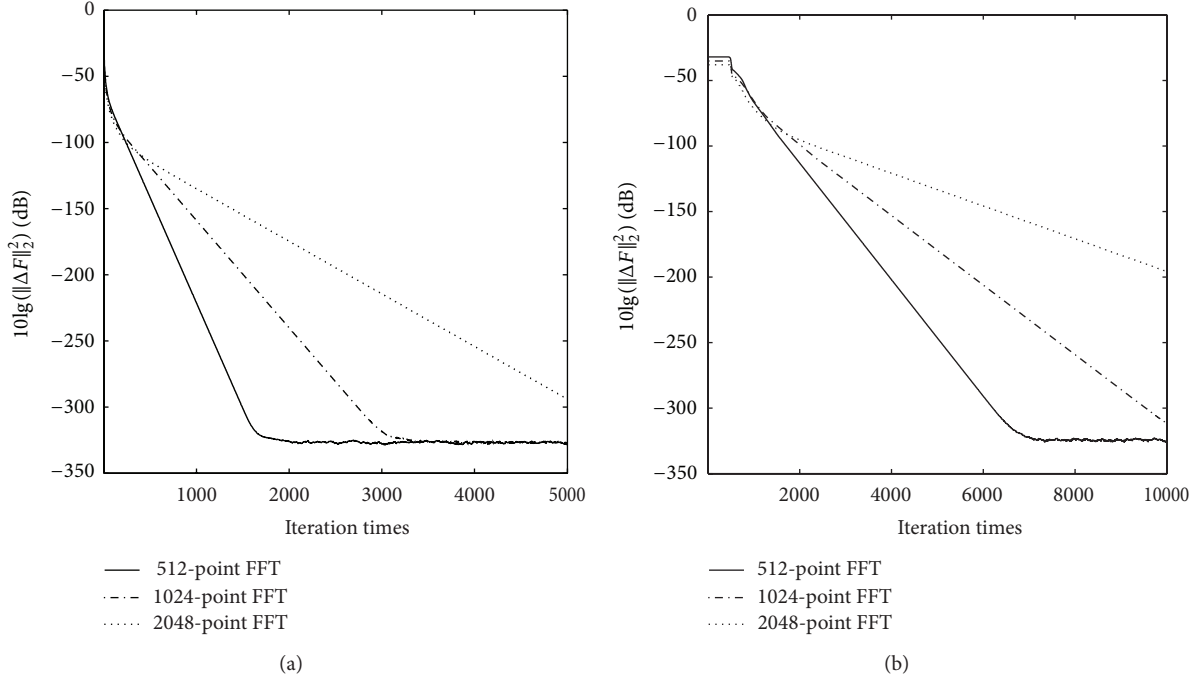


FIGURE 2: Norm of the error pattern: (a) amplitude-only and (b) phase-only.

number to 5000 and 10000 for the two cases, respectively. Figure 2 shows the convergence properties of the norm of the error pattern. We can see that the method has a low convergence rate, as it converges logarithmically in the latter part of the iteration. We can also see that the bigger the FFT points number is, the lower the method converges. Figure 2 also illustrates that although the norm of the error pattern can converge to a very low value, it does not reach zero. It means that the method can hardly synthesize a pattern that fully meets the requirements of the desired pattern.

4. Improved FFT Method for Pattern Synthesis

For planar arrays, the elements in the error pattern $\Delta F^{(i)}$ are given by

$$\Delta F_{kl}^{(i)} = \begin{cases} (F_{kl}^e - |F_{kl}^{(i)}|) \cdot e^{j\varphi_{kl}^{(i)}}, & (k, l) \in U \\ 0, & (k, l) \notin U. \end{cases} \quad (18)$$

First we divide U into U_s and U_m , which are the sets representing the side lobe region and the main lobe region, respectively. When $(k, l) \in U_s$, $F_{kl}^e - |F_{kl}^{(i)}| < 0$ and the value tends to converge towards zero more slowly as the procedure iterates. So, to change the slowly varying characteristics, we propose the following updating equation for the error pattern:

$$\Delta F_{kl}^{(i)} = \begin{cases} (\alpha^{(i)} \cdot F_{kl}^e - |F_{kl}^{(i)}|) \cdot e^{j\varphi_{kl}^{(i)}}, & (k, l) \in U_s \\ (F_{kl}^e - |F_{kl}^{(i)}|) \cdot e^{j\varphi_{kl}^{(i)}}, & (k, l) \in U_m \\ 0, & (k, l) \notin U, \end{cases} \quad (19)$$

where $\alpha^{(i)}$ is a scaling factor within the range $[0, 1]$. The smaller the value of $\alpha^{(i)}$ is, the more intense the excitation changes. In (19), when $(k, l) \in U_m$, the error pattern remains unchanged, since for main lobe shaping synthesis, we need to approximate $|F_{kl}^{(i)}| - F_{kl}^e$ to a certain error level, whereas in the side lobe region, only $F_{kl}^e \geq |F_{kl}^{(i)}|$ is required. So, the final updating equation replacing (9) is given by

$$F_{kl}^{(i)'} = \begin{cases} \alpha^{(i)} \cdot F_{kl}^e \cdot e^{j\varphi_{kl}^{(i)}}, & (k, l) \in U_s \\ F_{kl}^e \cdot e^{j\varphi_{kl}^{(i)}}, & (k, l) \in U_m \\ F_{kl}^{(i)}, & (k, l) \notin U. \end{cases} \quad (20)$$

To analyze the convergence properties of the proposed method, we still use the prior examples and consider a linear array with 60 elements spacing by half wavelength. The maximum iteration times are 5000 and 10000 as before. As illustrated in Figures 3 and 4, although the curves are not smooth, the norm of the error pattern can converge to zero for all the cases. In both figures, we can also see that the iteration times of the $\alpha = 0$ case are much less than that of $\alpha = 0.99$. Figures 5 and 6 show the influence of α value on the maximum iteration times and the array directivity. It is shown that as α grows near one, the iterations times increase rapidly but the directivity only changes a little. So we can say that the proposed method can give a good performance by setting α to zero. The radiation patterns obtained using $\alpha = 0.0$ are shown in Figure 7, where θ is measured from one end of the linear array to the other end.

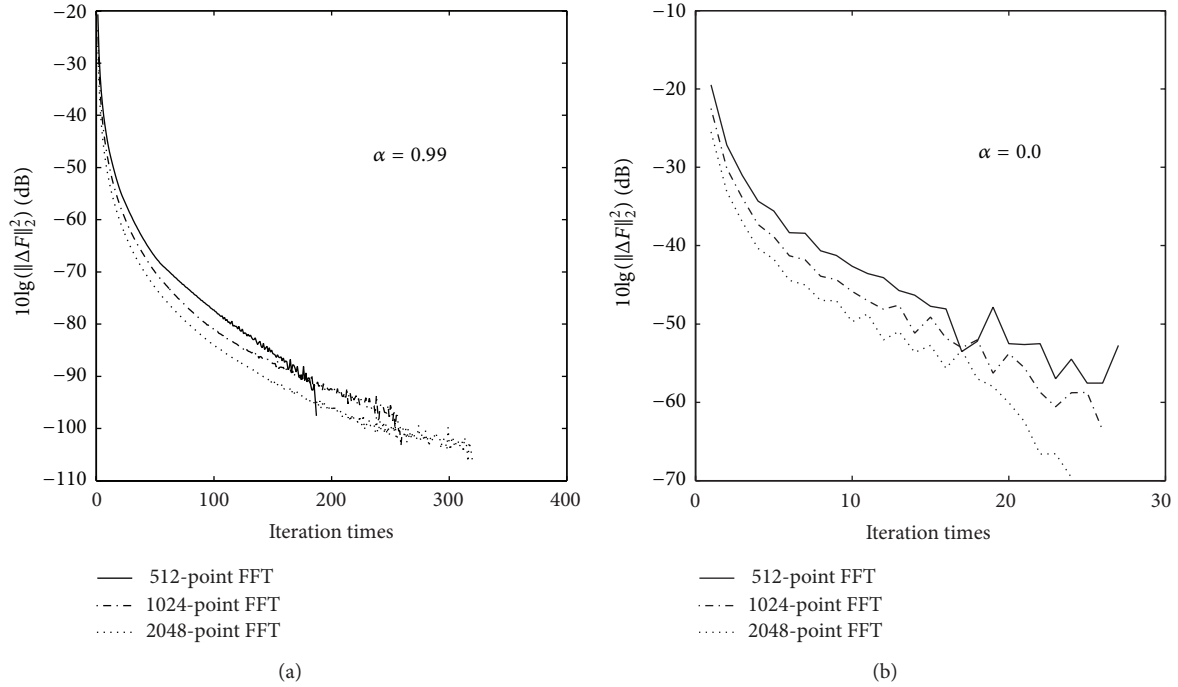


FIGURE 3: Norm of the error pattern for the amplitude-only tapering: (a) $\alpha = 0.99$ and (b) $\alpha = 0.0$.

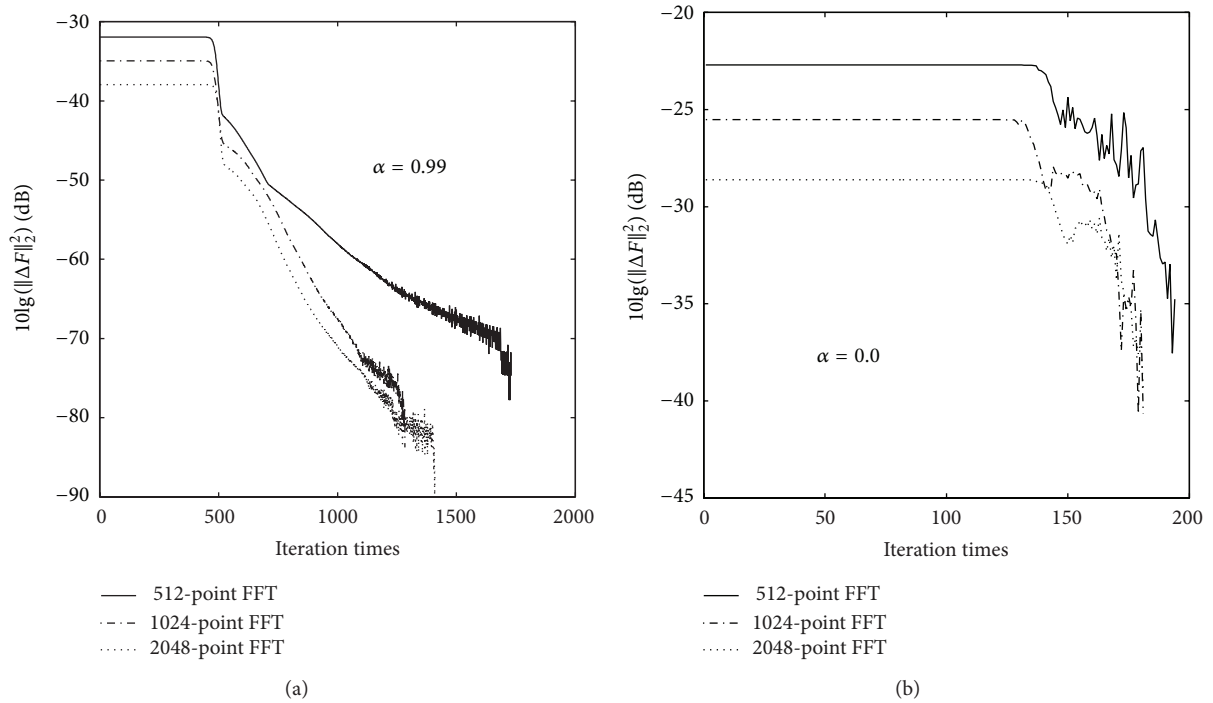


FIGURE 4: Norm of the error pattern for the phase-only tapering: (a) $\alpha = 0.99$ and (b) $\alpha = 0.0$.

5. Example for Planar Array Pattern Synthesis

Consider a 60×60 planar array with elements spacing by 0.65λ in both directions. The desired pattern has a maximum side lobe level of -40 dB and two -60 dB notches

at rectangular sectors $\{-0.1 \leq u \leq 0.1, 0.2 \leq v < 0.3\}$ and $\{0.3 \leq u \leq 0.4, -0.1 \leq v < 0.1\}$. The procedure suggested in [14] is adopted. First the 256×256 points FFT is used. At the following two phases, 512×512 and 1024×1024 points FFT are performed, with the previous results being

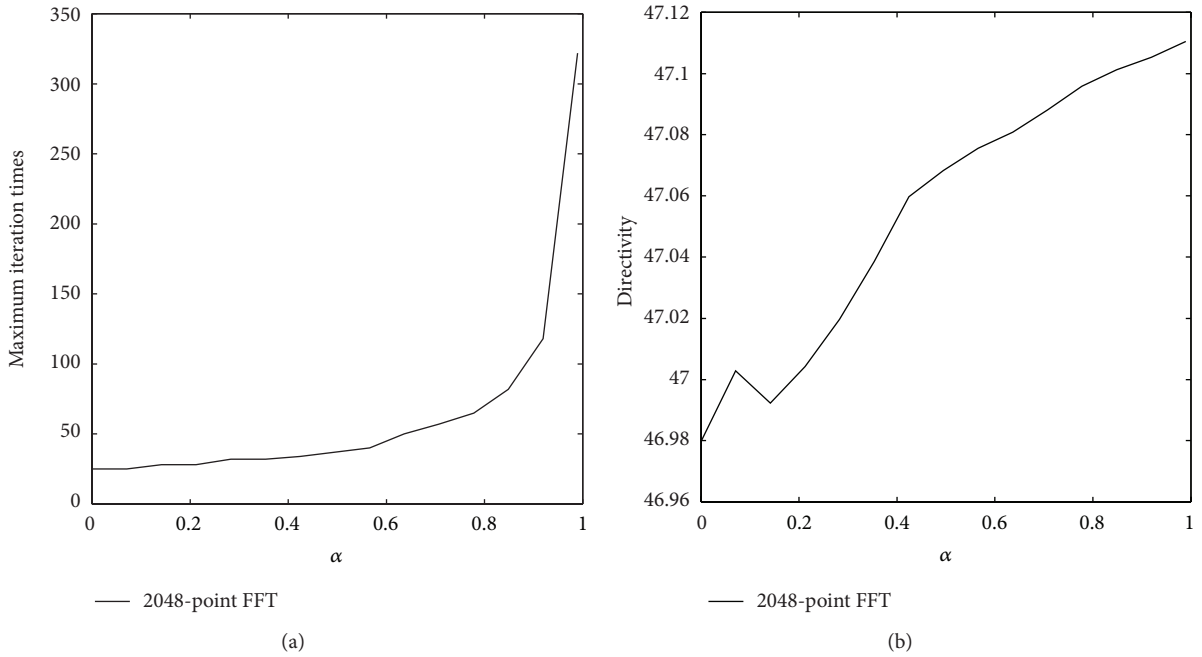


FIGURE 5: Maximum iteration times (a) and directivity of the array (b) versus α for the amplitude-only tapering.

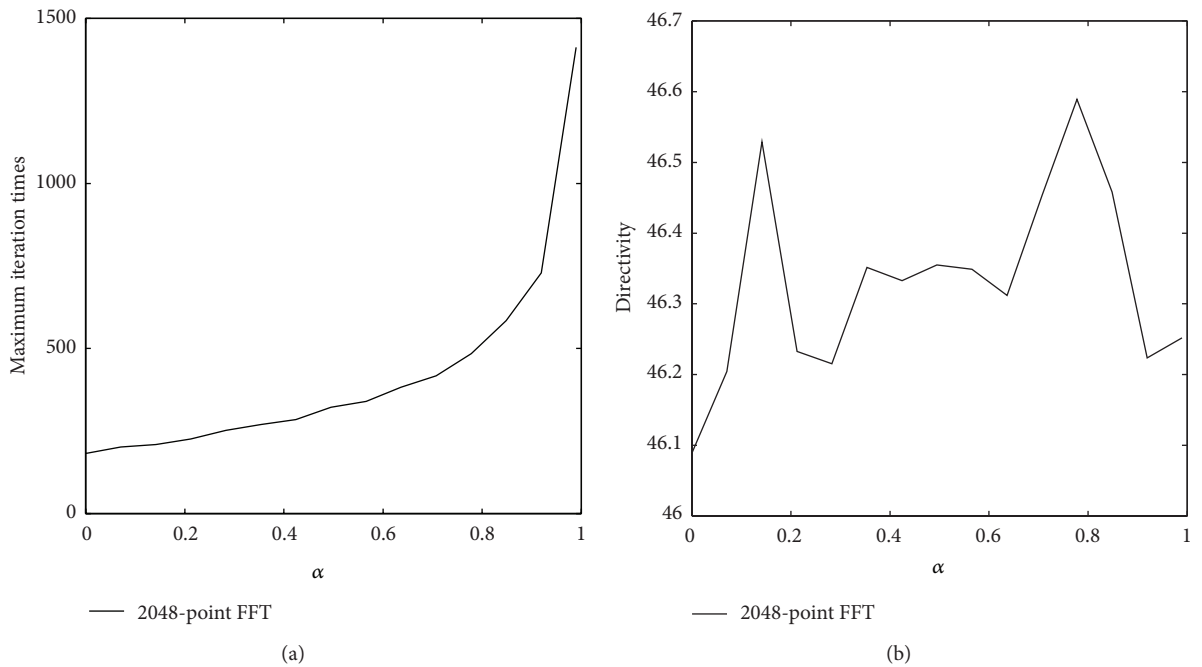


FIGURE 6: Maximum iteration times (a) and directivity of the array (b) versus α for the phase-only tapering.

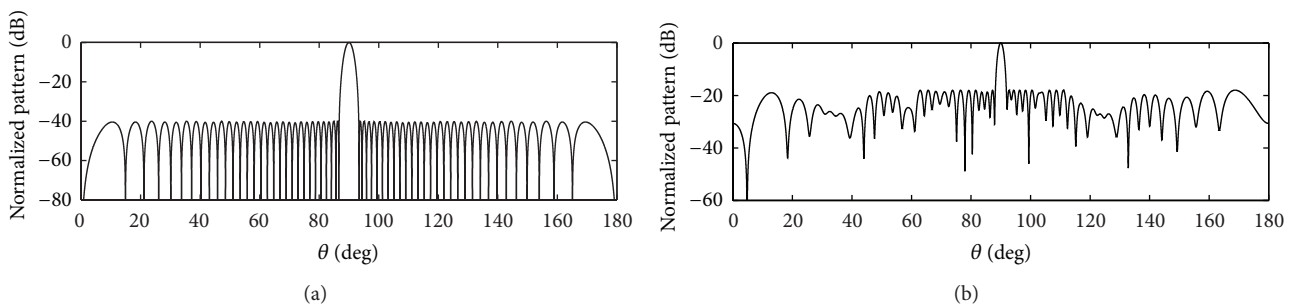


FIGURE 7: Normalized pattern: (a) amplitude-only tapering and (b) phase-only tapering.

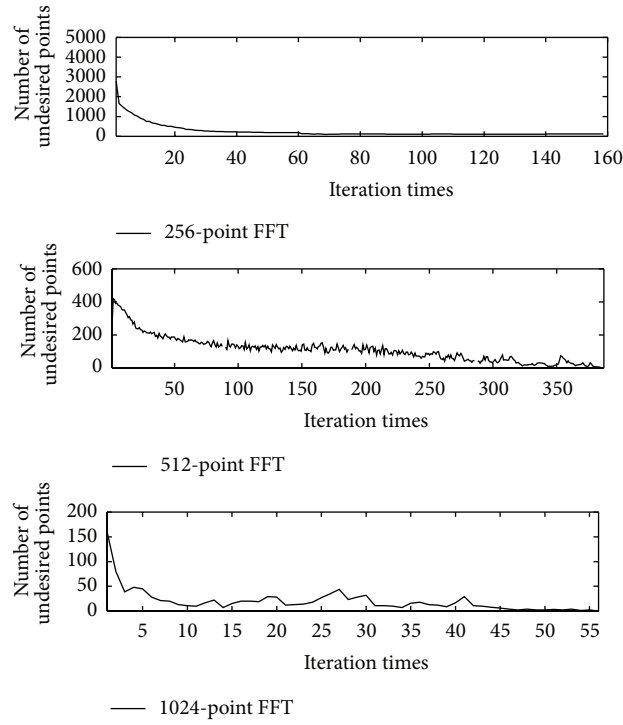


FIGURE 8: Number of undesired points versus iteration times.

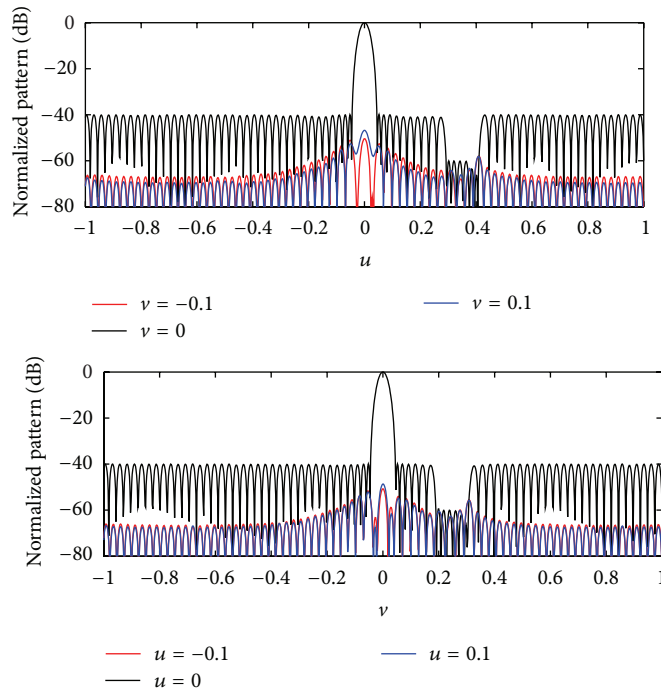


FIGURE 9: Normalized pattern at u -cut and v -cut planes.

the initial excitations for the next phase. At each phase, the maximum iteration time is 1000, and the scaling factor α is set to zero. Figure 8 gives the convergence property of the number of undesired radiation points. It shows that, after the previous two phases, the final phase converges very quickly.

The 1D radiation patterns containing the two notch sectors are shown in Figure 9. Figure 10 presents the 2D radiation pattern, where the visible space is determined by (8). The normalized amplitude and phase of the excitations are given in Figure 11.

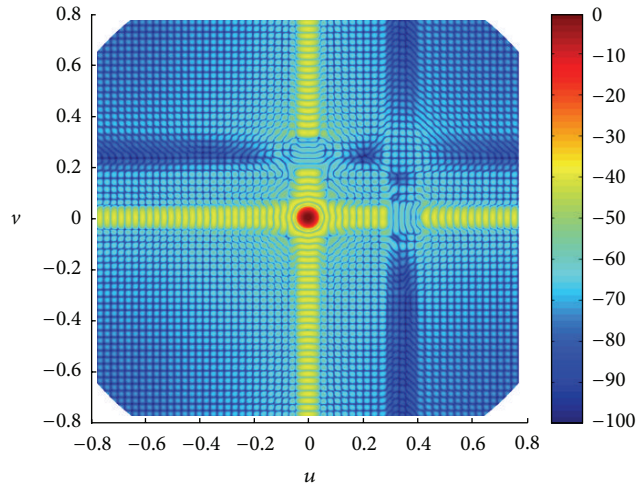


FIGURE 10: 2D radiation pattern.

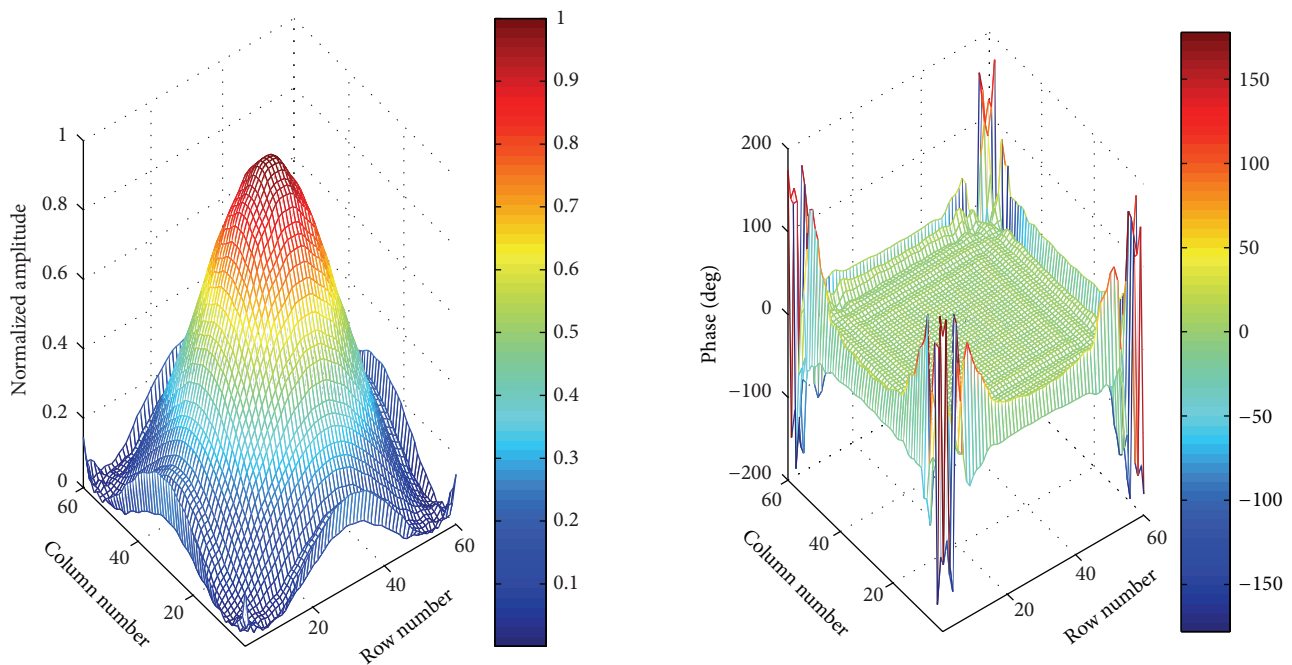


FIGURE 11: Normalized amplitude and phase of the excitations.

6. Conclusion

The iterative FFT method is capable of synthesizing a large planar array. In this paper, the method is validated by theoretical and simulative analyses. But the original method has a low convergence rate, and the synthesized results are usually unable to achieve the optimal solution. A scaling factor is introduced to form an improved method, which can avoid the drawbacks of the original method. Analysis and simulation results showed the effectiveness of the improved method.

Conflict of Interests

The authors declare that there is no conflict of interests regarding the publication of this paper.

References

- [1] B. P. Ng, M. H. Er, and C. Kot, "Flexible array synthesis method using quadratic programming," *IEEE Transactions on Antennas and Propagation*, vol. 41, no. 11, pp. 1541–1550, 1993.

- [2] T. Isernia, P. D. Iorio, and F. Soldovieri, "An effective approach for the optimal focusing of array fields subject to arbitrary upper bounds," *IEEE Transactions on Antennas and Propagation*, vol. 48, no. 12, pp. 1837–1847, 2000.
- [3] S. Boyd and L. Vandenberghe, *Convex Optimization*, Cambridge University Press, 2009.
- [4] O. M. Bucci, L. Caccavale, and T. Isernia, "Optimal far-field focusing of uniformly spaced arrays subject to arbitrary upper bounds in nontarget directions," *IEEE Transactions on Antennas and Propagation*, vol. 50, no. 11, pp. 1539–1554, 2002.
- [5] F. Ares, J. Fondevila-Gomez, G. Franceschetti, E. Moreno-Piquero, and J. A. Rodriguez-Gonzalez, "Synthesis of very large planar arrays for prescribed footprint illumination," *IEEE Transactions on Antennas and Propagation*, vol. 56, no. 2, pp. 584–589, 2008.
- [6] D. H. Schaubert, A. O. Boryssenko, A. van Ardenne, J. G. B. de Vaate, and C. Craeye, "The square kilometer array (SKA) antenna," in *Proceedings of the IEEE International Symposium on Phased Array Systems and Technology*, pp. 351–358, October 2003.
- [7] J. Nocedal and S. J. Wright, *Numerical Optimization*, Springer, New York, NY, USA, 2006.
- [8] F. J. Ares-Pena, J. A. Rodriguez-Gonzalez, E. Villanueva-Lopez, and S. R. Rengarajan, "Genetic algorithms in the design and optimization of antenna array patterns," *IEEE Transactions on Antennas and Propagation*, vol. 47, no. 3, pp. 506–510, 1999.
- [9] D. Marcano and F. Durán, "Synthesis of antenna arrays using genetic algorithms," *IEEE Antennas and Propagation Magazine*, vol. 42, no. 3, pp. 12–20, 2000.
- [10] L. Shi, Y. Deng, H. Sun, R. Wang, J. Ai, and H. Yan, "An improved real-coded genetic algorithm for the beam forming of spaceborne SAR," *IEEE Transactions on Antennas and Propagation*, vol. 60, no. 6, pp. 3034–3040, 2012.
- [11] W. T. Li, X. W. Shi, and Y. Q. Hei, "An improved particle swarm optimization algorithm for pattern synthesis of phased arrays," *Progress in Electromagnetics Research*, vol. 82, pp. 319–332, 2008.
- [12] K. V. Deligkaris, Z. D. Zaharis, D. G. Kampitaki, S. K. Goudos, I. T. Rekanos, and M. N. Spasos, "Thinned planar array design using boolean PSO with velocity mutation," *IEEE Transactions on Magnetics*, vol. 45, no. 3, pp. 1490–1493, 2009.
- [13] T. H. Ismail and Z. M. Hamici, "Array pattern synthesis using digital phase control by quantized particle swarm optimization," *IEEE Transactions on Antennas and Propagation*, vol. 58, no. 6, pp. 2142–2145, 2010.
- [14] W. P. M. N. Keizer, "Fast low-sidelobe synthesis for large planar array antennas utilizing successive fast fourier transforms of the array factor," *IEEE Transactions on Antennas and Propagation*, vol. 55, no. 3, pp. 715–722, 2007.
- [15] J. L. Gomez-Tornero, A. J. Martinez-Ros, and R. Verdu-Monedero, "FFT synthesis of radiation patterns with wide nulls using tapered leaky-wave antennas," *IEEE Antennas and Wireless Propagation Letters*, vol. 9, pp. 518–521, 2010.
- [16] K. Yang, Z. Zhao, and Q. H. Liu, "Fast pencil beam pattern synthesis of large unequally spaced antenna arrays," *IEEE Transactions on Antennas and Propagation*, vol. 61, no. 2, pp. 627–634, 2013.

Research Article

A Generalized Oblique Projection Filter with Flexible Parameter for Interference Suppression

Yi-ming Wang,^{1,2} Xing-peng Mao,¹ Hong Hong,¹ Jie Zhang,² and Yu-mei Cui¹

¹ School of Electronics and Information Engineering, Harbin Institute of Technology, Harbin, Heilongjiang 150001, China

² The First Institute of Oceanography, SOA, Qing Dao, Shandong 266061, China

Correspondence should be addressed to Xing-peng Mao; mxp@hit.edu.cn

Received 25 April 2014; Accepted 20 October 2014

Academic Editor: Michelangelo Villano

Copyright © 2015 Yi-ming Wang et al. This is an open access article distributed under the Creative Commons Attribution License, which permits unrestricted use, distribution, and reproduction in any medium, provided the original work is properly cited.

A generalized oblique projection (GOP) with an adjustable parameter defined as interference suppression cost (ISC) is proposed. Therefore, an optional optimized signal to interference-plus-noise ratio (SINR) and user controlled actions on the interference filtering are presented in this GOP framework. Theoretical analysis and numerical simulation demonstrate that when the ISC is derived from minimum variance distortionless response (MVDR) algorithm, the SINR performance of GOP filter is better than both MVDR and oblique projection (OP) filters. Further, an application of GOP filter in ionospheric clutter cancellation in a high frequency surface wave radar (HFSWR) system is given. The ISC is designed specifically to introduce an extra coherent loss to the clutters and a satisfying clutter suppression result is achieved. Besides the examples given, more designs of GOP filter can be inspired by the flexibility of ISC. As a generalized form of OP filter, GOP filter expands the connotation of oblique projection based technique and could be used in spatial filtering, polarization filtering, and other array signal processing applications.

1. Introduction

As an effective subspace based method, oblique projection [1–3] is used to project measurements into a low-rank subspace along a direction that is oblique to the subspace. In fact, this kind of method is an extension of the widely used orthogonal projection and has been applied in radars [4–6], communications [7, 8], navigations [9], image processing [10], and many other areas [11, 12]. The subspaces of the oblique projection processed can be either orthogonal or nonorthogonal, which relaxed the orthogonal requirement between subspaces.

The advantage of the oblique projection in retaining the target signals and mitigating the interference has been a promising technique and greatly extended its applications in array signals processing. The oblique projection utilizes the difference between the desired and unwanted signals to extract the target while suppressing interference. As the array, which is formed by a group of sensors sited in a predetermined pattern, generates a featured directional steering vector, spatial information has been used in constructing

an oblique projection operator [13–16]. Except for the spatial information, polarization information is also explored in oblique projection to distinguish the target and interference [4, 17]. Conventional oblique projection based filtering techniques focus on eliminating the interference completely, which may imply a maximized signal to interference ratio (SIR).

One of the problems with the emphasis of maximizing SIR output is that the target signal may be distorted [18]. The oblique projection can resolve it well, whereas the other problem is that when the angle separation between subspaces is small, the noise will be amplified, which leads to a loss in signal to interference-plus-noise ratio (SINR). One way to tackle this problem is to expand single processing domain to multiple domains. When more domains are cooperated, the angle separation can be improved. A collaborative range-angle-polarization filter [19], which takes advantage of the differences between the signal and interferences in the joint domains, is constructed based on the vector sensitive array.

However, when the target and interference are quite close in multidomain, the angle separation of subspaces is still

small. To fundamentally solve the problem, a generalized oblique projection (GOP) filter is proposed based on the further research of the traditional oblique projection (OP) operator. Theoretical analysis and simulation results demonstrate that the GOP filter has an improved SINR output capability. Some of the unique properties of the GOP and the flexibilities of interference suppression cost (ISC) by using conventional adaptive signal processing technologies [20, 21] or being designed according to a specific high frequency radar application are also explored.

The remaining sections of this paper are organized as follows. In Section 2, the linear model, especially its explicit form in two scenarios of array spatial and polarization filtering, is presented. It is followed by a brief introduction of the OP filter and short analysis of its SINR performance. In Section 3, the generalized form of GOP operator is derived. Four fundamental properties with proofs are given. In Section 4, the spatial GOP is derived and the SINR performance of GOP, OP, and MVDR is evaluated followed by numerical simulations. In Section 5, the GOP filter in polarization domain is discussed and practical application in the ionospheric clutter cancellation problem of a high frequency radar system is demonstrated. Finally, the last section concludes the present work in this paper.

2. Array Received Signal Model and Oblique Projection Filter

2.1. The Linear Model. As the signals are characterized as a weighted sum of modes, a linear algebraic framework is applied to vector-valued signals such as those obtained from a sensor array [1]. Assume there are full rank matrices $\mathbf{A} \in \mathbf{S}^{k \times m}$ and $\mathbf{B} \in \mathbf{H}^{k \times t}$ with their columns being linearly independent. The subspaces spanned by them are hence disjoint (unnecessarily orthogonal), which are composed of k observations and m or t parameters. Also, when the additive Gaussian white noise \mathbf{n} is considered, the received linear signal model can be described as

$$\mathbf{x} = \mathbf{A}\omega + \mathbf{B}\vartheta + \mathbf{n}, \quad (1)$$

where ω, ϑ represent mode weights for vectors \mathbf{A} and \mathbf{B} , respectively.

The linear model presented here is based on the concept of subspaces, which are not required to be orthogonal. In practical scenarios, spatial subspaces and polarization subspaces can be constructed.

Scenario 1: Array Signal Model in Spatial Domain. The signals received by a uniform linear array (ULA) are a mixture of desired target echoes and interferences from various spatial directions. Under far field assumption, the received signal of the N element array can be described as

$$\mathbf{x}(t) = \mathbf{a}_{\theta_1, \varphi_1} \cdot s(t) + \sum_{m=2}^{M-1} \mathbf{a}_{\theta_m, \varphi_m} \cdot i(t) + \mathbf{n}(t), \quad (2)$$

where the spatial steering vector of m th signal is given by

$$\begin{aligned} \mathbf{a}_{\theta_m, \varphi_m} &= \left[1 \quad e^{-j2\pi d \sin \theta_m \sin \varphi_m f/c} \quad \dots \quad e^{-j2\pi(N-1)d \sin \theta_m \sin \varphi_m f/c} \right]^T \end{aligned} \quad (3)$$

with θ, φ denoting respective azimuth and pitch angles and d being the distance between adjacent sensor elements.

The subspaces spanned by column vector $\mathbf{a}_{\theta_1, \varphi_1}$ are defined as the target subspace with the description of $\langle \mathbf{a}_{\theta_1, \varphi_1} \rangle$ and $\langle \mathbf{a}_{\theta_2, \varphi_2} \dots \mathbf{a}_{\theta_m, \varphi_m} \rangle$ is defined as interference subspace, correspondingly.

Scenario 2: Array Signal Model in Polarization Domain. In a polarization sensor with biorthogonal polarized antennas, the target subspace and the interference subspace are spanned by their polarization vectors marked by \mathbf{P}_s and \mathbf{P}_i , respectively. The signals received can therefore be described as

$$\mathbf{x}(t) = \mathbf{P}_s s(t) + \mathbf{P}_i i(t) + \mathbf{n}(t), \quad (4)$$

where $\mathbf{P}_s = [\cos \gamma_s \quad \sin \gamma_s e^{j\eta_s}]^T$, $\mathbf{P}_i = [\cos \gamma_i \quad \sin \gamma_i e^{j\eta_i}]^T$, and γ_s, γ_i and η_s, η_i depict the respective amplitude relationship and the phase difference between orthogonal electric fields of the target signal and interference.

2.2. Oblique Projection Filter. Consider two full-column-rank complex matrices $\mathbf{A} \in \mathbf{S}^{n \times m}$ and $\mathbf{B} \in \mathbf{H}^{n \times k}$ with $m + k \leq n$; then the columns of \mathbf{A} and \mathbf{B} are both linearly independent and disjoint. Let $\langle \mathbf{A} \rangle$ and $\langle \mathbf{B} \rangle$ denote the subspaces spanned by the columns of \mathbf{A} and \mathbf{B} , respectively; then the oblique projection operator $\mathbf{E}_{\mathbf{AB}}$ onto \mathbf{A} along \mathbf{B} is defined as

$$\mathbf{E}_{\mathbf{AB}} = \mathbf{A} \left(\mathbf{A}^H \mathbf{P}_{\mathbf{B}}^\perp \mathbf{A} \right)^{-1} \mathbf{A}^H \mathbf{P}_{\mathbf{B}}^\perp, \quad (5)$$

where $\mathbf{P}_{\mathbf{B}}^\perp$ is

$$\mathbf{P}_{\mathbf{B}}^\perp = \mathbf{I} - \mathbf{B} \left(\mathbf{B}^H \mathbf{B} \right)^{-1} \mathbf{B}^H. \quad (6)$$

Then $\mathbf{E}_{\mathbf{AB}}$ has the following properties:

$$\begin{aligned} \mathbf{E}_{\mathbf{AB}}^2 &= \mathbf{E}_{\mathbf{AB}}, \\ \mathbf{E}_{\mathbf{AB}} \mathbf{A} &= \mathbf{A}, \\ \mathbf{E}_{\mathbf{AB}} \mathbf{B} &= \mathbf{0}. \end{aligned} \quad (7)$$

Therefore, we have the output of OP filter as

$$\begin{aligned} \widehat{\mathbf{x}}_{\text{OP}}(t) &= \mathbf{E}_{\mathbf{AB}} \mathbf{x}(t) = \mathbf{E}_{\mathbf{AB}} (\mathbf{A}s(t) + \mathbf{B}i(t) + \mathbf{n}(t)) \\ &= \mathbf{A}s(t) + \mathbf{E}_{\mathbf{AB}} \mathbf{n}(t). \end{aligned} \quad (8)$$

The scalar form of the OP filter output is

$$\widehat{s}_{\text{OP}}(t) = \frac{\mathbf{A}^H}{\|\mathbf{A}\|^2} \mathbf{E}_{\mathbf{A,B}} \mathbf{x}(t) = s(t) + \frac{\mathbf{A}^H}{\|\mathbf{A}\|^2} \mathbf{E}_{\mathbf{A,B}} \mathbf{n}(t). \quad (9)$$

The OP operator recovers the desired signal and eliminates interference completely. Therefore, the SINR of the output can be expressed as

$$\begin{aligned} \text{SINR} &= \frac{P_s}{P_i + P_n} = \frac{E \left\{ \left| \mathbf{A}^H \mathbf{E}_{\text{AB}} \mathbf{A} s(t) / \|\mathbf{A}\|^2 \right|^2 \right\}}{E \left\{ \left| \mathbf{A}^H \mathbf{E}_{\text{AB}} \mathbf{n}(t) / \|\mathbf{A}\|^2 \right|^2 \right\}} \\ &= \frac{\sigma_s^2 \|\mathbf{A}\|^2}{\sigma_n^2 \text{trace} \{ \mathbf{E}_{\text{AB}} \mathbf{E}_{\text{AB}}^H \}} = \frac{\sigma_s^2}{\sigma_n^2} \|\mathbf{A}\|^2 \sin^2 \psi, \end{aligned} \quad (10)$$

where σ_s^2, σ_n^2 stand for the power of target and additive noise, respectively, and the principle angle between \mathbf{A} and \mathbf{B} is defined as

$$\psi = \arccos \left(\frac{\|\mathbf{A}^H \mathbf{B}\|}{\|\mathbf{A}\| \|\mathbf{B}\|} \right). \quad (11)$$

As observed from (8), a portion of noise is retained, mixed with the target signal. The noise power after filtering is given by

$$P_n = E \left\{ \|\mathbf{E}_{\text{AB}} \mathbf{n}(t)\|^2 \right\} = \frac{1}{\sin^2(\psi)} \sigma_n^2. \quad (12)$$

From (9) and (12), we can observe that the noise power after filtering is closely related to the principle angle. When subspaces $\langle \mathbf{A} \rangle$ and $\langle \mathbf{B} \rangle$ get close, which implies a small principle angle, the noise power will be amplified. In this situation, although the interference is totally eliminated, the enhanced noise power may result in a significant SINR loss. This is an inevitable problem of the OP filter.

3. Generalized Oblique Projection Filter

The OP filter focuses on the suppression of interference and lacks of the control of the noise power. To obtain a flexible control of the power of the noise and interference simultaneously, a novel oblique projection is proposed, which is named GOP.

3.1. Generalized Oblique Projection Operator. Taking the noise into consideration and introducing an ISC of ζ , the GOP operator can be derived by solving the following linear constrained optimum problem as

$$\begin{aligned} \min \quad & \mathbf{w}^H \mathbf{w} \\ \text{s.t.} \quad & \mathbf{w}^H \mathbf{A} = 1 \\ & \mathbf{w}^H \mathbf{B} = \zeta, \end{aligned} \quad (13)$$

where \mathbf{A} and \mathbf{B} are the vectors that span target subspace and interference subspace.

From the constraint equation in (13), we have

$$\mathbf{w}^H \mathbf{B} - \zeta \mathbf{w}^H \mathbf{A} = \mathbf{w}^H (\mathbf{B} - \zeta \mathbf{A}) = 0 \quad (14)$$

which implicates $\mathbf{B} - \zeta \mathbf{A} \in \langle \mathbf{w} \rangle^\perp$.

Also, we have

$$\begin{aligned} \mathbf{w}^H \mathbf{A} &= \mathbf{w}^H (\mathbf{P}_{(\mathbf{B}-\zeta\mathbf{A})} \mathbf{A} + \mathbf{P}_{(\mathbf{B}-\zeta\mathbf{A})}^\perp \mathbf{A}) \\ &= \mathbf{w}^H \mathbf{P}_{(\mathbf{B}-\zeta\mathbf{A})}^\perp \mathbf{A} = 1, \end{aligned} \quad (15)$$

where the orthogonal projection operator of $\mathbf{B} - \zeta \mathbf{A}$ is defined as

$$\begin{aligned} \mathbf{P}_{(\mathbf{B}-\zeta\mathbf{A})}^\perp &= \mathbf{I} - (\mathbf{B} - \zeta \mathbf{A}) \\ &\cdot [(\mathbf{B} - \zeta \mathbf{A})^H \cdot (\mathbf{B} - \zeta \mathbf{A})]^{-1} (\mathbf{B} - \zeta \mathbf{A})^H. \end{aligned} \quad (16)$$

Therefore, the optimum problem in (13) can be transformed into the following:

$$\begin{aligned} \min \quad & \mathbf{w}^H \mathbf{w} \\ \text{s.t.} \quad & \mathbf{w}^H \mathbf{P}_{(\mathbf{B}-\zeta\mathbf{A})}^\perp \mathbf{A} = 1 \\ & \mathbf{B} - \zeta \mathbf{A} \in \langle \mathbf{w} \rangle^\perp. \end{aligned} \quad (17)$$

To solve this problem, a cost function is constructed by Lagrange multiplier method as

$$F(w) = \mathbf{w}^H \mathbf{w} + \lambda (\mathbf{w}^H \mathbf{P}_{(\mathbf{B}-\zeta\mathbf{A})}^\perp \mathbf{A} - 1). \quad (18)$$

Taking derivative of (18) with respect to \mathbf{w} , the optimum weight is obtained as

$$\mathbf{w} = -\frac{\lambda}{2} \mathbf{P}_{(\mathbf{B}-\zeta\mathbf{A})}^\perp \mathbf{A}. \quad (19)$$

Substitute w into the constraint condition $\mathbf{w}^H \mathbf{P}_{(\mathbf{B}-\zeta\mathbf{A})}^\perp \mathbf{A} = 1$; we have

$$-\frac{\lambda}{2} \mathbf{A}^H \mathbf{P}_{(\mathbf{B}-\zeta\mathbf{A})}^\perp \mathbf{P}_{(\mathbf{B}-\zeta\mathbf{A})}^\perp \mathbf{A} = 1. \quad (20)$$

Consider that $\mathbf{P}_{(\mathbf{B}-\zeta\mathbf{A})}^\perp \mathbf{P}_{(\mathbf{B}-\zeta\mathbf{A})}^\perp = \mathbf{P}_{(\mathbf{B}-\zeta\mathbf{A})}^\perp$ and $\mathbf{P}_{(\mathbf{B}-\zeta\mathbf{A})}^\perp \mathbf{P}_{(\mathbf{B}-\zeta\mathbf{A})}^\perp = \mathbf{P}_{(\mathbf{B}-\zeta\mathbf{A})}^\perp$; the cost factor is

$$\lambda = -2 (\mathbf{A}^H \mathbf{P}_{(\mathbf{B}-\zeta\mathbf{A})}^\perp \mathbf{A})^{-1}. \quad (21)$$

Substitute λ into (19); we have the explicit weight as

$$\begin{aligned} \mathbf{w} &= \mathbf{P}_{(\mathbf{B}-\zeta\mathbf{A})}^\perp \mathbf{A} (\mathbf{A}^H \mathbf{P}_{(\mathbf{B}-\zeta\mathbf{A})}^\perp \mathbf{A})^{-1} \\ &= \left((\mathbf{A}^H \mathbf{P}_{(\mathbf{B}-\zeta\mathbf{A})}^\perp \mathbf{A})^{-1} \mathbf{A}^H \mathbf{P}_{(\mathbf{B}-\zeta\mathbf{A})}^\perp \right)^H \\ &= \left(\frac{\mathbf{A}^H}{\|\mathbf{A}\|^2} \mathbf{E}_{\mathbf{A}, \mathbf{B}, \zeta} \right)^H, \end{aligned} \quad (22)$$

where the GOP operator is derived from (22) as

$$\mathbf{E}_{\mathbf{A}, \mathbf{B}, \zeta} = \mathbf{A} (\mathbf{A}^H \mathbf{P}_{(\mathbf{B}-\zeta\mathbf{A})}^\perp \mathbf{A})^{-1} \mathbf{A}^H \mathbf{P}_{(\mathbf{B}-\zeta\mathbf{A})}^\perp. \quad (23)$$

Compare (23) with (5); the expressions of GOP and OP share the similar expression. It will be shown that the GOP operator presented is related to the OP operator and orthogonal projection operator. However, GOP is the extended form of them and some special properties are generated by the GOP.

3.2. *Properties of the GOP.* Four fundamental properties of the GOP are presented. The idempotence of GOP and the oblique projection abilities are given, respectively, in Property 1. The connections of OP and orthogonal projection with GOP are shown in Property 2. The enlargement of the principle angle by GOP compared to OP is discussed in Property 3, which implies a reduction of the noise power output. Lastly, in Property 4, the maximized SINR condition in GOP is presented.

Property 1. Consider

$$\begin{aligned} \mathbf{E}_{\mathbf{A},\mathbf{B},\zeta}^2 &= \mathbf{E}_{\mathbf{A},\mathbf{B},\zeta}, \\ \mathbf{E}_{\mathbf{A},\mathbf{B},\zeta}\mathbf{A} &= \mathbf{A}, \\ \mathbf{E}_{\mathbf{A},\mathbf{B},\zeta}\mathbf{B} &= \zeta\mathbf{A}. \end{aligned} \quad (24)$$

Examine (24); the GOP operator has equivalent filtering effect when the operator is multiplied. It recovers the desired signal without amplitude and phase distortion, whereas part of the interference is projected into the target subspace and is reserved by GOP. The target signal after GOP filtering can be expressed as

$$\begin{aligned} \widehat{\mathbf{S}}_{\text{GOP}}(t) &= \frac{\mathbf{A}^H}{\|\mathbf{A}\|^2} \mathbf{E}_{\mathbf{A},\mathbf{B},\zeta} \mathbf{x}(t) \\ &= s(t) + \zeta i(t) + \frac{\mathbf{A}^H}{\|\mathbf{A}\|^2} \mathbf{E}_{\mathbf{A},\mathbf{B},\zeta} \mathbf{n}(t). \end{aligned} \quad (25)$$

Proof. Since $\mathbf{P}_{(\mathbf{B}-\zeta\mathbf{A})}^\perp$ is a square matrix and \mathbf{A} is a column vector, we have

$$\begin{aligned} \mathbf{E}_{\mathbf{A},\mathbf{B},\zeta}^2 &= \mathbf{A} \left(\mathbf{A}^H \mathbf{P}_{(\mathbf{B}-\zeta\mathbf{A})}^\perp \mathbf{A} \right)^{-1} \mathbf{A}^H \mathbf{P}_{(\mathbf{B}-\zeta\mathbf{A})}^\perp \\ &\quad \cdot \mathbf{A} \left(\mathbf{A}^H \mathbf{P}_{(\mathbf{B}-\zeta\mathbf{A})}^\perp \mathbf{A} \right)^{-1} \mathbf{A}^H \mathbf{P}_{(\mathbf{B}-\zeta\mathbf{A})}^\perp \\ &= \mathbf{A} \left(\mathbf{A}^H \mathbf{P}_{(\mathbf{B}-\zeta\mathbf{A})}^\perp \mathbf{A} \right)^{-1} \left(\mathbf{A}^H \mathbf{P}_{(\mathbf{B}-\zeta\mathbf{A})}^\perp \mathbf{A} \right) \\ &\quad \times \left(\mathbf{A}^H \mathbf{P}_{(\mathbf{B}-\zeta\mathbf{A})}^\perp \mathbf{A} \right)^{-1} \mathbf{A}^H \mathbf{P}_{(\mathbf{B}-\zeta\mathbf{A})}^\perp \\ &= \mathbf{A} \left(\mathbf{A}^H \mathbf{P}_{(\mathbf{B}-\zeta\mathbf{A})}^\perp \mathbf{A} \right)^{-1} \mathbf{A}^H \mathbf{P}_{(\mathbf{B}-\zeta\mathbf{A})}^\perp = \mathbf{E}_{\mathbf{A},\mathbf{B},\zeta}, \end{aligned} \quad (26)$$

$$\mathbf{E}_{\mathbf{A},\mathbf{B},\zeta}\mathbf{A} = \mathbf{A} \left(\mathbf{A}^H \mathbf{P}_{(\mathbf{B}-\zeta\mathbf{A})}^\perp \mathbf{A} \right)^{-1} \left(\mathbf{A}^H \mathbf{P}_{(\mathbf{B}-\zeta\mathbf{A})}^\perp \mathbf{A} \right) = \mathbf{A}.$$

Since $\mathbf{B} - \zeta\mathbf{A}$ is a column vector, from (16) we have

$$\begin{aligned} \mathbf{P}_{(\mathbf{B}-\zeta\mathbf{A})}^\perp (\mathbf{B} - \zeta\mathbf{A}) &= 0, \\ \mathbf{E}_{\mathbf{A},\mathbf{B},\zeta} (\mathbf{B} - \zeta\mathbf{A}) &= \mathbf{A} \left(\mathbf{A}^H \mathbf{P}_{(\mathbf{B}-\zeta\mathbf{A})}^\perp \mathbf{A} \right)^{-1} \mathbf{A}^H \mathbf{P}_{(\mathbf{B}-\zeta\mathbf{A})}^\perp (\mathbf{B} - \zeta\mathbf{A}) \\ &= 0 \implies \mathbf{E}_{\mathbf{A},\mathbf{B},\zeta} \mathbf{B} = \zeta\mathbf{A}. \end{aligned} \quad (27)$$

□

Property 2. The ISC ζ can be real or complex, and its absolute value $|\zeta| \in [0, 1]$. When $\zeta = \langle \mathbf{A}, \mathbf{B} \rangle / \|\mathbf{A}\| \|\mathbf{B}\|$, GOP becomes an orthogonal operator, and

$$\mathbf{E}_{\mathbf{A},\mathbf{B},\zeta} = \mathbf{P}_{\mathbf{A}}, \quad \zeta = \frac{\langle \mathbf{A}, \mathbf{B} \rangle}{\|\mathbf{A}\| \|\mathbf{B}\|}. \quad (28)$$

When $\zeta = 0$, GOP degrades to an OP and shares the same expression in (5), and

$$\mathbf{E}_{\mathbf{A},\mathbf{B},\zeta} = \mathbf{E}_{\mathbf{A},\mathbf{B}}, \quad \zeta = 0. \quad (29)$$

Proof. Suppose ζ equals the inner product of \mathbf{A} and \mathbf{B} ;

$$\begin{aligned} \langle \mathbf{A}, (\mathbf{B} - \zeta\mathbf{A}) \rangle &= \mathbf{A}^H (\mathbf{B} - \zeta\mathbf{A}) \\ &= \mathbf{A}^H \mathbf{B} - \frac{\mathbf{A}^H \mathbf{A} \mathbf{A}^H \mathbf{B}}{\|\mathbf{A}\| \|\mathbf{B}\|} = 0. \end{aligned} \quad (30)$$

Therefore, subspace $\langle \mathbf{A} \rangle$ is orthogonal to subspace $\langle \mathbf{B} - \zeta\mathbf{A} \rangle$, and substitute (16) into (23); we have

$$\mathbf{E}_{\mathbf{A},\mathbf{B},\zeta} = \left(\mathbf{E}_{\mathbf{A},\mathbf{B},\zeta} \right)^H = \mathbf{A} \left(\mathbf{A}^H \mathbf{A} \right)^{-1} \mathbf{A}^H = \mathbf{P}_{\mathbf{A}}, \quad (31)$$

where $\mathbf{P}_{\mathbf{A}}$ represents the orthogonal projection of \mathbf{A} . Suppose ζ is set to zero; hence

$$\begin{aligned} \mathbf{E}_{\mathbf{A},\mathbf{B},\zeta} &= \mathbf{A} \left(\mathbf{A}^H \mathbf{P}_{(\mathbf{B}-\zeta\mathbf{A})}^\perp \mathbf{A} \right)^{-1} \mathbf{A}^H \mathbf{P}_{(\mathbf{B}-\zeta\mathbf{A})}^\perp \\ &= \mathbf{A} \left(\mathbf{A}^H \mathbf{P}_{\mathbf{B}}^\perp \mathbf{A} \right)^{-1} \mathbf{A}^H \mathbf{P}_{\mathbf{B}}^\perp = \mathbf{E}_{\mathbf{A},\mathbf{B}}. \end{aligned} \quad (32)$$

Correspondingly, the target signal recovered by GOP and OP is identical in this case:

$$\widehat{\mathbf{S}}_{\text{GOP}}(t) = \widehat{\mathbf{S}}_{\text{OP}}(t), \quad \zeta = 0. \quad (33)$$

□

Property 3. The principle angle of GOP is adjusted by ζ . When $\zeta \in (0, \cos \psi]$, the principle angle of GOP can be enlarged, which is given by

$$\psi' > \psi, \quad \zeta \in (0, \cos \psi], \quad (34)$$

where ψ' represents the principle angle of GOP and ψ represents the principle angle of OP under the same \mathbf{A} and \mathbf{B} . With a proper setting of the ISC, the principle angle between subspaces can be enlarged.

Proof. The square of the cosine of the new principle angle is

$$\begin{aligned}
\cos^2 \psi' &= \frac{(\mathbf{A}^H \mathbf{B}')^H (\mathbf{A}^H \mathbf{B}')}{\|\mathbf{A}^H\|^2 \|\mathbf{B}'\|^2} \\
&= \frac{(\mathbf{B} - \zeta \mathbf{A})^H \mathbf{A} \mathbf{A}^H (\mathbf{B} - \zeta \mathbf{A})}{\mathbf{A}^H \mathbf{A} (\mathbf{B} - \zeta \mathbf{A})^H (\mathbf{B} - \zeta \mathbf{A})} \\
&= \frac{(\mathbf{B}^H \mathbf{A}^H \mathbf{A} \mathbf{B} / \mathbf{A}^H \mathbf{A}) - \zeta (\mathbf{A}^H \mathbf{B} + \mathbf{B}^H \mathbf{A}) + \zeta^2 \mathbf{A}^H \mathbf{A}}{\mathbf{B}^H \mathbf{B} - \zeta (\mathbf{A}^H \mathbf{B} + \mathbf{B}^H \mathbf{A}) + \zeta^2 \mathbf{A}^H \mathbf{A}} \\
&= \frac{(\cos \psi - \zeta)^2}{\zeta^2 - 2\zeta \cos \psi + 1} \\
&= \frac{1}{1 + (1 - \cos^2 \psi) / (\cos \psi - \zeta)^2}.
\end{aligned} \tag{35}$$

Since (35) is a monotonically declining function of ζ under the condition of $\zeta \in [0, \cos \psi]$, it is evident that

$$\psi' = \psi, \quad \zeta = 0, \tag{36}$$

$$\text{or } \psi' > \psi, \quad \zeta \in (0, \cos \psi]. \tag{37}$$

Equation (37) demonstrates that when ζ is set in the range of $(0, \cos \psi]$, the principle angle of GOP is enlarged. According to the expression of output noise power in (12), the noise power of GOP will be less than that of OP:

$$P'_n < P_n. \tag{38}$$

□

Property 4. Suppose INR is known a priori; a maximized SINR, which is the SINR upper bound of GOP, can be obtained and the corresponding ICS is given as

$$\zeta_{\text{opt}} = \frac{\cos \psi}{1 + N \cdot \text{INR} \sin^2 \psi}, \tag{39}$$

such that the maximum SINR is obtained as

$$\text{SINR}_{\text{max}} = \frac{(\text{SIR} + N \cdot \text{SNR} \sin^2 \psi) N \cdot \text{SNR}}{\text{SIR} + N \cdot \text{SNR}}, \tag{40}$$

where N represents the number of array elements.

Proof. The SINR output of the GOP filter can be expressed as

$$\begin{aligned}
\text{SINR} &= \frac{P_s}{P'_i + P'_n} = \frac{P_s}{\zeta^2 P_i + P_n / N \sin^2 \psi'} \\
&= \left(\frac{\zeta^2}{\text{SIR}} + \frac{1}{N \sin^2 \psi' \text{SNR}} \right)^{-1} \\
&= \left(\frac{\zeta^2}{\text{SIR}} + \frac{1 - 2\zeta \cos \psi + \zeta^2}{N \sin^2 \psi \text{SNR}} \right)^{-1}.
\end{aligned} \tag{41}$$

To have the maximum value of SINR, the first order derivative of (41) with respect to ζ is taken; therefore the optimum ζ_{opt} that will give the maximum SINR in (40) is obtained as in (39). □

4. GOP in Spatial Filtering

By using the spatial difference between the target and interference, spatial filtering is an effective method to reduce the power of unwanted signals including output noise. In the construction of spatial GOP filter, the design of ISC parameter is flexible. It can be generated by using the conventional adaptive spatial filtering methods such as minimum variance distortionless response (MVDR) algorithm [20].

The constrained criterion of MVDR is described as

$$\begin{aligned}
\min_{\mathbf{w}} \quad & \mathbf{w}^T \mathbf{R} \mathbf{w} \\
\text{s.t.} \quad & \mathbf{w}^H \mathbf{A} = 1,
\end{aligned} \tag{42}$$

where \mathbf{A} is the spatial vector for the target signal and $\mathbf{R} = E\{\mathbf{x}(t)\mathbf{x}^H(t)\}$ represents the covariance matrix of the received signal.

The weight of MVDR can be obtained as

$$\mathbf{w}_{\text{MVDR}} = \mathbf{R}^{-1} \mathbf{A} (\mathbf{A}^H \mathbf{R}^{-1} \mathbf{A})^{-1}. \tag{43}$$

Therefore, the ISC obtained from \mathbf{w}_{MVDR} is expressed as

$$\zeta_{\text{MVDR}} = \mathbf{w}_{\text{MVDR}}^H \mathbf{B} = \left(\mathbf{R}^{-1} \mathbf{A} (\mathbf{A}^H \mathbf{R}^{-1} \mathbf{A})^{-1} \right)^H \mathbf{B}. \tag{44}$$

It should be noted that the restoration of the target is not related to ζ , which is the fundamental property of GOP as given in (25). The interference suppression effect is determined by ζ only. As a result, except for MVDR, more adaptive beamforming methods can be utilized. However, as the information required by MVDR is usually easy to obtain, it is more representative to derive ζ from \mathbf{w}_{MVDR} . In the following part, the SINR performance of the MVDR, OP, and GOP with ζ given in (44) is analyzed and compared.

4.1. SINRs Comparison of GOP and MVDR. The SINR performance of the GOP and MVDR filter is evaluated. The SINRs for GOP and MVDR filter are given in (45) and (46), respectively, as

$$\text{SINR}_{\text{GOP}} = \frac{E\{|\mathbf{w} \mathbf{A} s(n)|^2\}}{E\{|\mathbf{w} \mathbf{B} i(n)|^2\} + E\{|\mathbf{w} \mathbf{n}(n)|^2\}} \tag{45}$$

$$= \frac{E\{|\mathbf{w} \mathbf{A}|^2\} \sigma_s^2}{E\{|\mathbf{w} \mathbf{B}|^2\} \sigma_i^2 + |\mathbf{w}|^2 \sigma_n^2},$$

where $\mathbf{w} = \mathbf{A}^H \mathbf{E}_{\mathbf{A}, \mathbf{B}, \zeta} / \|\mathbf{A}\|^2$. Consider

$$\begin{aligned}
\text{SINR}_{\text{MVDR}} &= \frac{E\{|\mathbf{w}_{\text{MVDR}} \mathbf{A} s(n)|^2\}}{E\{|\mathbf{w}_{\text{MVDR}} \mathbf{B} i(n)|^2\} + E\{|\mathbf{w}_{\text{MVDR}} \mathbf{n}(n)|^2\}} \\
&= \frac{E\{|\mathbf{w}_{\text{MVDR}} \mathbf{A}|^2\} \sigma_s^2}{E\{|\mathbf{w}_{\text{MVDR}} \mathbf{B}|^2\} \sigma_i^2 + |\mathbf{w}_{\text{MVDR}}|^2 \sigma_n^2}.
\end{aligned} \tag{46}$$

Observing (13), (42), (43), and (44), we get

$$\begin{aligned}\mathbf{w}^H \mathbf{A} &= \mathbf{w}_{\text{MVDR}}^H \mathbf{A}, \\ \mathbf{w}^H \mathbf{B} &= \mathbf{w}_{\text{MVDR}}^H \mathbf{B}.\end{aligned}\quad (47)$$

Substitute (47) into (45) and (46); it can be observed that the difference of output SINRs is decided by the power of noise after filtering.

Investigating the objective function in (13), we get \mathbf{w}_{GOP} which satisfies $\min(\mathbf{w}_{\text{GOP}}^H \mathbf{w}_{\text{GOP}})$; hence $|\mathbf{w}_{\text{GOP}}|^2 \leq |\mathbf{w}_{\text{MVDR}}|^2$. This leads to

$$\text{SINR}_{\text{GOP}} \geq \text{SINR}_{\text{MVDR}}. \quad (48)$$

Both of these filters attempt to reduce the interference and noise while producing the distortionless response. However, the GOP filter has a better treatment to the noise and interference which results in a higher SINR.

4.2. SINRs Comparison of GOP and OP. The SINR performance of the GOP and OP filter is evaluated. The SINR for OP filter is written as

$$\begin{aligned}\text{SINR}_{\text{OP}} &= \frac{E \{ |\mathbf{w}_{\text{OP}} \mathbf{A} s(n)|^2 \}}{E \{ |\mathbf{w}_{\text{OP}} \mathbf{B} i(n)|^2 \} + E \{ |\mathbf{w}_{\text{OP}} \mathbf{n}(n)|^2 \}} \\ &= \frac{\sigma_s^2}{\sigma_n^2 \|\mathbf{E}_{\text{AB}}\|^2 / \|\mathbf{A}\|^2},\end{aligned}\quad (49)$$

where $\mathbf{w}_{\text{OP}} = \mathbf{A}^H \mathbf{E}_{\text{A,B}} / \|\mathbf{A}\|^2$.

Let the ratio between SINRs of GOP and OP filter be

$$\begin{aligned}k &= \frac{\text{SINR}_{\text{GOP}}}{\text{SINR}_{\text{OP}}} \\ &= \frac{\|\mathbf{E}_{\text{AB}}\|^2 \sigma_n^2 / \|\mathbf{A}\|^2}{\zeta^2 \sigma_i^2 + \|\mathbf{A}^H \mathbf{E}_{\text{A,B},\zeta} / \|\mathbf{A}\|^2\|^2 \sigma_n^2} \\ &= \frac{1}{N \zeta^2 \text{INR} \sin^2 \psi + \|\mathbf{B} - \zeta \mathbf{A}\|^2 / N} \\ &= \frac{1}{Z \zeta^2 - 2 \cos \psi \zeta + 1},\end{aligned}\quad (50)$$

where $Z = 1 + N \sin^2 \psi \text{INR}$, $\|\mathbf{A}\|^2 = N$, and N is the number of the array elements.

As the value of k is determined by the principle angle, INR, the number of array elements, and ISC simultaneously, it is not easy to be analyzed without numerical evaluations. However, we can make a reasonable assumption under two extreme cases, where spatial difference between the target and interference approaches 90 degrees or 0 degrees.

Case 1 ($\psi \rightarrow 90^\circ$). The angular separation between target and interference is nearly orthogonal, which means the spatial difference is maximized. An aggressive action is taken,

and the interference is expected to be eliminated completely. Rewrite (50) as

$$k_1 = \frac{1}{N \sin^2 \psi \varepsilon_1 + 2 \delta_1 + 1 + \zeta^2}, \quad (51)$$

where $\varepsilon_1 = \zeta^2 \text{INR}$ and $\delta_1 = \zeta \cos \psi$.

To evaluate (51) numerically, let $\psi = 89.8^\circ$ and $\zeta = 0$; we have $\sin^2 \psi \approx 1$, $\zeta^2 = 0$, and $\delta_1 = 0$. Since the INR is bounded by a practical maximum of 60 dB, we have $\varepsilon_1 = 0$, $k_1 = 1$, and

$$\text{SINR}_{\text{GOP}} = \text{SINR}_{\text{OP}}. \quad (52)$$

Case 2 ($\psi \rightarrow 0^\circ$). When the angular separation between target and interference is very close, the principle angle is near zero. For OP filter, its SINR is not satisfying due to the amplified noise power as given in (12). However, the proposed GOP filter can be expected to be more conservative in rejecting the interference and shifting the focus in reducing the noise power output. That means when INR is low, which means noise power is comparably high, the ISC is approaching one. However, if noise power is comparably much lower than interference, resulting in a very high INR, the ISC is approaching zero to facilitate interference suppression. We rewrite (50) as

$$k_2 = \frac{1}{N \varepsilon_2 + \delta_2 + \zeta^2}, \quad (53)$$

where $\varepsilon_2 = (\zeta \sin \psi)^2 \text{INR}$ and $\delta_2 = 2 \zeta \cos \psi + 1$.

To evaluate (53) numerically, let $\psi = 0.01^\circ$ and $\zeta \in [10^{-5}, 1]$; we have $\sin^2 \psi = 0$; hence $\varepsilon_2 = 0$. Therefore, we have $\delta_2 + \zeta^2 \geq 1$, $k_2 \geq 1$, and

$$\text{SINR}_{\text{GOP}} \geq \text{SINR}_{\text{OP}}. \quad (54)$$

From the theoretical analysis of the two cases, the SINR outputs from both filters have an identical performance when the spatial difference between the target and interference is large. However, GOP filter has a superior performance than OP filter when the spatial difference is small.

Moreover, according to Property 4 of GOP, there is an optimized ζ_{opt} in maximizing SINR output if the INR can be obtained in advance. By substituting (39), (50) can be rewritten as

$$\begin{aligned}k &= \frac{1}{Z (\zeta_{\text{opt}} - \cos \psi / Z)^2 + 1 - \cos^2 \psi / Z} \\ &= \frac{1}{1 - \cos^2 \psi / Z} \geq 1,\end{aligned}\quad (55)$$

where $\zeta_{\text{opt}} = \cos \psi / Z$.

Therefore, we have

$$\text{SINR}_{\text{GOP}} \geq \text{SINR}_{\text{OP}}. \quad (56)$$

4.3. Simulations. Assume an ULA of 10 antenna elements with half wavelength spacing between adjacent elements; the carrier frequency is $f_0 = 5$ MHz. Under the conditions of

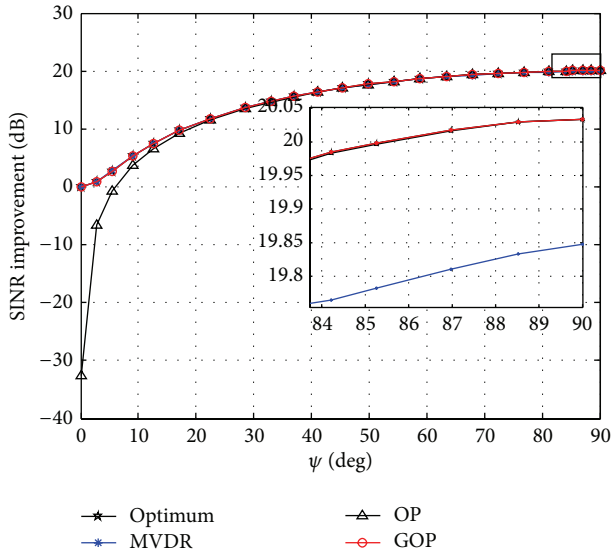


FIGURE 1: SINR improvement versus ψ .

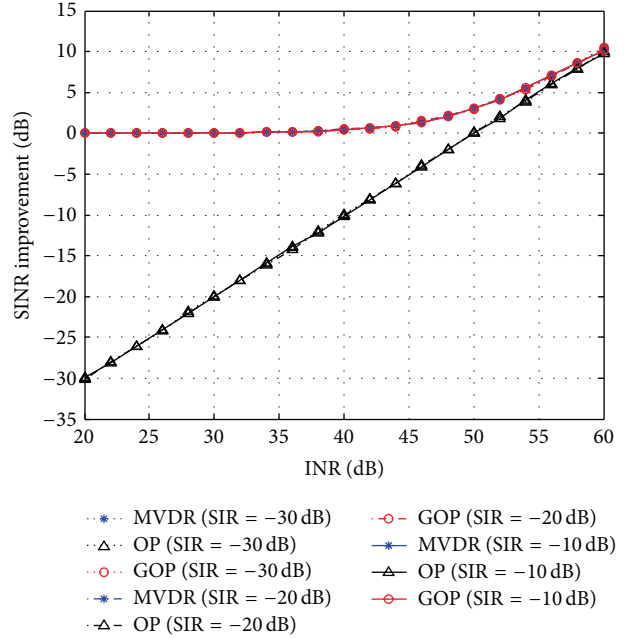


FIGURE 3: SINR improvement versus INR for Case 2.

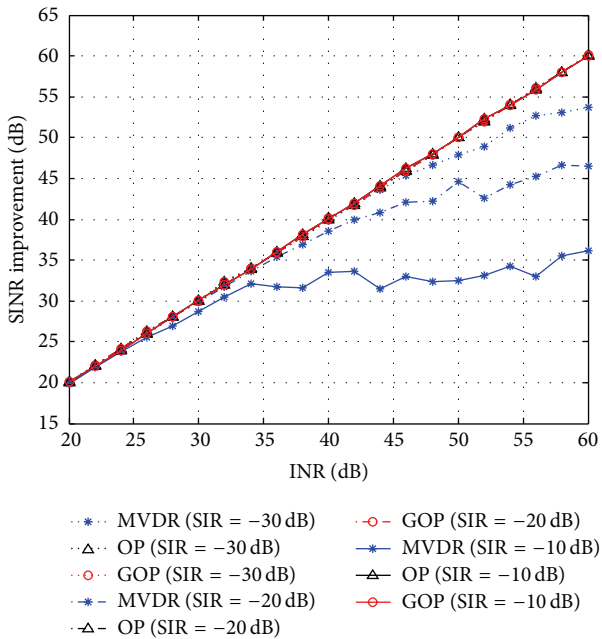


FIGURE 2: SINR improvement versus INR for Case 1.

SINR = 10 dB and SIR = -10 dB, the SINR improvement versus ψ for MVDR, OP, GOP, and GOP with optimum ISC is shown in Figure 1.

From Figure 1, it can be observed that the principle angles have great impacts on the SINR performance of the three spatial filters. With the principle angle less than 10 degrees, a sharper decrease appears in SINR for the OP filter than both GOP and MVDR filters. However, when the principle angle increases to nearly 90 degrees, GOP and OP filters perform slightly better than MVDR filter. The GOP spatial filter demonstrates a superior performance than OP and

MVDR filters in the whole angle range; further it coincides with the maximized SINR derived in (40).

In the following, the principle angle is fixed and the performances of three filters under different INRs are investigated. The INRs span from 20 dB to 60 dB while the SIRs are of -10 dB, -20 dB, and -30 dB, respectively. The principle angles are set to near 90 degrees and 0 degrees, respectively, which correspond to the cases in Section 4.2.

In Figures 2 and 3, the principle angles are set to 89.8 degrees and 0.18 degrees, respectively, which correspond to Cases 1 and 2. It is found that the ISC varies slightly around zero when the INRs change for Case 1, and ISC varies in range of $[2.7 \times 10^{-5}, 1]$ for Case 2. As shown in Figure 2, the SINR improvements of the GOP and OP increase linearly with INRs; however, the MVDR shows an inferior SINR improvement. In Figure 3, the principle angle is small, which means that the spatial difference between the target and interference reduces. The noise power amplifying effect of OP is significant, resulting in a severe SINR performance loss. In contrast, the GOP and MVDR filters have better SINR improvements, which exceed 30 dB at highest than OP filter. In general, the GOP filter generates a superior performance than both OP and MVDR filters. The numerical simulations have verified the theoretical analysis of the spatial filters presented.

5. GOP in Polarization Filtering of HF Radar

High frequency surface wave radar (HFSWR) [22] operates in the short wave band, which facilitates the over-the-horizon detection over the sea surface. However, signals in this band will also get reflected by the ionosphere, leading to a strong interference to the target detection or sea state remote sensing. In this section, we explored the polarization information

in the HFSWR and extended the application of the GOP filter in polarization filtering; further, a challenging ionospheric clutter mitigation problem in HFSWR is addressed.

5.1. Generalized Oblique Projection Polarization Filter. As the linear signal model presented in (4), a pair of the polarization parameters represent the amplitude relationship and the phase difference between the echoes received by the orthogonal dual-polarized radar sensor.

Suppose the polarization parameters of the target and interference are different; then the target polarization subspace $\langle \mathbf{P}_s \rangle$ and interference polarization subspace $\langle \mathbf{P}_i \rangle$ are disjoint. Note that the polarization subspace is independent of the specific radar signal waveforms. The polarization subspace is constructed by the difference of the polarization state. Therefore, the target and interference subspaces in (23) can be given as

$$\mathbf{A} = \begin{bmatrix} \cos \gamma_s \\ \sin \gamma_s e^{j\eta_s} \end{bmatrix}, \quad \mathbf{B} = \begin{bmatrix} \cos \gamma_i \\ \sin \gamma_i e^{j\eta_i} \end{bmatrix}, \quad (57)$$

where γ and η are the polarization pair with subscripts s and i representing target and interference.

There are two sets of the parameters that need to be decided, that is, the echoes polarization set and the ISC. The polarization angle is obtained as

$$\gamma = \text{tg}^{-1} \left(\frac{|x_V(t)|}{|x_H(t)|} \right) \quad (58)$$

and the polarization phase difference as

$$\eta = \arg(x_V(t)) - \arg(x_H(t)), \quad (59)$$

where $x_V(t)$, $x_H(t)$ represent the vertically and horizontally polarized signal components and $\arg(\cdots)$ indicates phase of the signal.

By the inflexibility of the polarized state in the temporal domain and the frequency domain [18], these parameters can be calculated using frequency transformed signal also. The ISC is a free variable, which can be designed according to the specific application.

However, it can be proved that if the ISC is set to zero, this GOP polarization filter becomes OP polarization filter. In constrained condition, that is, subspace $\langle \mathbf{P}_s \rangle$ is orthogonal to $\langle \mathbf{P}_i \rangle$, the GOP polarization filter degrades into an orthogonal polarization filter.

5.2. Ionospheric Clutter Cancellation in HFSWR. The characteristics of the ionosphere reflected echoes received by HFSWR are

- (1) nonstationary,
- (2) multiclutters,
- (3) widely spread in range and Doppler bins.

In addition to that, there are ionospheric clutters returning from the sea surface, which make their polarization states close to the target, or the spatial difference between the

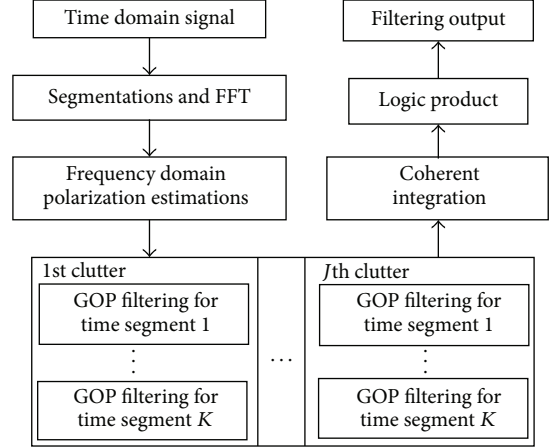


FIGURE 4: Ionospheric clutter mitigation process flow.

clutters and target is not obvious. Those characteristics lead to an unsolved clutter mitigation problem so far.

As the radar arrays cannot effectively distinguish the target and interference spatially in this scenario, the array polarization diversity and the coherent integration process are explored. To handle those characteristics, segmentations of the time domain signals are introduced in an effort to approach the real clutter parameters, and multiple GOP filters with flexible parameters ζ are constructed. The flowchart to illustrate the ionospheric clutter mitigation process is shown in Figure 4.

In the dual-polarized HFSWR system, the time domain signal is range processed. After proper signal segmentations, the polarization states are estimated according to (58) and (59) with frequency transformed signal components. The signals returned from the ship target over sea surface will retain vertically polarized state, whereas the ionosphere reflected clutters will be ellipse polarized with strong horizontally polarized components. The target and clutter polarization subspaces (\mathbf{A} and \mathbf{B} for GOP) are therefore obtained by the polarization threshold. A total number of K segments of the time divided data after filtering are connected and coherent integration is performed. However, by the special design of GOP polarization filter, an extra integration loss to the ionospheric clutter will be brought in.

By Property 1 of GOP, the target polarization subspaces are retained, while the ionospheric clutters are controlled by the free variable ζ which is designed to introduce random phase shift. Therefore, after GOP processing, a significant coherent integration loss will be introduced to the ionospheric clutters when the time divided segments are reconnected and fast Fourier transformed. However, the target's amplitude and phase are unchanged and its coherent integration performance is not affected.

The free variable of $\zeta(n)$ is designed as

$$\zeta(n) = \text{rnd}(\delta_1, \delta_2, n) e^{j\text{rnd}(\beta_1, \beta_2, n)}, \quad n \in [1, K], \quad (60)$$

where $\text{rnd}(\delta_1, \delta_2, n)$ represents random arrays from the uniform distribution with amplitude range $[\delta_1, \delta_2]$ and random

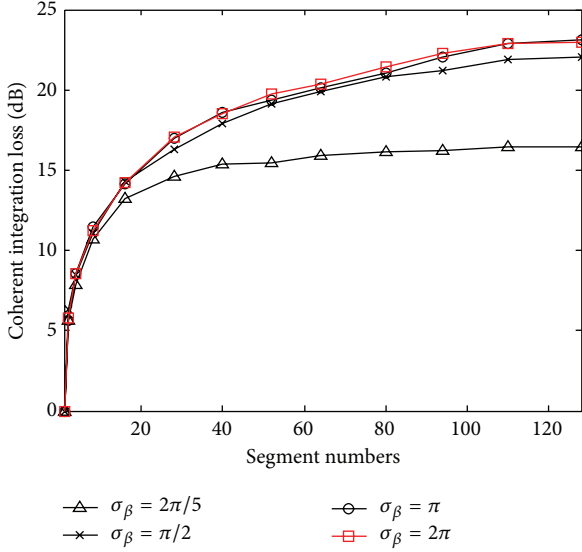


FIGURE 5: Coherent loss versus segment numbers under different phase ranges.

phase term $e^{j\text{rnd}(\beta_1, \beta_2, n)}$ with phase range $[\beta_1, \beta_2]$ and n denotes the sequence number of ζ generated.

In deciding the parameters of ζ , the number of segmentation and the phase ranges are of importance. In Figure 5, the segmentation number is chosen to be 64 and at that point phase range of $[0, 2\pi]$ is picked by simulation results of ideal exponential signals. The reasons are that more segmentation numbers can only introduce at most 3 dB loss further, while more segments indicate shorter time in coherent integration and result in more estimation errors, which may degrade the performance of the filter. Therefore, the parameters are obtained in consideration of the extra coherent loss and potential estimation error.

After logic product process [18], which reserves the smallest points in Doppler spectrum from all the filtering results, the final output in each range bin is obtained as

$$\mathbf{Y}(\omega) = \sum_{n=1}^N \left\{ \delta(\omega - \omega_n) \times \min_{j=1}^J \left(\text{FFT} \left[\sum_{k=1}^K \mathbf{E}_{\mathbf{A}, \mathbf{B}, \xi, k, j} \mathbf{x}_k(n_{\text{seg}, k}) \right] \right) \right\}, \quad (61)$$

where N represents the length of FFT, ω_n represents the frequency at point n , J represents the total number of the clutters, K is the total number of segmentations, $\mathbf{E}_{\mathbf{A}, \mathbf{B}, \xi, k, j}$ is the k th GOP in time domain for the suppression of j th clutter, and $\mathbf{x}_k(n_{\text{seg}, k})$ is the k th time segmented data with $n_{\text{seg}, k}$ denoting the sampled points in the corresponding segment.

In the HFSWR field experiment, the vertically polarized signal was transmitted with a carrier frequency of 7 Mhz by a half-wave dipole antenna. The data was collected by a distant polarized high frequency linear array with 15-meter separation between the vertically and horizontally polarized elements. The coherent integration time was 4 minutes.

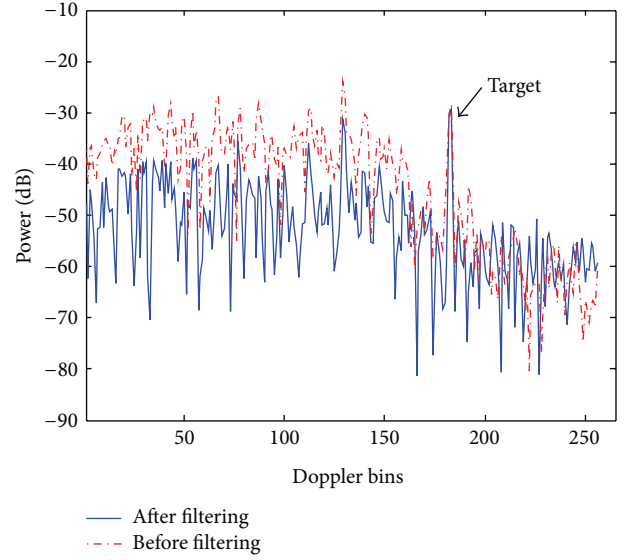


FIGURE 6: Doppler spectrum at range bin 79.

Figure 6 gives the Doppler spectrum after integration at range bin 79, which is obtained from experimentally derived data with red dashed line denoting spectrum before filtering and blue solid line denoting spectrum after process. It can be observed that there are several peaks well above -30 dB before filtering, which create an unfavorable ship detection environment. However, the ship target at Doppler bin 183 can be distinguished easily since the ionospheric clutters are suppressed by about 10 dB in average, whereas the target signal is undistorted.

Besides ship detection, the other focus can be drawn on the sea state remote sensing. A successful sea state inversion algorithm depends on the correct and accurate extractions of Bragg. In Figure 7, the double first order Bragg peaks at Doppler bins (in between the vertically green dashed lines) are contaminated by the ionospheric clutters. After GOP filtering, the contaminations of ionosphere are minimized; moreover the SINR of the negative Bragg peaks was raised around 12 dB, which facilitates its extraction algorithms.

The Doppler spectrums from all the range bins are then collected together, forming a range-Doppler spectrum. Figure 8(a) presents the original range-Doppler spectrum which is contaminated by the ionospheric clutters from range bins 73 to 96, whereas Figure 8(b) describes the spectrum after being processed by GOP filters. Obviously, the ionospheric clutters which widely spread in range and Doppler bins are suppressed effectively. The average SINR improvement is above 10 dB in this experiment.

6. Conclusions

In this paper, a novel GOP with adjustable ISC parameter has been proposed. It is proved to be an extension of OP and four fundamental properties are presented with proofs. The construction of GOP filters is demonstrated with examples of spatial and polarization filtering, respectively. In the first example, with ISC derived from adaptive beamforming

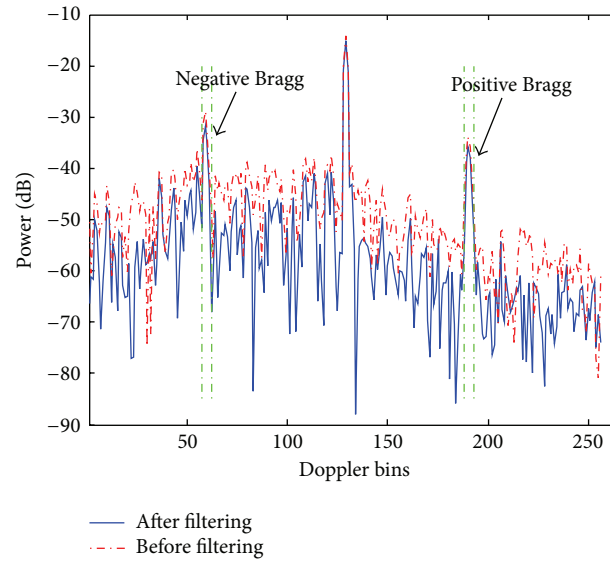


FIGURE 7: Doppler spectrum at range bin 89.

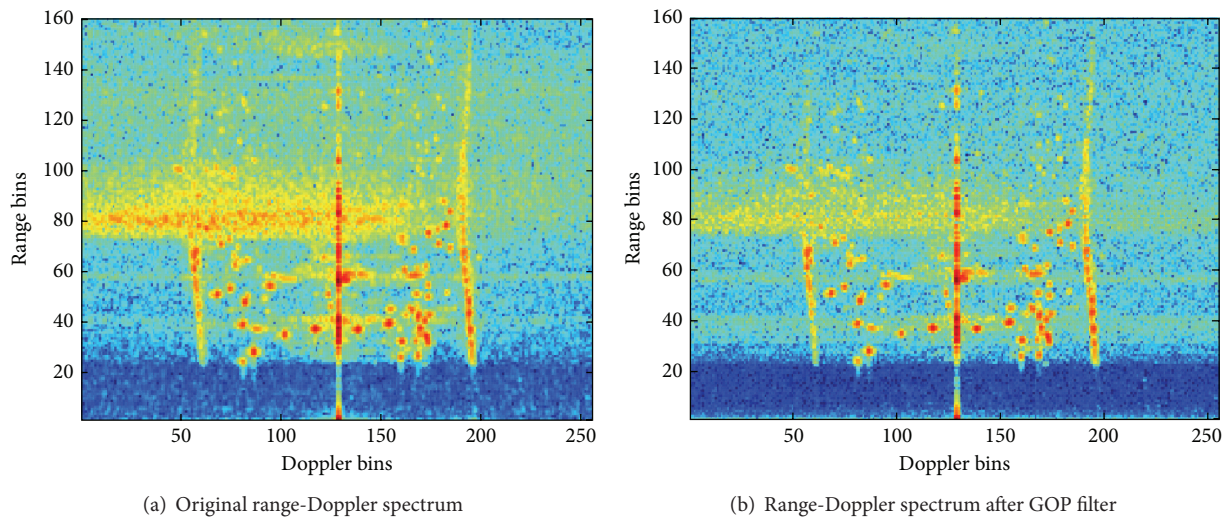


FIGURE 8: Range-Doppler spectrum of HFSWR.

algorithm, the SINR performance of GOP filter is shown to be better than MVDR and OP filters both theoretically and numerically. A GOP polarization filter is constructed with manually designed ISC in the second example. An extra coherent loss is introduced to the ionospheric clutters by purpose and a satisfying clutter suppression result in HFSWR is achieved. Besides the examples given, more designs of GOP filter can be inspired by the flexibilities of ISC. It can be concluded that GOP filter is a promising filtering technique for interference suppression and capable of being used in spatial filtering, polarization filtering, and other array signal processing applications.

Conflict of Interests

The authors declare that there is no conflict of interests regarding the publication of this paper.

Acknowledgments

This project is sponsored by the National Marine Technology Program for Public Welfare (no. 200905029), National Natural Science Foundation of China (no. 61171180), and Team Research Foundation for Fundamental Research Program in FIO, China (no. GY0213T03).

References

- [1] R. T. Behrens and L. L. Scharf, "Signal processing applications of oblique projection operators," *IEEE Transactions on Signal Processing*, vol. 42, no. 6, pp. 1413–1424, 1994.
- [2] L. Rebollo-Neira, "Oblique matching pursuit," *IEEE Signal Processing Letters*, vol. 14, no. 10, pp. 703–706, 2007.
- [3] G. W. Stewart, "On the numerical analysis of oblique projectors," *SIAM Journal on Matrix Analysis and Applications*, vol. 32, no. 1, pp. 309–348, 2011.

- [4] X.-P. Mao, A.-J. Liu, H.-J. Hou, H. Hong, R. Guo, and W.-B. Deng, "Oblique projection polarisation filtering for interference suppression in high-frequency surface wave radar," *IET Radar, Sonar and Navigation*, vol. 6, no. 2, pp. 71–80, 2012.
- [5] X. P. Mao, A. J. Liu, W. B. Deng, B. Cao, and Q. Y. Zhang, "An oblique projecting polarization filter," *Acta Electronica Sinica*, vol. 38, no. 9, pp. 2003–2008, 2010 (Chinese).
- [6] Q.-Y. Zhang, B. Cao, L. Jin, and N.-T. Zhang, "Oblique projection polarization filtering-based interference suppressions for radar sensor networks," *EURASIP Journal on Wireless Communications and Networking*, vol. 2010, Article ID 605103, 2010.
- [7] X. Yu and L. Tong, "Joint channel and symbol estimation by oblique projections," *IEEE Transactions on Signal Processing*, vol. 49, no. 12, pp. 3074–3083, 2001.
- [8] Q. Zhang, B. Cao, J. Wang, and N. Zhang, "Polarization filtering technique based on oblique projections," *Science China F*, vol. 53, no. 5, pp. 1056–1066, 2010.
- [9] Y. Cui, K. Liu, and J. Wang, "Direction-of-arrival estimation for coherent GPS signals based on oblique projection," *Signal Processing*, vol. 92, no. 1, pp. 294–299, 2012.
- [10] Y. Hu, X. Zhang, F. Zhu, and H. Lv, "Image recognition using iterative oblique projection," *Electronics Letters*, vol. 41, no. 20, pp. 1109–1110, 2005.
- [11] G. Hellboug, R. Weber, C. Capdessus, and A.-J. Boonstra, "Oblique projection beamforming for RFI mitigation in radio astronomy," in *Proceedings of the IEEE Statistical Signal Processing Workshop (SSP '12)*, pp. 93–96, IEEE, August 2012.
- [12] P. De, "New methods for sensing bandlimited signals in cognitive radio," in *Proceedings of the IEEE 65th Vehicular Technology Conference (VTC '07-Spring)*, pp. 1916–1920, Dublin, Ireland, April 2007.
- [13] R. Boyer, "Oblique projection for source estimation in a competitive environment: algorithm and statistical analysis," *Signal Processing*, vol. 89, no. 12, pp. 2547–2554, 2009.
- [14] M. L. McCloud and L. L. Scharf, "A new subspace identification algorithm for high-resolution DOA estimation," *IEEE Transactions on Antennas and Propagation*, vol. 50, no. 10, pp. 1382–1390, 2002.
- [15] R. Boyer and G. Bouleux, "Oblique projections for direction-of-arrival estimation with prior knowledge," *IEEE Transactions on Signal Processing*, vol. 56, no. 4, pp. 1374–1387, 2008.
- [16] H. Hong, X.-P. Mao, C. Hu, R. Guo, W.-B. Deng, and P. Jiang, "Narrow-band null phase-shift spatial filter based on oblique projection," in *Proceedings of the IEEE Radar Conference (RADAR '13)*, pp. 1–5, Ottawa, Canada, May 2013.
- [17] Z. H. Xu, Y. P. Ni, and L. Jin, "Resolution theory of polarization sensitive array signals," in *Proceedings of the CIE International Conference on Radar (ICR '06)*, pp. 1–4, IEEE, Shanghai, China, October 2006.
- [18] X. P. Mao and Y. T. Liu, "Null phase-shift polarization filtering for high-frequency radar," *IEEE Transactions on Aerospace and Electronic Systems*, vol. 43, no. 4, pp. 1397–1408, 2007.
- [19] Y.-M. Wang, X.-P. Mao, J. Zhang, and H. Hong, "A multi-domain collaborative filter based on polarization sensitive frequency diverse array," in *Proceedings of the IEEE Radar Conference*, pp. 0507–0511, Cincinnati, Ohio, USA, May 2014.
- [20] M. Souden, J. Benesty, and S. Affes, "A study of the LCMV and MVDR noise reduction filters," *IEEE Transactions on Signal Processing*, vol. 58, no. 9, pp. 4925–4935, 2010.
- [21] Y. M. Cui, X. P. Mao, and H. Hong, "A novel adaptive filter for interference suppression," in *Proceedings of the IEEE Region 10 Conference*, vol. 31194, pp. 1–5, IEEE, 2013.
- [22] H. C. Chan, "Characterization of ionospheric clutter in HF surface wave radar," Tech. Rep. 2003-114, Defence R&D Canada, Ottawa, Canada, 2003.

Research Article

Two-Dimensional Direction of Arrival (DOA) Estimation for Rectangular Array via Compressive Sensing Trilinear Model

Huaxin Yu,¹ Xiaofeng Qiu,² Xiaofei Zhang,^{1,3} Chenghua Wang,¹ and Gang Yang¹

¹ Key Laboratory of Radar Imaging and Microwave Photonics, Nanjing University of Aeronautics and Astronautics, Ministry of Education, Nanjing 210016, China

² Institute of Command Information System, PLA University of Science and Technology, Nanjing 210007, China

³ Laboratory of Modern Acoustics of Ministry of Education, Nanjing University, Nanjing 210093, China

Correspondence should be addressed to Xiaofei Zhang; njxnd88@126.com

Received 15 March 2014; Revised 21 July 2014; Accepted 17 September 2014

Academic Editor: Hang Hu

Copyright © 2015 Huaxin Yu et al. This is an open access article distributed under the Creative Commons Attribution License, which permits unrestricted use, distribution, and reproduction in any medium, provided the original work is properly cited.

We investigate the topic of two-dimensional direction of arrival (2D-DOA) estimation for rectangular array. This paper links angle estimation problem to compressive sensing trilinear model and derives a compressive sensing trilinear model-based angle estimation algorithm which can obtain the paired 2D-DOA estimation. The proposed algorithm not only requires no spectral peak searching but also has better angle estimation performance than estimation of signal parameters via rotational invariance techniques (ESPRIT) algorithm. Furthermore, the proposed algorithm has close angle estimation performance to trilinear decomposition. The proposed algorithm can be regarded as a combination of trilinear model and compressive sensing theory, and it brings much lower computational complexity and much smaller demand for storage capacity. Numerical simulations present the effectiveness of our approach.

1. Introduction

Array signal processing has received a significant amount of attention during the last decades due to its wide application in radar, sonar, radio astronomy, and satellite communication [1]. The direction of arrival (DOA) estimation of signals impinging on an antenna array is a fundamental problem in array signal processing, and many DOA estimation methods [2–7] have been proposed for its solution. They contain estimation of signal parameters via rotational invariance techniques (ESPRIT) algorithm [2, 3], multiple signal classification (MUSIC) algorithm [4], Root-MUSIC [5], matrix pencil methods [6], and so on. Compared with linear arrays, uniform rectangular array can identify two-dimensional DOA (2D-DOA). 2D-DOA estimation with rectangular array has received considerable attention in the field of array signal processing [7–12]. ESPRIT algorithms in [8–11] have exploited the invariance property for 2D-DOA estimation in uniform rectangular array. Parallel factor

analysis (PARAFAC) in [12], which is also called trilinear decomposition method, was proposed for 2D-DOA estimation for uniform rectangular array, and it has better angle estimation performance than ESPRIT. MUSIC algorithm, as a subspace method, has good angle estimation performance and matches irregular arrays. It has been proved that two-dimensional MUSIC (2D-MUSIC) algorithm [13] can be used for 2D-DOA estimation. However, the requirement of two-dimensional (2D) spectrum searching renders much higher computational complexity.

Compressive sensing [14, 15] has attracted a lot of attention recently, and it has been applied to image processing, machine learning, channel estimation, radar imaging, and penalized regression [16]. According to the theory of compressive sensing, a signal that is sparse in some domain can be recovered via fewer samples than required by the Nyquist sampling theorem. The DOAs of sources form a sparse vector in the potential signal space, and, therefore, compressive sensing can be applied to DOA estimation.

The superresolution property and ability of resolving coherent sources can be achieved when we apply it to the source location [17]. Lots of the DOA estimation methods with compressive sensing just use one snapshot and are very sensitive to the noise. For multiple snapshots, ℓ_1 -SVD method [16] employed ℓ_1 norm to enforce sparsity and singular value decomposition to reduce complexity and sensitivity to noise, and sparse recovery for weighted subspace fitting in [17] improved the ℓ_1 -SVD method via the weight to the subspace.

Compared to matrix decomposition, trilinear decomposition has a distinctive and attractive feature: it is often unique [18–22]. In the signal processing field, trilinear decomposition can be regarded as a generalization of ESPRIT and joint approximate diagonalization [19–22]. The compressive sensing trilinear model-based algorithm discussed in this paper can be regarded as a combination of trilinear model and compressive sensing theory, which brings much lower computational complexity and much smaller demand for storage capacity.

The framework of compressive sensing for sparse low-rank tensor is proposed in [23] and used for signal detection and multiple-input-multiple-output radar in [24, 25]. In this paper, the problem of 2D-DOA estimation for rectangular array is linked to compressive sensing trilinear model. Exploiting this link, we derive a compressive sensing trilinear model-based 2D-DOA estimation algorithm for rectangular array. Firstly, we compress the received data to get a compressed trilinear model and then obtain the estimates of compressed direction matrices through performing trilinear decomposition for the compressed model. Finally, we formulate a sparse recovery problem through the estimated compressed direction matrices and apply the orthogonal matching pursuit (OMP) [26] to resolve it for 2D-DOA estimation. Due to compression, the proposed method has much lower computational complexity than conventional trilinear decomposition method [12] and 2D-MUSIC algorithm and requires much smaller storage capacity. We illustrate that the proposed algorithm has better angle estimation performance than ESPRIT algorithm. Furthermore, our algorithm can obtain paired elevation angles and azimuth angles automatically. We also derive the Cramer-Rao bound (CRB) for 2D-DOA estimation in rectangular array. Numerical simulations present the effectiveness of our approach.

The remainder of this paper is structured as follows. Section 2 presents the data model, and Section 3 proposes the compressed sensing trilinear model-based algorithm for 2D-DOA estimation in rectangular array. In Section 4, the simulation results are presented to verify improvement of the proposed algorithm, while the conclusions are drawn in Section 5.

Notation. Bold lower (upper) case letters are adopted to represent vectors (matrices). $(\cdot)^T$, $(\cdot)^H$, $(\cdot)^*$, $(\cdot)^{-1}$, and $(\cdot)^+$ denote transpose, conjugate transpose, conjugate, matrix inversion, and pseudoinverse operations, respectively. \mathbf{I}_P stands for a $P \times P$ identity matrix. $D_n(\mathbf{A})$ denotes a diagonal matrix with the entries of the matrix \mathbf{A} 's n th row on the main diagonal. The i th entry of a given column vector \mathbf{g} is denoted by $\mathbf{g}(i)$.

\odot , \otimes , and \oplus denote Khatri-Rao product, Kronecker product, and Hadamard product, respectively.

If \mathbf{A} is a p -by- q matrix and \mathbf{B} is an m -by- n matrix, then the Kronecker product $\mathbf{A} \otimes \mathbf{B}$ is the mp -by- nq block matrix:

$$\mathbf{A} \otimes \mathbf{B} = \begin{bmatrix} a_{11}\mathbf{B} & a_{12}\mathbf{B} & \cdots & a_{1q}\mathbf{B} \\ a_{21}\mathbf{B} & a_{22}\mathbf{B} & \cdots & a_{2q}\mathbf{B} \\ \vdots & \vdots & \ddots & \vdots \\ a_{p1}\mathbf{B} & a_{p2}\mathbf{B} & \cdots & a_{pq}\mathbf{B} \end{bmatrix}, \quad (1)$$

where a_{ij} is the (i, j) element of the matrix \mathbf{A} .

If \mathbf{A} is an I -by- F matrix and \mathbf{B} is a J -by- F matrix, then the Khatri-Rao product $\mathbf{A} \odot \mathbf{B}$ is the IJ -by- F block matrix:

$$\mathbf{A} \odot \mathbf{B} = [\mathbf{a}_1 \otimes \mathbf{b}_1, \dots, \mathbf{a}_F \otimes \mathbf{b}_F], \quad (2)$$

where \mathbf{a}_f and \mathbf{b}_f are the f th column of the matrices \mathbf{A} and \mathbf{B} , respectively.

If \mathbf{A} is an I -by- J matrix and \mathbf{B} is an I -by- J matrix, then the Hadamard product $\mathbf{A} \oplus \mathbf{B}$ is

$$\mathbf{A} \oplus \mathbf{B} = \begin{bmatrix} a_{11}b_{11} & a_{12}b_{12} & \cdots & a_{1J}b_{1J} \\ a_{21}b_{21} & a_{22}b_{22} & \cdots & a_{2J}b_{2J} \\ \vdots & \vdots & \ddots & \vdots \\ a_{I1}b_{I1} & a_{I2}b_{I2} & \cdots & a_{IJ}b_{IJ} \end{bmatrix}, \quad (3)$$

where a_{ij} and b_{ij} are the (i, j) element of the matrices \mathbf{A} and \mathbf{B} , respectively.

2. Data Model

A rectangular array consisted of $M \times N$ elements is shown in Figure 1, where the distance between two adjacent elements is d . We consider signals in the far field, in which case the signal sources are far away enough that the arriving waves are essentially planes over the array. We assume that the noise is independent of the sources. It is also assumed that there are K noncoherent or independent sources, and the number of sources is preknown. θ_k and ϕ_k are the elevation angle and the azimuth angle of the k th source, respectively. We assume the sources impinge on the array with different DOAs.

The received signal of the first subarray in the rectangular array is $\mathbf{x}_1(t) = \mathbf{A}_x \mathbf{s}(t) + \mathbf{n}_1(t)$, where $\mathbf{A}_x = [\mathbf{a}_x(\phi_1, \theta_1), \mathbf{a}_x(\phi_2, \theta_2), \dots, \mathbf{a}_x(\phi_K, \theta_K)] \in \mathbf{C}^{M \times K}$ with $\mathbf{a}_x(\phi_k, \theta_k) = [1, e^{j2\pi d \sin \theta_k \cos \phi_k / \lambda}, \dots, e^{j2\pi(M-1)d \sin \theta_k \cos \phi_k / \lambda}]^T$ and λ is the wavelength. $\mathbf{n}_1(t)$ is the received additive white Gaussian noise of the first subarray. $\mathbf{s}(t) \in \mathbf{C}^{K \times 1}$ is the source vector. The received signal of the n th subarray in the rectangular array is $\mathbf{x}_n(t) = \mathbf{A}_x \Phi^{n-1} \mathbf{s}(t) + \mathbf{n}_n(t)$, where $\Phi = \text{diag}(e^{j2\pi d \sin \theta_1 \sin \phi_1 / \lambda}, \dots, e^{j2\pi d \sin \theta_K \sin \phi_K / \lambda})$ and $\mathbf{n}_n(t)$ is the received additive white Gaussian noise of the n th subarray. Therefore, the received signal of the rectangular array is [27]

$$\mathbf{x}(t) = \begin{bmatrix} \mathbf{x}_1(t) \\ \mathbf{x}_2(t) \\ \vdots \\ \mathbf{x}_N(t) \end{bmatrix} = \begin{bmatrix} \mathbf{A}_x \\ \mathbf{A}_x \Phi \\ \vdots \\ \mathbf{A}_x \Phi^{N-1} \end{bmatrix} \mathbf{s}(t) + \begin{bmatrix} \mathbf{n}_1(t) \\ \mathbf{n}_2(t) \\ \vdots \\ \mathbf{n}_N(t) \end{bmatrix}. \quad (4)$$

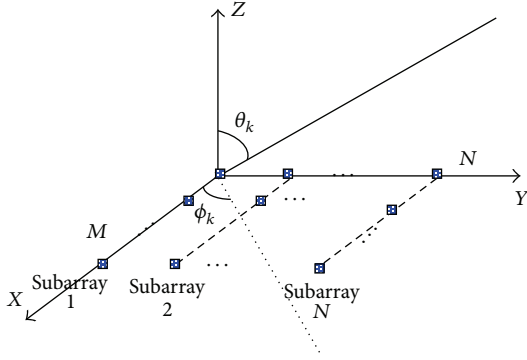


FIGURE 1: The structure of uniform rectangular array.

The signal $\mathbf{x}(t) \in \mathbf{C}^{MN \times 1}$ in (4) can also be denoted by

$$\mathbf{x}(t) = [\mathbf{A}_y \odot \mathbf{A}_x] \mathbf{s}(t) + \mathbf{n}(t), \quad (5)$$

where $\mathbf{A}_y = [\mathbf{a}_y(\phi_1, \theta_1), \mathbf{a}_y(\phi_2, \theta_2), \dots, \mathbf{a}_y(\phi_K, \theta_K)]$ with $\mathbf{a}_y(\phi_k, \theta_k) = [1, e^{j2\pi d \sin \theta_k \sin \phi_k / \lambda}, \dots, e^{j2\pi(N-1)d \sin \theta_k \sin \phi_k / \lambda}]^T$; $\mathbf{n}(t) = [\mathbf{n}_1(t)^T, \mathbf{n}_2(t)^T, \dots, \mathbf{n}_N(t)^T]^T \in \mathbf{C}^{MN \times 1}$. \odot denotes Khatri-Rao product.

According to the definition of Khatri-Rao product, the signal in (5) can be rewritten as

$$\mathbf{x}(t) = [\mathbf{a}_y(\phi_1, \theta_1) \otimes \mathbf{a}_x(\phi_1, \theta_1), \dots, \mathbf{a}_y(\phi_K, \theta_K) \otimes \mathbf{a}_x(\phi_K, \theta_K)] \mathbf{s}(t) + \mathbf{n}(t), \quad (6)$$

where \otimes denotes Kronecker product. We collect L samples and define $\mathbf{X} = [\mathbf{x}(1), \mathbf{x}(2), \dots, \mathbf{x}(L)] \in \mathbf{C}^{MN \times L}$, which can be expressed as

$$\begin{aligned} \mathbf{X} &= [\mathbf{A}_y \odot \mathbf{A}_x] \mathbf{S}^T + \mathbf{N} = \begin{bmatrix} \mathbf{X}_1 \\ \mathbf{X}_2 \\ \vdots \\ \mathbf{X}_N \end{bmatrix} \\ &= \begin{bmatrix} \mathbf{A}_x D_1(\mathbf{A}_y) \\ \mathbf{A}_x D_2(\mathbf{A}_y) \\ \vdots \\ \mathbf{A}_x D_N(\mathbf{A}_y) \end{bmatrix} \mathbf{S}^T + \begin{bmatrix} \mathbf{N}_1 \\ \mathbf{N}_2 \\ \vdots \\ \mathbf{N}_N \end{bmatrix}, \end{aligned} \quad (7)$$

where $\mathbf{S} = [\mathbf{s}(1), \mathbf{s}(2), \dots, \mathbf{s}(L)]^T \in \mathbf{C}^{L \times K}$ is source matrix and $\mathbf{N} = [\mathbf{n}(1), \mathbf{n}(2), \dots, \mathbf{n}(L)]$ is the received additive white Gaussian noise matrix. $\mathbf{N}_n \in \mathbf{C}^{M \times L}$ ($n = 1, \dots, N$) is the noise matrix. Thus, $\mathbf{X}_n \in \mathbf{C}^{M \times L}$ in (7) is denoted as

$$\mathbf{X}_n = \mathbf{A}_x D_n(\mathbf{A}_y) \mathbf{S}^T + \mathbf{N}_n, \quad n = 1, 2, \dots, N. \quad (8)$$

Equation (7) can also be denoted with the trilinear model [18, 28]

$$\begin{aligned} x_{m,n,l} &= \sum_{k=1}^K \mathbf{A}_x(m, k) \mathbf{A}_y(n, k) \mathbf{S}(l, k) + n_{m,n,l}, \\ m &= 1, \dots, M, \quad n = 1, \dots, N, \quad l = 1, \dots, L, \end{aligned} \quad (9)$$

where $\mathbf{A}_x(m, k)$ is the (m, k) element of the matrix \mathbf{A}_x and similarly for the others. $n_{m,n,l}$ is noise part. $\mathbf{X}_n \in \mathbf{C}^{M \times L}$ ($n = 1, \dots, N$) can be regarded as slicing the three-dimensional data in a series of slices, which is shown in Figure 2. There are two more matrix system rearrangements, in which we have $\mathbf{Y}_m = \mathbf{S} D_m(\mathbf{A}_x) \mathbf{A}_y^T + \mathbf{N}_m^y$, $m = 1, \dots, M$, and $\mathbf{Z}_l = \mathbf{A}_y D_l(\mathbf{S}) \mathbf{A}_x^T + \mathbf{N}_l^z$, $l = 1, \dots, L$, where \mathbf{N}_m^y and \mathbf{N}_l^z are noise matrices. Then, we form the matrices of $\mathbf{Y} \in \mathbf{C}^{M \times L \times N}$ and $\mathbf{Z} \in \mathbf{C}^{L \times N \times M}$:

$$\mathbf{Y} = \begin{bmatrix} \mathbf{Y}_1 \\ \mathbf{Y}_2 \\ \vdots \\ \mathbf{Y}_M \end{bmatrix} = [\mathbf{A}_x \odot \mathbf{S}] \mathbf{A}_y^T + \mathbf{N}^y, \quad (10)$$

$$\mathbf{Z} = \begin{bmatrix} \mathbf{Z}_1 \\ \mathbf{Z}_2 \\ \vdots \\ \mathbf{Z}_L \end{bmatrix} = [\mathbf{S} \odot \mathbf{A}_y] \mathbf{A}_x^T + \mathbf{N}^z, \quad (11)$$

where

$$\begin{aligned} \mathbf{N}^y &= \begin{bmatrix} \mathbf{N}_1^y \\ \mathbf{N}_2^y \\ \vdots \\ \mathbf{N}_M^y \end{bmatrix}, \\ \mathbf{N}^z &= \begin{bmatrix} \mathbf{N}_1^z \\ \mathbf{N}_2^z \\ \vdots \\ \mathbf{N}_L^z \end{bmatrix}. \end{aligned} \quad (12)$$

3. 2D-DOA Estimation Based on Compressive Sensing Trilinear Model

We link the problem of 2D-DOA estimation for rectangular array to compressive sensing trilinear model and derive a compressive sensing trilinear model-based 2D-DOA estimation algorithm. Firstly, we compress the received data to get a compressed trilinear model and then obtain the estimates of compressed direction matrices through performing trilinear decomposition for the compressed model. Finally, we formulate the sparse recovery problem for 2D-DOA estimation.

3.1. Trilinear Model Compression. We compress the three-way data $\underline{\mathbf{X}} \in \mathbf{C}^{M \times N \times L}$ into a smaller three-way data $\underline{\mathbf{X}}' \in \mathbf{C}^{M' \times N' \times L'}$, where $M' < M$, $N' < N$, and $L' < L$. The trilinear model compression processing is shown in Figure 3. We define the compression matrices as $\mathbf{U} \in \mathbf{C}^{M \times M'}$, $\mathbf{V} \in \mathbf{C}^{N \times N'}$, and $\mathbf{W} \in \mathbf{C}^{L \times L'}$, and the compression matrices \mathbf{U} , \mathbf{V} , and \mathbf{W} can be generated randomly or obtained by Tucker3 decomposition [23, 29]. We can use the Tucker3 decomposition,

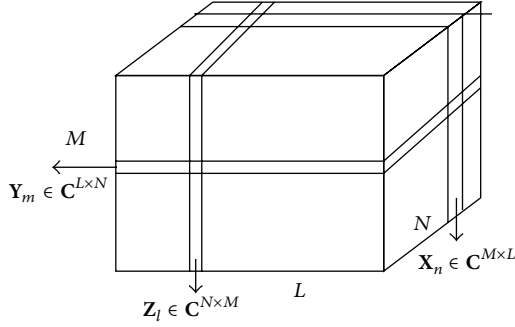


FIGURE 2: Trilinear model.

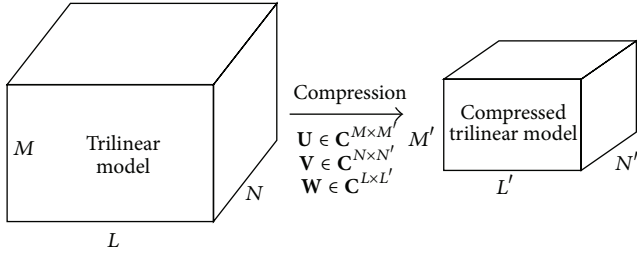


FIGURE 3: The compression of trilinear model.

where tensor is decomposed into the core tensor, to obtain the compression matrices. The compression matrices should satisfy the restricted isometry property. And random Gaussian, Bernoulli, and partial Fourier matrices satisfy the restricted isometry property with number of measurements nearly linear in the sparsity level [30, 31].

Then compress $\mathbf{X} \in \mathbb{C}^{MN \times L}$ in (7) to a smaller one as $\mathbf{X}' \in \mathbb{C}^{M'N' \times L'}$

$$\begin{aligned} \mathbf{X}' &= (\mathbf{V}^T \otimes \mathbf{U}^T) \mathbf{X} \mathbf{W}^T \\ &= (\mathbf{V}^T \otimes \mathbf{U}^T) [\mathbf{A}_y \circ \mathbf{A}_x] \mathbf{S}^T \mathbf{W}^T \\ &\quad + (\mathbf{V}^T \otimes \mathbf{U}^T) \mathbf{N} \mathbf{W}^T. \end{aligned} \quad (13)$$

According to the property of Khatri-Rao product [23], we know

$$(\mathbf{V}^T \otimes \mathbf{U}^T) [\mathbf{A}_y \circ \mathbf{A}_x] = (\mathbf{V}^T \mathbf{A}_y) \circ (\mathbf{U}^T \mathbf{A}_x). \quad (14)$$

Define $\mathbf{A}'_x = \mathbf{U}^T \mathbf{A}_x$, $\mathbf{A}'_y = \mathbf{V}^T \mathbf{A}_y$, and $\mathbf{S}' = \mathbf{W}^T \mathbf{S}$. Equation (11) is also denoted as

$$\mathbf{X}' = [\mathbf{A}'_y \circ \mathbf{A}'_x] \mathbf{S}'^T + \mathbf{N}', \quad (15)$$

where $\mathbf{N}' = (\mathbf{V}^T \otimes \mathbf{U}^T) \mathbf{N} \mathbf{W}^T$. \mathbf{X}' can be denoted by trilinear model. With respect to (10) and (11), we form the matrices of \mathbf{Y}' and \mathbf{Z}' according to the compressed data

$$\mathbf{Y}' = [\mathbf{A}'_x \circ \mathbf{S}'] \mathbf{A}'_y{}^T + \mathbf{N}'^y, \quad (16)$$

$$\mathbf{Z}' = [\mathbf{S}' \circ \mathbf{A}'_y] \mathbf{A}'_x{}^T + \mathbf{N}'^z, \quad (17)$$

where \mathbf{N}'^y and \mathbf{N}'^z are the noise part. The compressed trilinear model may degrade the angle estimation performance.

By trilinear model compression, the proposed method has much lower computational complexity than conventional trilinear decomposition method and requires much smaller storage capacity. Conventional compressive sensing is to compress the matrix, while our algorithm compresses the three-dimensional tensor.

3.2. Trilinear Decomposition. Trilinear alternating least square (TALS) algorithm is an iterative method for estimating the parameters of a trilinear decomposition [18, 28]. We concisely show the basic idea of TALS: (1) update one matrix each time via LS, which is conditioned on previously obtained estimates of the remaining matrices; (2) proceed to update the other matrices; (3) repeat until convergence of the LS cost function [21, 22]. TALS algorithm is discussed as follows.

According to (15), least squares (LS) fitting is

$$\min_{\mathbf{A}'_x, \mathbf{A}'_y, \mathbf{S}'} \|\mathbf{X}' - [\mathbf{A}'_y \circ \mathbf{A}'_x] \mathbf{S}'^T\|_F \quad (18)$$

and LS update for the matrix \mathbf{S}' is

$$\widehat{\mathbf{S}}'^T = [\widehat{\mathbf{A}}'_y \circ \widehat{\mathbf{A}}'_x]^+ \mathbf{X}', \quad (19)$$

where $\widehat{\mathbf{A}}'_x$ and $\widehat{\mathbf{A}}'_y$ are previously obtained estimates of \mathbf{A}'_x and \mathbf{A}'_y , respectively. According to (16), LS fitting is

$$\min_{\mathbf{A}'_x, \mathbf{A}'_y, \mathbf{S}'} \|\mathbf{Y}' - [\mathbf{A}'_x \circ \mathbf{S}'] \mathbf{A}'_y{}^T\|_F \quad (20)$$

and LS update for \mathbf{A}'_y is

$$\widehat{\mathbf{A}}'_y{}^T = [\widehat{\mathbf{A}}'_x \circ \widehat{\mathbf{S}}']^+ \mathbf{Y}', \quad (21)$$

where $\widehat{\mathbf{A}}'_x$ and $\widehat{\mathbf{S}}'$ stand for the previously obtained estimates of \mathbf{A}'_x and \mathbf{S}' . Similarly, according to (17), LS fitting is

$$\min_{\mathbf{A}'_x, \mathbf{A}'_y, \mathbf{S}'} \|\mathbf{Z}' - [\mathbf{S}' \circ \mathbf{A}'_y] \mathbf{A}'_x{}^T\|_F, \quad (22)$$

where $\widetilde{\mathbf{Z}}'$ is the noisy compressed signal. LS update for \mathbf{A}'_x is

$$\widehat{\mathbf{A}}'_x{}^T = [\widehat{\mathbf{S}}' \circ \widehat{\mathbf{A}}'_y]^+ \mathbf{Z}', \quad (23)$$

where $\widehat{\mathbf{A}}'_y$ and $\widehat{\mathbf{S}}'$ stand for the previously obtained estimates of \mathbf{A}'_y and \mathbf{S}' , respectively.

Define $\mathbf{E} = \mathbf{X} - [\widehat{\mathbf{A}}'_y \circ \widehat{\mathbf{A}}'_x] \widehat{\mathbf{S}}'^T$, where $\widehat{\mathbf{S}}'$, $\widehat{\mathbf{A}}'_y$, and $\widehat{\mathbf{A}}'_x$ present the estimates of \mathbf{S}' , \mathbf{A}'_y , and \mathbf{A}'_x , respectively. The sum of squared residuals (SSR) in trilinear model is defined as $\text{SSR} = \sum_{j=1}^L \sum_{i=1}^{MN} |e_{ij}|$, where e_{ij} is the (i, j) element of the matrix \mathbf{E} . According to (19), (21), and (23), the matrices \mathbf{S}' , \mathbf{A}'_y , and \mathbf{A}'_x are updated with least squares repeatedly until SSR attain apriorthreshold. The we obtain the final estimates $\widehat{\mathbf{S}}'$, $\widehat{\mathbf{A}}'_y$, and $\widehat{\mathbf{A}}'_x$.

Theorem 1 (see [22]). Considering $\mathbf{X}'_n = \mathbf{A}'_x D_n(\mathbf{A}'_y) \mathbf{S}'^T$, $n = 1, \dots, N'$, where $\mathbf{A}'_x \in \mathbf{C}^{M' \times K}$, $\mathbf{S}' \in \mathbf{C}^{L' \times K}$, and $\mathbf{A}'_y \in \mathbf{C}^{N' \times K}$, if

$$k_{\mathbf{A}'_x} + k_{\mathbf{A}'_y} + k_{\mathbf{S}'^T} \geq 2K + 2, \quad (24)$$

where $k_{\mathbf{A}}$ is the k -rank of the matrix \mathbf{A} [18], then \mathbf{A}'_x , \mathbf{S}' , and \mathbf{A}'_y are unique up to permutation and scaling of columns.

For the different DOAs and independent sources, we have $k_{\mathbf{A}'_x} = \min(M', K)$, $k_{\mathbf{A}'_y} = \min(N', K)$, and $k_{\mathbf{S}'^T} = \min(L', K)$ in the trilinear model in this paper, and then the inequality in (24) becomes

$$\begin{aligned} \min(M', K) + \min(N', K) + \min(L', K) \\ \geq 2K + 2. \end{aligned} \quad (25)$$

When $M' \geq K$, $N' \geq K$, and $L' \geq K$, the identifiable condition is $1 \leq K \leq \min(M', N')$.

When $M' \leq K$, $N' \leq K$, and $L' \geq K$, the identifiable condition is $\max(M', N') \leq K \leq M' + N' - 2$. Hence, the proposed algorithm is effective when $K \leq M' + N' - 2$ and the maximum number of sources that can be identified is $M' + N' - 2$.

After the trilinear decomposition, we obtain the estimates of the loading matrices

$$\begin{aligned} \widehat{\mathbf{A}}'_x &= \mathbf{A}'_x \mathbf{\Pi} \mathbf{\Delta}_1 + \mathbf{E}_1, \\ \widehat{\mathbf{S}}' &= \mathbf{S}' \mathbf{\Pi} \mathbf{\Delta}_2 + \mathbf{E}_2, \\ \widehat{\mathbf{A}}'_y &= \mathbf{A}'_y \mathbf{\Pi} \mathbf{\Delta}_3 + \mathbf{E}_3, \end{aligned} \quad (26)$$

where $\mathbf{\Pi}$ is a permutation matrix, and $\mathbf{\Delta}_1$, $\mathbf{\Delta}_2$, $\mathbf{\Delta}_3$ note for the diagonal scaling matrices satisfying $\mathbf{\Delta}_1 \mathbf{\Delta}_2 \mathbf{\Delta}_3 = \mathbf{I}_K$. \mathbf{E}_1 , \mathbf{E}_2 , and \mathbf{E}_3 are estimation error matrices. After the trilinear decomposition, the estimates of \mathbf{A}'_x , \mathbf{A}'_y , and \mathbf{S}' can be obtained. Scale ambiguity and permutation ambiguity are inherent to the trilinear decomposition problem. However, the scale ambiguity can be resolved easily by means of normalization, while the existence of permutation ambiguity is not considered for angle estimation.

3.3. Angle Estimation via Sparse Recovery. Use $\widehat{\mathbf{a}}'_{xk}$ and $\widehat{\mathbf{a}}'_{yk}$ to denote the k th column of estimates $\widehat{\mathbf{A}}'_x$ and $\widehat{\mathbf{A}}'_y$, respectively. According to the compression matrices, we have

$$\widehat{\mathbf{a}}'_{xk} = \mathbf{U}^T \partial_{xk} \mathbf{a}_{xk} + \mathbf{n}_{xk}, \quad k = 1, \dots, K, \quad (27a)$$

$$\widehat{\mathbf{a}}'_{yk} = \mathbf{V}^T \partial_{yk} \mathbf{a}_{yk} + \mathbf{n}_{yk}, \quad k = 1, \dots, K, \quad (27b)$$

where \mathbf{a}_{xk} and \mathbf{a}_{yk} are the k th column of \mathbf{A}_x , \mathbf{A}_y , respectively. \mathbf{n}_{xk} and \mathbf{n}_{yk} are the corresponding noise, respectively. ∂_{xk} and ∂_{yk} are the scaling coefficients. Construct two Vandermonde matrices $\mathbf{A}_{sx} \in \mathbf{C}^{M \times P}$ and $\mathbf{A}_{sy} \in \mathbf{C}^{N \times P}$ ($P \gg M$, $P \gg N$)

composed of steering vectors corresponding to each potential source location as its columns:

$$\begin{aligned} \mathbf{A}_{sx} &= [\mathbf{a}_{sx1}, \mathbf{a}_{sx2}, \dots, \mathbf{a}_{sxP}] \\ &= \begin{bmatrix} 1 & 1 & \dots & 1 \\ e^{j2\pi d\mathbf{g}(1)/\lambda} & e^{j2\pi d\mathbf{g}(2)/\lambda} & \vdots & e^{j2\pi d\mathbf{g}(P)/\lambda} \\ \vdots & \vdots & \vdots & \vdots \\ e^{j2\pi(M-1)d\mathbf{g}(1)/\lambda} & e^{j2\pi(M-1)d\mathbf{g}(2)/\lambda} & \dots & e^{j2\pi(M-1)d\mathbf{g}(P)/\lambda} \end{bmatrix}, \end{aligned} \quad (28a)$$

$$\begin{aligned} \mathbf{A}_{sy} &= [\mathbf{a}_{sy1}, \mathbf{a}_{sy2}, \dots, \mathbf{a}_{syP}] \\ &= \begin{bmatrix} 1 & 1 & \dots & 1 \\ e^{j2\pi d\mathbf{g}(1)/\lambda} & e^{j2\pi d\mathbf{g}(2)/\lambda} & \vdots & e^{j2\pi d\mathbf{g}(P)/\lambda} \\ \vdots & \vdots & \vdots & \vdots \\ e^{j2\pi(N-1)d\mathbf{g}(1)/\lambda} & e^{j2\pi(N-1)d\mathbf{g}(2)/\lambda} & \dots & e^{j2\pi(N-1)d\mathbf{g}(P)/\lambda} \end{bmatrix}, \end{aligned} \quad (28b)$$

where \mathbf{g} is a sampling vector and its p th elements is $\mathbf{g}(p) = -1 + 2p/P$, $p = 1, 2, \dots, P$. The matrices \mathbf{A}_{sx} and \mathbf{A}_{sy} can be regarded as the completed dictionaries. Then (27a)-(27b) can be expressed as

$$\widehat{\mathbf{a}}'_{xk} = \mathbf{U}^T \mathbf{A}_{sx} \mathbf{x}_s + \mathbf{n}_{xk}, \quad k = 1, \dots, K, \quad (29a)$$

$$\widehat{\mathbf{a}}'_{yk} = \mathbf{V}^T \mathbf{A}_{sy} \mathbf{y}_s + \mathbf{n}_{yk}, \quad k = 1, \dots, K, \quad (29b)$$

where \mathbf{x}_s and \mathbf{y}_s are sparse. The estimates of \mathbf{x}_s and \mathbf{y}_s can be obtained via l_0 -norm constraint:

$$\begin{aligned} \min \quad & \|\widehat{\mathbf{a}}'_{xk} - \mathbf{U}^T \mathbf{A}_{sx} \mathbf{x}_s\|_2^2, \\ \text{st.} \quad & \|\mathbf{x}_s\|_0 = 1, \end{aligned} \quad (30a)$$

$$\begin{aligned} \min \quad & \|\widehat{\mathbf{a}}'_{yk} - \mathbf{V}^T \mathbf{A}_{sy} \mathbf{y}_s\|_2^2, \\ \text{st.} \quad & \|\mathbf{y}_s\|_0 = 1, \end{aligned} \quad (30b)$$

where $\|\cdot\|_0$ denotes the l_0 -norm. $\|\mathbf{x}_s\|_0 = 1$; that is to say, there is only one nonzero element in the vector \mathbf{x}_s , similar to $\|\mathbf{y}_s\|_0 = 1$. We can use the OMP recovery method [26] to find the nonzero element in \mathbf{x}_s or \mathbf{y}_s . The OMP algorithm tries to recover the signal by finding the strongest component in the measurement signal, removing it from the signal, and searching the dictionary again for the strongest atom that is presented in the residual signal [32]. We extract the index of the maximum modulus of elements in \mathbf{x}_s and \mathbf{y}_s , respectively, noted as p_x and p_y . According to the corresponding columns in \mathbf{A}_{sx} and \mathbf{A}_{sy} , we obtain $\mathbf{g}(p_x)$ and $\mathbf{g}(p_y)$, which are estimates of $\sin \theta_k \cos \phi_k$ and $\sin \theta_k \sin \phi_k$. We define

$r_k = \mathbf{g}(p_x) + j\mathbf{g}(p_y)$, and then the elevation angles and azimuth angles can be obtained via

$$\hat{\theta}_k = \sin^{-1}(\text{abs}(r_k)), \quad k = 1, \dots, K, \quad (31a)$$

$$\hat{\phi}_k = \text{angle}(r_k), \quad k = 1, \dots, K, \quad (31b)$$

where $\text{abs}(\cdot)$ is the modulus value symbol and $\text{angle}(\cdot)$ is to get the angle of an imaginary number. As the columns of the estimated matrices $\hat{\mathbf{A}}'_x$ and $\hat{\mathbf{A}}'_y$ are automatically paired, then the estimated elevation angles and azimuth angles can be paired automatically.

3.4. The Procedures of the Proposed Algorithm. Till now, we have achieved the proposal for the compressive sensing trilinear model-based 2D-DOA estimation for rectangular array. We show major steps of the proposed algorithm as follows.

Step 1. Form the three-way matrix $\bar{\mathbf{X}} \in \mathbf{C}^{M \times N \times L}$, then compress the three-way matrix into a much smaller three-way matrix $\bar{\mathbf{X}}' \in \mathbf{C}^{M' \times N' \times L'}$ via the compression matrices $\mathbf{U} \in \mathbf{C}^{M \times M'}$, $\mathbf{V} \in \mathbf{C}^{N \times N'}$, and $\mathbf{W} \in \mathbf{C}^{L \times L'}$.

Step 2. Perform trilinear decomposition through TALS algorithm for the compressed three-way matrix to obtain the estimation of \mathbf{A}'_x , \mathbf{A}'_y , and \mathbf{S}' .

Step 3. Estimate the sparse vectors.

Step 4. Estimate 2D-DOA via (31a)-(31b).

Remark A. Because the trilinear decomposition brings the same permutation ambiguity for the estimates \mathbf{A}'_x , \mathbf{A}'_y , and \mathbf{S}' , the estimated elevation angles and azimuth angles are paired automatically.

Remark B. The conventional compressive sensing method formulates an angle sampling grid for sparse recovery to estimate angles. When it is applied to 2D-DOA estimation, both elevation and azimuth angles must be sampled, and it results in a two-dimensional sampling problem which brings much heavier cost for sparse signal recovery. In this paper, $\sin \theta_k \cos \phi_k$ (or $\sin \theta_k \sin \phi_k$) is bundled into a single variable in the range of -1 to 1 . The bundled variable is sampled for sparse recovery to obtain the estimates of $\sin \theta_k \cos \phi_k$ and $\sin \theta_k \sin \phi_k$, respectively. Afterwards, the elevation and azimuth angles are estimated through the estimates of $\sin \theta_k \cos \phi_k$ and $\sin \theta_k \sin \phi_k$.

Remark C. If the number of sources K is unknown, it can be estimated by performing singular value decomposition for received data matrix \mathbf{X} in (7) and finding the number of largest singular values [33]. We also use some lower-complexity algorithm in [34] for estimating the number of the sources.

Remark D. When the coherent sources impinge on the array, we can use the parallel profiles with linear dependencies

(PARALIND) model [35, 36], which is a generalization of PARAFAC suitable for solving problems with linear dependent factors, to resolve coherent DOA estimation problem.

3.5. Complexity Analysis and CRB. The proposed algorithm has much lower computational cost than conventional trilinear decomposition-based method. The proposed algorithm requires $O(K^3 + M'N'L'K)$ operations for a iteration, while the trilinear decomposition algorithm needs $O(K^3 + MNLK)$ operations [28] for a iteration, where $M' < M$, $N' < N$, and $L' < L$.

We define $\mathbf{A} = [\mathbf{a}_y(\theta_1) \otimes \mathbf{a}_x(\theta_1), \dots, \mathbf{a}_y(\theta_K) \otimes \mathbf{a}_x(\theta_K)]$. According to [37], we can derive the CRB

$$\text{CRB} = \frac{\sigma^2}{2L} \left\{ \text{Re} \left[\mathbf{D}^H \mathbf{\Pi}_A \mathbf{D} \oplus \hat{\mathbf{P}}_s^T \right] \right\}^{-1}, \quad (32)$$

where L denotes the number of samples, \mathbf{a}_k is the k th column of \mathbf{A} , and $\hat{\mathbf{P}}_s = (1/L) \sum_{t=1}^L \mathbf{s}(t) \mathbf{s}^H(t)$. σ^2 is the noise power. $\mathbf{\Pi}_A = \mathbf{I}_{MN} - \mathbf{A}(\mathbf{A}^H \mathbf{A})^{-1} \mathbf{A}^H$ and

$$\mathbf{D} = \left[\frac{\partial \mathbf{a}_1}{\partial \theta_1}, \frac{\partial \mathbf{a}_2}{\partial \theta_2}, \dots, \frac{\partial \mathbf{a}_K}{\partial \theta_K}, \frac{\partial \mathbf{a}_1}{\partial \phi_1}, \frac{\partial \mathbf{a}_2}{\partial \phi_2}, \dots, \frac{\partial \mathbf{a}_K}{\partial \phi_K} \right]. \quad (33)$$

The advantages of the proposed algorithm can be presented as follows.

- (1) The proposed algorithm can be regarded as a combination of trilinear model and compressive sensing theory, and it brings much lower computational complexity and much smaller demand for storage capacity.
- (2) The proposed algorithm has better 2D-DOA estimation performance than ESPRIT algorithm and close angle estimation performance to TALS algorithm, which will be proved by Figures 6-7.
- (3) The proposed algorithm can achieve paired elevation angles and azimuth angles automatically.

4. Numerical Simulations

In the following simulations, we assume that the numerical simulation results converge when the SSR $\leq 10^{-8}$. M , N , L , and K denote the number of antennas in x -axis, number of antennas in y -axis, samples, and sources, respectively. And we compress the parameters M , N , L to M' , N' , and L' (usually set $M = 16$, $N = 20$, $L = 100$, and $M' = N' = L' = 5$ in numerical simulations). $d = \lambda/2$ is considered in the simulation. We present 1000 Monte Carlo simulations to assess the angle estimation performance of the proposed algorithm. Define root mean squared error (RMSE) as

$$\text{RMSE} = \frac{1}{K} \sum_{k=1}^K \sqrt{\frac{1}{1000} \sum_{l=1}^{1000} (\hat{\phi}_{k,l} - \phi_k)^2 + (\hat{\theta}_{k,l} - \theta_k)^2}, \quad (34)$$

where ϕ_k and θ_k denote the perfect elevation angle and azimuth angle of k th source, respectively. $\hat{\phi}_{k,l}$ and $\hat{\theta}_{k,l}$ are

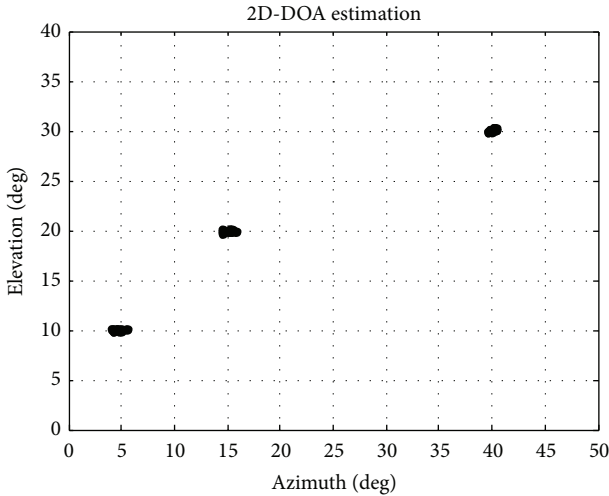


FIGURE 4: 2D-DOA estimation of our algorithm in SNR = -10 dB ($N = 20, M = 16, L = 100,$ and $K = 3$).

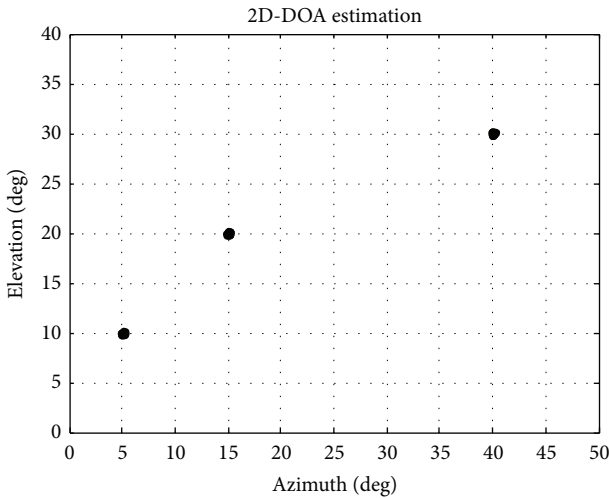


FIGURE 5: 2D-DOA estimation of our algorithm in SNR = 5 dB ($N = 20, M = 16, L = 100,$ and $K = 3$).

the estimates of ϕ_k and θ_k in the l th Monte Carlo trail. Assume that there are 3 noncoherent sources located at angles $(\phi_1, \theta_1) = (5^\circ, 10^\circ), (\phi_2, \theta_2) = (15^\circ, 20^\circ),$ and $(\phi_3, \theta_3) = (40^\circ, 30^\circ)$.

Figure 4 presents the 2D-DOA estimation of the proposed algorithm for uniform rectangular array with $N = 20, M = 16, L = 100, K = 3,$ and SNR = -10 dB. Figure 5 depicts the 2D-DOA estimation performance with SNR = 5 dB. Figures 4-5 illustrate that our algorithm is effective for 2D-DOA estimation.

Figure 6 shows the 2D-DOA estimation performance comparison of the proposed algorithm, the ESPRIT algorithm, the TALS algorithm, and the CRB for the uniform rectangular array with $N = 20, M = 16, L = 100,$ and $K = 3,$ while Figure 7 depicts the 2D-DOA estimation performance comparison with $N = 16, M = 16, L = 200,$ and $K = 3.$ It is indicated that our algorithm has better angle estimation

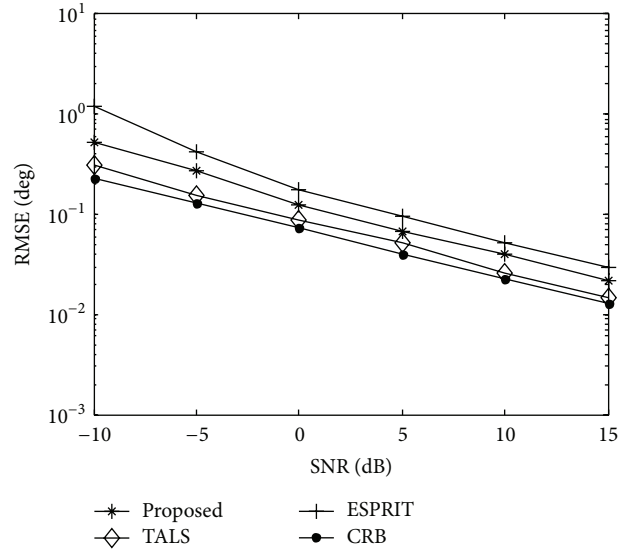


FIGURE 6: 2D-DOA estimation performance comparison ($N = 20, M = 16, L = 100,$ and $K = 3$).

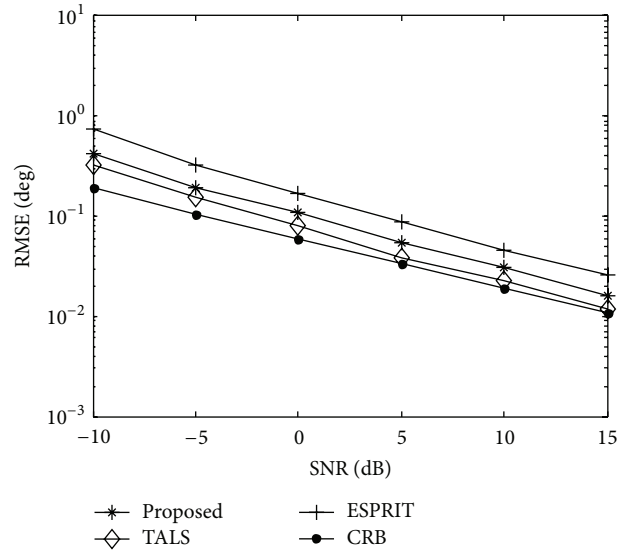


FIGURE 7: 2D-DOA estimation performance comparison ($N = 16, M = 16, L = 200,$ and $K = 3$).

performance than the ESPRIT algorithm and close angle estimation to TALS algorithm. The angle estimation performance of the proposed algorithm will be further improved through increasing the compressed parameters $M', N',$ and $L'.$

Figure 8 depicts the 2D-DOA estimation performance of the proposed algorithm with different value of N ($M = 16, L = 100,$ and $K = 3$), while Figure 9 presents the 2D-DOA estimation performance of the proposed algorithm with different value of $M.$ It is clearly shown that the angle estimation performance of our algorithm is gradually improved with the number of antennas increasing. Multiple

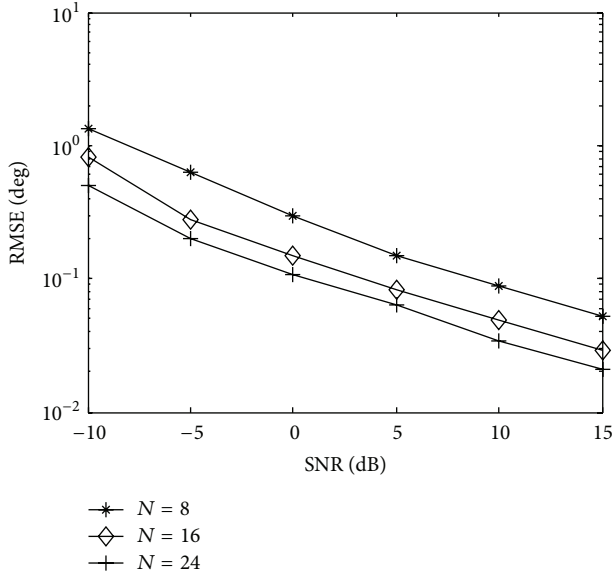


FIGURE 8: Angle estimation performance of our algorithm with different N ($M = 16$, $L = 100$, and $K = 3$).

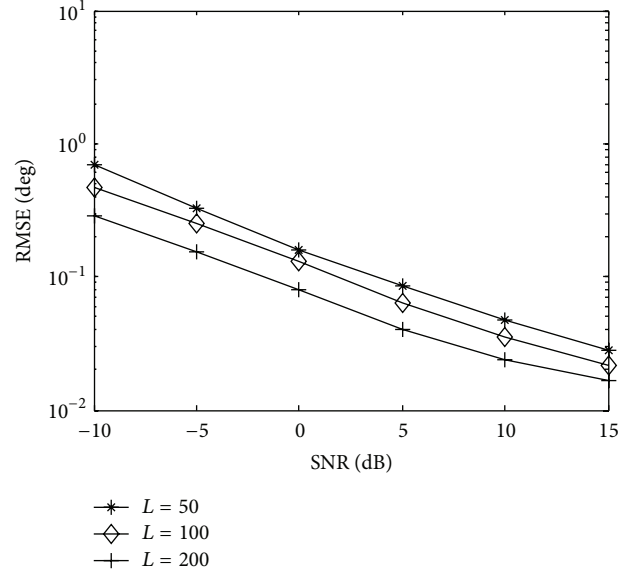


FIGURE 10: Angle estimation performance of our algorithm with different L ($N = 16$, $M = 20$, and $K = 3$).

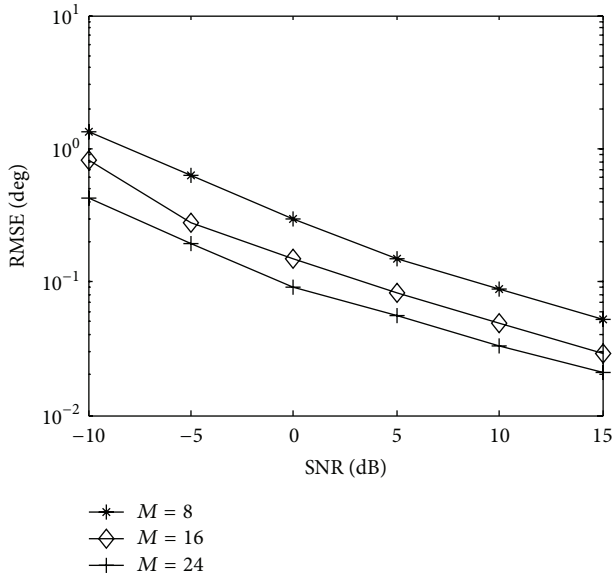


FIGURE 9: Angle estimation performance of our algorithm with different M ($N = 16$, $L = 100$, and $K = 3$).

antennas improve the angle estimation performance because of diversity gain.

Figure 10 presents 2D-DOA estimation performance of the proposed algorithm with different value of L ($N = 20$, $M = 16$, and $K = 3$). It illustrates that the angle estimation performance becomes better in collaboration with L increasing.

5. Conclusions

In this paper, we have addressed the 2D-DOA estimation problem for rectangular array and have derived a compressive

sensing trilinear model-based 2D-DOA estimation algorithm, which can obtain the automatically paired 2D-DOA estimate. The proposed algorithm has better angle estimation performance than ESPRIT algorithm and close angle estimation performance to conventional trilinear decomposition method. Furthermore, the proposed algorithm has lower computational complexity and smaller demand for storage capacity than conventional trilinear decomposition method. The proposed algorithm can be regarded as a combination of trilinear model and compressive sensing theory, and it brings much lower computational complexity and much smaller demand for storage capacity.

Conflict of Interests

The authors declare that there is no conflict of interests regarding the publication of this paper.

Acknowledgments

This work is supported by China NSF Grants (61371169, 61301108, 61471191, 61471192, and 61271327), Jiangsu Planned Projects for Postdoctoral Research Funds (1201039C), China Postdoctoral Science Foundation (2012M521099, 2013M541661), Open Project of Key Laboratory of Modern Acoustics of Ministry of Education (Nanjing University), the Aeronautical Science Foundation of China (20120152001), Qing Lan Project, Priority Academic Program Development of Jiangsu High Education Institutions, and the Fundamental Research Funds for the Central Universities (NS2013024, kfj130114, and kfj130115).

References

- [1] H. Krim and M. Viberg, "Two decades of array signal processing research: the parametric approach," *IEEE Signal Processing Magazine*, vol. 13, no. 4, pp. 67–94, 1996.
- [2] R. Roy and T. Kailath, "ESPRIT-estimation of signal parameters via rotational invariance techniques," *IEEE Transactions on Acoustics, Speech and Signal Processing*, vol. 37, no. 7, pp. 984–995, 1989.
- [3] F. Gao and A. B. Gershman, "A generalized ESPRIT approach to direction-of-arrival estimation," *IEEE Signal Processing Letters*, vol. 12, no. 3, pp. 254–257, 2005.
- [4] D. Kundu, "Modified MUSIC algorithm for estimating DOA of signals," *Signal Processing*, vol. 48, no. 1, pp. 85–90, 1996.
- [5] B. D. Rao and K. V. S. Hari, "Performance analysis of Root-Music," *IEEE Transactions on Acoustics, Speech, and Signal Processing*, vol. 37, no. 12, pp. 1939–1949, 1989.
- [6] N. Yilmazer, J. Koh, and T. K. Sarkar, "Utilization of a unitary transform for efficient computation in the matrix pencil method to find the direction of arrival," *IEEE Transactions on Antennas and Propagation*, vol. 54, no. 1, pp. 175–181, 2006.
- [7] Y. Chiba, K. Ichige, and H. Arai, "Reducing DOA estimation error in extended ES-root-MUSIC for uniform rectangular array," in *Proceedings of the 4th International Congress on Image and Signal Processing (CISP '11)*, vol. 5, pp. 2621–2625, October 2011.
- [8] T. Filik and T. E. Tuncer, "2-D paired direction-of-arrival angle estimation with two parallel uniform linear arrays," *International Journal of Innovative Computing, Information and Control*, vol. 7, no. 6, pp. 3269–3279, 2011.
- [9] Y.-Y. Wang and S.-C. Huang, "An ESPRIT-based algorithm for 2D-DOA estimation," *IEICE Transactions on Fundamentals of Electronics, Communications and Computer Sciences*, vol. E94.A, no. 9, pp. 1847–1850, 2011.
- [10] C. P. Mathews, M. Haardt, and M. D. Zoltowski, "Performance analysis of closed-form, ESPRIT based 2-D angle estimator for rectangular arrays," *IEEE Signal Processing Letters*, vol. 3, no. 4, pp. 124–126, 1996.
- [11] M. D. Zoltowski, M. Haardt, and C. P. Mathews, "Closed-form 2-D angle estimation with rectangular arrays in element space or beamspace via unitary ESPRIT," *IEEE Transactions on Signal Processing*, vol. 44, no. 2, pp. 316–328, 1996.
- [12] N. D. Sidiropoulos, R. Bro, and G. B. Giannakis, "Parallel factor analysis in sensor array processing," *IEEE Transactions on Signal Processing*, vol. 48, no. 8, pp. 2377–2388, 2000.
- [13] Y. Hua, "A pencil-MUSIC algorithm for finding two-dimensional angles and polarizations using crossed dipoles," *IEEE Transactions on Antennas and Propagation*, vol. 41, no. 3, pp. 370–376, 1993.
- [14] D. L. Donoho, "Compressed sensing," *IEEE Transactions on Information Theory*, vol. 52, no. 4, pp. 1289–1306, 2006.
- [15] E. J. Candes, J. Romberg, and T. Tao, "Robust uncertainty principles: exact signal reconstruction from highly incomplete frequency information," *IEEE Transactions on Information Theory*, vol. 52, no. 2, pp. 489–509, 2006.
- [16] D. Malioutov, M. Cetin, and A. S. Willsky, "A sparse signal reconstruction perspective for source localization with sensor arrays," *IEEE Transactions on Signal Processing*, vol. 53, no. 8, pp. 3010–3022, 2005.
- [17] N. Hu, Z. Ye, D. Xu, and S. Cao, "A sparse recovery algorithm for DOA estimation using weighted subspace fitting," *Signal Processing*, vol. 92, no. 10, pp. 2566–2570, 2012.
- [18] J. B. Kruskal, "Three-way arrays: rank and uniqueness of trilinear decompositions, with application to arithmetic complexity and statistics," *Linear Algebra and its Applications*, vol. 18, no. 2, pp. 95–138, 1977.
- [19] L. de Lathauwer, B. de Moor, and J. Vandewalle, "Computation of the canonical decomposition by means of a simultaneous generalized Schur decomposition," *SIAM Journal on Matrix Analysis and Applications*, vol. 26, no. 2, pp. 295–327, 2004.
- [20] L. de Lathauwer, "A link between the canonical decomposition in multi-linear algebra and simultaneous matrix diagonalization," *SIAM Journal on Matrix Analysis and Applications*, vol. 28, no. 3, pp. 642–666, 2006.
- [21] N. D. Sidiropoulos, G. B. Giannakis, and R. Bro, "Blind PARAFAC receivers for DS-CDMA systems," *IEEE Transactions on Signal Processing*, vol. 48, no. 3, pp. 810–823, 2000.
- [22] N. D. Sidiropoulos and X. Liu, "Identifiability results for blind beamforming in incoherent multipath with small delay spread," *IEEE Transactions on Signal Processing*, vol. 49, no. 1, pp. 228–236, 2001.
- [23] N. D. Sidiropoulos and A. Kyrillidis, "Multi-way compressed sensing for sparse low-rank tensors," *IEEE Signal Processing Letters*, vol. 19, no. 11, pp. 757–760, 2012.
- [24] X. F. Zhang, H. X. Yu, J. F. Li, and D. Ben, "Blind signal detection for uniform rectangular array via compressive sensing trilinear model," *Advanced Materials Research*, vol. 756–759, pp. 660–664, 2013.
- [25] R. Cao, X. Zhang, and W. Chen, "Compressed sensing parallel factor analysis-based joint angle and Doppler frequency estimation for monostatic multiple-input–multiple-output radar," *IET Radar, Sonar & Navigation*, vol. 8, no. 6, pp. 597–606, 2014.
- [26] J. A. Tropp and A. C. Gilbert, "Signal recovery from random measurements via orthogonal matching pursuit," *IEEE Transactions on Information Theory*, vol. 53, no. 12, pp. 4655–4666, 2007.
- [27] X. Zhang, F. Wang, and H. Chen, *Theory and Application of Array Signal Processing (version 2)*, National Defense Industry Press, Beijing, China, 2012.
- [28] X. Zhang, J. Li, H. Chen, and D. Xu, "Trilinear decomposition-based two-dimensional DOA estimation algorithm for arbitrarily spaced acoustic vector-sensor array subjected to unknown locations," *Wireless Personal Communications*, vol. 67, no. 4, pp. 859–877, 2012.
- [29] R. Bro, N. D. Sidiropoulos, and G. B. Giannakis, "A fast least squares algorithm for separating trilinear mixtures," in *Proceedings of the International Workshop on Independent Component Analysis and Blind Signal Separation*, pp. 289–294, January 1999.
- [30] R. A. DeVore, "Deterministic constructions of compressed sensing matrices," *Journal of Complexity*, vol. 23, no. 4–6, pp. 918–925, 2007.
- [31] S. Li and X. Zhang, "Study on the compressed matrices in compressed sensing trilinear model," *Applied Mechanics and Materials*, vol. 556–562, pp. 3380–3383, 2014.
- [32] F. Wang and X. Zhang, "Joint estimation of TOA and DOA in IR-UWB system using sparse representation framework," *ETRI Journal*, vol. 36, no. 3, pp. 460–468, 2014.
- [33] A. Di, "Multiple source location—a matrix decomposition approach," *IEEE Transactions on Acoustics, Speech, and Signal Processing*, vol. 33, no. 5, pp. 1086–1091, 1985.
- [34] J. Xin, N. Zheng, and A. Sano, "Simple and efficient nonparametric method for estimating the number of signals without eigendecomposition," *IEEE Transactions on Signal Processing*, vol. 55, no. 4, pp. 1405–1420, 2007.

- [35] R. Bro, R. A. Harshman, N. D. Sidiropoulos, and M. E. Lundy, "Modeling multi-way data with linearly dependent loadings," *Journal of Chemometrics*, vol. 23, no. 7-8, pp. 324–340, 2009.
- [36] X. Zhang, M. Zhou, and J. Li, "A PARALIND decomposition-based coherent two-dimensional direction of arrival estimation algorithm for acoustic vector-sensor arrays," *Sensors*, vol. 13, no. 4, pp. 5302–5316, 2013.
- [37] P. Stoica and A. Nehorai, "Performance study of conditional and unconditional direction-of-arrival estimation," *IEEE Transactions on Acoustics, Speech, and Signal Processing*, vol. 38, no. 10, pp. 1783–1795, 1990.

Research Article

Knowledge-Aided STAP Using Low Rank and Geometry Properties

Zhaocheng Yang,¹ Rodrigo C. de Lamare,² Xiang Li,¹ and Hongqiang Wang¹

¹ *Research Institute of Space Electronics, Electronics Science and Engineering School, National University of Defense Technology, Changsha 410073, China*

² *Communications Research Group, Department of Electronics, University of York, York YO10 5DD, UK*

Correspondence should be addressed to Zhaocheng Yang; yangzhaocheng@gmail.com

Received 27 April 2014; Accepted 17 July 2014; Published 12 August 2014

Academic Editor: Hang Hu

Copyright © 2014 Zhaocheng Yang et al. This is an open access article distributed under the Creative Commons Attribution License, which permits unrestricted use, distribution, and reproduction in any medium, provided the original work is properly cited.

This paper presents knowledge-aided space-time adaptive processing (KA-STAP) algorithms that exploit the low-rank dominant clutter and the array geometry properties (LRGP) for airborne radar applications. The core idea is to exploit the clutter subspace that is only determined by the space-time steering vectors, by employing the Gram-Schmidt orthogonalization approach to compute the clutter subspace. Simulation results illustrate the effectiveness of our proposed algorithms.

1. Introduction

Space-time adaptive processing (STAP) is considered an efficient tool for detection of slow targets by airborne radar systems in strong clutter environments [1–4]. However, due to the very high degrees of freedom (DoFs), the full-rank STAP has a slow convergence and requires about twice the DoFs of the independent and identically distributed (IID) training snapshots to yield an average performance loss of roughly 3 dB [1]. In real scenarios, it is hard to obtain so many IID training snapshots, especially in heterogeneous environments. Reduced-dimension/reduced-rank methods [1–10], parametric adaptive matched filter (PAMF) [11], and sparse beamformers [12, 13] have been considered to counteract the slow convergence of the full-rank STAP. However, it still fundamental for radar systems to improve the convergence performance of STAP algorithms or reduce their required sample support in heterogeneous environments because the number of required snapshots is large relative to those needed in IID scenarios. By exploiting the sparsity of the received signal, sparsity-based STAP algorithms are developed to reduce the sample support [14–16]. However, these algorithms usually require high computation complexity.

Recently developed knowledge-aided (KA) STAP algorithms have received a growing interest and become a key concept for the next generation of adaptive radar systems (see [17–30] and the reference therein). The core idea of KA-STAP is to incorporate prior knowledge, provided by digital elevation maps, land cover databases, road maps, global positioning system (GPS), previous scanning data, and other known features, to compute estimates of the clutter covariance matrix (CCM) with high accuracy [17, 18, 24]. Among the developed KA-STAP algorithms, they can be categorized into two cases: intelligent training and filter selection; and Bayesian filtering and data prewhitening [17]. In the former case, prior knowledge of the interference environments is used for the filter selection or the selection of the so-called filter training data. By using database information, [25] identifies and screens roadways from the training set and provides approximately 15 dB gains compared with no prior knowledge. Digital land classification data and digital elevation data are used to characterize clutter patches for secondary data selection and ensure independent secondary data samples [26]. Additionally, a geographic-map-aided radar detector is exploited to remove dynamic outliers from the training data [27]. In the latter case, prior knowledge

is incorporated directly by the filter to aid in suppressing the clutter. Colored loading (CL) implements the STAP filter in two steps: a prewhitening step using the prior matrix, followed by adaptive filtering [28]. Fully automatic methods for combining the matrix with prior knowledge and secondary data are considered in [23, 29]. Furthermore, in [30], an automatic combination of the inverse of the matrix with prior knowledge and the inverse of the estimated covariance matrix from secondary data is developed. Moreover, there is a class of approaches that exploit prior knowledge of the clutter ridge to form the STAP filter weights in [19–22]. The authors in [19] introduced a knowledge-aided parametric covariance estimation (KAPE) scheme by combining both prior knowledge and data observations within a parameterized model to capture instantaneous characteristics of the cell under test (CUT). A modified sample matrix inversion (SMI) procedure to estimate the CCM using a least-squares (LS) approach has been described in [20] to overcome the range-dependent clutter nonstationarity in conformal array configurations. However, both approaches require the pseudoinverse calculation to estimate the CCM and this often requires a computationally costly singular value decomposition (SVD) [19]. Although two weighting approaches with lower computations are discussed in [19], they are suboptimal approaches to the LS estimator (LSE) computed by the SVD and the performance of these approaches depends on the radar system parameters, especially the array characteristics [19]. Moreover, the latter approach has not considered the situation when prior knowledge has uncertainties. Under the assumption of the known clutter ridge in the angle-Doppler plane, the authors in [21] imposed a sparse regularization to estimate the clutter covariance excluding the clutter ridge. Although this kind of method can obtain a high resolution even with only one snapshot, it requires the designer to know the exact positions of the clutter ridge resulting in being sensitive to prior knowledge. Furthermore, the computational complexity caused by sparse recovery is expensive. A data independent STAP method based on prolate spheroidal wave functions (PSWF) has been considered in MIMO radar by incorporating the clutter ridge [22], where the computational complexity is significantly reduced compared with the approaches in [19, 20]. However, it is highly dependent on the ideal clutter subspace and is not robust against clutter subspace mismatches.

In this paper, we propose KA-STAP algorithms using prior knowledge of the clutter ridge that avoid the pseudoinverse calculation, require a low computational complexity, and mitigate the impact of uncertainties of prior knowledge. Specifically, for a side-looking uniformly spaced linear array (ULA), the proposed method selects a group of linearly independent space-time steering vectors that can represent the ideal clutter subspace using prior knowledge of the dominant low-rank clutter and the array geometry properties (LRGP). The orthogonal bases of the clutter ideal subspace are computed by a Gram-Schmidt orthogonalization procedure on the selected space-time steering vectors. Two robust approaches to compute the STAP filter weights are then presented based on the estimated clutter subspace. To overcome the performance degradation caused by the

internal clutter motion (ICM), we employ a covariance matrix taper (CMT) to the estimated CCM. The array calibration methods discussed in [19] can be applied to our proposed algorithm to mitigate the impact of nonideal factors, such as channel mismatch. Moreover, a reduced-dimension version of the proposed KA-STAP algorithm is devised for practical applications. Finally, simulation results demonstrate the effectiveness of our proposed algorithms.

The work is organized as follows. Section 2 introduces the signal model in airborne radar applications. Section 3 details the approach of the proposed KA-STAP algorithms and also discusses the computational complexity. The simulated airborne radar data are used to evaluate the performance of the proposed algorithms in Section 4. Section 5 provides the summary and conclusions.

2. Signal Model

The system under consideration is a side-looking pulsed Doppler radar with a ULA consisting of M elements on the airborne radar platform, as shown in Figure 1. The platform is at altitude h_p and moving with constant velocity v_p . The radar transmits a coherent burst of pulses at a constant pulse repetition frequency (PRF) $f_r = 1/T_r$, where T_r is the pulse repetition interval (PRI). The transmitter carrier frequency is $f_c = c/\lambda_c$, where c is the propagation velocity and λ_c is the wavelength. The number of pulses in a coherent processing interval (CPI) is N . The received signal from the iso-range of interest is represented by a space-time $NM \times 1$ data vector \mathbf{x} .

The received space-time clutter plus noise return from a single range bin can be represented by [4]

$$\mathbf{x} = \sum_{m=1}^{N_s} \sum_{n=1}^{N_c} \sigma_{m,n} \mathbf{v}(f_{s,m,n}, f_{d,m,n}) \odot \boldsymbol{\alpha}(m, n) + \mathbf{n}, \quad (1)$$

where \mathbf{n} is the Gaussian white thermal noise vector with the noise power σ_n^2 on each channel and pulse, N_s is the number of range ambiguities, N_c is the number of independent clutter patches over the iso-range of interest, $f_{s,m,n}$ and $f_{d,m,n}$ are the spatial and Doppler frequencies of the m th clutter patch, respectively, $\sigma_{m,n}$ is the complex amplitude for the m th clutter patch, $\boldsymbol{\alpha}(m, n) = \boldsymbol{\alpha}_d(m, n) \otimes \boldsymbol{\alpha}_s(m, n)$ is the space-time random taper vector characterizing the voltage fluctuation caused by nonideal factors, such as ICM and channel mismatch (where $\boldsymbol{\alpha}_d(m, n)$ and $\boldsymbol{\alpha}_s(m, n)$ are the temporal and spatial random tapers), and $\mathbf{v}(f_{s,m,n}, f_{d,m,n})$ is the $NM \times 1$ space-time steering vector for a clutter patch with $f_{s,m,n}$ and $f_{d,m,n}$.

The space-time steering vector is given as the Kronecker product of the temporal and spatial steering vectors, $\mathbf{v}(f_{s,m,n}, f_{d,m,n}) = \mathbf{v}_t(f_{d,m,n}) \otimes \mathbf{v}_s(f_{s,m,n})$, which are given by [1]

$$\begin{aligned} \mathbf{v}_t(f_{d,m,n}) &= [1, \dots, \exp(j2\pi(N-1)f_{d,m,n})]^T, \\ \mathbf{v}_s(f_{s,m,n}) &= [1, \dots, \exp(j2\pi(M-1)f_{s,m,n})]^T, \end{aligned} \quad (2)$$

where $()^T$ denotes the transpose operation, $f_{s,m,n} = d_a/\lambda_c \cos \theta_{m,n} \sin \phi_{m,n}$, $f_{d,m,n} = 2v_p T_r/\lambda_c \cos \theta_{m,n} \sin \phi_{m,n}$,

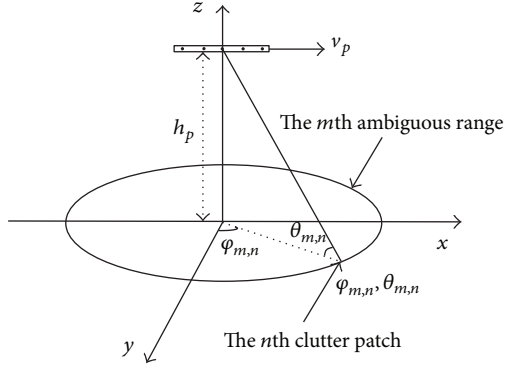


FIGURE 1: Airborne radar geometry with a ULA antenna.

and d_a is the intersensor spacing of the ULA. If we stack all clutter patches' amplitudes into a vector

$$\boldsymbol{\sigma} = [\sigma_{1,1}, \dots, \sigma_{1,N_c}, \dots, \sigma_{N_a,1}, \dots, \sigma_{N_a,N_c}]^T \quad (3)$$

and assume there are no nonideal factors, then the clutter plus noise received data denoted by (1) can be described as

$$\mathbf{x} = \mathbf{x}_c + \mathbf{n} = \mathbf{V}\boldsymbol{\sigma} + \mathbf{n}, \quad (4)$$

where \mathbf{V} denotes the clutter space-time steering matrix, given by

$$\mathbf{V} = \begin{bmatrix} \mathbf{v}(\phi_{1,1}, \theta_{1,1}, f_{1,1}), \dots, \\ \mathbf{v}(\phi_{1,N_c}, \theta_{1,N_c}, f_{1,N_c}), \dots, \\ \mathbf{v}(\phi_{N_a,1}, \theta_{N_a,1}, f_{N_a,1}), \dots, \\ \mathbf{v}(\phi_{N_a,N_c}, \theta_{N_a,N_c}, f_{N_a,N_c}) \end{bmatrix}. \quad (5)$$

Thus, the CCM based on (4) can be expressed as

$$\mathbf{R}_c = \mathbf{V}\boldsymbol{\Sigma}\mathbf{V}^H, \quad (6)$$

where $\boldsymbol{\Sigma} = E[\boldsymbol{\sigma}\boldsymbol{\sigma}^H]$. Under the condition that the clutter patches are independent from each other, $\boldsymbol{\Sigma} = \text{diag}(\mathbf{a})$, $\mathbf{a} = [a_{1,1}, a_{1,2}, \dots, a_{N_a,N_c}]^T$, and $a_{m,n} = E[|\sigma_{m,n}|^2]$ ($m = 1, \dots, N_a$, $n = 1, \dots, N_c$) for the statistics of the clutter patches. Here, $E[\cdot]$ denotes the expectation operator, $\text{diag}(\mathbf{a})$ stands for a diagonal matrix with the main diagonal taken from the elements of the vector \mathbf{a} , and $(\cdot)^H$ represents the conjugate transpose of a matrix.

The optimal filter that maximizes the output SINR for the Gaussian distribution clutter which is given by the full-rank STAP processor can be written as [4]

$$\mathbf{w}_{\text{opt}} = \mu \mathbf{R}^{-1} \mathbf{s}, \quad (7)$$

where μ is a constant which does not affect the SINR performance, \mathbf{s} is the $NM \times 1$ space-time steering vector in the target direction, and $\mathbf{R} = E[\mathbf{x}\mathbf{x}^H] = \mathbf{R}_c + \sigma_n^2 \mathbf{I}$ is the clutter plus noise covariance matrix (\mathbf{I} is the identity matrix).

3. KA-STAP Algorithms Using LRGP

In this section, we firstly review the method that estimates the CCM using an LS technique in [19, 20] and then detail the design and the computational complexity of the proposed KA-STAP algorithms using LRGP. The key difference between the proposed and existing algorithms lies in the way to compute the CCM.

3.1. CCM Estimated by LS. In practice, prior knowledge of certain characteristics of the radar system and the aerospace platform, such as platform heading, speed and altitude, array normal direction, and antenna phase steering, can be obtained from the Inertial Navigation Unit (INU) and the GPS data [19]. In other words, we can obtain the values of the number of range ambiguities N_a , the platform velocity v_p , and the elevation angle θ . Thus, we can develop KA-STAP algorithms based on this prior knowledge, for example, the methods described in [19–22]. In reality, the clutter consists of returns over a continuous geographical region, which we divide into a discrete set of clutter patches for analytical and computational convenience. The rest of the discussion is on the issues associated with choosing the number of clutter patches N_c . A possible approach is to assume a value of N_c and discretize the whole azimuth angle evenly into N_c patches for each range bin [19, 20]. In addition, it usually ignores range ambiguities, that is, $N_a = 1$, where the justification can be seen in [19]. Then, the parameter $\boldsymbol{\sigma}$ in (4) can be estimated using the observation data by solving the LS problem as follows [19, 20]:

$$\hat{\boldsymbol{\sigma}} = \arg \min_{\boldsymbol{\sigma}} \|\mathbf{x} - \mathbf{V}\boldsymbol{\sigma}\|^2, \quad (8)$$

where $\hat{\boldsymbol{\sigma}} = [\hat{\sigma}_1, \hat{\sigma}_2, \dots, \hat{\sigma}_{N_c}]^T$. Herein, the solution for the above problem based on an LS technique is given by

$$\hat{\boldsymbol{\sigma}} = [\mathbf{V}^H \mathbf{V}]^{-1} \mathbf{V}^H \mathbf{x}. \quad (9)$$

To avoid the effect of the target signal at CUT, the near range bins of the CUT are used to estimate $\boldsymbol{\sigma}$ [20], which is given by

$$\hat{\sigma}_{m,n}^2 = \frac{1}{L} \sum_{l=1}^L |\hat{\sigma}_{m,n,l}|^2, \quad (10)$$

where L is the total number of the secondary data. Then, the estimated CCM by the LS method (we call it LSE in the following) is

$$\hat{\mathbf{R}}_c = \mathbf{V} \hat{\boldsymbol{\Sigma}} \mathbf{V}^H. \quad (11)$$

Then the clutter plus noise covariance matrix is estimated as

$$\hat{\mathbf{R}} = \hat{\mathbf{R}}_c + \hat{\sigma}_n^2 \mathbf{I}, \quad (12)$$

where $\hat{\sigma}_n^2$ is the estimated noise power level which can be collected by the radar receiver when the radar transmitter operates in a passive mode [2]. Finally, the STAP filter weights can be computed according to (7) using $\hat{\mathbf{R}}$ instead of \mathbf{R} .

It should be noted that it often assumes a large number of clutter patches N_c to obtain a good estimation accuracy of the estimated CCM. Specifically, if the assumed number of clutter patches $N_c > NM$, then $[\mathbf{V}^H \mathbf{V}]^{-1}$ does not exist and has to be calculated by the pseudoinversion. However, the computational complexity of the terms $[\mathbf{V}^H \mathbf{V}]^{-1}$ is very high; that is, $O((N_c)^3) + O(N_c(NM)^2)$, which should be avoided in practice. Two suboptimal approximation weighting approaches with lower cost are discussed in [19]. But the performance of these approaches depends on the radar system parameters [19]. In addition, in the presence of nonideal factors in the clutter component and despite the inclusion of the estimated angle-independent channel mismatch in the space-time steering vectors \mathbf{V} and the use of the modified \mathbf{V} to solve the problem (8), the techniques do not consider the impact of the temporal random taper α_d . Nevertheless, the received data vector \mathbf{x} is formed by all nonideal factors. Thus, whether it is suitable to compute the parameter σ only considering the spatial random taper is worth being investigated, as will be discussed in Section 3.3.

3.2. Proposed KA-STAP Algorithm. To overcome the rank deficiency and the inverse of the matrix $\mathbf{V}^H \mathbf{V}$, in the following, we will detail the proposed KA-STAP algorithm to estimate the CCM using prior knowledge of LRGP. In this subsection, we only consider the ideal case of the received data, that is, the signal model in (4).

From (4), we know that the clutter return is a linear combination of returns from all clutter patches. Thus, we have

$$\text{span}(\mathbf{R}_c) = \text{span}(\mathbf{V}) = \text{span}(\mathbf{V}\mathbf{V}^H). \quad (13)$$

From (13), it can be seen that the clutter subspace is independent of the power of the clutter patches and is only determined by the clutter space-time steering vectors. Thus, the orthogonal basis of the clutter subspace \mathbf{U} can be calculated by \mathbf{V} or $\mathbf{V}\mathbf{V}^H$. The other problem to calculate the clutter subspace arising is that one should know the clutter rank first. Fortunately, some rules for estimating the clutter rank were discussed in previous literature, such as [1, 2, 31, 32]. Specifically, for a side-looking ULA, the estimated clutter rank is approximated by Brennan's rule as

$$\text{rank}(\mathbf{R}_c) \approx N_r = \lceil M + \beta(N - 1) \rceil, \quad (14)$$

where $\beta = 2v_p T_r / d_a$ and the brackets $\lceil \cdot \rceil$ indicate rounding to the nearest largest integer. In [32], this rule has been extended to the case with arbitrary arrays. Usually, $N_r \ll NM$ and the STAP algorithms can be performed in a low dimensional space so that the computational complexity and the convergence can be significantly improved [22].

After the clutter rank is determined, a low-complexity approach to computing the orthogonal bases of the clutter subspace is to perform the Gram-Schmidt orthogonalization procedure on the space-time steering vectors \mathbf{V} , where the implementation steps of the Gram-Schmidt orthogonalization are listed in Algorithm 1 and interested readers are referred to [33] for further details. Note that this procedure is at the computational cost of $O((N_c + 1)N_c NM / 2) \ll O(N_c^3 +$

Initialization:

$$\beta = 2v_p T_r / d_a, N, M, \hat{\sigma}_n^2.$$

Select a group of space-time steering vectors (for side-looking ULA)

$$\{\bar{\mathbf{v}}_p\}_{p=0}^{N_r},$$

$$\text{where } \bar{\mathbf{v}}_p(n, m) = \exp(j2\pi f_s (\beta n + m)),$$

$$N_r = M + \beta(N - 1), \text{ and } f_s = \frac{p}{N_r}, p = 0, 1, \dots, N_r - 1,$$

Compute calibrated space-time steering vectors

Estimate $\hat{\alpha}_s$ using the methods in [19],

where columns of $\hat{\mathbf{E}}_s$ are all equivalent to $\mathbf{1}_N \otimes \hat{\alpha}_s$,

$$\mathbf{V}_s = \mathbf{V} \odot \hat{\mathbf{E}}_s,$$

(In RD version, $\bar{\mathbf{V}}_s = \mathbf{S}_D^H \mathbf{V}_s$),

Compute \mathbf{U}_s

$$\mathbf{u}_{s,0} = \bar{\mathbf{v}}_{s,0} / \|\bar{\mathbf{v}}_{s,0}\|,$$

$$\tilde{\mathbf{u}}_{s,p} = \bar{\mathbf{v}}_{s,p} - \sum_{i=0}^{p-1} (\mathbf{u}_{s,i}^H \bar{\mathbf{v}}_{s,p}) \mathbf{u}_{s,i},$$

$$\mathbf{u}_{s,p} = \tilde{\mathbf{u}}_{s,p} / \|\tilde{\mathbf{u}}_{s,p}\|, p = 1, \dots, N_r - 1,$$

$$\mathbf{U}_s = [\mathbf{u}_{s,0}, \dots, \mathbf{u}_{s,N_r-1}].$$

(In RD version, $\bar{\mathbf{U}}_s$ instead of \mathbf{U}_s),

For each snapshot $l = 1, \dots, L$

$$\hat{\mathbf{y}}_{l,s} = \mathbf{U}_s^H \mathbf{x}_l,$$

Compute $\hat{\mathbf{R}}_c$

$$\hat{\mathbf{\Gamma}} = \text{diag} \left(\frac{1}{L} \sum_{l=1}^L \hat{\mathbf{y}}_{l,s} \odot \hat{\mathbf{y}}_{l,s}^* \right),$$

$$\hat{\mathbf{R}}_s = \hat{\mathbf{U}}_s \hat{\mathbf{\Gamma}}_s \hat{\mathbf{U}}_s^H,$$

Estimate $\hat{\mathbf{T}}_d$,

$$\hat{\mathbf{R}}_c = \hat{\mathbf{R}}_s \odot \hat{\mathbf{T}}_d,$$

(In RD version, $\bar{\mathbf{U}}_s$ instead of \mathbf{U}_s , $\hat{\mathbf{T}}_d$ instead of $\hat{\mathbf{T}}_d$)

Compute \mathbf{U}

Adopt the Lanczos algorithm to $\hat{\mathbf{R}}_c$ to compute \mathbf{U} ,

(In RD version, $\hat{\mathbf{R}}_c$ instead of $\hat{\mathbf{R}}_c$),

Filter weights computation

$$\hat{\mathbf{w}} = \frac{(\mathbf{I} - \mathbf{U}\mathbf{U}^H)\mathbf{s}}{\mathbf{s}^H(\mathbf{I} - \mathbf{U}\mathbf{U}^H)\mathbf{s}},$$

Or:

$$\hat{\mathbf{w}} = \mu \mathbf{U} \left(\hat{\mathbf{\Gamma}}^{-1} + \frac{1}{\hat{\sigma}_n^2} \mathbf{I} \right) \mathbf{U}^H \mathbf{s}.$$

(In RD version, $\bar{\mathbf{U}}$ instead of \mathbf{U})

ALGORITHM 1: The proposed KA-STAP algorithm.

$N_c^2 NM$). It should be also noted that the approach of the Gram-Schmidt orthogonalization can be applied to arbitrary arrays if we can obtain prior knowledge of the array geometry, some radar system parameters, and some information of the platform.

In particular, for the case of a side-looking ULA, we can further reduce the computational complexity to compute the clutter subspace eigenvectors. Since the dimension of the columns of \mathbf{V} should satisfy $N_c \gg N_r$, if we carry out the Gram-Schmidt orthogonalization procedure on the columns

of \mathbf{V} one by one, this will result in unnecessary computations due to the linear correlation among the columns. Thus, it is desirable to directly find a group of vectors that are linear independent or nearly linear independent (i.e., most of the vectors are linearly independent and only very few vectors are linearly correlated). Fortunately, for a ULA we have the following proposition.

Proposition 1. *For the case of a side-looking ULA and constant PRF, the clutter subspace belongs to the subspace computed by a group of space-time steering vectors $\{\bar{\mathbf{v}}_p\}_{p=0}^{N_r}$, which are given by*

$$\bar{\mathbf{v}}_p(n, m) = \exp(j2\pi f_s(\beta n + m)), \quad (15)$$

where

$$f_s = \frac{p}{N_r}, \quad p = 0, 1, \dots, N_r - 1. \quad (16)$$

Proof. Let us stack the above space-time steering vectors into a $N_r \times NM$ matrix $\tilde{\mathbf{V}}$, which is shown as

$$\tilde{\mathbf{V}} = \begin{bmatrix} 1 & 1 & \cdots & 1 \\ z_{0,0} & z_{0,1} & \cdots & z_{N,M} \\ \vdots & \vdots & \ddots & \vdots \\ z_{N_r-1,0} & z_{N_r-1,1} & \cdots & z_{N_r-1,M} \end{bmatrix}, \quad (17)$$

where

$$z_{n,m} = \exp\left(j2\pi \frac{\beta n + m}{N_r}\right). \quad (18)$$

Note that $\tilde{\mathbf{V}}$ is a Vandermonde matrix of dimension $N_r \times NM$. For $z_{n,m}$, $n = 0, \dots, N - 1$ and $m = 0, \dots, M - 1$, the number of linearly independent columns of $\tilde{\mathbf{V}}$ is determined by the number of distinct values of $\beta n + m$. If β is an integer, the number of distinct values of $\beta n + m$ is $N_r = \beta(N - 1) + M$. If β is a rational value (not an integer), the number of distinct values of $\beta n + m$ is larger than $N_r = \lceil M + \beta(N - 1) \rceil$. Therefore, $\tilde{\mathbf{V}}$ has full rank, which is equal to [1]

$$\text{rank}(\tilde{\mathbf{V}}) = \min(N_r, NM) = N_r. \quad (19)$$

The dimension of the clutter subspace is also N_r . Herein, the clutter subspace shares the same subspace with $\tilde{\mathbf{V}}$. We can then compute the clutter subspace by taking the Gram-Schmidt orthogonalization procedure on the rows of $\tilde{\mathbf{V}}$. Moreover, it should be noted that the computational complexity of the second approach is on the order of $O((N_r + 1)N_r NM/2) \ll O((N_c + 1)N_c NM/2) \ll O(N_c^3 + N_c^2 NM)$, which exhibits a much lower complexity compared with the LSE resulting in a very useful tool for practical applications. It also avoids the procedure to determine the values of the number of clutter patches N_c and the azimuth angle ϕ . \square

After computing the orthogonal basis of the clutter subspace, we try to design the STAP filter weights by two different kinds of methods. One is to use the minimum

norm eigen-canceler (MNE) derived in [5] to form the filter weights. Specifically, the MNE method is a linearly constrained beamformer with a minimum norm weight vector appearing orthogonal to the clutter subspace, which is described by [5]

$$\begin{aligned} \min_{\mathbf{w}} \quad & \mathbf{w}^H \mathbf{w}, \\ \text{subject to} \quad & \mathbf{U}^H \mathbf{w} = 0, \quad \mathbf{w}^H \mathbf{s} = 1. \end{aligned} \quad (20)$$

The solution to the above optimization problem in (20) is provided by [5]

$$\hat{\mathbf{w}} = \frac{(\mathbf{I} - \mathbf{U}\mathbf{U}^H) \mathbf{s}}{\mathbf{s}^H (\mathbf{I} - \mathbf{U}\mathbf{U}^H) \mathbf{s}}. \quad (21)$$

The other method tries to design the filter weights using both the orthogonal bases of the computed clutter subspace and the observation data. Let us first calculate the root eigenvalues by projecting the data on the clutter subspace \mathbf{U} , as described by

$$\hat{\boldsymbol{\gamma}} = \mathbf{U}^H \mathbf{x}. \quad (22)$$

Then, the clutter plus noise covariance matrix $\hat{\mathbf{R}}$ can be estimated by

$$\hat{\mathbf{R}} = \mathbf{U} \hat{\boldsymbol{\Gamma}} \mathbf{U}^H + \hat{\sigma}_n^2 \mathbf{I}, \quad (23)$$

where $\hat{\boldsymbol{\Gamma}} = \text{diag}(\hat{\boldsymbol{\gamma}} \hat{\boldsymbol{\gamma}}^*)$ and \odot denotes the Hadamard product. It should be noted that, in (23), $\mathbf{U} \hat{\boldsymbol{\Gamma}} \mathbf{U}^H$ is the estimated prior CCM. It introduces a linear combiner of the prior CCM and the sample covariance matrix (SCM) in [17, 24]. How to adaptively set the linear coefficients is also discussed in [23, 29]. Observing $\hat{\mathbf{R}}$ in (23), it corresponds to the case that the linear combiner of the prior CCM and the SCM with only thermal noise. Finally, the STAP filter weights can be computed by

$$\hat{\mathbf{w}} = \mu \mathbf{U} \left(\hat{\boldsymbol{\Gamma}}^{-1} + \frac{1}{\hat{\sigma}_n^2} \mathbf{I} \right) \mathbf{U}^H \mathbf{s}, \quad (24)$$

where we use the fact that $\hat{\mathbf{R}}^{-1} = \mathbf{U} (\hat{\boldsymbol{\Gamma}}^{-1} + (1/\hat{\sigma}_n^2) \mathbf{I}) \mathbf{U}^H$. The whole procedure of the proposed KA-STAP algorithm is summarized in Algorithm 1.

3.3. Proposed KA-STAP Employing CMT. In practice, there are many nonideal effects, such as the ICM and the channel mismatch [3], which result in performance degradation of the proposed algorithm. In the following, we will detail the proposed KA-STAP employing CMT.

For the angle-independent channel mismatch (since the main beam is usually fixed in a CPI, the angle-dependent channel mismatch can be approximated by spatial random tapers only related to the main beam and seen as angle-independent [3]), we can assume the spatial taper $\boldsymbol{\alpha}_s$ is a random vector but stable over a CPI due to the narrowband case considered in the paper [3]. Herein, the clutter plus noise

received data vector in presence of channel mismatch is given by [3]

$$\mathbf{x} = (\mathbf{V} \odot \Xi_s) \boldsymbol{\sigma} + \mathbf{n}, \quad (25)$$

where the columns of Ξ_s are all equivalent to $\mathbf{1}_N \otimes \boldsymbol{\alpha}_s$ and $\mathbf{1}_N$ denotes the all 1 vector with dimension N . When considering ICM, the received data can be represented as [3]

$$\mathbf{x} = (\mathbf{V}_s \boldsymbol{\sigma}) \odot (\boldsymbol{\alpha}_d \otimes \mathbf{I}_M) + \mathbf{n}, \quad (26)$$

where $\mathbf{V}_s = \mathbf{V} \odot \Xi_s$ and $\boldsymbol{\alpha}_d$ is the temporal taper accounting for the ICM. Then, the clutter plus noise covariance matrix is

$$\mathbf{R} = \mathbf{R}_s \odot \mathbf{T}_d + \sigma_n^2 \mathbf{I}, \quad (27)$$

where

$$\begin{aligned} \mathbf{R}_s &= \mathbf{V}_s \Sigma \mathbf{V}_s^H, \\ \mathbf{T}_d &= E \left[\boldsymbol{\alpha}_d \boldsymbol{\alpha}_d^H \right] \otimes \mathbf{1}_{M,M}, \end{aligned} \quad (28)$$

where \mathbf{T}_d denotes the space-time CMT accounting for the ICM and $\mathbf{1}_{M,M}$ is the $M \times M$ all 1 matrix. One common model, referred to as the Billingsley model, is suitable for a land scenario. Its temporal autocorrelation is detailed in [3]. Another common model, presented by Ward in [1], is suitable for a water scenario. The temporal autocorrelation of the fluctuations is Gaussian in shape with the form:

$$\zeta(m) = \exp \left\{ -\frac{8\pi^2 \sigma_v^2 T_r^2}{\lambda_c^2} m^2 \right\}, \quad (29)$$

where σ_v is the variance of the clutter spectral spread in m^2/s^2 . Then, \mathbf{T}_d can be given

$$\mathbf{T}_d = \text{Toeplitz}(\zeta(0); \dots; \zeta(N-1)). \quad (30)$$

In this paper, we consider the latter one.

Since $\boldsymbol{\alpha}_d$ is a random vector and its temporal autocorrelation has the form of (30), we assume the elements of $\boldsymbol{\alpha}_d$ do not equate to zeros, and we assume $\bar{\boldsymbol{\alpha}}_d = [1/\alpha_{d,1}, \dots, 1/\alpha_{d,N}]^T$. If we multiply both sides of (26) by $\bar{\boldsymbol{\alpha}}_d \otimes \mathbf{I}_M$, then it becomes

$$\mathbf{x}_s = \mathbf{x} \odot (\boldsymbol{\alpha}_d \otimes \mathbf{I}_M) = \mathbf{V}_s \boldsymbol{\sigma} + \mathbf{n}_s, \quad (31)$$

where $\mathbf{n}_s = \mathbf{n} \odot (\boldsymbol{\alpha}_d \otimes \mathbf{I}_M)$. In this situation, similarly as the analysis in Section 3.2, we can employ the Gram-Schmidt orthogonalization procedure to compute a matrix with eigenvectors of \mathbf{V}_s , which is denoted as \mathbf{U}_s . Then the root eigenvalues $\boldsymbol{\gamma}_s$ can be calculated by

$$\boldsymbol{\gamma}_s = \mathbf{U}_s^H \mathbf{x}_s. \quad (32)$$

We can then compute \mathbf{R}_s as

$$\mathbf{R}_s = \mathbf{U}_s \boldsymbol{\Gamma}_s \mathbf{U}_s^H, \quad (33)$$

where

$$\begin{aligned} \boldsymbol{\Gamma}_s &= \text{diag} (E [\boldsymbol{\gamma}_s \odot \boldsymbol{\gamma}_s^*]) \\ &= \text{diag} (E [(\mathbf{U}_s \mathbf{x}_s) \odot (\mathbf{U}_s \mathbf{x}_s)^*]) \\ &= \text{diag} ((\mathbf{U}_s \odot \mathbf{U}_s^*) E [(\mathbf{x}_s \odot \mathbf{x}_s^*)]) \\ &= \text{diag} ((\mathbf{U}_s \odot \mathbf{U}_s^*) E [(\mathbf{x} \odot \mathbf{x}^*)]) \\ &= \text{diag} (E [(\mathbf{U}_s \mathbf{x}) \odot (\mathbf{U}_s \mathbf{x})^*]). \end{aligned} \quad (34)$$

Here, it uses the fact that the expectation of the amplitude of the temporal taper caused by the ICM is one, which agrees with the ICM models introduced previously. From (34), we observe that \mathbf{R}_s can be estimated using the received data \mathbf{x} directly without $\boldsymbol{\alpha}_d$. It also suggested that the KAPE approach could directly use the received data and the calibrated space-time steering vectors (only the spatial taper without the temporal taper) to compute the parameter $\boldsymbol{\sigma}$.

In order to obtain the clutter plus noise covariance matrix \mathbf{R} , we should estimate \mathbf{R}_s and \mathbf{T}_d in (27). Regarding the estimation of \mathbf{R}_s , we can firstly use the array calibration methods discussed in [19] to estimate the spatial taper (denoted as $\hat{\boldsymbol{\alpha}}_s$), which will not be discussed here due to space limitations. The reader is referred to the literature [19] for further details. Then, substituting $\hat{\boldsymbol{\alpha}}_s$ into \mathbf{V}_s , we obtain the estimate $\hat{\mathbf{V}}_s$ and then compute the eigenvector matrix $\hat{\mathbf{U}}_s$. Finally, the estimate of $\hat{\boldsymbol{\Gamma}}_s$ can be approximated using estimates obtained by the averages over the available snapshots instead of the expectation operation. Regarding the estimation of \mathbf{T}_d , it can be obtained via a rough knowledge of the interference environment (e.g., forest versus desert, bandwidth, etc.) [6].

After computing the estimates $\hat{\mathbf{R}}_s$ and $\hat{\mathbf{T}}_d$, we can compute the CCM as $\hat{\mathbf{R}}_c = \hat{\mathbf{R}}_s \odot \hat{\mathbf{T}}_d$. Since $\hat{\mathbf{R}}_c$ has low rank, we adopt the Lanczos algorithm to compute the clutter subspace \mathbf{U} , where the computational complexity is on the order of $O((NM)^2 N_r')$ (N_r' is the clutter rank of $\hat{\mathbf{R}}_c$). Finally, the STAP filter weights are computed according to (21) or (24). The whole procedure can be seen in Algorithm 1.

Prior Knowledge Uncertainty Impact. In the proposed algorithms, prior knowledge uncertainty, such as velocity misalignment and yaw angle misalignment, will have a great impact on the performance. However, the scheme that employs the CMT will mitigate this impact. To illustrate this, we take a typical airborne radar system, for example. The parameters of the radar system are listed at the beginning of Section 4. Consider a far field scenario, the elevation angle will be close to zero resulting in $\cos \theta \approx 1$. Let v_{pu} and ϕ_u denote the velocity deviation and the yaw angle deviation, respectively. Then, for a discretized azimuth angle ϕ , the spatial frequency f_s and Doppler frequency f_d can be represented as

$$\begin{aligned} f_s &= \frac{d_a}{\lambda_c} \sin \phi, \\ f_d &= \frac{2(v_p + v_{pu}) T_r}{\lambda_c} \sin(\phi + \phi_u). \end{aligned} \quad (35)$$

From (35), we see that prior knowledge uncertainty will affect the position and shape of the clutter ridge, which leads to the mismatch between the exact and the assumed space-time steering vectors. Figure 2 provides a more direct way to illustrate the impact of prior knowledge uncertainty on the clutter ridge in the spatiotemporal plane. By employing a CMT, the clutter spectra will become wider along the clutter ridge in the figure including the exact clutter ridge. From this point of view, the impact of prior knowledge

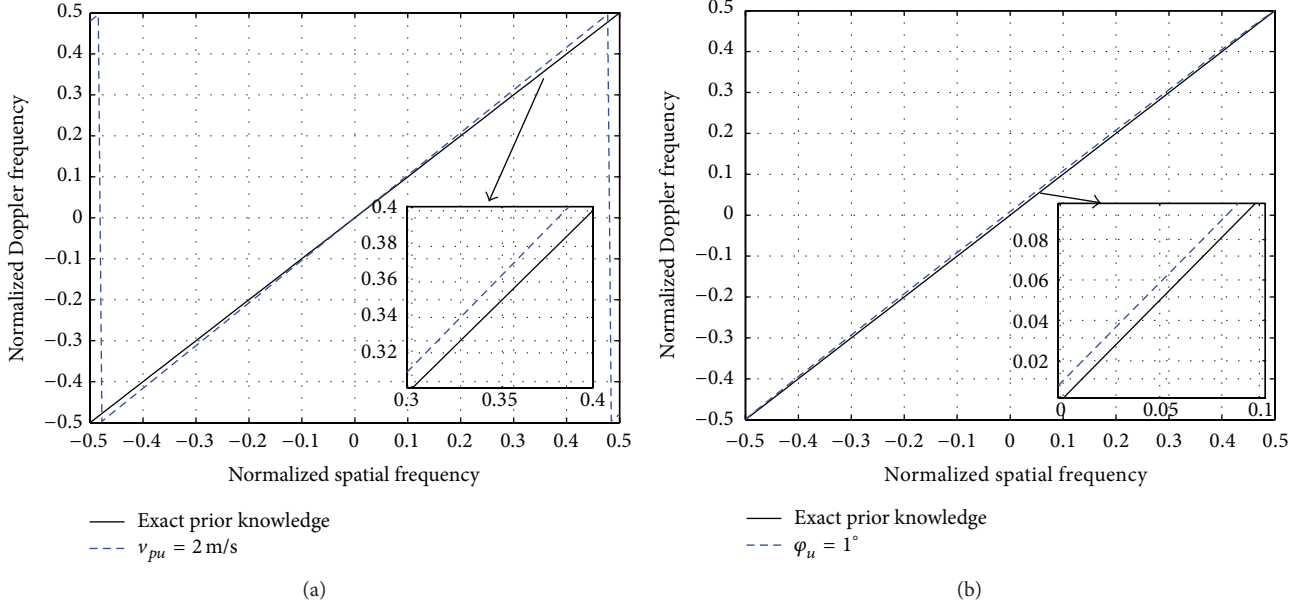


FIGURE 2: Impact of prior knowledge uncertainty to the clutter ridge in the spatiotemporal plane with (a) velocity deviation $v_{pu} = 2$ m/s and (b) $\phi_u = 1^\circ$.

uncertainty is mitigated. Because the methods in [20–22] do not consider any strategies to mitigate the impact of prior knowledge uncertainty, the performance will depend highly on the accuracy of prior knowledge. The KAPE approach in [19] also adopts the CMT and can mitigate the impact of prior knowledge uncertainty in a sense. But the differences between the proposed algorithm and the KAPE approach lie in three aspects. First, the KAPE approach estimates the CCM using the LS or some approximate approaches. On the contrary, the proposed algorithm estimates the CCM using the Gram-Schmidt orthogonalization procedure (that is not an approximation). Furthermore, for a side-looking ULA radar, the proposed algorithm directly selects a group of linearly independent space-time steering vectors using the LRGP and then takes the Gram-Schmidt orthogonalization procedure to compute the clutter subspace. Second, the proposed algorithm shows evidence that is feasible to directly use the received data vector and the calibrated space-time steering vectors (only the spatial taper without the temporal taper) to compute the parameter σ . Third, the proposed algorithm with an RD version in the following section is presented to further reduce the complexity.

3.4. Proposed Reduced-Dimension (RD) KA-STAP Algorithms.

From the above discussions, one aspect to be noted is that it is impractical to use all the DoFs available at the ULA for reasons of computational complexity when NM is too large. In such situations, a common approach is to break the full DoFs problem into a number of smaller problems via the application of an $MN \times D$ (with $D \ll MN$) transformation matrix \mathbf{S}_D to the data [1]. Our proposed KA-STAP algorithms can be easily extended to this kind of approach. By applying

the reduced-dimension transformation matrix \mathbf{S}_D to the data and the space-time steering vectors, we obtain

$$\bar{\mathbf{x}} = \mathbf{S}_D^H \mathbf{x}, \quad \bar{\mathbf{V}} = \mathbf{S}_D^H \mathbf{V}, \quad (36)$$

where “ $\bar{\cdot}$ ” denotes the results after the transformation. Then, the reduced-dimension CCM $\bar{\mathbf{R}}_c$ becomes

$$\bar{\mathbf{R}}_c = \mathbf{S}_D^H \mathbf{R}_c \mathbf{S}_D = \bar{\mathbf{V}} \bar{\mathbf{\Sigma}} \bar{\mathbf{V}}^H = \bar{\mathbf{U}} \bar{\mathbf{\Gamma}} \bar{\mathbf{U}}^H. \quad (37)$$

In a manner similar to that of the proposed full-DoF KA-STAP algorithm described in Section 3.2, we compute the orthogonal bases of the clutter subspace $\bar{\mathbf{U}}$, estimate the CCM $\hat{\bar{\mathbf{R}}}_c = \bar{\mathbf{U}} \hat{\bar{\mathbf{\Gamma}}} \bar{\mathbf{U}}^H$, and then calculate the STAP filter weights according to (21) or (24). When employing a CMT to the ideal clutter covariance matrix, the final RD clutter covariance matrix can be estimated as

$$\hat{\bar{\mathbf{R}}}_c = \hat{\bar{\mathbf{R}}}_s \circ \hat{\bar{\mathbf{T}}}_d = \left(\hat{\bar{\mathbf{U}}}_s \hat{\bar{\mathbf{\Gamma}}}_s \hat{\bar{\mathbf{U}}}_s^H \right) \circ \hat{\bar{\mathbf{T}}}_d, \quad (38)$$

where $\hat{\bar{\mathbf{U}}}_s$ is computed by taking the Gram-Schmidt orthogonalization procedure to $\hat{\bar{\mathbf{V}}}_s = \mathbf{S}_D^H \hat{\mathbf{V}}_s$, $\hat{\bar{\mathbf{\Gamma}}}_s$ is calculated via (34) using $\bar{\mathbf{x}}$ and $\hat{\bar{\mathbf{U}}}_s$ instead of \mathbf{x} and $\hat{\mathbf{U}}_s$, and $\hat{\bar{\mathbf{T}}}_d$ denotes the estimated RD CMT. Again, the STAP filter weights can be computed according to (21) or (24). By inspecting (37) and (38), we find that the computational complexity of our proposed RD-KA-STAP algorithm is related to D instead of NM ($D \ll NM$), which leads to great computation savings.

In this paper, we focus on the reduced-dimension technique known as extended factored (EFA) algorithm or multi-bin element-space post-Doppler STAP algorithm [1]. The simulations with this technique will show the performance of our proposed RD-KA-STAP algorithm.

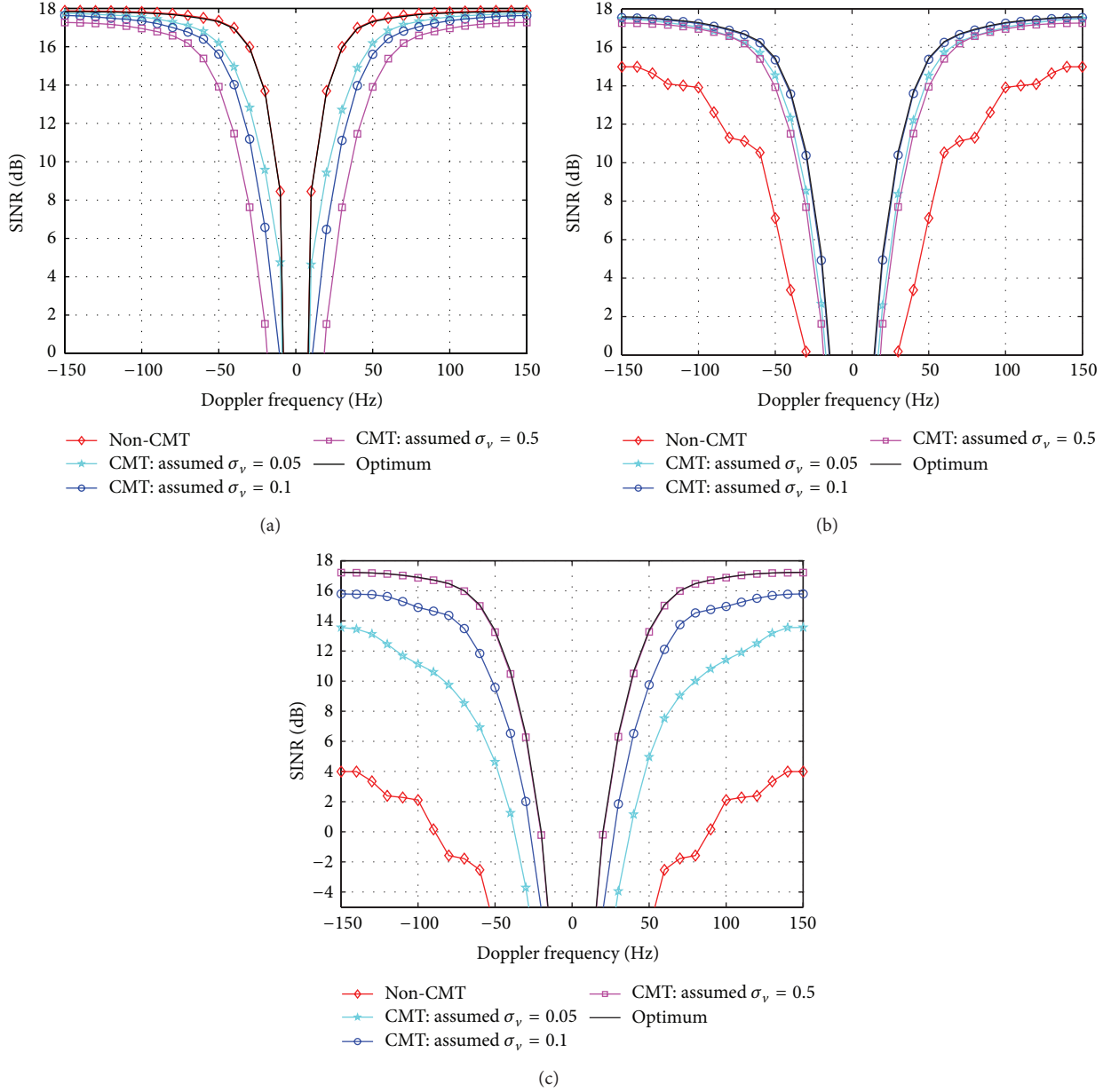


FIGURE 3: Impacts of ICM on SINR performance against Doppler frequency with 4 snapshots and the target Doppler frequency space from -150 to 150 Hz. (a) $\sigma_v = 0$; (b) $\sigma_v = 0.1$; (c) $\sigma_v = 0.5$.

3.5. Complexity Analysis. Here we illustrate the computational complexity of the proposed algorithms (shortened as LRGP KA-STAP and LRGP RD-KA-STAP) and other existing algorithms, namely, the sample matrix inversion algorithm (SMI), the EFA algorithm in [1], the joint-domain-localized (JDL) algorithm in [7], the CSMIECC algorithm in [20], and the KAPE algorithm in [19]. In Table 1, D denotes the size of the reduced dimension. We can see that the computational complexity of our proposed algorithms is significantly lower than the CSMIECC and the KAPE algorithms ($N_r \ll N_c, NM$), which require the pseudoinverse of the matrix $\mathbf{V}^H \mathbf{V}$. With regard to the SMI algorithm, our proposed

algorithms also show a lower computational complexity because the number of snapshots used for training the filter weights of the SMI is in the order of $2NM$.

Although the computational complexity of the EFA and JDL algorithms is lower than our proposed LRGP KA-STAP algorithm, two aspects should be noted. One is that the number of snapshots used for training filter weights is much larger than our proposed algorithms. The other is that the computational complexity of EFA and JDL is proportional to the number of Doppler frequencies of interest (we only list the computation complexity for one Doppler frequency), while our proposed algorithms only have to compute the CCM once

TABLE I: Computational complexity of algorithms.

Algorithm	Estimate the CCM	Compute filter weights
SMI	$O(L(NM)^2)$	$O((NM)^3)$
EFA	$O(L(D)^2) + O\left(L\frac{N}{2}\log_2(N)\right)$	$O(D^3)$
JDL	$O(L(D)^2) + O\left(L\frac{NM}{2}\log_2(NM)\right)$	$O(D^3)$
CSMIECC	$O(L(NM)^2) + O(N_c(NM)^2) + O(N_c^3 + N_c^2NM)$	$O((NM)^3)$
KAPE	$O(N_c(NM)^2) + O(N_c^3 + N_c^2NM)$	$O((NM)^3)$
LRGP KA-STAP	$O\left(\frac{(N_r + 1)N_rNM}{2} + LN_rNM\right) + O(N_r(NM)^2)$	$O(N_r(NM)^2)$
LRGP RD-KA-STAP	$O\left(\frac{(N_r + 1)N_rD}{2} + LN_rD\right) + O(N_rD^2)$	$O(D^3)$

for different Doppler frequencies of interest. Moreover, the computational complexity of our proposed LRGP RD-KA-STAP is lower than the EFA since L in EFA is in the order of $2D$, where D is usually larger than N_r .

4. Performance Assessment

In this section, we assess the proposed KA-STAP algorithms by computing the output SINR performance and probability of detection performance using simulated radar data. The output SINR is defined by

$$\text{SINR} = \frac{|\widehat{\mathbf{w}}^H \mathbf{s}|^2}{|\widehat{\mathbf{w}}^H \mathbf{R} \widehat{\mathbf{w}}|}. \quad (39)$$

Throughout the simulations, unless otherwise stated, the simulated scenarios use the following parameters: side-looking ULA, uniform transmit pattern, $M = 8$, $N = 8$, $f_c = 450$ MHz, $f_r = 300$ Hz, $v_p = 50$ m/s, $d_a = \lambda_c/2$, $\beta = 1$, $N_r = \lceil M + \beta(N - 1) \rceil = 15$, $h_p = 9000$ m, signal-to-noise ratio (SNR) of 0 dB, the target located at 0° azimuth with Doppler frequency 100 Hz, clutter-to-noise ratio (CNR) of 50 dB, and unitary thermal noise power (here, SNR and CNR are defined relative to noise power per channel and per pulse). All presented results are averaged over 100 independent Monte Carlo runs.

4.1. Impact of ICM on the SINR Performance. In this subsection, we evaluate the impact on the SINR performance with different ICM for our proposed algorithms. In the examples, we consider four different ICM cases with $\sigma_v = 0$, $\sigma_v = 0.1$, and $\sigma_v = 0.5$. The number of snapshots for training is 4. In Figures 3(a), 3(b), and 3(c), we show the SINR performance against the target Doppler frequency of our proposed LRGP KA-STAP algorithm both with and without a CMT. From the figures, we observe the following conclusions. (i) When there is non-ICM, the proposed LRGP KA-STAP algorithm without a CMT can obtain the optimum performance since the computed clutter subspace is exact. However, it degrades the SINR performance with the increase of σ_v , resulting in extra sensitivity to the ICM. That is because the computed clutter subspace cannot represent the true clutter subspace.

(ii) Our proposed LRGP KA-STAP algorithm with a CMT illustrates a robust characteristic to the ICM. When the estimated parameter σ_v of CMT is correct, we can achieve the optimum SINR performance. Furthermore, the range of values of CMT mismatch is demonstrated in which the estimated spreading exhibits acceptable SINR performance, which can be useful in applications. This can be interpreted as that the computed clutter subspace via the application of the CMT to the ideal clutter subspace spans a similar space to the true clutter subspace.

4.2. Impact of Inaccurate Prior Knowledge on the SINR Performance. In this subsection, we focus on the impact of inaccurate prior knowledge on the SINR performance of our proposed algorithms. In the first example, we consider the impact of the velocity misalignment by showing the SINR performance against the target Doppler frequency, as shown in Figure 4. Consider three different cases: the velocity misalignments of prior knowledge are (a) 0.5 m/s, (b) 1 m/s, and (c) 2 m/s, compared with true platform velocity. The potential Doppler frequency space from -150 to 150 Hz is examined and 4 snapshots are used to train the filter weights. The plots show that the proposed LRGP KA-STAP algorithm without a CMT is sensitive to the velocity misalignment, while the LRGP KA-STAP algorithm with a CMT is robust to that. The reason for this is that the velocity misalignment of prior knowledge will lead to the mismatch between the computed clutter subspace and the true clutter subspace. Although the computed clutter subspace via the CMT cannot avoid this situation, it can mitigate this impact. Because the velocity misalignment between the clutter patches and the platform can be seen as the Doppler spreading of the clutter patches. Moreover, the results also show that a slightly larger value of the estimated parameter σ_v will result in an improved SINR performance for the velocity misalignment case.

The evaluation of the impact caused by the yaw angle misalignment is shown in Figure 5, where we also consider three different cases: the yaw angle misalignments of prior knowledge are (a) 0.2° , (b) 0.5° , and (c) 1° . The curves also indicate that (i) the proposed LRGP KA-STAP algorithm without a CMT is sensitive to the yaw angle misalignment, while the LRGP KA-STAP algorithm with a CMT is robust

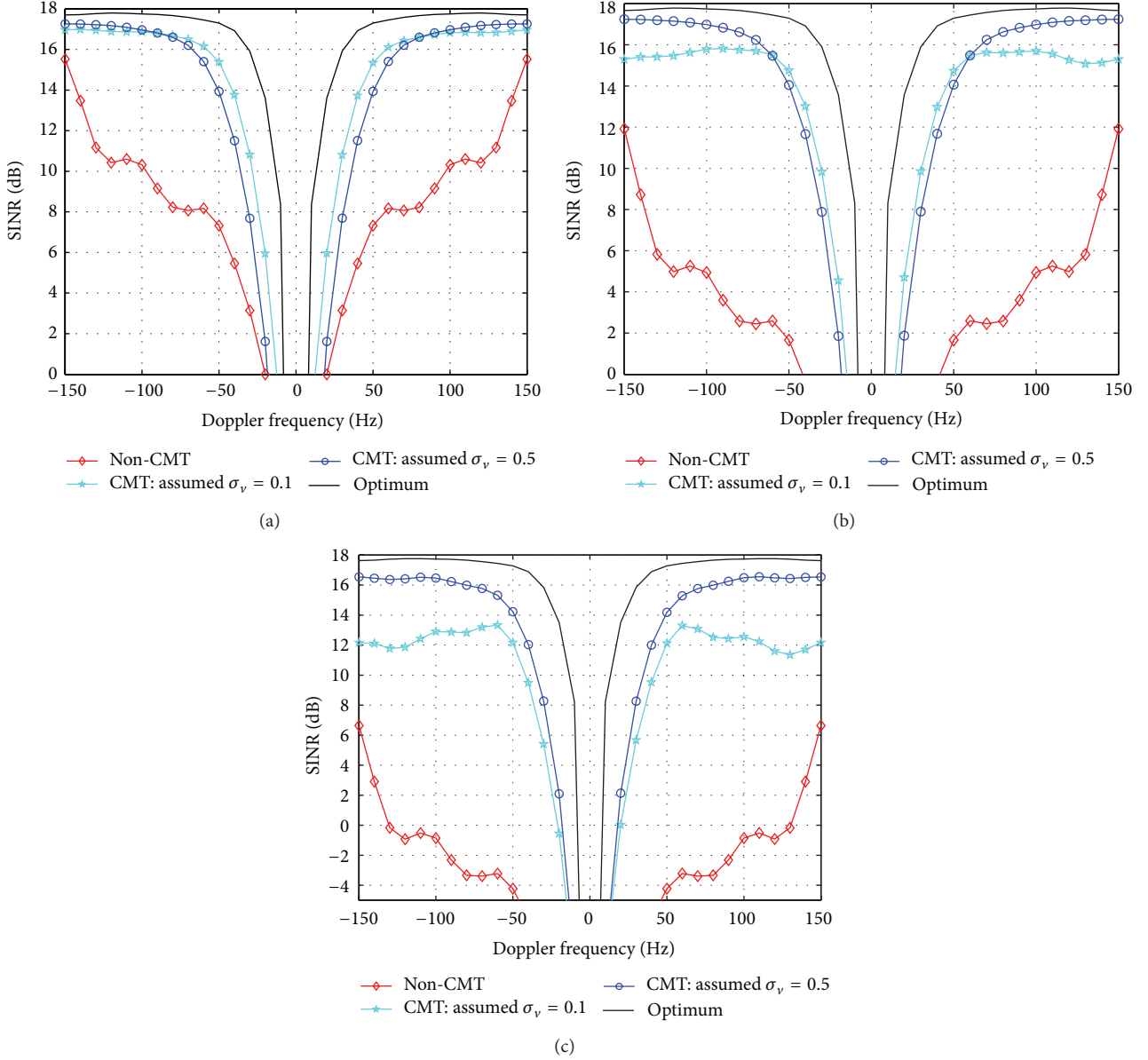


FIGURE 4: Impacts of velocity misalignment of prior knowledge on SINR performance against Doppler frequency with 4 snapshots and the target Doppler frequency space from -150 to 150 Hz. (a) Velocity misalignment 0.5 m/s; (b) velocity misalignment 1 m/s; (c) velocity misalignment 2 m/s.

to that; (ii) a slightly larger value of the estimated parameter σ_v will result in an improved SINR performance. The misalignment of the yaw angle will lead to a Doppler frequency mismatch between the radar platform and the clutter patches. While the CMT mainly aims at mitigating the performance degradation caused by the clutter Doppler spreading, the CMT will lead to an improved estimated clutter subspace and will exhibit robustness against the yaw angle misalignment.

4.3. Comparison with Conventional STAP Algorithms. To provide further investigation about the performance of our proposed algorithms, we compare the SINR performance versus the snapshots of our proposed LRGP KA-STAP and LRGP

RD-KA-STAP algorithms with the Loaded SMI (LSMI), the EFA algorithm (3 Doppler bins), the 3×3 JDL algorithm, Stoica's scheme in [23] (the prior knowledge covariance matrix is computed in the same way as the CSMIECC algorithm), and the CSMIECC algorithm (the combination parameter is set to 0.6) in [20], where the simulation results are shown in Figure 6. Here, we consider a scenario of ICM with $\sigma_v = 0.5$ and assume the diagonal loading factors for all algorithms are set to the level of the thermal noise power. The parameter σ_v for our proposed algorithms is assumed to be 1 . The curves in the figure illustrate that our proposed algorithms have a very fast SINR convergence speed, which only needs three snapshots for training, and offer significant

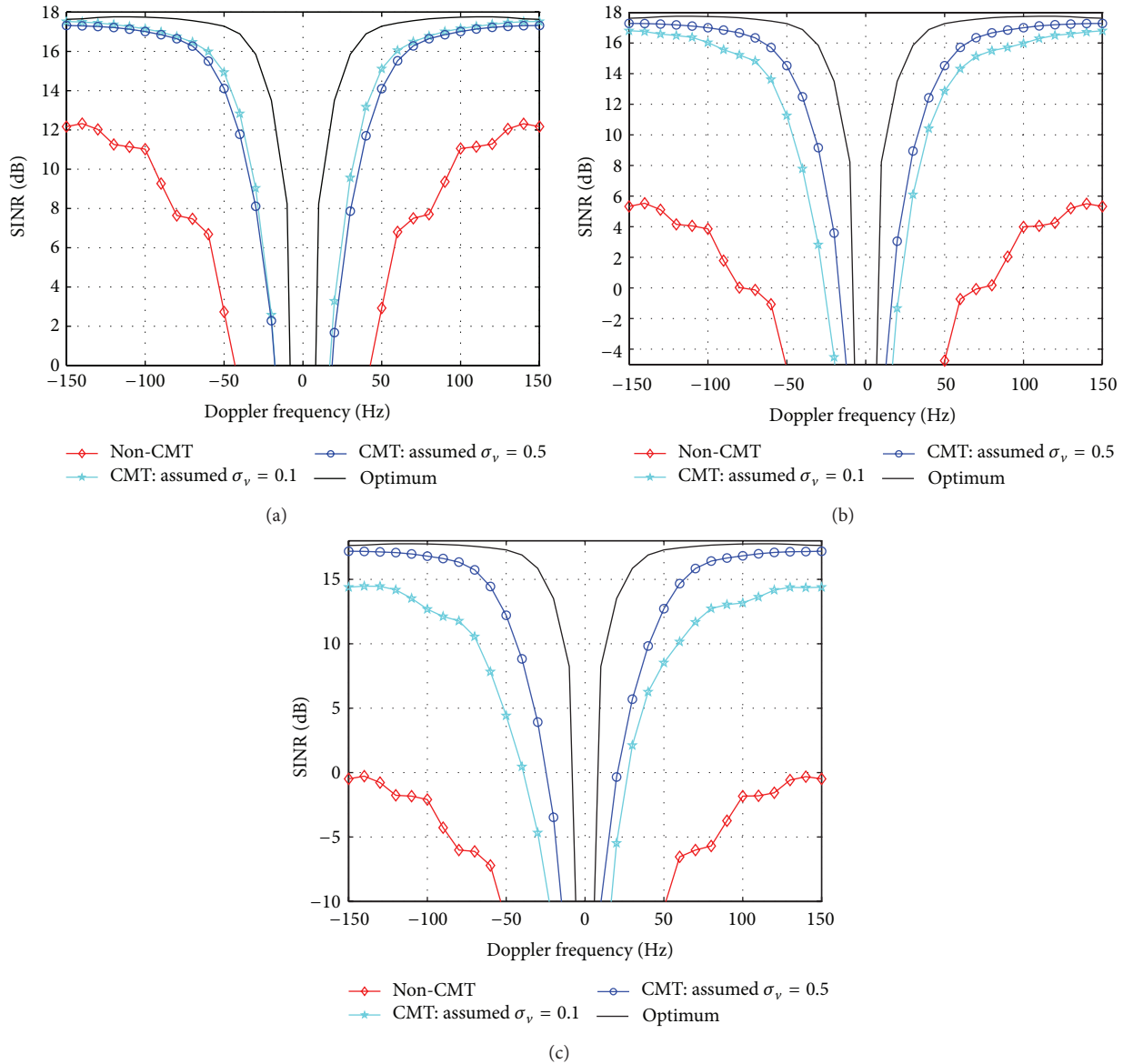


FIGURE 5: Impacts of yaw angle misalignment of prior knowledge on SINR performance against Doppler frequency with 4 snapshots and the target Doppler frequency space from -150 to 150 Hz: (a) yaw angle misalignment 0.2° , (b) yaw angle misalignment 0.5° , and (c) yaw angle misalignment 1° .

better SINR steady-state performance compared with the LSMI, EFA, JDL, Stoica’s scheme, and CSMIECC algorithms. This is because the proposed algorithms provide a much better estimation of the CCM by using prior knowledge of the data, the low clutter rank property, the geometry of the array, and the interference environment. It should be noted that the SINR performance of the LRGP RD-KA-STAP algorithm is worse than that of LRGP KA-STAP with full-DOFs. This is due to the fact that the reduced DOFs will lead to lower computational complexity at the cost of performance degradation.

The results in Figure 7 illustrate the SINR performance versus the target Doppler frequency. The number of snapshots

used for training in the LSMI, EFA, JDL, Stoica’s scheme, and CSMIECC algorithms is set to 48, while we set it to 4 in our proposed algorithms. It is found that our proposed LRGP KA-STAP algorithm provides the best SINR performance among all algorithms and forms the narrowest clutter null resulting in improved performance for the detection of slow targets. It is also shown that the performance of the proposed LRGP RD-KA-STAP algorithm is worse than that of LRGP KA-STAP with full-DOFs but better than other algorithms in most Doppler bins. Note that although the LRGP RD-KA-STAP algorithm performs slightly worse than other algorithms in Doppler range of -60 to 60 Hz, it requires much less snapshots for training filter weights.

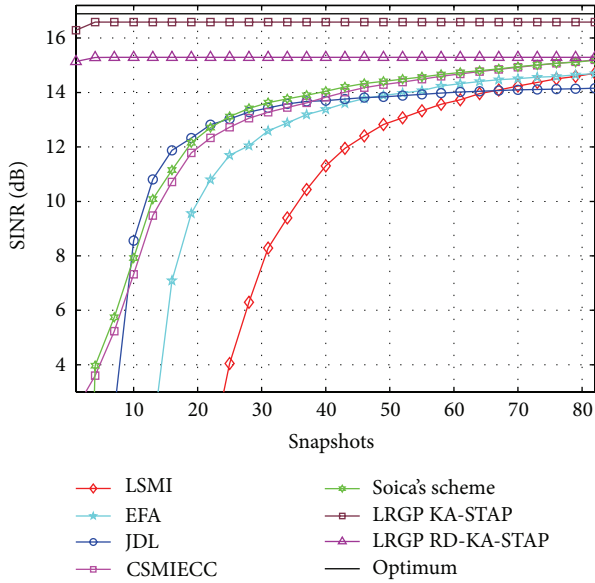


FIGURE 6: SINR performance against the number of snapshots considering ICM, where $\sigma_v = 0.5$.

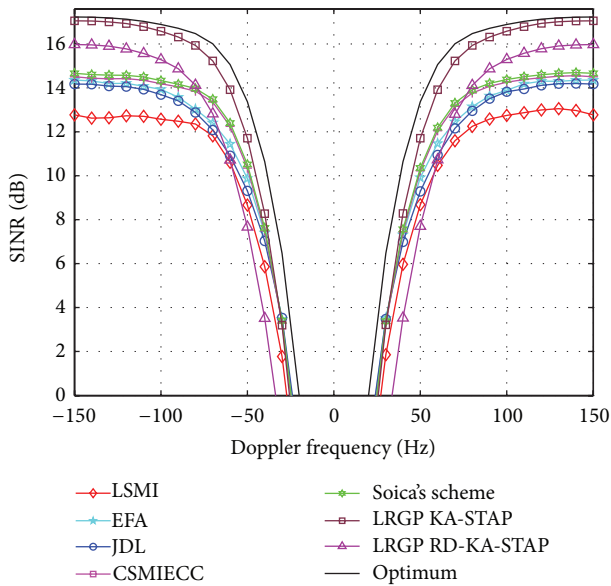


FIGURE 7: SINR performance versus the target Doppler frequency. The number of snapshots used for training in the LSMI, EFA, JDL, and CSMIECC algorithms is set to 48, while we only use 4 snapshots for our proposed algorithms.

As shown in Figure 8, we present the probability of detection performance versus the target SNR for all algorithms. The false alarm rate is set to 10^{-3} and for simulation purposes the threshold and probability of detection estimates are based on 10,000 samples. We suppose the target is injected in the boresight with Doppler frequency 100 Hz. We note that the proposed algorithms provide suboptimal detection performance using very short snapshots but, remarkably,

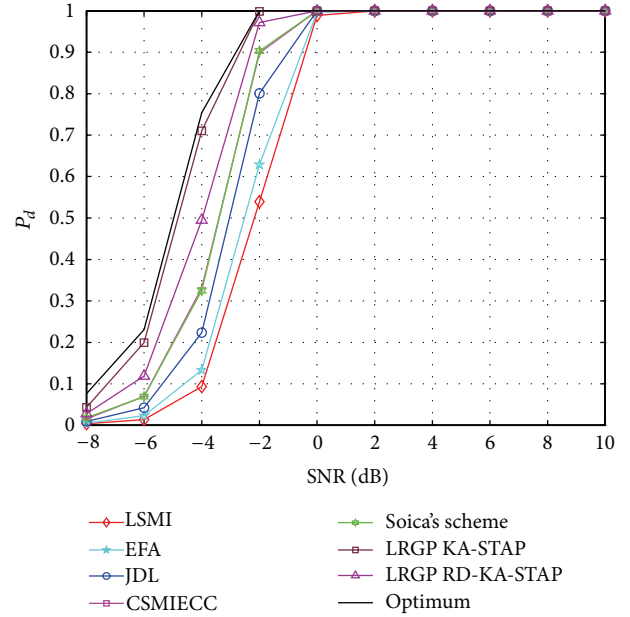


FIGURE 8: Probability of detection performance against the target SNR. Suppose the target is injected in the boresight with Doppler frequency 100 Hz, and other parameters setting for all algorithms are the same as that in the second example.

obtain much higher detection rate than other algorithms at an SNR level from -8 dB to 0 dB.

5. Conclusions

In this paper, novel KA-STAP algorithms have been proposed by using prior knowledge of LRGP to obtain an accurate estimation of the CCM with a very small number of snapshots. By exploiting the fact that the clutter subspace is only determined by the space-time steering vectors, we have developed a Gram-Schmidt orthogonalization approach to compute the clutter subspace. In particular, for a side-looking ULA, we have proposed a scheme to directly select a group of linearly independent space-time steering vectors to compute the orthogonal bases of the clutter subspace. Compared with the LSE algorithm, it has not only exhibited a low complexity, but also shown a simple way to compute the CCM. To overcome the performance degradation caused by the nonideal effects and prior knowledge uncertainty, the proposed KA-STAP algorithm that combines the CMT has been presented and a reduced-dimension version has been devised for practical applications. This has also provided evidence that it is feasible to directly use the received data vector and the calibrated space-time steering vectors (only the spatial taper without the temporal taper) to compute the assumed clutter amplitude. The simulation results have shown that our proposed algorithms outperform other existing algorithms in terms of SINR steady-state performance, SINR convergence speed, and detection performance for a very small number of snapshots and also exhibit robustness against errors in prior knowledge.

Conflict of Interests

The authors declare that there is no conflict of interests regarding the publication of this paper.

Acknowledgments

This work is funded in part by the National Natural Science Foundation of China (61201334, 61101182, and 61171133) and the Hunan Provincial Innovation Foundation for Postgraduate.

References

- [1] J. Ward, "Space-time adaptive processing for airborne radar," Tech. Rep. 1015, MIT Lincoln Laboratory, Lexington, Mass, USA, 1994.
- [2] R. Klemm, *Principles of Space-Time Adaptive Processing*, Institute of Electrical Engineering, London, UK, 2006.
- [3] J. R. Guerci, *Space-time Adaptive Processing for Radar*, Artech House, 2003.
- [4] W. L. Melvin, "A STAP overview," *IEEE Aerospace and Electronic Systems Magazine*, vol. 19, no. 1, pp. 19–35, 2004.
- [5] A. M. Haemovich and M. Berin, "Eigenanalysis-based space-time adaptive radar: performance analysis," *IEEE Transactions on Aerospace and Electronic Systems*, vol. 33, no. 4, pp. 1170–1179, 1997.
- [6] J. R. Guerci and J. S. Bergin, "Principal components, covariance matrix tapers, and the subspace leakage problem," *IEEE Transactions on Aerospace and Electronic Systems*, vol. 38, no. 1, pp. 152–162, 2002.
- [7] H. Wang and L. Cai, "On adaptive spatial-temporal processing for airborne surveillance radar systems," *IEEE Transactions on Aerospace and Electronic Systems*, vol. 30, no. 3, pp. 660–670, 1994.
- [8] R. C. de Lamare, L. Wang, and R. Fa, "Adaptive reduced-rank LCMV beamforming algorithms based on joint iterative optimization of filters: Design and analysis," *Signal Processing*, vol. 90, no. 2, pp. 640–652, 2010.
- [9] R. Fa, R. C. de Lamare, and L. Wang, "Reduced-rank STAP schemes for airborne radar based on switched joint interpolation, decimation and filtering algorithm," *IEEE Transactions on Signal Processing*, vol. 58, no. 8, pp. 4182–4194, 2010.
- [10] R. Fa and R. C. de Lamare, "Reduced-rank STAP algorithms using joint iterative optimization of filters," *IEEE Transactions on Aerospace and Electronic Systems*, vol. 47, no. 3, pp. 1668–1684, 2011.
- [11] J. R. Román, M. Rangaswamy, D. W. Davis, Q. Zhang, B. Himed, and J. H. Michels, "Parametric adaptive matched filter for airborne radar applications," *IEEE Transactions on Aerospace and Electronic Systems*, vol. 36, no. 2, pp. 677–692, 2000.
- [12] Z. Yang, R. C. de Lamare, and X. Li, " L_1 -regularized STAP algorithms with a generalized sidelobe canceler architecture for airborne radar," *IEEE Transactions on Signal Processing*, vol. 60, no. 2, pp. 674–686, 2012.
- [13] Z. Yang, R. C. de Lamare, and X. Li, "Sparsity-aware space-time adaptive processing algorithms with L_1 -norm regularisation for airborne radar," *IET Signal Processing*, vol. 6, no. 5, pp. 413–423, 2012.
- [14] Z. Yang, X. Li, H. Wang, and W. Jiang, "On clutter sparsity analysis in space-time adaptive processing airborne radar," *IEEE Geoscience and Remote Sensing Letters*, vol. 10, no. 5, pp. 1214–1218, 2013.
- [15] Z. Yang, X. Li, H. Wang, and W. Jiang, "Adaptive clutter suppression based on iterative adaptive approach for airborne radar," *Signal Processing*, vol. 93, no. 12, pp. 3567–3577, 2013.
- [16] Z. Yang, X. Li, H. Wang, and L. Nie, "Sparsity-based space-time adaptive processing using complex-valued homotopy technique for airborne radar," *IET Signal Processing*, vol. 8, no. 5, pp. 552–564, 2014.
- [17] J. R. Guerci and E. J. Baranoski, "Knowledge-aided adaptive radar at DARPA," *IEEE Signal Processing Magazine*, vol. 23, no. 1, pp. 41–50, 2006.
- [18] M. C. Wicks, M. Rangaswamy, R. Adve, and T. B. Hale, "Space-time adaptive processing," *IEEE Signal Processing Magazine*, vol. 23, no. 1, pp. 51–65, 2006.
- [19] W. L. Mevin and G. A. Showman, "An approach to knowledge-aided covariance estimation," *IEEE Transactions on Aerospace and Electronic Systems*, vol. 42, no. 3, pp. 1021–1042, 2006.
- [20] W. Xie, K. Duan, F. Gao, Y. Wang, and Z. Zhang, "Clutter suppression for airborne phased radar with conformal arrays by least squares estimation," *Signal Processing*, vol. 91, no. 7, pp. 1665–1669, 2011.
- [21] I. W. Selesnick, S. U. Pillai, K. Y. Li, and B. Himed, "Angle-Doppler processing using sparse regularization," in *Proceedings of the IEEE International Conference on Acoustics, Speech, and Signal Processing (ICASSP '10)*, pp. 2750–2753, March 2010.
- [22] C. Chen and P. P. Vaidyanathan, "MIMO radar space-time adaptive processing using prolate spheroidal wave functions," *IEEE Transactions on Signal Processing*, vol. 56, no. 2, pp. 623–635, 2008.
- [23] P. Stoica, J. Li, X. Zhu, and J. Guerci, "On using a priori knowledge in space-time adaptive processing," *IEEE Transactions on Signal Processing*, vol. 56, no. 6, pp. 2598–2602, 2008.
- [24] J. R. Guerci, *Cognitive Radar: The Knowledge-Aided Fully Adaptive Approach*, Artech House, London, UK, 2010.
- [25] J. S. Bergin, P. M. Techau, W. L. Melvin, and J. R. Guerci, "GMTI STAP in target-rich environments: site-specific analysis," in *Proceedings of the IEEE Radar Conference*, pp. 391–396, Long Beach, Calif, USA, April 2002.
- [26] J. S. Bergin, C. M. Teixeira, P. M. Techau, and J. R. Guerci, "Improved clutter mitigation performance using knowledge-aided space-time adaptive processing," *IEEE Transactions on Aerospace and Electronic Systems*, vol. 42, no. 3, pp. 997–1008, 2006.
- [27] E. Conte, A. de Maio, A. Farina, and G. Foglia, "Design and analysis of a knowledge-aided radar detector for Doppler processing," *IEEE Transactions on Aerospace and Electronic Systems*, vol. 42, no. 3, pp. 1058–1079, 2006.
- [28] K. Gerlach and M. L. Picciolo, "Airborne/spacebased radar STAP using a structured covariance matrix," *IEEE Transactions on Aerospace and Electronic Systems*, vol. 39, no. 1, pp. 269–281, 2003.
- [29] X. Zhu, J. Li, and P. Stoica, "Knowledge-aided space-time adaptive processing," *IEEE Transactions on Aerospace and Electronic Systems*, vol. 47, no. 2, pp. 1325–1336, 2011.
- [30] R. Fa, R. C. de Lamare, and V. H. Nascimento, "Knowledge-aided STAP algorithm using convex combination of inverse covariance matrices for heterogeneous clutter," in *Proceeding of the IEEE International Conference on Acoustics, Speech, and Signal Processing (ICASSP '10)*, pp. 2742–2745, Dallas, Tex, USA, March 2010.

- [31] Q. Zhang and W. B. Mikhael, "Estimation of the clutter rank in the case of subarraying for space-time adaptive processing," *Electronics Letters*, vol. 33, no. 5, pp. 419–420, 1997.
- [32] N. A. Goodman and J. M. Stiles, "On clutter rank observed by arbitrary arrays," *IEEE Transactions on Signal Processing*, vol. 55, no. 1, pp. 178–186, 2007.
- [33] R. A. Horn and C. R. Johnson, *Matrix Analysis*, Cambridge University Press, Cambridge, UK, 1985.

Research Article

Spatial Spectrum-Based Imaging for UWB Through-the-Wall MIMO Arrays

Biying Lu, Xin Sun, Yang Zhao, and Zhimin Zhou

College of Electronic Science and Engineering, National University of Defense Technology, Changsha, Hunan 410073, China

Correspondence should be addressed to Biying Lu; lubiyang@nudt.edu.cn

Received 2 April 2014; Revised 23 June 2014; Accepted 28 June 2014; Published 21 July 2014

Academic Editor: Ahmed Shaharyar Khwaja

Copyright © 2014 Biying Lu et al. This is an open access article distributed under the Creative Commons Attribution License, which permits unrestricted use, distribution, and reproduction in any medium, provided the original work is properly cited.

To keep the system complexity at a reasonable level and conform to the propagation demands, MIMO arrays are usually sparse in through-the-wall applications, which results in corrupted and gapped data. The corresponding imaging results are seriously affected by the high-level sidelobes. To solve this problem, a new imaging model for ultra-wideband (UWB) MIMO arrays is constructed via spatial spectrum theory in this paper. Based on the model, the characteristics of the spatial spectrum for the MIMO array and its effects on imaging are discussed. To improve the imaging quality, a through-the-wall imaging enhancement method is proposed via spatial spectrum estimation. Synthetic and experimental results show that, unlike the conventional amplitude weighting methods and nonlinear techniques, the proposed method can efficiently suppress sidelobes in the imagery, especially for the sparse MIMO array, and consequently improve the target image quality without degrading the mainlobe resolution. The proposed method has been successfully used in our real through-the-wall radar system.

1. Introduction

Ultra-wideband (UWB) through-the-wall imaging (TWI) approaches that can detect objects through obstacles, such as walls, doors, and other opaque materials, are considered powerful tools for a variety of civilian and military applications [1–5].

In TWI applications, the imaging component of the application is considered the most important because it is usually the first step for the subsequent processes, such as detection, identification, and wall parameters estimation [6–10]. Currently, to obtain a satisfying target image, two types of radars are widely used: synthetic aperture radar (SAR) and multiple input multiple output (MIMO) radar. Although SAR has better resolution, it has a heavy time cost. By using the high-speed electronic switch, the time to acquire a dataset in a MIMO system is greatly reduced, compared to SAR systems. Therefore, MIMO radar is preferred over SAR in real applications, especially for moving target imaging.

By using the proper array design method, we can obtain an optimal array configuration. However, in certain

real cases, the equipment complexity and the shape may be our first consideration. Therefore, we make the tradeoff between size and performance [11]. For example, to achieve the Nyquist sampling criterion, the interelement space (d) must be kept below half of the wavelength (λ) for the MIMO array [12]. However, conforming to this criterion will lead to a large number of array elements, even for a small aperture. Usually, when a MIMO array is used in TWI applications, the element spacing is made significantly higher than $\lambda/2$ to keep the system complexity at reasonable levels and to increase the element size to achieve an acceptable SNR. Furthermore, for a typical TWI radar system, the most commonly used frequency range is from 1 GHz to 3 GHz to support the range resolution and wall propagation ability. Therefore, for the ultra-wideband signal, even if more elements can be placed in the equipment, the elements are usually dense in the low frequency band but sparse in the high frequency band. In such a case, the MIMO array will not be optimal but it will be sparse with gapped virtual elements, which would otherwise diminish the array imaging performance. As a result, the image quality of the TWI results, in real

applications, is significantly limited by the ratio of the main to sidelobe amplitude.

To suppress the sidelobes and improve the image quality, many imaging methods for through-the-wall imaging, including the back projection (BP) method [13, 14], the beamforming method [15, 16], and the tomography method [17, 18], are presented in recent years. In these methods, the sidelobes are reduced by applying an amplitude weighting function to the data prior to the final IFFT. However, the sidelobes have been reduced at the expense of the main lobe width, which determines the ultimate resolution of the imagery [19]. For example, the Hanning main lobe is twice as wide (null-to-null) as the sinc function. These methods are consequently a compromise between a narrow main lobe (high resolution) and low sidelobes.

To retain the main lobe resolution while reducing the sidelobes, several nonlinear signal processing methods are introduced into radar imaging. Typical methods include spatially variant apodization (SVA), super-SVA, and the CLEAN technique [19–22]. By using interpolation or extrapolation operations, these methods are successfully used in SAR signal data processing to minimize the effects of corrupted and gapped data. However, for MIMO radar, because of the more complicated signal channels, the distribution of the received data is significantly different from that in SAR. In this situation, the performance of these methods is seriously affected.

Based on the rigorous derivation of the UWB MIMO array and experimental validation via real TWI radar systems, we proposed in this paper a through-the-wall imaging enhancement method via spatial spectrum theory. Unlike the conventional amplitude weighting methods and nonlinear techniques, the proposed method can effectively suppress the sidelobes from imagery, especially for the UWB sparse MIMO array, and consequently enhance the target image quality without degrading the main lobe resolution.

This paper is organized as follows. In Section 2, the imaging model for the MIMO array is constructed via spatial spectrum theory. Then, the spatial spectrum of the UWB MIMO array is deeply analyzed. The effects of the spatial spectrum distribution on PSF are discussed, and the spatial spectrum characteristics for the typical TWI UWB MIMO array are obtained. In Section 4, to improve the image quality, an imaging enhancement method by spatial spectrum estimation is proposed. Synthetic and experimental processing results are given in Section 5. Conclusions end this paper.

2. Spatial Spectrum-Based Imaging Model for a MIMO Array

We assume a MIMO array has M transmitters and N receivers, as shown in Figure 1. For convenience, in the following derivation we choose one transmitter and one receiver, and the polar coordinate origin is assumed at the target center. We assume a stepped frequency waveform as the

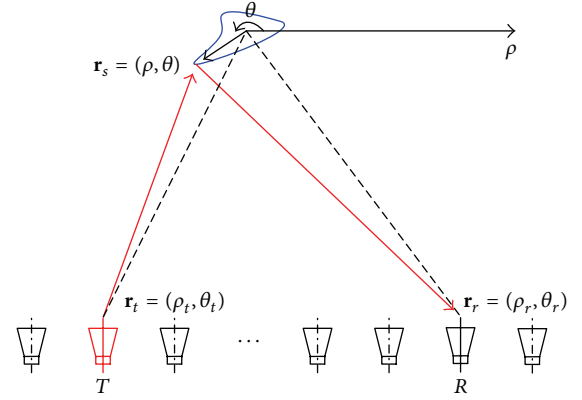


FIGURE 1: The geometry of the MIMO array imaging scene.

transmitted signal, which has a frequency range of $[f_0, f_{P-1}]$ and a frequency increment of Δf :

$$s(t) = \sum_{p=0}^{P-1} e^{j2\pi f_p t}, \quad (1)$$

$$f_p = (f_0 + p\Delta f), \quad p = 0, 1, \dots, P-1,$$

where f_0 is the start frequency. The variable P denotes the frequency numbers.

We consider a general bistatic radar scene with a target as shown in Figure 1. The transmitter located at $\mathbf{r}_t = (R_t, \theta_t)$ transmits the EM wave. The wave arrives at the reflection point located at $\mathbf{r}_s = (\rho, \theta)$ and is backscattered. Under the assumption of free space propagation, the total received backscattered field of the distributed target by the receiver at $\mathbf{r}_r = (R_r, \theta_r)$ can be expressed as

$$G(f_p, \mathbf{r}_t, \mathbf{r}_r) = \int_{\rho} \int_{\theta} \sigma(\rho, \theta) e^{j2\pi(f_p/c)(|\mathbf{r}_t - \mathbf{r}_s| + |\mathbf{r}_r - \mathbf{r}_s|)} d\rho d\theta, \quad (2)$$

where $\sigma(\rho, \theta)$ is the reflection function of the target. Assuming $\rho \ll \rho_t$ and $\rho \ll \rho_r$, the following approximation holds:

$$|\mathbf{r}_t - \mathbf{r}_s| \approx \rho_t - \rho \cos(\theta - \theta_t), \quad (3a)$$

$$|\mathbf{r}_r - \mathbf{r}_s| \approx \rho_r - \rho \cos(\theta - \theta_r). \quad (3b)$$

Then, (2) becomes

$$\begin{aligned} G(f_p, \mathbf{r}_t, \mathbf{r}_r) &= e^{j2\pi(f_p/c)(\rho_t + \rho_r)} \\ &\times \int_{\rho} \int_{\theta} \sigma(\rho, \theta) e^{-j2\pi(f_p/c)[\rho \cos(\theta - \theta_t) + \rho \cos(\theta - \theta_r)]} d\rho d\theta. \end{aligned} \quad (4)$$

The fixed value $e^{j2\pi(f_p/c)(\rho_t+\rho_r)}$ outside the integrals can be neglected. We define $x = \rho \cos \varphi$, $y = \rho \sin \varphi$ in the equivalent Descartes coordinates and the wavenumber $k = 2\pi f_p/c$ in the expression. Then, we rewrite (2) in the Descartes coordinate system:

$$\begin{aligned} G(k, \mathbf{r}'_t, \mathbf{r}'_r) &= \int_x \int_y \sigma(x, y) e^{-jk[(\cos \theta_t + \cos \theta_r)x + (\sin \theta_t + \sin \theta_r)y]} dx dy \quad (5) \\ &= \int_x \int_y \sigma(x, y) e^{-j[(k_{t,x} + k_{r,x})x + (k_{t,y} + k_{r,y})y]} dx dy, \end{aligned}$$

where \mathbf{r}'_t and \mathbf{r}'_r denote the positions of the transmitter and receiver, respectively, in Descartes coordinates. $k_{t,x} = k \cos \theta_t$ and $k_{t,y} = k \sin \theta_t$ are the transmitter wavenumbers in the directions of the x -axis and y -axis. $k_{r,x} = k \cos \theta_r$ and $k_{r,y} = k \sin \theta_r$ are the receiver wavenumbers in the directions of the x -axis and y -axis.

We further define the virtual wavenumbers $k_{v,x} = k_{t,x} + k_{r,x}$ and $k_{v,y} = k_{t,y} + k_{r,y}$. Then, the spatial spectrum $G(k_{v,x}, k_{v,y})$ can be expressed as the 2D Fourier transform of the target reflection function, $\sigma(x, y)$

$$G(k_{v,x}, k_{v,y}) = \int_x \int_y \sigma(x, y) e^{-j(k_{v,x}x + k_{v,y}y)} dx dy. \quad (6)$$

If the wavenumbers are expressed in the form of vectors as $\mathbf{k}_v = [k_{v,x}, k_{v,y}]^T$, $\mathbf{k}_t = [k_{t,x}, k_{t,y}]^T$, and $\mathbf{k}_r = [k_{r,x}, k_{r,y}]^T$, then

$$\mathbf{k}_v = \mathbf{k}_t + \mathbf{k}_r = 2k \cos \frac{\theta_t - \theta_r}{2} \left[\cos \frac{\theta_t + \theta_r}{2} \sin \frac{\theta_t + \theta_r}{2} \right]^T. \quad (7)$$

Here, the vector \mathbf{k}_v is the wavenumber for the virtual element, which, as shown in Figure 2, is the vector sum of the transmitter wavenumber \mathbf{k}_t and the receiver wavenumber \mathbf{k}_r .

Therefore, by taking the inverse Fourier transform of the spatial spectrum of the target scattering, that is, $G_M(k_x, k_y)$, the target image can be obtained:

$$I(x, y) = \int_{k_x} \int_{k_y} G_M(k_x, k_y) \exp[j(k_x x + k_y y)] dk_x dk_y. \quad (8)$$

As a result, for the MIMO array constructed by M transmitters and N receivers, the spatial spectrum of the

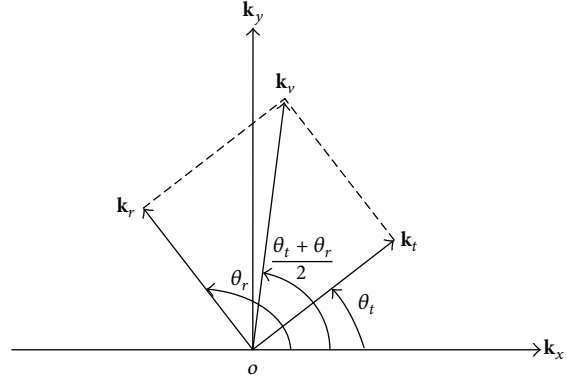


FIGURE 2: The relationship between the virtual element wavenumber, the transmitter wavenumber, and the receive wavenumber.

received signal is determined by the array structure. By using an ideal point target located at the origin, that is, $\sigma(x, y) = \delta(x)\delta(y)$, the point spread function (PSF) of the array system can be demonstrated by (9) in the spatial spectrum domain:

$$P_M(k_x, k_y) = \begin{cases} 1, & (k_x, k_y) \in \mathbf{K} \\ 0, & (k_x, k_y) \notin \mathbf{K} \end{cases} \quad (9)$$

where \mathbf{K} is the support area of the spatial spectrum. After the inverse Fourier transform is performed, the spatial expression of the PSF is

$$\begin{aligned} \text{PSF}_M(x, y) &= \int_{k_x} \int_{k_y} P_M(k_x, k_y) \\ &\quad \times \exp[j2\pi(k_x x + k_y y)] dk_x dk_y. \end{aligned} \quad (10)$$

According to (9) and (10), for a MIMO imaging system, the PSF is equivalent to the support area of the spatial spectrum, and the performance of the imaging system can be depicted by the support area of the spatial spectrum.

3. Spatial Spectrum Analysis for the UWB MIMO Array

As we know, an imaging system can be fully characterized by the point spread function (PSF) defined as the response of the imaging system to an ideal point source. Equation (10) presents the relationship between the spatial spectrum distribution and the PSF. In this section, the effects of the spatial spectrum distribution on PSF are first discussed. Then, the spatial spectrum of the typical through-the-wall UWB MIMO array is analyzed.

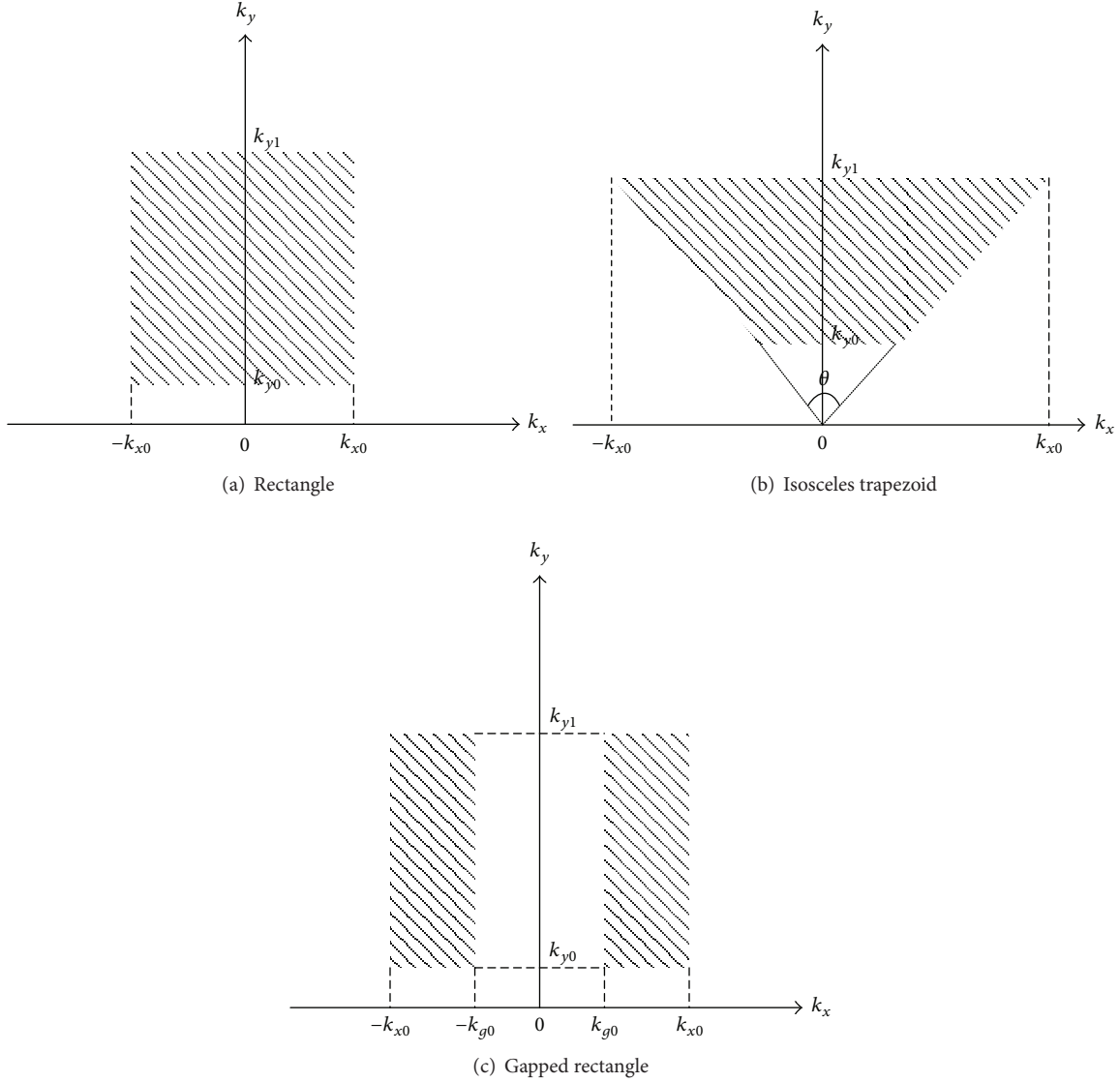


FIGURE 3: Geometric shapes of the spatial spectrum support area.

3.1. *Effects of the Spatial Spectrum Distribution on the PSF.* For an imaging system, the ideal support area of the spatial spectrum is an evenly sampled rectangle, as shown in Figure 3(a). The corresponding PSF is

$$\begin{aligned} \text{PSF}_r(x, y) &= \int_{-k_{x0}}^{k_{x0}} \exp(j2\pi x k_x) dk_x \\ &\cdot \int_{k_{y0}}^{k_{y1}} \exp(j2\pi y k_y) dk_y \\ &= \phi \frac{\sin(\pi \Delta k_x x)}{\pi x} \frac{\sin(\pi \Delta k_y y)}{\pi y}, \end{aligned} \quad (11)$$

where $\Delta k_x = 2k_{x0}$, $\Delta k_y = k_{y1} - k_{y0}$, and $\phi = e^{j\pi(k_{y1} + k_{y0})y}$ are the phase term. The resolution of the image is

$$\rho_x = \frac{1}{\Delta k_x}, \quad (12a)$$

$$\rho_y = \frac{1}{\Delta k_y}. \quad (12b)$$

In this situation, the highest level of the sidelobe for the sinc function is -13.3 dB, and the sidelobes are orthogonal and spread along the x - and y -axes (see Figure 4(d)).

Unfortunately, the support area of a wideband wide beam imaging system is an annulus sector. In this situation, a trapezoid is used instead of a rectangle to approximate the actual spectral support area to increase the resolution [23, 24]. Furthermore, the support area of the acquired

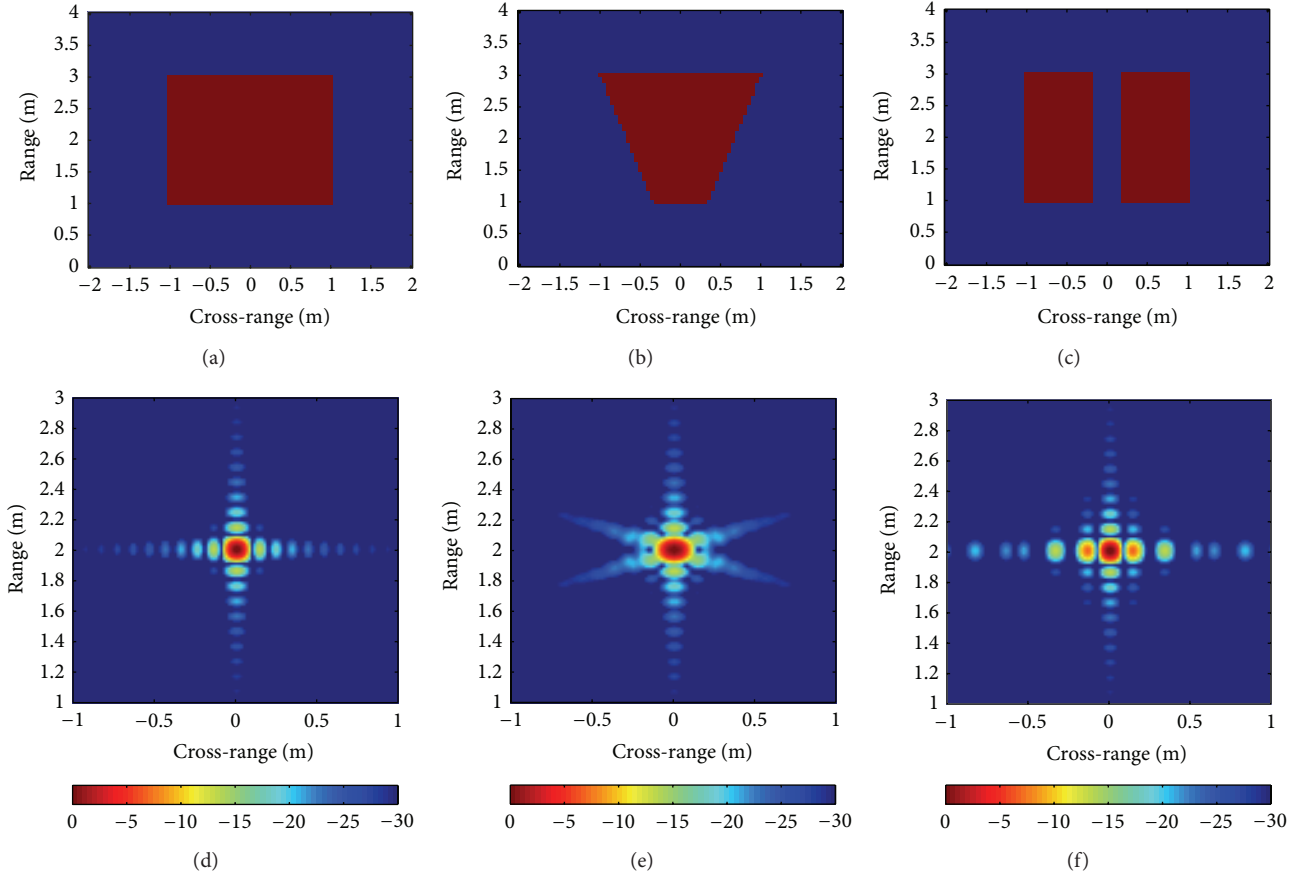


FIGURE 4: Three different support areas of the spatial spectrum and the corresponding target images: (a) rectangle, (b) isosceles trapezoid, (c) gapped rectangle, (d) target image for Figure 4(a), (e) target image for Figure 4(b), and (f) target image for Figure 4(c).

spectrum is often not continuous due to incomplete data. In radar imaging, a target may be illuminated by the radar from several separate angular regions to improve cross-range resolution, and, consequently, the sampled data will have missing columns [25, 26]. For the imaging system using fixed aperture, sparse arrays rather than filled arrays are preferred to reduce the number of array elements, which means that spatial samples can more easily be missed [22, 27, 28].

For the isosceles trapezoid shown in Figure 3(b), the PSF is given as

$$\begin{aligned}
 \text{PSF}_t(x, y) &= \int_{k_{y0}}^{k_{y1}} \int_{-k_y \tan \theta/2}^{k_y \tan \theta/2} \exp(j2\pi x k_x) \exp(j2\pi y k_y) dk_x dk_y \\
 &= \left(\cos \left[\pi (k_{y1} + k_{y0}) \left(y + x \tan \frac{\theta}{2} \right) \right] \right. \\
 &\quad \times \left. \sin \left[\pi (k_{y1} - k_{y0}) \left(y + x \tan \frac{\theta}{2} \right) \right] \right) \\
 &\quad \times \left(\pi x \left(y + x \tan \frac{\theta}{2} \right) \right)^{-1}
 \end{aligned}$$

$$\begin{aligned}
 &+ \left(\cos \left[\pi (k_{y1} + k_{y0}) \left(y - x \tan \frac{\theta}{2} \right) \right] \right) \\
 &\quad \times \sin \left[\pi (k_{y1} - k_{y0}) \left(y - x \tan \frac{\theta}{2} \right) \right] \\
 &\quad \times \left(\pi x \left(y - x \tan \frac{\theta}{2} \right) \right)^{-1},
 \end{aligned} \tag{13}$$

where θ is the processing angle shown in Figure 3(b). Equation (13) indicates that the sidelobes are nonorthogonal and spread along the linear axes with $y = \pm x \tan \theta/2$ (see Figure 4(e)).

For the gapped spatial spectrum shown in Figure 3(c), the PSF is given as

$$\begin{aligned}
 \text{PSF}_g(x, y) &= \left(\int_{-k_{x0}}^{k_{x0}} \exp(j2\pi k_x x) dk_x - \int_{-k_{g0}}^{k_{g0}} \exp(j2\pi k_x x) dk_x \right)
 \end{aligned}$$

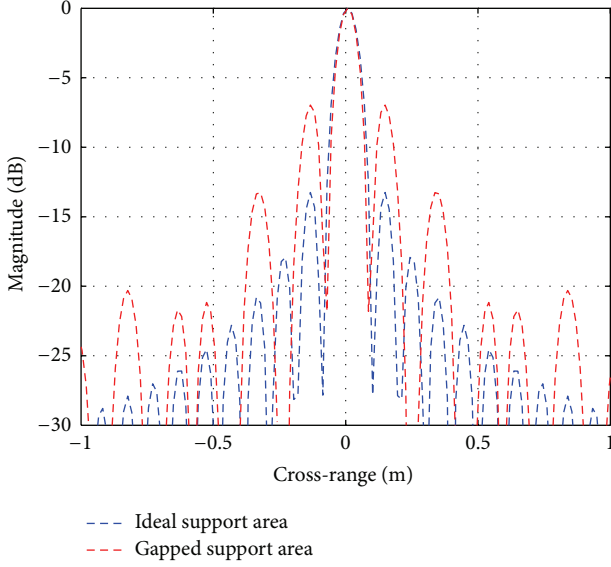


FIGURE 5: The PSF figures in the cross-range direction. In the figure, the blue lines denote the PSF for the ideal support area, that is, Figure 4(a). The red lines denote the PSF for the gapped support area, that is, Figure 4(c).

$$\begin{aligned} & \times \int_{k_{y0}}^{k_{y1}} \exp(j2\pi k_y) dk_y \\ & = \frac{\sin(2\pi k_{x0}x) - \sin(2\pi k_{g0}x)}{\pi x} \cdot \frac{\sin(2\pi(k_{y1} - k_{y0})y)}{\pi y}. \end{aligned} \quad (14)$$

To analyze the effects of the gapped spatial spectrum on the imaging result, Figure 4 shows three support areas of the spatial spectrum, that is, rectangle, isosceles trapezoid and gapped rectangle, and the corresponding target images. For the rectangle and gapped rectangle support area, the sidelobes are orthogonal and spread along the x - and y -axes. When the support area is an isosceles trapezoid, its sidelobes are no longer orthogonal. Additionally, by comparing Figure 4(d) and Figure 4(f), we can find that when the support area is gapped, the sidelobes are significantly enhanced. As a result, the target imaging quality in Figure 4(f) is seriously affected. The PSF figures in the cross-range direction for the ideal support area and the gapped support area are given in Figure 5. The red lines and the blue lines correspond to Figure 4(d) and Figure 4(f), respectively. The main lobe is approximately unchanged, but the sidelobes are significantly different. The highest level of the sidelobes is -13.3 dB in the case of ideal support area and -7.0 dB when the support area is gapped, as in Figure 4(c).

According to the derivation and figures, the PSF performance is determined by the spatial spectrum distribution. Furthermore, the distribution and levels of the sidelobes are determined by the shape and density of the spatial spectrum, respectively.

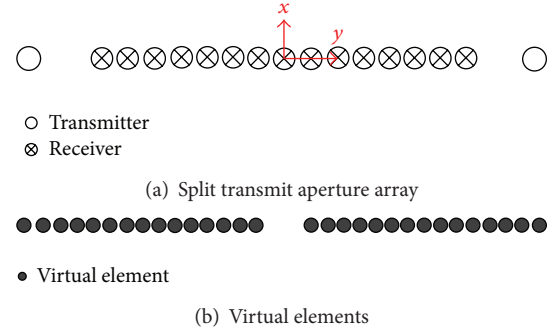


FIGURE 6: Split transmit virtual aperture array and its virtual elements.

3.2. Spatial Spectrum of the Typical TWI UWB MIMO Array. Three characteristics of the spatial spectrum for the UWB MIMO array can be determined. First, a large processing angle is needed in the low frequency band to obtain a satisfying azimuth resolution. However, in real practice, the processing angle is usually limited. Therefore, the support area is no longer nearly rectangular but is described by an annulus sector. In this situation, the trapezoid is usually used instead of the rectangle to approximate the actual spectral support area. Second, to keep the system complexity reasonable, the elements are usually sparse and the element spacing is significantly higher than $\lambda/2$. For the ultra-wideband signal, the spatial spectrum will be dense in the low frequency band and sparse in the high frequency band. Third, for some MIMO arrays with special structures, the corresponding spatial spectrums may be gapped.

In order to explain the characteristics, here we take a sparse array, for example. The configuration of the array is shown in Figure 6(a), and the receiver array consists of 15 elements with an interelement spacing of 0.2 m. Two transmit elements are located at $(-2$ m, 0 m) and $(2$ m, 0 m), at the ends of the array. The physical aperture length of the array is 4 m. Using the concept of a virtual phase center, a virtual aperture with 30 virtual transmit/receive (T/R) elements is synthesized, as shown in Figure 6(b). The interelement spacing of the synthesized virtual aperture is 0.1 m except for a gap of 0.6 m at the midpoint, synthesizing a total aperture length of 3.4 m. The gap at the midpoint is due to the separation of the transmit elements.

The transmitted signal is a stepped frequency waveform, with a range from 0.5 GHz to 1 GHz. The increment frequency is 2 MHz. For a point target located at $(0$ m, 5 m), we obtain the spatial spectrum support area shown in Figure 7. There are 30 dotted lines in the figure, corresponding to the 30 virtual elements, and the envelope of the support area is an isosceles trapezoid. For each dotted line, the points are dense when k_y is small (corresponding to low frequency) and sparse when k_y is large (corresponding to high frequency). Unfortunately, the support area is missing in the middle region, which is caused by the gap in the virtual elements.

To analyze the effects of the gapped spatial spectrum on target imaging, the result and profile in the cross-range direction are presented in Figures 8 and 9, respectively. The

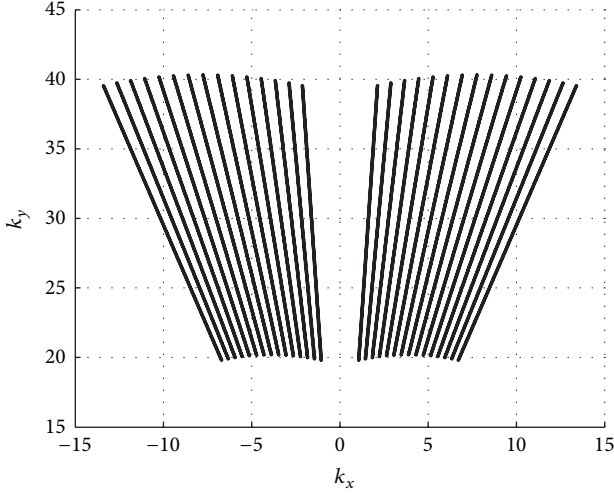


FIGURE 7: Support area of the spatial spectrum for this array.

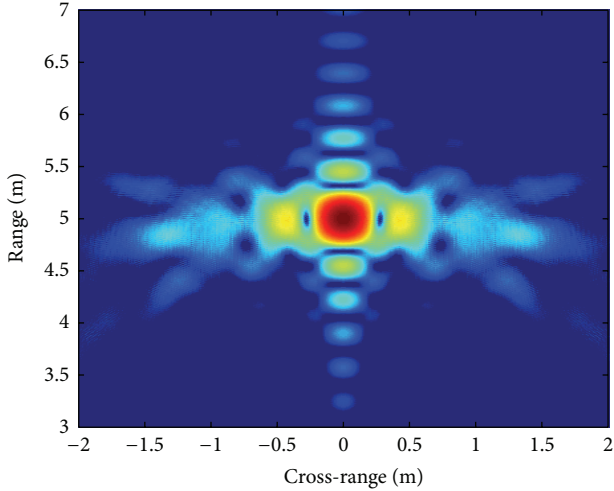


FIGURE 8: The target imaging result.

whole target image is severely affected, and the highest level of the sidelobes is -10.67 dB.

4. Through-the-Wall Imaging Enhancement via Spatial Spectrum Estimation

As shown in the analysis above, the serious sidelobes problem in the STVA system is caused by the missing spatial spectrum. To suppress the sidelobes, conventional methods are applied using a weighting function, such as the Hanning, Hamming, or Blackman functions. However, these weighting methods suppress the sidelobes at the expense of the main lobe resolution. A through-the-wall imaging enhancement method via a spatial spectrum estimation for suppressing the sidelobes without degrading the main lobe resolution is presented in this section.

The principle of our method is to extrapolate the missing support area using the existing spatial spectrum. Then,

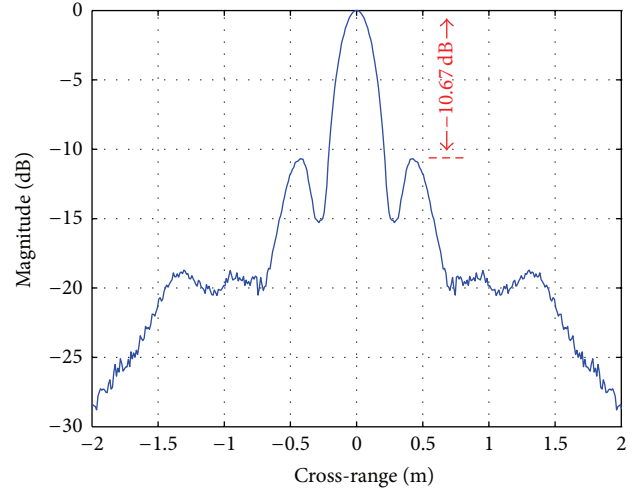


FIGURE 9: The profile in the cross-range direction of the target image.

according to the filled support area, the sidelobes-suppressed image can be obtained by applying the two-dimensional inverse Fourier transform.

The common method for obtaining the support area of the spatial spectrum for the target image is the Stolt interpolation, which is widely used in far-field-based imaging. However, in TWI MIMO radar applications, the distribution of the spatial spectrum is so complicated that the interpolation processing is inaccurate. According to the derived relationship between the image and the spatial spectrum, in our method, the support area is obtained by taking the 2D Fourier transform of the image. Thus, the steps of our method are as follows.

Step 1. Perform the imaging processing for the received echo. Here, we take the BP imaging method as an example. In the imaging operation, the region of interest is divided into a finite number of pixels in the range and cross-range directions. The complex amplitude image value for the pixel located at $\mathbf{x} = (x, y)$ is obtained by applying frequency-dependent phases and weights to all the received data:

$$I(x, y) = \iiint w \cdot S(f_m, \mathbf{x}_T, \mathbf{x}_R) \cdot \exp\left(\frac{j2\pi f_m r(\mathbf{x}_T, \mathbf{x}, \mathbf{x}_R)}{c}\right) d\mathbf{x}_T d\mathbf{x}_R df_m, \quad (15)$$

where w is the weighting function to shape the beam. $S(\cdot)$ is the received echo. \mathbf{x}_T and \mathbf{x}_R denote the transmitter and receiver positions. $r(\mathbf{x}_T, \mathbf{x}, \mathbf{x}_R)$ is the compensation signal distance for pixel \mathbf{x} , which is computed as follows:

$$r(\mathbf{x}_T, \mathbf{x}_q, \mathbf{x}_R) = \sqrt{(x_T - x_q)^2 + (y_T - y_q)^2} + \sqrt{(x_q - x_R)^2 + (y_q - y_R)^2}. \quad (16)$$

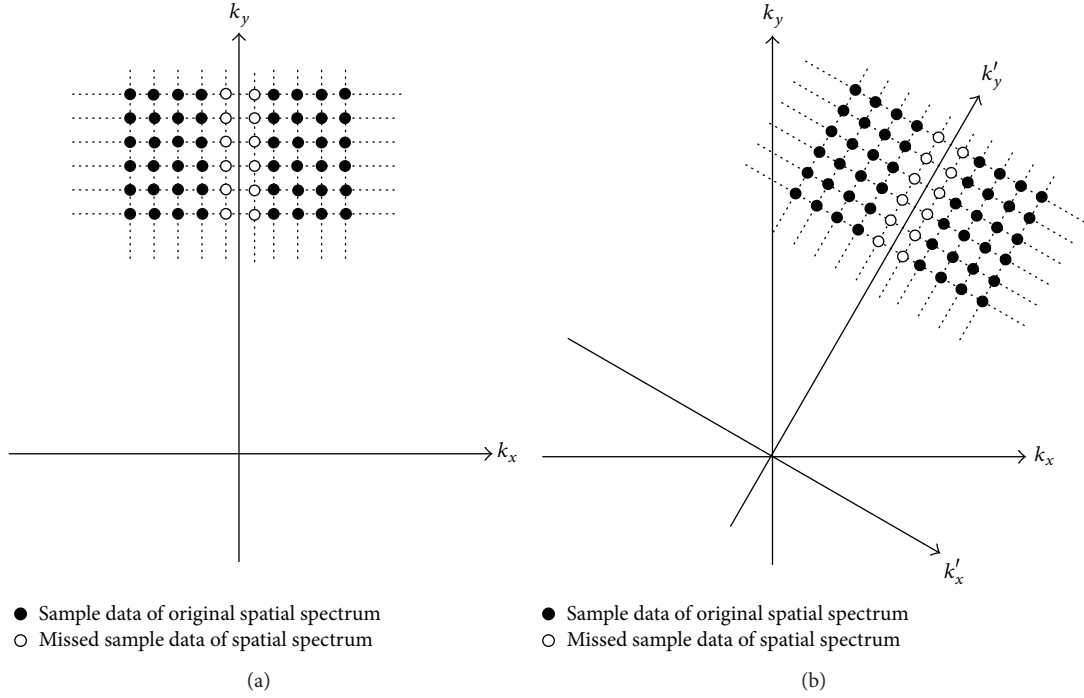


FIGURE 10: The missing sample data of the spatial spectrum can be estimated by the existing data. (a) The target is in the middle line of the array. (b) The target is not in the middle line of the array. In this situation, a transfer matrix is needed.

Step 2. Take the 2D Fourier transform of the imaging result, $I(x, y)$. Then, the corresponding support area of the spatial spectrum is obtained:

$$E(k_x, k_y) = \iint I(x, y) \exp[-j(k_x x + k_y y)] dx dy. \quad (17)$$

Here, $E(k_x, k_y)$ is the obtained support area of the spatial spectrum.

Step 3. Extrapolate the missing spatial spectrum. As shown in Figure 10, the black points denote the sample data in the original spatial spectrum and the white points are the missing spatial spectrum. Therefore, the missing spatial spectrum can be forecasted by the existing data. To obtain an accurate result, the left and right data are used to make forward and back forecasting, respectively. The forward forecasting and the back forecasting AR models are given in (18) and (19), respectively:

$$E_L(k_{x,p}, k_{y,q_0}) = -\sum_{i=1}^L b_L(i) E(k_{x,p-i}, k_{y,q_0}), \quad (18)$$

$$E_H(k_{x,p}, k_{y,q_0}) = -\sum_{i=1}^H b_H(i) E(k_{x,p+i}, k_{y,q_0}), \quad (19)$$

where the variables L and H denote the order of each model. The variables $b_L(i)$ and $b_H(i)$ denote the coefficient in the models. Here, the model order is evaluated by the forecasting

error, and the model coefficient is computed by the Burg algorithm.

Step 4. Update the k_{y,q_0} to estimate the missing spatial spectrum. Then, the filled spatial spectrum, denoted by $E'(k_x, k_y)$, is obtained.

Step 5. Take the 2D inverse Fourier transform of $E'(k_x, k_y)$. Then, the enhanced image, $I'(x, y)$, is obtained:

$$I'(x, y) = \iint E'(k_x, k_y) \exp[j(k_x x + k_y y)] dk_x dk_y. \quad (20)$$

When the target is not in the middle line of the array, the spatial spectrum will not be symmetrical along k_y , but will be symmetrical along k_v (see Figure 2). In this situation, (18) and (19) need to be reconstructed in a new coordinate system. By using the transfer matrix, the variables k_x and k_y in these expressions are replaced by k'_x and k'_y in the new coordinate system. The transfer matrix is

$$\begin{bmatrix} k'_x \\ k'_y \end{bmatrix} = \begin{bmatrix} \sin \frac{\theta_t + \theta_r}{2} & -\cos \frac{\theta_t + \theta_r}{2} \\ -\cos \frac{\theta_t + \theta_r}{2} & \sin \frac{\theta_t + \theta_r}{2} \end{bmatrix} \begin{bmatrix} k_x \\ k_y \end{bmatrix}, \quad (21)$$

where $(\theta_t + \theta_r)/2$ is the angle of vector k_v , which is marked in Figure 2.

Additionally, in TWI MIMO radar applications, different targets have different incident angles and received angles.

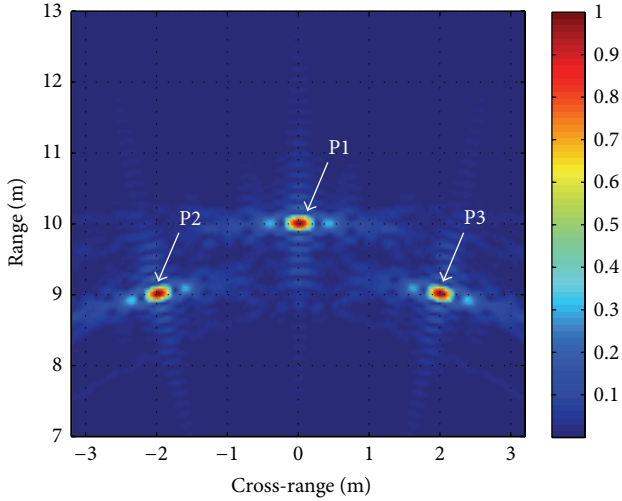


FIGURE 11: The original imaging result by the back projection imaging method.

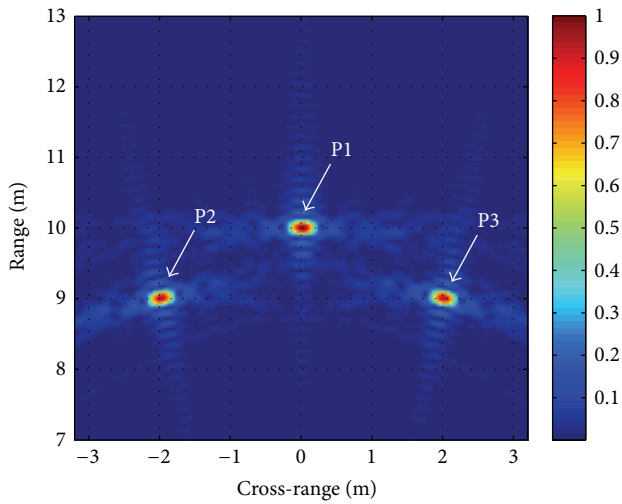


FIGURE 12: The processed result by the proposed method.

Therefore, the spatial spectrums of the targets will be located at different places. To minimize the effects of the overlapped spectrum, the whole image area can be divided into several small subregions. Then, the extrapolation can be applied in each subregion.

5. Simulated and Experimental Results

The simulation and experiments used to validate the proposed method are described in this section. In the simulation, the abovementioned array, which is shown in Figure 6, is adopted. In the coordinate system, the x-axis is along the array and the origin is the middle point of the array. Three point targets, located at (0 m, 10 m), (-2 m, 9 m), and (2 m, 9 m), are in free space. The stepped frequency signal, with a range from 1 GHz to 2 GHz, is used. The increment frequency is 5 MHz.

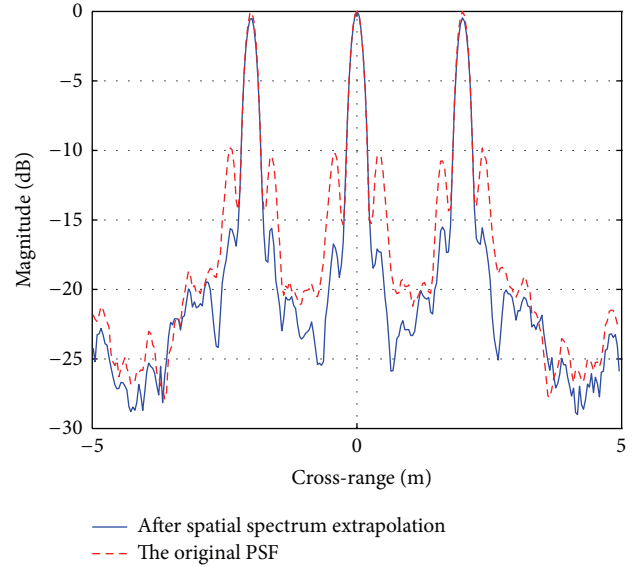


FIGURE 13: The sidelobes are suppressed by the proposed method. The PSLR for each target decreased from -10.0 dB to -15.9 dB, -17.1 dB, and -15.9 dB, respectively. The main lobes in this figure are all unchanged.

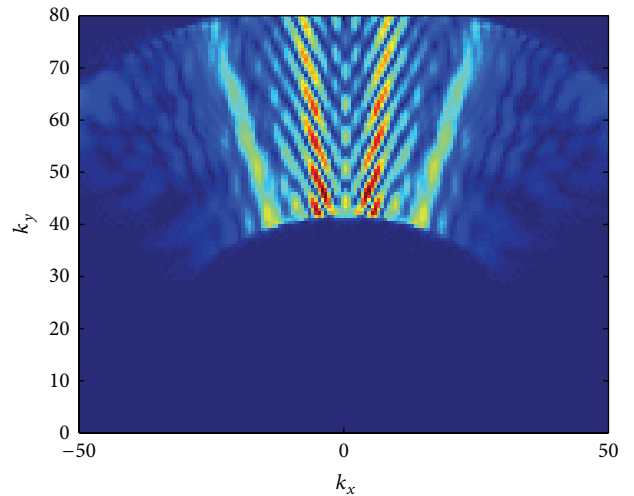


FIGURE 14: The spatial spectrums for the three targets overlap largely when we take the 2D Fourier transform of the whole image area.

Using the back projection (BP) imaging method, the original image is given in Figure 11. Figure 12 is the processed result made by our proposed method. The sidelobes of the three targets are shown to be efficiently suppressed. To analyze the algorithm performance quantitatively, the peak sidelobe ratio (PSLR) for each target is computed, which are suppressed from -10.0 dB to -15.9 dB, -17.1 dB, and -15.9 dB (see Figure 13). The main lobes for the three targets are unchanged.

Because the spatial spectrums of the targets overlap (see Figure 14), in our processing, we divide the imaging area into several subregions. Therefore, the spatial spectrum for

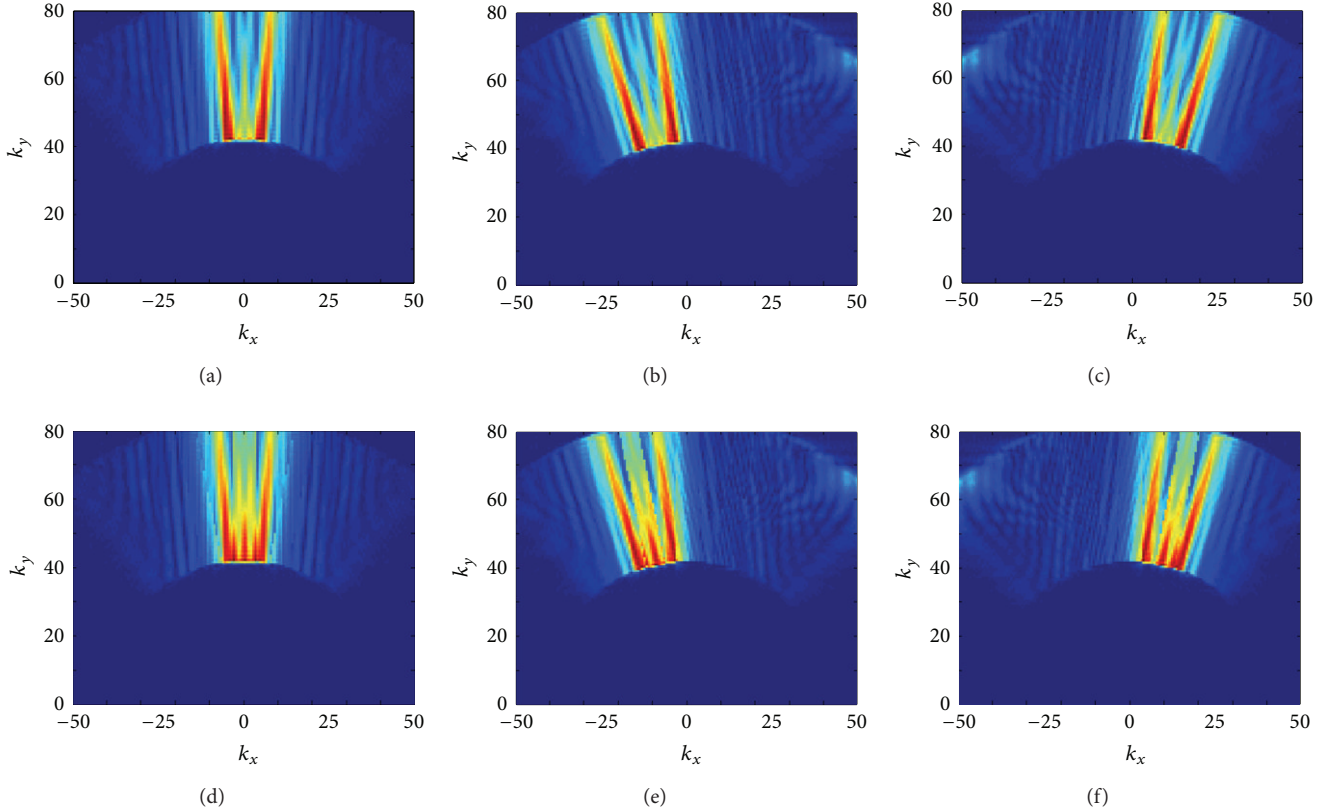


FIGURE 15: By dividing the imaging area into several subregions, the spatial spectrum for each target is obtained. (a–c) The gapped spatial spectrum for three targets, namely, P1, P2, and P3, respectively. (e–f) The extrapolated spatial spectrum for each target, that is, P1, P2, and P3.

each target is obtained by the 2D Fourier transform, which is shown in Figure 15. From Figures 15(a)–15(c), the spatial spectrums for these three targets are shown to be gapped. After spatial spectrum estimation, the missing spectrums are filled in (see Figures 15(d)–15(f)).

To validate the performance of the proposed method, the through-the-wall imaging experiments are processed in a real environment. In this experiment, a sparse STVA array, which has two transmitters and six receivers, is used. The length of the array is 4.1 m, and two transmitters are placed at the two ends of the array. The height of the array is 1.5 m and the interelement space of the receivers is 0.25 m. The antennas used in the system are Archimedes antennas. A transceiver module is designed to transmit and receive the EM wave. The waveform used in the system is stepped frequency signal. Its frequency range is from 1 GHz to 2 GHz, with the increment step of 2 MHz. The principle of the radar system is given in Figure 16.

Imaging data were collected by the radar system. Radar system is placed at the left side of a cinderblock building at a distance of 23.7 m. The antennas are parallel to the side wall. As shown in Figure 17, the thickness of the left-side cinderblock wall is 30 cm. The width of the left wall is 10 m and its extent is 4 m of the first floor. During the acquisition of the data, a 172-cm-tall man stands behind the wall and moves slightly (see Figure 17).

A standard differential back projection (BP) imaging algorithm is adopted to process the acquired data. It is noted that the wall parameters are estimated and compensated by using the image-domain method (see [14] for details). Figure 18 is the original imaging result. The human imaging has strong sidelobes and the image quality is severely affected. Using the proposed method, the processed result is shown in Figure 19. Compared with Figure 18, the sidelobes are efficiently suppressed and the image quality is significantly enhanced.

To validate the algorithm performance for the static target behind the wall, another experiment is processed. In the experiment, we use a 30 cm trihedral as the target. The trihedral is placed in the abovementioned building, with 2 m behind the side cinderblock wall (see Figure 20). The radar system is placed at the left side of the building, with a distance of 9 m.

By using the BP imaging method and background subtract technique, the original imaging result is obtained (see Figure 21). As shown in the figure, the trihedral is present in the image, but it has strong sidelobes. Then we use the proposed method to extrapolate its spatial spectrum, and consequently, the processing result is obtained (see Figure 22). It is shown that, after processed by the proposed method, the target imaging is significantly enhanced and its sidelobes are suppressed.

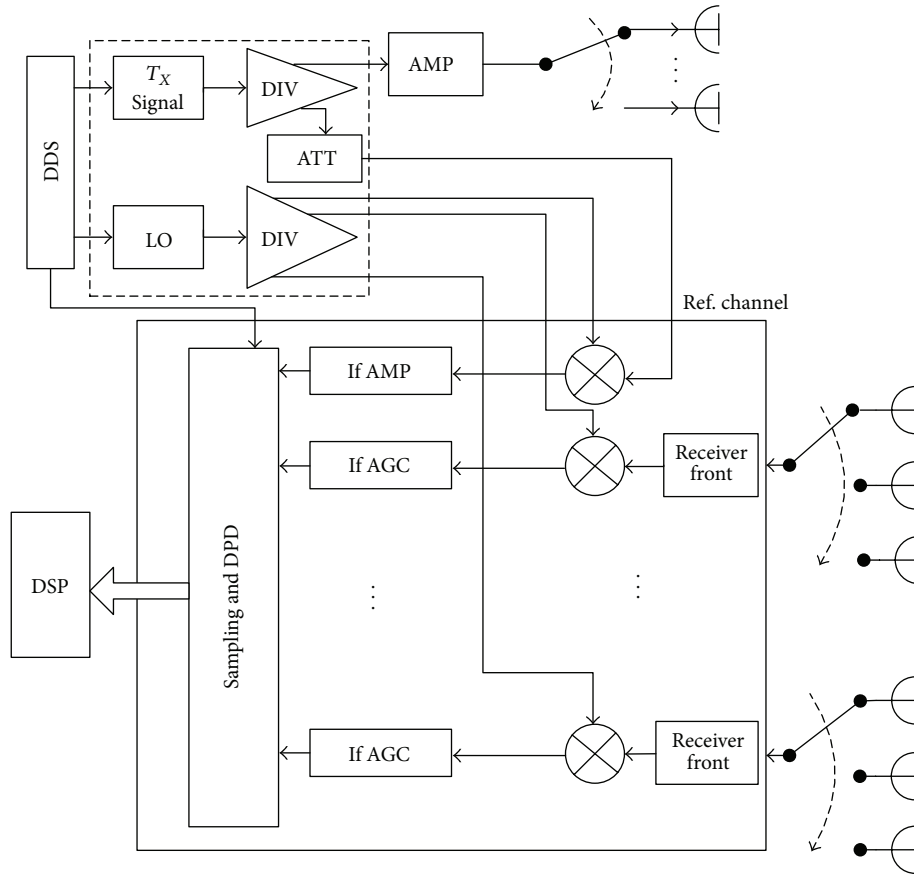


FIGURE 16: The principle diagram of through-the-wall radar system.

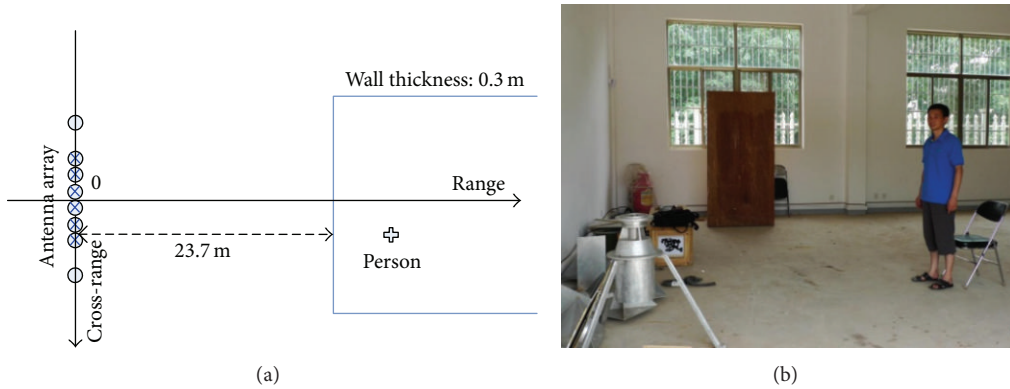


FIGURE 17: Imaging of a person inside a building: (a) the geometry of the imaging and (b) a man stands behind the left-side cinderblock wall.

6. Conclusion

In this paper, we construct an imaging model for an UWB MIMO radar via the spatial spectrum. The rigorous derivation of the model shows that the more spatial spectrum is used, the better imaging performance will be obtained. Therefore, when designing a MIMO array, the best solution is to make full use of the spatial spectrum. Unfortunately, to keep the system complexity at a reasonable level and conform to the propagation demands, MIMO arrays are usually sparse

in through-the-wall applications, which results in corrupted and gapped data. The corresponding imaging results are seriously affected by the high-level sidelobes.

Aiming at this problem, we proposed a spatial spectrum-based imaging enhancement method in this paper. By estimating the missing spatial spectrum, the effects of the gapped virtual elements can be significantly minimized. The processing results of the synthetic and experimental data show that the proposed method can efficiently improve the

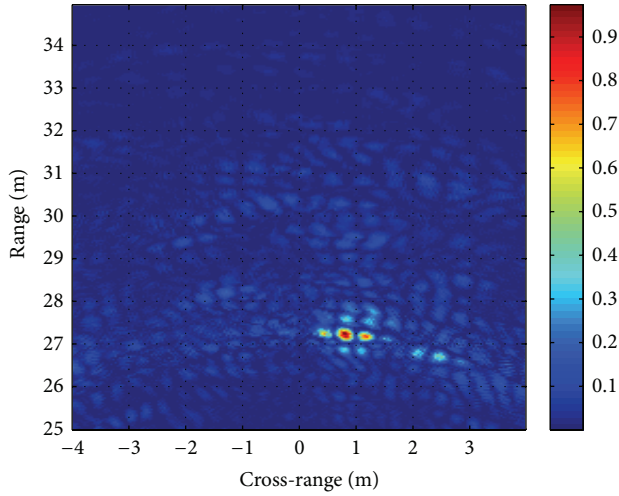


FIGURE 18: The original imaging result by the standard differential BP imaging algorithm.

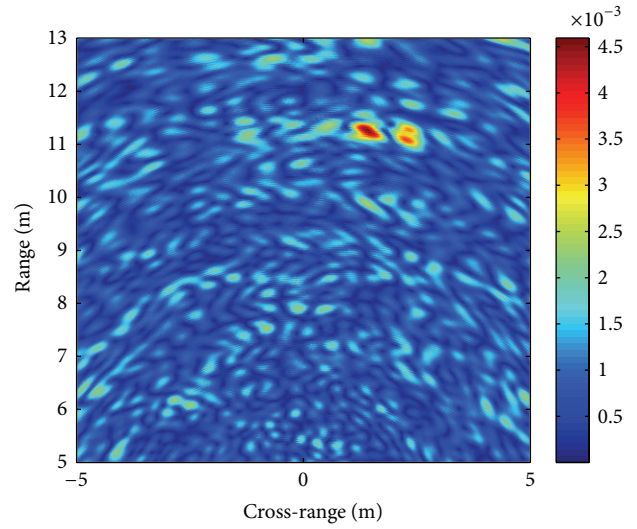


FIGURE 21: The original imaging result of the trihedral. In the figure, target has strong sidelobes.

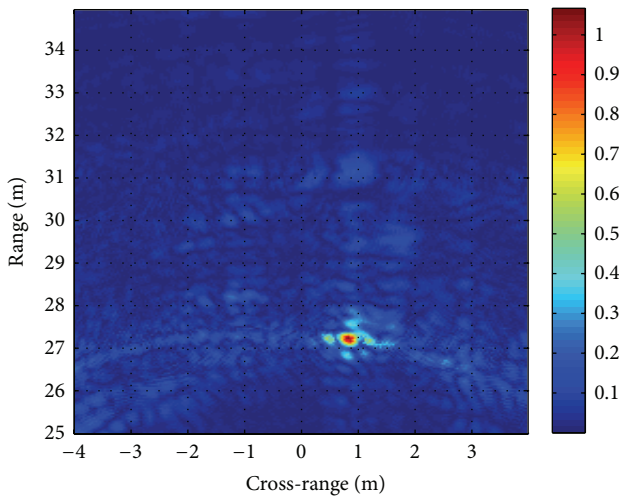


FIGURE 19: The processing result by the method proposed in this paper.

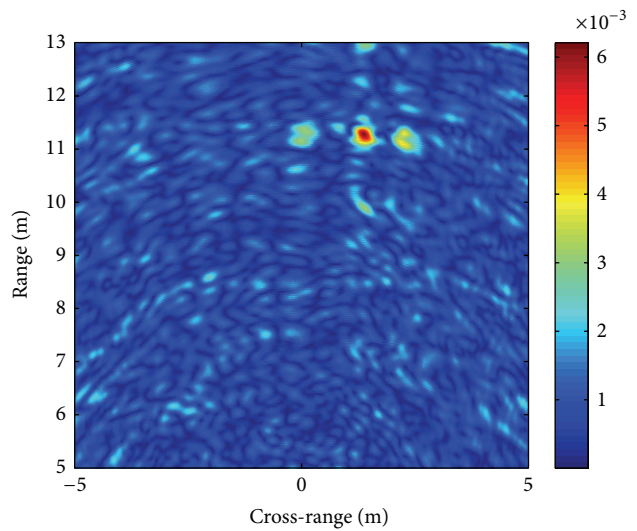


FIGURE 22: By using the proposed method, the sidelobes are suppressed.



FIGURE 20: In the static target experiment, a trihedral is used as the target and placed 2 m behind the wall.

imaging quality for both the moving target and static target in through-the-wall applications. Unlike the conventional amplitude weighting methods and nonlinear techniques, the proposed method does not degrade the main lobe resolution when suppressing the sidelobes. At present, the proposed method has been successfully applied to our real through-the-wall radar system.

Conflict of Interests

The authors declare that there is no conflict of interests regarding the publication of this paper.

Acknowledgment

This work was supported in part by the National Natural Science Foundation of China under Grants 61372161 and 61271441.

References

- [1] M. G. Amin, *Through-the-Wall Radar Imaging*, CRC press, 2010.
- [2] G. E. Smith and B. G. Mobasseri, "Robust through-the-wall radar image classification using a target-model alignment procedure," *IEEE Transactions on Image Processing*, vol. 21, no. 2, pp. 754–767, 2012.
- [3] V. H. Tang, A. Bouzerdoum, and S. L. Phung, "Two-stage through-the-wall radar image formation using compressive sensing," *Journal of Electronic Imaging*, vol. 22, no. 2, pp. 1–15, 2013.
- [4] K. E. Browne, R. J. Burkholder, and J. L. Volakis, "Fast optimization of through-wall radar images via the method of Lagrange multipliers," *IEEE Transactions on Antennas and Propagation*, vol. 61, no. 1, pp. 320–328, 2013.
- [5] C. Debes, A. M. Zoubir, and M. G. Amin, "Enhanced detection using target polarization signatures in through-the-wall radar imaging," *IEEE Transactions on Geoscience and Remote Sensing*, vol. 50, no. 5, pp. 1968–1979, 2012.
- [6] F. Ahmad and M. G. Amin, "Through-the-wall human motion indication using sparsity-driven change detection," *IEEE Transactions on Geoscience and Remote Sensing*, vol. 51, no. 3, pp. 881–890, 2013.
- [7] M. Dehmollaian and K. Sarabandi, "Refocusing through building walls using synthetic aperture radar," *IEEE Transactions on Geoscience and Remote Sensing*, vol. 46, no. 6, pp. 1589–1599, 2008.
- [8] A. H. Muqaibel and A. Safaai-Jazi, "A new formulation for characterization of materials based on measured insertion transfer function," *IEEE Transactions on Microwave Theory and Techniques*, vol. 51, no. 8, pp. 1946–1951, 2003.
- [9] H. Wang, Z. O. Zhou, and L. J. Kong, "Wall parameters estimation for moving target localization with through-the-wall radar," in *Proceedings of the International Conference on Microwave and Millimeter Wave Technology (ICMMT '07)*, pp. 1–4, IEEE Computer Society, Guilin, China, 2007.
- [10] X. Li, D. X. An, X. T. Huang, and S. R. Peng, "Estimation of wall parameters based on range profiles," *Science China Information Sciences*, vol. 54, no. 10, pp. 2178–2189, 2011.
- [11] W.-Q. Wang, "Virtual antenna array analysis for MIMO synthetic aperture radars," *International Journal of Antennas and Propagation*, vol. 2012, Article ID 587276, 10 pages, 2012.
- [12] J. L. Schwartz and B. D. Steinberg, "Ultrasparse, ultrawideband arrays," *IEEE Transactions on Ultrasonics, Ferroelectrics, and Frequency Control*, vol. 45, no. 2, pp. 376–393, 1998.
- [13] M. Mohsin Riaz and A. Ghafoor, "Through-wall image enhancement based on singular value decomposition," *International Journal of Antennas and Propagation*, vol. 2012, Article ID 961829, 20 pages, 2012.
- [14] T. Jin, B. Chen, and Z. Zhou, "Image-domain estimation of wall parameters for autofocusing of through-the-wall SAR imagery," *IEEE Transactions on Geoscience and Remote Sensing*, vol. 51, no. 3, pp. 1836–1843, 2013.
- [15] F. Ahmad, M. G. Amin, and G. Mandapati, "Autofocusing of through-the-wall radar imagery under unknown wall characteristics," *IEEE Transactions on Image Processing*, vol. 16, no. 7, pp. 1785–1795, 2007.
- [16] F. Ahmad, Y. Zhang, and M. G. Amin, "Three-dimensional wideband beamforming for imaging through a single wall," *IEEE Geoscience and Remote Sensing Letters*, vol. 5, no. 2, pp. 176–179, 2008.
- [17] F. Soldovieri, R. Solimene, and R. Pierri, "A simple strategy to detect changes in through the wall imaging," *Progress In Electromagnetics Research M*, vol. 7, pp. 1–13, 2009.
- [18] W. Zhang and A. Hoorfar, "Three-dimensional real-time through-the-wall radar imaging with diffraction tomographic algorithm," *IEEE Transactions on Geoscience and Remote Sensing*, vol. 51, no. 7, pp. 4155–4163, 2013.
- [19] H. C. Stankwitz, R. J. Dallaire, and J. R. Fienup, "Nonlinear apodization for sidelobe control in SAR imagery," *IEEE Transactions on Aerospace and Electronic Systems*, vol. 31, no. 1, pp. 267–279, 1995.
- [20] T. K. Sjögren, V. T. Vu, and M. I. Pettersson, "2D apodization in UWB SAR using linear filtering," in *Proceedings of the IEEE International Geoscience and Remote Sensing Symposium (IGARSS '11)*, pp. 1689–1692, Vancouver, Canada, July 2011.
- [21] X. Zhuge, A. G. Yarovoy, and L. P. Ligthart, "A sidelobe reduction technique for enhancing images of UWB sparse MIMO array," in *Proceedings of the International Radar Conference-Surveillance for a Safer World*, pp. 1–6, 2009.
- [22] H. C. Stankwitz and M. R. Kosek, "Sparse aperture fill for SAR using super-SVA," in *Proceedings of the IEEE National Radar Conference*, pp. 70–75, Ann Arbor, Mich, USA, May 1996.
- [23] L. Wang, X. Huang, Z. Zhimin, and S. Xiaokun, "Control sidelobes in UWB SAR images," in *Proceedings of the IEEE International Geoscience and Remote Sensing Symposium*, pp. 4630–4632, Seoul, The Republic of Korea, July 2005.
- [24] R. Goodman, S. Tummala, and W. Carrara, "Issues in ultra-wideband, widebeam SAR image formation," in *Proceedings of the IEEE International Radar Conference*, pp. 479–485, Alexandria, VA, USA, May 1995.
- [25] K. E. Browne, R. J. Burkholder, and J. L. Volakis, "Through-wall opportunistic sensing system utilizing a low-cost flat-panel array," *IEEE Transactions on Antennas and Propagation*, vol. 59, no. 3, pp. 859–868, 2011.
- [26] E. G. Larsson, P. Stoica, and J. Li, "Amplitude spectrum estimation for two-dimensional gapped data," *IEEE Transactions on Signal Processing*, vol. 50, no. 6, pp. 1343–1354, 2002.
- [27] B. Lu, Y. Zhao, X. Sun, and Z. Zhou, "Design and analysis of ultra wide band split transmit virtual aperture array for through the wall imaging," *International Journal of Antennas and Propagation*, vol. 2013, Article ID 934509, 9 pages, 2013.
- [28] H. J. Wang, Y. Su, Y. T. Zhu, and H. B. Xu, "MIMO radar imaging based on spatial spectral-domain filling," *Acta Electronica Sinica*, vol. 36, no. 6, pp. 1242–1246, 2009.

Research Article

Joint 2D Direction-of-Arrival and Range Estimation for Nonstationary Sources

Jian Chen, Hui Zhao, Xiaoying Sun, and Guohong Liu

College of Communication and Engineering, Jilin University, Changchun 130012, China

Correspondence should be addressed to Hui Zhao; zhaohui12@mails.jlu.edu.cn and Guohong Liu; liugh10@mails.jlu.edu.cn

Received 10 March 2014; Accepted 1 July 2014; Published 17 July 2014

Academic Editor: Michelangelo Villano

Copyright © 2014 Jian Chen et al. This is an open access article distributed under the Creative Commons Attribution License, which permits unrestricted use, distribution, and reproduction in any medium, provided the original work is properly cited.

Passive localization of nonstationary sources in the spherical coordinates (azimuth, elevation, and range) is considered, and a parallel factor analysis based method is addressed for the near-field parameter estimation problem. In this scheme, a parallel factor analysis model is firstly constructed by computing five time-frequency distribution matrices of the properly chosen observation data. In addition, the uniqueness of the constructed model is proved, and both the two-dimensional (2D) direction-of-arrival (DOA) and range can be jointly obtained via trilinear alternating least squares regression (TALS). The investigated algorithm is well suitable for near-field nonstationary source localization and does not require parameter-pairing or multidimensional search. Several simulation examples confirm the effectiveness of the proposed algorithm.

1. Introduction

Bearing estimation has been a strong interest in radar and sonar as well as communication. In the last three decades, various high-resolution algorithms for direction finding of multiple narrowband sources assume that the propagating waves are considered to be plane waves at the sensor array. However, when the sources are located in the Fresnel region [1] of the array aperture, the wavefronts emitted from these sources are spherical rather than planar at each sensor position and characterized by both the DOA and the range parameters; thus, the existing DOA estimation schemes, such as MUSIC and ESPRIT [2], would fail in estimating near-field localization parameters.

By applying the Fresnel approximation to the near-field sources localization, the two-dimensional (2D) MUSIC method, the high-order ESPRIT method, and the path-following method were, respectively, proposed in [3–7] in order to cope with the problem of estimating azimuth and range. In recent years, several methods that can obtain azimuth, elevation, and range have been developed. For instance, in [8], an original 3D higher order statistics based localization algorithm has been presented. By translating

the 1D uniform linear array of near-field into a virtual rectangular array of virtual far-field, Challa and Shamsunder [9] proposed a unitary-ESPRIT method. Aberd Meraim and Hua [10] used only the second-order statistics and proposed a higher resolution 3D near-field source localization; however, a parameter-pairing process leading to the poor performance in lower signal-to-noise ratio had to be taken into account. References [11, 12] also proposed fourth-order cumulant based algorithms to estimate 2D DOA and range, but they all coincided with [10]. All abovementioned algorithms rely on the assumption that impinging source signals are stationary; when nonstationary FM signals exist, they will show an unsatisfactory performance.

While quadratic time-frequency distribution [13, 14] has been sought out and properly investigated into sensor and spatial signal processing, and its evaluation of the observation data across the sensor array yields spatial time-frequency distribution (STFDs), the main advantage of STFDs is that it can well handle signals of nonstationary waveforms that are highly localized in the time-frequency domain and effectively improve the robustness of localization methods by spreading the noise power into the whole time-frequency domain. The STFDs based algorithm to locate near-field nonstationary

sources has been presented in [15] and showed a satisfactory parameters estimation accuracy; however, it required 2D search and only estimated 1D DOA and range.

In this paper, by exploiting favorable characteristics of a uniform cross array, we present a joint 2D DOA and range estimation algorithm. We first compute five time-frequency matrices to construct a parallel factor (PARAFAC) analysis model. Then, we obtain three-dimensional (3D) near-field parameters via trilinear alternating least squares regression (TALS). Compared with the other methods, the main contribution for the proposed method can be summarized as follows: (1) we obtain 3D near-field sources parameters (elevations, azimuths, and ranges) of nonstationary signals rather than stationary waves; (2) we creatively incorporate STFDs with parallel factor analysis to well avoid both parameter pairing and multidimensional search.

The rest of this paper is organized as follows. Section 2 introduces the signal model of near-field localization based on cross array. Section 3 develops a joint estimation algorithm of three parameters in near-field. Section 4 shows simulation results. Section 5 presents the conclusion of the whole paper.

2. Near-Field Signal Model Based Cross Array

2.1. Near-Field Signal Model. We consider a near-field scenario of M uncorrelated narrowband signals impinging on a cross array signed with the x - and y -axes (Figure 1), which consists of $L = 4P + 1$ elements with interelement spacing d . Let the array center be the phase point; the signals received by the $(l, 0)$ th and the $(0, l)$ th can be, respectively, expressed as

$$\begin{aligned} x_{l,0}(t) &= z_{l,0}(t) + n_{l,0}(t) \\ &= \sum_{m=1}^M s_m(t) e^{j(\gamma_{xm}l + \phi_{xm}l^2)} + n_{l,0}(t), \end{aligned} \quad (1)$$

$$\begin{aligned} x_{0,l}(t) &= z_{0,l}(t) + n_{0,l}(t) \\ &= \sum_{m=1}^M s_m(t) e^{j(\gamma_{ym}l + \phi_{ym}l^2)} + n_{0,l}(t), \end{aligned} \quad (2)$$

with $n(t)$ being additive noise, and

$$\begin{aligned} \gamma_{xm} &= -2\pi \frac{d}{\lambda} \sin \alpha_m \cos \theta_m, \\ \phi_{xm} &= \pi \frac{d^2}{\lambda r_m} (1 - \sin^2 \alpha_m \cos^2 \theta_m), \\ \gamma_{ym} &= -2\pi \frac{d}{\lambda} \sin \alpha_m \sin \theta_m, \\ \phi_{ym} &= \pi \frac{d^2}{\lambda r_m} (1 - \sin^2 \alpha_m \sin^2 \theta_m), \end{aligned} \quad (3)$$

where α_m , θ_m , and r_m indicate elevation, azimuth, and range of m th signal, respectively, and λ is wavelength of source signal.

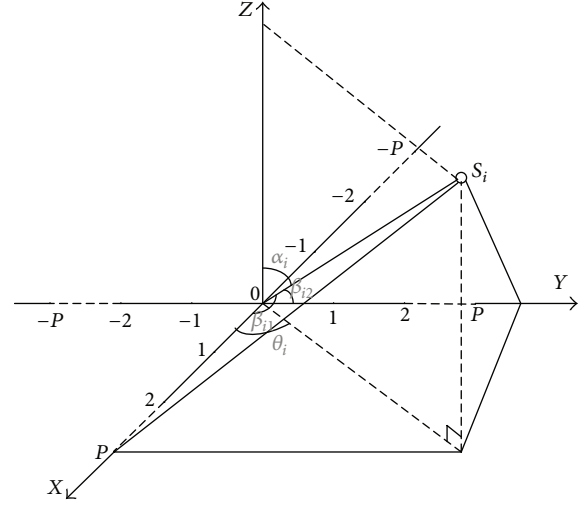


FIGURE 1: Sensor-source configuration for the near-field problem.

The m th source signal with phase $\psi_m(t)$ can be modeled as

$$s_m(t) = D_m e^{j\psi_m(t)}, \quad (4)$$

where $m = 1, 2, \dots, M$ and D_m is the amplitude of the m th source signal.

2.2. Assumption of Signal Model. The main problem addressed in this paper is to jointly estimate the sets of parameters $(\alpha_m, \theta_m, r_m)$; then the following assumptions are assumed to hold.

- (1) The source signal $s(t)$ is narrowband, independent, and nonstationary process.
- (2) The additive noise is spatially white Gaussian with zero-mean and independent from the source signals.
- (3) For unique estimation, we require $d = \lambda/4$, $M \leq N - 1$, and $-\gamma_{xm} + \phi_{xm} \neq \gamma_{xm} + \phi_{xm}$ as well as $-\gamma_{ym} + \phi_{ym} \neq \gamma_{ym} + \phi_{ym}$.

2.3. Parallel Factor Analysis. We need to introduce the following notation that will be used in the sequel.

Definition 1 (see [16]). Let $x_{k,n,p}$ stand for the (k, n, p) element of a three-dimensional tensor \mathbf{X} , if

$$x_{k,n,p} = \sum_{m=1}^M a_{k,m} b_{n,m} c_{p,m}, \quad (5)$$

where $a_{k,m}$ denotes the (k, m) element of matrix \mathbf{A} , and similarly for the others. Equation (5) indicates $x_{k,n,p}$ as a sum of triple products, which is variably known as the trilinear model, trilinear decomposition, triple product decomposition, canonical decomposition, or parallel factor (PARAFAC) analysis.

Definition 2 (see [16]). For a matrix $\mathbf{B} \in C^{I \times J}$, if all $I < J$ columns of \mathbf{B} are linearly independent but there exists

a collection of $I + 1$ linearly dependent columns of \mathbf{B} , then it has Kruskal-rank (k -rank) $k_{\mathbf{B}} = I$.

Theorem 3 (see [16]). Consider a three-dimensional tensor \mathbf{X} as defined in (5), and M represents the common dimension; if

$$k_{\mathbf{A}} + k_{\mathbf{B}} + k_{\mathbf{C}^T} \geq 2M + 2, \quad (6)$$

then \mathbf{A} , \mathbf{B} , and \mathbf{C} are unique up to permutation and (complex) scaling of columns.

3. PARAFAC Based 3D Near-Field Sources Localization

3.1. *Computation of the Spatial Time-Frequency Distribution Matrices.* The discrete form of Cohen's class of time-frequency distribution of a signal $x(t)$ can be expressed as

$$D_{XX}(t, f) = \sum_{k=-\infty}^{\infty} \sum_{\tau=-\infty}^{\infty} \varphi(k, \tau) x(t+k+\tau) \cdot x^*(t+k-\tau) e^{-j4\pi f\tau}, \quad (7)$$

where $\varphi(k, \tau)$ is the time-frequency kernel and the superscript * denotes complex conjugate. Replacing $x(t)$ by the data snapshot $x_{-l-1,0}(t)$ and $x_{-l,0}(t)$, we obtain

$$D_{-l-1,-l}^x(t, f) = \sum_{k=-\infty}^{\infty} \sum_{\tau=-\infty}^{\infty} \varphi(k, \tau) x_{-l-1}(t+k+\tau) \cdot x_{-l,0}^*(t+k-\tau) e^{-j4\pi f\tau}. \quad (8)$$

Substituting (1) into (8), $D_{-l-1,-l}^x(t, f)$ can be extended to the following form:

$$D_{-l-1,-l}^x(t, f) = D_{z_{-l-1}(t), z_{-l}(t)}(t, f) + D_{z_{-l-1}(t), n_{-l}(t)}(t, f) + D_{n_{-l-1}(t), z_{-l}(t)}(t, f) + D_{n_{-l-1}(t), n_{-l}(t)}(t, f). \quad (9)$$

Under the assumptions (1) and (2), it is obvious that

$$E[D_{-l-1,-l}^x(t, f)] = E[D_{z_{-l-1}(t), z_{-l}(t)}(t, f)] = \sum_{m=1}^M E[D_{s_m}(t, f)] e^{j(-\gamma_{xm} + \phi_{xm})} e^{j2\phi_{xm}}, \quad (10)$$

where $D_{s_m}(t, f)$ indicates the STFDs of source $s_m(t)$.

Using a rectangular window of old length N , the pseudo Wigner-Ville distribution (PWVD) of $s_m(t)$ is given by

$$D_{s_m}(t, f) = \sum_{\tau=-(N-1)/2}^{(N-1)/2} x_m(t+\tau) x_m^*(t-\tau) e^{-j4\pi f\tau}. \quad (11)$$

Assume that the third-order derivative of the phase can be negligible over the rectangular window length N , and $f_m =$

$d\psi_m(t)/(2\pi dt)$, $\psi_m(t+\tau) - \psi_m(t-\tau) - 4\pi f_m\tau = 0$; then we obtain the approximated expression as

$$D_{s_m}(t, f) = \sum_{\tau=-(N-1)/2}^{(N-1)/2} D_M^2 = LD_M^2. \quad (12)$$

We construct matrix \mathbf{D}_1 with the (k, q) th element being given by

$$\begin{aligned} \mathbf{D}_1(k, q) &= E[D_{q-k-1, q-k}^x(t, f)] \\ &= \sum_{m=1}^M E[D_{s_m}(t, f)] e^{j(-\gamma_{xm} + \phi_{xm})} e^{j2(k-q)\phi_{xm}}. \end{aligned} \quad (13)$$

On the other hand, following the same process described above, we can easily obtain

$$\begin{aligned} \mathbf{D}_2(k, q) &= E[D_{l+1, l}^x(t, f)] = E[D_{k-q+1, k-q}^x(t, f)] \\ &= \sum_{m=1}^M E[D_{s_m}(t, f)] e^{j(\gamma_{xm} + \phi_{xm})} e^{j2(k-q)\phi_{xm}}, \\ \mathbf{D}_3(k, q) &= E[D_{-l-1, -l}^y(t, f)] = E[D_{q-k-1, q-k}^y(t, f)] \\ &= \sum_{m=1}^M E[D_{s_m}(t, f)] e^{j(-\gamma_{ym} + \phi_{ym})} e^{j2(k-q)\phi_{ym}}, \\ \mathbf{D}_4(k, q) &= E[D_{l+1, l}^y(t, f)] = E[D_{k-q+1, k-q}^y(t, f)] \\ &= \sum_{m=1}^M E[D_{s_m}(t, f)] e^{j(\gamma_{ym} + \phi_{ym})} e^{j2(k-q)\phi_{ym}}, \\ \mathbf{D}_5(k, q) &= E[D_{l, l+1}^y(t, f)] = E[D_{q-k, q-k+1}^y(t, f)] \\ &= \sum_{m=1}^M E[D_{s_m}(t, f)] e^{j(-\gamma_{ym} - \phi_{ym})} e^{-j2(q-k)\phi_{ym}}. \end{aligned} \quad (14)$$

And their matrices form becomes

$$\begin{aligned} \mathbf{D}_1(t, f) &= \mathbf{A} \mathbf{D}_s(t, f) \mathbf{\Omega}_1^* \mathbf{\Phi}_1 \mathbf{A}^H, \\ \mathbf{D}_2(t, f) &= \mathbf{A} \mathbf{D}_s(t, f) \mathbf{\Omega}_1 \mathbf{\Phi}_1 \mathbf{A}^H, \\ \mathbf{D}_3(t, f) &= \mathbf{A} \mathbf{D}_s(t, f) \mathbf{\Omega}_2^* \mathbf{\Phi}_2 \mathbf{A}^H, \\ \mathbf{D}_4(t, f) &= \mathbf{A} \mathbf{D}_s(t, f) \mathbf{\Omega}_2 \mathbf{\Phi}_2 \mathbf{A}^H, \\ \mathbf{D}_5(t, f) &= \mathbf{A} \mathbf{D}_s(t, f) \mathbf{\Omega}_2^* \mathbf{\Phi}_2^* \mathbf{A}^H, \end{aligned} \quad (15)$$

where $\mathbf{A} = [\mathbf{a}_1, \mathbf{a}_2, \dots, \mathbf{a}_M]$, $\mathbf{a}_m = [1, e^{j2\phi_{xm}}, \dots, e^{j2(N-1)\phi_{xm}}]$, $\mathbf{\Omega}_1 = \text{diag}(e^{j\gamma_{x1}}, e^{j\gamma_{x2}}, \dots, e^{j\gamma_{xM}})$, $\mathbf{\Phi}_1 = \text{diag}(e^{j\phi_{x1}}, e^{j\phi_{x2}}, \dots, e^{j\phi_{xM}})$, $\mathbf{\Omega}_2 = \text{diag}(e^{j\gamma_{y1}}, e^{j\gamma_{y2}}, \dots, e^{j\gamma_{yM}})$, and $\mathbf{\Phi}_2 = \text{diag}(e^{j\phi_{y1}}, e^{j\phi_{y2}}, \dots, e^{j\phi_{yM}})$.

3.2. *Construction of the Parallel Factor Analysis Model.* Considering the situation of limited samples, we build a parallel

factor analysis model that uses the spatial time-frequency distribution as

$$\tilde{\mathbf{D}} = \begin{bmatrix} \mathbf{D}_1(t, f) \\ \mathbf{D}_2(t, f) \\ \mathbf{D}_3(t, f) \\ \mathbf{D}_4(t, f) \\ \mathbf{D}_5(t, f) \end{bmatrix} = \begin{bmatrix} \mathbf{A}\mathbf{D}_s(t, f)\mathbf{\Omega}_1^*\mathbf{\Phi}_1\mathbf{A}^H \\ \mathbf{A}\mathbf{D}_s(t, f)\mathbf{\Omega}_1^*\mathbf{\Phi}_1\mathbf{A}^H \\ \mathbf{A}\mathbf{D}_s(t, f)\mathbf{\Omega}_2^*\mathbf{\Phi}_2\mathbf{A}^H \\ \mathbf{A}\mathbf{D}_s(t, f)\mathbf{\Omega}_2^*\mathbf{\Phi}_2\mathbf{A}^H \\ \mathbf{A}\mathbf{D}_s(t, f)\mathbf{\Omega}_2^*\mathbf{\Phi}_2\mathbf{A}^H \end{bmatrix} + \nu_1. \quad (16)$$

Letting $\mathbf{C} = \mathbf{A}^*$, the Khutrr-Rao product [16] for (16) shows

$$\tilde{\mathbf{D}} = (\mathbf{M} \otimes \mathbf{A}) \mathbf{C}^T + \nu_1, \quad (17)$$

where

$$\mathbf{M} = \begin{bmatrix} g^{-1}(\mathbf{D}_s(t, f)\mathbf{\Omega}_1^*\mathbf{\Phi}_1) \\ g^{-1}(\mathbf{D}_s(t, f)\mathbf{\Omega}_1^*\mathbf{\Phi}_1) \\ g^{-1}(\mathbf{D}_s(t, f)\mathbf{\Omega}_2^*\mathbf{\Phi}_2) \\ g^{-1}(\mathbf{D}_s(t, f)\mathbf{\Omega}_2^*\mathbf{\Phi}_2) \\ g^{-1}(\mathbf{D}_s(t, f)\mathbf{\Omega}_2^*\mathbf{\Phi}_2) \end{bmatrix}, \quad (18)$$

$g^{-1}(\mathbf{D}_s(t, f)\mathbf{\Omega}_1^*\mathbf{\Phi}_1)$ denoting a row vector consisting of diagonal matrix $\mathbf{D}_s(t, f)\mathbf{\Omega}_1^*\mathbf{\Phi}_1$.

Similarly, (17) also yields

$$\begin{aligned} \tilde{\mathbf{X}} &= (\mathbf{A} \otimes \mathbf{C}) \mathbf{M}^T + \nu_2, \\ \tilde{\mathbf{Y}} &= (\mathbf{C} \otimes \mathbf{M}) \mathbf{A}^T + \nu_3. \end{aligned} \quad (19)$$

3.3. Estimation of 2D Direction-of-Arrival and Range. As it stands, \mathbf{A} and \mathbf{C} are both Vander-monde matrices, and then they have Kruskal-rank (k -rank) $k_{\mathbf{A}} = k_{\mathbf{C}^T} = M$. On the other hand, the k -rank of \mathbf{M} will be $k_{\mathbf{D}} = \min(5, M)$. When the condition that the number of signals being $M \geq 2$ holds, then \mathbf{A} , \mathbf{C} , and \mathbf{M} are unique up to permutation and scaling of columns. With trilinear alternating least squares regression, we obtain that

$$\begin{aligned} \tilde{\mathbf{C}}^T &= \arg \min_{\mathbf{C}^T} \|\tilde{\mathbf{D}} - (\mathbf{M} \otimes \mathbf{A}) \mathbf{C}^T\|_F^2, \\ \tilde{\mathbf{M}}^T &= \arg \min_{\mathbf{M}^T} \|\tilde{\mathbf{X}} - (\mathbf{A} \otimes \mathbf{C}) \mathbf{M}^T\|_F^2, \\ \tilde{\mathbf{A}}^T &= \arg \min_{\mathbf{A}^T} \|\tilde{\mathbf{Y}} - (\mathbf{C} \otimes \mathbf{M}) \mathbf{A}^T\|_F^2. \end{aligned} \quad (20)$$

Then using these estimates, we can get each pair $(\gamma_{xm}, \varphi_{ym}, \varphi_{ym})$ as follows:

$$\begin{aligned} \tilde{\gamma}_{xm} &= \frac{1}{2} \arg \left(\frac{\tilde{\mathbf{M}}(2, m)}{\tilde{\mathbf{M}}(1, m)} \right), \\ \tilde{\gamma}_{ym} &= \frac{1}{2} \arg \left(\frac{\tilde{\mathbf{M}}(4, m)}{\tilde{\mathbf{M}}(3, m)} \right), \\ \tilde{\varphi}_{ym} &= \frac{1}{2} \arg \left(\frac{\tilde{\mathbf{M}}(3, m)}{\tilde{\mathbf{M}}(5, m)} \right). \end{aligned} \quad (21)$$

Finally, the sources parameters can be estimated as

$$\begin{aligned} \tilde{\alpha}_m &= a \sin \left(\frac{\lambda}{2\pi d} (\tilde{\gamma}_{xm}^2 + \tilde{\gamma}_{ym}^2)^{1/2} \right), \\ \tilde{\theta}_m &= a \tan \left(\frac{\tilde{\gamma}_{ym}}{\tilde{\gamma}_{xm}} \right), \\ \tilde{r}_m &= \frac{\pi d^2 (1 - \sin^2 \tilde{\alpha}_m \sin^2 \tilde{\theta}_m)}{\lambda \tilde{\varphi}_{ym}}. \end{aligned} \quad (22)$$

4. Computer Simulation Results

In this section, we explicit several simulation results to evaluate the performance of proposed method. For all examples, a symmetrical cross array with a number of 17 elements and interelements spacing of 0.25λ , where λ is the wavelength of the narrowband source signals. The noise used in this section is zero-mean, Gaussian distributed, and temporally white, and the root mean square error (RMSE) is defined as (23). All the following presented results are obtained by averaging the results of 200 independent Monte Carlo simulations. Consider

$$\text{RMSE}(\theta) = \sqrt{\frac{1}{N}(\theta - \tilde{\theta})^2}, \quad (23)$$

where N denotes the number of independent Monte Carlo simulations.

In the first example, we examine the performance of the elevation, azimuth, and range estimations accuracy versus the SNR. The snapshot number is set at 512. Two linear frequency-modulated signals arrival at the sensor array with start and end frequencies (0.1, 0) and (0.5, 0.4), their 3D near-field parameters locate at $(25^\circ, 15^\circ, 0.3\lambda)$ and $(10^\circ, 30^\circ, 0.4\lambda)$. For the comparison, the fourth-order cumulant based method [9] is also displayed, in which the source signals are non-Gaussian and stationary process. When the SNR varies from 0 dB to 25 dB, the RMSEs of the 2D direction-of-arrival and range estimations using the proposed method and the fourth-order cumulant based method are shown in Figure 2. From Figure 2, we can see that the proposed method outperforms the fourth-order cumulant based method in elevation and azimuth as well as range estimation for all available SNRs. In addition, the RMSE of range estimations for the first source that is closer to the array is less than the second one. This phenomenon is in well agreement with the theoretical analysis that the sources closer to sensor array would hold a smaller standard deviation than the ones far away from the array.

In the second example, the proposed method is used to deal with the situation that two near-field FM signals are impinging on the sensor array shown in Figure 1. The elevation, azimuth, and range of the near-field sources are located at $(35^\circ, 40^\circ, 1/6\lambda)$ and $(20^\circ, 60^\circ, 0.4\lambda)$. Moreover, the snapshot number and SNR are set at 512 and 10 dB. Table 1 establishes the mean and variance of the elevation, azimuth, and range estimations using the proposed method. From Table 1, we can see that the proposed method shows

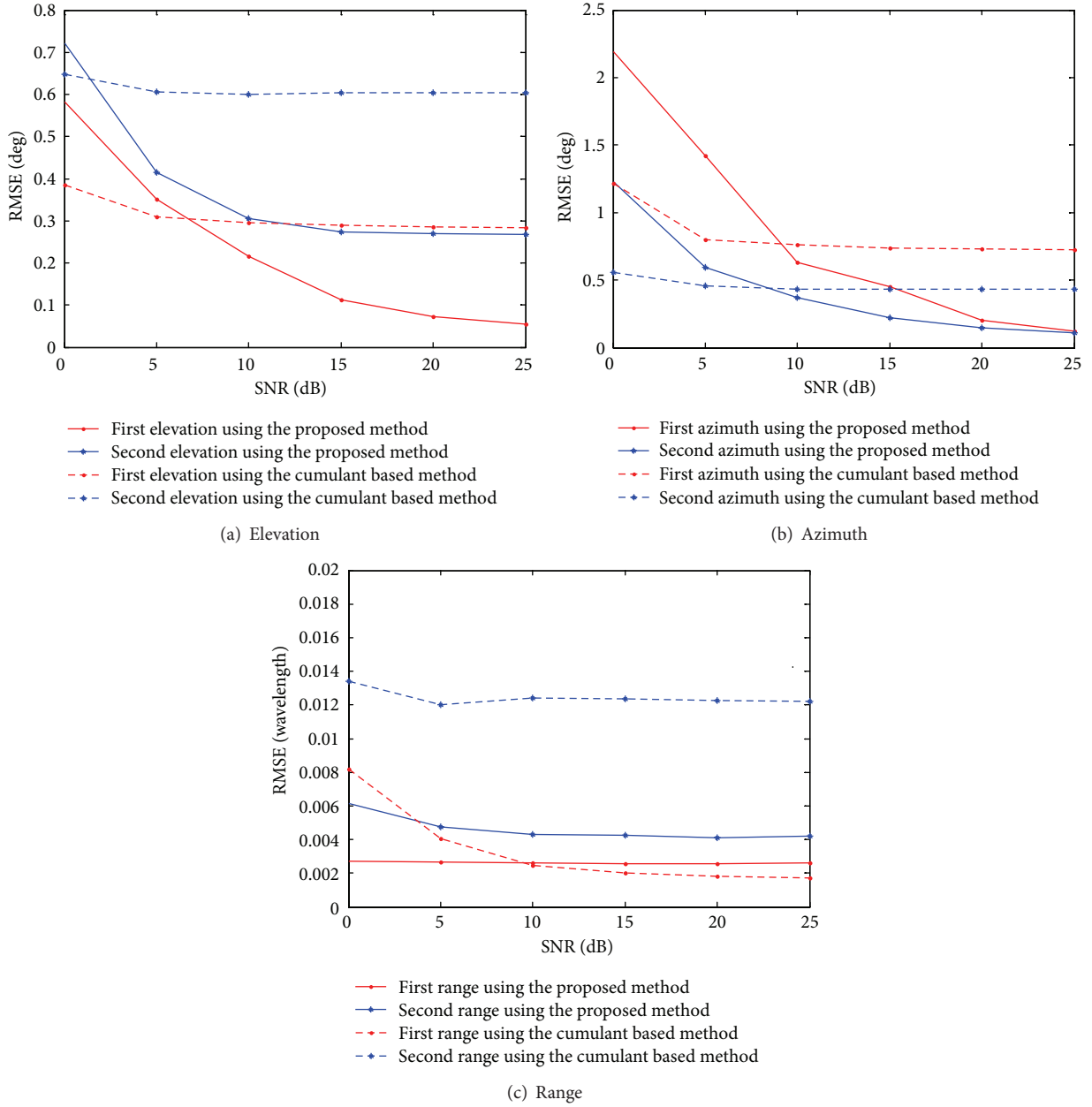


FIGURE 2: The RMSEs of the elevation, azimuth, and range estimation using the proposed method and the fourth-order cumulant based method versus SNRs.

TABLE 1: The mean and variance of the proposed method for the second example.

		True	Mean	Variance
Source 1	Elevation (°)	35	34.1036	0.0854
	Azimuth (°)	40	38.8652	0.0514
	Range	$1/6\lambda$	0.1956λ	8.7246×10^{-7}
Source 2	Elevation (°)	20	19.8274	0.0963
	Azimuth (°)	60	59.3610	0.1827
	Range	0.4λ	0.4449λ	7.6641×10^{-6}

a satisfactory performance in localizing the 3D near-field nonstationary sources.

In the last example, we consider the situation when far-field and near-field nonstationary sources are incoming on the sensor array mentioned above, and they are located at $(35^\circ, 40^\circ, 1/6\lambda)$ and $(20^\circ, 60^\circ, \text{inf})$, respectively. The snapshot number is fixed at 512. When the SNR varies from 0 dB to 25 dB, the RMSEs of the 2D direction-of-arrival and range estimations using the proposed method are shown in Figure 3. In addition, the results of the fourth-order cumulant based method are also displayed in the same figure for

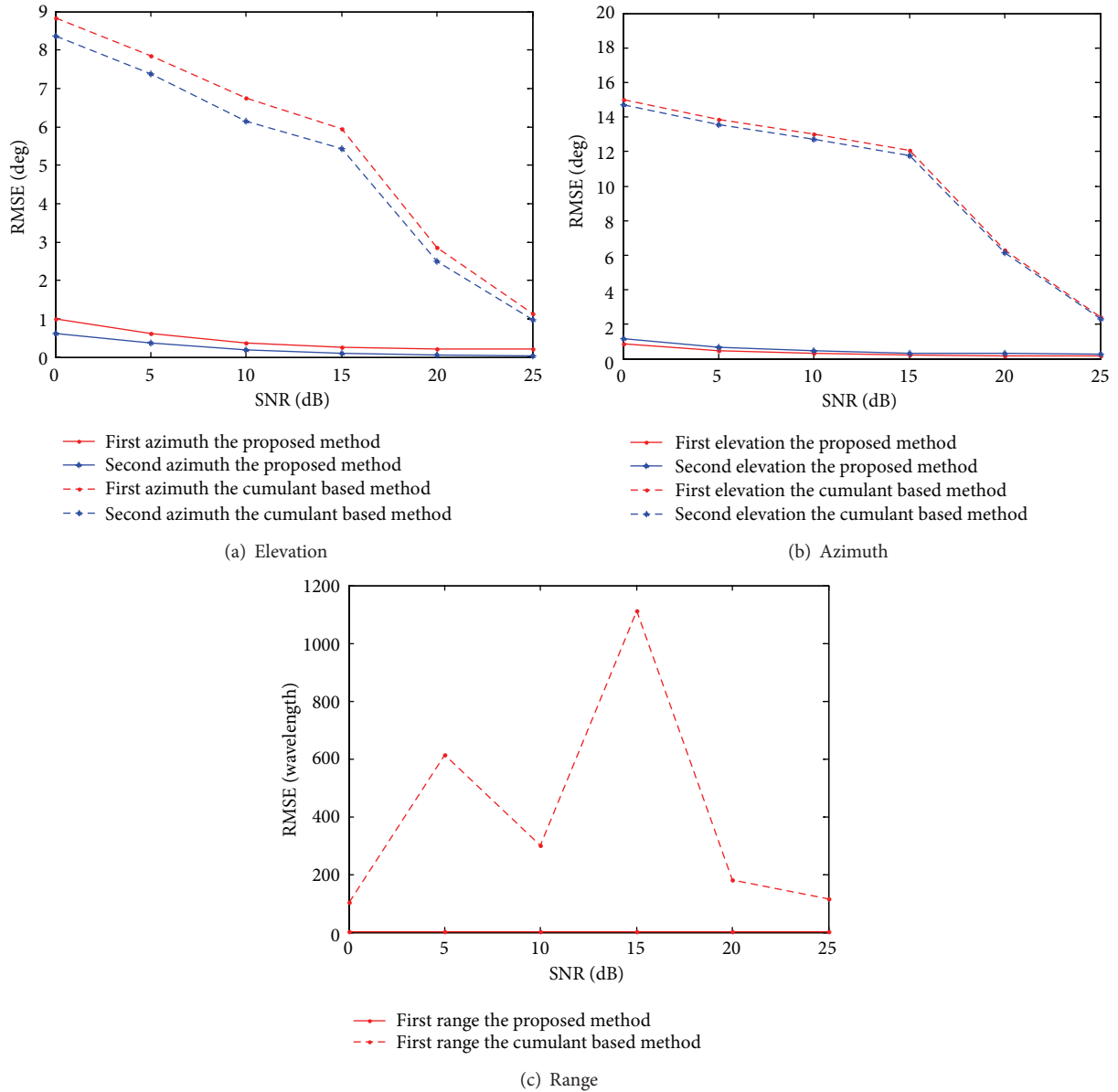


FIGURE 3: The RMSEs of the elevation, azimuth, and range estimation using the proposed method and the fourth-order cumulant based method versus SNRs.

comparison. From Figure 3, it can be seen that the proposed method still performs a satisfactory estimation accuracy for the case that far-field and near-field sources exist simultaneously. However, the fourth-order cumulant based method shows a poor performance in the same situation.

5. Conclusion

We have developed a spatial time-frequency distribution based algorithm for 3D near-field nonstationary source localization problems. Additionally, with parallel factor analysis technique, there is no parameter pairing or multidimensional searching. Finally, the computer simulation results indicate that using spatial time-frequency distribution and parallel

factor together significantly solves the problem of the joint estimation of elevation, azimuth, and range of nonstationary signals. However, the spatial time-frequency averaging methods may lead to the additional computation load.

Conflict of Interests

The authors declare that there is no conflict of interests regarding the publication of this paper.

Acknowledgments

This work is supported by the National Natural Science Foundation of China (61171137) and Specialized Research Fund

for the Doctoral Program of Higher Education (2009006112-0042).

References

- [1] J. Liang, X. Zeng, B. Ji, J. Zhang, and F. Zhao, "A computationally efficient algorithm for joint range-DOA-frequency estimation of near-field sources," *Digital Signal Processing: A Review Journal*, vol. 19, no. 4, pp. 596–611, 2009.
- [2] H. Krim and M. Viberg, "Two decades of array signal processing research," *IEEE Signal Processing Magazine*, vol. 13, no. 4, pp. 67–94, 1996.
- [3] Y. D. Huang and M. Barkat, "Near-field multiple source localization by passive sensor array," *IEEE Transactions on Antennas and Propagation*, vol. 39, no. 7, pp. 968–975, 1991.
- [4] A. J. Weiss and B. Friedlander, "Range and bearing estimation using polynomial rooting," *IEEE Journal of Oceanic Engineering*, vol. 18, no. 2, pp. 130–137, 1993.
- [5] W. J. Zhi and M. Y. Chia, "Near-field source localization via symmetric subarrays," in *Proceedings of the IEEE International Conference on Acoustics, Speech and Signal Processing (ICASSP '07)*, vol. 2, pp. II-1121–II-1124, Honolulu, Hawaii, USA, April 2007.
- [6] D. Starer and A. Nehora, "Path-following algorithm for passive localization of near-field sources," in *Proceedings of the 5th ASSP Workshop on Spectrum Estimation and Modeling*, 1990, pp. 677–680.
- [7] D. Starer and A. Nehorai, "Passive localization on near-field sources by path following," *IEEE Transactions on Signal Processing*, vol. 42, no. 3, pp. 677–680, 1994.
- [8] R. N. Challa and S. Shamsunder, "High-order subspace-based algorithms for passive localization of near-field sources," in *Proceedings of the 29th Asilomar Conference on Signals, Systems and Computers*, pp. 771–781, 1995.
- [9] R. N. Challa and S. Shamsunder, "3-D spherical localization of multiple non-Gaussian sources using cumulants," in *Proceedings of the 8th IEEE Signal Processing Workshop on Statistical Signal and Array Processing (SSAP '96)*, pp. 101–104, June 1996.
- [10] K. Aberd Meraim and Y. Hua, "3-D near field source localization using second order statistics," in *Proceedings of the 31st Asilomar Conference on Signals, Systems and Computers*, pp. 381–384, 1997.
- [11] C. M. Lee, K. S. Yoon, J. H. Lee, and K. K. Lee, "Efficient algorithm for localising 3-D narrowband multiple sources," *IEE Proceedings: Radar, Sonar and Navigation*, vol. 148, no. 1, pp. 23–26, 2001.
- [12] K. Deng and Q. Yin, "Closed form parameters estimation for 3-D near field sources," in *Proceedings of the IEEE International Conference on Acoustics, Speech and Signal Processing (ICASSP '06)*, pp. IV1133–IV1136, Toulouse, France, May 2006.
- [13] M. G. Amin and Y. Zhang, "Direction finding based on spatial time-frequency distribution matrices," *Digital Signal Processing: A Review Journal*, vol. 10, no. 4, pp. 325–359, 2000.
- [14] Y. M. Zhang, W. F. Ma, and M. G. Amin, "Subspace analysis of spatial time-frequency distribution matrices," *IEEE Transactions on Signal Processing*, vol. 49, no. 4, pp. 747–759, 2001.
- [15] L. A. Cirillo, A. M. Zoubir, and M. G. Amin, "Estimation of near-field parameters using spatial time-frequency distributions," in *Proceedings of the IEEE International Conference on Acoustics, Speech and Signal Processing (ICASSP '07)*, vol. 3, pp. III1141–III1144, Honolulu, Hawaii, USA, April 2007.
- [16] R. A. Harshman, "Foundation of the PARAFAC procedure: models and conditions for an explanatory multimodal factor analysis," *UCLA Working Papers in Phonetics*, vol. 16, pp. 1–84, 1970.

Research Article

Joint DOD and DOA Estimation for High Speed Target Using Bistatic MIMO Radar

Jinli Chen,^{1,2,3} Jiaqiang Li,^{1,2,3} Peng Li,^{1,2} Yanping Zhu,^{1,2} and Weijun Long⁴

¹ College of Electronic and Information Engineering, Nanjing University of Information Science and Technology, Nanjing 210044, China

² Jiangsu Key Laboratory of Meteorological Observation and Information Processing, Nanjing University of Information Science and Technology, Nanjing 210044, China

³ Collaborative Innovation Center on Forecast and Evaluation of Meteorological Disasters, Nanjing University of Information Science and Technology, Nanjing 210044, China

⁴ College of Electronic and Information Engineering, Nanjing University of Aeronautics and Astronautics, Nanjing 210016, China

Correspondence should be addressed to Jinli Chen; chen820803@yeah.net

Received 28 February 2014; Revised 24 June 2014; Accepted 3 July 2014; Published 16 July 2014

Academic Editor: Ahmed Shaharyar Khwaja

Copyright © 2014 Jinli Chen et al. This is an open access article distributed under the Creative Commons Attribution License, which permits unrestricted use, distribution, and reproduction in any medium, provided the original work is properly cited.

In bistatic multiple-input multiple-output (MIMO) radar, range migration and invalidly synthesized virtual array resulting from the serious mismatch of matched filter make it difficult to estimate direction of departure (DOD) and direction of arrival (DOA) of high speed target using the traditional superresolution algorithms. In this study, a method for joint DOD and DOA estimation of high speed target using bistatic MIMO radar is proposed. After multiplying the received signals with the conjugate of the delayed versions of the transmitted signals, Fourier transform (FT) of the multiplied signals over both fast time and slow time is employed. Then, the target components of radar return corresponding to the different transmitted waveforms can be perfectly separated at the receivers by extracting the target frequency-domain data along slow-time frequency dimension when the delay between the transmitted signals and their subsequent returns is timed. By splicing the separated target components distributed along several range cells, the virtual array can be formed, and then DOD and DOA of high speed target can be estimated using the superresolution algorithm with the range migration and the mismatch of matched filter properly removed. Simulation results have proved the validity of the proposed algorithm.

1. Introduction

Bistatic radar with the widely separated transmitter and receiver has the advantages of covert receivers, giving increased immunity to antiradiation missiles and electronic countermeasures, and possible antistealth capabilities [1]. However, the need for synchronization between the transmitter and receiver leads to an increase in complexity. Unlike bistatic phased-array radar, bistatic multiple-input multiple-output (MIMO) radar is characterized by using multiple transmit antennas to simultaneously transmit orthogonal waveforms. Therefore, bistatic MIMO radar will simultaneously illuminate a very broad angular sector instead of a focused angular sector. The virtual array can be formed by matching the received signals with the transmitted signals, and then the direction of arrivals (DOAs) and the direction of

departures (DODs) of targets can be estimated by processing the output of virtual array using the existing angle estimation algorithms, that is, the algorithms proposed in [2–4]. Due to the broad illuminated angular sector and the target location determined by its DOA and DOD in this case, the beam scanning and range information of the target are redundant and then the time and space synchronization are relaxed in bistatic MIMO radar [2, 3].

With the military technology evolution and the increasing exploitation of space resources, high speed maneuvering targets, that is, aircraft, missile, and space debris, pose severe challenges to modern radar in recent years. Joint DOD and DOA estimation methods have been widely investigated in bistatic MIMO radar [2–8]. But all of them, which are designed for low speed target, will be seriously deteriorated when dealing with the target moving at a high speed.

The successful virtual array formation and effective target energy accumulation during the long observation time are vital for angle estimation in bistatic MIMO radar. However, the variety of the phase caused by the large-scale Doppler frequency of high speed target within the repetition interval of radar signal results in the severe distortion of target echo. Then significant mismatch loss would occur in matched filters. That is, the virtual array cannot be effectively formed for high speed target [9]. Meanwhile, during the long observation time, the target with high speed easily goes through several range cells so that the target energy is distributed along multiple range cells [10–14]. As a consequence, for high speed target, the angle estimation performances of the existing methods, that is, the proposed methods in [6–8], are limited with both the mismatch loss in matched filter and the target residence time in a single range cell. Persy and Dipietro [15] have introduced the keystone transform to compensate for the linear range migration during the long integration time for synthetic aperture radar (SAR) ground moving targets imaging without knowing the target motion information. For high speed target, it is highly possible that both Doppler frequency ambiguity and target radial acceleration exist. However, in this situation, the detection performance of the keystone transform would be seriously reduced. At the same time, the data interpolation operator is employed to implement the keystone transform, which results in the large computational load. Dorp [16] introduced the keystone transform into MIMO radar for correcting the envelope migration of high speed target. It is worth pointing out that time division, rather than code division, strategy for transmitting signals is applied in MIMO radar to synthesize the virtual elements one by one at different time. The basic idea of the transmitter time division is to avoid the effect of the large-scale Doppler frequency on the virtual array formation. However, for high speed target, the switching time between the transmitters is normally longer than the inverse of the relative Doppler frequency of the target. Thus, the phase variety of the return signal caused by the target's Doppler frequency during the virtual array forming time alters the array manifold and then degrades the accuracy of the angle estimation. In [17], a long-time integration method based on Hough transform is proposed to detect the weak target without acceleration. This method is capable of overcoming the problem of the range migration, but it performs poorly under the condition that the virtual array is unsuccessfully formed because of the large-scale Doppler frequency of target, and its computational burden is also very huge. A novel long-time coherent detection method, Radon-Fourier transform (RFT), is proposed in [18–20], which realizes the echo spatial-temporal decoupling via joint searching along range and velocity dimensions. RFT may obtain the significant coherent integration gain without the Doppler ambiguity restriction, but, for the high speed maneuvering target detection using bistatic MIMO radar, a huge computational complexity is needed for five-dimensional joint searching of range, velocity, acceleration, DOD, and DOA. In [21], the space-time RFT for wideband digital array radar is proposed for high speed target detection by jointly realizing digital beamforming (DBF), range

compression, and long-time coherent integration. However, prior to the spatial and temporal information processing for bistatic MIMO radar, the virtual array should be effectively formed when dealing with the target moving at a high speed.

In bistatic MIMO radar, suffering from the range migration and the invalidly synthesized virtual array when dealing with high speed target, the performances of the existing angle estimation methods will rapidly degrade. This paper makes an effort to provide a method for overcoming the effect of the large-scale Doppler frequency on the virtual array formation and removing range migration during the long-time integration, thus facilitating the angle estimation for high speed target in bistatic MIMO radar. In order to overcome the effect of the large-scale Doppler frequency on the virtual array formation, the two-dimensional (2D) Fourier transform (FT) is employed to transform the multiplied signals, which are obtained by multiplying the received signals with the conjugate of the delayed versions of the transmitted signals, into the fast-time frequency and slow-time frequency domains, and then the target components of the radar return corresponding to the different transmitted waveforms perfectly separated by extracting the target frequency-domain data. By splicing the separated target components that are distributed along several range cells, the virtual array is synthesized with the range migration removed. Thus, the DOD and DOA of high speed target can be obtained from the output of virtual array using the superresolution algorithm. Simulation results demonstrate the effectiveness of the proposed method.

The remainder of this paper is organized as follows. In Section 2, the signal model for high speed target in bistatic MIMO radar is established. In Section 3, the proposed angle estimation algorithm for high speed target is described. Moreover, the simulation results of the proposed algorithm are presented and the performances are investigated in Section 4. Finally, Section 5 concludes the paper.

2. Signal Model

Consider a bistatic MIMO radar system [2] with M closely spaced transmit elements and N closely spaced receive elements, as shown in Figure 1. Both the transmit array and the receive array are uniform linear arrays and the spacing between adjacent elements of the transmit array and the receive array is denoted by d_t and d_r , respectively. We assume that the range between the target and the transmit array or receive array is much larger than the aperture of the transmit array or receive array. M different continuous coded periodic signals with identical bandwidth are employed, which are temporally orthogonal. The vector including M orthogonal transmitted baseband coded signals can be expressed as [2]

$$\mathbf{S}(\bar{t}, t_l) = [S_1(\bar{t}, t_l) \ S_2(\bar{t}, t_l) \ \cdots \ S_M(\bar{t}, t_l)]^T, \quad (1)$$

where $[\cdot]^T$ denotes the vector/matrix transpose, $\bar{t} = t + t_l$, $t_l = lT$ is the slow time, t ($0 \leq t < T$) is the fast time, T is the period of the transmitted signal, and $S_m(\bar{t}, t_l)$, $m = 1, 2, \dots, M$, denotes the transmitted baseband coded signal of the m th transmitter.

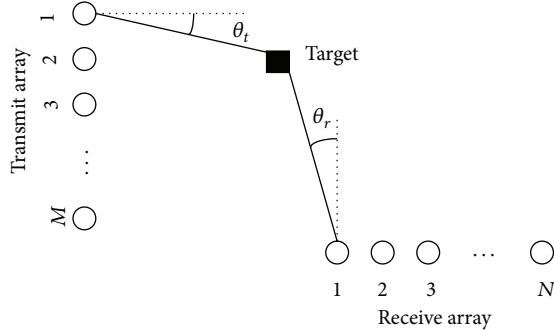


FIGURE 1: Bistatic MIMO radar scenario.

We assume that there are P high speed targets with different Doppler frequencies located at the same initial range cell. The directions of P targets with respect to the transmit array normal (i.e., DODs) are denoted by $\theta_{t1}, \theta_{t2}, \dots, \theta_{tP}$, respectively, and the directions of P targets with respect to the receive array normal (i.e., DOAs) are denoted by $\theta_{r1}, \theta_{r2}, \dots, \theta_{rP}$, respectively. Thus, $(\theta_{tp}, \theta_{rp})$ denotes the location of the p th target. Because the range walk of target within the observation time is much smaller than the target range, DODs and DOAs of targets are assumed to be constant during the observation time. The radial velocities of the p th target ($p = 1, 2, \dots, P$) with respect to the transmit array and the receive array are v_{tp} and v_{rp} , respectively, and then $v_p = v_{tp} + v_{rp}$ are the sum of two radial velocities for the p th target. The radial accelerations of the p th target with respect to the transmit array and the receive array are a_{tp} and a_{rp} , respectively, and then $a_p = a_{tp} + a_{rp}$ are the sum of two radial accelerations for the p th target. The received baseband signal through reflections of P targets can be written as [2, 3, 13, 14]

$$\mathbf{X}(\tilde{t}, t_l) = \sum_{p=1}^P \mathbf{a}_r(\theta_{rp}) \rho_p \mathbf{a}_t^T(\theta_{tp}) \mathbf{S} \left(\tilde{t} - \frac{v_p \tilde{t}}{c} - \frac{a_p \tilde{t}^2}{2c}, t_l \right) \times e^{-j2\pi(f_{dp} \tilde{t} + (a_p/2\lambda) \tilde{t}^2)} + \boldsymbol{\omega}(\tilde{t}, t_l), \quad (2)$$

where $\mathbf{X}(\tilde{t}, t_l) = [X_1(\tilde{t}, t_l) X_2(\tilde{t}, t_l) \dots X_N(\tilde{t}, t_l)]^T \in \mathbb{C}^{N \times 1}$ is the received signal vector; ρ_p denotes the complex amplitude of the reflected signal of the p th target involving the reflection coefficients and path losses of the target; $\mathbf{a}_r(\theta_{rp}) = [1 e^{-j(2\pi/\lambda)d_r \sin \theta_{rp}} \dots e^{-j(2\pi/\lambda)(N-1)d_r \sin \theta_{rp}}]^T$ and $\mathbf{a}_t(\theta_{tp}) = [1 e^{-j(2\pi/\lambda)d_t \sin \theta_{tp}} \dots e^{-j(2\pi/\lambda)(M-1)d_t \sin \theta_{tp}}]^T$ are the steering vectors of the receive array and transmit array, respectively, where λ denotes the wavelength; $f_{dp} = f_1(v_{tp} + v_{rp})/c = f_1 v_p/c$ denotes the Doppler frequency of the p th target, where f_1 is the radar carrier frequency; and the noise vector $\boldsymbol{\omega}(\tilde{t}, t_l)$ is assumed to be independent and identically distributed, and zero-mean complex white Gaussian distribution with $\boldsymbol{\omega}(\tilde{t}, t_l) \sim N^c(0, \sigma_\omega^2 \mathbf{I}_N)$, where σ_ω^2 is noise variance and \mathbf{I}_N is the identity matrix with the size of $N \times N$. The contribution of the target's acceleration to the envelope migration during the observation time can be neglected and the effect of the target's velocity on the envelope migration during the fast time can also be ignored. The reason is that

the range change caused by the above two factors is much less than the radar range resolution. Under this condition, (2) can be simplified as

$$\mathbf{X}(\tilde{t}, t_l) \approx \sum_{p=1}^P \mathbf{a}_r(\theta_{rp}) \rho_p \mathbf{a}_t^T(\theta_{tp}) \mathbf{S} \left(\tilde{t} - \frac{v_p \tilde{t}}{c}, t_l \right) e^{-j2\pi f_{dp} \tilde{t}} \cdot e^{-j2\pi f_{dp} t_l} e^{-j\pi a_p t_l^2 / \lambda} + \boldsymbol{\omega}(\tilde{t}, t_l). \quad (3)$$

By (3), in general cases, the envelope migration of high speed target echo caused by the high velocity of the target would exceed one range cell during the integration time, thus affecting the accumulation of target energy. There are three exponential terms in (3). The first and the second are the Doppler terms with respect to the fast time and the slow time induced by the target's radial velocity. It is highly possible that the variety of the phase caused by the large-scale Doppler frequency of high speed target within the fast time is more than half of a turn of the unit circle; that is, $f_{dp} > 1/2T$. So the sharp distortion of target echo will occur, which results in the severe mismatch loss in matched filters, and then virtual array cannot be effectively formed. The third is the frequency modulation term because of the target's radial acceleration ignoring the effect of the target's radial acceleration on the phase variety during the fast time. Due to the range migration and the unsuccessfully formed virtual array, bistatic MIMO radar is incapable of effectively estimating DOD and DOA of high speed target.

3. Joint DOD and DOA Estimation for High Speed Target

Assume that the number of the range cells that the p th high speed target has gone through at the slow time t_l is denoted by $z_p(t_l)$, $p = 1, 2, \dots, P$, which is an integer and can be written as

$$z_p(t_l) = \left\lceil \frac{v_p t_l}{\delta} \right\rceil, \quad (4)$$

where $\delta = c/B$ is the range resolution of bistatic radar, B is the bandwidth of the transmitted signal, and $\lceil \cdot \rceil$ means the ceil operator of integer. Ignoring the truncated effect of the integer operator on the envelope migration of echo, (3) can be rewritten as

$$\mathbf{X}(\tilde{t}, t_l) \approx \sum_{p=1}^P \mathbf{a}_r(\theta_{rp}) \rho_p \mathbf{a}_t^T(\theta_{tp}) \mathbf{S} \left(\tilde{t} - \frac{z_p(t_l) \delta}{c}, t_l \right) e^{-j2\pi f_{dp} \tilde{t}} \cdot e^{-j2\pi f_{dp} t_l} e^{-j\pi a_p t_l^2 / \lambda} + \boldsymbol{\omega}(\tilde{t}, t_l). \quad (5)$$

Assume that during the observation time the total number of the across range cells of target is element of $[-Z, Z]$, where Z is an integer corresponding to the maximum possible number of the across range cells and minus

denotes that the target moves towards the radar. Multiplying the received signal of the m th receive element with the conjugate of the delayed version of the m th transmitted signal $S_m(\bar{t} - (z\delta/c), t_l)$, $z \in [-Z, Z]$, one can construct a signal $Y_{mn}(t, t_l, z)$ corresponding to the z th searching across range cell as follows:

$$\begin{aligned}
Y_{mn}(t, t_l, z) &= \sum_{\substack{p=1 \\ p \in C_{z_l}}}^P \beta_p(z) e^{-j(2\pi/\lambda)(n-1)d_r \sin \theta_{rp}} \\
&\quad \cdot e^{-j(2\pi/\lambda)(m-1)d_r \sin \theta_{lp}} e^{-j2\pi f_{dp} t} \\
&\quad \cdot e^{-j2\pi f_{dp} t_l} e^{-j\pi a_p t_l^2 / \lambda} \\
&\quad + \phi_{mn}(t, t_l, z) + W_{mn}(t, t_l, z), \\
m &= 1, 2, \dots, M, \quad n = 1, 2, \dots, N,
\end{aligned} \tag{6}$$

where C_{z_l} denotes the set for the variable p , that is, when $p \in C_{z_l}$ the equality $z_p(t_l) = z$ should hold, $\beta_p(z) = \rho_p e^{j\psi(z)}$, $\psi(z)$ is the initial phase of the p th target reflected signal when this target is located at the z th range cell, and $W_{mn}(t, t_l, z) = \omega_n(t, t_l) S_m^*(t + t_l - (z\delta/c), t_l)$, where $[\cdot]^*$ denotes complex conjugate. The first term in the right hand side of (6) holds under the condition $S_m(t + t_l - (z_p(t_l)\delta/c), t_l) S_m^*(t + t_l - (z\delta/c), t_l) = 1$ with $z_p(t_l) = z$, which becomes a sinusoid signal over the fast time. The second term in the right hand side of (6) is given by

$$\begin{aligned}
&\phi_{mn}(t, t_l, z) \\
&= \sum_{\substack{p=1 \\ p \in C_{z_l}}}^P \beta_p(z) e^{-j(2\pi/\lambda)(n-1)d_r \sin \theta_{rp}} \\
&\quad \cdot \sum_{\substack{i=1 \\ i \neq m}}^M e^{-j(2\pi/\lambda)(i-1)d_r \sin \theta_{lp}} S_i \left(t + t_l - \frac{z\delta}{c}, t_l \right) \\
&\quad \times S_m^* \left(t + t_l - \frac{z\delta}{c}, t_l \right) \\
&\quad \cdot e^{-j2\pi f_{dp} t} \cdot e^{-j2\pi f_{dp} t_l} e^{-j\pi a_p t_l^2 / \lambda} \\
&\quad + \sum_{\substack{p=1 \\ p \notin C_{z_l}}}^P \beta_p e^{-j(2\pi/\lambda)(N-1)d_r \sin \theta_{rp}} \mathbf{a}_t^T(\theta_{lp}) \\
&\quad \cdot \mathbf{S} \left(t + t_l - \frac{z_p(t_l)\delta}{c}, t_l \right) S_m^* \left(t + t_l - \frac{z\delta}{c}, t_l \right) e^{-j2\pi f_{dp} t} \\
&\quad \cdot e^{-j2\pi f_{dp} t_l} e^{-j\pi a_p t_l^2 / \lambda}.
\end{aligned} \tag{7}$$

Following that, a Fourier transform (FT) to the variable t is employed to transform the signal $Y_{mn}(t, t_l, z)$ into the fast-time frequency domain, which can be written as

$$\begin{aligned}
Y_{mn}(f, t_l, z) &= \int_0^T Y_{mn}(t, t_l) e^{-j2\pi f t} dt \\
&= \sum_{\substack{p=1 \\ p \in C_{z_l}}}^P \beta_p(z) e^{-j(2\pi/\lambda)(n-1)d_r \sin \theta_{rp}} \\
&\quad \cdot e^{-j(2\pi/\lambda)(m-1)d_r \sin \theta_{lp}} \\
&\quad \cdot \frac{\sin[\pi(f + f_{dp})T]}{\pi(f + f_{dp})T} \\
&\quad \cdot e^{-j\pi(f + f_{dp})T} \cdot e^{-j2\pi f_{dp} t_l} e^{-j\pi a_p t_l^2 / \lambda} \\
&\quad + \phi_{mn}(f, t_l, z) + W_{mn}(f, t_l, z).
\end{aligned} \tag{8}$$

Because of the high target speed and low repetition frequency of radar signal, it is highly possible that under-sampling will occur [13, 14]. In this situation, the target's true Doppler frequency can be expressed as [13, 14]

$$f_{dp} = f_{dp0} + \frac{n_p}{T}, \tag{9}$$

where f_{dp0} is the ambiguous Doppler frequency and n_p is the fold factor. Substituting (9) into (8), we can obtain

$$\begin{aligned}
Y_{mn}(f, t_l, z) &= \sum_{\substack{p=1 \\ p \in C_{z_l}}}^P \beta_p(z) e^{-j(2\pi/\lambda)(n-1)d_r \sin \theta_{rp}} \\
&\quad \cdot e^{-j(2\pi/\lambda)(m-1)d_r \sin \theta_{lp}} \cdot \frac{\sin[\pi(f + f_{dp})T]}{\pi(f + f_{dp})T} \\
&\quad \cdot e^{-j\pi(f + f_{dp})T} \cdot e^{-j2\pi f_{dp0} t_l} \cdot e^{-j2\pi(n_p/T)t_l} \\
&\quad \cdot e^{-j\pi a_p t_l^2 / \lambda} + \phi_{mn}(f, t_l, z) + W_{mn}(f, t_l, z).
\end{aligned} \tag{10}$$

It is worth pointing out that $2\pi(n_p/T)t_l$ in the fifth exponential term is integer times of 2π because of $t_l = lT$ and the integer n_p . This term in (10) becomes $e^{-j2\pi(n_p/T)t_l} = 1$. So (10) can be rewritten as

$$\begin{aligned}
Y_{mn}(f, t_l, z) &= \sum_{\substack{p=1 \\ p \in C_{z_l}}}^P \beta_p(z) e^{-j(2\pi/\lambda)(n-1)d_r \sin \theta_{rp}} \\
&\quad \cdot e^{-j(2\pi/\lambda)(m-1)d_r \sin \theta_{lp}} \cdot \frac{\sin[\pi(f + f_{dp})T]}{\pi(f + f_{dp})T} e^{-j\pi(f + f_{dp})T} \\
&\quad \cdot e^{-j2\pi f_{dp0} t_l} \cdot e^{-j\pi a_p t_l^2 / \lambda} + \phi_{mn}(f, t_l, z) + W_{mn}(f, t_l, z).
\end{aligned} \tag{11}$$

Assume that the reflected signal of the p th target located at the z th range cell is distributed along the repetition period index $l = L_{p\min}, L_{p\min} + 1, \dots, L_{p\max}$. Following that, a Fourier transform is taken to the signal $Y_{mn}(f, t_l, z)$ with variable t_l , and with the principle of stationary phase [22] we have

$$\begin{aligned}
Y_{mn}(f, f_l, z) &\approx \sum_{\substack{p=1 \\ p \in C_{zl}}}^P \beta_p(z) e^{-j(2\pi/\lambda)(n-1)d_r \sin \theta_{rp}} \\
&\cdot e^{-j(2\pi/\lambda)(m-1)d_r \sin \theta_{rp}} \\
&\cdot \frac{\sin \left[\pi (f + f_{dp}) T \right]}{\pi (f + f_{dp}) T} e^{-j\pi(f+f_{dp})T} \\
&\cdot \text{rect} \left[\frac{f_l + f_{dp0}}{(L_{p\max} - L_{p\min}) T \cdot a_p / \lambda} \right] \\
&\times e^{j\pi(f_l + f_{dp0})^2 / (a_p / \lambda)} \\
&\times e^{-j\pi f_l (L_{p\max} + L_{p\min}) T} + \zeta_{mn}(f, f_l, z),
\end{aligned} \tag{12}$$

where $\text{rect}[u] = \begin{cases} 1, & |u| \leq 1/2 \\ 0, & |u| > 1/2 \end{cases}$, $\zeta_{mn}(f, f_l, z) = \phi_{mn}(f, f_l, z) + W_n(f, f_l, z)$, and $\phi_{mn}(f, f_l, z)$, $W_n(f, f_l, z)$ are the Fourier transform of $\phi_{mn}(f, t_l, z)$ and $W_{mn}(f, t_l, z)$, respectively. Thus, Fourier transforms over both fast time and slow time have transformed the multiplied signals into the fast-time frequency and slow-time frequency domains. However, in the slow-time frequency domain, the target's acceleration broadens the spectrum and the Doppler frequency ambiguity occurs.

Due to the P target echoes existing in the initial range cell, that is, $z = 0$, the frequency-domain data $Y_{mn}(f, f_l, z = 0)$ ($m = 1, 2, \dots, M$, $n = 1, 2, \dots, N$) corresponding to the initial range cell can be exploited to estimate the Doppler frequencies and the ambiguous Doppler frequencies of P targets. When $f = -f_{dp}$ and $f_l = -f_{dp0}$, $p = 1, 2, \dots, P$, $Y_{mn}(f, f_l, z = 0)$ will generate the peaks. In order to improve the signal-to-noise ratio (SNR) for detection, the frequency-domain data with all transmitters and receivers of the bistatic MIMO radar is incoherently accumulated. Therefore, f_{dp} and f_{dp0} can be estimated as

$$(\hat{f}_{dp}, \hat{f}_{dp0}) = \arg \max_{f, f_l} \sum_{m=1}^M \sum_{n=1}^N |Y_{mn}(-f, -f_l, z = 0)|. \tag{13}$$

Unfortunately, because the estimated \hat{f}_{dp} is integer times of the repetition frequency of radar signal, the fold factor n_p in (9) cannot be solved by the estimated \hat{f}_{dp} and \hat{f}_{dp0} . Then the p th target's velocity v_p can be obtained only by the estimated unambiguous Doppler frequency corresponding to the fast-time frequency domain, which can be expressed as

$$\hat{v}_p = \lambda \cdot \hat{f}_{dp}. \tag{14}$$

Using the very short echo time, the Fourier transform over fast-time domain has poor frequency resolution so

that the Doppler frequency shifting value caused by target's acceleration during the observation time is much less than half of the fast-time frequency resolution. Then the target's energy can be approximately regarded as being concentrated in the same fast-time frequency cell during the observation time. However, due to the high frequency resolution of Fourier transform over slow-time domain, the target's energy may be distributed along several slow-time frequency cells.

The frequency-domain data of the p th target can be extracted from $Y_{mn}(f, f_l, z)$ along the slow-time frequency dimension when $f = -f_{dp} = -\hat{v}_p/\lambda$, which can be written as

$$\begin{aligned}
Y_{mn} \left(-\frac{\hat{v}_p}{\lambda}, f_l, z \right) &= e^{-j(2\pi/\lambda)(n-1)d_r \sin \theta_{rp}} \\
&\cdot e^{-j(2\pi/\lambda)(m-1)d_r \sin \theta_{rp}} \\
&\cdot H_p \left(-\frac{\hat{v}_p}{\lambda}, f_l, z \right) \\
&+ \zeta_{mn} \left(-\frac{\hat{v}_p}{\lambda}, f_l, z \right), \quad p \in C_z,
\end{aligned} \tag{15}$$

where $H_p(-\hat{v}_p/\lambda, f_l, z) = \beta_p(z) e^{-j\pi(\hat{v}_p/\lambda + f_{dp})T} \cdot \text{rect}[(f_l + f_{dp0}) / ((L_{p\max} - L_{p\min}) T \cdot a_p / \lambda)] \cdot e^{-j\pi(f_l + f_{dp0})^2 / (a_p / \lambda)} e^{-j\pi f_l (L_{p\max} + L_{p\min}) T}$.

In fact, $Y_{mn}(-\hat{v}_p/\lambda, f_l, z)$ can be considered as the separated target component from the m th transmitter to the n th receiver via the p th target located at the z th range cell, $m = 1, 2, \dots, M$, $n = 1, 2, \dots, N$. The separated target components for the p th target with all transmitters and receivers of bistatic MIMO radar can be expressed as

$$\begin{aligned}
\mathbf{Y} \left(-\frac{\hat{v}_p}{\lambda}, f_l, z \right) &= \mathbf{A}(\theta_{rp}, \theta_{tp}) H_p \left(-\frac{\hat{v}_p}{\lambda}, f_l, z \right) \\
&+ \boldsymbol{\zeta} \left(-\frac{\hat{v}_p}{\lambda}, f_l, z \right), \quad p \in C_{zl},
\end{aligned} \tag{16}$$

where $\mathbf{Y}(-\hat{v}_p/\lambda, f_l, z) = [Y_1(-\hat{v}_p/\lambda, f_l, z), Y_2(-\hat{v}_p/\lambda, f_l, z), \dots, Y_{MN}(-\hat{v}_p/\lambda, f_l, z)]^T$, $\mathbf{A}(\theta_{rp}, \theta_{tp}) = \mathbf{a}_{r1}(\theta_{rp}) \otimes \mathbf{a}_{t1}(\theta_{tp})$, \otimes is the Kronecker product, and the vector $\mathbf{W}_l \in \mathbb{C}^{MN \times 1}$ represents a noise vector.

Assume that the p th target moves away from radar. Analyzing the results of (13), we find that the indexes of the range cells that the p th high speed target has gone through during the long observation time are $z_p = 0, 1, \dots, Z_p$, respectively. Then the separated target components distributed along all the across range cells for the p th target are spliced as follows:

$$\begin{aligned}
\tilde{\mathbf{Y}}_{pl} &= \left[\mathbf{Y} \left(-\frac{\hat{v}_p}{\lambda}, f_l, 0 \right), \mathbf{Y} \left(-\frac{\hat{v}_p}{\lambda}, f_l, 1 \right), \dots, \right. \\
&\left. \mathbf{Y} \left(-\frac{\hat{v}_p}{\lambda}, f_l, Z_p \right) \right],
\end{aligned} \tag{17}$$

where $\tilde{\mathbf{Y}}_{pl} \in \mathbb{C}^{MN \times Z_p}$ is the output of the formed virtual array with MN virtual elements at the slow-time index l . Using (17),

we can form the covariance matrix of $\tilde{\mathbf{Y}}_{pl}$ for the p th target from the spliced data of L snapshots, which is given by

$$\mathbf{R}_p = \frac{1}{Z_p L} \sum_{l=1}^L \tilde{\mathbf{Y}}_{pl} \cdot \tilde{\mathbf{Y}}_{pl}^H = \frac{1}{Z_p} \sum_{z=0}^{Z_p} \frac{1}{L} \sum_{l=1}^L \mathbf{Y} \left(-\frac{\hat{v}_p}{\lambda, f_l, z} \right) \mathbf{Y}^H \left(-\frac{\hat{v}_p}{\lambda, f_l, z} \right), \quad (18)$$

where $(\cdot)^H$ denotes the Hermitian transpose. It is worth pointing out that the estimation precision of covariance matrix after splicing the separated target components that are distributed along all the across range cells can be remarkably improved due to the average of the covariance matrixes corresponding to all the across range cells. Thus, the angle estimation precision can also be increased using the more accurate covariance matrix.

Assume that the p th target moves towards radar. Analyzing the results of (13), we find that the indexes of the range cells that the p th high speed target has gone through during the long observation time are $z_p = 0, -1, \dots, -Z_p$, respectively. Then the separated target components for the p th target distributed along all the across range cells are spliced as follows:

$$\tilde{\mathbf{Y}}_{pl} = \left[\mathbf{Y} \left(-\frac{\hat{v}_p}{\lambda, f_l, 0} \right), \mathbf{Y} \left(-\frac{\hat{v}_p}{\lambda, f_l, -1} \right), \dots, \mathbf{Y} \left(-\frac{\hat{v}_p}{\lambda, f_l, -Z_p} \right) \right]. \quad (19)$$

After synthesizing the virtual array with the range migration removed, most of the existing superresolution angle estimation algorithms can be applied to obtain DOD and DOA of the high speed target. In this paper, only the ESPRIT algorithm is used for angle estimation because of its simplicity and efficiency. Using (19), we can form the covariance matrix of $\tilde{\mathbf{Y}}_{pl}$ for the p th target from the spliced data of L snapshots, which can be written as

$$\mathbf{R}_p = \frac{1}{Z_p L} \sum_{l=1}^L \tilde{\mathbf{Y}}_{pl} \cdot \tilde{\mathbf{Y}}_{pl}^H = \frac{1}{Z_p} \sum_{z=-Z_p}^0 \frac{1}{L} \sum_{l=1}^L \mathbf{Y} \left(-\frac{\hat{v}_p}{\lambda, f_l, z} \right) \mathbf{Y}^H \left(-\frac{\hat{v}_p}{\lambda, f_l, z} \right). \quad (20)$$

Performing the eigendecomposition on the $MN \times MN$ sample covariance matrix \mathbf{R}_p [5], we then have

$$\mathbf{R}_p = \mathbf{U}_s \Sigma_s \mathbf{U}_s^H + \mathbf{U}_n \Sigma_n \mathbf{U}_n^H, \quad (21)$$

where Σ_s is a scalar representing the largest eigenvalue because of only one existing target in \mathbf{R}_p , Σ_n is a diagonal matrix constructed by the remaining $MN - 1$ eigenvalues, $\mathbf{U}_s \in \mathbb{C}^{MN \times 1}$ is the signal subspace composed of the eigenvector corresponding to the largest eigenvalue, and $\mathbf{U}_n \in \mathbb{C}^{MN \times (MN-1)}$ is the noise subspace containing the remaining

$MN - 1$ eigenvectors of \mathbf{R}_p . Because the signal subspace spans the same space with the steering matrix, we have $\mathbf{U}_s = \mathbf{A}(\theta_{rp}, \theta_{tp})T$, where T is a nonzero scalar.

Define $\mathbf{A}'(\theta_{rp}, \theta_{tp}) = \mathbf{a}_{t1}(\theta_{tp}) \otimes \mathbf{a}_{r1}(\theta_{rp})$, which is row equivalent to $\mathbf{A}(\theta_{rp}, \theta_{tp})$ [7]. Suppose that \mathbf{U}'_s is a $MN \times 1$ signal subspace vector formed from \mathbf{U}_s by the same row interchange operations as $\mathbf{A}'(\theta_{rp}, \theta_{tp})$ is formed from $\mathbf{A}(\theta_{rp}, \theta_{tp})$. Let \mathbf{U}_{s1} and \mathbf{U}_{s2} be the first and the last $(N - 1)M$ rows of \mathbf{U}_s , and let \mathbf{U}'_{s1} and \mathbf{U}'_{s2} be the first and the last $(M - 1)N$ rows of \mathbf{U}'_s .

Then let us define the average estimators as follows [7]:

$$r_{rp} = \frac{1}{M(N-1)} \sum_{i=1}^{M(N-1)} \frac{\mathbf{U}_{s2}(i)}{\mathbf{U}_{s1}(i)}, \quad (22)$$

$$r_{tp} = \frac{1}{N(M-1)} \sum_{i=1}^{N(M-1)} \frac{\mathbf{U}'_{s2}(i)}{\mathbf{U}'_{s1}(i)},$$

where $\mathbf{U}_{s1}(i)$ and $\mathbf{U}_{s2}(i)$ are the i th elements in \mathbf{U}_{s1} and \mathbf{U}_{s2} , respectively, and $\mathbf{U}'_{s1}(i)$ and $\mathbf{U}'_{s2}(i)$ are the i th elements in \mathbf{U}'_{s1} and \mathbf{U}'_{s2} , respectively. Therefore, the DOA θ_{rp} and DOD θ_{tp} for the p th target, $p = 1, 2, \dots, P$, can be written as

$$\hat{\theta}_{rp} = \arcsin \left(-\lambda \cdot \frac{\text{angle}(r_{rp})}{2\pi d_r} \right), \quad (23)$$

$$\hat{\theta}_{tp} = \arcsin \left(-\lambda \cdot \frac{\text{angle}(r_{tp})}{2\pi d_t} \right).$$

The DOAs and DODs for the other targets can also be estimated by the same method. In summary, the DOAs and DODs of high speed targets for bistatic MIMO radar can be estimated via the following procedure.

Step 1. The signal $Y_{mn}(t, t_l, z)$ corresponding to the z th searching across range cell is constructed by multiplying the received signal of the n th receive element with the conjugate of the delayed version of the m th transmitted signal $S_m(\bar{t} - (z\delta/c), t_l)$, $z \in [-Z, Z]$.

Step 2. Following that, a Fourier transform (FT) to the variable t is employed to transform the signal $Y_{mn}(t, t_l, z)$ into the fast-time frequency domain, thus obtaining the signal $Y_{mn}(f, t_l, z)$.

Step 3. A Fourier transform is taken to the signal $Y_{mn}(f, t_l, z)$ with variable t_l , and we have the signal $Y_{mn}(f, f_l, z)$.

Fourier transforms over both fast time and slow time shown in Steps 2 and 3 have transformed the multiplied signals into the fast-time frequency and slow-time frequency domains.

Step 4. The frequency-domain data of the p th target $Y_{mn}(-\hat{v}_p/\lambda, f_l, z)$ can be extracted from $Y_{mn}(f, f_l, z)$ along the slow-time frequency dimension, which can be considered as the separated target component from the m th transmitter to the n th receiver via the p th target located at the z th range

cell. Then the separated target components for the p th target with all transmitters and receivers of bistatic MIMO radar are expressed as $\mathbf{Y}(-\hat{v}_p/\lambda, f_l, z)$.

Step 5. The separated target components for the p th target distributed along all the across range cells are spliced. Thus, the output of the formed virtual array for the p th high speed target is expressed as $\tilde{\mathbf{Y}}_{pl}$.

Step 6. The DOD and DOA of p th high speed target can be obtained from the output of virtual array $\tilde{\mathbf{Y}}_{pl}$ using the superresolution algorithm, that is, ESPRIT algorithm. The DOAs and DODs for the other targets can also be estimated by repeating Steps 4–6.

4. Simulation Result

Some numerical examples are presented to illustrate the performance of the proposed method. A bistatic MIMO radar with $M = 6$ transmitters and $N = 8$ receivers is adopted. Radar carrier frequency $f_1 = 10$ GHz, and the spacing between adjacent elements used for both transmit array and receive array is $d_t = d_r = 1.5$ cm. The Gold sequences are selected as the transmitted baseband signals of bistatic MIMO radar, which are nearly orthogonal binary codes with good autocorrelation and intercorrelation. The duration of a code is assumed to be $0.1 \mu\text{s}$, the period length of Gold sequence is 1023, and then the repetition period of the transmitted signals is $102.3 \mu\text{s}$. Suppose that the number of the repetition periods for the transmitted signals during the observation time is 128.

4.1. Results of 2D Fourier Transform of the Multiplied Signals. Assume that three high speed targets located at the same initial range cell and their DODs and DOAs are $(\theta_{t1}, \theta_{r1}) = (30^\circ, 60^\circ)$, $(\theta_{t2}, \theta_{r2}) = (5^\circ, 40^\circ)$, and $(\theta_{t3}, \theta_{r3}) = (25^\circ, 10^\circ)$, respectively. The sums of two radial velocities with respect to the transmit array and the receive array for three targets are given by 7500 m/s, 9000 m/s, and 6500 m/s, respectively. The sums of two radial accelerations with respect to the transmit array and the receive array for three targets are 400 m/s^2 , 500 m/s^2 , and 450 m/s^2 , respectively. The SNRs of three targets are all -25 dB. The received signals are multiplied with the conjugate of the delayed versions of the transmitted signals, and then the Fourier transform (FT) of the multiplied signals over both fast time and slow time is employed.

Figures 2(a)–2(f) show the results of 2D Fourier transform of the multiplied signals corresponding to the different searching across range cells, where the peak value indicates the existing target. By comparing the results of Figures 2(a)–2(f), we can show that the target's energy is concentrated in the same fast-time frequency cell when the target is located at the different range cells. The outputs are below noise level and unobservable as in Figures 2(a) and 2(f) with the searching range cell indexes $z = -1, 4$. However, there are three or two peaks that are much higher than the noise background and may easily be detected as in Figures 2(b), 2(c), 2(d), and 2(e) with the searching range cell indexes $z = 0, 1, 2, 3$. Thus, the energy of one target is distributed along the range cells

with the indexes $z = 0, 1, 2$, while the other two go through the range cells with the indexes $z = 0, 1, 2, 3$. The estimated target's velocities are 7625.8 m/s, 9092.3 m/s, and 6452.6 m/s, which are obtained by the estimated unambiguous Doppler frequency corresponding to the fast-time frequency domain. The relative errors of velocity estimation are large because of poor frequency resolution in fast-time frequency dimension. However, the Doppler frequency ambiguity occurs in the slow-time frequency dimension.

4.2. DOD and DOA Estimation for High Speed Target. In this simulation, we evaluate the DOD and DOA estimation performance of the proposed method and the standard ESPRIT method [5] that is employed in bistatic MIMO radar for angle estimation. The simulation parameters for the three targets are the same as those in Section 4.1. Figure 3 shows the obtained result by using the standard ESPRIT method for all three high speed targets with 150 Monte Carlo tests. We can observe that the high speed targets are unsuccessfully localized by the standard ESPRIT method due to the invalidly formed virtual array and the range migration. Figure 4 shows the obtained result by using the proposed method for all three high speed targets over 150 Monte Carlo tests. It is clear that the DOAs and DODs of the three high speed targets are well estimated and automatically paired. The crosses denote the true locations of the three high speed targets in Figures 3 and 4.

4.3. Angle Estimation Performance for High Speed Target versus SNR. In this simulation, the SNRs of three targets identically range from -30 dB to 0 dB, while the other parameters for the three targets are the same as those in Section 4.1. The root mean square error (RMSE) of two-dimensional angle estimation is defined as

$$\text{RMSE} = \sqrt{\frac{1}{\text{LC}} \sum_{i=1}^{\text{LC}} [(\hat{\theta}_{ti} - \theta_t)^2 + (\hat{\theta}_{ri} - \theta_r)^2]}, \quad (24)$$

where LC is the number of the independent trials and $\hat{\theta}_{ti}$ and $\hat{\theta}_{ri}$ are the estimates of true DOD θ_t and DOA θ_r in the i th Monte Carlo trial. Figure 5 shows the RMSEs of DOD and DOA estimation versus SNR for target 1, which is located at $(30^\circ, 60^\circ)$ with the velocity $v_1 = 7500$ m/s and $a_1 = 400 \text{ m/s}^2$. The number of Monte Carlo tests is 200. It is shown that the standard ESPRIT method fails to estimate the angles of the high speed target, while the proposed method has a marked performance improvement over the standard ESPRIT method.

Because only the DOD and DOA estimation problem for high speed target is considered in this paper, the Cramer-Rao bounds (CRBs) for target's motion parameters of different order [23] are not given. Moreover, the CRBs for target's DOD and DOA parameters in bistatic MIMO radar are derived under the condition that the virtual array can be successfully formed by matched filters [2], which cannot be used as a proper benchmark for evaluating the performance of the proposed method. The proposed method is provided for

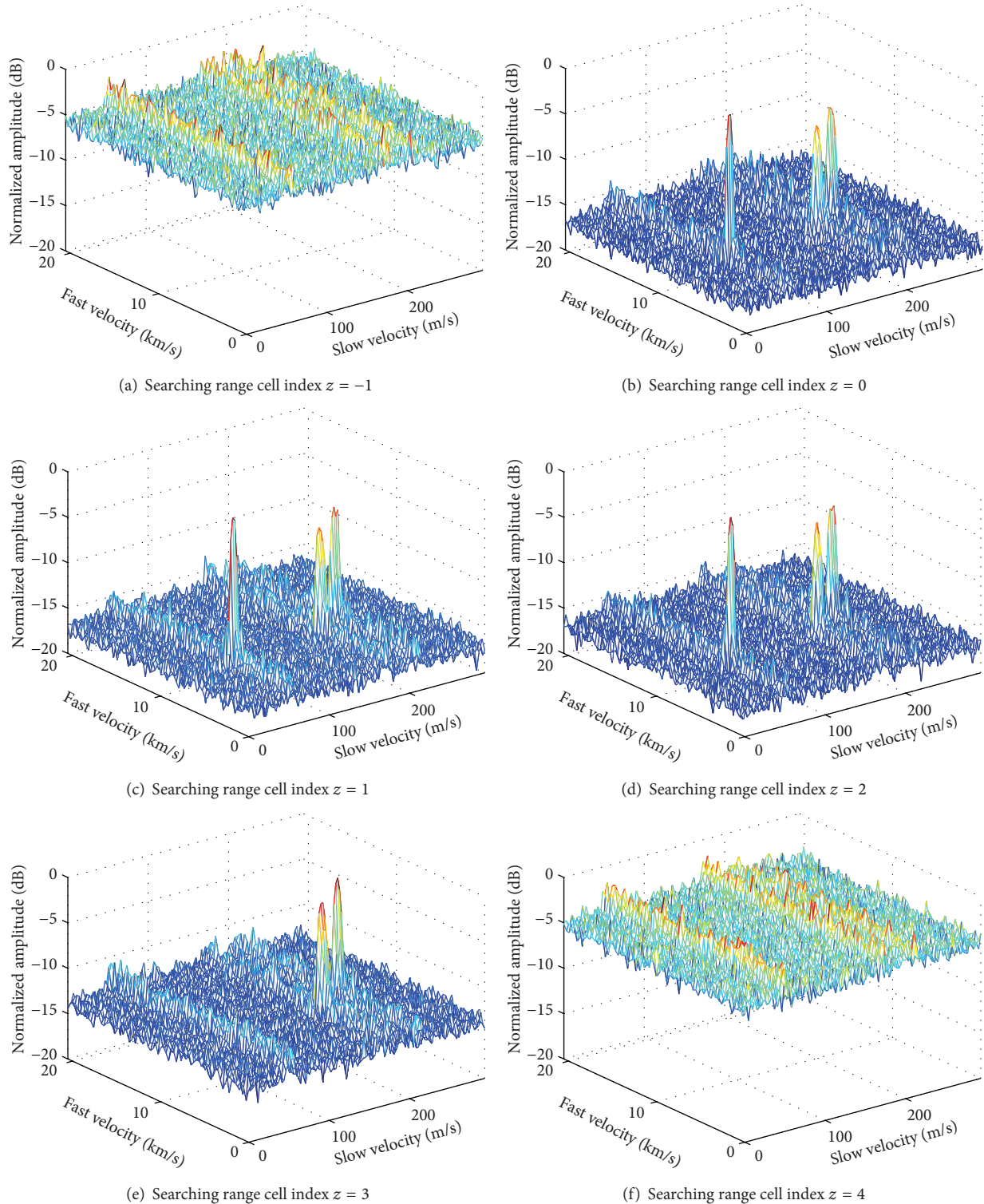


FIGURE 2: Results of 2D Fourier transform of the multiplied signals.

overcoming the effect of the large-scale Doppler frequency on the virtual array formation and removing range migration during the long-time integration, thus facilitating the angle estimation for high speed target in bistatic MIMO radar. Therefore, it is a good way to make the angle estimation

performance of the standard ESPRIT method when dealing with the low speed target without acceleration serve as a benchmark for performance comparison as shown in Figure 5. It is clearly shown that the standard ESPRIT method has a good performance in the estimation of DOD and DOA

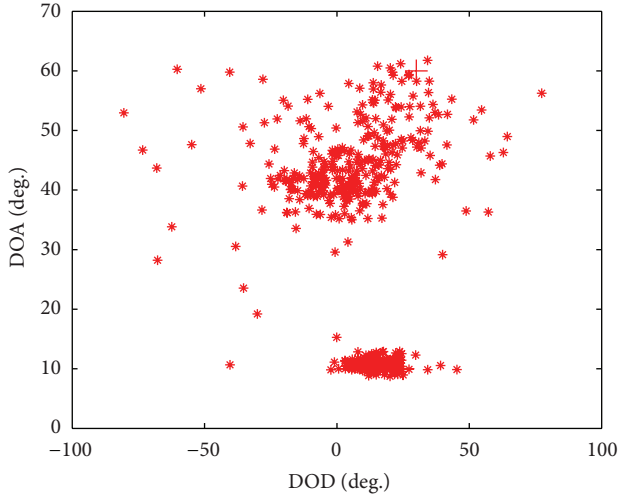


FIGURE 3: Estimation results of the standard ESPRIT method for three high speed targets.

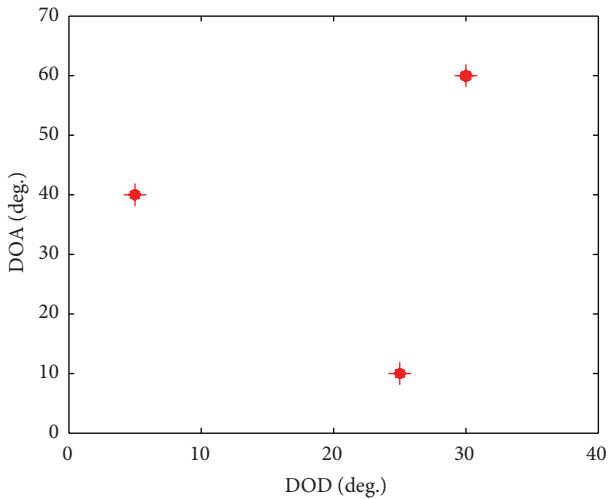


FIGURE 4: Estimation results of the proposed method for three high speed targets.

of the low speed target due to the effective virtual array formed by conventional matched filters and absence of range walk, while the proposed method exploited to estimate angles of the high speed target performs only a little worse than the standard ESPRIT method used for dealing with the low speed target. Moreover, for the high speed target, the angle estimation performances of the proposed method in the case of target acceleration $a_1 = 0 \text{ m/s}^2$ and the proposed method using the target energy only in the initial range cell are also shown in Figure 5. These results illustrate that whether there exists target acceleration, the proposed method has a robust performance, and the proposed method using the target energy in all the across range cells attains better performance compared with that using the target energy only in the initial range cell. Thus, splicing the separated target components

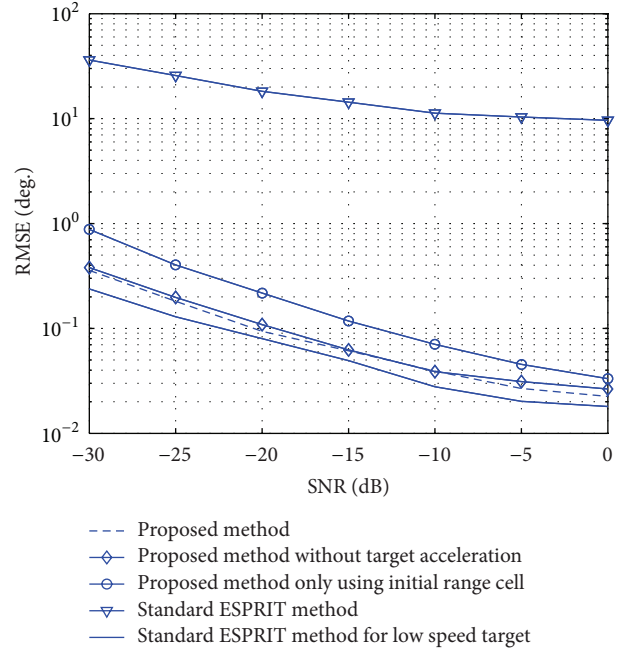


FIGURE 5: RMSEs of DOD and DOA estimation versus SNR for target 1.

that are distributed along several range cells can improve the angle estimation accuracy.

5. Conclusions

A method for high speed target angle estimation using bistatic MIMO radar is proposed. For the target with high velocity, range migration always occurs and the serious mismatch induced by the target’s large-scale Doppler frequency usually exists in matched filter, which creates difficulties for target parameter estimation. After 2D Fourier transform of the multiplied signals which are obtained by multiplying the received signals with the conjugate of the delayed versions of the transmitted signals, the proposed method perfectly separates the target components of the radar return corresponding to the different transmitted waveforms and then splices the separated target components that are distributed along several range cells to successfully synthesize the virtual array. Thus, the DOD and DOA of high speed target can be estimated by using the superresolution algorithm. The effectiveness of the proposed method has been demonstrated by the numerical experimental results.

Conflict of Interests

The authors declare that there is no conflict of interests regarding the publication of this paper.

Acknowledgments

This work was supported in part by the National Natural Science Foundation of China under Grant no. 61302188,

Grant no. 61372066, Grant no. 61071164, Grant no. 61071163, Grant no. 61271327, and Grant no. 41075115, in part by the Natural Science Foundation of Jiangsu Province of China under Grant BK20131005, and in part by the project funded by the Priority Academic Program Development of Jiangsu Higher Education Institutions. The authors wish to thank the anonymous reviewers for their valuable comments and suggestions which greatly improved the paper.

References

- [1] N. J. Willis and H. D. Griffiths, *Advances in Bistatic Radar*, SciTech Publishing, Raleigh, NC, USA, 2007.
- [2] H. D. Yan, J. Li, and G. S. Liao, "Multitarget identification and localization using bistatic MIMO radar systems," *EURASIP Journal on Advances in Signal Processing*, vol. 2008, Article ID 283483, 8 pages, 2008.
- [3] J. Li, S. Q. Zhu, X. X. Chen, L. Lv, G. S. Liao, and M. L. Yi, "Sparse recovery for bistatic MIMO radar imaging in the presence of array gain uncertainties," *International Journal of Antennas and Propagation*, vol. 2014, Article ID 807960, 6 pages, 2014.
- [4] Y. H. Cao, Z. J. Zhang, S. H. Wang, and F. Z. Dai, "Direction finding for bistatic MIMO radar with uniform circular array," *International Journal of Antennas and Propagation*, vol. 2013, Article ID 674878, 6 pages, 2013.
- [5] C. Duofang, C. Baixiao, and Q. Guodong, "Angle estimation using ESPRIT in MIMO radar," *Electronics Letters*, vol. 44, no. 12, pp. 770–771, 2008.
- [6] M. L. Bencheikh, Y. D. Wang, and H. He, "Polynomial root finding technique for joint DOA DOD estimation in bistatic MIMO radar," *Signal Processing*, vol. 90, no. 9, pp. 2723–2730, 2010.
- [7] C. Jinli, G. Hong, and S. Weimin, "Angle estimation using ESPRIT without pairing in MIMO radar," *Electronics Letters*, vol. 44, no. 24, pp. 1422–1423, 2008.
- [8] J. Li, X. Zhang, R. Cao, and M. Zhou, "Reduced-dimension MUSIC for angle and array gain-phase error estimation in bistatic MIMO radar," *IEEE Communications Letters*, vol. 17, no. 3, pp. 443–446, 2013.
- [9] H. A. Khan and D. J. Edwards, "Doppler problems in orthogonal MIMO radars," in *Proceedings of the IEEE Radar Conference*, pp. 244–247, April 2006.
- [10] D. Kirkland, "Imaging moving targets using the second-order keystone transform," *IET Radar, Sonar and Navigation*, vol. 5, no. 8, pp. 902–910, 2011.
- [11] Y. Jungang, H. Xiaotao, J. Tian, J. Thompson, and Z. Zhimin, "New approach for SAR imaging of ground moving targets based on a keystone transform," *IEEE Geoscience and Remote Sensing Letters*, vol. 8, no. 4, pp. 829–833, 2011.
- [12] Y. Liu, Q. S. Wu, G. C. Sun, M. D. Xing, B. C. Liu, and Z. Bao, "Parameter estimation of moving targets in the SAR system with a low PRF sampling rate," *Science China: Information Sciences*, vol. 55, no. 2, pp. 337–347, 2012.
- [13] J. Su, M. Xing, G. Wang, and Z. Bao, "High-speed multi-target detection with narrowband radar," *IET Radar, Sonar and Navigation*, vol. 4, no. 4, pp. 595–603, 2010.
- [14] M. Xing, J. Su, G. Wang, and Z. Bao, "New parameter estimation and detection algorithm for high speed small target," *IEEE Transactions on Aerospace and Electronic Systems*, vol. 47, no. 1, pp. 214–224, 2011.
- [15] R. P. Persy and R. C. Dipietro, "SAR imaging of moving targets," *IEEE Transactions on Aerospace and Electronic Systems*, vol. 35, no. 1, pp. 188–200, 1999.
- [16] P. V. Dorp, "LFMCW based MIMO imaging processing with Keystone Transform," in *Proceedings of the 10th European Radar Conference*, pp. 467–470, October 2013.
- [17] J. K. Zeng and Z. S. He, "Detection of weak target for MIMO radar based on Hough transform," *Journal of Systems Engineering and Electronics*, vol. 20, no. 1, pp. 76–80, 2009.
- [18] J. Xu, J. Yu, Y. Peng, and X. Xia, "Radon-fourier transform for radar target detection, I: generalized doppler filter bank," *IEEE Transactions on Aerospace and Electronic Systems*, vol. 47, no. 2, pp. 1186–1202, 2011.
- [19] J. Xu, J. Yu, Y. Peng, and X. Xia, "Radon-fourier transform for radar target detection (II): blind speed sidelobe suppression," *IEEE Transactions on Aerospace and Electronic Systems*, vol. 47, no. 4, pp. 2473–2489, 2011.
- [20] J. Yu, J. Xu, Y. Peng, and X. Xia, "Radon-Fourier transform for radar target detection (III): optimality and fast implementations," *IEEE Transactions on Aerospace and Electronic Systems*, vol. 48, no. 2, pp. 991–1004, 2012.
- [21] J. Xu, J. Yu, Y.-N. Peng, X.-G. Xia, and T. Long, "Space-time Radon-Fourier transform and applications in radar target detection," *IET Radar, Sonar & Navigation*, vol. 6, no. 9, pp. 846–857, 2012.
- [22] W. G. Carrara, R. S. Goodman, and R. M. Majewski, *Spotlight Synthetic Aperture Radar: Signal Processing Algorithms*, Artech House, Norwood, Mass, USA, 1995.
- [23] J. Xu, X. Xia, S. Peng, J. a. Yu, and L. Qian, "Radar maneuvering target motion estimation based on generalized Radon-Fourier transform," *IEEE Transactions on Signal Processing*, vol. 60, no. 12, pp. 6190–6201, 2012.

Research Article

SAGE-Based Algorithm for Direction-of-Arrival Estimation and Array Calibration

Kunlai Xiong, Zheng Liu, and Wenli Jiang

College of Electronic Science and Engineering, National University of Defense Technology, Changsha, Hunan 410073, China

Correspondence should be addressed to Kunlai Xiong; comecloud@163.com

Received 21 December 2013; Revised 23 April 2014; Accepted 12 May 2014; Published 15 June 2014

Academic Editor: Michelangelo Villano

Copyright © 2014 Kunlai Xiong et al. This is an open access article distributed under the Creative Commons Attribution License, which permits unrestricted use, distribution, and reproduction in any medium, provided the original work is properly cited.

Most existing array processing algorithms are very sensitive to model uncertainties caused by the mutual coupling and sensor location error. To mitigate this problem, a novel method for direction-of-arrival (DOA) estimation and array calibration in the case of deterministic signals with unknown waveforms is presented in this paper. The analysis begins with a comprehensive perturbed array output model, and it is effective for various kinds of perturbations, such as mutual coupling and sensor location error. Based on this model, the Space Alternating Generalized Expectation-Maximization (SAGE) algorithm is applied to jointly estimate the DOA and array perturbation parameters, which simplifies the multidimensional search procedure required for finding maximum likelihood (ML) estimates. The proposed method inherits the characteristics of good convergence and high estimation precision of the SAGE algorithm. At the same time, it forms a unified framework for DOA and array perturbation parameters estimation in the presence of mutual coupling and sensor location error. The simulation results demonstrate the effectiveness of the algorithm.

1. Introduction

The problem of estimating direction-of-arrival (DOA) of multiple narrowband signals plays an important role in many fields, including radar, wireless communications, seismology, and sonar. The performance of most existing DOA estimation methods relies crucially on perfect knowledge of the array manifold. In practice, however, the array manifold is often affected by the mutual coupling, gain/phase uncertainty, sensor location error, and so forth. Without array manifold calibration, the performance of DOA estimation may deteriorate significantly.

To mitigate this problem, various array calibration methods have been proposed. Those methods formulate the array perturbations with unknown parameters and estimate those parameters together with the source directions, so as to realize array calibration and DOA estimation. Most of the existing methods only focus on certain type of array imperfection, such as mutual coupling [1–4], gain/phase uncertainty [5–7], and sensor location error [8, 9]. The DOA estimation problem in the presence of more than one type of array perturbation has also been studied in a small amount of literatures [10, 11]. However, the method

in [10] is computationally much expensive as it requires multidimensional parameter searching, while the method in [11] needs to know the directions of the calibration sources.

Among all popular DOA estimation methods, the maximum likelihood (ML) approach provides the best asymptotic performance and remains stable in scenarios involving small numbers of snapshots, coherent signals, and low signal-to-noise ratios (SNR). The main drawback of the ML approach is the high computational complexity caused by optimization of the likelihood function. To reduce this difficulty, the Expectation-Maximization (EM) algorithm has been derived for both deterministic and stochastic signal models with known noise covariance structure [12, 13]. The Space Alternating Generalized EM (SAGE) algorithm is a variation of the widely used EM algorithm, which updates subsets of parameters sequentially in one iteration. Through the augmentation scheme specified by the EM or SAGE algorithm, the complicated multidimensional search involved in maximizing likelihood functions can be simplified to one-dimensional search. It was proved in [14] that SAGE converges faster than EM while retaining the advantages of numerical simplicity and stability due to its flexible augmentation scheme. Both the EM algorithm and the SAGE algorithm are earlier applied

to DOA estimation problem in accurately calibrated arrays. However, because the directional information can hardly be extracted directly when array perturbation exists, there is little literature using EM or SAGE algorithm to estimate DOA in perturbed arrays. In [15], we present a comprehensive perturbed output model, which makes the relationship between the array output and the perturbation parameters clearer. The sparse Bayesian method and EM algorithm are applied to estimate DOA and perturbation parameters in the case of stochastic signals.

In this paper, we focus on deterministic and unknown narrowband signals. And a single type of array imperfection is considered, with mutual coupling and sensor location error treated as typical examples. Based on the comprehensive perturbed array output model proposed in [15], we derive an SAGE-based algorithm, which applies the SAGE algorithm to jointly estimate DOA and perturbation parameters. Compared to the existing method, the proposed algorithm can achieve higher estimation precision; at the same time, it follows a unified framework to address the DOA estimation problem in the presence of array imperfections, with typical perturbations of mutual coupling and sensor location error taken into consideration.

This paper is outlined as follows. The comprehensive perturbed array output model is described in Section 2. The SAGE algorithm for DOA estimation and array calibration is developed in Section 3. Numerical results are presented and discussed in Section 4. Section 5 concludes this work.

2. Perturbed Array Output Formulation

Consider that K unknown and deterministic narrowband signals impinge onto an M element uniform linear array from directions of $\boldsymbol{\vartheta} = [\vartheta_1, \dots, \vartheta_K]^T$, where $K < M$. We take the first array sensor as the reference. The perturbed array output is given as follows:

$$\mathbf{x}(t) = \sum_{k=1}^K \mathbf{a}'(\vartheta_k) s_k(t) + \mathbf{v}(t) = \mathbf{A}'(\boldsymbol{\vartheta}) \mathbf{s}(t) + \mathbf{v}(t), \quad (1)$$

where the array responding matrix $\mathbf{A}'(\boldsymbol{\vartheta}) = [\mathbf{a}'(\vartheta_1), \dots, \mathbf{a}'(\vartheta_K)]$ and $\mathbf{a}'(\theta)$ is the perturbed responding vector. The observe vector $\mathbf{x}(t) = [x_1(t), \dots, x_M(t)]^T$ is sampled at time instances $t = t_1, \dots, t_N$, where N represents the number of snapshots. The signal vector $\mathbf{s}(t) = [s_1(t), \dots, s_K(t)]^T$, and $s_k(t)$ is the waveform of the k th signal. The noise vector $\mathbf{v}(t) = [v_1(t), \dots, v_M(t)]^T$ is independent, identically complex, and normally distributed with zero mean and covariance matrix $\sigma^2 \mathbf{I}$, where σ is an unknown noise spectral parameter. The two types of typical array perturbations, including mutual coupling and sensor location error, are concerned in this paper, and the array geometry is assumed to be linear to simplify notations. The sensor location error is also assumed to exist along the array axes and thus does not destroy the linear geometry of the array.

The perturbed array responding vector has diverse expressions in the case of different array imperfections. When mutual coupling is present, the vector is $\mathbf{a}'(\boldsymbol{\vartheta}) = \mathbf{C}\mathbf{a}(\boldsymbol{\vartheta})$ [2],

with \mathbf{C} representing the mutual coupling matrix. The mutual coupling matrix can be written more explicitly as $\mathbf{C} = \text{toeplitz}([1, b_1, \dots, b_p, \mathbf{0}_{(M-p-1) \times 1}^T])^T$, where $b_p \in \mathbb{C}$ is the coupling coefficient of the two sensors displaced by $p - 1$ times the interelement spacing of the ULA, and b_p is very small when $p > P$ and is, thus, neglected. The perturbed array responding vector in the presence of sensor location error is $\mathbf{a}'(\boldsymbol{\vartheta}) = [e^{j2\pi(d_1 + \tilde{d}_1) \sin \theta / \lambda}, \dots, e^{j2\pi(d_M + \tilde{d}_M) \sin \theta / \lambda}]^T$, with $\tilde{d}_1, \dots, \tilde{d}_M$ being the location errors of the M sensors [8]. In this paper, we take the first array sensor as the reference; thus $\tilde{d}_1 = 0$ and $\tilde{d}_1 = 0$.

Although the directional information of the incident signals is still reserved in the perturbed array outputs, it can hardly be extracted directly based on the array output formulation in (1), as the structure of $\mathbf{A}'(\boldsymbol{\vartheta})$ is not available beforehand due to the unknown array imperfections. In order to highlight the perturbation-free signal components and also make the relationship between the array output and the perturbation parameters clearer, we have established the following comprehensive formulation of the perturbed array output in [15]:

$$\mathbf{x}(t) = \mathbf{A}'(\boldsymbol{\vartheta}) \mathbf{s}(t) + \mathbf{v}(t) = \mathbf{A}(\boldsymbol{\vartheta}) \mathbf{s}(t) + \mathbf{Q}(t) \mathbf{c} + \mathbf{v}(t). \quad (2)$$

Equation (2) adapts to the typical array perturbations, including mutual coupling and sensor location error, with \mathbf{c} standing for a column vector consisting of the array perturbation parameters, $\mathbf{c} \in \mathbb{C}^{P \times 1}$ for mutual coupling, and $\mathbf{c} \in \mathbb{R}^{(M-1) \times 1}$ for sensor location error. We use P to denote the dimension of \mathbf{c} uniformly for notational convenience; that is, $\mathbf{c} = [c_1, \dots, c_P]^T$, and $P = M - 1$ in the case of sensor location error. The explicit formulation of $\mathbf{A}'(\boldsymbol{\vartheta})$ varies with respect to the array perturbation type, and the following equation holds for $\mathbf{Q}(t)$ and \mathbf{c} :

$$\mathbf{Q}(t) \mathbf{c} = [\mathbf{A}'(\boldsymbol{\vartheta}) - \mathbf{A}(\boldsymbol{\vartheta})] \mathbf{s}(t) \triangleq \boldsymbol{\Psi} \boldsymbol{\Phi}(\boldsymbol{\vartheta}) \mathbf{s}(t), \quad (3)$$

where $\boldsymbol{\Psi}$ is a function of \mathbf{c} and independent of the signal directions, while $\boldsymbol{\Phi}(\boldsymbol{\vartheta})$ is independent of \mathbf{c} and relies on the signal directions; they diverge largely according to the array perturbation type. However, for each of the typical perturbations, it holds for $\mathbf{Q}(t)$ that $[\mathbf{Q}(t)]_{:,p} = \mathbf{G}_p \boldsymbol{\Phi}(\boldsymbol{\vartheta}) \mathbf{s}(t)$ with $\mathbf{G}_p = \partial \boldsymbol{\Psi} / \partial c_p$. Such an expression of $\mathbf{Q}(t)$ is concluded by taking the differentiations of both sides of (3) with respect to c_p . In order to explain (2) and (3) more explicitly, we itemize the expressions of \mathbf{c} , $\boldsymbol{\Psi}$, $\boldsymbol{\Phi}(\boldsymbol{\vartheta})$, and $\mathbf{Q}(t)$.

Mutual Coupling. Equation (2) can be rewritten as follows in the case of mutual coupling:

$$\begin{aligned} \mathbf{x}(t) &= \mathbf{A}(\boldsymbol{\vartheta}) \mathbf{s}(t) + (\mathbf{C} - \mathbf{I}_M) \mathbf{A}(\boldsymbol{\vartheta}) \mathbf{s}(t) + \mathbf{v}(t) \\ &= \mathbf{A}(\boldsymbol{\vartheta}) \mathbf{s}(t) + \mathbf{Q}(t) \mathbf{c} + \mathbf{v}(t). \end{aligned} \quad (4)$$

By combining (3) and (4), it can be concluded that $\boldsymbol{\Psi} = (\mathbf{C} - \mathbf{I}_M) = \text{toeplitz}([0, b_1, \dots, b_p, \mathbf{0}_{(M-p-1) \times 1}^T])^T$, $\boldsymbol{\Phi}(\boldsymbol{\vartheta}) = \mathbf{A}(\boldsymbol{\vartheta})$, $c_p = b_p$, $[\mathbf{Q}(t)]_{:,p} = \mathbf{G}_p \mathbf{A}(\boldsymbol{\vartheta}) \mathbf{s}(t)$, and $\mathbf{G}_p = \partial \boldsymbol{\Psi} / \partial c_p = \partial \mathbf{C} / \partial b_p$ contain nonzero elements of 1 only on the $\pm p$ diagonals.

Sensor Location Error. Equation (2) can be rewritten as follows in the case of sensor location error:

$$\begin{aligned} \mathbf{x}(t) &= \mathbf{A}(\boldsymbol{\vartheta}) \mathbf{s}(t) + \text{diag}\left([0, \tilde{d}_2, \dots, \tilde{d}_M]^T\right) \\ &\quad \times \mathbf{A}(\boldsymbol{\vartheta}) \text{diag}\left(\frac{j2\pi}{\lambda} [\sin \vartheta_1, \dots, \sin \vartheta_K]^T\right) \times \mathbf{s}(t) + \mathbf{v}(t) \\ &= \mathbf{A}(\boldsymbol{\vartheta}) \mathbf{s}(t) + \mathbf{Q}(t) \mathbf{c} + \mathbf{v}(t). \end{aligned} \quad (5)$$

The first equation in (5) is concluded via first-order Taylor expansion under the assumption of small sensor location errors, and $\boldsymbol{\Psi} = \text{diag}([0, \tilde{d}_2, \dots, \tilde{d}_M]^T)$, $\Phi(\boldsymbol{\vartheta}) = \mathbf{A}(\boldsymbol{\vartheta}) \text{diag}((j2\pi/\lambda) [\sin \vartheta_1, \dots, \sin \vartheta_K]^T)$, $c_p = \tilde{d}_{p+1}$, $\mathbf{G}_p = \partial \boldsymbol{\Psi} / \partial c_p$ have their $(p+1, p+1)$ th element being the only nonzero value of 1.

3. SAGE-Based Algorithm for DOA Estimation and Array Calibration

It is well known that both EM algorithm and SAGE algorithm have been applied to the question of DOA estimation without array imperfections. And they can achieve the global convergence. The EM algorithm is a general numerical method for finding maximum likelihood estimates which is characterized by simple implementation and stable convergence. The SAGE algorithm is a generalized form of the EM algorithm, which allows a more flexible optimization scheme and converges faster than the EM algorithm. Instead of estimating all parameters at once in EM, SAGE breaks up the problem into several smaller ones and uses EM to update the parameter subset associated with each reduced problem. In this section, based on the existing comprehensive perturbed array output model, we propose an SAGE-based algorithm to jointly estimate DOA and array perturbation parameters. At the same time, for comparing the performance of the SAGE and EM algorithms in array self-calibration problem, the EM-based algorithm is also considered.

Based on the comprehensive model of the perturbed array output in (2), we construct the augmented data as follows for separating different signal components of array output:

$$\begin{aligned} \mathbf{y}_k(t) &= \mathbf{a}'(\vartheta_k) s_k(t) + \mathbf{v}_k(t) \\ &= \mathbf{a}(\vartheta_k) s_k(t) + \mathbf{Q}_k(t) \mathbf{c} + \mathbf{v}_k(t), \end{aligned} \quad (6)$$

$$k = 1, \dots, K,$$

where $\mathbf{Q}_k(t) \mathbf{c} = [\mathbf{a}'(\vartheta_k) - \mathbf{a}(\vartheta_k)] s_k(t)$, $[\mathbf{Q}_k(t)]_{:,p} = (\partial / \partial c_p) [\mathbf{a}'(\vartheta_k) - \mathbf{a}(\vartheta_k)] s_k(t) \triangleq \mathbf{G}_{k,p} \phi(\vartheta_k) s_k(t)$. $\mathbf{G}_{k,p}$ and $\phi(\vartheta_k)$ diverge largely according to the array perturbation type.

Mutual Coupling. Equation (6) can be rewritten as follows in the case of mutual coupling:

$$\begin{aligned} \mathbf{y}_k(t) &= \mathbf{a}(\vartheta_k) s_k(t) + (\mathbf{C} - \mathbf{I}_M) \mathbf{a}(\vartheta_k) s_k(t) + \mathbf{v}_k(t) \\ &= \mathbf{a}(\vartheta_k) s_k(t) + \mathbf{Q}_k(t) \mathbf{c} + \mathbf{v}_k(t), \end{aligned} \quad (7)$$

$$k = 1, \dots, K.$$

It can be concluded that $\phi(\vartheta_k) = \mathbf{a}(\vartheta_k)$, $\mathbf{c} = [c_1, \dots, c_P]^T = [b_1, \dots, b_P]^T$, and $\mathbf{G}_{k,p} = \partial \mathbf{C} / \partial b_p$ contain nonzero elements of 1 only on the $\pm p$ diagonals.

Sensor Location Error. Equation (6) can be rewritten as follows in the case of sensor location error:

$$\begin{aligned} \mathbf{y}_k(t) &= \mathbf{a}(\vartheta_k) s_k(t) + \text{diag}\left([0, \tilde{d}_2, \dots, \tilde{d}_M]^T\right) \\ &\quad \times \mathbf{a}(\vartheta_k) \frac{j2\pi}{\lambda} \sin \vartheta_K \times s_k(t) + \mathbf{v}_k(t) \\ &= \mathbf{a}(\vartheta_k) s_k(t) + \mathbf{Q}_k(t) \mathbf{c} + \mathbf{v}_k(t), \end{aligned} \quad (8)$$

$$k = 1, \dots, K.$$

It can be concluded that $\phi(\vartheta_k) = \mathbf{a}(\vartheta_k)(j2\pi/\lambda) \sin \vartheta_K$, $\mathbf{c} = [c_1, \dots, c_P]^T = [\tilde{d}_2, \dots, \tilde{d}_M]^T$, and $\mathbf{G}_{k,p}$ have their $(p+1, p+1)$ th element being the only nonzero value of 1. $\mathbf{v}_k(t)$ is a portion of noise extracted from $\mathbf{v}(t)$, and $\mathbf{v}_k(t) \sim \mathcal{N}(\mathbf{0}, \rho_k \sigma^2 \mathbf{I}_M)$, $0 \leq \rho_k \leq 1$.

In the framework of the EM algorithm, the noise process $\mathbf{v}_k(t)$, ($k = 1, \dots, K$) is independent and $\rho_k = 1/K$, so the likelihood of $\mathbf{y}_K(t)$ is given by

$$\begin{aligned} p_{\text{EM}}(\mathbf{y}_k(t) | \Omega_k(t)) \\ = \left| \pi \frac{\sigma^2}{K} \mathbf{I}_M \right|^{-1} \exp \left\{ -\frac{K}{\sigma^2} \left\| \mathbf{y}_k(t) - \mathbf{a}'(\vartheta_k) s_k(t) \right\|_2^2 \right\}, \end{aligned} \quad (9)$$

where $\Omega_k(t)$ is the subset of all unknown parameters set $\Omega = \{\boldsymbol{\vartheta}, \{\mathbf{s}(t_n)\}_{n=1}^N, \mathbf{c}, \sigma^2\}$ and, correspondingly, $\Omega(t) = \{\boldsymbol{\vartheta}, \mathbf{s}(t), \mathbf{c}, \sigma^2\}$. Because $\mathbf{v}_k(t_n)$, ($k = 1, \dots, K, n = 1, \dots, N$) is independent, we can infer that $\mathbf{y}_k(t_n)$, ($k = 1, \dots, K, n = 1, \dots, N$) is independent. Hence, the unified log-likelihood of $\{\mathbf{y}_1(t_n), \dots, \mathbf{y}_K(t_n)\}_{n=1}^N$ is given by

$$\begin{aligned} \mathcal{L}_{\text{EM}}(\{\mathbf{y}_1(t_n), \dots, \mathbf{y}_K(t_n)\}_{n=1}^N) \\ = \sum_{k=1}^K \mathcal{L}_{\text{EM}}(\{\mathbf{y}_k(t_n)\}_{n=1}^N) \\ = KMN \ln \sigma^2 + \frac{K}{\sigma^2} \sum_{n=1}^N \sum_{k=1}^K \left\| \mathbf{y}_k(t_n) - \mathbf{a}'(\vartheta_k) s_k(t_n) \right\|_2^2. \end{aligned} \quad (10)$$

In the framework of the SAGE algorithm, $\mathbf{v}_1(t) = \dots = \mathbf{v}_K(t) = \mathbf{v}(t)$ and $\rho_k = 1$, so the likelihood of $\mathbf{y}_K(t)$ is given by

$$\begin{aligned} p_{\text{SAGE}}(\mathbf{y}_k(t) | \Omega_k(t)) \\ = \left| \pi \sigma^2 \mathbf{I}_M \right|^{-1} \exp \left\{ -\frac{1}{\sigma^2} \left\| \mathbf{y}_k(t) - \mathbf{a}'(\vartheta_k) s_k(t) \right\|_2^2 \right\}. \end{aligned} \quad (11)$$

Because $\mathbf{v}_1(t) = \dots = \mathbf{v}_K(t) = \mathbf{v}(t)$ for the SAGE algorithm, we can infer that $\mathbf{y}_1(t), \dots, \mathbf{y}_K(t)$ have the same distribution. Hence, the unified log-likelihood of $\{\mathbf{y}_1(t_n), \dots, \mathbf{y}_K(t_n)\}_{n=1}^N$ is the mean of the log-likelihood of $\{\mathbf{y}_k(t_n)\}_{n=1}^N$ for different k value.

Consider

$$\begin{aligned} \mathcal{L}_{\text{SAGE}}(\{\mathbf{y}_1(t_n), \dots, \mathbf{y}_K(t_n)\}_{n=1}^N) \\ = \frac{1}{K} \sum_{k=1}^K \mathcal{L}_{\text{SAGE}}(\{\mathbf{y}_k(t_n)\}_{n=1}^N) \\ = MN \ln \sigma^2 + \frac{1}{K\sigma^2} \sum_{n=1}^N \sum_{k=1}^K \|\mathbf{y}_k(t_n) - \mathbf{a}'(\vartheta_k) s_k(t_n)\|_2^2. \end{aligned} \quad (12)$$

According to (10) and (12), the log-likelihood of $\{\mathbf{y}_1(t_n), \dots, \mathbf{y}_K(t_n)\}_{n=1}^N$ for the EM and SAGE algorithms can be unified, written as

$$\begin{aligned} \mathcal{L}(\{\mathbf{y}_1(t_n), \dots, \mathbf{y}_K(t_n)\}_{n=1}^N) \\ = KMN \ln \sigma^2 + \frac{1}{\rho\sigma^2} \sum_{n=1}^N \sum_{k=1}^K \|\mathbf{y}_k(t_n) - \mathbf{a}'(\vartheta_k) s_k(t_n)\|_2^2 \\ = KMN \ln \sigma^2 + \frac{1}{\rho\sigma^2} \sum_{n=1}^N \sum_{k=1}^K \|\mathbf{y}_k(t_n) - \mathbf{a}(\vartheta_k) s_k(t_n) - \mathbf{Q}_k(t_n) \mathbf{c}\|_2^2. \end{aligned} \quad (13)$$

where $\rho = 1/K$ for the EM algorithm and $\rho = 1$ for the SAGE algorithm. The second expression in (13) is mainly used for optimizing \mathbf{c} .

Both EM and SAGE algorithms update each unknown parameter by iterative method. Each iteration consists of an E-step and an M-step. Given the estimate of the $(q-1)$ th iteration $\Omega^{(q-1)}$, the q th iteration consists of the following steps.

E-Step. Calculate

$$\begin{aligned} \mathcal{F}(\Omega^{(q)}; \Omega^{(q-1)}) \\ = \mathbb{E} \left[\mathcal{L}(\{\mathbf{y}_1(t_n), \dots, \mathbf{y}_K(t_n)\}_{n=1}^N) \mid \{\mathbf{x}(t_n)\}_{n=1}^N, \Omega^{(q-1)} \right], \end{aligned} \quad (14)$$

where the superscript (q) stands for the iteration index and $\mathbb{E}[\bullet]$ denotes expectation operator. Equation (11) is equivalent to computing the following conditional expectations:

$$\begin{aligned} \mathbf{y}_k^{(q)}(t) &= \mathbb{E}[\mathbf{y}_k(t) \mid \mathbf{x}(t), \Omega^{(q-1)}] \\ &= \mathbf{a}'(\vartheta_k^{(q-1)}) s_k^{(q-1)}(t) \\ &\quad + \rho [\mathbf{x}(t) - \mathbf{A}'(\mathbf{c}^{(q-1)}, \boldsymbol{\vartheta}^{(q-1)}) \mathbf{s}^{(q-1)}(t)], \end{aligned} \quad (15)$$

$$\begin{aligned} \mathbf{R}_{\mathbf{y}_k}^{(q)} &= \mathbb{E} \left[\frac{1}{N} \sum_{n=1}^N \mathbf{y}_k(t_n) \mathbf{y}_k^H(t_n) \mid \{\mathbf{x}(t_n)\}_{n=1}^N, \Omega^{(q-1)} \right] \\ &= \frac{1}{N} \sum_{n=1}^N \mathbf{y}_k^{(q)}(t_n) (\mathbf{y}_k^{(q)}(t_n))^H. \end{aligned} \quad (16)$$

For emphasizing the dependence on array perturbation parameters, we use $\mathbf{A}'(\mathbf{c}^{(q-1)}, \boldsymbol{\vartheta}^{(q-1)})$ to denote the perturbed responding matrix in (15), which is different in above context.

M-Step. The unknown parameters Ω are updated by maximizing $\mathcal{F}(\Omega^{(q)}; \Omega^{(q-1)})$, which can be realized by setting its differentiations of those parameters to zero.

Consider

$$\vartheta_k^{(q)} = \arg \max_{\theta} \frac{(\mathbf{a}'(\mathbf{c}^{(q-1)}, \theta))^H \mathbf{R}_{\mathbf{y}_k}^{(q)} \mathbf{a}'(\mathbf{c}^{(q-1)}, \theta)}{\|\mathbf{a}'(\mathbf{c}^{(q-1)}, \theta)\|_2^2}, \quad (17)$$

$$k = 1, \dots, K,$$

$$s_k^{(q)}(t_n) = \frac{(\mathbf{a}'(\mathbf{c}^{(q-1)}, \vartheta_k^{(q)}))^H \mathbf{y}_k^{(q)}(t_n)}{\|\mathbf{a}'(\mathbf{c}^{(q-1)}, \vartheta_k^{(q)})\|_2^2}, \quad (18)$$

$$k = 1, \dots, K; \quad n = 1, \dots, N,$$

$$(\sigma^2)^{(q)} = \frac{1}{KMN} \mathbb{E} \left[\sum_{n=1}^N \sum_{k=1}^K \|\mathbf{y}_k(t_n) - \mathbf{a}'(\vartheta_k) s_k(t_n)\|_2^2 \right], \quad (19)$$

$$\begin{aligned} \mathbf{c}^{(q)} &= \left\{ \mathbb{E} \left[\sum_{n=1}^N \sum_{k=1}^K \mathbf{Q}_k^H(t_n) \mathbf{Q}_k(t_n) \right] \right\}^{-1} \\ &\quad \times \mathbb{E} \left[\sum_{n=1}^N \sum_{k=1}^K \mathbf{Q}_k^H(t_n) (\mathbf{y}_k(t_n) - \mathbf{a}(\vartheta_k) s_k(t_n)) \right]. \end{aligned} \quad (20)$$

As can be seen from (15) to (18), the update processes of ϑ_k and $\{s_k(t_n)\}_{n=1}^N$ are mainly dependent on the corresponding augmented data $\{\mathbf{y}_k(t_n)\}_{n=1}^N$, and it does not matter with $\{\mathbf{y}_1(t_n), \dots, \mathbf{y}_{k-1}(t_n), \mathbf{y}_{k+1}(t_n), \dots, \mathbf{y}_K(t_n)\}_{n=1}^N$. We know that the parameters \mathbf{c} and σ^2 exist in all signal components model, so the update processes are rested on $\{\mathbf{y}_1(t_n), \dots, \mathbf{y}_K(t_n)\}_{n=1}^N$. The iteration process can be divided into two parts: sequential update ϑ_k and $\{s_k(t_n)\}_{n=1}^N$ for different k values and unified update \mathbf{c} and σ^2 by using all of augmented data. The formulation of $\mathbf{Q}_k(t)$ is very complicated, the iteration strategy of those parameters given above is not usable directly. In appendix, we carry out some deeper analysis to simplify the implementation of the iteration.

4. Simulation Results

The simulations in this section illustrate the performance of our proposed algorithm. The proposed algorithm gives a unified framework for DOA estimation in the presence of mutual coupling and sensor location error. In the first experiment, the scenario when mutual coupling exists is considered. For comparison, we also apply S-S method [2] and Y-L method [3] to the same batch of data, as well as the curves of the Cramer-Rao lower bound (CRLB) [16]. In the second experiment, the scenario when sensor location error exists is considered. The maximum likelihood method [8] (denoted by ML method), IMTAM [8], and CRLB are also implemented for the performance comparison.

We consider a nominally uniform linear array of 8 sensors with interelement spacing equaling half a wavelength of the

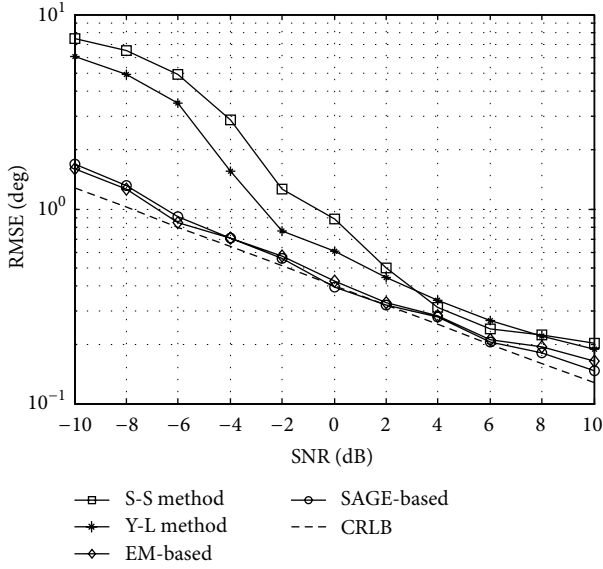


FIGURE 1: RMSE of DOA estimates of different methods against SNR.

incident signals. Suppose that two equal-power independent signals impinge onto the array from directions of -9° and 25° . The snapshot number is fixed at 200. The algorithm is terminated if the increase in the data likelihood function is smaller than 10^{-4} or the maximal number of iterations has arrived. The maximal number of iterations in the simulation is set to be 200. The average root-mean-square error (RMSE) of the DOA estimates is considered for statistical direction estimation precision evaluation, which is defined as

$$\text{RMSE}_\theta = \sqrt{\frac{\sum_{w=1}^W \|\hat{\theta}^{(w)} - \theta^{(w)}\|^2}{K \times W}}, \quad (21)$$

where W denotes the number of Monte Carlo experiments. We set $W = 500$ in the simulation. $\hat{\theta}^{(w)}$ and $\theta^{(w)}$ are the estimated and true directions in the w th simulation. Similarly, the RMSE of the mutual coupling coefficients is used for the array calibration precision evaluation, which is defined as

$$\text{RMSE}_c = \xi \times \sqrt{\frac{\sum_{w=1}^W \|\hat{c}^{(w)} - c\|_2^2}{W}}, \quad (22)$$

where c keeps constant in each scenario, $\hat{c}^{(w)}$ is the estimated coupling coefficient vector in the w th simulation, ξ is a tuning factor introduced to enhance the sense of the RMSE, $\xi = \|c\|_2$ for mutual coupling, and $\xi = \lambda^{-1}$ for sensor location error.

4.1. Statistical Performance in the Presence of Mutual Coupling.

For each Monte Carlo experiment, we suppose that the coupling coefficient vector includes two coupling coefficients. Each coefficient is a random complex data. The range of real and imaginary parts of coefficients is 0.1~0.6. Figure 1 shows the RMSE of DOA estimates of different methods against

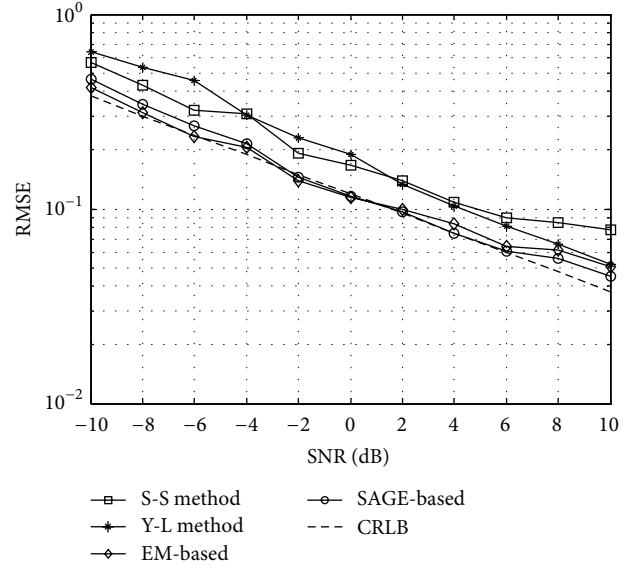


FIGURE 2: RMSE of coupling coefficients of different methods against SNR.

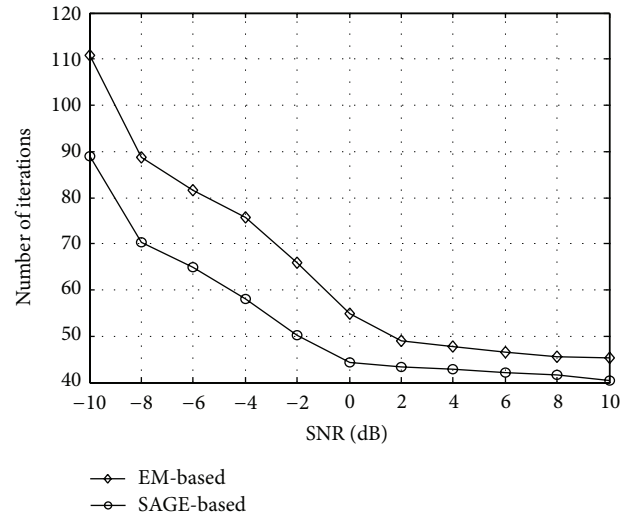


FIGURE 3: The average number of iterations needed for convergence against SNR.

input SNR. The results illustrate that both SAGE-based and EM-based algorithms can lead to significant improvement in estimation accuracy, especially for low levels of SNR, and they improve with a similar speed as that of the CRLB when the SNR increases. Figure 2 shows the RMSE of mutual coupling coefficients versus input SNR. The results illustrate that both S-S method and Y-L method cannot achieve high estimation precision, while the SAGE-based and EM-based algorithms can achieve the better performance. They are always close to the CRLB.

Figure 3 shows the average number of iterations needed for convergence versus input SNR. Since each iteration of the SAGE-based and EM-based algorithms requires similar computations, their total computational costs are determined

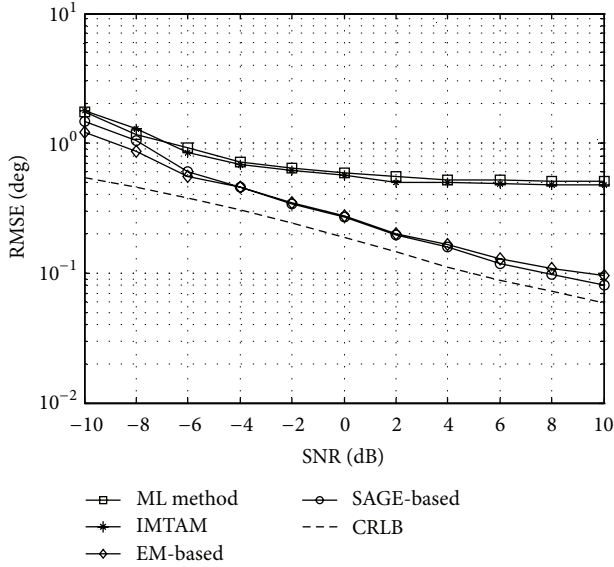


FIGURE 4: RMSE of DOA estimates of different methods against SNR.

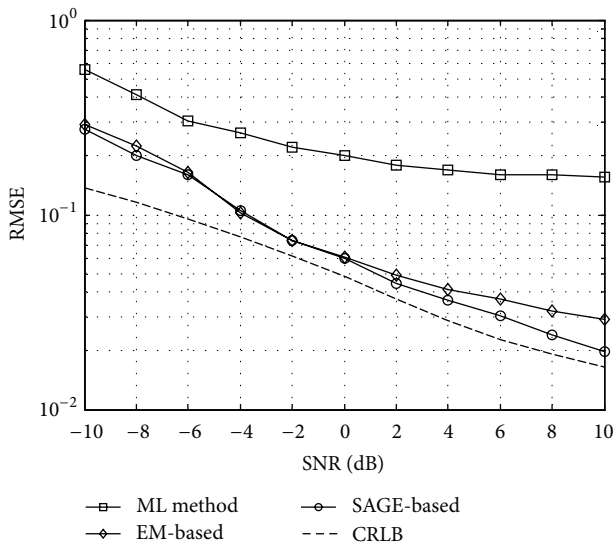


FIGURE 5: RMSE of sensor location error of different methods against SNR.

by the number of iterations. It can be observed that the number of iterations needed by the SAGE-based algorithm is always smaller than that by the EM-based algorithm over the whole range of SNR.

4.2. Statistical Performance in the Presence of Sensor Location Error. In the second experiment, we suppose that the sensor locations are not accurately calibrated. They depart from the nominal positions by 0, 0.08, 0.12, 0.16, 0.04, -0.12, -0.08, and -0.16 times the half-wavelength; that is, $\mathbf{c} = [0.08, 0.12, 0.16, 0.04, -0.12, -0.08, -0.16]^T$. The nominal sensor positions are used to initialize the algorithm; that is, $\mathbf{c}^{[0]} = [0, 0, 0, 0, 0, 0, 0]^T$. The initial DOA estimate is given by $\mathfrak{D}^{[0]} = [-5, 20]$.

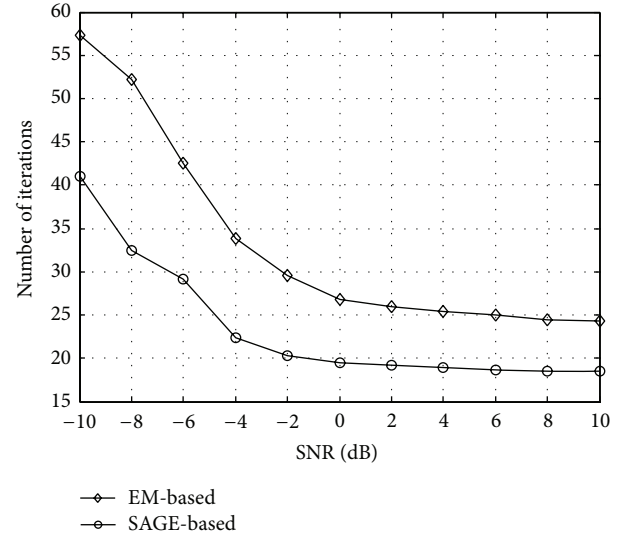


FIGURE 6: The average number of iterations needed for convergence against SNR.

Figure 4 shows RMSE of DOA estimates of different methods against SNR. As can be shown in Figure 4, the SAGE-based and EM-based algorithms perform similarly over the entire SNR range. They are always close to CRLB. Both of them have significant improvement in estimation accuracy than ML method and IMTAM method. Figure 5 shows RMSE of sensor location error of different methods against SNR. We can easily observe that ML method fails to estimate sensor location error effectively (no array calibration result is available from IMTAM), while the SAGE-based and EM-based algorithms provide reasonable results. Figure 6 shows the average number of iterations needed for convergence versus each SNR. As can be shown in Figure 6, as the SNR increases, the numbers of iterations required by both algorithms are reduced quickly, and the SAGE-based algorithm gets a faster convergence rate over the entire SNR range.

5. Conclusion

In this paper, the DOA and array perturbation parameters estimation problem in the case of deterministic signals with unknown waveforms is studied. An SAGE-based method for DOA estimation and array calibration in the presence of mutual coupling and sensor location perturbation is proposed. First, a comprehensive array output model that is applicable to two typical array perturbations is introduced. Based on this model, we construct the augmented data needed by the SAGE algorithm and establish the augmented data unified likelihood for N snapshots. Then, the E-step and M-step of the SAGE algorithm for DOA and perturbation parameters estimation are derived. The implementation of the proposed method follows the standard SAGE iterations and thus has guaranteed convergence and high estimation precision. For comparison, the EM-based algorithm is also studied, which applies the EM algorithm to jointly estimate DOA and perturbation parameters. The simulation results show that the EM-based algorithm can obtain higher

estimation precisions than the existing methods, and the SAGE-based algorithm converges faster than the EM-based algorithm while retaining the advantage of high estimation precisions. Therefore, the SAGE-based algorithm is an attractive method for DOA estimation and array calibration.

Appendix

Implementation of the Iteration

According to (14), (15), and (17), one can obtain that

$$\begin{aligned} R_{s_k}^{(q)} &= \mathbb{E} \left[\frac{1}{N} \sum_{n=1}^N s_k(t_n) s_k^H(t_n) \mid \{\mathbf{x}(t_n)\}_{n=1}^N, \Omega^{(q-1)} \right] \\ &= \frac{(\mathbf{a}'(\mathbf{c}^{(q-1)}, \vartheta_k^{(q)}))^H \mathbf{R}_{y_k}^{(q)} \mathbf{a}'(\mathbf{c}^{(q-1)}, \vartheta_k^{(q)})}{\|\mathbf{a}'(\mathbf{c}^{(q-1)}, \vartheta_k^{(q)})\|_2^4}, \end{aligned} \quad (\text{A.1})$$

$k = 1, \dots, K,$

$$\begin{aligned} \mathbf{R}_{y_k s_k}^{(q)} &= \mathbb{E} \left[\frac{1}{N} \sum_{n=1}^N \mathbf{y}_k(t_n) s_k^H(t_n) \mid \{\mathbf{x}(t_n)\}_{n=1}^N, \Omega^{(q-1)} \right] \\ &= \frac{\mathbf{R}_{y_k}^{(q)} \mathbf{a}'(\mathbf{c}^{(q-1)}, \vartheta_k^{(q)})}{\|\mathbf{a}'(\mathbf{c}^{(q-1)}, \vartheta_k^{(q)})\|_2^2}, \quad k = 1, \dots, K. \end{aligned} \quad (\text{A.2})$$

Moreover, according to (15), (16), (18), and (A.1), we can get that

$$\begin{aligned} &\frac{1}{N} \mathbb{E} \left[\sum_{n=1}^N \|\mathbf{y}_k(t_n) - \mathbf{a}'(\vartheta_k) s_k(t_n)\|_2^2 \right] \\ &= \text{tr} \left[\mathbf{R}_{y_k}^{(q)} - \mathbf{a}'(\mathbf{c}^{(q-1)}, \vartheta_k^{(q)}) (\mathbf{R}_{y_k s_k}^{(q)})^H \right. \\ &\quad \left. - \mathbf{R}_{y_k s_k}^{(q)} (\mathbf{a}'(\mathbf{c}^{(q-1)}, \vartheta_k^{(q)}))^H \right. \\ &\quad \left. + R_{s_k}^{(q)} \mathbf{a}'(\mathbf{c}^{(q-1)}, \vartheta_k^{(q)}) (\mathbf{a}'(\mathbf{c}^{(q-1)}, \vartheta_k^{(q)}))^H \right] \\ &= \text{tr} \left\{ \left[\mathbf{I}_M - \frac{\mathbf{a}'(\mathbf{c}^{(q-1)}, \vartheta_k^{(q)}) (\mathbf{a}'(\mathbf{c}^{(q-1)}, \vartheta_k^{(q)}))^H}{\|\mathbf{a}'(\mathbf{c}^{(q-1)}, \vartheta_k^{(q)})\|_2^2} \right] \mathbf{R}_{y_k}^{(q)} \right\}, \end{aligned}$$

$k = 1, \dots, K.$

(A.3)

Denote $\mathbf{h}_k = (1/N) \mathbb{E}[\sum_{n=1}^N \mathbf{Q}_k^H(t_n) (\mathbf{y}_k(t_n) - \mathbf{a}(\vartheta_k) s_k(t_n))]$, $\Sigma_k = (1/N) \mathbb{E}[\sum_{n=1}^N \mathbf{Q}_k^H(t_n) \mathbf{Q}_k(t_n)]$; then the elements of the vector and the matrix can be computed according to $[\mathbf{Q}_k(t)]_{:,p} = \mathbf{G}_{k,p} \phi(\vartheta_k) s_k(t)$ as follows:

$$\begin{aligned} (\mathbf{h}_k)_p &= \phi^H(\vartheta_k) \mathbf{G}_{k,p}^H \\ &\quad \times \frac{1}{N} \mathbb{E} \left[\sum_{n=1}^N (\mathbf{y}_k(t_n) s_k^H(t) - \mathbf{a}(\vartheta_k) s_k(t_n) s_k^H(t)) \right] \\ &= \phi^H(\vartheta_k) \mathbf{G}_{k,p}^H (\mathbf{R}_{y_k s_k}^{(q)} - \mathbf{a}(\vartheta_k) R_{s_k}^{(q)}) \end{aligned}$$

$$\begin{aligned} &= \phi^H(\vartheta_k) \mathbf{G}_{k,p}^H \left[\mathbf{I}_M - \frac{\mathbf{a}(\vartheta_k^{(q)}) (\mathbf{a}'(\mathbf{c}^{(q-1)}, \vartheta_k^{(q)}))^H}{\|\mathbf{a}'(\mathbf{c}^{(q-1)}, \vartheta_k^{(q)})\|_2^2} \right] \\ &\quad \times \frac{\mathbf{R}_{y_k}^{(q)} \mathbf{a}'(\mathbf{c}^{(q-1)}, \vartheta_k^{(q)})}{\|\mathbf{a}'(\mathbf{c}^{(q-1)}, \vartheta_k^{(q)})\|_2^2}, \end{aligned} \quad (\text{A.4})$$

$$\begin{aligned} (\Sigma_k)_{p_1, p_2} &= \frac{1}{N} \mathbb{E} \left[\sum_{n=1}^N s_k^*(t) \phi^H(\vartheta_k) \mathbf{G}_{k,p_1}^H \mathbf{G}_{k,p_2} \phi(\vartheta_k) s_k(t) \right] \\ &= \frac{1}{N} \mathbb{E} \left[\sum_{n=1}^N s_k(t) s_k^*(t) \right] \phi^H(\vartheta_k) \mathbf{G}_{k,p_1}^H \mathbf{G}_{k,p_2} \phi(\vartheta_k) \\ &= \frac{(\mathbf{a}'(\mathbf{c}^{(q-1)}, \vartheta_k^{(q)}))^H \mathbf{R}_{y_k}^{(q)} \mathbf{a}'(\mathbf{c}^{(q-1)}, \vartheta_k^{(q)})}{\|\mathbf{a}'(\mathbf{c}^{(q-1)}, \vartheta_k^{(q)})\|_2^4} \\ &\quad \times \phi^H(\vartheta_k) \mathbf{G}_{k,p_1}^H \mathbf{G}_{k,p_2} \phi(\vartheta_k), \end{aligned} \quad (\text{A.5})$$

where $(\mathbf{h}_k)_p$ represents the p th element of \mathbf{h}_k , and $(\Sigma_k)_{p_1, p_2}$ represents the (p_1, p_2) th element of Σ_k .

Finally, (15), (16), and (A.3)–(A.5) can be substituted into (17)–(20) to yield more convenient steps for updating the unknown parameters and implementing the iterations.

Conflict of Interests

The authors declare that there is no conflict of interests regarding the publication of this paper.

References

- [1] Z. Liu, Z. Huang, F. Wang, and Y. Zhou, "DOA estimation with uniform linear arrays in the presence of mutual coupling via blind calibration," *Signal Processing*, vol. 89, no. 7, pp. 1446–1456, 2009.
- [2] F. Sellone and A. Serra, "A novel online mutual coupling compensation algorithm for uniform and linear arrays," *IEEE Transactions on Signal Processing*, vol. 55, no. 2, pp. 560–573, 2007.
- [3] Z. Ye and C. Liu, "On the resiliency of MUSIC direction finding against antenna sensor coupling," *IEEE Transactions on Antennas and Propagation*, vol. 56, no. 2, pp. 371–380, 2008.
- [4] A. J. Weiss and B. Friedlander, "Mutual coupling effects on phase-only direction finding," *IEEE Transactions on Antennas and Propagation*, vol. 40, no. 5, pp. 535–541, 1992.
- [5] A. J. Weiss and B. Friedlander, "Eigenstructure methods for direction finding with sensor gain and phase uncertainties," *Circuits, Systems, and Signal Processing*, vol. 9, no. 3, pp. 271–300, 1990.
- [6] Y. Li and M. H. Er, "Theoretical analyses of gain and phase error calibration with optimal implementation for linear equispaced array," *IEEE Transactions on Signal Processing*, vol. 54, no. 2, pp. 712–723, 2006.
- [7] A. Liu, G. Liao, C. Zeng, Z. Yang, and Q. Xu, "An eigenstructure method for estimating doa and sensor gain-phase errors," *IEEE Transactions on Signal Processing*, vol. 59, no. 12, pp. 5944–5956, 2011.

- [8] Y.-M. Chen, J.-H. Lee, C.-C. Yeh, and J. Mar, "Bearing estimation without calibration for randomly perturbed arrays," *IEEE Transactions on Signal Processing*, vol. 39, no. 1, pp. 194–197, 1991.
- [9] A. J. Weiss and B. Friedlander, "Array shape calibration using sources in unknown locations—a maximum likelihood approach," *IEEE Transactions on Acoustics, Speech, and Signal Processing*, vol. 37, no. 12, pp. 1958–1966, 1989.
- [10] C. M. S. See, "Method for array calibration in high-resolution sensor array processing," *IEE Proceedings: Radar, Sonar and Navigation*, vol. 142, no. 3, pp. 90–96, 1995.
- [11] B. C. Ng and C. M. Samson, "Sensor-array calibration using a maximum-likelihood approach," *IEEE Transactions on Antennas and Propagation*, vol. 44, no. 6, pp. 827–835, 1996.
- [12] M. Feder and E. Weinstein, "Parameter estimation of superimposed signals using the EM algorithm," *IEEE Transactions on Acoustics, Speech, and Signal Processing*, vol. 36, no. 4, pp. 477–489, 1988.
- [13] M. I. Miller and D. R. Fuhrmann, "Maximum-likelihood narrow-band direction finding and the EM algorithm," *IEEE Transactions on Acoustics, Speech, and Signal Processing*, vol. 38, no. 9, pp. 1560–1577, 1990.
- [14] P. J. Chung and J. F. Böhme, "Comparative convergence analysis of EM and SAGE algorithms in DOA estimation," *IEEE Transactions on Signal Processing*, vol. 49, no. 12, pp. 2940–2949, 2001.
- [15] Z.-M. Liu and Y.-Y. Zhou, "A unified framework and sparse Bayesian perspective for direction-of-arrival estimation in the presence of array imperfections," *IEEE Transactions on Signal Processing*, vol. 61, no. 15, pp. 3786–3798, 2013.
- [16] Z. M. Liu, "Conditional cramer-rao lower bounds for DOA estimation and array calibration," *IEEE Signal Processing Letters*, vol. 21, pp. 361–364, 2014.